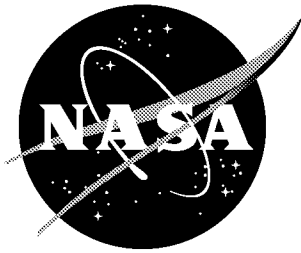


NASA/CP-2002-211741



Multiscale Modeling, Simulation and Visualization and Their Potential for Future Aerospace Systems

*Compiled by
Ahmed K. Noor
Old Dominion University
Center for Advanced Engineering Environments
Langley Research Center, Hampton, Virginia*

July 2002

The NASA STI Program Office ... in Profile

Since its founding, NASA has been dedicated to the advancement of aeronautics and space science. The NASA Scientific and Technical Information (STI) Program Office plays a key part in helping NASA maintain this important role.

The NASA STI Program Office is operated by Langley Research Center, the lead center for NASA's scientific and technical information. The NASA STI Program Office provides access to the NASA STI Database, the largest collection of aeronautical and space science STI in the world. The Program Office is also NASA's institutional mechanism for disseminating the results of its research and development activities. These results are published by NASA in the NASA STI Report Series, which includes the following report types:

- **TECHNICAL PUBLICATION.** Reports of completed research or a major significant phase of research that present the results of NASA programs and include extensive data or theoretical analysis. Includes compilations of significant scientific and technical data and information deemed to be of continuing reference value. NASA counterpart of peer-reviewed formal professional papers, but having less stringent limitations on manuscript length and extent of graphic presentations.
- **TECHNICAL MEMORANDUM.** Scientific and technical findings that are preliminary or of specialized interest, e.g., quick release reports, working papers, and bibliographies that contain minimal annotation. Does not contain extensive analysis.
- **CONTRACTOR REPORT.** Scientific and technical findings by NASA-sponsored contractors and grantees.

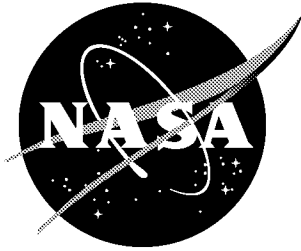
- **CONFERENCE PUBLICATION.** Collected papers from scientific and technical conferences, symposia, seminars, or other meetings sponsored or co-sponsored by NASA.
- **SPECIAL PUBLICATION.** Scientific, technical, or historical information from NASA programs, projects, and missions, often concerned with subjects having substantial public interest.
- **TECHNICAL TRANSLATION.** English-language translations of foreign scientific and technical material pertinent to NASA's mission.

Specialized services that complement the STI Program Office's diverse offerings include creating custom thesauri, building customized databases, organizing and publishing research results ... even providing videos.

For more information about the NASA STI Program Office, see the following:

- Access the NASA STI Program Home Page at <http://www.sti.nasa.gov>
- E-mail your question via the Internet to help@sti.nasa.gov
- Fax your question to the NASA STI Help Desk at (301) 621-0134
- Phone the NASA STI Help Desk at (301) 621-0390
- Write to:
NASA STI Help Desk
NASA Center for AeroSpace Information
7121 Standard Drive
Hanover, MD 21076-1320

NASA/CP-2002-211741



Multiscale Modeling, Simulation and Visualization and Their Potential for Future Aerospace Systems

*Compiled by
Ahmed K. Noor
Old Dominion University
Center for Advanced Engineering Environments
Langley Research Center, Hampton Virginia*

Proceedings of a workshop sponsored by the National Aeronautics and
Space Administration and Old Dominion University, Center for Advanced
Engineering Environments, Hampton, Virginia, and held at
NASA Langley Research Center, Hampton, Virginia
March 5-6, 2002

National Aeronautics and
Space Administration

Langley Research Center
Hampton, Virginia 23681-2199

July 2002

Available from:

NASA Center for Aerospace Information (CASI)
7121 Standard Drive
Hanover, MD 21076-1320
(301) 621-0390

National Technical Information Service (NTIS)
5285 Port Royal Road
Springfield, VA 22161-2171
(703) 605-6000

Preface

This document contains the proceedings of the Training Workshop on Multiscale Modeling, Simulation and Visualization and Their Potential for Future Aerospace Systems held at NASA Langley Research Center, Hampton, Virginia, March 5 – 6, 2002. The workshop was jointly sponsored by Old Dominion University and NASA. Workshop attendees came from NASA, other government agencies, industry, and universities. The objectives of the workshop were to review the diverse activities in hierarchical approach to material modeling from continuum to atomistics; applications of multiscale modeling to advanced and improved material synthesis; defects, dislocations, and material deformation; fracture and friction; thin-film growth; characterization at nano and micro scales; and, verification and validation of numerical simulations, and to identify their potential for future aerospace systems.

Ahmed K. Noor
Old Dominion University
Center for Advanced Engineering Environments
Hampton, Virginia

Contents

Preface	iii
Attendees	vii
Perspectives on Multiscale Modeling, Simulation and Visualization	1
Ahmed K. Noor Old Dominion University, NASA Langley Research Center, Hampton, VA	
Concurrent Coupling of Length Scales	41
Noam Bernstein Naval Research Laboratory, Washington, D.C	
The Future of Computational Materials Science: The Role of Atomistics	65
Michael I. Baskes Los Alamos National Laboratory, Los Alamos, NM	
Materials Modeling and Simulation as a Technology for Advanced Materials Development	93
Gregg Caldwell 3M Center, Advanced Materials Technology Center, St. Paul, MN	
Computational Modeling to Support Materials Design	125
David L. McDowell Georgia Institute of Technology, Atlanta, GA	
Quantum Simulations of Solids, Liquids and Nanostructures	153
Giulia Galli Lawrence Livermore National Laboratory, Livermore, CA	
Exploration in Accurate Atomistic, Coarse Grain and Mesoscopic Simulations of Structured Solutions	173
John C. Shelley Schrodinger, Inc., Portland, OR	
A Multiscale Modeling Approach to Crack Initiation in Aluminum Polycrystals	201
Anthony R. Ingraffea Cornell University, Ithaca, NY	
Scale-Bridging in Dislocation-Based Multiscale Modeling	223
Kyung-Suk Kim Brown University, Providence, RI	

Yield Criteria for BCC Metals That Include Effects of Non-Glide Stresses Based on Understanding the Atomic Level Features of Dislocation Motion	241
Vaclav Vitek University of Pennsylvania, Philadelphia, PA	
Multiscale Modeling of Crystalline Metals with Experimental Verification	269
Sia Nemat-Nasser University of California, San Diego, La Jolla, CA	
Multiscale Simulation of Grain Growth in Nanocrystalline Thin Films	299
Dorel Moldovan Argonne National Laboratory, Argonne, IL	
Anisotropic Materials Properties: Functional Forms for Multiscale Modeling	331
Nicholas P. Bailey Cornell University, Ithaca, NY	
Multiscale Modeling for Linking Growth, Microstructure, and Properties of Inorganic Microporous Films	343
Dion G. Vlachos University of Delaware, Newark, DE	
Multiscale Modeling of Polycrystalline Materials	371
Olga Shenderova North Carolina State University, Raleigh, NC	
On the Role of Plasticity Length Scale Parameters in Multiscale Modeling	397
Wole O. Soboyejo Princeton University, Princeton, NJ	

**ODU-NASA Training Workshop on Multiscale Modeling, Simulation and
Visualization**

and Their Potential for Future Aerospace Systems

Pearl Young Theatre, NASA Langley Research Center

Hampton, VA 23681

March 5 - 6, 2002

Attendees List

1. Nicholas P. Bailey
Cornell University
117 Clark Hall
Ithaca, NY 14853
(607) 255-5522
Email: nbailey@ccmr.cornell.edu
2. Dr. Michael I. Baskes
Los Alamos National Laboratory
MS G755
Los Alamos, NM 87545
(505) 667-1238; Fax (505) 667-8021
Email: baskes@lanl.gov
3. Dr. Noam Bernstein
Naval Research Laboratory
4555 Overlook Avenue, S.W.
Washington D.C. 20375
(202) 404-8628
Email: bernstei@dave.nrl.navy.mil
4. Gregg Caldwell
3M Center
Advanced Materials Technology Center
St. Paul, MN 55144-1000
(651) 736-1360; Fax (651) 737-2590
Email: gcaldwell@mmm.com
5. Dr. Kyeongjae (K.J.) Cho
Stanford University
Mechanical Engineering
Materials Science and Engineering
MC 4040
Stanford, CA 94305-4040
(650) 623-4354; Fax (650) 623-1778
Email: kjcho@stanford.edu
6. Oscar Dillon
National Science Foundation
4201 Wilson Blvd., Rm. 545
Arlington, VA 22230
Email: odillon@nsf.gov
7. Dr. Guilla A. Galli
Lawrence Livermore National Laboratory
7000 East Avenue
Mail Stop L-415
Livermore, CA 94550
(925) 423-4223; Fax (925) 422-6594
Email: galli@llnl.gov
8. Dr. Anthony R. Ingraffea
Civil and Environmental Engineering
643 Rhodes Hall
Cornell University
Ithaca, NY 14853
(607) 254-8844; Fax (607) 254-8815
Email: aril@cornell.edu
9. Dr. Kyung-Suk Kim
Brown University
Providence, RI 02912
(401) 863-1456; Fax (401) 863-1157
Email: kim@engin.brown.edu
10. Dr. David L. McDowell
Department of Mechanical Engineering
Georgia Institute of Technology
801 Ferst Dr., N.W.
Atlanta, GA 30332-0405
(404) 894-8414; Fax (404) 894-9140
Email: david.mcdowell@me.gatech.edu

11. Dr. Dorel Moldovan
Materials Science Division, Bldg. 212
Argonne National Laboratory
9700 S. Cass Ave.
Argonne, IL 60439
(630) 252-1366; Fax (630) 252-4987
Email: dorelm@anl.gov
12. Aiichiro Nakano
Concurrent Computing Laboratory for
Materials Simulation
Department of Computer Science
Louisiana State University, Coates Hall
Baton Rouge, LA 70803-4020
(225) 578-1342; Fax: (225) 578
Email: nakano@bit.csc.lsu.edu
13. Sia Nemat-Nasser
University of California, San Diego
Center of Excellence of Advanced
Materials
9500 Gilman Drive
La Jolla, CA 92093-0416
(619) 534-4914; Fax (619) 534-2727
Email: sia@mae.ucsd.edu
14. Dr. Ahmed K. Noor
Director, Center for Advanced
Engineering Environments
Old Dominion University
Mail Stop 201
NASA Langley Research Center
Hampton, VA 23681
(757) 864-1978; Fax (757) 864-8089
15. Dr. John C. Shelley
Schrodinger, Inc.
1500 SW First Avenue
Suite 1180
Portland, OR 97201
(503) 229-1150; Fax (503) 229-4532
Email: jshelley@schrodinger.com
16. Dr. Olga Shenderova
North Carolina State University
Materials Science and Engineering
Raleigh, NC 27695
(919) 513-4390; Fax (919) 515-7724
Email: oashend@eos.ncsu.edu
17. Wole Soboyejo
Princeton University
Princeton Materials Institute and
Department of Mechanical and
Aerospace Engineering
Princeton, NJ 08544
Email: soboyejo@princeton.edu
18. Deepak Srivastava
NASA Ames Research Center
Senior Scientist and Task Leader
Nanotechnology at CSC/NAS
MS T27A-1
Moffett Field, CA 94035-1000
(650) 704-3486
Email: deepak@nas.nasa.gov
19. Dr. Vaclav Vitek
Dept. Materials Science and Engineering
University of Pennsylvania
3231 Walnut Street
Philadelphia, PA 19104
(215) 898-7883; Fax (215) 573-2128
Email: vitek@lrsm.upenn.edu
20. Dionisios G. Vlachos
University of Delaware
Chemical Engineering
325 Colburn Lab
Newark, DE 19716
(302) 831-2830
Email: vlachos@che.udel.edu

Perspectives on Multiscale Modeling, Simulation and Visualization

Ahmed K. Noor
Center for Advanced Engineering Environments
Old Dominion University
NASA Langley Research Center
Hampton, VA

INTRODUCTION

In recent years intense effort has been devoted to the modeling and simulations of physical phenomena occurring on a vast range of spatial and temporal length scales. Multiscale modeling and simulations are being used in fields as diverse as materials science, nano/microelectronics, environmental remediation, safe stewardship of nuclear weapons and biotechnology. This endeavor has prompted the development of multiscale modeling and simulation strategies, interrogative visualization facilities, as well as versatile and powerful software systems.

An attempt is made in this overview to give broad definitions to the terms and to set the stage for the succeeding presentations. The presentation is divided into four parts (Figure 1). In the first part, examples of future aerospace systems are given, along with some of their major characteristics and the enabling technologies. The second part provides a brief overview of some aspects of multiscale modeling and simulation as one of the enabling technologies for future aerospace systems. The third part describes the future research and learning environments required for the realization of the full potential of multiscale modeling and simulation. The fourth part lists the objectives of the workshop and some of the sources of information on multiscale modeling and simulation

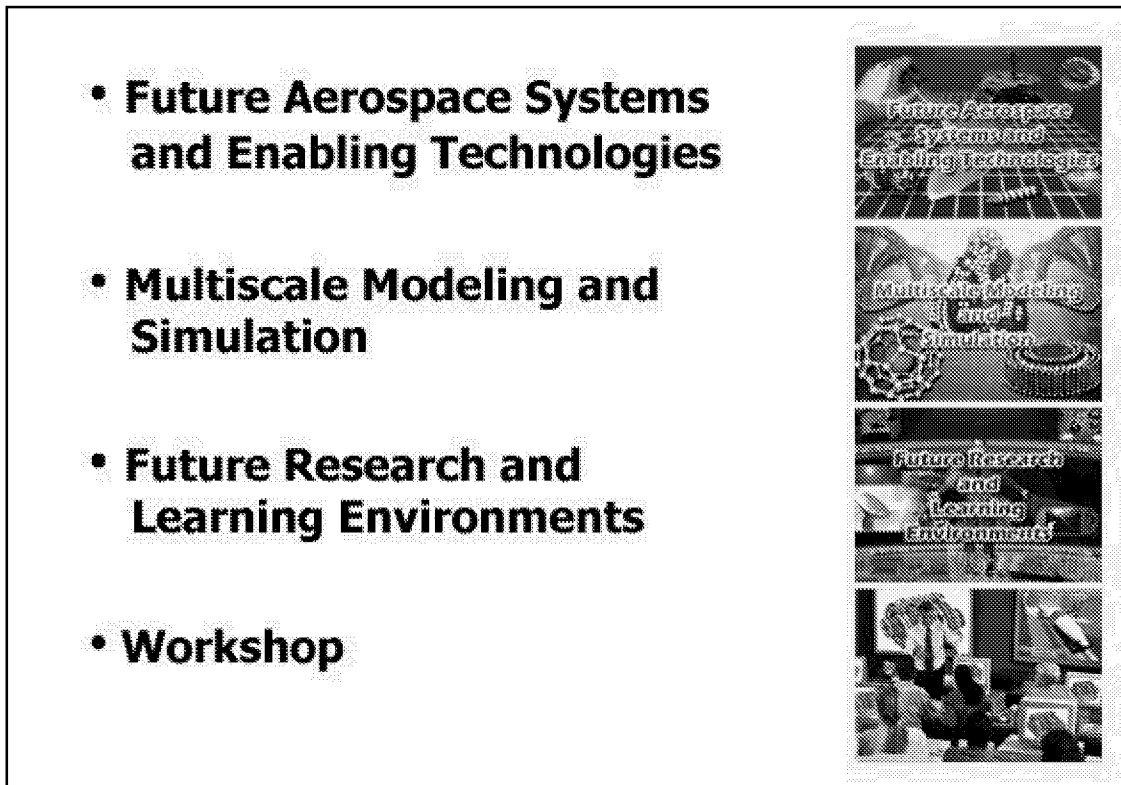


Figure 1

EXAMPLES OF FUTURE AEROSPACE SYSTEMS AND SOME OF THEIR CHARACTERISTICS

The realization of NASA's ambitious goals in aeronautics and space with the current national budget constraints will require new kinds of aerospace systems and missions that use novel technologies and manage risk in new ways. Future aerospace systems must be autonomous, evolvable, resilient, and highly distributed. Two examples are given in Figure 2. The first is a biologically inspired aircraft with self-healing wings that flex and react like living organisms. It is built of a multifunctional material with fully integrated sensing and actuation, and unprecedented levels of aerodynamic efficiencies and aircraft control. The second is an integrated human-robotic outpost, with biologically inspired robots. The robots could enhance the astronaut's capabilities to do large-scale mapping, detailed exploration of regions of interest, and automated sampling of rocks and soil. They could enhance the safety of the astronauts by alerting them to mistakes before they are made, and letting them know when they are showing signs of fatigue, even if they are not aware of it.

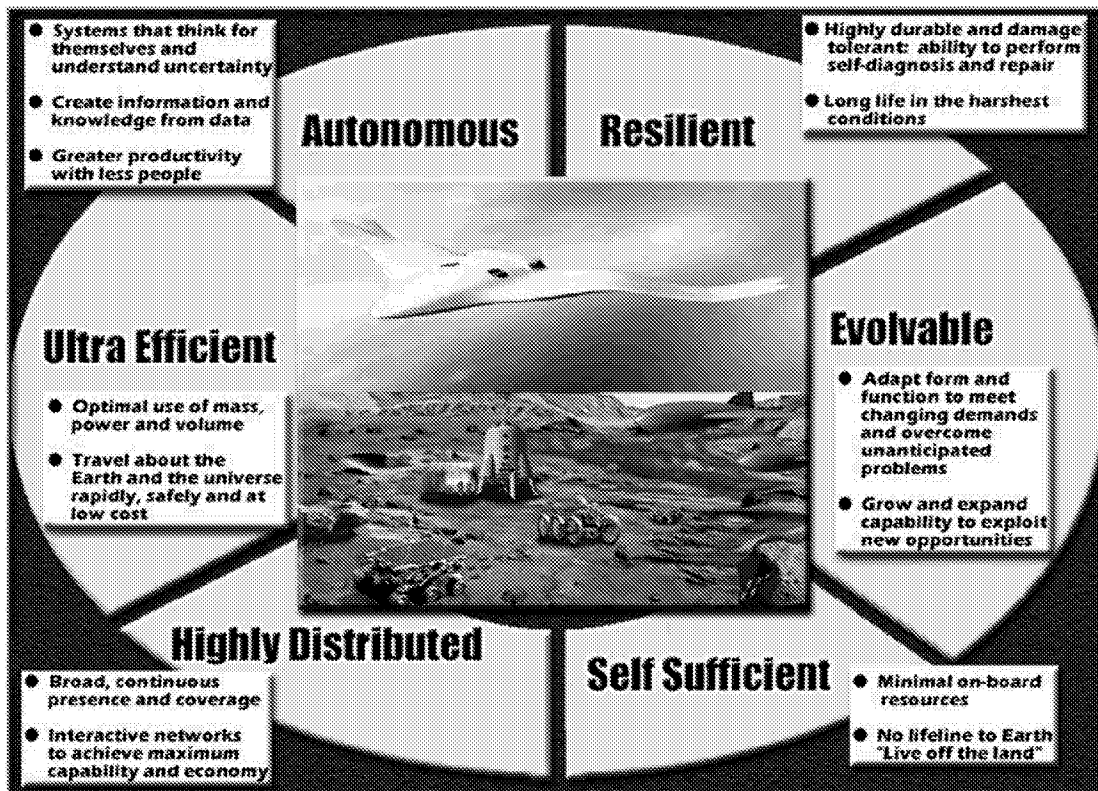


Figure 2

ENABLING TECHNOLOGIES FOR FUTURE AEROSPACE SYSTEMS

The characteristics of future aerospace systems identified in Figure 3 are highly coupled and require the synergistic coupling of the revolutionary and other leading-edge technologies listed in Figure 3. The three revolutionary technologies are nanotechnology, biotechnology and information/knowledge technology. The other leading-edge technologies are high-productivity computing; high-capacity communication; multiscale modeling, simulation and visualization; intelligent software agents; human performance, and human-computer symbiosis.

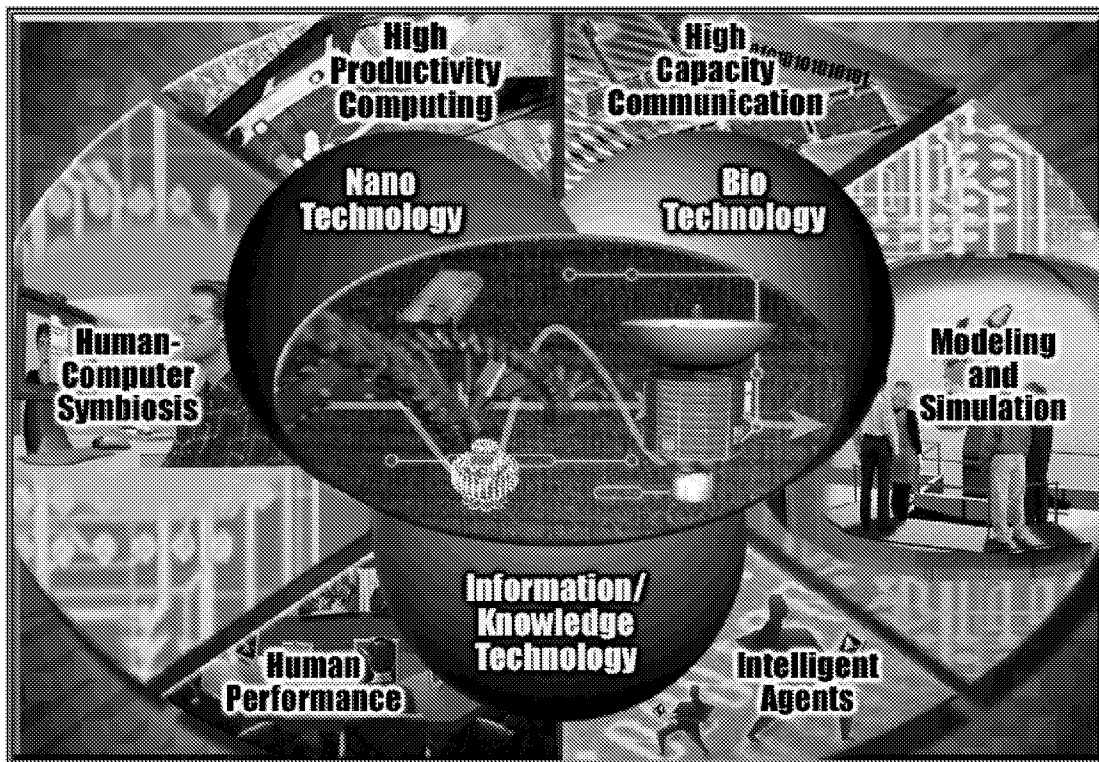


Figure 3

DEFINITION AND GOAL OF MULTISCALE MODELING

The term multiscale modeling has been used in reference to various activities for exploiting insights arising either from distinct methodologies, or from attempts to incorporate multiple mechanisms, occurring at disparate spatial and/or temporal scales, into the same modeling paradigm. The overall goal of multiscale modeling is to predict the response of complex systems across all relevant spatial and temporal scales (Figure 4).

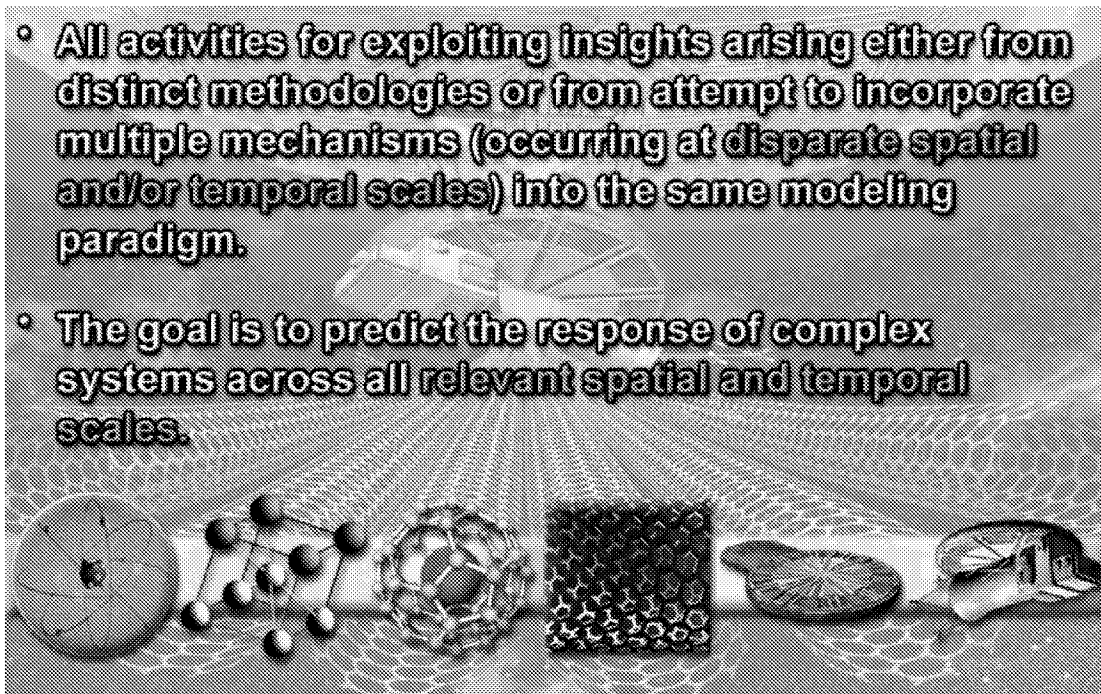


Figure 4

SOME OF THE APPLICATIONS OF MULTISCALE MODELING AND SIMULATION

Applications of multiscale modeling and simulation methodologies include (Figure 5):

1. Material synthesis and development
2. Material characterization and degradation (e.g., damage, failure and plasticity)
3. Phase transformations in materials (e.g., recrystallization)
4. Turbulence modeling
5. Atmospheric modeling
6. Modeling of biological systems
7. Systems on a chip
8. Signal processing and analysis

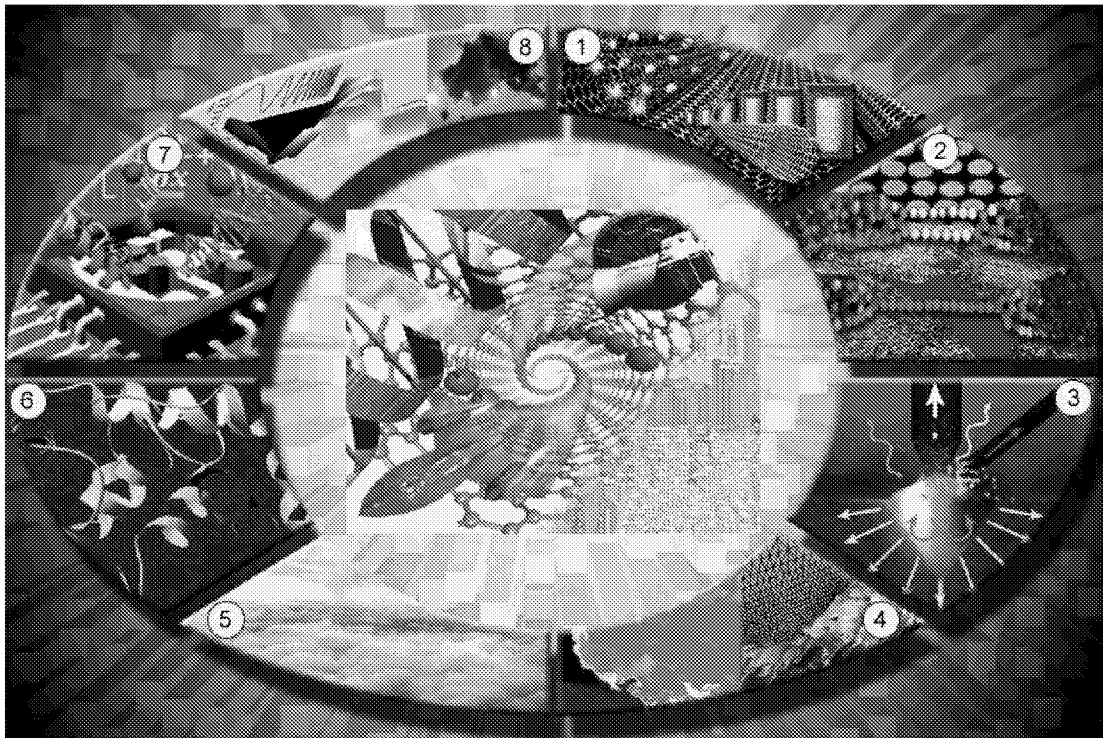


Figure 5

APPROACHES FOR MULTISCALE MODELING

Three categories of approaches can be identified for multiscale modeling, namely (Figure 6).

- Parameters passing, hierarchical modeling approaches in which a hierarchy of approaches and mathematical/computational models with different physical levels of description is pieced together. The output of the smaller-scale models is used as input for the larger-scale models.
- Handshaking approaches in which several computational approaches (and mathematical models) are used concurrently and use some sort of handshaking procedure to communicate
- Approaches that host more than one physical level of description in the same mathematical model. Example is provided by the Lattice-Boltzman equation which incorporates atomistic, kinetic, and continuum fluid description.

Examples of the three categories are given subsequently.

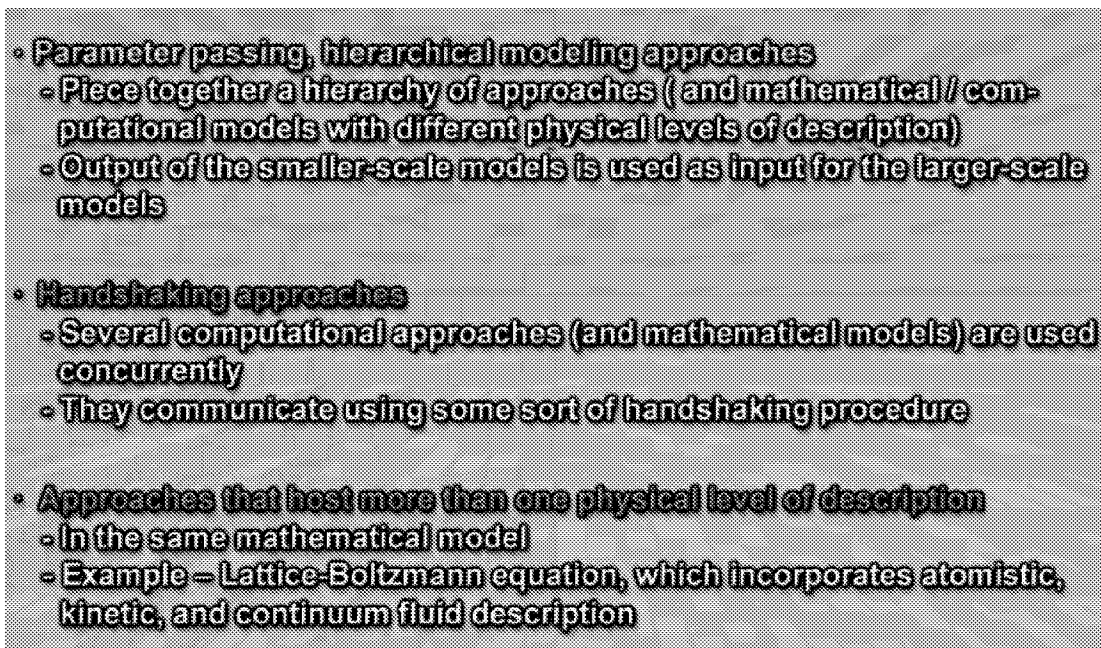


Figure 6

EXAMPLES OF HIERARCHICAL MATERIAL MODELING

Hierarchical material modeling has been used to predict and explain the mechanical properties of metals at dimensions ranging from a fraction of a nanometer to meters. The focus is on four major length scales – the atomic (nanoscopic) scale (nanometers), the microscale (micrometers), and mesoscale (millimeters), and the macroscale (centimeters and above). Fundamental physical and mathematical principles are rigorously applied to the modeling at each scale, and then data are then passed to the next scale up (Figure 7).

For nanocomposite structures, six different levels can be identified in the hierarchy; namely, nanotubes and nanopolymers, fibers and matrix, ply, laminate, subcomponent and component. The techniques/theories used to go from each scale to the next are identified in Figure 7. In the hierarchical sensitivity analysis an opposite path is taken from that of the hierarchical modeling. The sensitivity coefficients with respect to each of the constituent and effective ply properties can be expressed as a linear combination of the sensitivity coefficients with respect to the laminate stiffnesses.

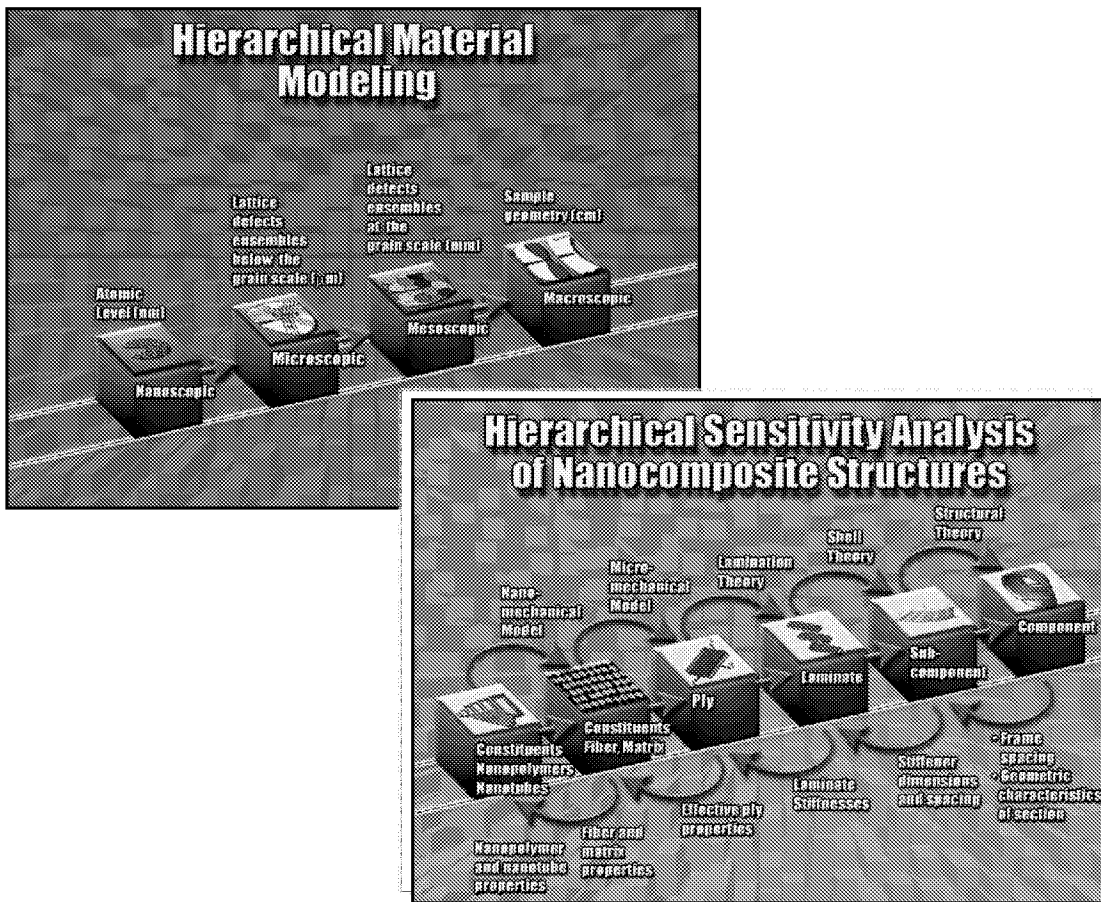


Figure 7

EXAMPLES OF HANDSHAKING APPROACHES

Two examples are given in Figure 8 for the multiscale modeling approaches that attempt to link several computational approaches in a combined model. The first is dynamic fracture analysis and the second is functionalized AFM tip (molecular robotics). In both examples, electronic structure model (quantum mechanics) is combined with a molecular dynamics model, which in turn is embedded into a continuum model (discretized) by finite elements.

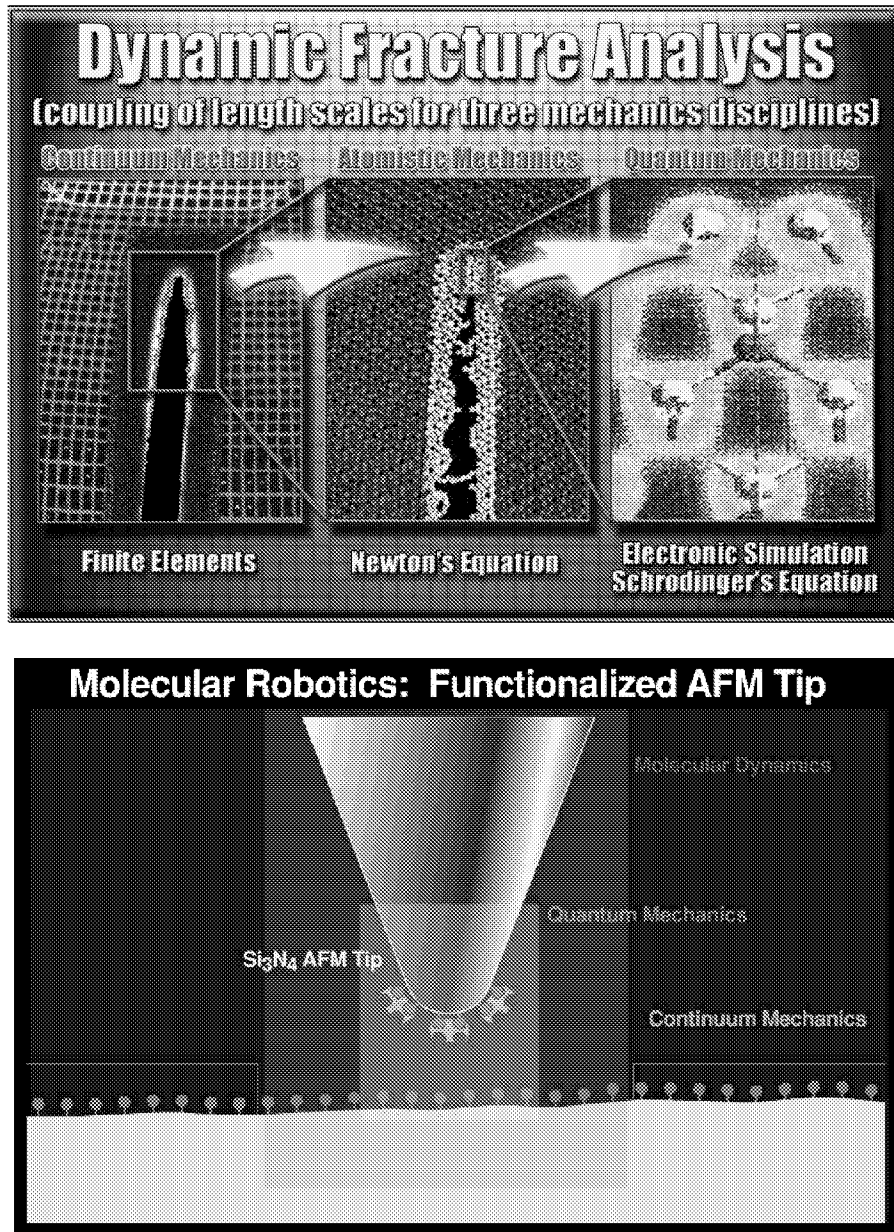


Figure 8

HIERARCHY OF SCALES IN FRACTURE

The hierarchy of scale that may determine the response of a crack in a relatively ductile polycrystalline metal are shown in Figure 9. Zooming in to the near-tip region, the plastic zone governed by the macroscopic plastic flow is observed. Inside that zone the material is polycrystalline, with the plastic deformation being different in different grains. Closer to the tip of the crack plastic deformation occurs via localized slip on particular slip planes, caused by the motion of individual dislocations. The atomic arrangement on either side of the crack is shown in the bottom left part of the figure.

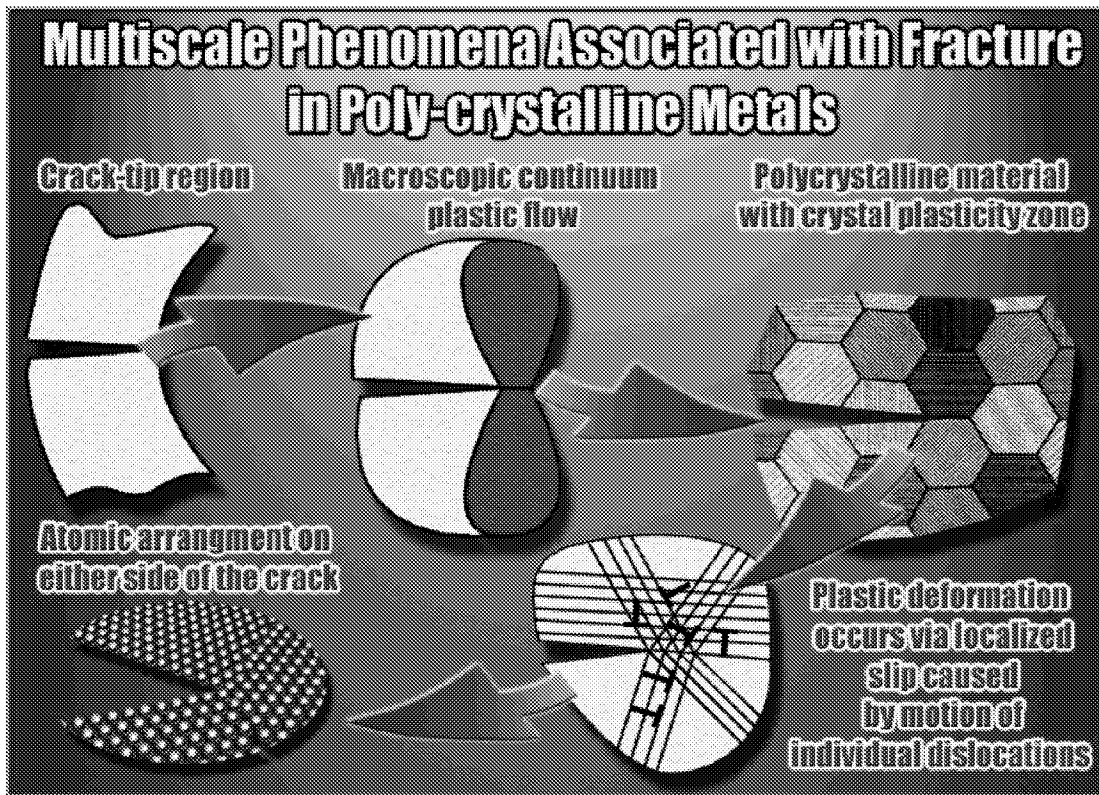


Figure 9

LENGTH AND TIME SCALES IN HIERARCHICAL MODELING

In computationally driven material development, a hierarchy of material models are used, associated with phenomena occurring at length scales from 10^{-10} to 1m and time scales from 10^{-15} second to years (Figure 10). The disciplines involved in these scales include quantum mechanics; molecular dynamics; nanomechanics; micro, meso and macromechanics; process simulation and; engineering design. However, many gaps still exist in the hierarchy of models, and to date, no rational way exists to integrate these models and to couple them in order to relate the phenomena at the very small length scales with the macroscopic behavior.

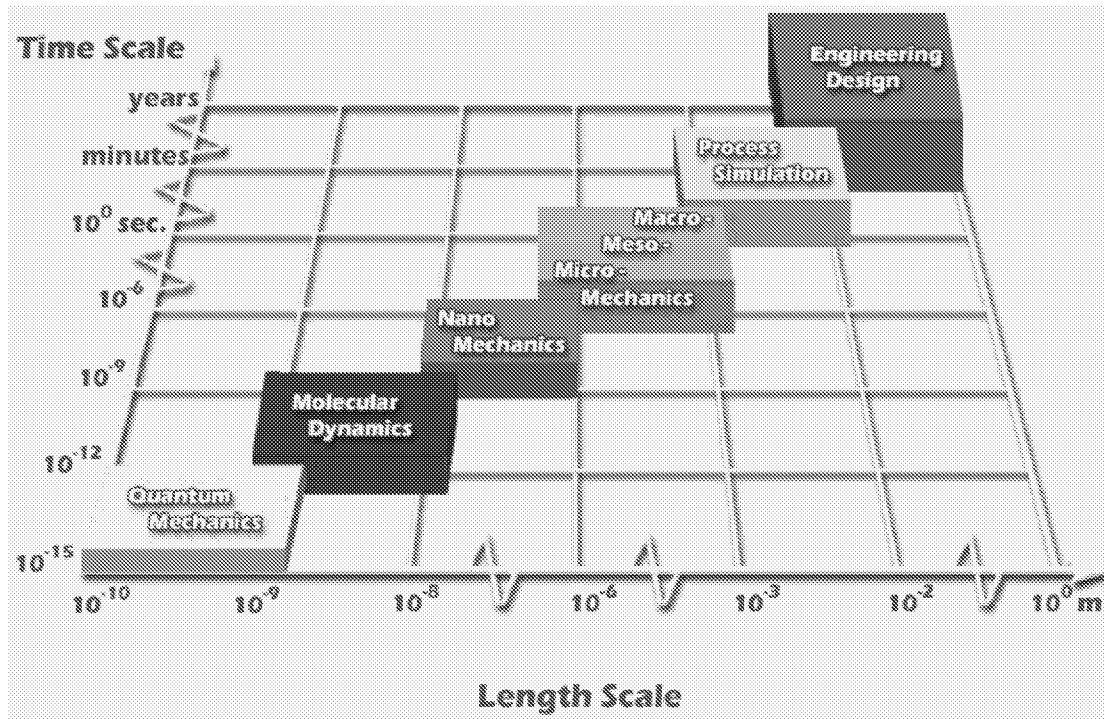


Figure 10

LATTICE-BOLTZMANN METHOD

The Lattice-Boltzmann method (LBM) is an example of the modeling approaches that host more than one physical level of description (Figure 11). Unlike conventional methods which solve the discretized macroscopic Navier-Stokes equations, the LBM is based on microscopic particle models and mesoscopic kinetic equations. It is a derivative of the lattice gas automata methods, and is especially useful for modeling interfacial dynamics, flows over porous media, and multiphase flows.

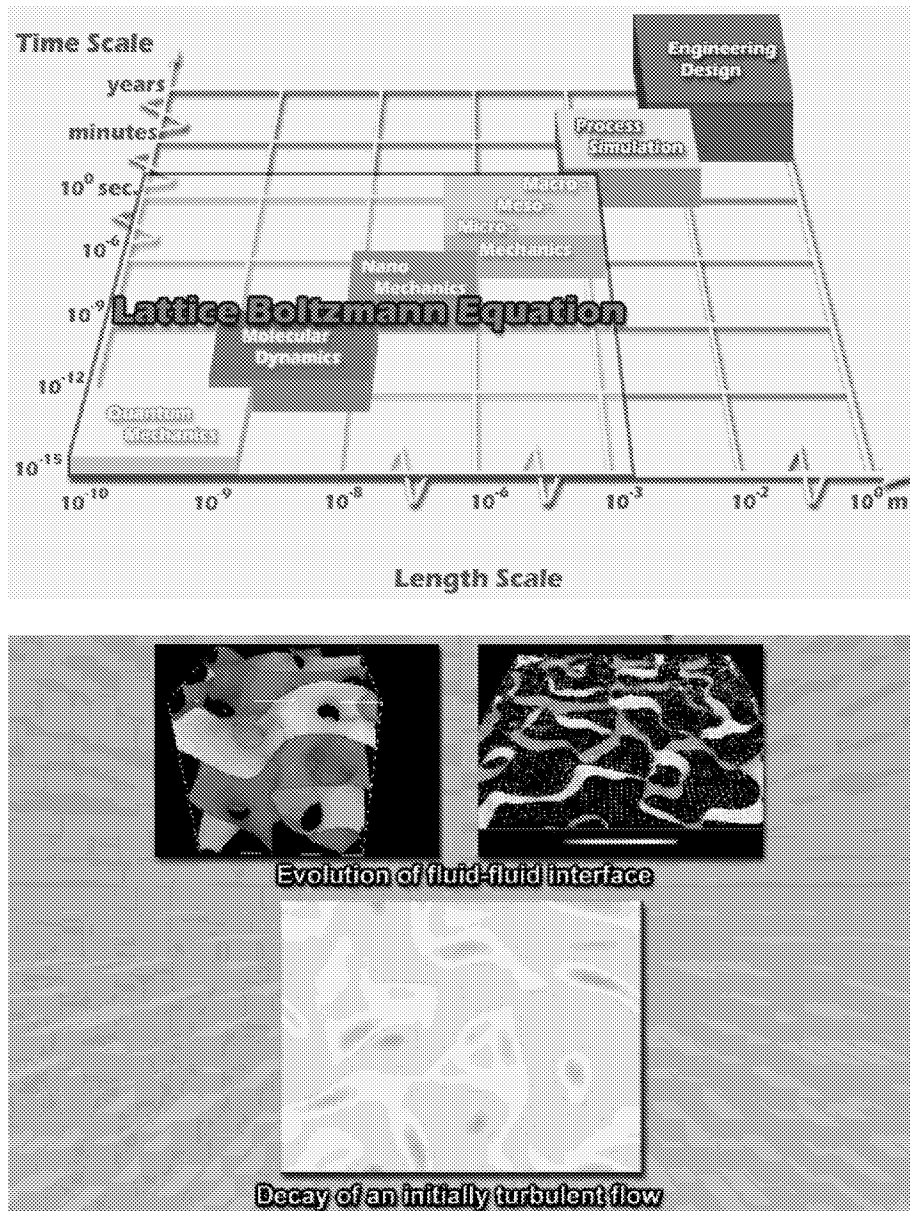


Figure 11

QUANTUM MECHANICS

Quantum mechanics is a means to understand and predict the interactions between atoms and molecules and to model chemical reactions at that scale (Figure 12). It uses models based on electronic structure. The solution of Schrodinger equation provides electronic wave functions. Other properties are obtained from these functions.

The practical time and length scales are often a million times too small for industrial design. To overcome this difficulty, a hierarchy of methodologies is used with quantum mechanics at the foundation.

- **Study of electronic structure of solids, surfaces or clusters - Properties that are determined below the molecular scale**
- **Predicts the interactions between atoms and molecules, and models the chemical reactions at that scale**
- **Quantum-Mechanical equation of motion**
Time dependent Schrodinger Equation
- **Electronic states of many-particle systems**
 - **Hartree-Fock Approximation**
 - **Density functional theory**
 - **Quantum Monte-Carlo Methods**

Figure 12

MOLECULAR DYNAMICS

Molecular dynamics is a means to study matter at the atomic level and to predict the static and dynamic properties from the underlying interactions between the molecules (Figure 13). It allows the prediction of systems 100 to 10,000 larger than quantum mechanics for periods 1,000 to 1,000,000 times longer.

To go from quantum mechanics to molecular dynamics requires averaging over the electrons to obtain spring constants, discrete charges and van der Waals parameters.

Recently, a team of researchers from Lawrence Livermore National Laboratory, IBM, and the Max Planck Institute for Metal Research in Germany were able to simulate the interactions of one billion atoms and discover cracks traveling faster than the speed of sound (767 mph in air at sea level and room temperature). They used half the 8,192 processors of the ASCI white computer for five full days (about million processor hours).

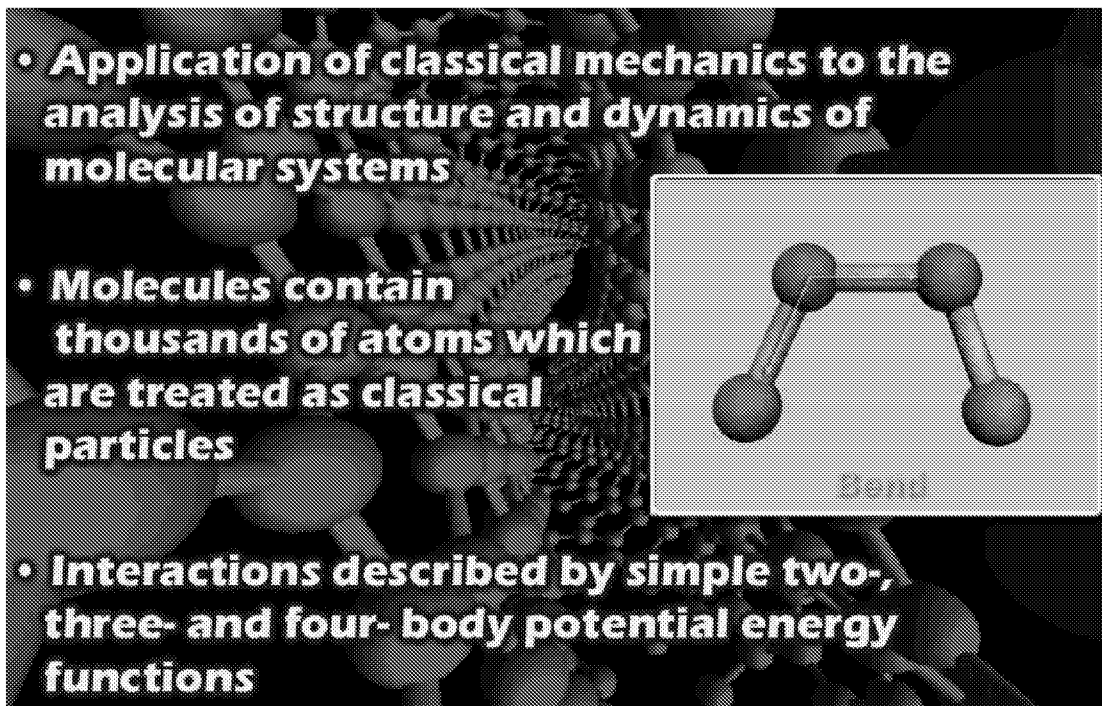


Figure 13

NANOMECHANICS

Nanomechanics deals with mechanics problems associated with modeling, design, fabrication and application of 3-D structures and systems with submicron (nm-scale) dimensions (Figure 14). Nanoscale systems have a number of interesting features which distinguish them from micro- and macro-scale systems.

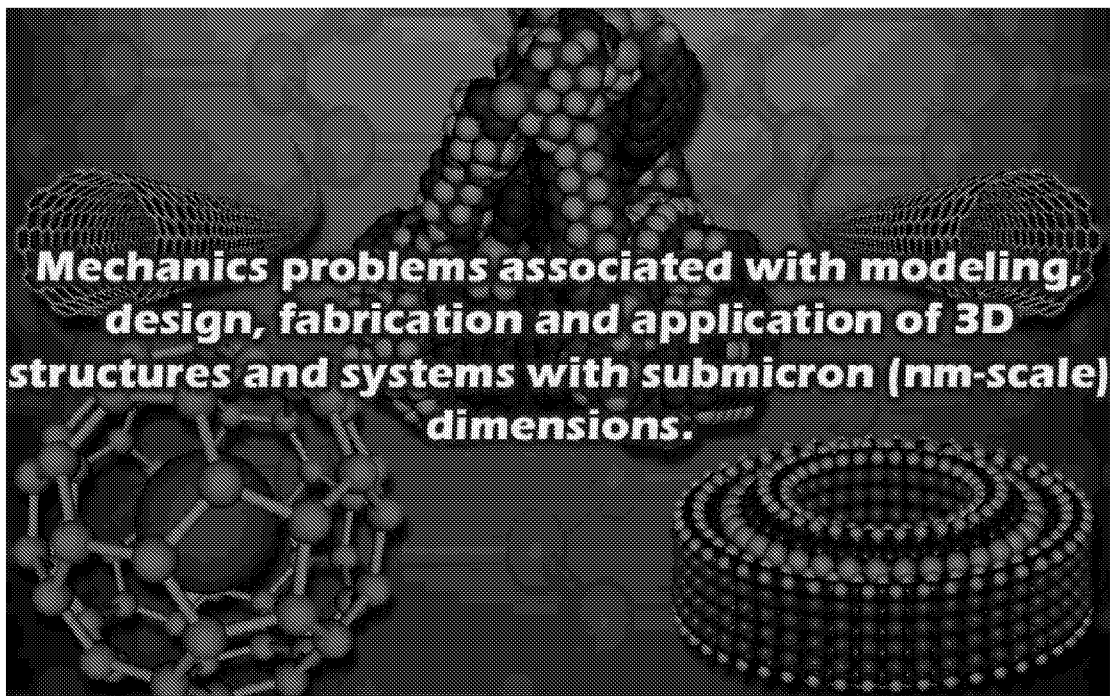


Figure 14

CONTINUUM MECHANICS VS. NANOMECHANICS

Continuum mechanics is used to predict the phenomena described by uniform collective behavior of atoms (for example, elastic response of materials). By contrast, nanomechanics is used to predict the phenomena described by dramatic changes in the state of few atoms (for example, corrosion and fatigue). To accomplish this, the atoms whose state is affected need to be identified, their behavior at the nm length scale modeled and connected to the solid's macroscopic response (Figure 15).

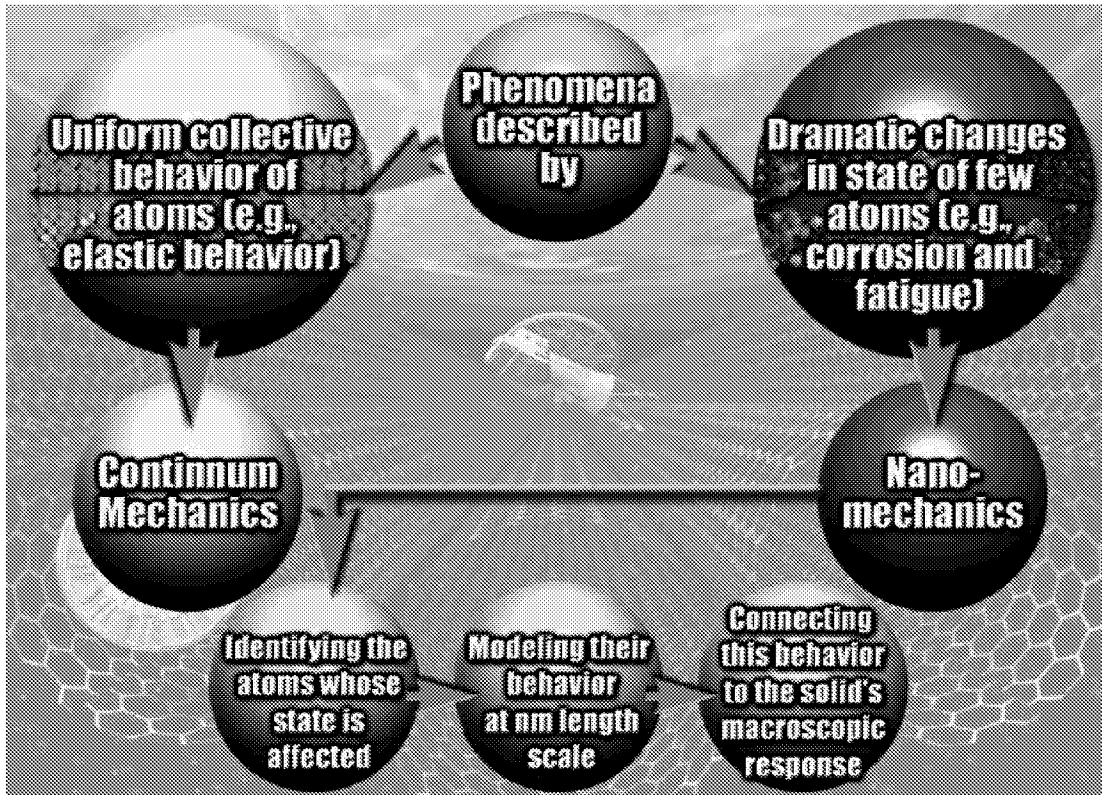


Figure 15

KEY COMPONENTS OF ADVANCED MULTISCALE RESEARCH ENVIRONMENT

Multiscale modeling is a unifying paradigm to enable integration of science and engineering. It allows rigorous correlation of different science and engineering models, representations, languages and metrics. It overcomes engineering process fragmentation.

The realization of the strategic value of multiscale modeling requires an advanced research environment that links diverse teams of scientists, engineers and technologists. The essential components of the environment can be grouped into three categories: intelligent tools and facilities, nontraditional methods, and advanced interfaces (Figure 16). The three categories are described subsequently.

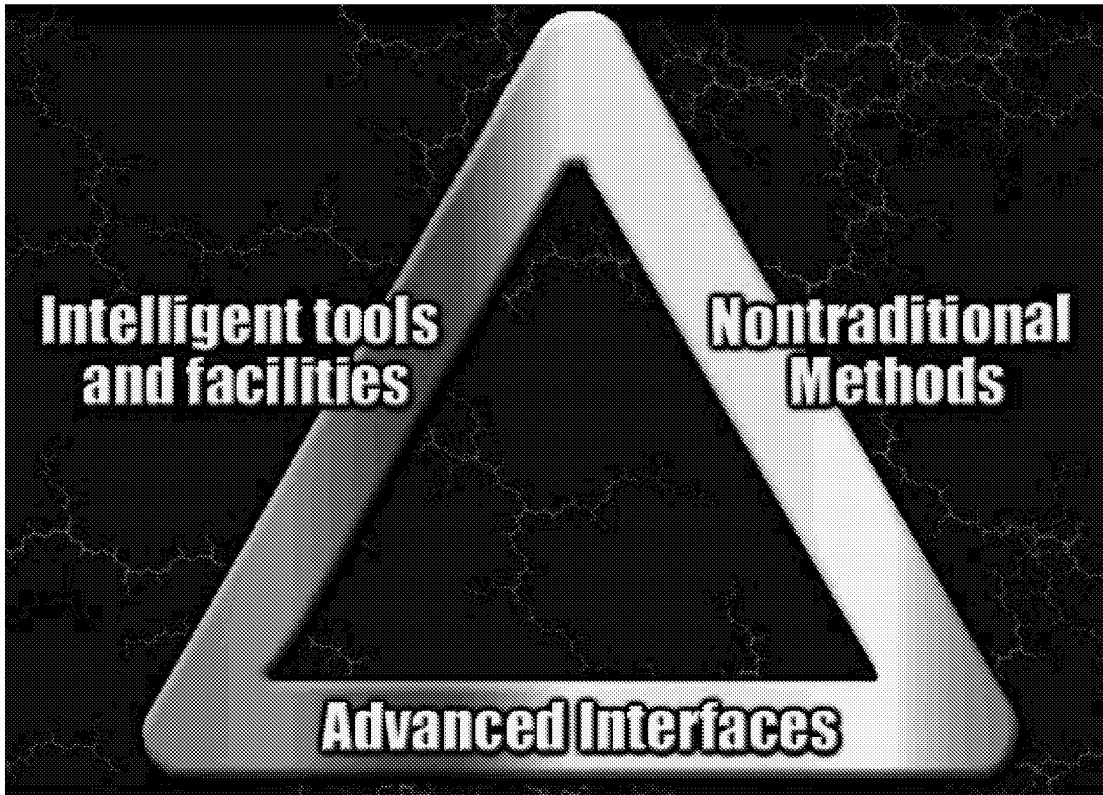


Figure 16

INTELLIGENT TOOLS AND FACILITIES

These include high fidelity – rapid modeling, simulation and interrogative visualization tools, synthetic immersive environments; close coupling of simulations and experiments; computer simulation of physical experiments and remote control of these experiments. In all of these tools, extensive use should be made of intelligent software agents and information technology (Figure 17).

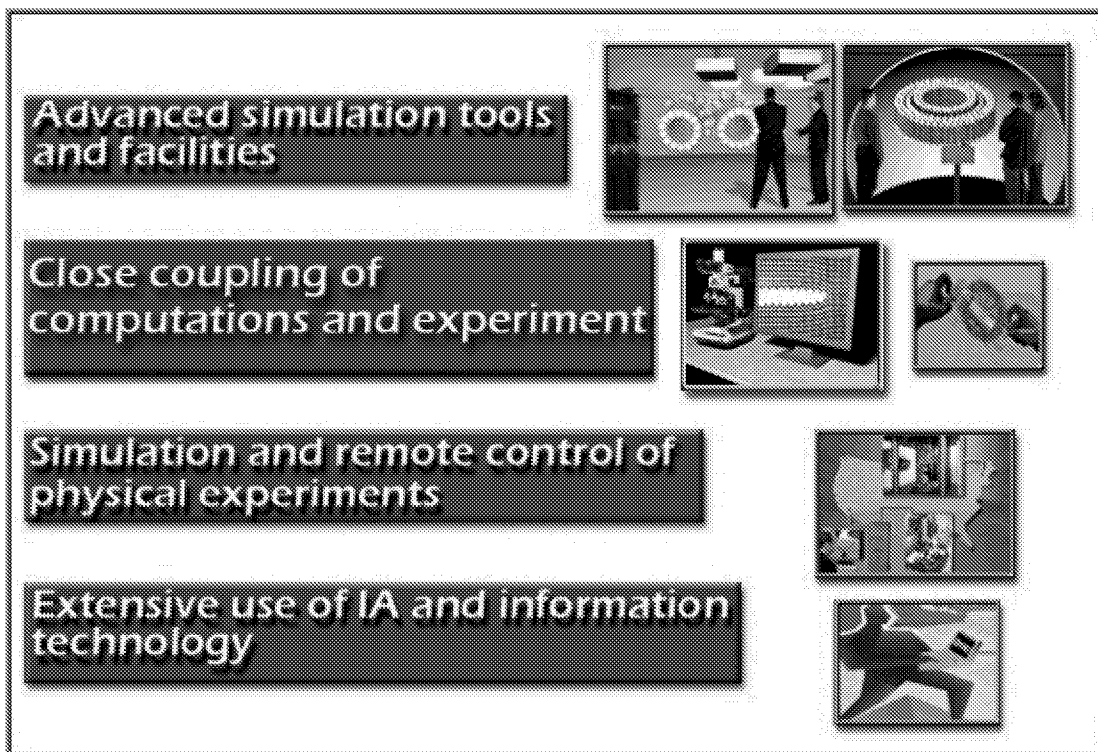


Figure 17

NONTRADITIONAL METHODS

These include novel mathematical tools for multiscale data representation (e.g., wavelets, ridgelets and curvelets) and multiresolution methods; verification and validation strategies; and nondeterministic approaches for handling various types of uncertainties in geometry, material properties, boundary conditions, loading and operational environment (Figure 18).

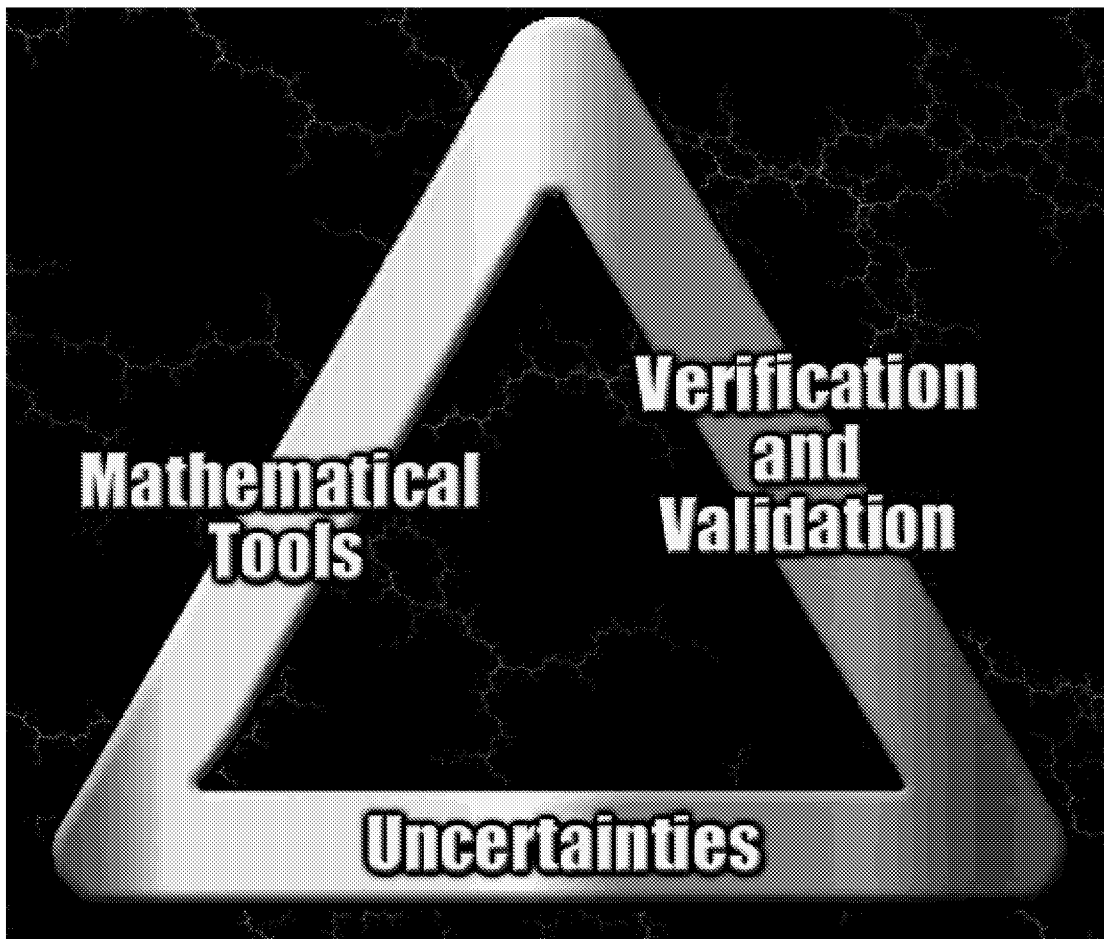


Figure 18

MULTISCALE DATA PRESENTATION

In recent years a number of novel concepts related to multiscale data representation and wavelet bases have appeared. *Wavelets* are functions of compact support – small waves. They are well-suited for describing local phenomena (e.g., point of zero-dimensional singularities). They oscillate and have zero net area.

In dimensions greater than one *ridgelets* and *curvelets* are used for representing sharp variations, or singularities. Ridgelets are used for linelike and planelike phenomena and curvelets are used for representing sharp variations across curves (Figure 19).

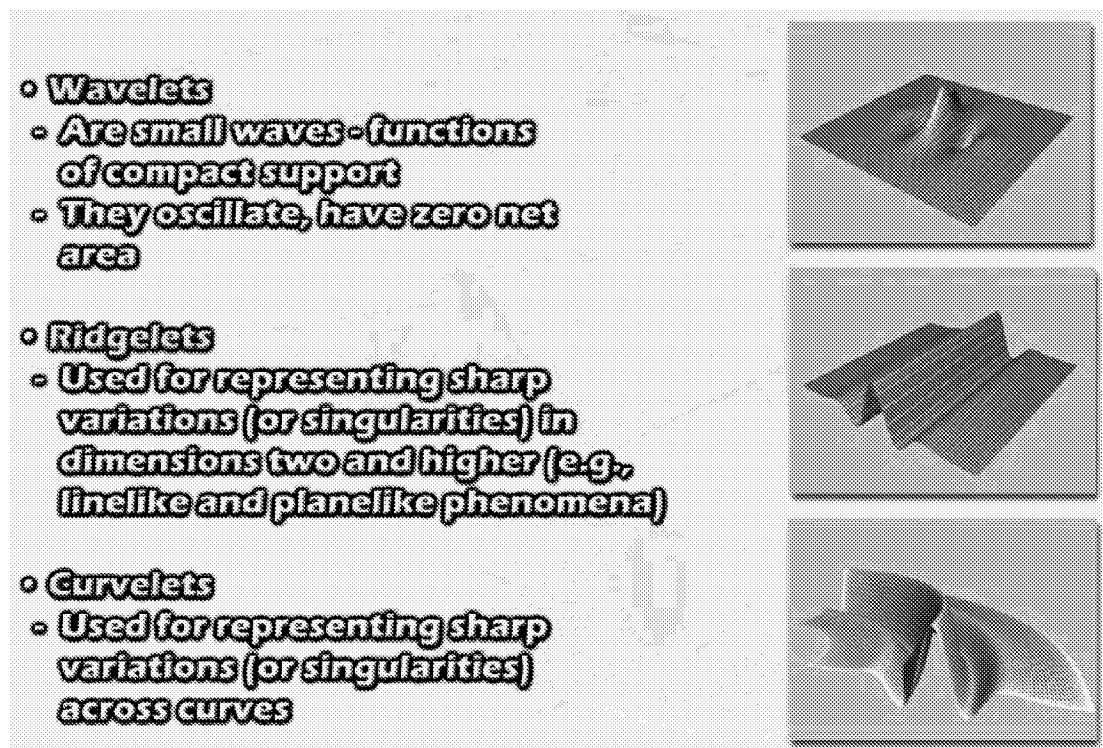


Figure 19

MULTIRESOLUTION METHODS

In typical multiresolution methods a sequence of system descriptions at a sequence of representative scales are constructed, combining local processing at each scale with various inter-scale interactions. For example, the evolving solution at each scale is typically used to construct the equations on coarser scales and to accelerate the solution on finer scales. In this way, large-scale changes are effectively performed on coarse grids, based on information previously gathered from finer grids (Figure 20).

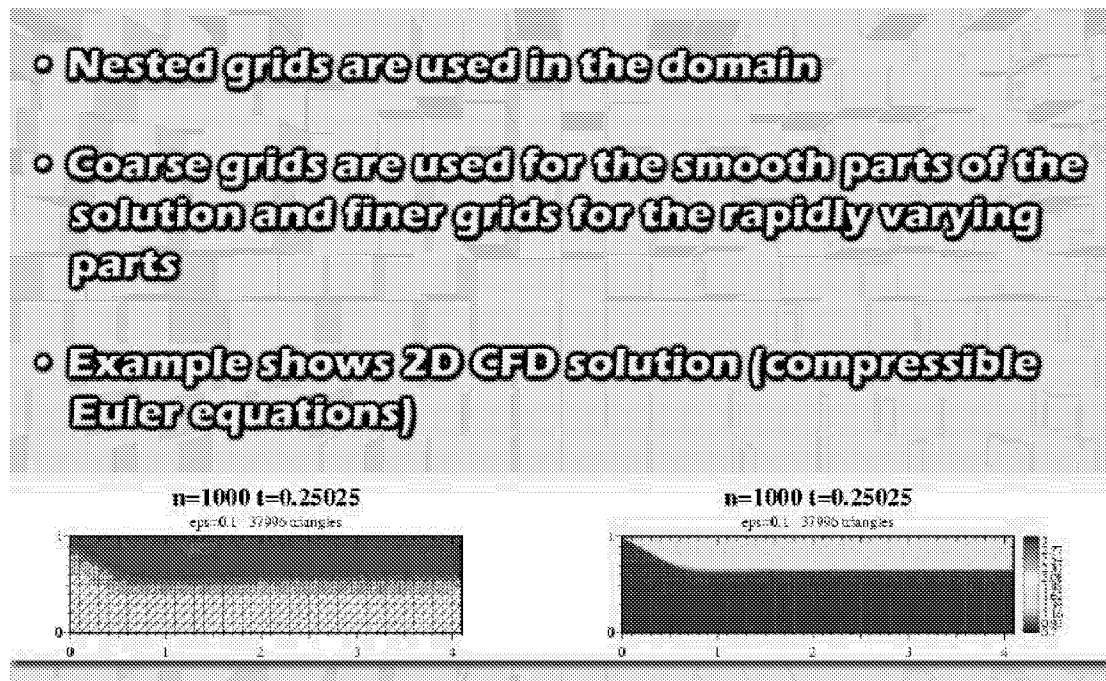


Figure 20

VERIFICATION AND VALIDATION OF NUMERICAL SIMULATIONS

Quantifying the level of confidence, or reliability and accuracy of numerical simulations has recently received increased levels of attention in research and engineering applications. During the past few years, new technology development concepts and terminology have arisen. Terminology such as virtual prototyping and virtual testing is now being used to describe computer simulation for design, evaluation and testing of new engineering systems.

The two major phases of modeling and simulation of an engineering system are depicted in Figure 21. The first phase involves developing a conceptual and mathematical model of the system. The second phase involves discretization of the mathematical model, computer implementation, numerical solution and representation or visualization of the solution. In each of these phases there are uncertainties, variabilities and errors.

Verification and validation are the primary methods for building and quantifying confidence in numerical simulations. *Verification* is the process of determining that a model implementation accurately represents the conceptual/mathematical model and the solution to the model. Correct answer is provided by highly accurate solutions. *Validation* is the process of determining the degree to which a model is an accurate representation of the real system. Correct answer is provided by experimental data.

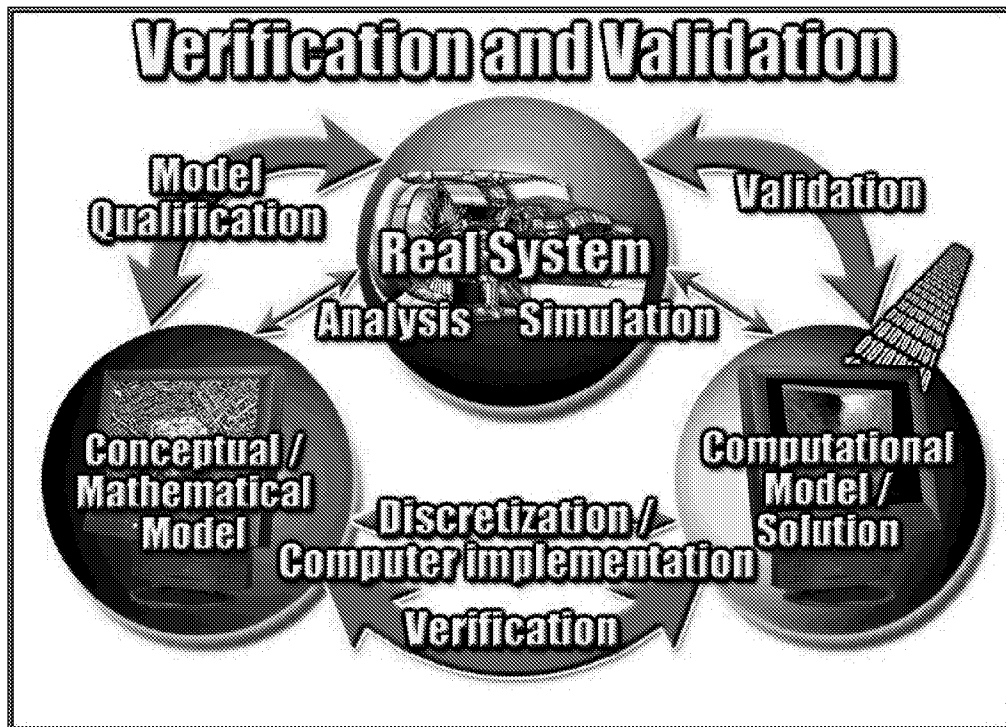


Figure 21

TYPES OF UNCERTAINTIES

A number of different uncertainty representations and classification have been proposed. Among these classifications are the three-type classification – statistical, model, and fundamental uncertainties; the two type classification – uncertainty of information and uncertainty of the reasoning process, and the six-type classification (see Figure 22):

- *Probabilistic uncertainty*, which arises due to chance or randomness,
- *Fuzzy uncertainty* due to linguistic imprecision (e.g., set boundaries are not sharply defined)
- *Model uncertainty* which is attributed to lack of information about the model characteristics,
- *Uncertainty due to limited (fragmentary) information* available about the system (e.g., in the early stage of the design process),
- *Resolutinal uncertainty* which is attributed to limitation of resolution (e.g., sensor resolution), and
- *Ambiguity* (e.g., one to many relations)

Accounting for uncertainties in the design of engineering systems involves representation and propagation of uncertainty, from model parameters to estimating the performance; bounding uncertainties; model updating and validation; and assessment of the impact of uncertainties on the reliability and certification of the system.

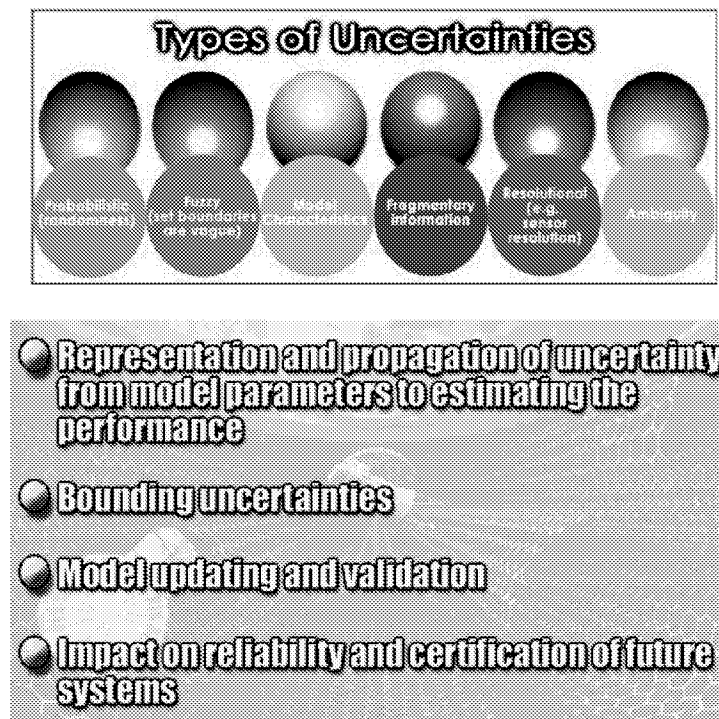


Figure 22

PRINCIPLE OF COMPLEXITY

One of the important consequences of uncertainty is its effect on precision. Three types of models can be identified depending on the complexity and the precision, namely: mathematical models, model-free methods, and fuzzy systems. In a typical complex system a combination of the three should be used. As the uncertainty and/or complexity of an engineering system increases, the ability to predict its response diminishes, until a threshold is reached beyond which precision and relevance become almost mutually exclusive. Consider, for example, numerical simulations in which sophisticated computational models are used for predicting the response, performance, and reliability of the engineering system, but the system parameters are little more than guesses. Such simulations can be characterized as *Correct but Irrelevant Computation* (CBIC); that is, forcing precision where it is not possible (Figure 23).

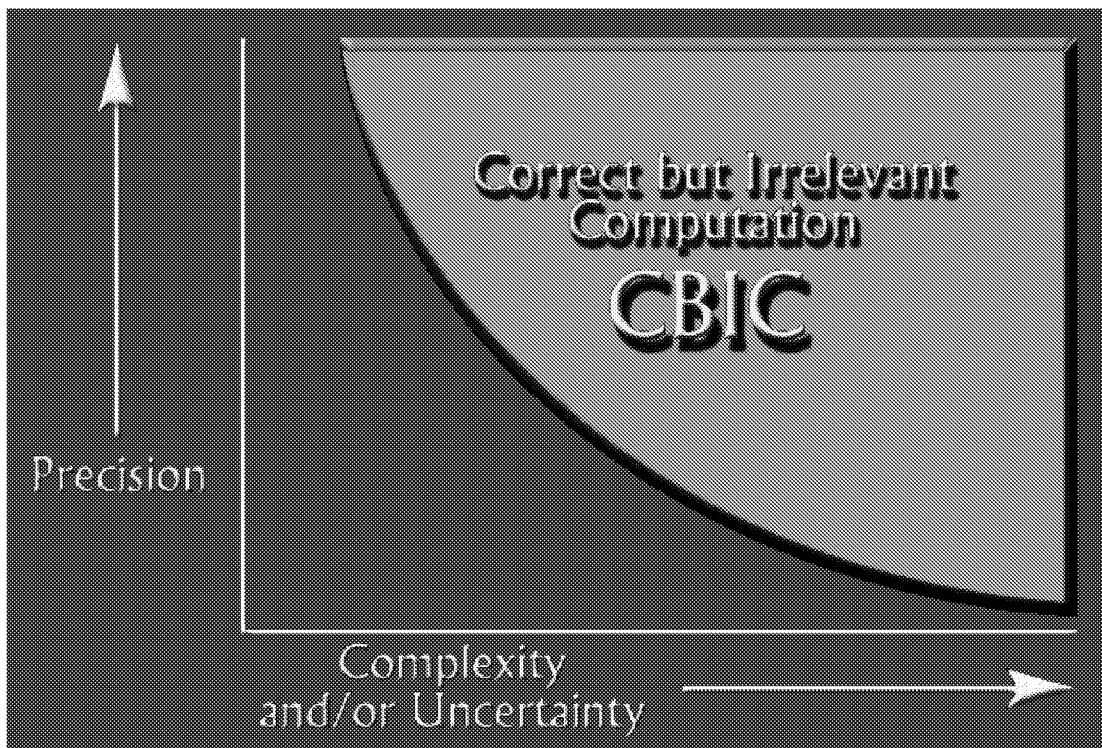


Figure 23

NONDETERMINISTIC ANALYSIS APPROACHES

Three general approaches can be used for the analysis of systems with uncertainties; namely (Figure 24): probabilistic methods for random processes; fuzzy sets; and set theoretical or antioptimization methods. The domain of application of each of these techniques is identified in Figure 24.

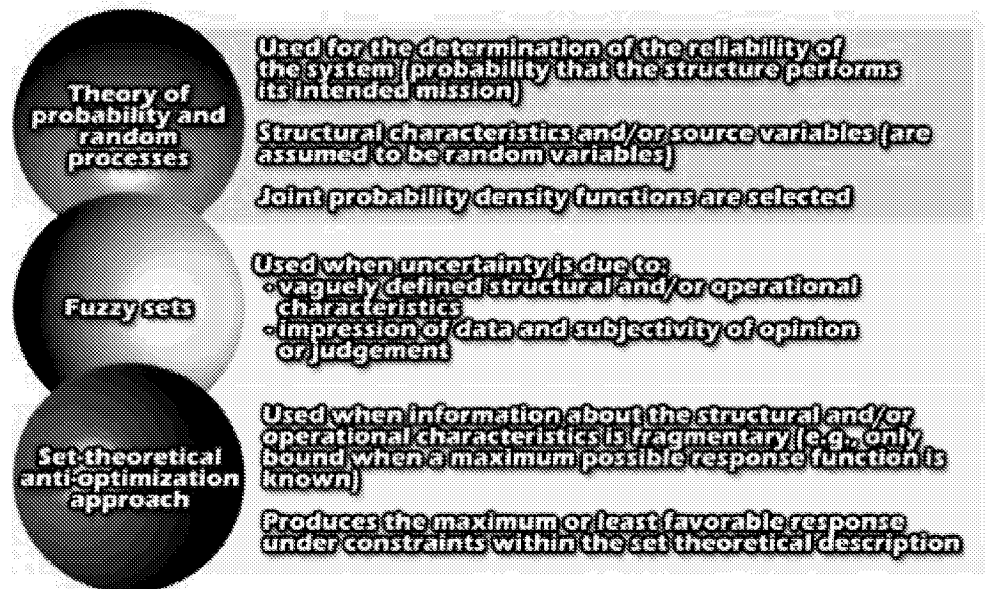


Figure 24

ADVANCED HUMAN/COMPUTER INTERFACES

Although the WIMP (windows, icons, menus, and pointing devices) paradigm has provided a stable global interface, it will not scale to match the myriad form factors and uses of platforms in the future collaborative distributed environment. Perceptual user interfaces (PUI's) are likely to meet those needs. PUI's integrate perceptive, multimodal and multimedia interfaces to bring human capabilities to bear on creating more natural intuitive interfaces. They enable multiple styles of interactions, such as speech only, speech and gesture, vision, and synthetic sound, each of which may be appropriate in different applications (Figure 25). These new technologies will enable broad uses of computers as assistants or agents that will interact in more human-like ways.

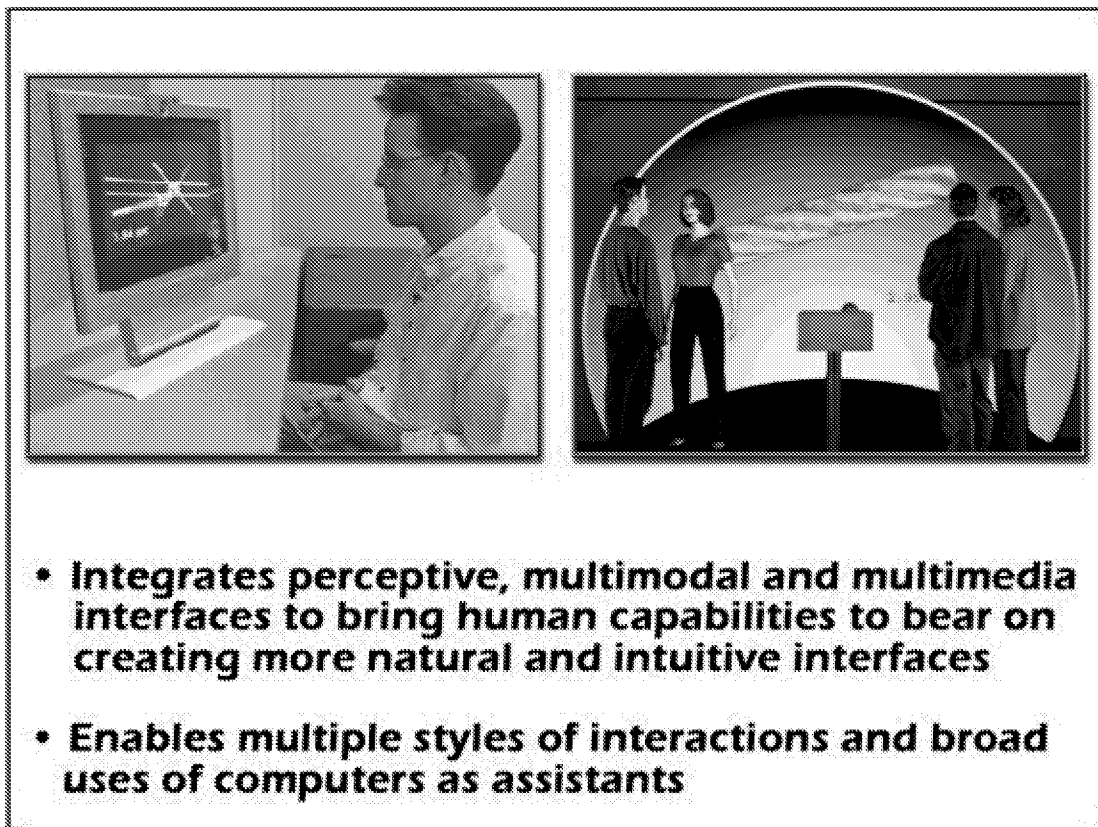


Figure 25

ADVANCED LEARNING ENVIRONMENTS

In order to meet the life-long learning demands of the future and broaden the awareness among the researchers and engineers of nondeterministic approaches, three categories of learning environments are needed; namely, expert-led group learning environment; self-paced individual learning environment; and collaborative learning environment (Figure 26). The three environments, in combination, can reduce the time and cost of learning, as well as sustain and increase worker competencies in high tech organizations.

The human instructors in these environments will serve many roles, including inspiring, motivating, observing, evaluating, and steering the learners, both individually and in distributed teams.

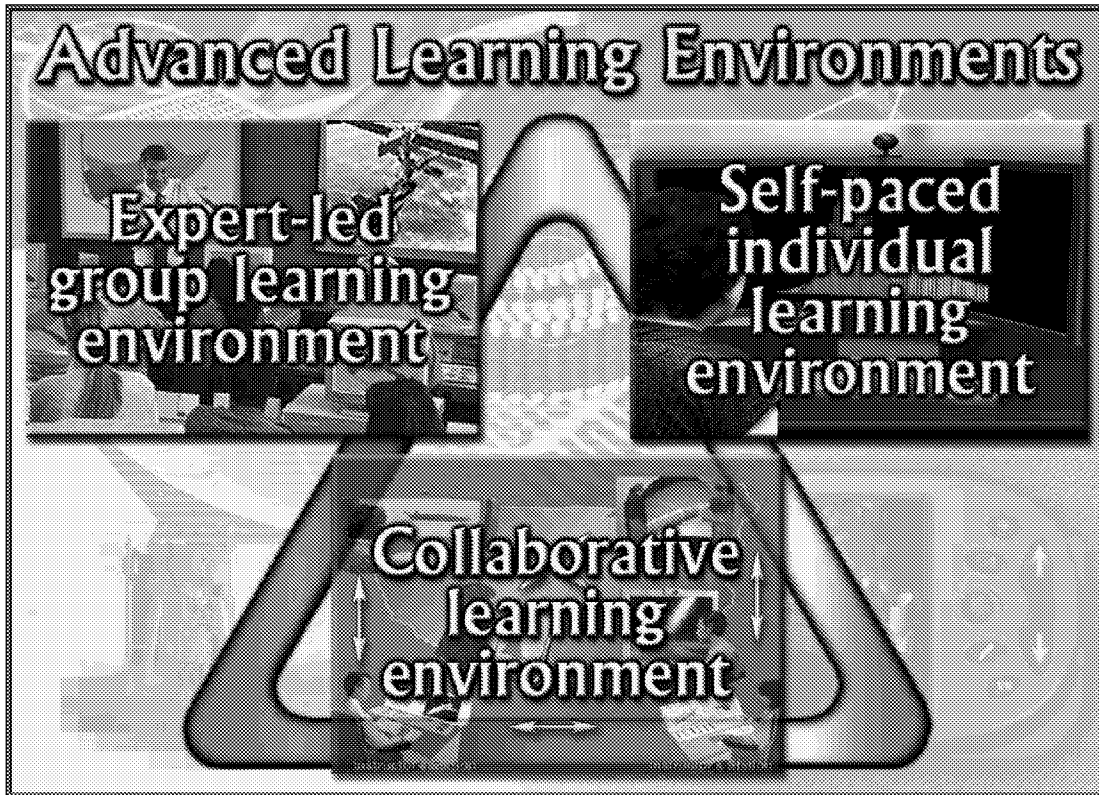


Figure 26

EXPERT-LED LEARNING ENVIRONMENT

The human instructors in expert-led distributed learning in a virtual environment serve as coaches, guides, facilitators, and course managers. Their presentations focus on a broad overview of the topic and its diverse applications (Figure 27), and end with more penetrating, what-if questions that can enhance the critical thinking and creativity of the learners. Elaborate visualization and multimedia facilities are used in the presentations. Routine instructional and training tasks are relegated to the self-paced individual learning environment.

Role of Instructor



- Gives broad overview of the topic
- Shows diverse applications
- Uses advanced multimedia facilities
- Ends the lecture with penetrating what-if questions

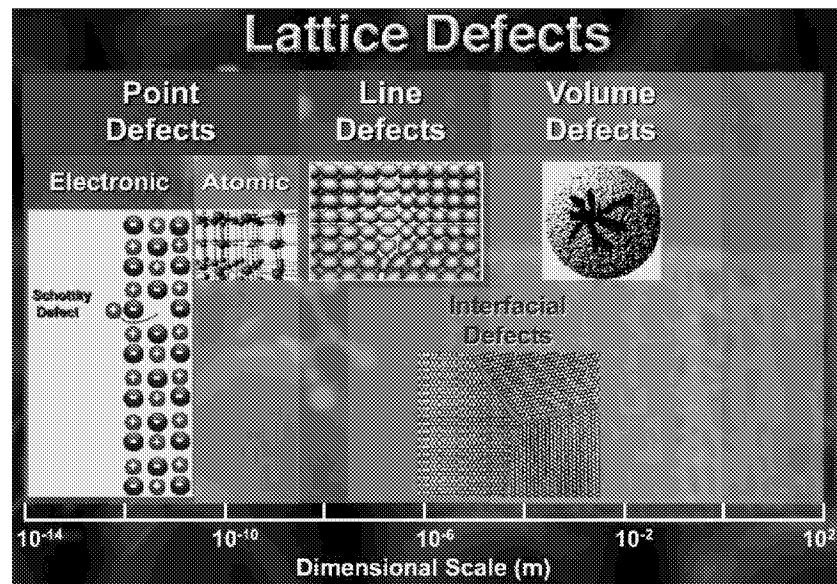


Figure 27

SELF-PACED LEARNING ENVIRONMENT

The individual learning environment engages the learner and provides a high degree of tailored interactivity. It can be used for self-paced instruction of routine material not covered in the lecture. Using virtual instructors assigned by the human instructors can enhance such instruction. It can be used to study the physical phenomena occurring at different length scales using advanced visualization, multimedia and multisensory immersive facilities. The individual learning environment can serve to carry out numerical and virtual experiments - computer simulation of physical experiments (Figure 28).

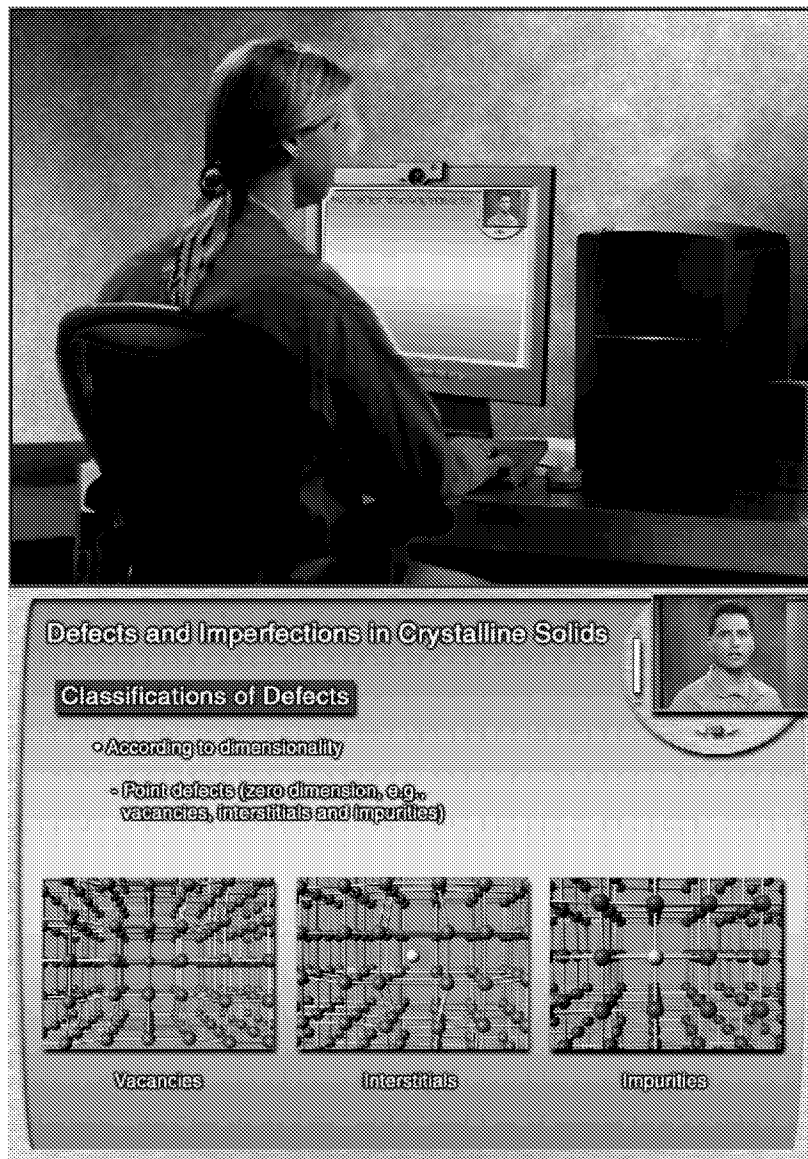


Figure 28

SELF-PACED LEARNING ENVIRONMENT

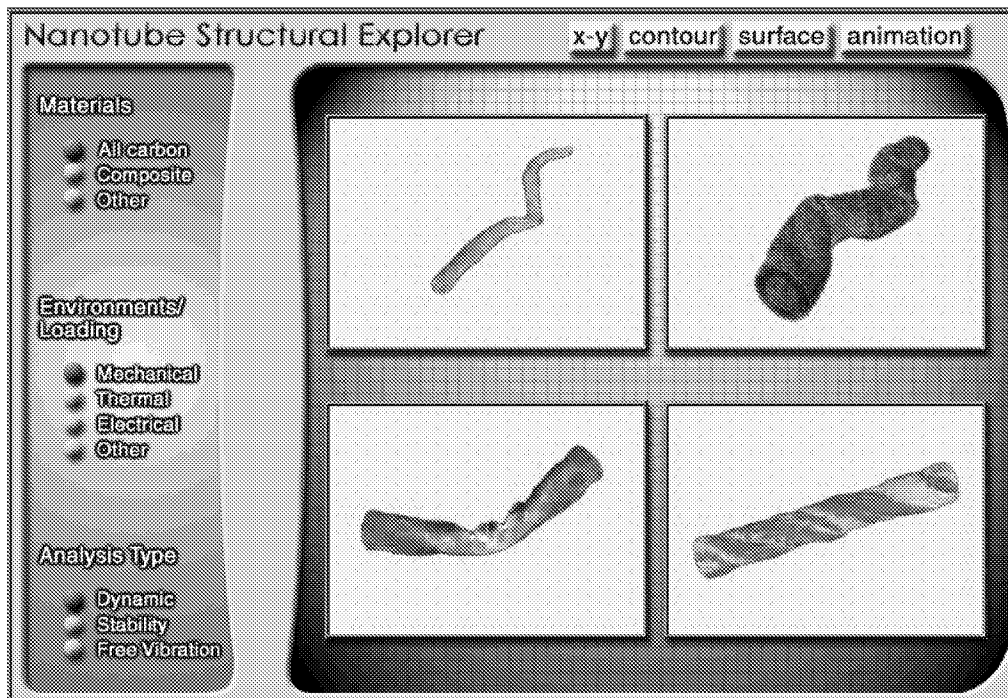
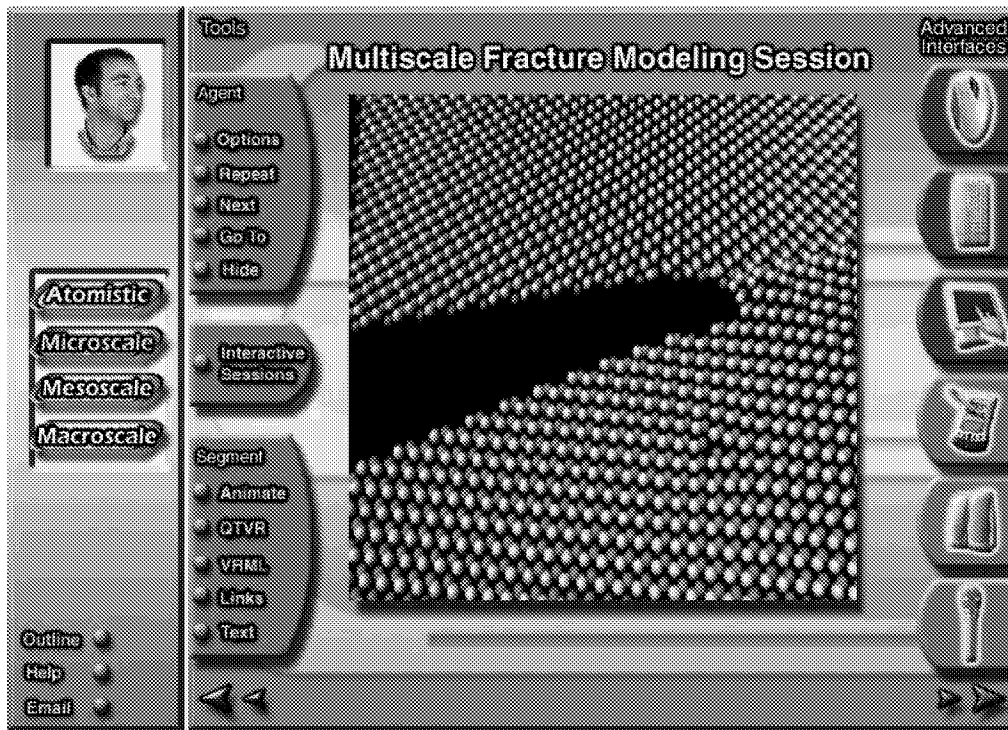


Figure 28 (continued)

COLLABORATIVE / DISTRIBUTED LEARNING ENVIRONMENT

Collaborative learning environments teach teamwork and group problem solving. Instructors and learners can be geographically dispersed. Eventually, they can be brought together through immersive telepresence facilities to share their experiences in highly heterogeneous environments involving different computing platforms, software, and other facilities, and they will be able to work together to design complex engineering systems beyond what is traditionally done in academic settings. Because participants can be virtually collocated without leaving their industry and government laboratories, collaborative learning environments can enable the formation of learning networks linking universities, industry and government labs. The ultimate goal of these learning facilities is to create an intellectual environment where academic and experiential learning are effectively and efficiently co-mingled. In such an environment, academic rigor is learned in concert with professional job performance, and academic complexities are addressed within the industrial concern (Figure 29).

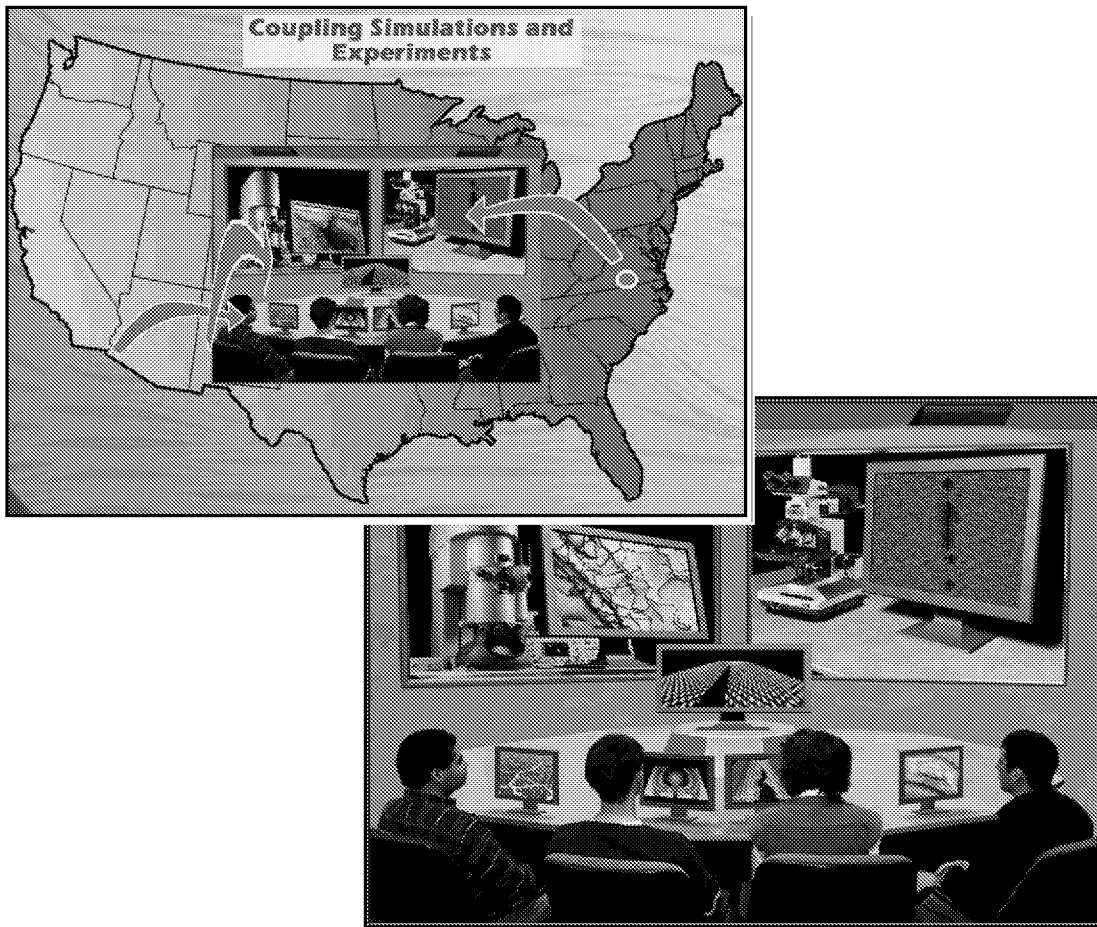


Figure 29

COLLABORATIVE / DISTRIBUTED LEARNING ENVIRONMENT

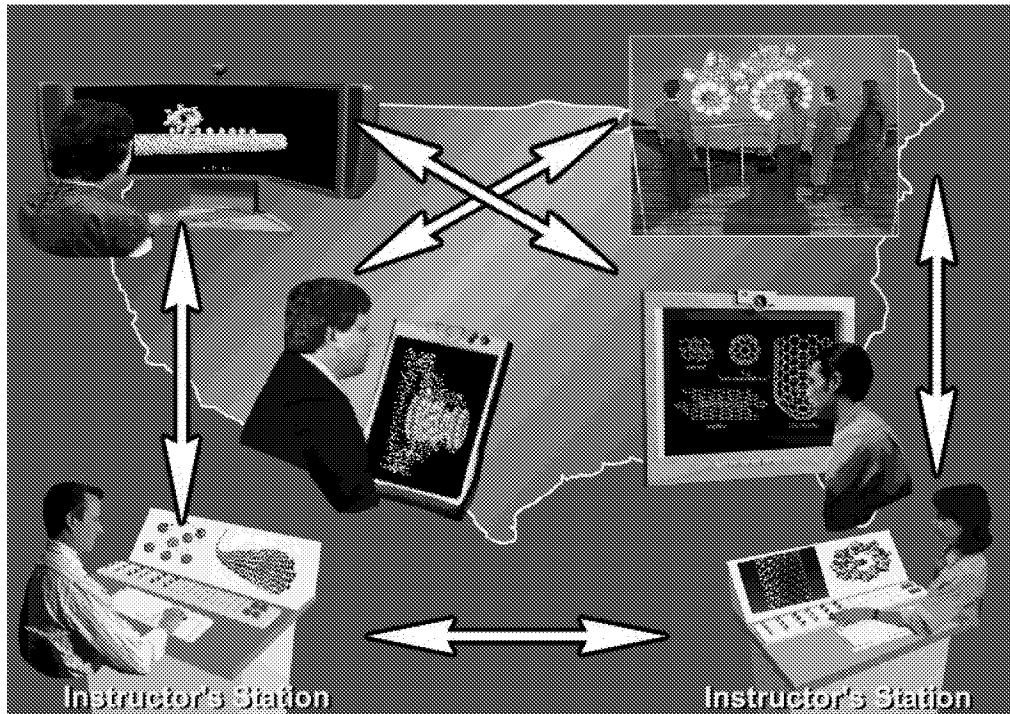
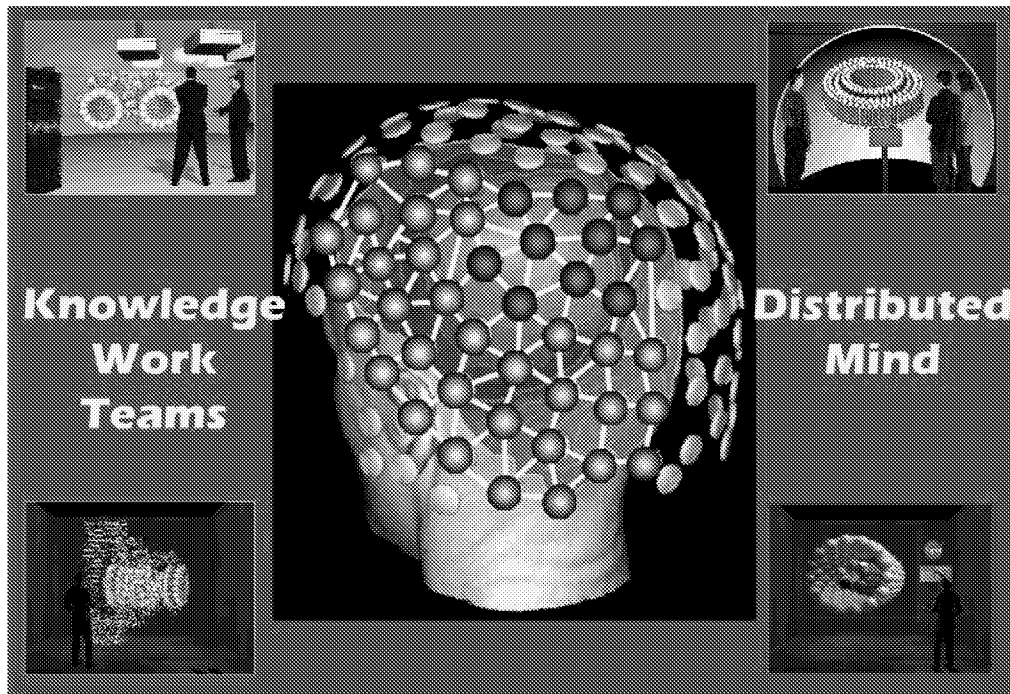


Figure 29 (continued)

VIRTUAL CLASSROOM

Online training and virtual classrooms are typically used to provide learning environments with custom self-instruction, flexible tutorial support, and choice of both the place and time of learning. Three categories of facilities are used in these environments; namely: *instruction*, including multimedia lectures, links to other resources and tools for searching, browsing, and using archived knowledge; *communication*, including email, UseNet, chat centers, video and Internet conferencing; and *course management and performance evaluation* (Figure 30).

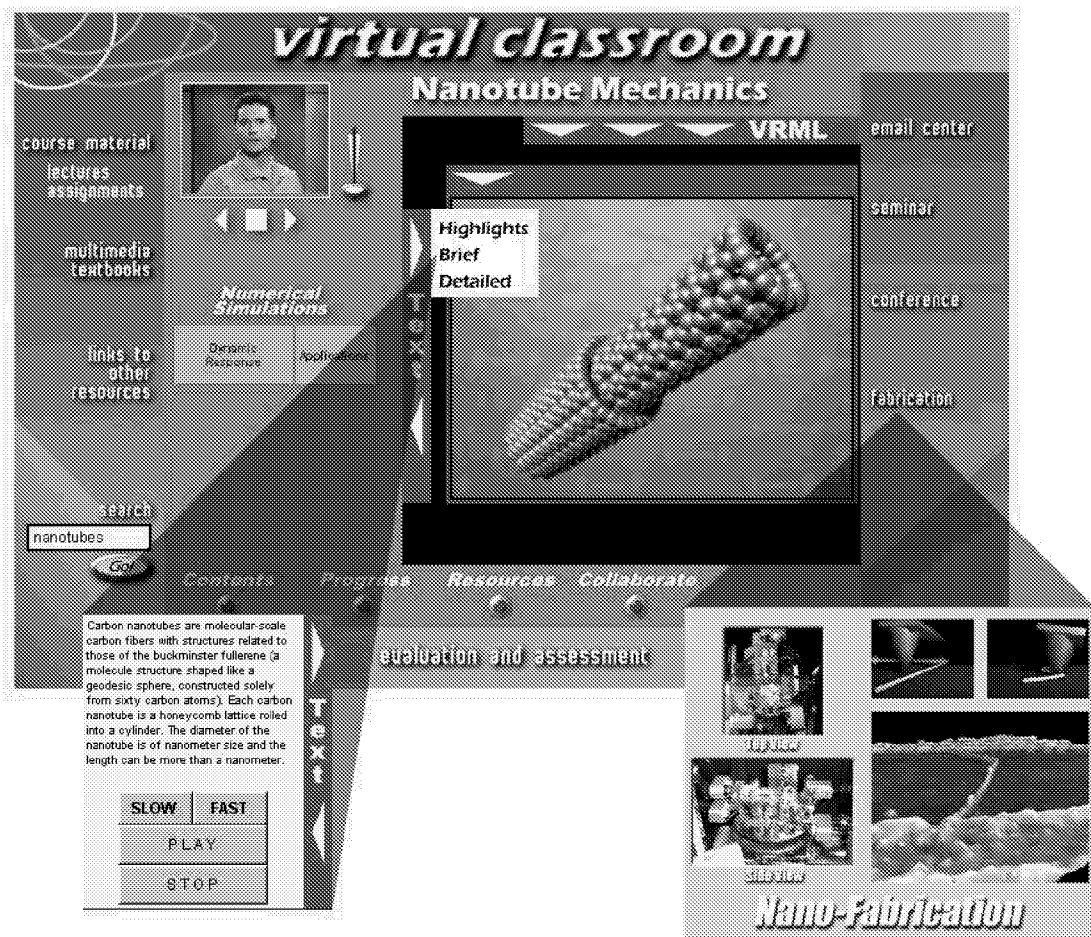


Figure 30

MULTISCALE MODELING AND SIMULATION NETWORK

The realization of the full potential of multiscale modeling and simulation in the design, and development of future complex systems requires, among other things, the establishment of research and learning networks. The networks connect diverse, geographically dispersed teams from NASA, other government labs, university consortia, industry, technology providers, and professional societies (Figure 31).

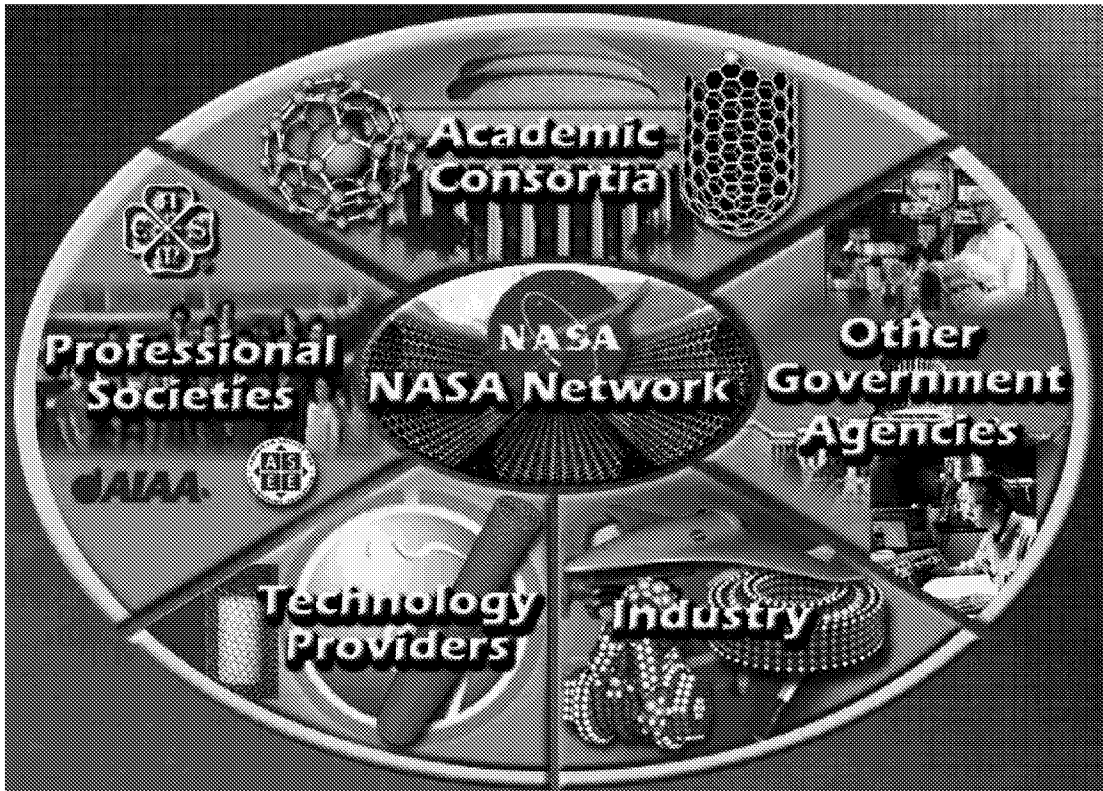


Figure 31

EVOLUTION OF NEW TECHNOLOGY

The multiscale modeling, simulation and visualization, and their associated technologies, as any other technology, have gone through three phases. The first is that of *naïve euphoria* – unrealistic expectations resulting from overreaction to immature technology. The second is *cynicism*, or frustration associated with unmet expectation. The third is that of *realistic expectations* – gradually realizing the true benefits from the technologies (Figure 32).

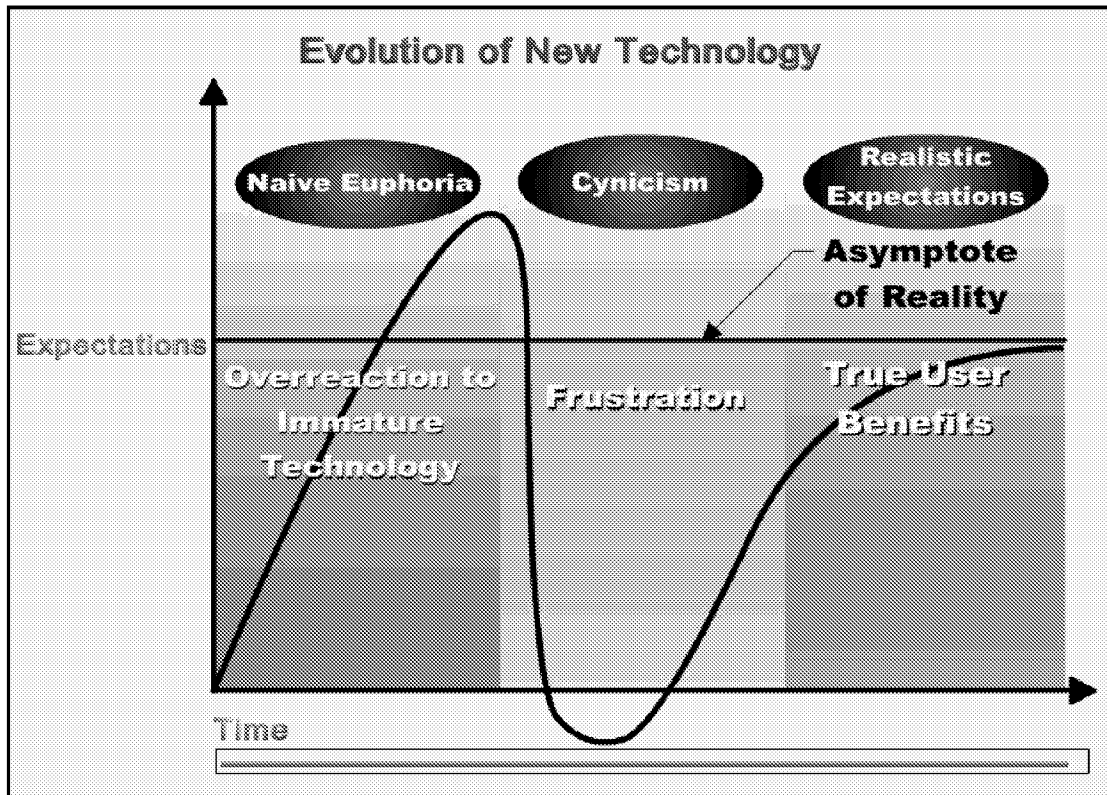


Figure 32

OBJECTIVE AND FORMAT OF WORKSHOP

The objectives of the workshop are to: a) provide a broad overview of the diverse activities related to multiscale modeling, simulation and visualization, and b) identify the potential of these technologies to future aerospace systems (Figure 33). The nineteen presentations illuminate some of the key issues in multiscale modeling and simulation, particularly in the area of material modeling and synthesis, and provide fresh ideas for future research and development.

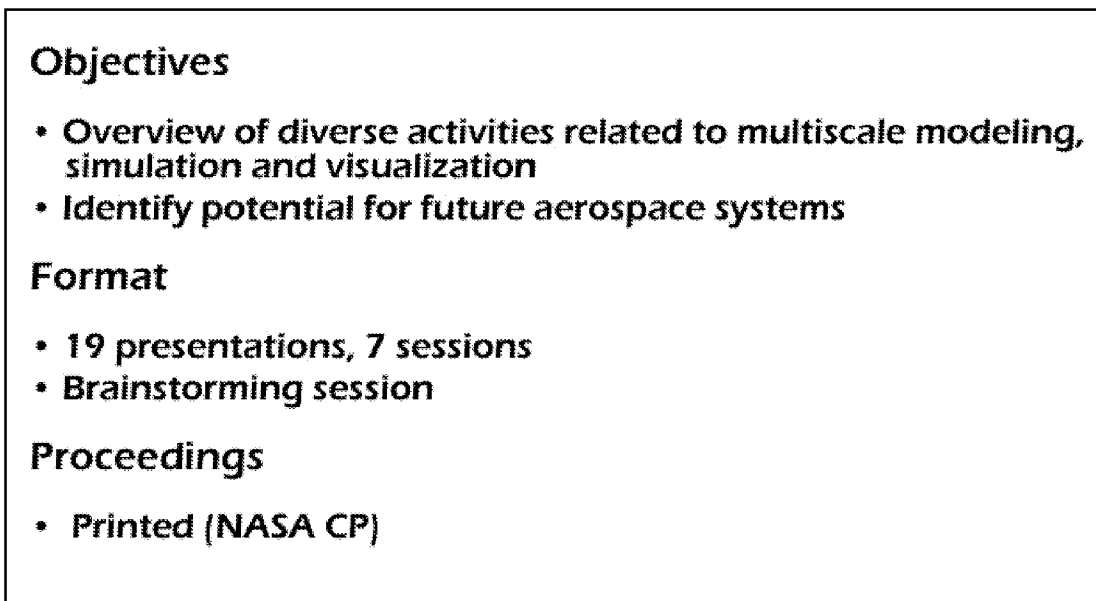


Figure 33

ISSUES RELATED TO MULTISCALE MODELING, SIMULATION AND VISUALIZATION

The issues related to, and the pacing items for, multiscale modeling, simulation and visualization can be grouped into five major categories, and are identified in Figure 34.

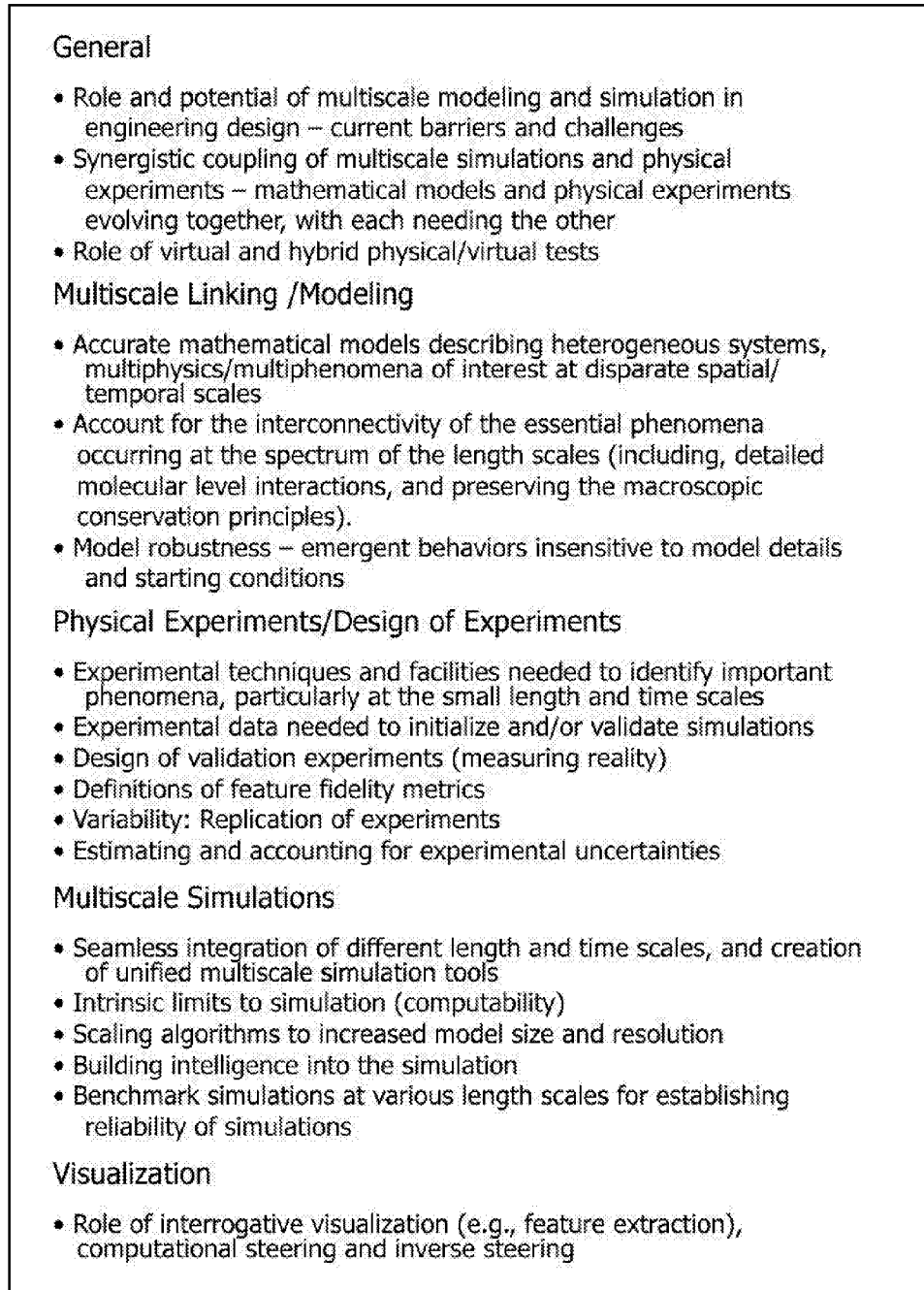


Figure 34

INFORMATION ON MULTISCALE MODELING, SIMULATION AND VISUALIZATION

Extensive literature now exists on multiscale modeling and simulation. A short list of books, monographs, conference proceedings, survey papers and websites is given subsequently.

Books, Monographs and Conference Proceedings

- Phillips, R., “*Crystals, Defects and Microstructures: Modeling Across Scales*”, Cambridge University Press, Cambridge, UK. 2001. pp. 780.
- Kubin, L. P., Selinger, R. L., Bassani, J. L., and Cho, K. (editors), “*Multiscale Modeling of Materials – 2000*”, Proceeding of a symposium held Nov. 27 – Dec. 1, 2000, Boston, MA, Materials Research Society, Volume 653, 2001.
- Murayama, Y., “*Mesosopic Systems – Fundamentals and Applications*”, John Wiley & Sons, Inc. Chichester, United Kingdom, 2001.
- Ohno, K., Isfarjani, K., and Kawazoe, Y., “*Computational Materials Science – from Ab Initio to Monte Carlo Methods*”, Springer-Verlag, Berlin, Germany, 1999.
- Cronin, J. and O’Malley, R.E. (editors), “*Analyzing Multiscale Phenomena Using Singular Perturbation Methods*”, Proceedings of Symposia in Applied Mathematics, Volume 56, American Mathematical Society, 1999.
- Bulatov, Vasily, V., Diaz de la Rubia, T., Phillips, R., Kaxiras, E., and Ghoniem, N. (editors), “*Multiscale Modelling of Materials*”, Proceedings of a symposium held Nov. 30 – Dec. 3, 1998, Boston, MA, Materials Research Society, Volume 538, 1998.
- Raabe, D., “*Computational Materials Science – The Simulation of Materials Microstructures and Properties*”, Wiley-VCH Verlag GmbH. D-69469 Weinheim (Federal Republic of Germany), 1998.
- Golden, K.M., Grimmet, G.R., James, R.D., and Milton, G.W. (editors), “*Mathematics of Multiscale Materials*”, Springer-Verlag New York, Inc., 1998.
- Dahmen, W., Kurdilla, A.J., and Oswald, P. (editors), “*Multiscale Wavelet Methods for Partial Differential Equations (Wavelet Analysis and Its Applications, V. 6)*”, Academic Press, 1997.
- Hiller, J. R., Johnston, I. D., and Styer, D. F., “*Quantum Mechanics Simulations – The Consortium for Upper-Level Physics Software*”, John Wiley & Sons, Inc., New York, 1995.
- Rapaport, D., “*The Art of Molecular Dynamics Simulation*”, Cambridge University Press, Cambridge, United Kingdom, 1995.
- Cohen, A., “*Wavelets and Multiscale Signal Processing*”, CRC Press, 1995.

Journal Articles

- Needleman, A., and Van der Giessen, E., “*Micromechanics of Fracture: Connecting Physics to Engineering*”, MRS Bulletin, Materials Research Society, Volume 26, No 3, March 2001.
- Diaz de la Rubia, T. D., and Bulatov, V. V., (guest editors) “*Materials Research by Means of Multiscale Computer Simulation*”, MRS Bulletin, Materials Research Society, pp. 169 – 170, March 2001.
- Tolles, W. M., “*Self-Assembled Materials*”, Materials Challenges for the Next Century, MRS Bulletin, Materials Research Society, October 2000, pp. 36 – 38.
- Hafner, J., “*Atomic-Scale Computational Materials Science*”, Acta Materiala, Volume 48 (2000), pp. 71 – 92.
- Needleman, A., “*Computational Mechanics at the Mesoscale*”, Acta Materiala, Volume 48 (2000), pp. 105 – 124.
- Wild, A., “*Multi-discipline, Multi-scale modeling of Microsystems: An Overview*”, Proceeding of the IEEE International Caracas Conference on Devices, Circuits and Systems, ICCDCS, 2000, Piscataway, NJ, USA, pp. C110-1 – C110-5.
- Lemarchand, C., Chaboche, J. L., Devincere, B., and Kubin, L. P., “*Multiscale Modeling of Plastic Deformation*”, Journal de Physique IV, Proceedings of the 1998 3rd European Mechanics of Materials Conference on Mechanics and Multi—physics Processes in Solids: Experiments, Modeling, Applications (EUROMECH – MECAMAT ’98), Oxford, United Kingdom, 1999.

Websites

- “*Predicting Material Behavior from the Atomic Level Up*”, *Multiscale Modeling*
<http://www.llnl.gov/str/Moriarty.html>.
- “*Exploring the Fundamental Limits of Simulation*”
<http://www.llnl.gov/str/March01/Galli.htm>
- “*Multiscale Materials Modeling Presentations*”
<http://www.tc.cornell.edu/Research/Multiscale/Presentations/>
- “*Visual Quantum Mechanics*”
<http://phys.educ.ksu.edu/>

Concurrent Coupling of Length Scales

Noam Bernstein
Center for Computational Materials Science
Naval Research Laboratory, Washington, DC

CONCURRENT COUPLING OF LENGTH SCALES

This work on concurrent coupling of length scales was started by Farid Abraham at IBM Almaden and Jeremy Broughton (then at NRL), together with Prof. Tim Kaxiras at Harvard and myself. The work has been supported by the Office of Naval Research and the Naval Research Laboratory, and computer time was provided by the DOD HPCMO Challenge Program.

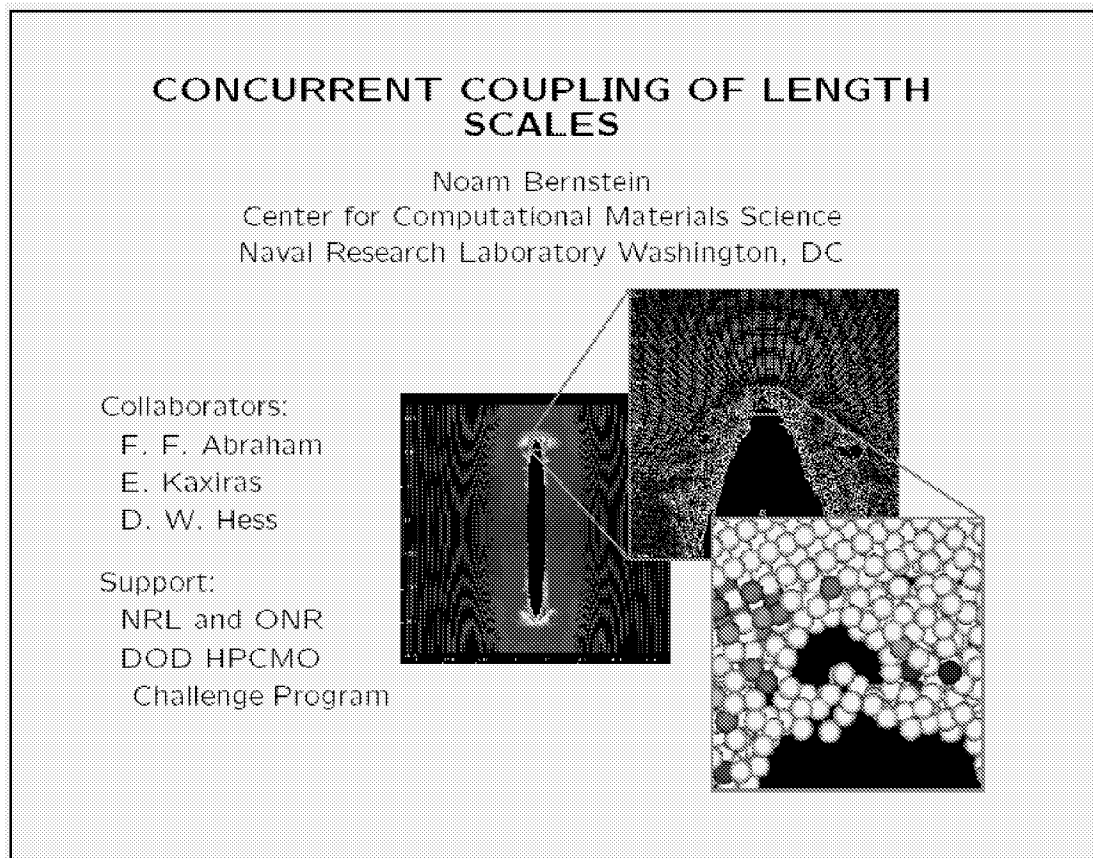


Figure 1

OVERVIEW

The talk begins with an overview of the coupling of length scales (CLS) concept. In particular, I discuss the differences between “sequential” and “concurrent” coupling of length scales approaches. After a brief introduction to the relevant issues in fracture, I describe our first approach to the CLS method. I describe the method we developed, and some results and lessons we learned from that work. I then describe our current CLS approach for simulating fracture. After presenting the method and results, I present some future directions and conclusions.

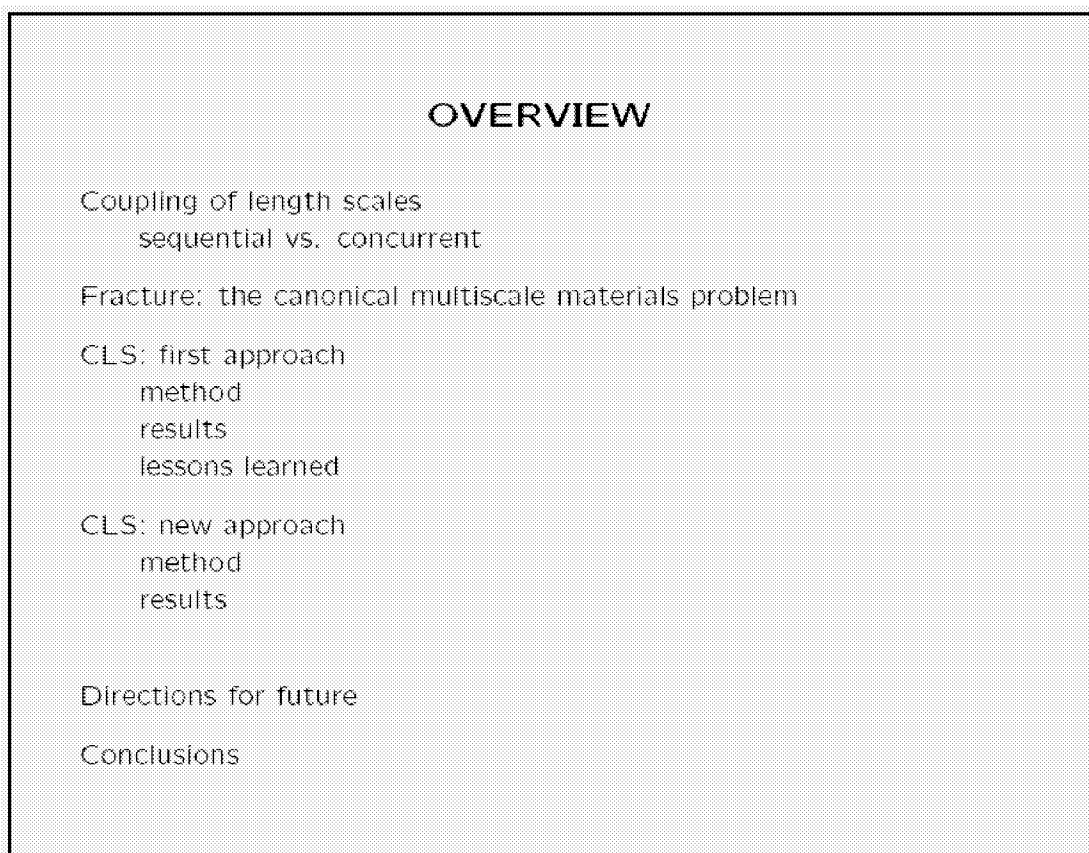


Figure 2

COUPLING OF LENGTH SCALES

Many material properties are controlled by processes that occur on a wide range of length scales. Each of these processes is most appropriately (accurately and efficiently) described by different physical models.

One prototypical example is fracture. On the shortest length scales there are a few hundred atoms near the crack tip where breaking of interatomic bonds is significant. For this region a classical description of the nuclei is sufficient, but the electrons should be described quantum-mechanically for the greatest accuracy. Farther from the crack tip there are tens of thousands of atoms where bonds are highly strained but not broken. In this region empirical potentials (EPs) do a good job of describing the interactions between the atoms. The elastic deformation that drives fracture can extend over much larger, macroscopic length scales, and in the vast majority of this region is very accurately and efficiently described by continuum mechanics.

How to best describe a system with all of these different processes and regions is still an open question.

COUPLING OF LENGTH SCALES

Material properties controlled by processes over many length scales
Different processes best described by different models

Example: fracture

- Short scale – 10^2 atoms
 - breaking atomic bonds
 - classical nuclei, quantum-mechanical bonds
- Medium scale – 10^4 atoms
 - highly strained bonds
 - classical nuclei, empirical interactions
- Long scale – 10^{23} atoms
 - elastic deformation
 - continuum mechanics

How can you treat all of these aspects?

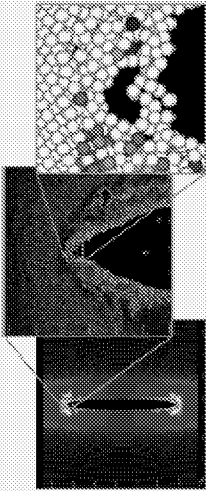


Figure 3

SEQUENTIAL COUPLING

Sequential coupling is an approach where an accurate method is used to simulate a number of configurations in a small system. From these simulations some parameters for a faster but more empirical method are extracted. One popular example is kinetic monte carlo for surface growth, where barriers to adatom motion can be computed with density-functional theory. Another is discrete dislocation dynamics, where the mobilities are computed using atomistic simulations.

In any implementation some general features are needed for the sequential approach to apply. One is a separation of time scales. If the essential events of the faster method occur on the same time scales as the details of the processes computed using the slower system, the two can't be separated. The other major requirement is that there exists a faster and more empirical theory to use, and that it has a reasonable number of parameters than can be practically computed using the more accurate method.

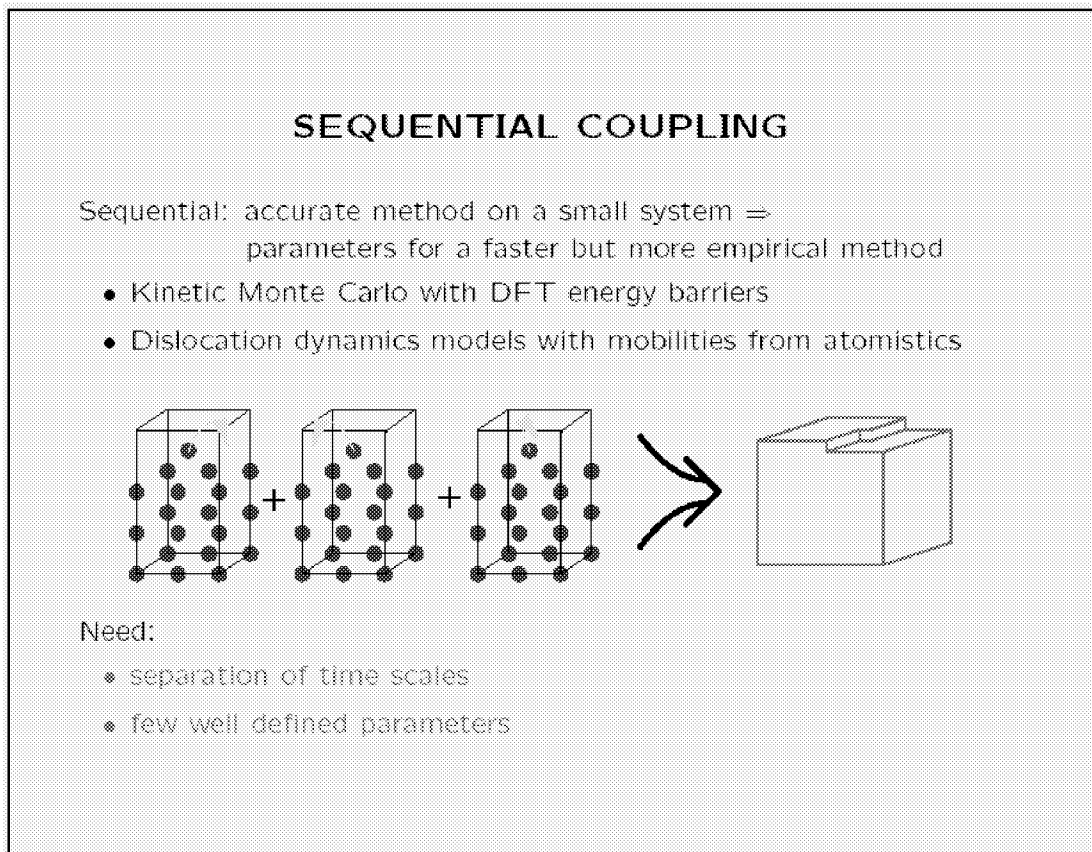


Figure 4

CONCURRENT COUPLING

An alternative to the sequential approach is concurrent coupling, where a large system is simulated using a fast method with limited applicability, and where needed a slower, more accurate method is used. Two good examples where this approach is important are fracture and friction. In fracture the crack tip bond breaking can be described with a quantum-mechanical model of bonding, while the rest of the sample is described with empirical potentials. In friction it might be necessary to describe surface-surface interaction using quantum-chemical approaches while using continuum elasticity to simulate the contact forces.

The essential requirement for the concurrent approach is that the slower method is only required to describe a localized region. The main importance of the concurrent approach is that it can be applied to dynamics, and to systems where the boundary conditions on the region that must be described accurately are changing with time. In these situations information is flowing in both directions between the regions described by the different methods. This makes it difficult to summarize the effect of one on the other in terms of a boundary conditions or a few parameters.

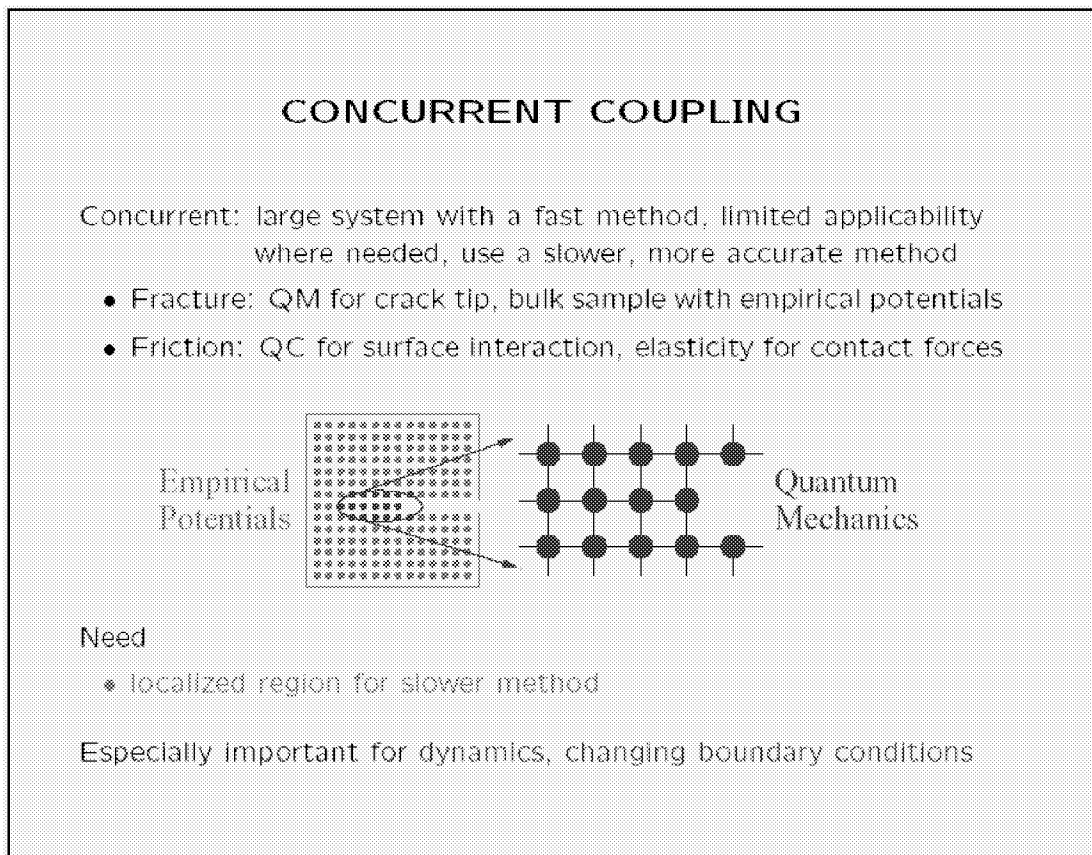


Figure 5

FRACTURE

Fracture is a phenomenon of great technological importance. It would be very useful to be able to predict fracture properties, ideal from first-principles. It would also be useful to be able to understand fracture properties well enough to control them. Fracture is also interesting for purely scientific reasons. Why is it that materials break in the way they do, some through brittle fracture, others through plasticity and ductile fracture?

Silicon in particular is an interesting example of the transition between brittle and ductile fracture. Over a few degrees temperature variation its stress to fracture changes by almost a factor of two.¹ For this reason it has become a model system for the brittle to ductile transition.

¹ P. B. Hirsch and S. G. Roberts, "The brittle-ductile transition in silicon," *Phil. Mag. A*, Vol. 64, 1991, pp. 55-80.

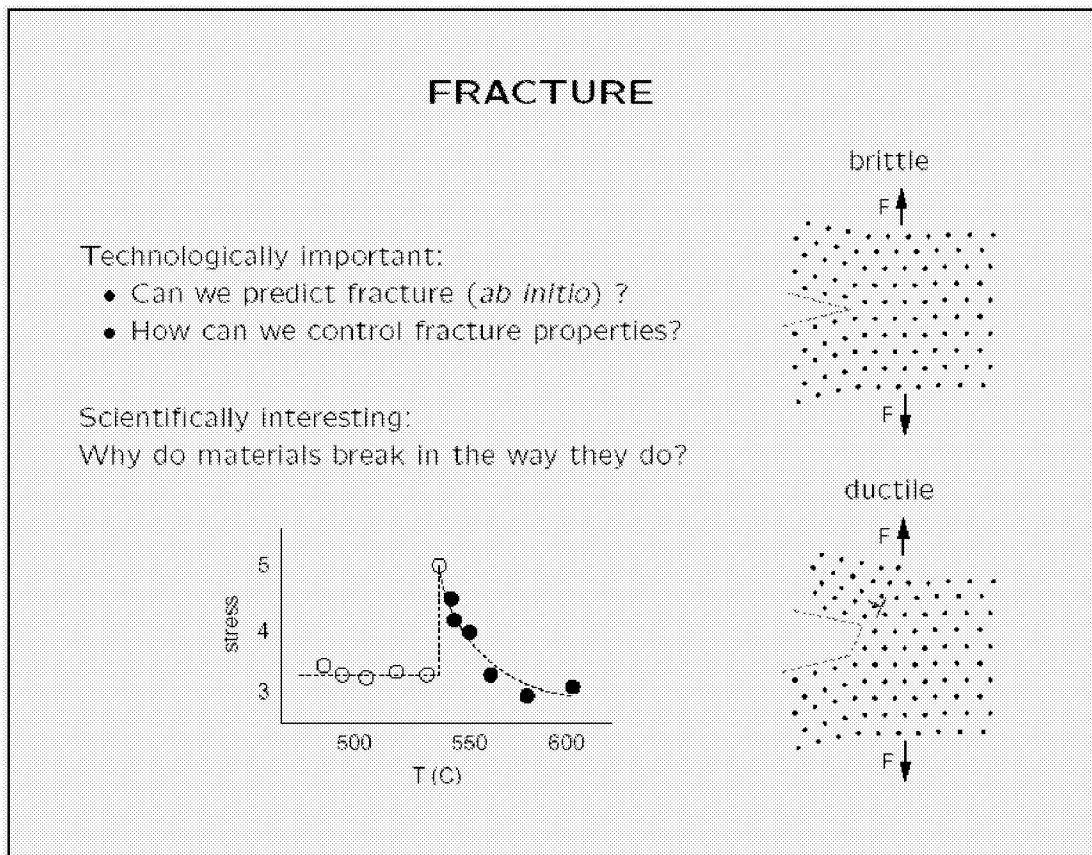


Figure 6

ORIGINAL CLS METHOD

The original CLS method^{2,3} used a well defined Hamiltonian to express the total energy of the system. This energy consisted of contributions from three regions: continuum elasticity, empirical potentials, and tight-binding (TB). The first was evaluated using 2-D finite elements. The second used the Stillinger- Weber (SW) interatomic potential for Si.⁴ The third used the Si TB model of Bernstein and Kaxiras⁵ with an approximate solution for the forces on the atoms. The dynamics for each region were advanced forward in time in sync.

² F. F. Abraham, J. Q. Broughton, N. Bernstein, and E. Kaxiras, "Spanning the continuum to quantum length scales in a dynamic simulation of brittle fracture," *Europhys. Lett.*, Vol. 44, 1998, pp. 783-787.

³ J. Q. Broughton, F. F. Abraham, N. Bernstein, and E. Kaxiras, "Concurrent coupling of length scales: Methodology and application," *Phys. Rev. B*, Vol. 60, 1999, pp. 2391-2403.

⁴ F. H. Stillinger and T. A. Weber, "Computer simulation of local order in condensed phases of silicon," *Phys. Rev. B*, Vol. 31, 1985, pp. 5262-5271.

⁵ N. Bernstein and E. Kaxiras, "Nonorthogonal tight-binding Hamiltonians for defects and interfaces in silicon," *Phys. Rev. B*, Vol. 56, 1997, pp. 10488-10496.

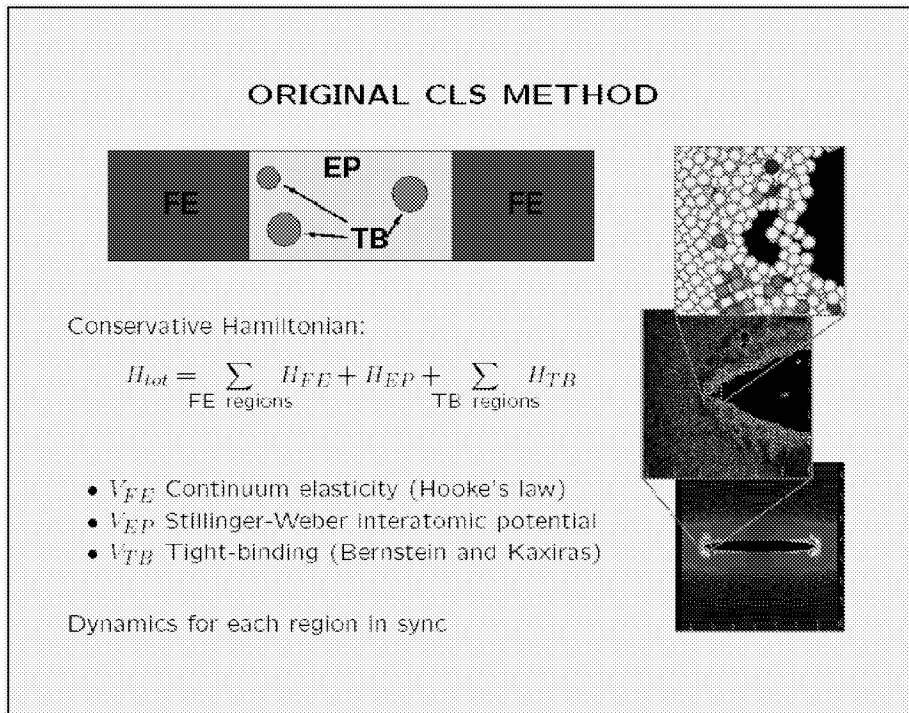


Figure 7

ORIGINAL CLS RESULTS

The picture shows a visualization of the crack tip after substantial propagation using the original CLS method without the tight-binding region. The whole sample is an 11 Å thick, periodically repeated system about 4000 Å by 3600 Å on a side. There are 1.5×10^6 empirical potential atoms, and another three 3×10^5 finite element nodes representing about 7.7×10^6 atoms.

In the image, color coded by the local energy of each atom, there are elastic waves emanating from the crack, as well as voids and amorphous tendrils near the crack. The amorphous tendrils are left behind rapidly propagating dislocations.

This type of morphology is indicative of fracture that is not at all brittle. The energy release rate, a measure of the elastic energy that's driving the fracture process is about 130 J/m^3 , many times larger than the experimental results of about 2.5 J/m^3 .⁷

⁷ J. A. Hauch, D. Holland, M. P. Marder, and H. L. Swinney, "Dynamic fracture in single crystal silicon," Phys. Rev. Lett., Vol. 82, 1999, pp. 3823-3826.

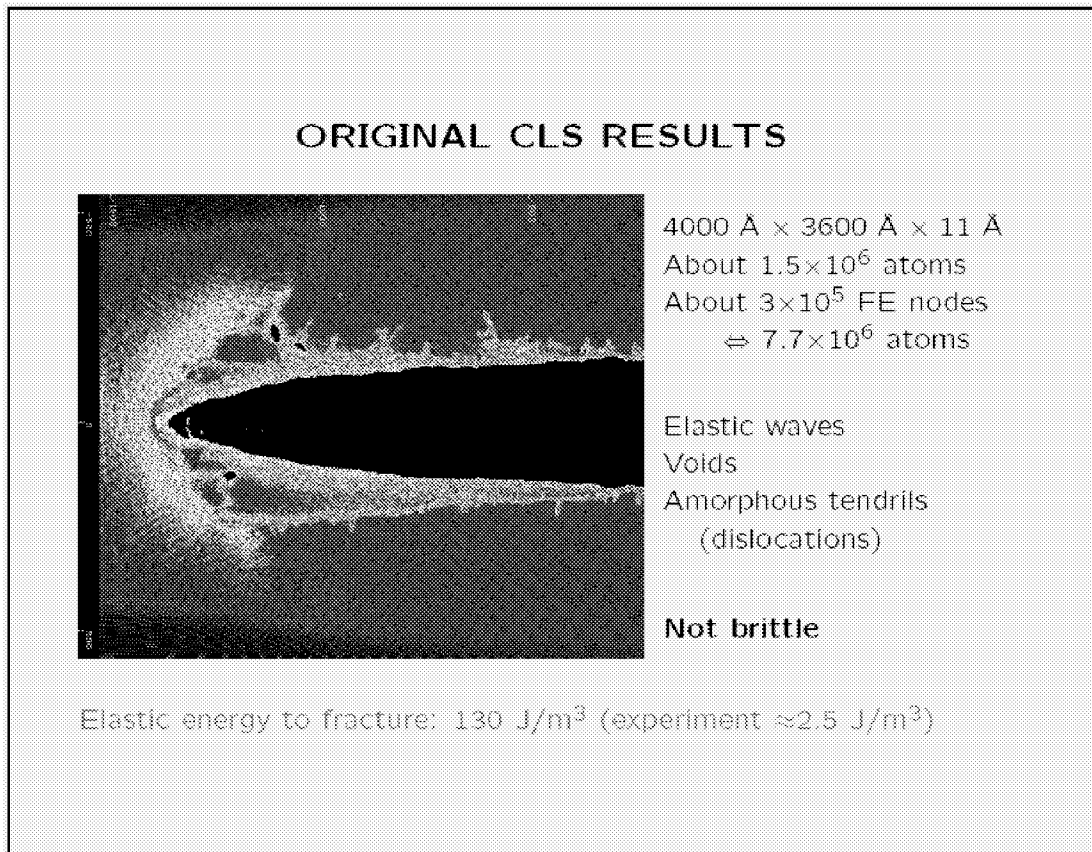


Figure 8

LESSONS FROM ORIGINAL CLS

The original CLS approach combined continuum mechanics, empirical potentials, and tight-binding. The results showed that the simulations were stable, and efficient enough to run for long times. However, the empirical potentials were not accurate enough to describe the bond breaking process, nor were the approximations used to evaluate the TB forces. There was also a wide range of relevant time scales between the finite element and tight-binding regions. One conclusion is that it may not be obvious *a priori* what will prove to be a sufficiently accurate method. The other is that the simulation duration is limited by the computational demands of the TB region.

A back-of-the-envelope estimate of the time scales is simple: The length of the run is limited by the most accurate method, TB, which take about 10 s for a 1 fs time step. One day of runtime is about 1000 time steps, or about 1 ps. There is a characteristic velocity, the speed of sound, which is of order 4 km/s, giving a length scale of about 40 Å. A region on this length scale can almost always be simulated efficiently enough atomistically, and the complications involved in coupling atomistics to continuum mechanics are not needed.

The inaccuracies in the approximations used for the TB, together with the separation of time scales, led us to modify the approach without finite elements and a more accurate solution of the TB forces.

LESSONS FROM ORIGINAL CLS

continuum mechanics, empirical potentials, tight binding

Results:

- Stable, long running simulations
- Empirical potential, tight-binding solution not accurate enough
- Wide range of time scales: FEM vs. TB

Conclusions:

- Sufficient accuracy may not be obvious *a priori*
- Simulation duration limited by TB region

Run is limited by most accurate method: TB 10 s/1 fs time step

1 day of simulation \approx 1000 time steps \approx 1 ps

Implied length scale $l = t \times v = 40 \text{ \AA}$

No FEM, improved TB

Figure 9

NEW CLS

The new concurrent CLS approach used only atomistic methods to calculate the forces on atoms, which were then used to do molecular dynamics (MD) simulations. Most of the atoms in the fracture system were described using the EDIP empirical potential.⁸

The TB region was described with the same model as before⁵, but the forces were evaluated using a different method.⁹ This method computed the single electron density matrix in real space by summing the Green's function at a number of complex energies. The complex energies are computed from the poles of an approximate Fermi function. One advantage to this method is that it is possible to compute the density matrix in a localized portion of a large system. Another is that using the sparsity of the TB model Hamiltonian and overlap matrices, one can compute a sparse Green's function matrix.

⁸ J. F. Justo, M. Z. Bazant, E. Kaxiras, V. V. Bulatov, and S. Yip, "Interatomic potential for silicon defects and disordered phases," Phys. Rev. B, Vol. 58, 1998, pp. 2539-2550.

⁹ N. Bernstein, "Linear scaling nonorthogonal tight-binding molecular dynamics for nonperiodic systems," N. Bernstein, Europhys. Lett., Vol. 55, 2001, pp. 52-58.

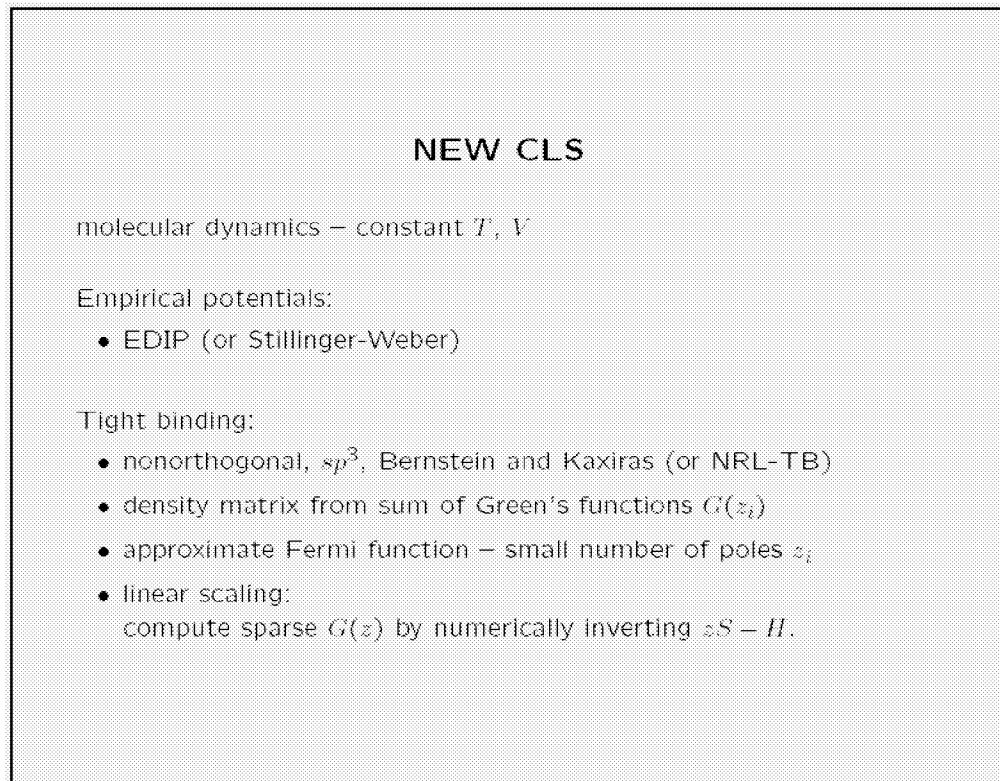


Figure 10

COUPLING AND TB

An essential ingredient in the coupling scheme is computing the Green's function, and therefore the density matrix, in a finite part of a larger system. To do this we compute the Green's function using iterative inversion, applying a constraint to the Green's function matrix elements at the boundary of the TB region.

The mechanical coupling between the two regions is achieved simply. The EP atoms are included in the EP calculation, and are subject to forces from the EP calculation. The TB atoms are included in the TB calculation, and are subject to forces from the TB calculation. The boundary atoms are included in both calculations, but are subject only to EP forces.

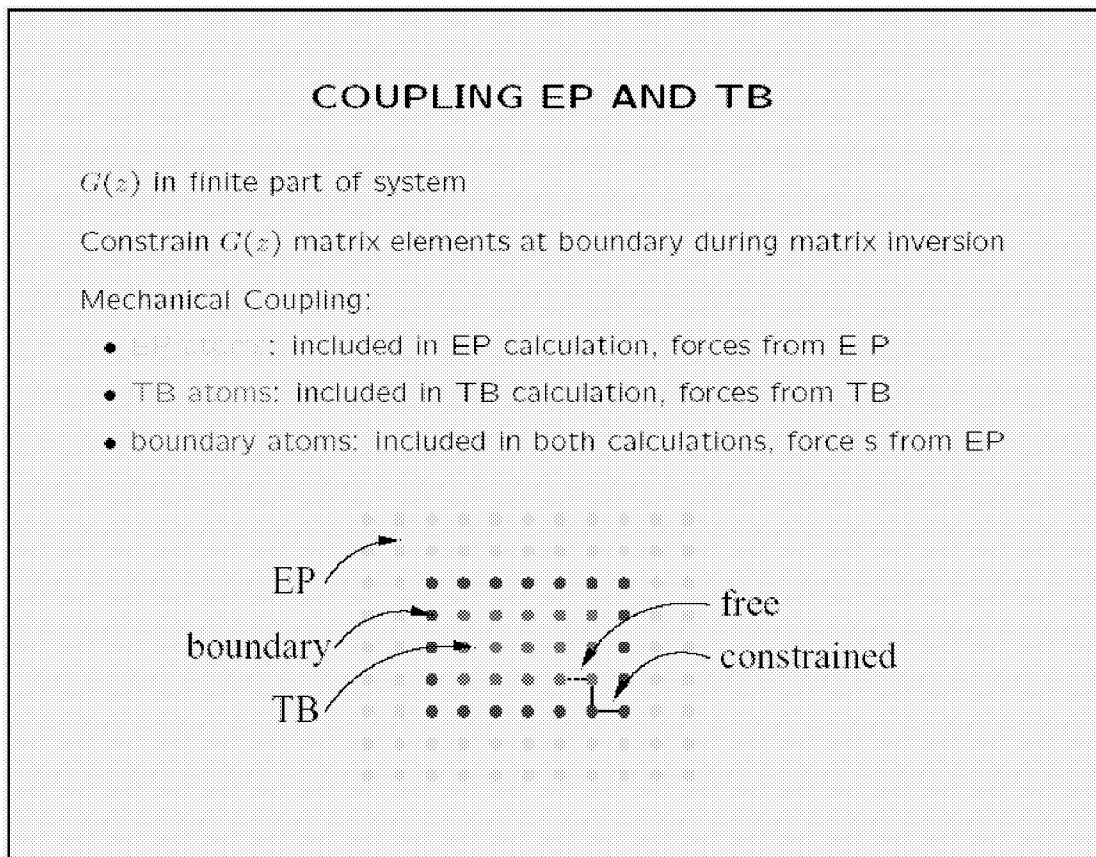


Figure 11

FRACTURE WITH TB

Using this approach, we simulated fracture in silicon coupling the EDIP empirical potential to the TB model of Bernstein and Kaxiras. A seed crack was created in the system, and the sample was loaded in tension (mode I) by moving the atoms along the displacement field for the continuum elasticity solution for a finite crack in an infinite plate.¹⁰ The entire system consists of about 5×10^4 atoms, with about 1000 atoms in the TB region. This results in a sample size of about 400 \AA by 250 \AA , in a 12 \AA thick, periodically repeated slab. The image below shows a 80 \AA by 65 \AA region around the crack tip.

¹⁰ K. B. Broberg, Cracks and Fracture, Academic Press, San Diego, 1999.

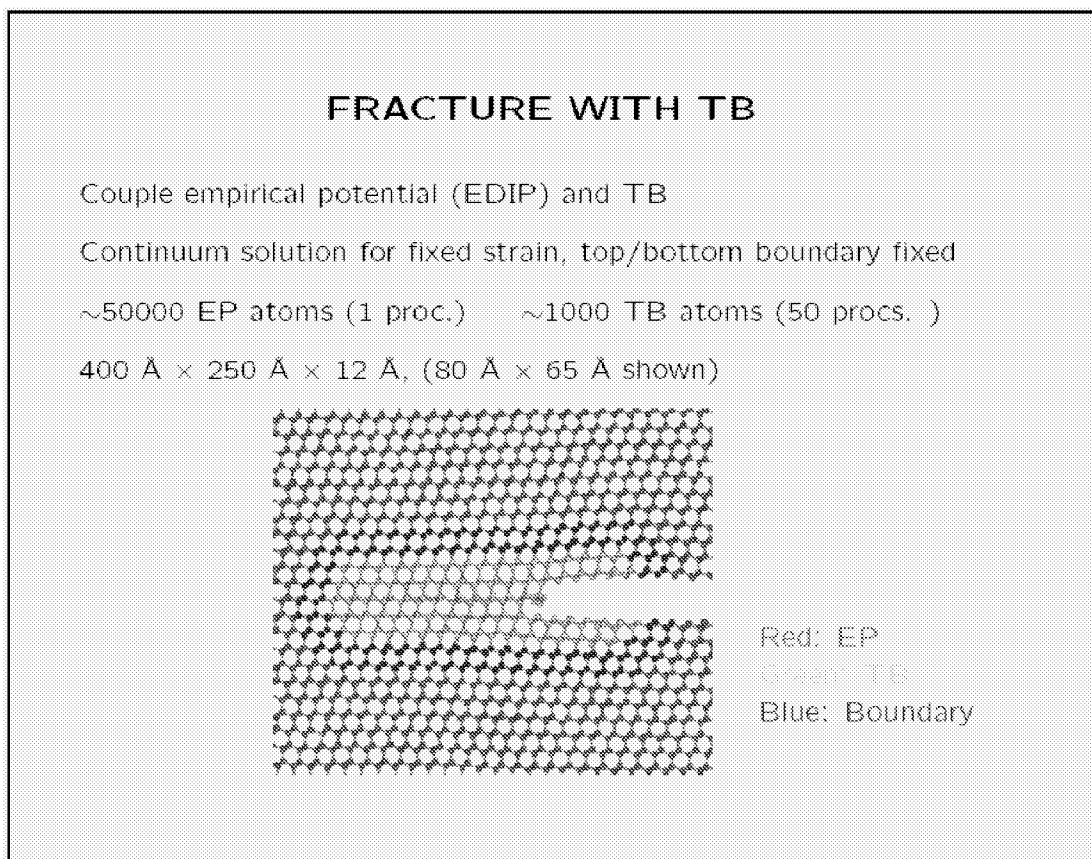


Figure 12

BRITTLE FRACTURE

The image on the left shows a visualization of the crack at the end of the MD simulation. The Si sample has failed through brittle fracture. The crack has propagated via interplanar cleavage, remaining atomically sharp and leaving behind a smooth crack face.

On the right is a plot of the crack speed as a function of loading, measure through the energy release rate G . The vertical line is the Griffith criterion, the point at which the elastic energy reduction due to crack propagation is exactly equal to the surface energy of the increased exposed surface. The blue line indicates the results of the present simulation, in very good agreement with the black dots representing the experimental results of Hauch *et al.*⁷ The red line approximates the results for the empirical potentials, which fracture only at much higher loadings than experiment or the new CLS approach.

The crack speed, which is about half of the Rayleigh wave speed, is similar in all sets of results.

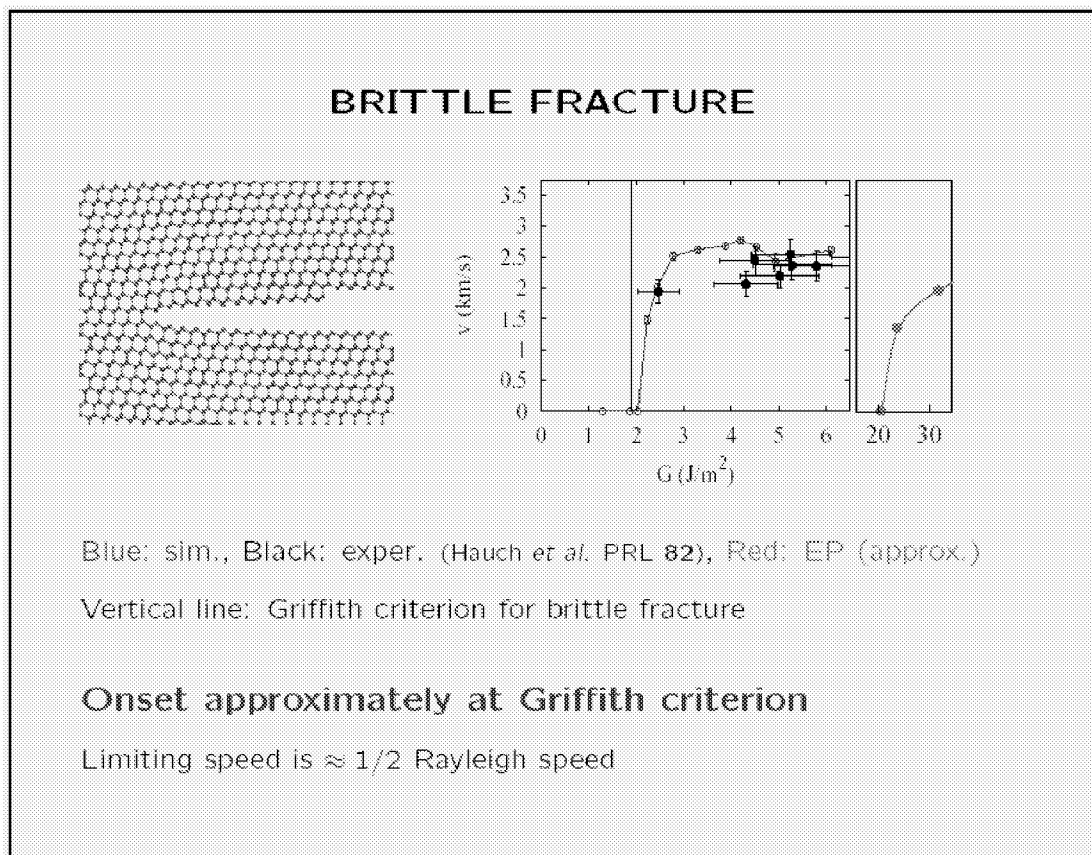


Figure 13

DISCUSSION

The results of the new CLS with an accurate calculation of the TB forces are clearly different from the EP results. However, it is unclear how the quantum-mechanical description of bonding makes a difference - what are the relevant fundamental material parameters that are different in the two descriptions?

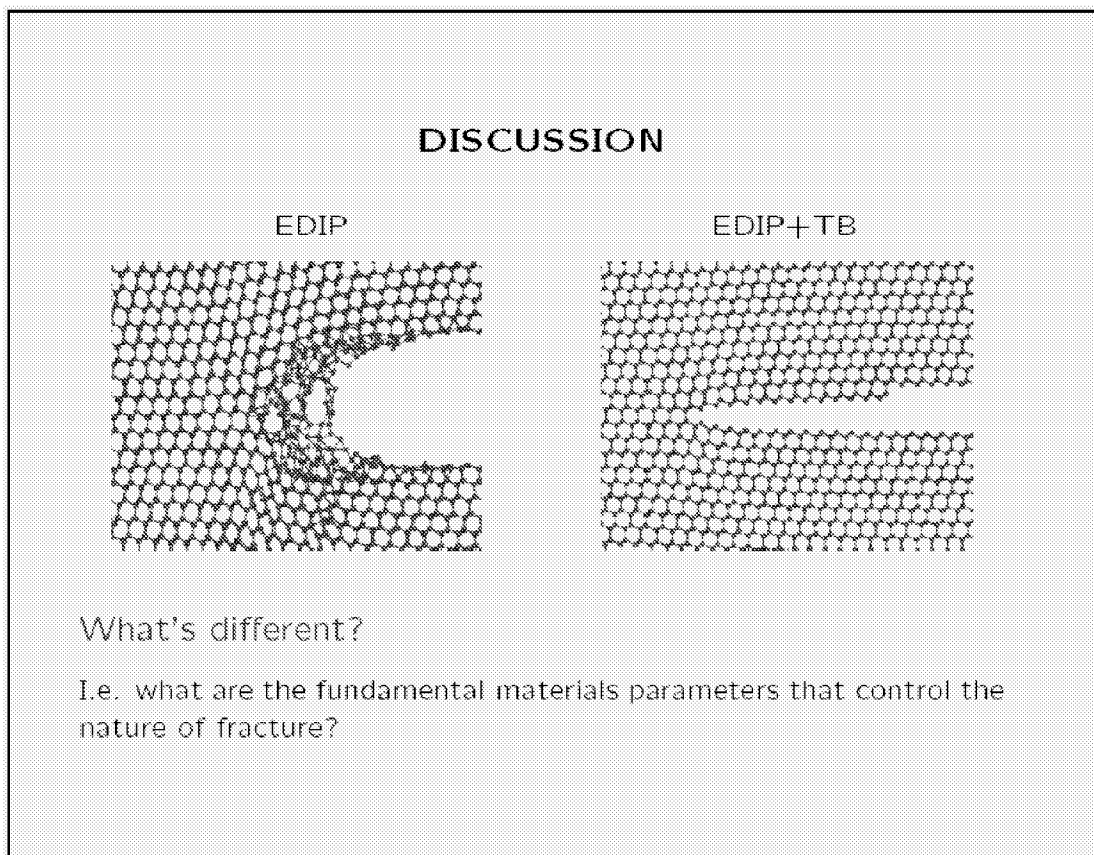


Figure 14

ENERGIES

One important class of approaches for predicting the fracture properties of a material is based on energetics. For example, the Rice criterion makes a quantitative prediction about whether a material will be brittle or ductile based on the ratio between the surface energy and the unstable stacking fault energy, which is the energy barrier to nucleating or propagating a dislocation.¹¹

However, a comparison of this ratio for density-functional theory,¹² the TB model used here, and the two empirical potentials,⁸ does not show a systematic difference between the TB model and both of the EP models. Apparently the Rice criterion does not provide a good explanation for the differences between the EP simulation and the CLS method using the TB model.

¹¹ J. R. Rice, "Dislocation nucleation from a crack tip: an analysis based on the Peierls concept", *J. Mech. Phys. Solids*, Vol. 40, 1992, pp. 239-271.

¹² E. Kaxiras and M. S. Duesbery, "Free energies of generalized stacking faults in Si and implications for the brittle-ductile transition," *Phys. Rev. Lett.*, Vol. 70, 1993, pp. 3752-3755.

ENERGIES ...				
Energetics (Rice criterion): Compare				
• γ_s surface energy : make new crack surface				
• γ_{us} unstable stacking fault energy : make dislocations				
	LDA	BK-TB	EDIP	SW
c_{11}	166	145	175	162
c_{12}	63.3	84.5	65	82
c_{44}	79.3	53.4	71	60
γ_s (111) Ideal	1.7	1.0	1.1	1.4
γ_{us} glide relaxed	1.9	2.5	1.9	3.1
γ_{us} shuffle relaxed	1.7	1.1	1.3	0.8
γ_s/γ_{us} (glide)	0.90	0.40	0.59	0.45
γ_s/γ_{us} (shuffle)	1.02	0.90	0.85	1.71
Apparently not Rice criterion				
(LDA from Kaxiras and Duesbery, EDIP and SW from Justo et al.)				

Figure 15

... VS. FORCES

An alternative to energy criteria is a criterion based on forces, independently proposed in various forms by Abraham and Marder.

Forces depend on the way energy varies over a displacement distance. For dislocations, the distance is set by the lattice constant, which is the same for all reasonable models of a given material. For surfaces, on the other hand, the distance is set by two factors. In reality it is set by the physics of bonding. Any model of bonding makes some approximations that can greatly change this range. For example, first-principles methods in general involve much longer range interactions than empirical potentials, especially for covalently bonded materials such as Si.

Since the surface energies for all the models are reasonable, the range of interaction ranges in the different models can greatly vary the forces that atoms feel as two surfaces are pulled apart.

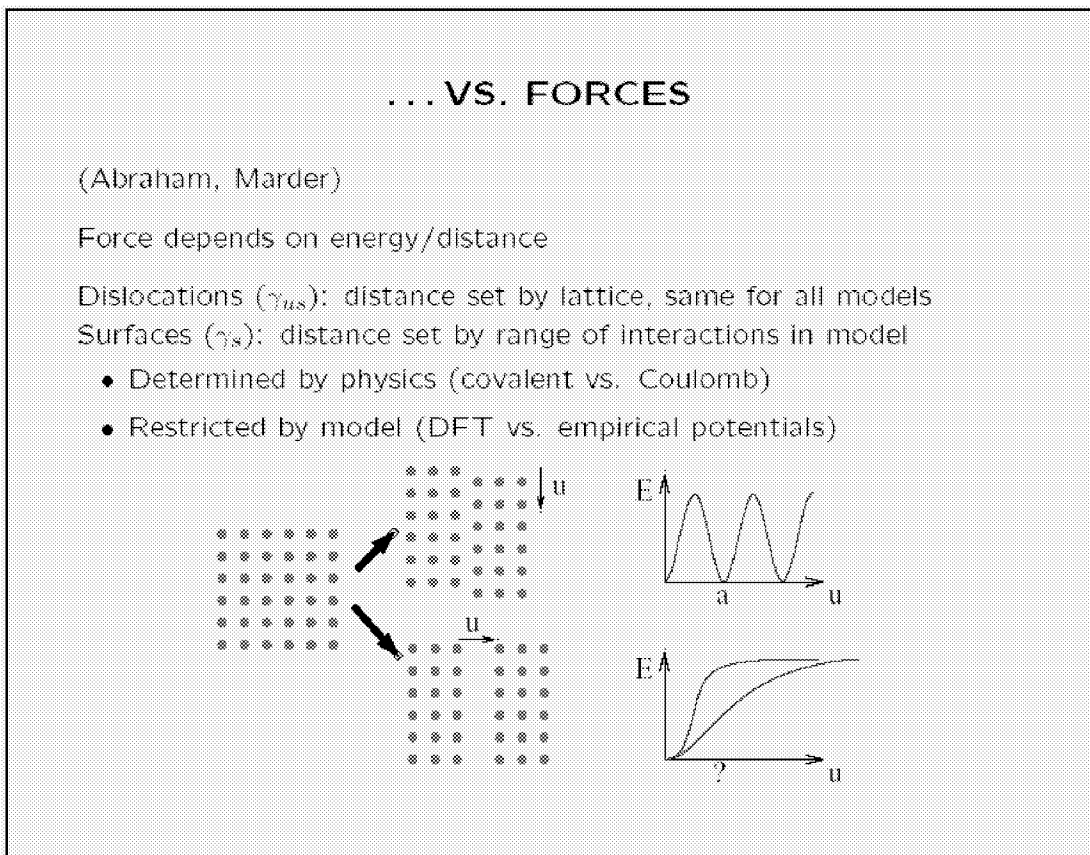


Figure 16

RANGE: ENERGIES VS. FORCES

The plot on the left is the energy required to rigidly pull apart two slabs of material as a function of the distance between them. This energy is normalized by the relevant comparable dislocation related energy, the unstable stacking fault energy. The plot on the right is the derivative of the energy as a function of distance, normalized by the Peierls stress which is the maximum derivative of the unstable stacking fault energy path.

While the difference in ranges between the first-principles LDA, TB, and EP calculations is apparent, it does not show any systematic variations. The maximum force for the TB model is comparable to that of EDIP, and in fact much lower than for SW. If this force criterion were applicable, the TB simulation would look at least qualitatively like EDIP and unlike this is not the case, this type of force based criterion does not explain the differences either.

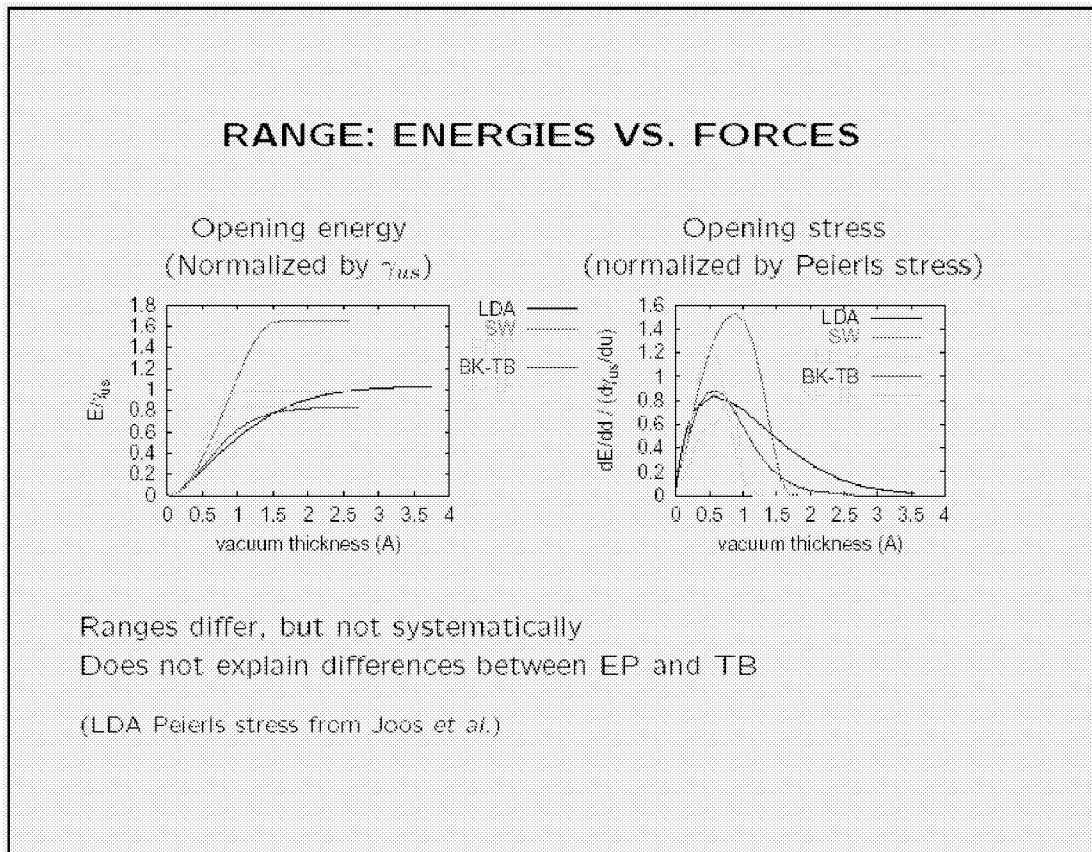


Figure 17

WHAT IS CAUSING THE DIFFERENCE?

Energetics does not seem to explain the differences between the CLS and EP simulations, since the Rice criterion gives comparable ductility values for both.

One important observation is that at a range of stresses above the Griffith criterion, where it is energetically favorable to fracture, the EP crack does not propagate, but the CLS crack does. This implies that lattice trapping from some source is important in the EP simulation. However, the stresses in the TB model (as computed by rigidly pulling apart two slabs) are comparable to those in the EP models. Therefore, something must be reducing the stresses needed to break a bond at the crack tip in the TB calculation.

There are several possible sources for such weakening, including non-local effects and coupling between different strain components at the crack tip.

WHAT IS CAUSING THE DIFFERENCE?

Energetics: NO
Rice criterion comparable

Just above Griffith criterion:
EP crack won't propagate
TB crack will

Stress induced lattice trapping: MAYBE
Stresses in TB and EP comparable
Even short-range TB (with higher decohesion stress) is brittle

Hypothesis:
decohesion stresses at crack tip are weakened in TB calculations

Several possibilities: non-local effects, coupling

Figure 18

WEAKENING: NON-LOCAL EFFECTS

The Rice criterion (and its stress analog) are local. They assume that the relevant energies can be measured by creating the entire surface at once. However, in the real crack, a half surface is already present. It is possible that the broken bonds to the right of the crack tip weaken the bonds ahead of the crack tip.

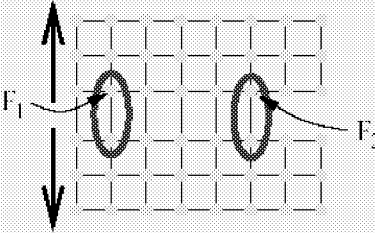
To measure this effect we created a penny crack in an otherwise ideal Si crystal, and rigidly pulled apart the two slabs. We monitored the forces on the atoms adjacent to the crack tip, and compared them with the forces on atoms in the bulk, far from the crack tip. In the EP calculations the forces on these two atoms were identical. Using TB the crack tip bond was indeed weakened. The difference in the peak forces between the crack-tip bond and the bulk bond was only about 2%, too small to explain the qualitative differences between the EP and CLS fracture simulation results.

Other possible hypotheses for the reduced lattice trapping in the CLS simulations are currently being investigated.

WEAKENING: NON-LOCAL EFFECTS

Rice criterion (and stress analog): "local" \Rightarrow
Assume entire surface is formed at the same time, but . . .
In crack, half surface is already present

Do adjacent broken bonds weaken bonds ahead of crack tip?



Create penny crack, pull apart slabs, monitor forces on surface atoms

EP: peak forces are identical
TB: Force on crack-tip-bond atom weaker by $< 2\%$

Figure 19

CLS METHOD – FUTURE DIRECTIONS

There are a number of limitations in the current implementation of the CLS approach coupling an empirical potential to a tight-binding description of a system. The first is that the code is limited to single component systems. The second is that Coulomb interactions due to the movement of electrons in the system are not included.

We are planning a number of improvements to the code to address these issues. These include the extension to multicomponent systems, making it possible to study more complex, technologically relevant materials. Another is charge self-consistency, which will be even more important for heteroatomic systems where bonds are partially ionic. The last improvement is for full scalability of both the EP and TB region calculations on parallel computers, making it possible to study larger systems.

The code is being developed and will be released through the DOD HPC CHSSI program.

CLS METHOD – FUTURE DIRECTIONS

Limitations in current implementation:

- Single component systems
- No charge self-consistency

Planned improvements:

- Multicomponent systems
more complex materials
- Charge self-consistency
more complex materials
- Full scalability (EP, QM regions)
larger systems

CHSSI - DOD High Performance Computing software development project

Figure 20

FUTURE APPLICATIONS

Using some of these improvements, we are planning to use the CLS approach to study structural and mechanical properties. Planned applications include high strain-rate plastic deformation, as well as additional study of fracture. We hope to be able to simulate more complex, technologically relevant systems including other brittle insulators, e.g. semiconductors used for micro-electromechanical systems (MEMS) construction such as SiC and diamond, as well as high-toughness ceramic coatings. Although there are some technical challenges, we will also explore the application of this method to fracture in metals. Another field of application is friction and stiction, which are often the limiting factor for MEMS devices. Central to these phenomena is the interaction between surface chemistry and the mechanical loading.

FUTURE APPLICATIONS

Structural, mechanical properties:

High strain rate plastic deformation

Fracture in more complex, technologically relevant systems

- Other brittle insulators
 - MEMS semiconductors (Si, SiC, diamond)
 - high-toughness coatings: ceramics
- Metals?

Friction and stiction: (NSF NIRT – JHU, Naval Academy)

- Big limitation for MEMS
- Interaction between surface chemistry and mechanical loading

Figure 21

CONCLUSIONS

The concurrent coupling of length scales approach simulates a large system with a fast method with limited applicability, and where needed using a slower but more accurate method. The essential requirement for this approach is that the region where the slower method is needed be localized.

The approach is most useful where there is no separation of time scales between the processes in the two regions. This leads to an interplay in dynamics between the two regions, making it impractical to compute the changing boundary conditions on the two regions *a priori*.

The benefits of the approach are a combination of accuracy and speed.

CONCLUSIONS

Concurrent coupling of length scales:
large system with a fast method, limited applicability
where needed, use a slower, more accurate method

Requirement: localized region for slower method

Most useful when:

- Not much separation of time scales
- interplay in dynamics between regions
boundary conditions on inner region changing,
too complex to be computed ahead of time

Benefits: combination of accuracy and speed

Figure 22

**The Future of Computational Materials Science:
The Role of Atomistics**

Michael I. Baskes
Los Alamos National Laboratory
Los Alamos, NM

OUTLINE

This talk will start with a tutorial on computational methods and techniques. Two examples of atomistic calculations will be presented: mechanical properties and phase transformations. The author's view of the future of computational materials science will be presented.

**THE FUTURE OF COMPUTATIONAL
MATERIALS SCIENCE:
THE ROLE OF ATOMISTICS**

**M. I. BASKES
LOS ALAMOS NATIONAL LABORATORY**

Methods
Techniques
Examples
 mechanical properties
 phase transformations
Future



Figure 1

METHODS USED DEPEND ON THE ENTITY BEING MODELED

The concept of *entity* is introduced. Each entity is connected to a specific method that may be used for calculations involving that entity. This talk will concentrate on semi-empirical methods. These methods have a basis in physics or chemistry, but use experimental data.

<u>Method</u>	<u>Entity</u>	<u>Examples</u>
first principles	electron	density functional theory (DFT) quantum chemistry (QC)
semi-empirical	atom	embedded atom method (EAM) modified EAM (MEAM) N-body, glue
empirical	atom, grain, dislocation	Lennard-Jones (LJ), Potts dislocation dynamics (DD)
phenomenological	continuum field	Ficks Law elasticity/plasticity

Figure 2

ATOMISTIC MODELS HAVE TWO PURPOSES (I)

There are two clear purposes for performing calculations at the atomic level. The first purpose is to obtain quantitative properties of specific materials for use in models using higher level entities. Examples are given for first principles and semi-empirical methods.

ATOMISTIC MODELS HAVE TWO PURPOSES (I)

- **Obtain quantitative properties of specific materials**
 - **First principles**
 - **lattice constant**
 - **structural stability**
 - **elastic modulus**
 - **Semi-empirical potentials (fit to experimental data)**
 - **thermal expansion**
 - **melting point**
 - **yield strength**



Figure 3

ATOMISTIC MODELS HAVE TWO PURPOSES (II)

The second and equally important purpose of atomistic modeling is to obtain understanding of physical processes. Examples are given for empirical, semi-empirical, and first-principles methods.

ATOMISTIC MODELS HAVE TWO PURPOSES (II)

- Obtain understanding of physical processes
 - Model system (empirical) potentials
 - how specific properties affect collective behavior
 - dependence of yield strength on stacking fault energy
 - Semi-empirical potentials (fit to experimental data)
 - plasticity
 - phase transformations
 - First principles
 - diffusion



Figure 4

WE USED THREE WORKHORSE TECHNIQUES

Techniques for atomistic calculations are presented. The requirements and output for each technique are summarized.

WE USE THREE WORKHORSE TECHNIQUES

- **Molecular statics**
 - Requires total energy as a function of all atom positions
 - Convenient to also have forces
 - Yields minimum energy configuration
- **Molecular dynamics**
 - Requires force on each atom as a function of all atom positions
 - Follows the atomic motion (vibrations) using Newton's second law
- **Monte Carlo**
 - Requires total energy as a function of all atom positions
 - Yields a catalog of the most probable atomic configurations



Figure 5

WHAT MOLECULAR STATICS GIVES YOU

The detailed information about what can be obtained from a molecular statics or energy minimization calculation is presented.

WHAT MOLECULAR STATICS GIVES YOU

- Structural Energies
- Defect Formation Energies
- Saddle Point Energies
- Defect Geometries
- Elastic Constants (0 K)



Figure 6

WHAT MOLECULAR DYNAMICS GIVES YOU

The detailed information about what can be obtained from a molecular dynamics calculation is presented. Note that mechanisms and temperature dependent properties are obtainable.

WHAT MOLECULAR DYNAMICS GIVES YOU

- Mechanisms
- Reaction Rates
- Diffusion Rates
- Interface Mobility
- Elastic Constants (T)
- Thermal Expansion
- Thermodynamics

Figure 7

WHAT MONTE CARLO GIVES YOU

The detailed information about what can be obtained from a Monte Carlo calculation is presented. Note that equilibrium properties are obtainable.

WHAT MONTE CARLO GIVES YOU

- Equilibrium at Temperature
 - positions
 - composition
- Thermal Expansion
- Thermodynamics

Figure 8

LIMITATIONS OF COMPUTATIONAL MATERIALS SCIENCE

There are severe limitations in what computational materials science can do. Most important is our lack of information about underlying physical mechanisms.

LIMITATIONS OF COMPUTATIONAL MATERIALS SCIENCE

- Lack of understanding of underlying mechanisms
 - mechanical properties
 - phase transformations
- Inability to query long enough times
 - processing - development of microstructure
 - properties - realistic strain rates
- Inability to process large enough samples
 - boundary conditions
 - microstructure
- Inadequate potential interactions
 - multi-components

NISA

 **Los Alamos**

Figure 9

WE CAN USE ATOMISTIC CALCULATIONS TO HELP UNDERSTAND MECHANICAL BEHAVIOR

We choose mechanical behavior as an example of atomistic calculations. The calculations will be used to investigate the strain gradient mechanism in plasticity.

WE CAN USE ATOMISTIC CALCULATIONS TO HELP UNDERSTAND MECHANICAL BEHAVIOR

- Classical materials science, physics, and mechanical engineering postulate that mechanical properties do not depend upon sample size
- Recent experiments (torsion, indentation, bending) have shown that this postulate breaks down for small size samples
- This behavior has been explained by postulating the importance of strain gradients
- Atomistic calculations can investigate the “real” size mechanism

NISA

 **Los Alamos**

Figure 10

RECENT EXPERIMENTS SUGGEST A LENGTH SCALE IS INHERENT IN PLASTICITY

Conventional theory = elasticity or plasticity theory. Experiments are torsion of small wires by Fleck and Hutchinson, indentation by, McElhaney, interfacial force microscopy (very fine scale indentation) by Houston et al. Large scale calculations were performed at Sandia.

RECENT EXPERIMENTS SUGGEST A LENGTH SCALE IS INHERENT IN PLASTICITY

- **Conventional theory predicts that yield stress is independent of sample size (no inherent length scale)**
- **Recent experiments show that yield stress depends on sample size**
- **Molecular dynamics (MD) using the Embedded Atom Method will be used to investigate shear deformation in nickel**
- **Calculations are performed using 100 to 100 million atoms**

NISA

 **Los Alamos**

Figure 11

YIELD STRESSES BECOMES INDEPENDENT OF STRAIN RATE AT SMALL STRAIN RATES

We show the yield stress normalized by the shear modulus vs. the strain rate. Note that the strain rates accessible in mMD are very large. The points represent the results of the MD calculations at various wire sizes indicated on the figure. The aspect ratio of the wire was held fixed at 2:1. The data shows that the yield stress becomes independent of strain rate for “low” strain rates. A simple inertial dislocation model is able to qualitatively describe this data. From the atom positions, we determine that the yield process is controlled by dislocation nucleation from the free (x-direction) surfaces.

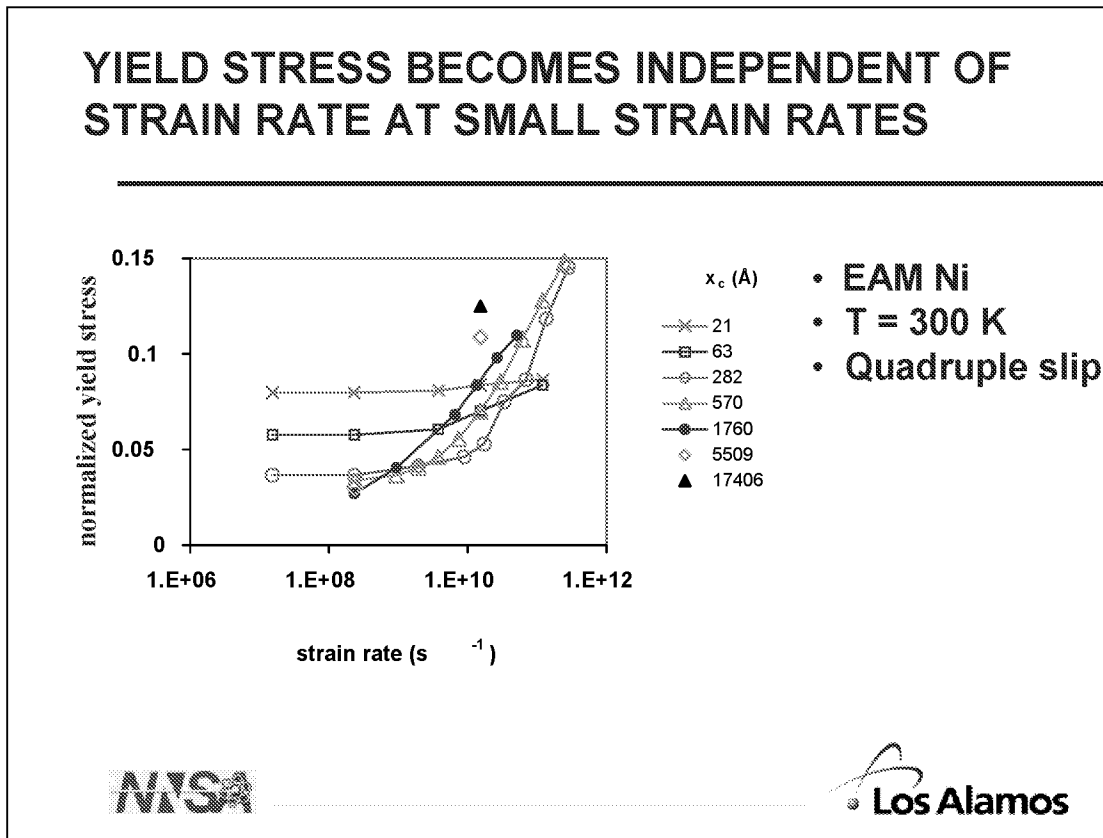


Figure 13

YIELD STRESS IS PRIMARILY DETERMINED BY SAMPLE SIZE

Using the results of the MD simulations at the lowest strain rates, the shear stress, normalized by the shear modulus as resolved on the slip plane of maximum stress is plotted vs. a characteristic size, the volume to surface ratio. Also shown are the results of numerous experiments: interfacial force microscopy (IFM), indentation, and torsion. All of the data falls on an approximate straight line showing power law dependence of the yield stress on size.

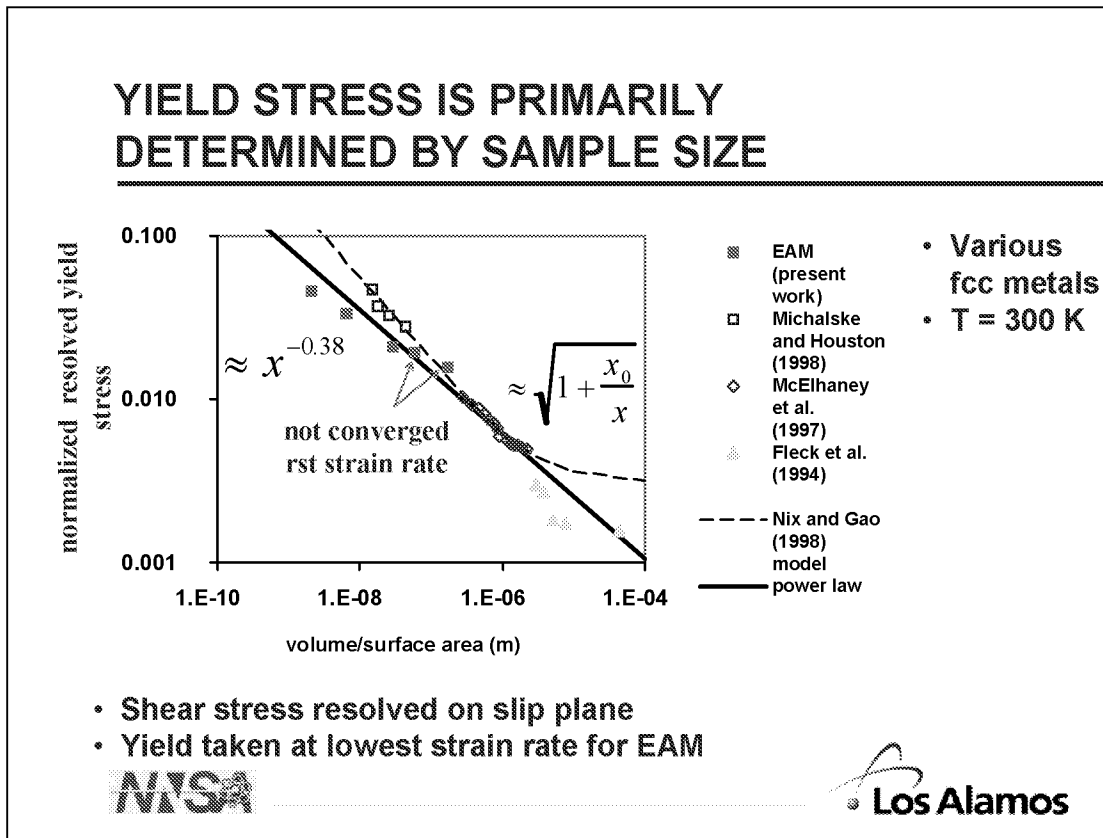


Figure 14

FACTORS THAT INFLUENCE THE YIELD STRENGTH IN FCC METALS

The calculations presented above plus numerous other calculations lead us the following summary of factors that influence the yield strength in fcc materials. Geometry effects, specifically size, are seen to be most important. Test conditions and material properties have a smaller effect.

FACTORS THAT INFLUENCE THE YIELD STRENGTH IN FCC METALS			
	<u>Factor</u>	<u>Extent</u>	<u>Dependence</u>
Geometry	Sample size	1000	$x^{-0.4}$
	Aspect ratio	10	independent (> 4)
	Orientation	4	resolved stress
Test conditions	Strain rate	10	independent (< $\epsilon_c(x)$)
	Temperature	1.2	-
Material	Shear modulus	10	proportional to μ
	Initial Dislocation density	10	-




Figure 15

WHAT WE HAVE LEARNED ABOUT PLASTICITY MECHANISMS

We may summarize what we have learned about plasticity from the MD calculations. In these small samples yield is determined by dislocation emission, not dislocation pileup as is commonly assumed. Deformation is found to be quite inhomogeneous even when a uniform strain is imposed. Finally we see a strong sample size dependence on the yield stress even in the absence of an externally applied strain gradient. These results force us to seriously question the strain gradient models in the literature.

WHAT WE HAVE LEARNED ABOUT PLASTICITY MECHANISMS

- **Yield depends on sample size even in the absence of an applied strain gradient**
- **Inhomogeneous deformation is the rule, not the exception**
- **Strain rates in the inertial regime are important**
- **The yield mechanism is dislocation emission (at least in small samples) - not dislocation pileup**

NISA

 **Los Alamos**

Figure 16

WHAT WE HAVEN'T LEARNED ABOUT PLASTICITY

Unfortunately MD atomistic calculations are not able to answer many questions of plasticity. These questions point out the clear need for modeling with different entities at large length scales.

WHAT WE HAVEN'T LEARNED ABOUT PLASTICITY

- What happens at low (realistic) strain rates
 - Other mechanisms, e.g. climb
- Hardening
 - Restricted geometry (sample size)
- Cell/microstructure formation
 - Limited sample size
- Alloying additions

NISA

 Los Alamos

Figure 17

WE CAN USE ATOMISTIC CALCULATIONS TO HELP DESIGN NEW MATERIALS

Our second example of atomistic calculations is in the area of material design.

WE CAN USE ATOMISTIC CALCULATIONS TO HELP DESIGN NEW MATERIALS

- **Pb-based solder has long been the workhorse of the electronics industry**
- **We now recognize the deleterious effects of Pb on the environment**
- **A major thrust has been initiated to replace Pb-based solder with a Sn alloy**
- **Atomistic calculations can predict properties of Sn alloys that are difficult to measure**

NISA

 **Los Alamos**

Figure 18

GEOMETRY FOR REACTIVE WETTING CALCULATIONS

The left figure shows a side view of a Cu substrate with a periodic array of small liquid Sn drops impinging on the surface. The right figure shows a top view of the sample. Modified Embedded Atom Method (MEAM) potentials are used to describe the interactions at the atomic level. These potentials describe the properties of Cu, Sn, and Cu/Sn alloys quite well.

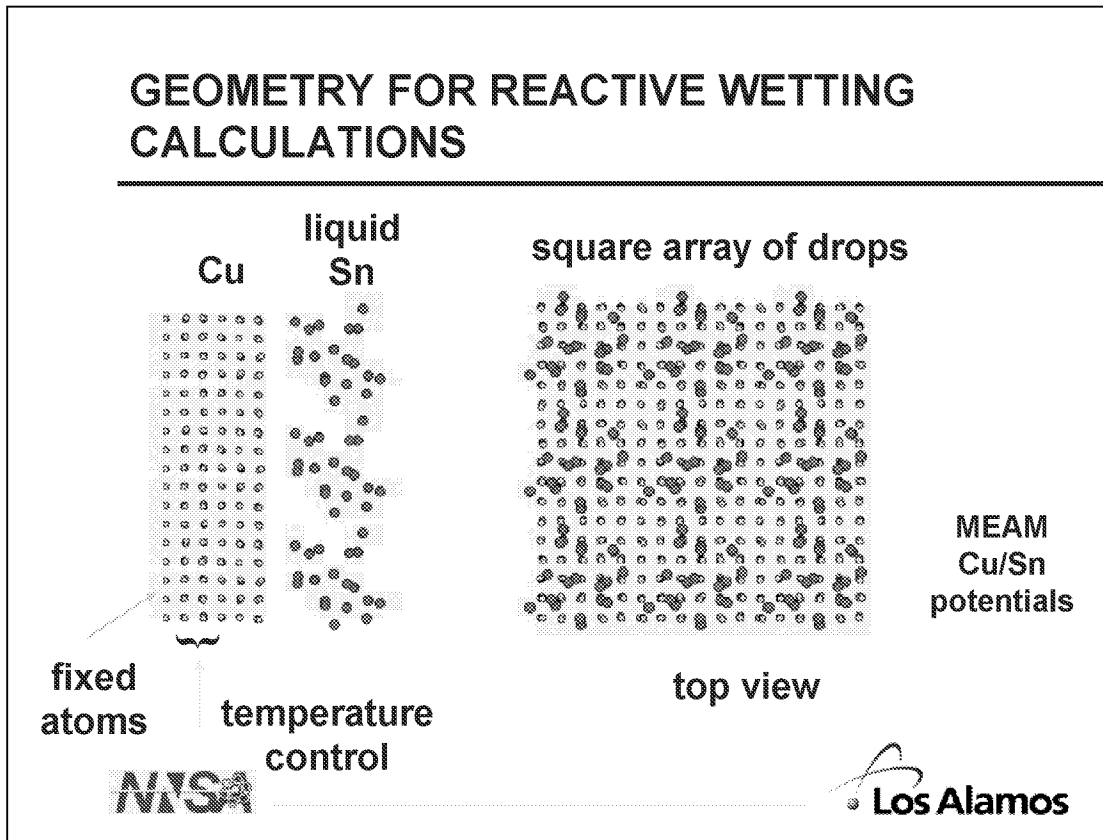


Figure 19

TIN REACTS WITH THE Cu SURFACE AT HIGH TEMPERATURE

Using MD calculations, we see that at 700 K the Sn forms an ordered overlayer on the Cu (100) surface. At 800 K the Sn reacts with the Cu leading to a mixed layer. Experiment shows reaction at much lower temperatures.

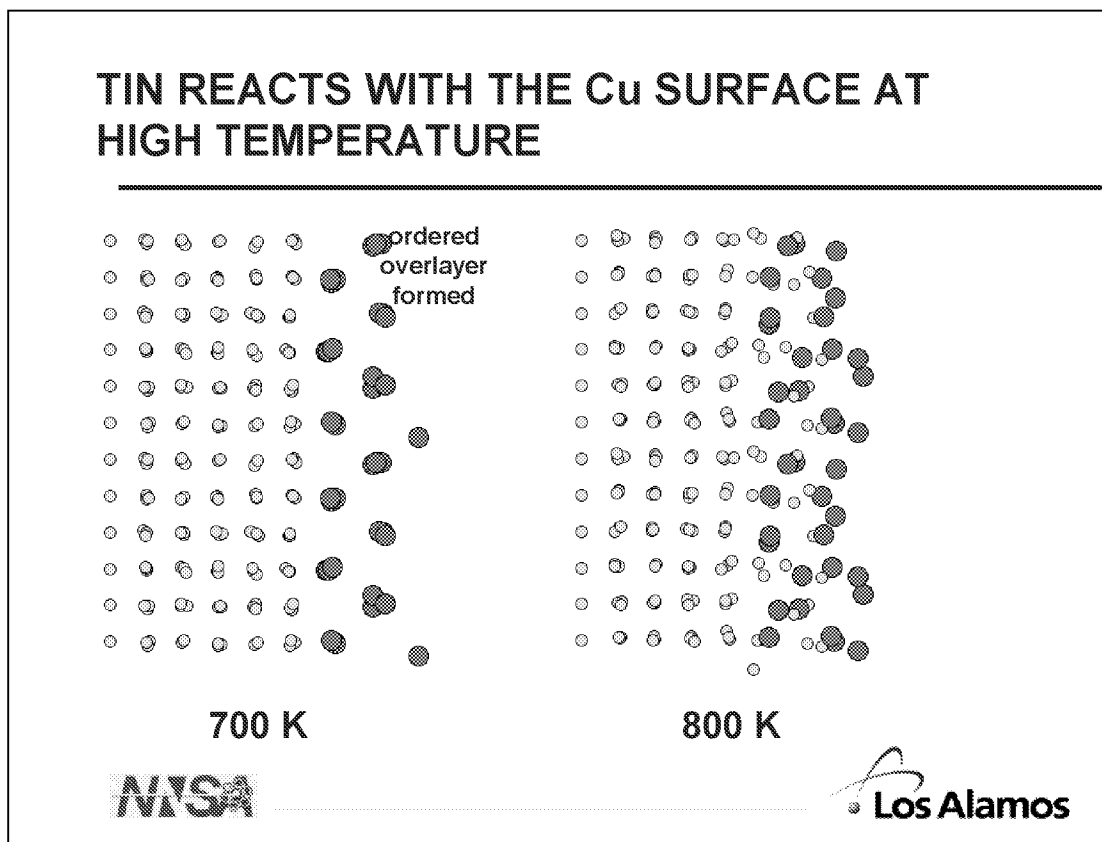


Figure 20

A STEPPED SURFACE FACILITATES REACTION

We investigate the effect of surface defects on the reaction temperature. The figure at the top left shows the initial defective surface. We now see that at temperatures as low as room temperature, the Sn reacts with the Cu substrate.

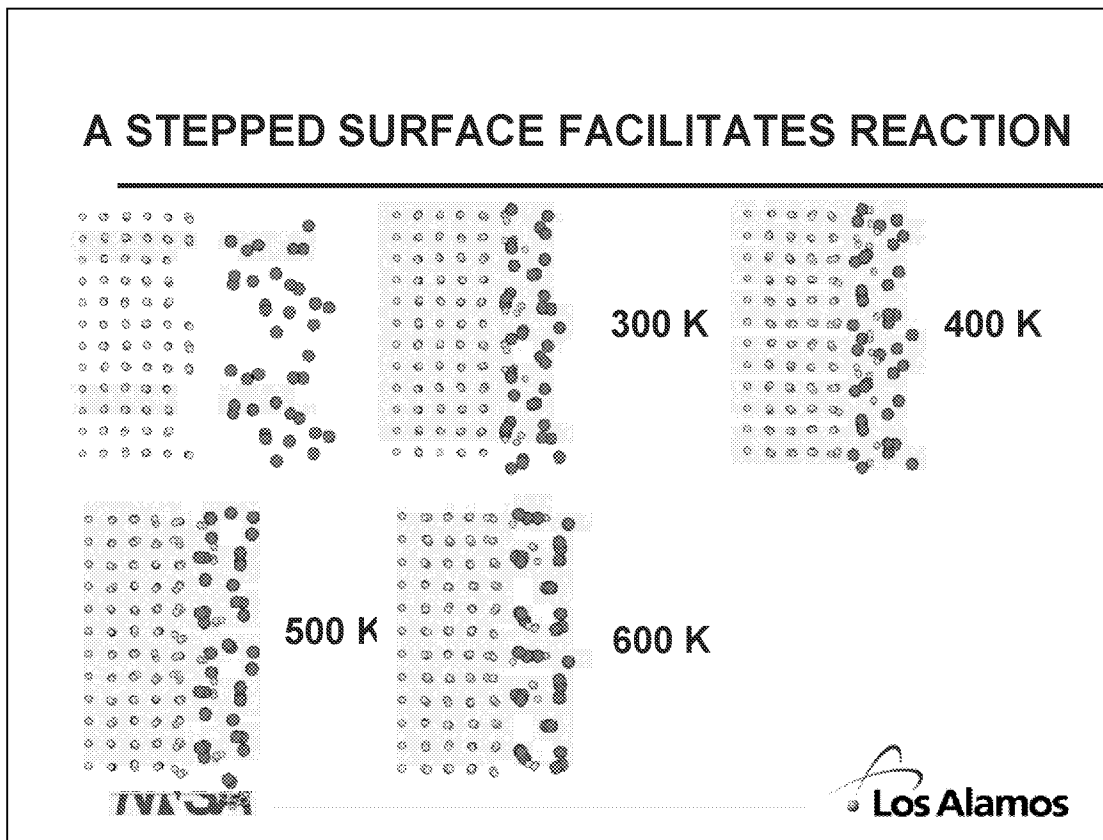


Figure 21

WHAT WE LEARNED ABOUT WETTING MECHANISMS

It is clear that surface defects are critical in the examination of the reactive wetting of Sn on Cu... It is satisfying to note that the MEAM potentials are able to represent the complicated processes occurring at the Cu/Sn interface.

WHAT WE LEARNED ABOUT WETTING MECHANISMS

- Liquid tin reacts with a smooth Cu (100) at temperatures greater than 800 K
- Below 800 K an ordered layer of tin forms
- A roughened surface reacts with liquid tin down to temperatures as low as room temperature
- Reactive wetting is controlled by surface defects

NISA

 **Los Alamos**

Figure 22

WHAT WE HAVEN'T LEARNED ABOUT WETTING

As in the previous case of mechanical behavior, it is seen that additional calculations are needed if we are to seriously approach the alloy design question.

WHAT WE HAVEN'T LEARNED ABOUT WETTING

- Solder alloy and surface impurity effects
 - Need potentials for Cu/Sn/X
- Diffusion mediated mechanisms
 - Time limitations
- Bond strength

NISA

 **Los Alamos**

Figure 23

**DEVELOP MODELS BASED ON ENTITIES
WITH INFORMATION PASSED FROM LOWER LEVEL**

We suggest that the most likely way for success in multi-scale modeling is the hierarchical scheme shown at the right. Calculations of the various entities are performed and information is extracted to be passed to the next level of computation. It is important to closely compare results to experiment at all levels of calculation.

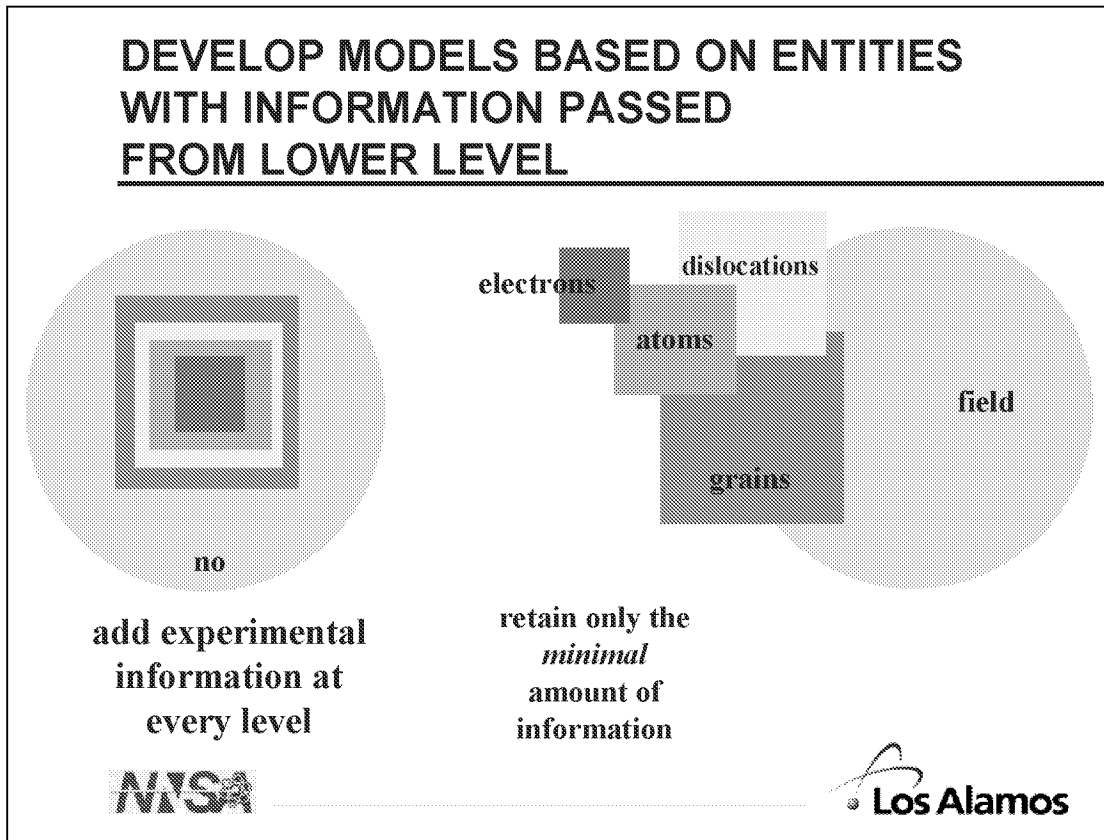


Figure 24

**IMPACT OF COMPUTATIONAL MATERIALS
SCIENCE ON ALLOY DEVELOPMENT**

We feel that within the next two decades it is quite likely that computational materials science will be strongly influencing multi-component alloy development in the area of phase stability. In contrast the probability for strongly influencing alloy design through the prediction of properties is small. Somewhat intermediate is the ability of predict phase transformations and microstructure.

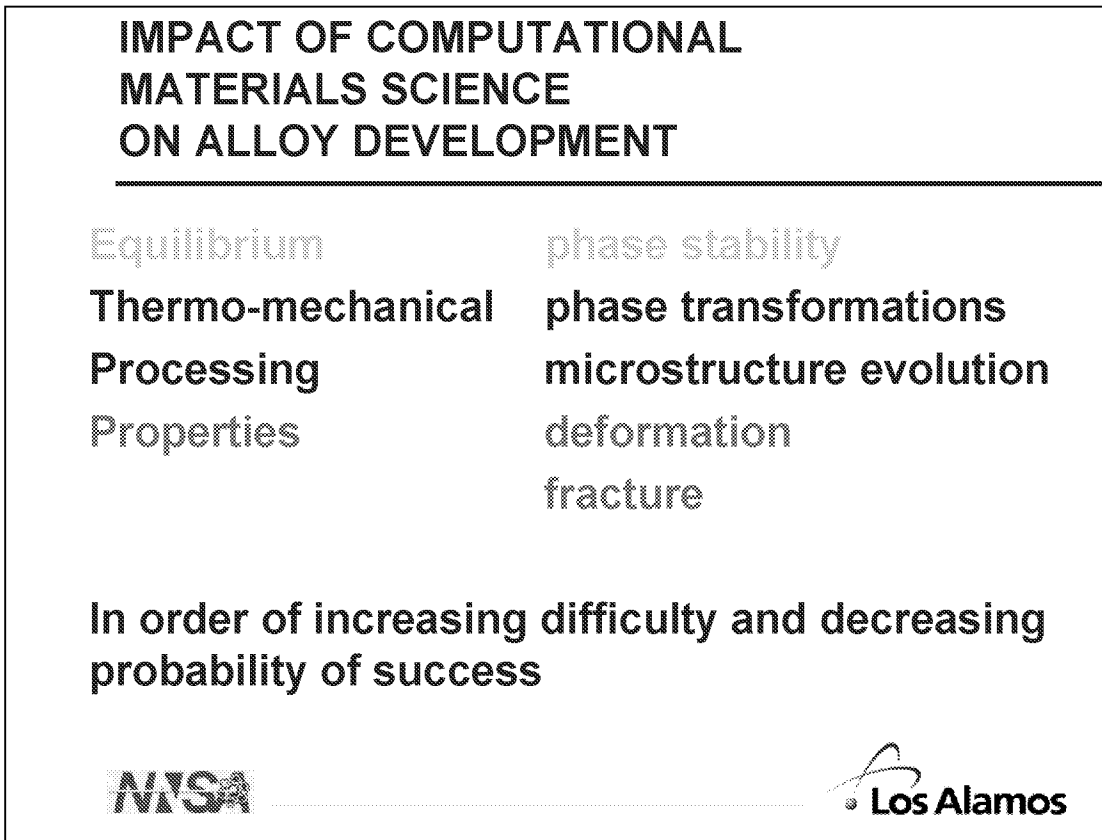


Figure 25

KEY ISSUES FOR THE FUTURE

We summarize the key issues for the future.

KEY ISSUES FOR THE FUTURE

- **Reliable potentials - tradeoff**
 - Reliability
 - Material classes
 - Multi-component systems
 - Computational speed
- **Information extraction**
 - Connection to larger size (longer time) models
 - Visualization of mechanisms
- **Changing entities - don't do it all with atoms**

Figure 26

**Materials Modeling and Simulation as a Technology Platform
for Advanced Materials Development**

Gregg Caldwell
3M Materials Modeling, Advanced Materials Tech Center
St. Paul, MN

OUTLINE

Outline

- Materials Modeling Technology at **3M**.
- Bottom Up
 - Atomistic Simulations of Organic Fluoromaterials.
 - Predicting Solubility Parameters of Molecules.
- Top Down
 - The Need for Property Predictions Via Molecular Simulations: Pavement Markings Performance.
- The Middle Out
 - Self Assembly of Materials and the Mesoscale.
- Summary.

Figure 1

MATERIALS MODELING TECHNOLOGY AT 3M

The AMTC has significant expertise in modeling material behavior. The group is focused on the prediction of performance by using an integrated approach for various length and times scales - atomistic, molecular, polymer, mesoscale, fluid transport (including microfluidics), thru applied mechanics. The goal is to accelerate materials development with modeling and simulation and help develop new products and processes through computational methods.

Materials Modeling Technology at 3M

- Advanced Materials Technology Center
 - drives strong **3M** global growth short-term and long-term through building and applying expertise in chosen materials-related technology areas, anticipating new technology platforms aligned with major **3M** growth opportunities.
- Materials Modeling Technology Group
 - accelerate **3M** innovation by using mathematical and computational models of materials.
 - provide an integrated approach among the various length scales and time scales of materials behavior.

Figure 2

MATERIALS MODELING

The modeling group within the AMTC use a hierarchal approach to materials modeling. The challenge of bridging the gaps in size and time scales is recognized with a “bottom up” and “top down” approach used to link well understood design and constitutive modeling approaches with first principles approaches.

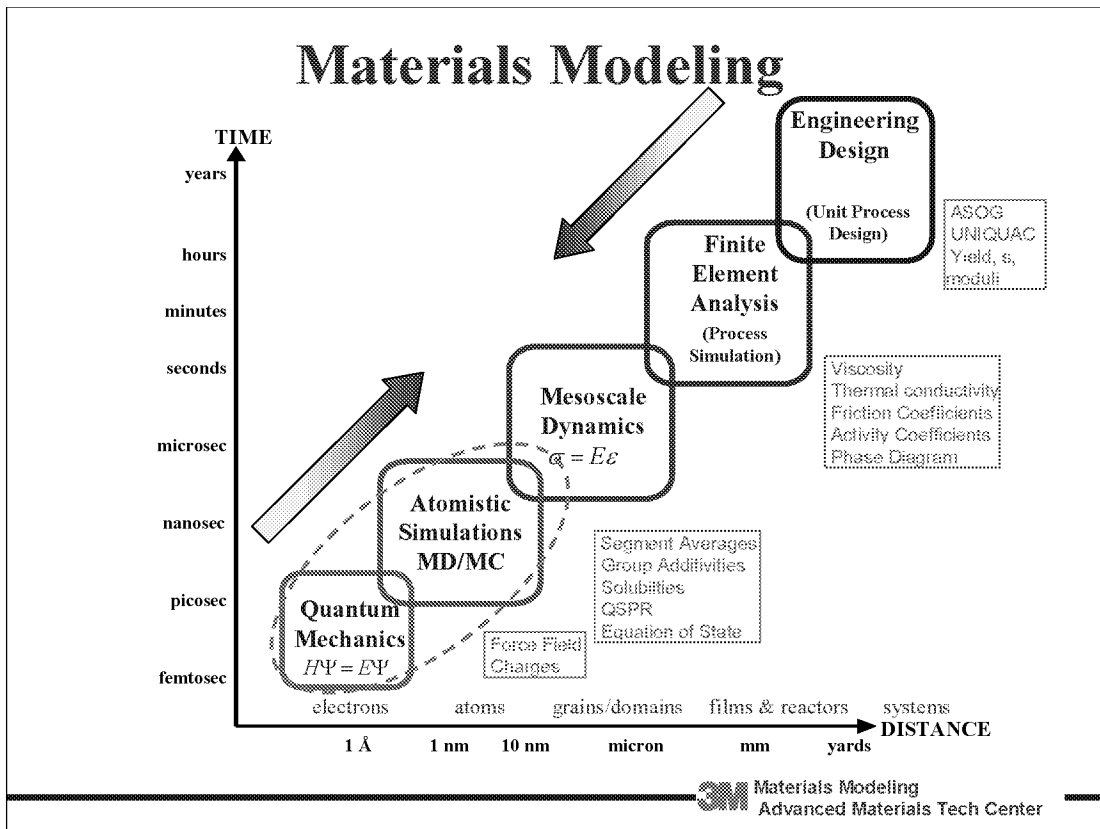


Figure 3

ATOMISTIC SIMULATION OF ORGANIC FLUOROMATERIALS

Polytetrafluoroethylene (PTFE) is an important industrial polymer due to some of its remarkable properties. Other fluorinated materials also have significant industrial interest and the ability to predict structure and possibly performance of these materials would be of great value.

Unlike the zig-zag shape of the polyethylene backbone, X-ray crystallography studies show¹ that polytetrafluoroethylene (PTFE) has a helical conformation due, in part, to larger van der Waals interactions among fluorine atoms. The first order phase transitions (20°C) below the melting point are believed to be due to a chirality transformation from a well ordered helical form to disordered ones and disordering among polymer chains.

In order to look at this transformation a molecular dynamics (MD) approach is necessary. The accuracy of the MD calculations is only as good as the underlying force field.

1. Bunn C.W. and Howells E. R. *Nature*, **174**, 549 (1954).
2. Mayo S.L., Olafson B.D., Goddard W.A., *J. Phys. Chem.*, **94**, 8897 (1990)

Atomistic Simulations of Organic Fluoromaterials

- Selected a general force field for organic molecules:
 - Dreiding².
- The basic force field had limitations:
 - Did not deal with fluorinated systems correctly.
- A collaboration between **3M**'s Materials Modeling Group and the Materials Process and Simulation Center led by Bill Goddard at the California Institute of Technology.

Figure 4

DREIDING EXP 6 FORCE FIELD

Early experiments¹ demonstrated that the backbone dihedral angles in PTFE are displaced by 17° from a truly trans state (that is 0°.) This can be attributed to the large non-bond interactions among fluorine atoms attached to the carbon backbone. In order to accommodate these unfavorable steric interactions, the carbon backbone must deform slightly. As a result, PTFE forms two stereo helical conformations.

Full quantum mechanical calculations for PTFE, however, still remains a challenge due to the large number of atoms involved. However, molecular mechanics/dynamics methodologies have been widely used to model macromolecules and large systems. In order to carry out correct analysis from classical molecular methods, the critical issue is to obtain a highly accurate classical force field (FF) that models the atomic interactions among different atoms.

As a first step, the torsional parameter of the Dreiding² force field was modified based on *ab initio* studies.

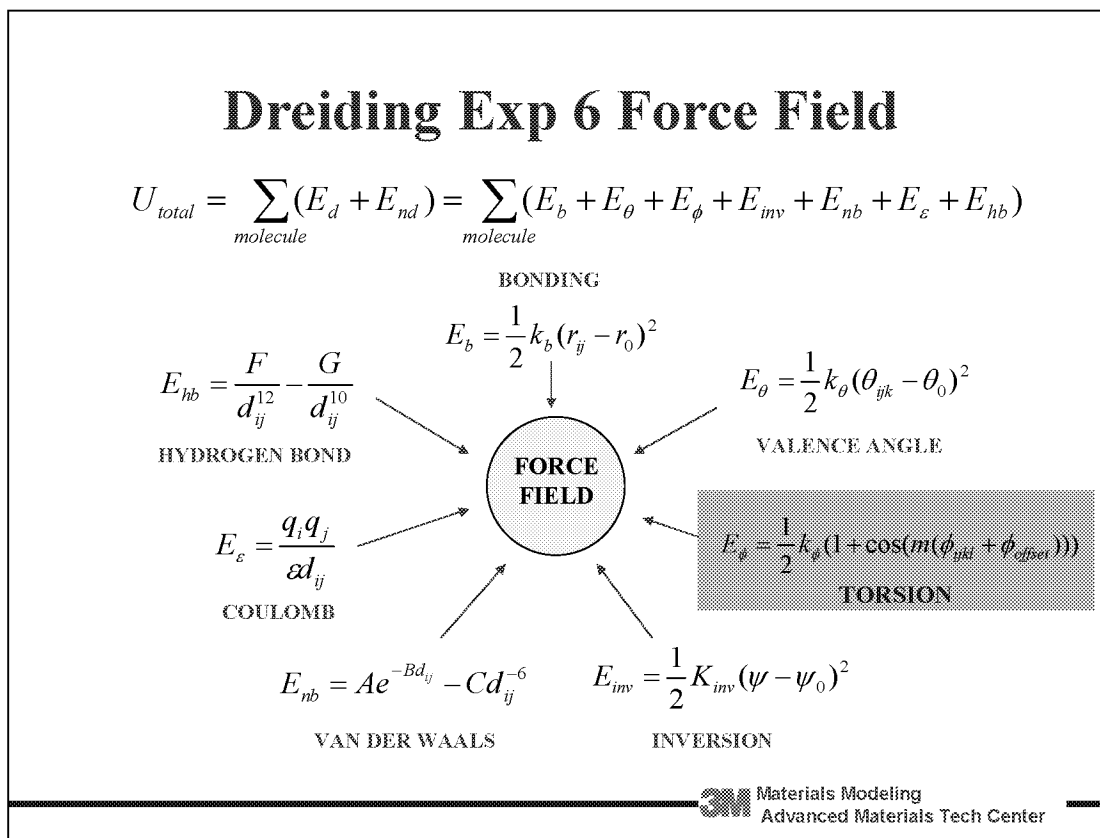


Figure 5

QUANTUM MECHANICS

To parameterize the torsional potential, we carried out a series of *ab initio* calculations for fluorinated alkanes from C₂F₆ up to C₁₀F₂₂. (B3LYP with 6-31G* basis set).

To capture the conformational characteristics classically, we used the standard Dreiding Force Field to describe covalent bonds, angles, and non-bond interactions. The van der Waals parameters for fluorine were taken from a previous study³. The torsional potential was tuned to best represent helical displacements for fluorinated systems. The torsional potential used was a 6-term dihedral.

3. Karasawa N, Goddard W.A, *Macromolecules*, **25**, 7268 (1992).

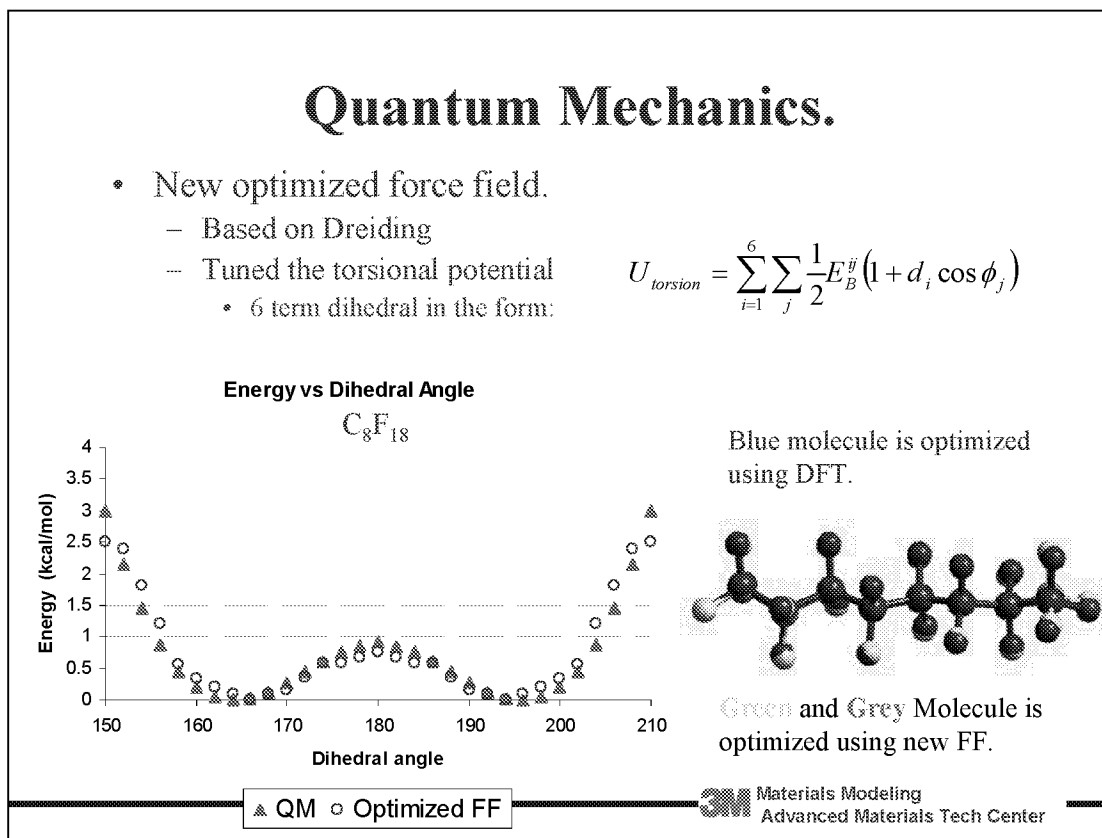


Figure 6

VALIDATION – C₂₀F₄₂

Perfluoro-n-icosane (C₂₀F₄₂) was used to validate the modified force field. Like other chain molecules, the crystal structure is composed of stacking layers. Within each layer, the molecules form a two-dimensional lattice. The phase transitions are first order and mainly due to dis-order in rotational motions within each molecule or translational motion among molecules. Perfluoro-n-icosane has three solid phases⁴, namely, **M** (monoclinic) for T < 146 K; **I** (intermediate) for 146 < T < 200 K, and **R** (rhombohedral) for T > 200 K.

- Schwickert, H. J., Strobl, G., Kimmig, M., *Chem. Phys.* **1991**, 95, 2800.

Validation – C₂₀F₄₂

- Crystal Structure:
 - At least 2 stable crystal phases⁴.
- A phase stable at ambient temperature.
 - rhombohedral phase (R)
 - » Each unit cell occupied by 3 molecules
 - » a = b = 5.7 Å, c = 85.0 Å
 - » α = β = 90°; γ = 120°
 - » ρ = 2.16 g/cm³
- A phase stable at low temperature.
 - Monoclinic phase
 - » Each unit cell occupied by 2 molecules.
 - » A = 9.65 Å, b = 5.7 Å, c = 28.3 Å
 - » α = γ = 90°; β ~ 97°
 - » ρ = 2.16 g/cm³

top view

R L

Materials Modeling
Advanced Materials Tech Center

Figure 7

VALIDATION – C₂₀F₄₂ LOW TEMPERATURE PHASE

The unit cell in the simulation of the M-phase C₂₀F₄₂ consists of two molecules. One is left-handed, and the other is right-handed. After constant pressure energy minimization from molecular mechanics, the computed cell parameters are listed together with experimental data.

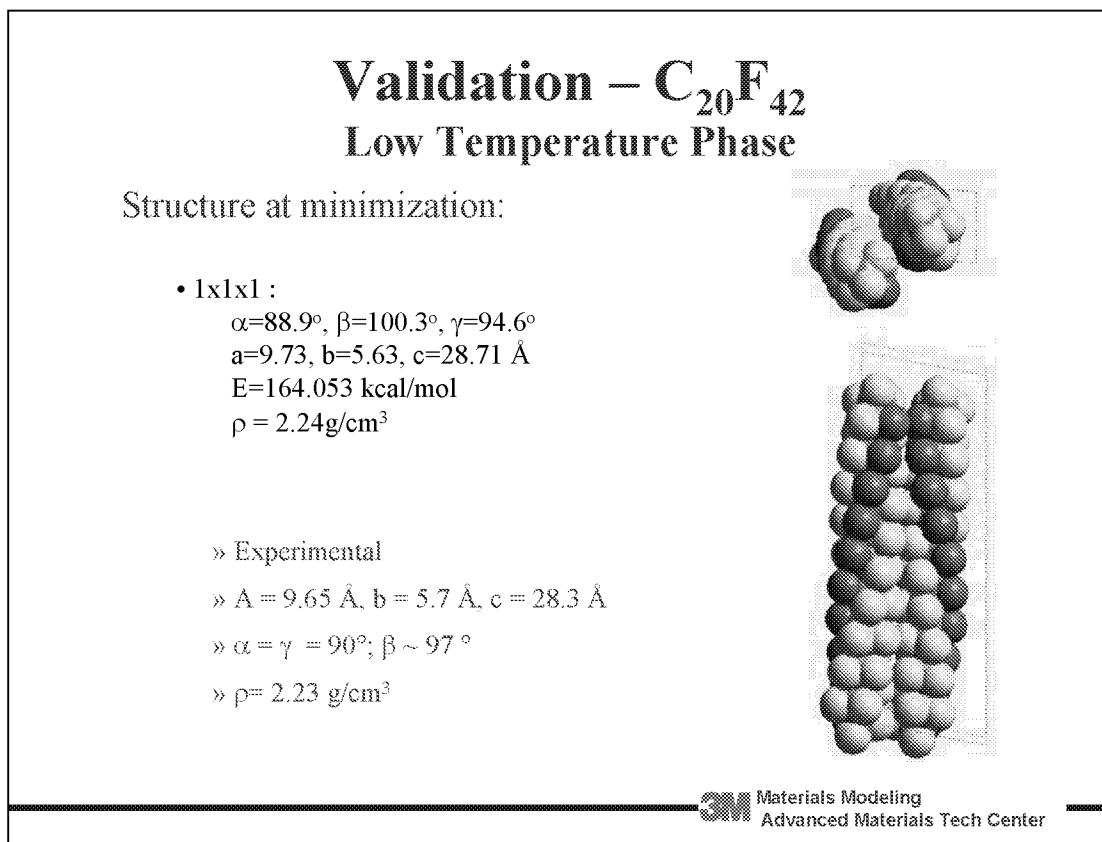


Figure 8

VALIDATION – C₂₀F₄₂ HIGH TEMPERATURE PHASE

The high temperature phase having three molecules in the unit cell is much more difficult. Three different cases were tried:

- Case 1: All the molecules in the unit cell were left handed.
- Case 2: All the molecules in the unit cell were right handed.
- Case 3: The molecules were alternating left and right handed.

The results of the third case were the closest match to the experimental crystal structure after minimization.

Validation – C₂₀F₄₂ high temperature phase

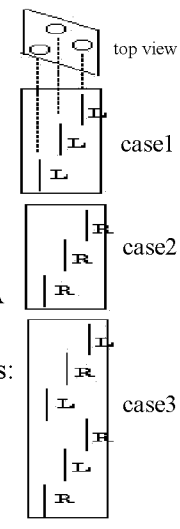
- This is more difficult!
 - How do the 3 molecules arrange themselves in the unit cell?
 - Crystal structure implies the ordering of the helices has disappeared.
 - What is happening?

Experimental:
 $a = b = 5.7 \text{ \AA}$, $c = 85.0 \text{ \AA}$
 $\alpha = \beta = 90^\circ$; $\gamma = 120^\circ$
 $\rho = 2.16 \text{ g/cm}^3$

Tried 3 Cases:

- * case 1 - all left-handed helices:
 $\alpha = 90.7^\circ$, $\beta = 89.3^\circ$, $\gamma = 118.3^\circ$
 $a = 5.62 \text{ \AA}$, $b = 5.60 \text{ \AA}$, $c = 84.73 \text{ \AA}$
- * case 2 - all right-handed helices:
 $\alpha = 89.7^\circ$, $\beta = 90.3^\circ$, $\gamma = 120.0^\circ$
 $a = 5.63 \text{ \AA}$, $b = 5.72 \text{ \AA}$, $c = 84.81 \text{ \AA}$
- * case 3 - alternative right-left helices:
 $\alpha = 89.9^\circ$, $\beta = 89.9^\circ$, $\gamma = 119.2^\circ$
 $a = 5.61 \text{ \AA}$, $b = 5.69 \text{ \AA}$,
 $c = 169.8 \text{ \AA}$ (equiv. $C = 84.9 \text{ \AA}$)

(minimization)



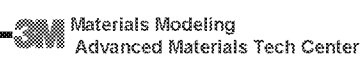


Figure 9

VALIDATION – C20F42

A 3X3 supercell of the M-phase was constructed (each layer is colored differently for clarity). The molecules are packed in a very ordered array.

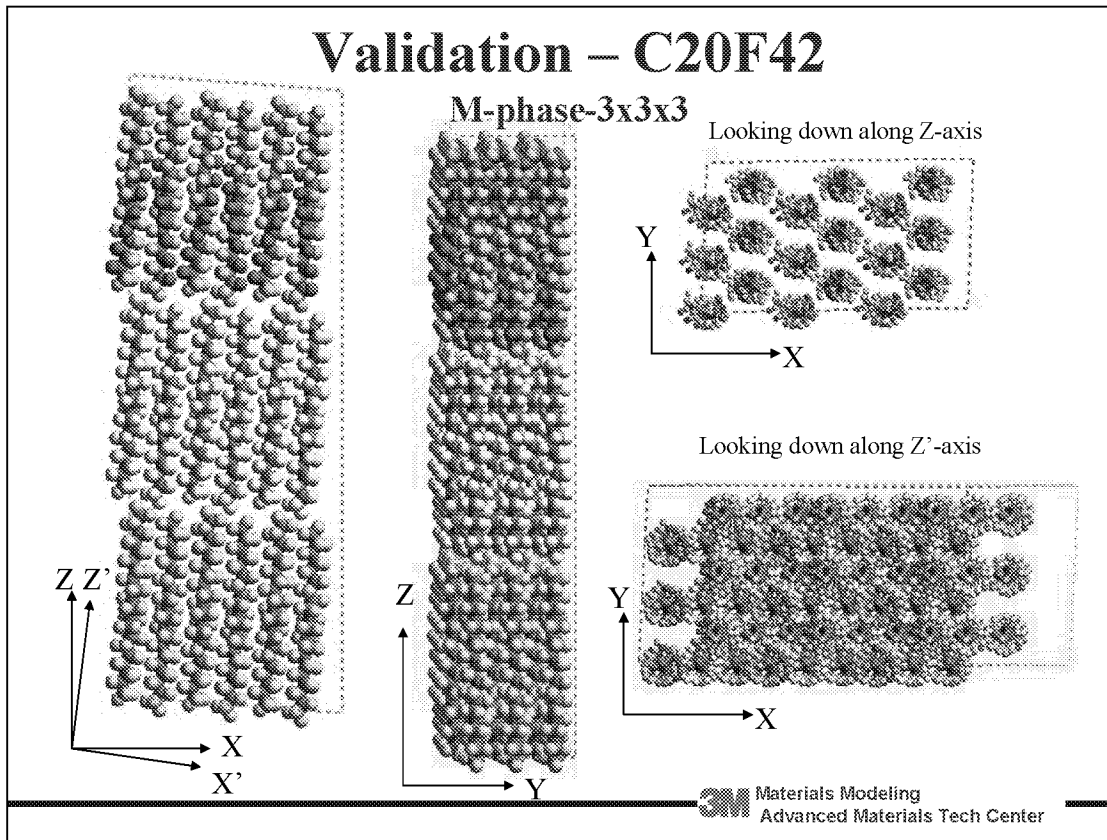


Figure 10

VALIDATION – C₂₀F₄₂

Molecular dynamics was then run at 120K (below the first transition) and at 240K (above the second transition). After 70ps of dynamics at the lower temperature, the well ordered crystal structure is maintained. When the temperature is increased, however, the crystal structure tends to disorder. This is due to a change in the helicity of each molecule. The barrier to change from a left handed helix to a right handed helix is $\sim 1\text{kcal mol}^{-1}$. During the higher temperature dynamics a bond changes from $+15^\circ$ to -15° . This in turn causes the other bonds in the molecule to switch thus changing its handedness. The adjacent molecular then changes handedness and the order of the entire crystal is changed.

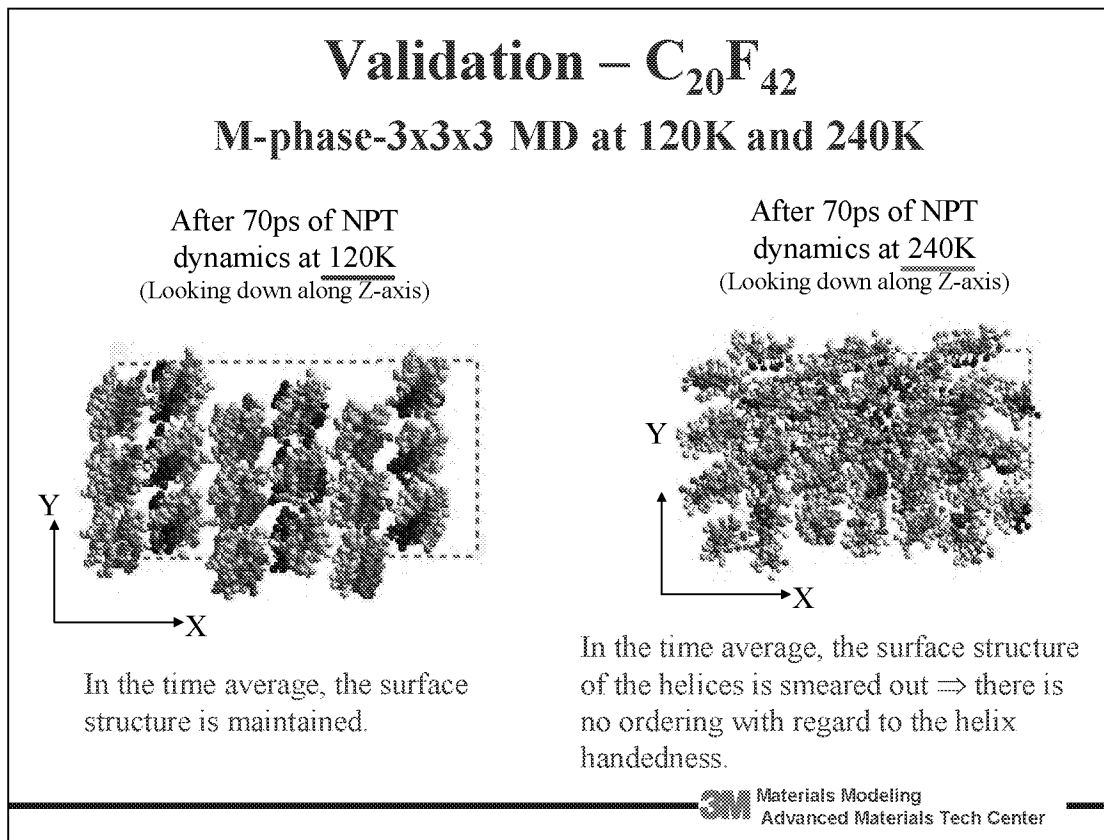


Figure 11

X-RAY DIFFRACTION PROFILE OF THE STRUCTURES FROM MD

Simulated X-ray patterns averaged over the dynamics time period shows the difference in order in the molecules helicity at different temperatures. At low temperature (120K) the molecule has a lot of order in the higher 2θ region. At higher temperature (240K) this order disappears as the molecules switch helicities.

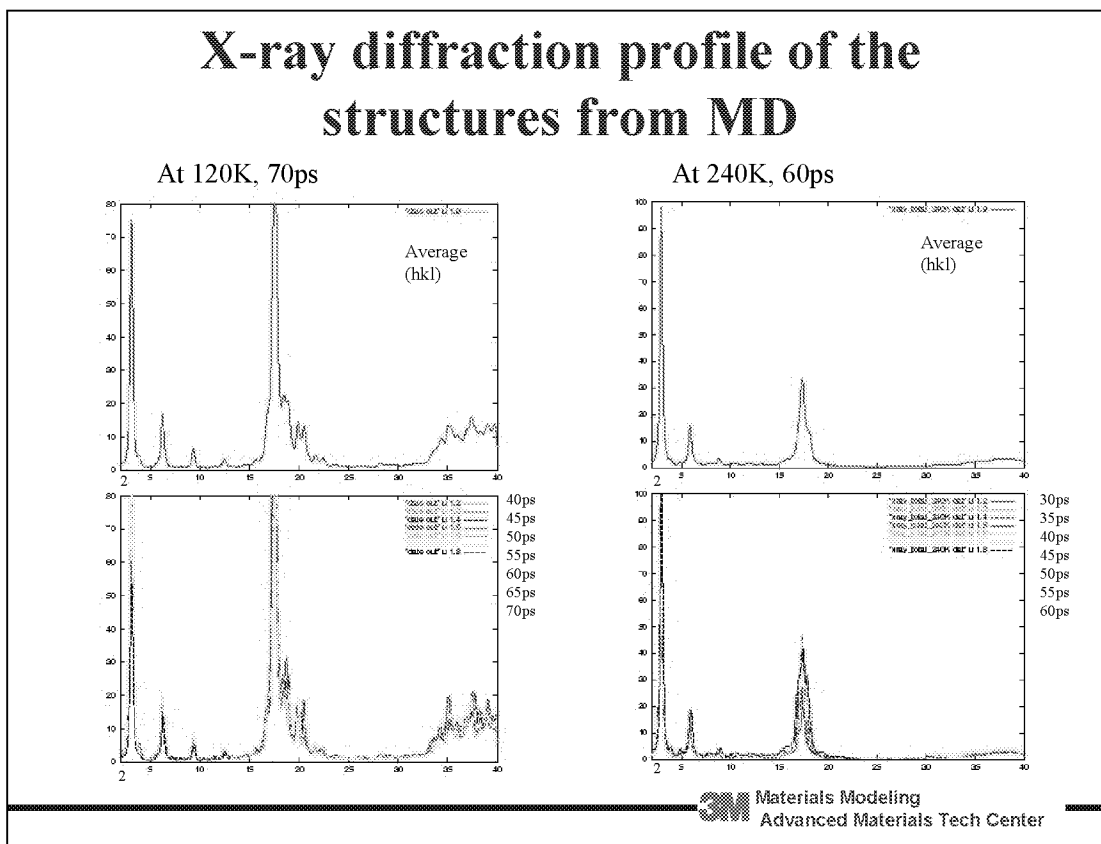


Figure 12

VALIDATION

A recent paper⁵ described the SAM formation of $C_{20}F_{42}$ by vapor depositing the compound onto a glass slide. Meridial X-ray patterns of our simulated high temperature phase are in excellent agreement with the experimental X-ray patterns.

5. Nishino T., Meuro M., Nakamae K., Matsushita M., and Ueda Y., *Langmuir*, **1999**, *15*, 4321

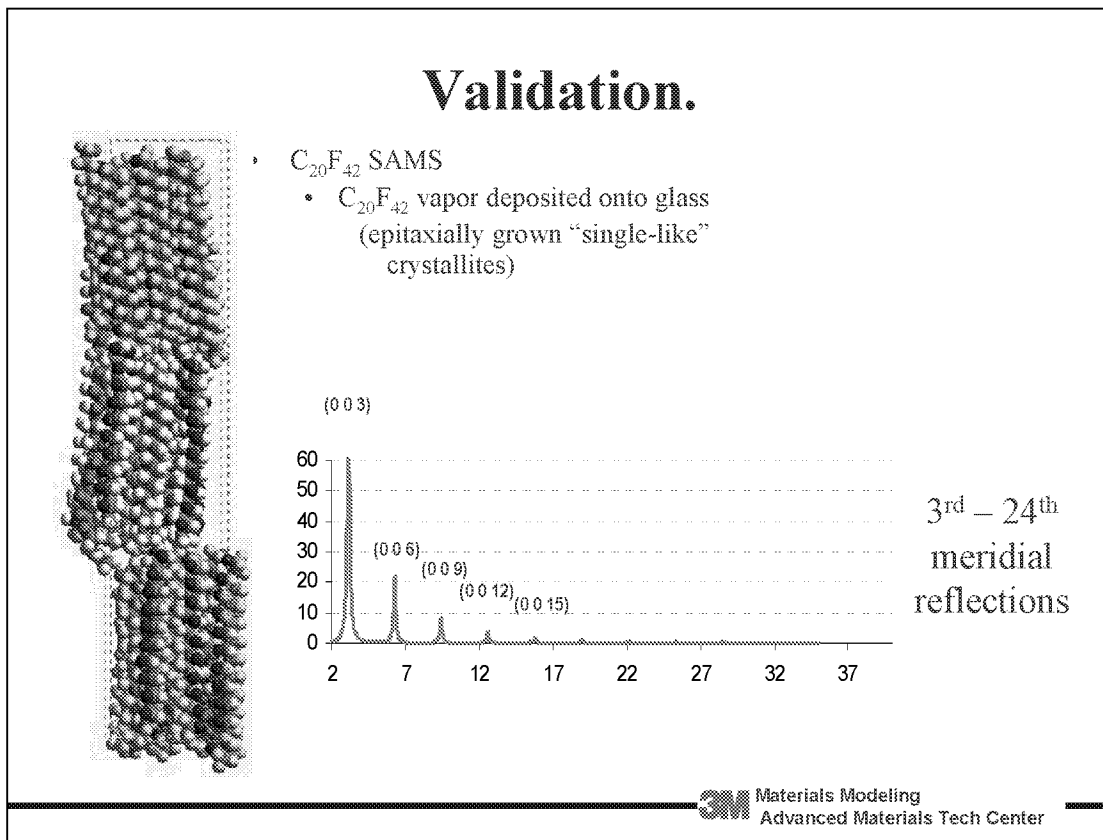


Figure 13

PREDICTING SOLUBILITY PARAMETERS OF MOLECULES

It is of great value to be able to estimate from first principles the Hildebrand solubility parameter for any given solvent or polymer. Predictions of this type may be of practical use for selection of polymers in blending, for understanding polymer kinetics and monomer distribution compositions in copolymers, or for the proper selection of solvents in new formulations and synthesis processes.

Predicting Solubility Parameters of Molecules

- In the literature, there sometimes as many values of δ as there are researchers measuring them.
- Distribution can be pretty large (especially for polymeric materials).
 - general rule of thumb - compare values from the same researchers only.
- Can modeling give a quick, reproducible, way of calculating cohesive energy densities (CED) and solubility parameters?
- A collaboration between the **3M**'s Materials Modeling Group and the Materials Process and Simulation Center led by Bill Goddard at the California Institute of Technology

Figure 14

SIMULATION DETAILS

A simple hierarchical approach was again used in the simulation procedure. First, accurate charges were obtained for each molecule using quantum mechanics. Molecular dynamics were then carried out on an ensemble of the molecules and results averaged.

Simulation Details

- Atomic charges calculated via Hartree-Fock studies (6-31G** basis set) employing Jaguar.
 - Both Mulliken and Electrostatic Derived Atomic Charges Employed and Compared.
- Molecular dynamics simulations carried out with the Cerius² employing the Dreiding Force Field.
- Molecular Dynamics Simulation protocol and CED/Solubility Parameter analysis carried out via the program CED developed Mario Blanco, Bill Goddard, and co-workers at the California Institute of Technology

 Materials Modeling
Advanced Materials Tech Center

Figure 15

SOLUBILITY PARAMETERS

A search of the literature found 39 compounds with reliable solubility parameters determined experimentally. The experimental points are from a collection of literature sources and there is quite a range of experimental values for each compound.

Computational approaches to calculating the solubility parameter provide a consistent approach allowing much easier comparisons between compounds.

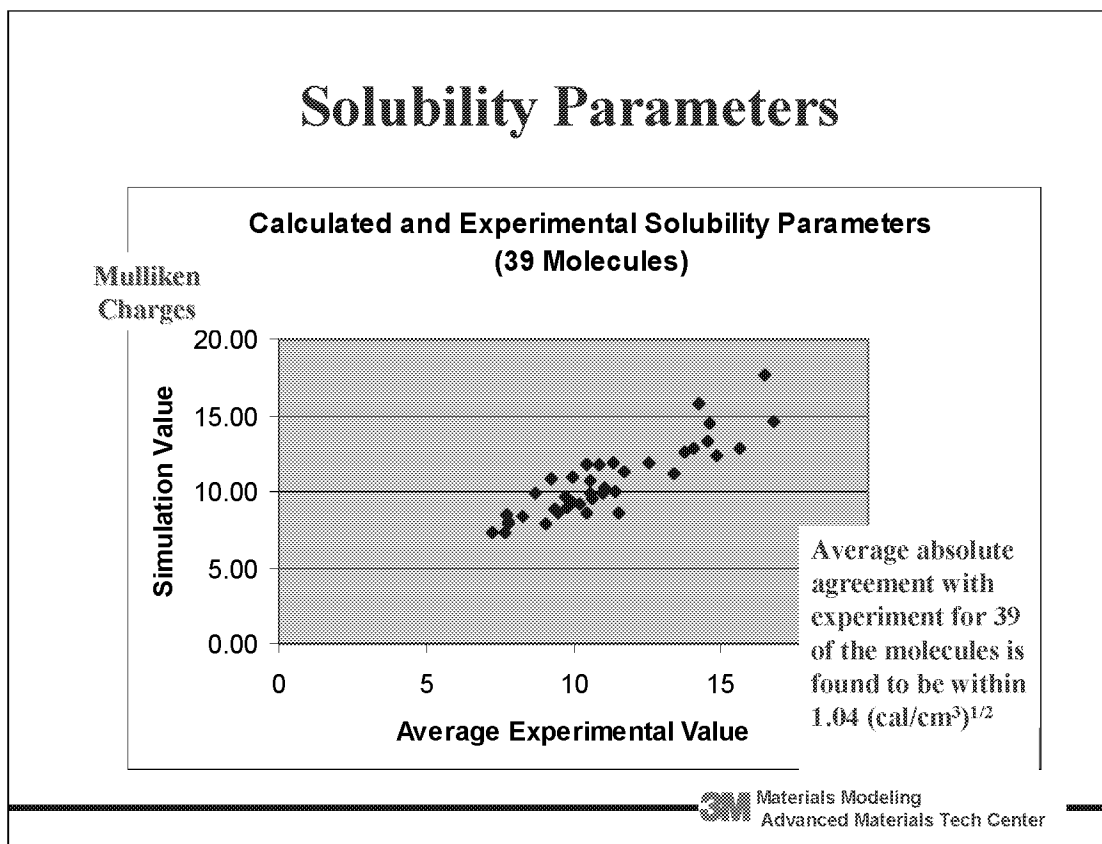


Figure 16

PREDICTING SOLUBILITY PARAMETERS SUMMARY

The method shows good agreement with experimental results and 3M is utilizing this as way of overcoming the need for time-consuming experiments.

Predicting Solubility Parameters Summary

- With Mulliken Charges, the average absolute agreement with experiment for 39 of the molecules is found to be $1.04(\text{cal}/\text{cm}^3)^{1/2}$.
- With Electrostatic Charges, the average absolute agreement with experiment for 16 of the molecules is found to be $0.88(\text{cal}/\text{cm}^3)^{1/2}$.
- Simulations in progress to complete Cerius2/electrostatic charge simulations for comparison with Mulliken charge-based simulations.
- Simulations in progress with Discover and the Compass force field to compare accuracy with the Dreiding Force Field.
- Methodology is being incorporated into the research process at **3M** to replace the need for time-consuming experiments.

Figure 17

PREDICTING SOLUBILITY PARAMETERS APPLICATIONS

From an industrial stand point, predicting solubility parameters has many applications.

Predicting Solubility Parameters Applications

- Polymer/polymer miscibility for design of polymer blends
- Polymer/polymer immiscibility for design of phase separating materials.
- Polymer/additive miscibility for optimization of additive selection.
- Polymer/solvent or molecule/solvent miscibility for solvent selection.
- Solvent/solvent miscibility to design of solvent blends.

- Molecular descriptor for development of Quantitative Structure Activity Relations.

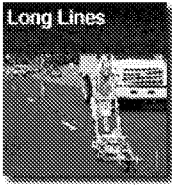
Figure 18

NEED FOR PROPERTY PREDICTIONS VIA MOLECULAR SIMULATIONS PAVEMENT MARKINGS PERFORMANCE

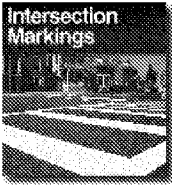
The Traffic Control Material Division of 3M Company is a recognized market leader in products for traffic management enhancing safety for all of us. This leadership comes from delivering innovative solutions to cities, counties, states and countries that need them. One of these solutions, pavement markings, utilized 3M retro reflective technology for lane markings. The customers want markings with road presence that means, durable markings with good adhesion and lasting retro reflectivity.

The Need for Property Predictions Via Molecular Simulations Pavement Markings Performance

- Road Presence
 - Adhesion
 - Wear Resistance
- Ease of Application
 - Wide Application Window
 - Minimum Road Surface Preparation
- Visibility and Recognition
 - Color
 - Retroreflective Performance



Long Lines



Intersection Markings



Raised Pavement Markers

 Materials Modeling
Advanced Materials Tech Center

Figure 19

MATERIAL PROPERTIES FOR MARKING PERFORMANCE

A major goal in the development of pavement marking tapes is conformance: the ability of the tape to maximize road contact and hence road adhesion. Intrinsic properties of the materials are needed as input of continuum models based on finite element technology. The most important ones for our application are: Young's modulus, yield stress, glass transition, thermal and hygroscopic expansion coefficients, viscosity, contact angle with various pavement types and permeability both to water and oil.

Our models have been used to predict the conformance of a particular tape in various roads. This slide has an example of the performance on two different roads with very different aggregates. Notice how performance depends on the type of road, conformance goes from 77% in one to only 33% in another one.

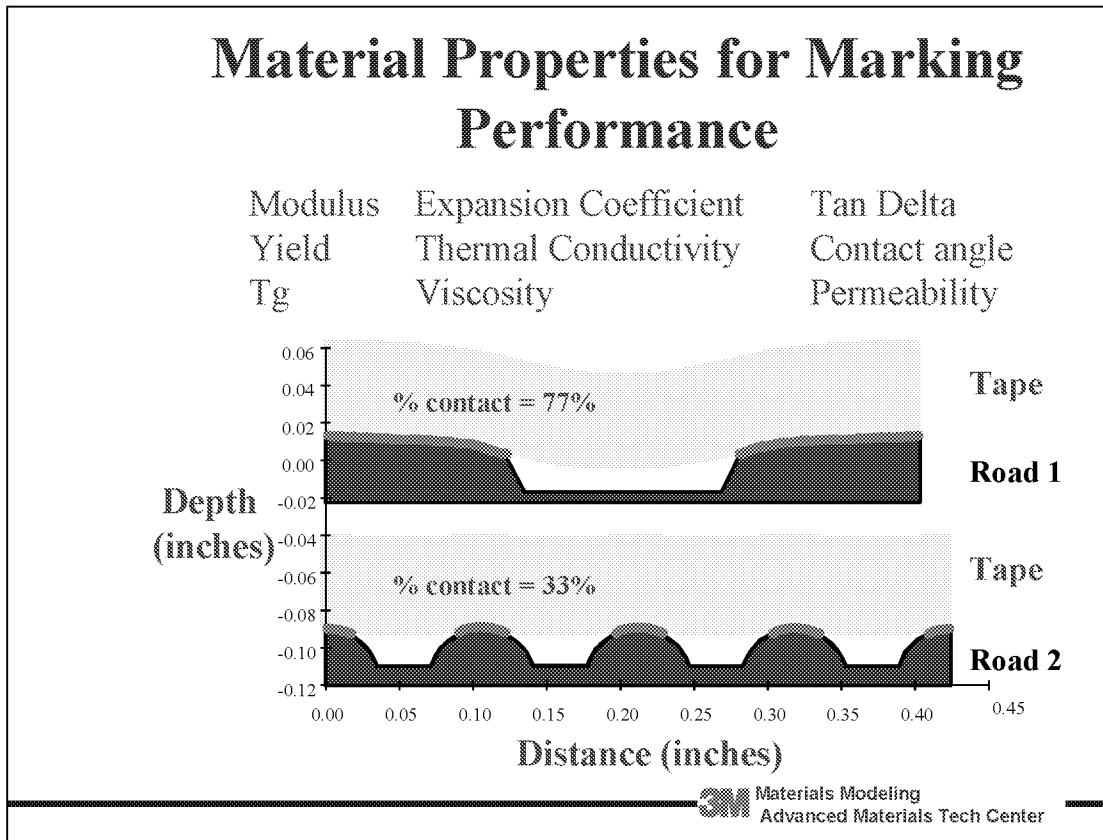


Figure 20

ACTUALS VS. PREDICTED ROAD CONTACT

The chart summarizes results obtained with the finite element models. It compares predicted values with measured values in two different sections of the same road: the wheel track zone and the oil drip zone. The wheel track zone corresponds to the area of the lane where the wheels pass. The oil drip zone corresponds to the center of the lane, i.e., the area between the two wheel tracks.

Our models capture correctly the ability of tapes to conform to various roads.

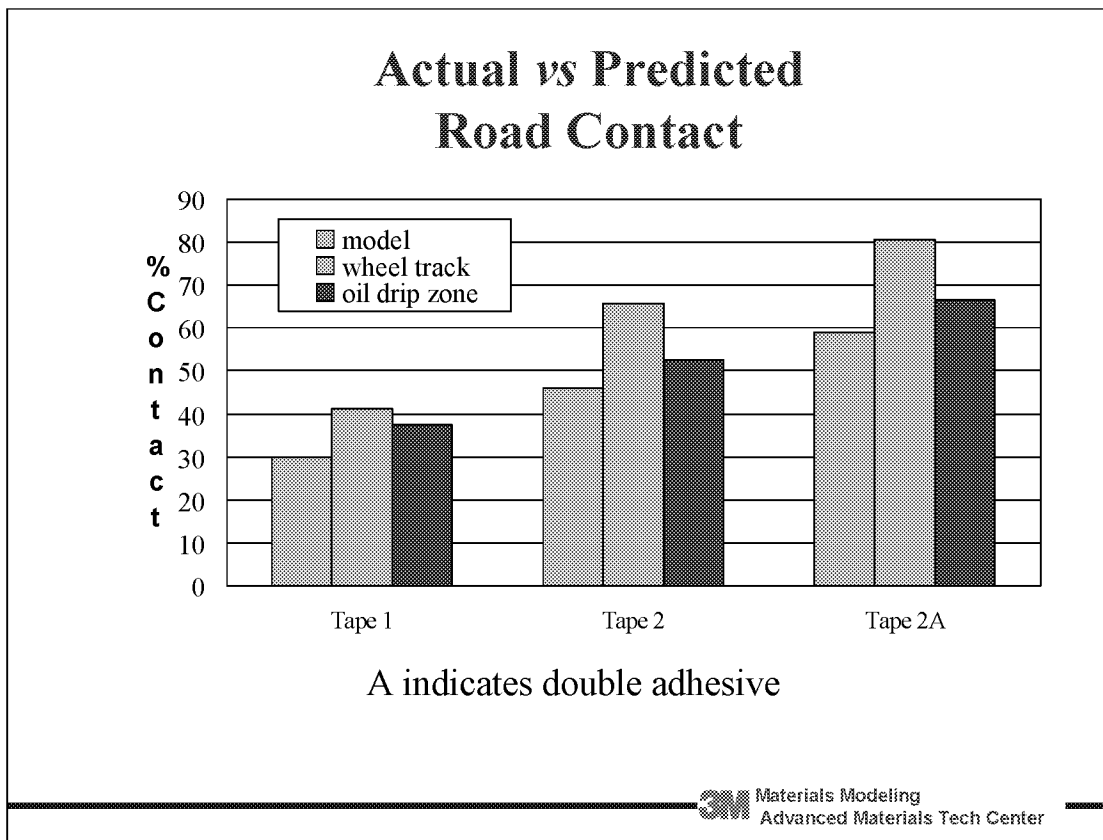


Figure 21

MATERIALS MODELING

New technology trends such as materials that interact, exchange or sense environmental changes, nanotechnology, microfluidics and micro machines are requiring information previously unavailable from traditional materials modeling methods, either fully atomistic or from a finite element side.

To address this gap, mesoscale models with a characteristic size located between the atomistic scale and the continuum model scale are being investigated for numerous applications.

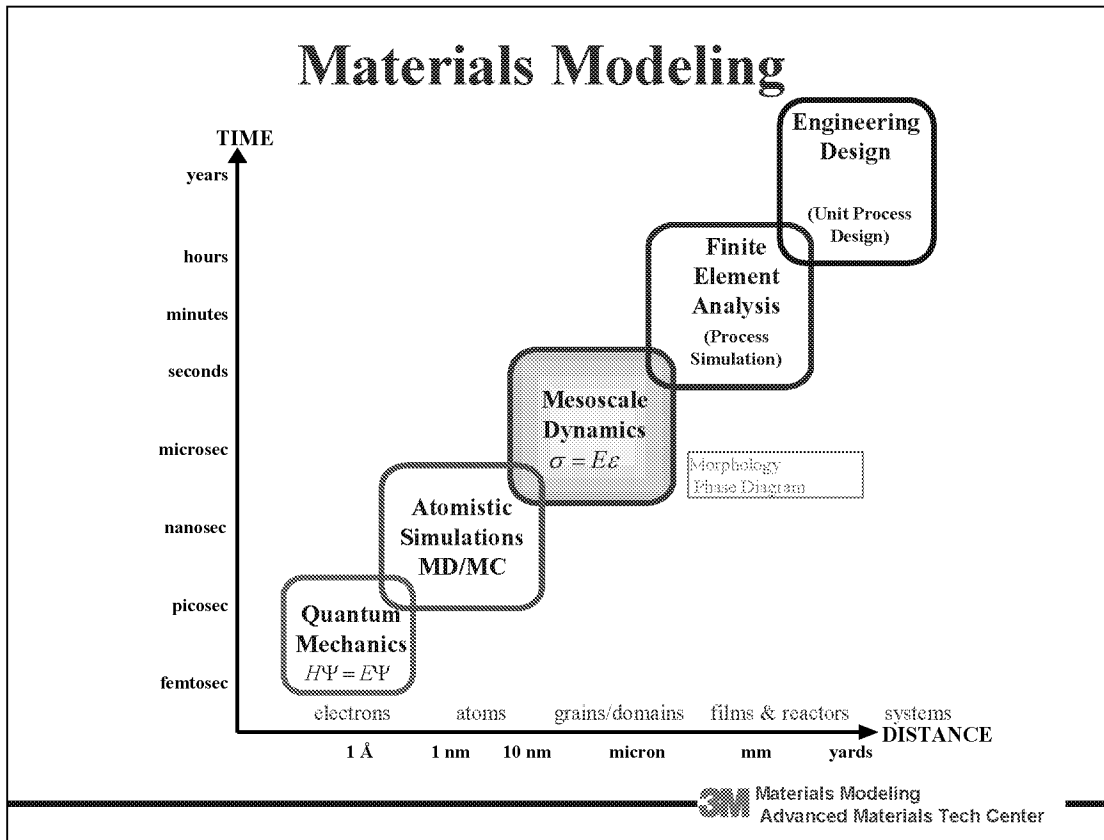


Figure 22

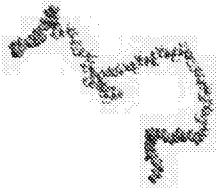
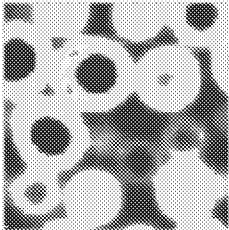
SELF ASSEMBLY

Of particular interest in soft-condensed materials is the self assembly of various components to form a structured fluid. The length and time scales at which these structures are formed are prohibitive for atomistic simulations, and mesoscale models are required to capture the rapid molecular kinetics as well as the slow thermodynamic relaxations of macro scale properties.

By coarse graining the description of the molecules we gain orders of magnitude in both length and time-scales.

Self Assembly

- Self-assembly of fluids has length and time scales which are prohibitive for fully atomistic studies.
- What is needed are tools that capture the the chemistry of the materials whilst coarse-graining the model.

Atomistic	Mesoscopic
	
Length: Nm	100's of nm (or more)
Units: Atoms	Beads representing many atoms
Time: Ns	as much as milli-seconds
Dynamics: $F=ma$	Diffusion, hydrodynamics

 Materials Modeling
Advanced Materials Tech Center

Figure 23

EXAMPLES OF MOLECULAR SELF ASSEMBLY

Molecular self assembly is engineered for the development of a large variety of materials. Surfactants present themselves as unique building blocks. They are used to coat surfaces with monolayers. In solutions they aggregate into very complex structures that have been used as templates for other materials (such as porous systems) or as nano-sized packets (such as vesicles) or to catalyze specific reactions (such as carriers to enzymes). Molecular self assembly has also been used to carry out engineered nucleation for the formation of zeolites and clathrates. Further, ordering within zeolites pores or clathrate complexes can be used for separation or selective reactions.

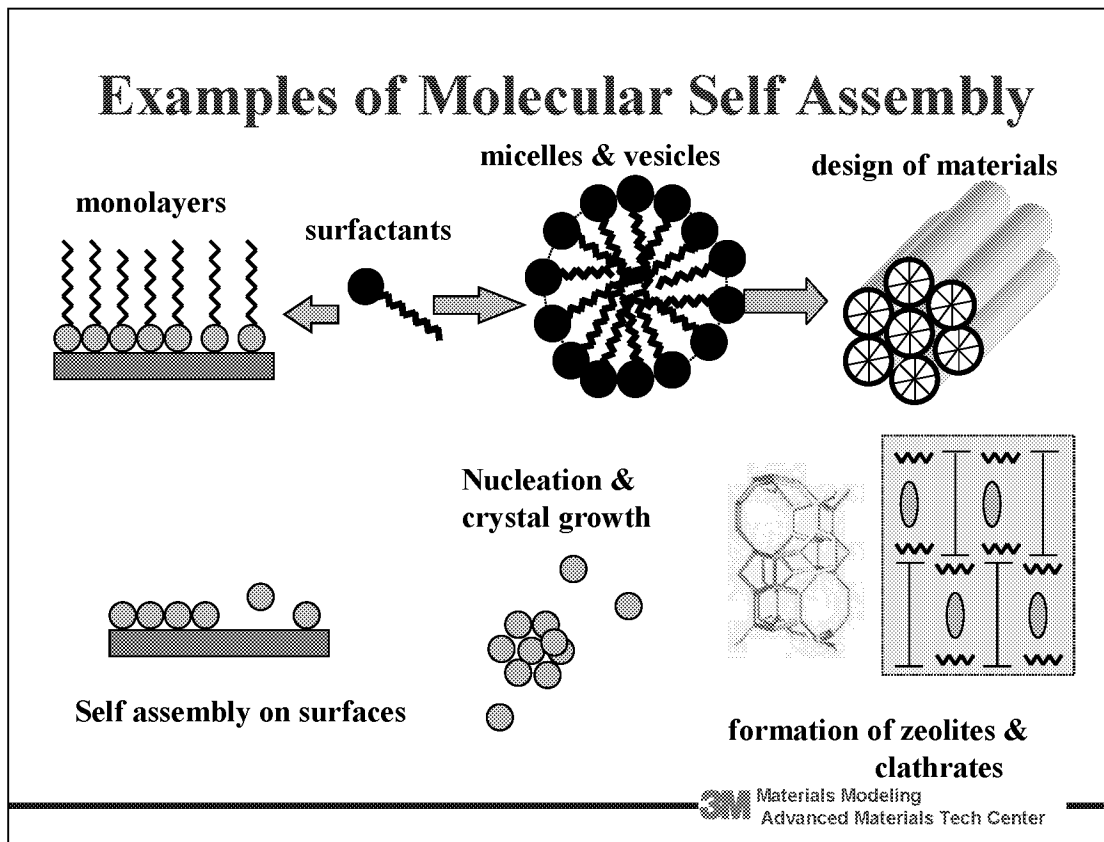


Figure 24

SELF ASSEMBLY IN MICELLES

Specifically amphiphiles (or surfactants) provide a rich set of highly complex self assembled aggregates at various solution conditions. As one increase the surfactant concentration the monomers aggregate into spherical micelles. Increasing the surfactant concentration further, or adding electrolytes or various additives result in worm like micelles, bilayers, vesicles or bicontinuous phases.

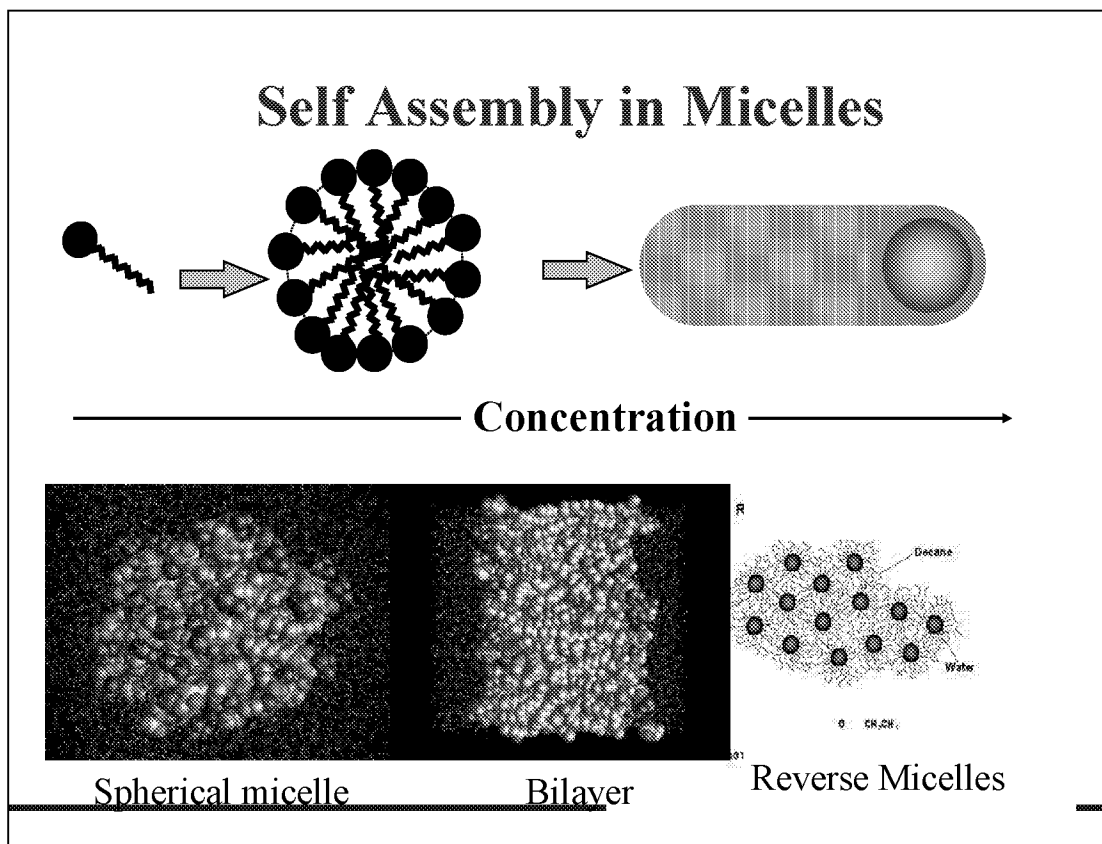


Figure 25

MESOSCOPIC SIMULATION – BLOCK COPOLYMER SYSTEMS

Self assembling block copolymer materials have important commercial applications as thermoplastic elastomers, and compatibilizers in polymer blends. Recently more advanced applications for these materials are being developed. These include using block copolymers morphologies as templates for the production of nanostructures and in nanoscale lithography for example.

While most blends of homopolymers are not compatible and show phase separation, block copolymers can only phase separate on a microscopic scale due to the connectivity of blocks. Depending on composition a large variety of micro-phase separated structures may be obtained. Mechanical properties of copolymers like the tensile strength may be significantly enhanced as compared to the corresponding homopolymers.

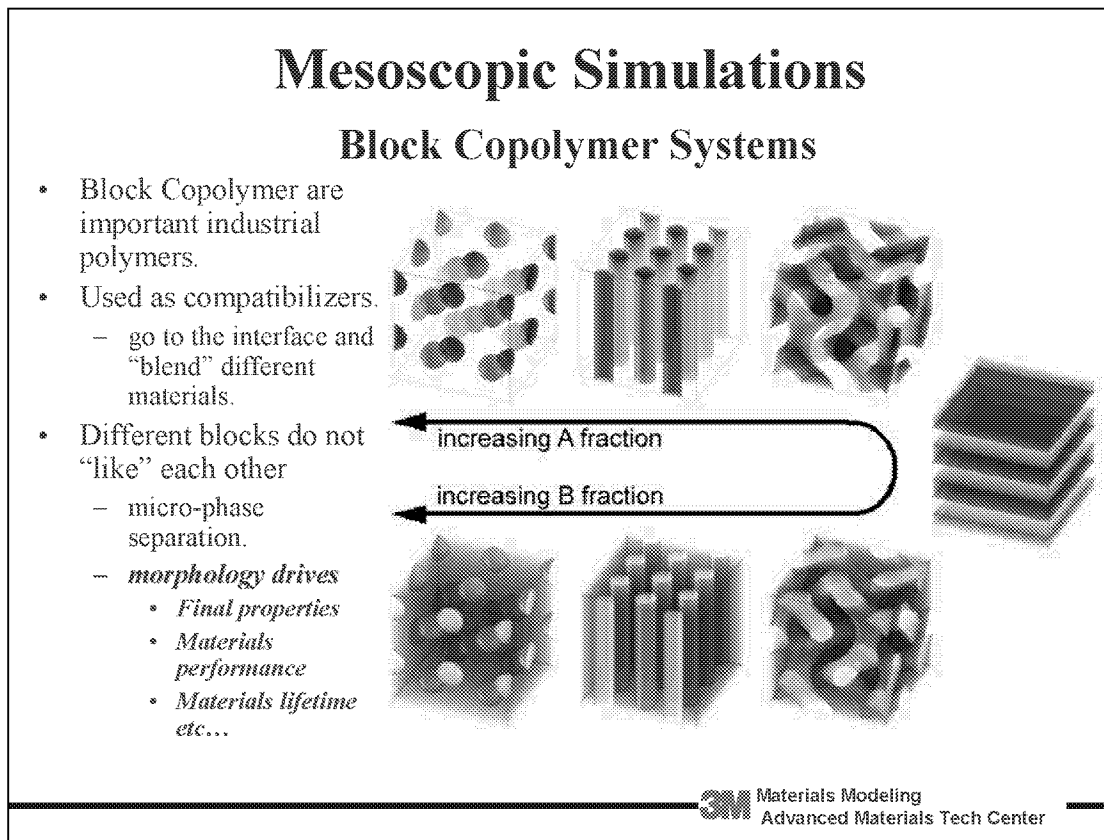


Figure 26

THE PHASE DIAGRAM

Like surfactants, changing concentrations of the various components of block copolymers, result in a number of possible morphologies.

The polymers are represented by an ideal Gaussian chain model.⁶ The non-ideality of the polymer is accounted for in an external potential.

The free energy of this system can be obtained in terms of these external potentials, which in turn can be related to the density fields via a density functional relationship.

In our group, we have been able to obtain computationally the phase diagram of a diblock copolymer. For this, we have used MesoDyn, a free energy method for blends and copolymer systems developed by Frajcie and implemented by Accelrys. Notice the right prediction of the various phases shown in the previous slide.

6. www.accelrys.com

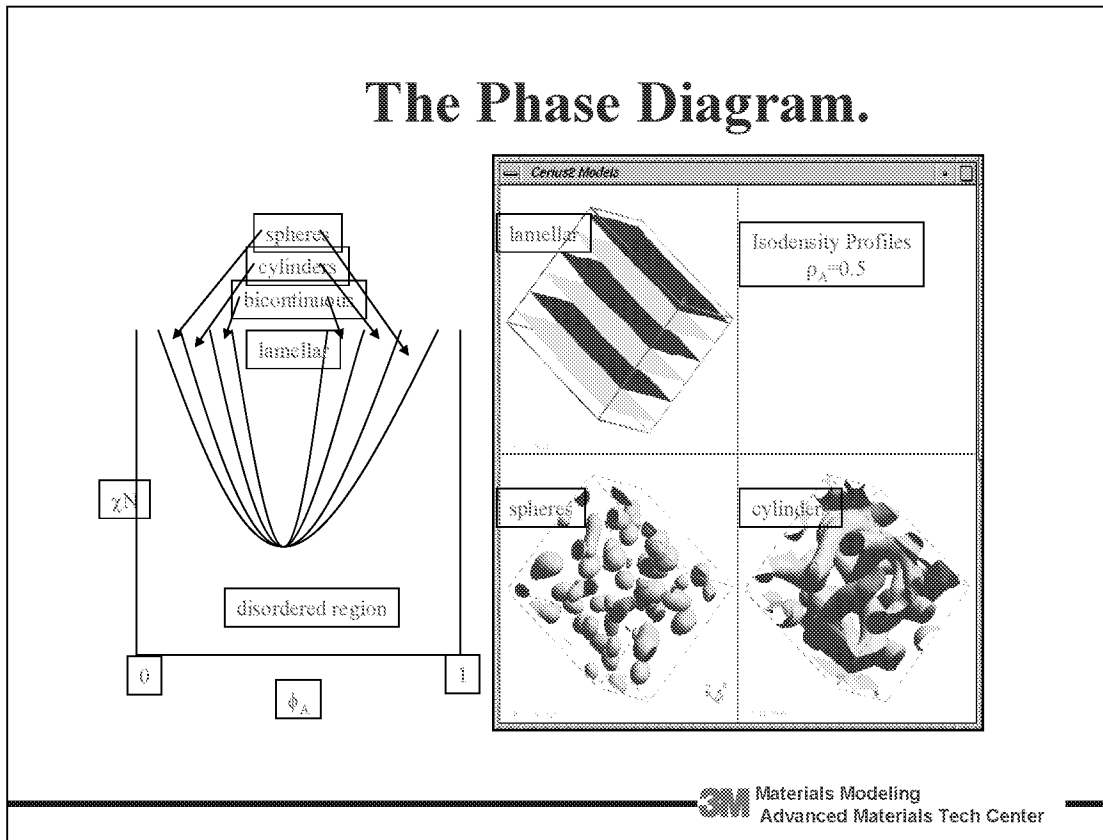


Figure 27

TIME EVOLUTION FOR LAMELLAE FORMATION

Typical processing times are orders of magnitude shorter than relaxation times. This results in non-equilibrium morphologies being trapped in the process. The systems are chemically the same, but have different material properties because various morphologies have been frozen in by processing.

Being able to predict the morphology at various process times and the corresponding properties associated to that state would be a great benefit in industrial design.

MesoDyn was also used to study the evolution of the A-B diblock copolymer toward its equilibrium morphology.

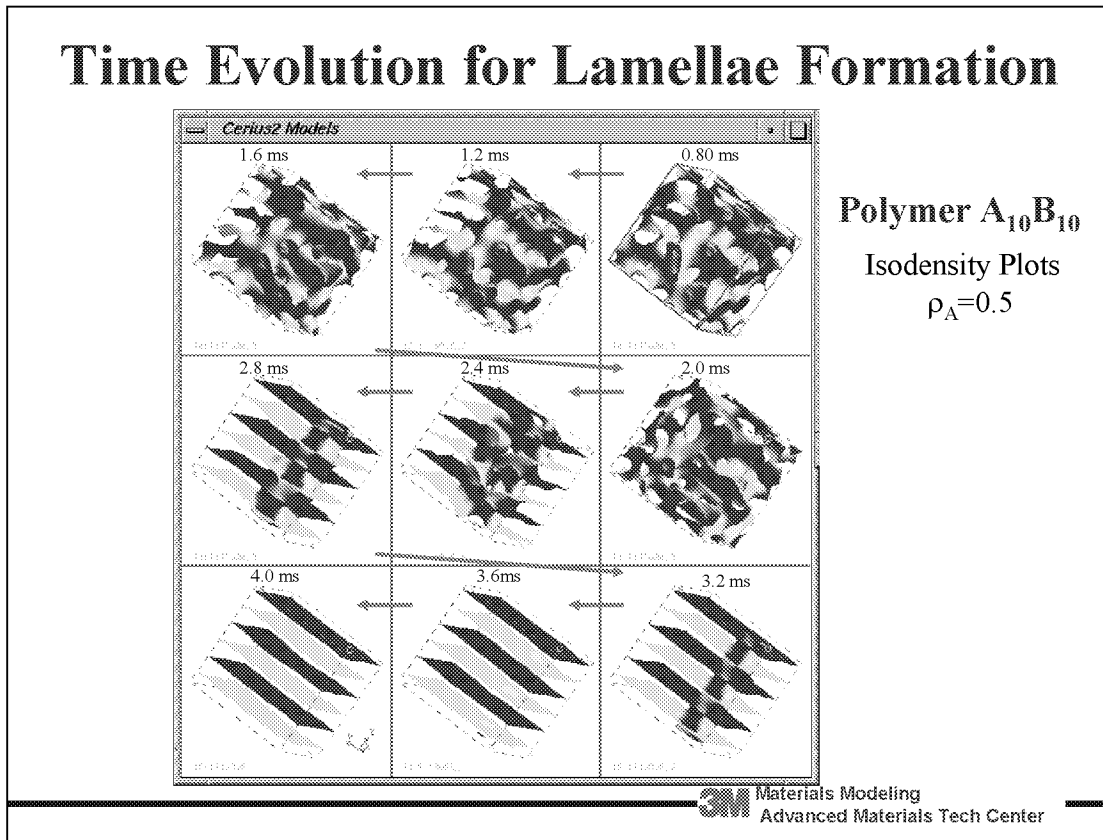


Figure 28

SUMMARY

Summary

- Applied research studies are being carried out via atomistic simulations for:
 - polymer surfaces and polymer/polymer interfaces.
 - self-assembled molecular and polymeric materials.
 - organic/inorganic interfacial systems.
 - structure/property prediction.
- Hybrid atomistic/coarse grain methodologies are being incorporated into the **3M** research program to expand the range of interfaces and materials that can be studied.

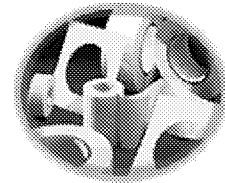


Figure 29

Computational Modeling to Support Materials Design

David L. McDowell
Georgia Institute of Technology
Atlanta, GA

COMPUTATIONAL MODELING TO SUPPORT MATERIALS DESIGN

The objectives of materials design may differ substantially from traditional objectives of life cycle engineering or assessment of durability. Rather than just selecting off-the-shelf materials, it is increasingly the case that we can consider alternatives among materials via computation. Since each new component and application has somewhat different functional requirements, it is desirable as well to develop the machinery that permits computational assessment of the relative suitability among a range of microstructures, or to be able to choose composition and process route that result in a microstructure that delivers the desired structure-property relations. This paper considers several projects at Georgia Tech that address multiscale modeling within the overall vision of materials design.

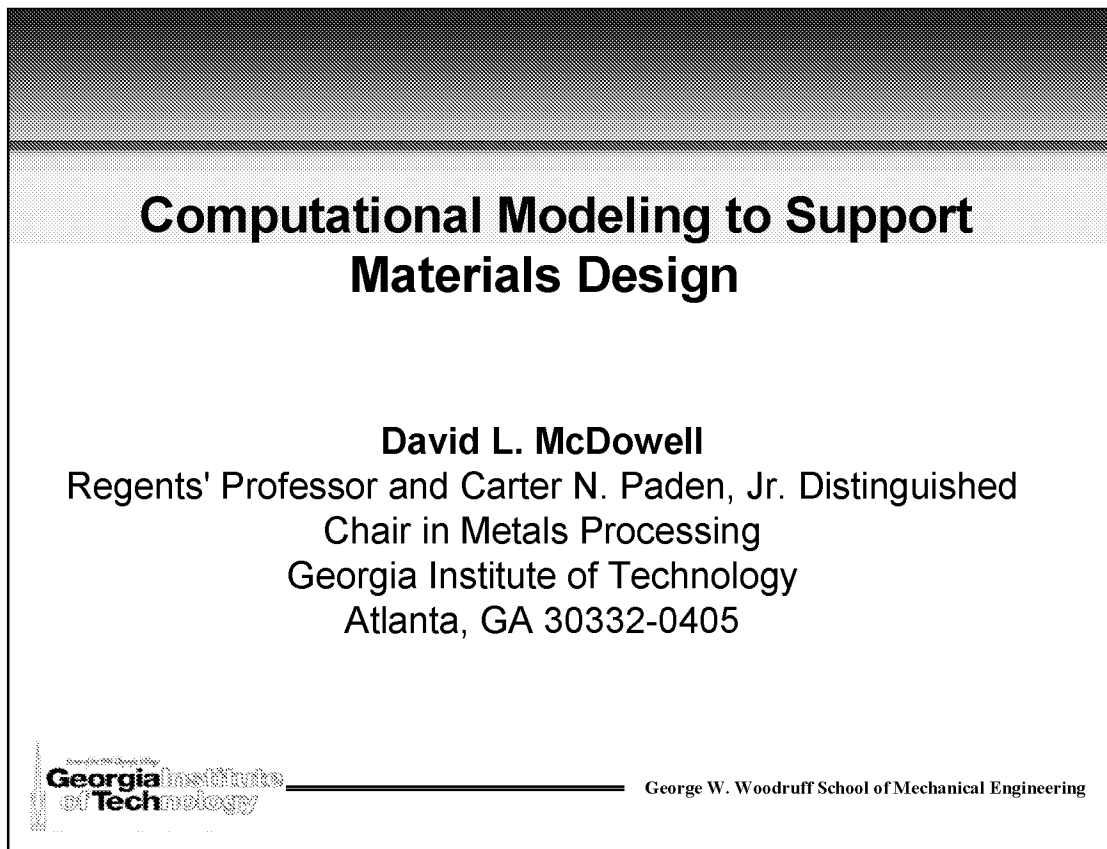


Figure 1

MULTISCALE MODELING- WHAT IS IT?

In general, as one moves from increasingly fine length scales with high resolution, high fidelity mechanics models to more coarse scale representations at higher length scales, it is inevitable the (i) one loses description of dynamical state in favor of thermodynamical state and (ii) the number of model degrees of freedom decrease as one adopts lower order continuum models (compared, for example, to atomistic calculations). Note that although we normally speak of homogenization of properties over increasing length scales (cascade upwards), we must also understand the connection of macroscopic response to phenomena occurring at individual scales below this level, i.e., we must be able to deconstruct the multiscale description to extract salient statistics regarding evolving characteristics such as damage, inelastic deformation, and so on.

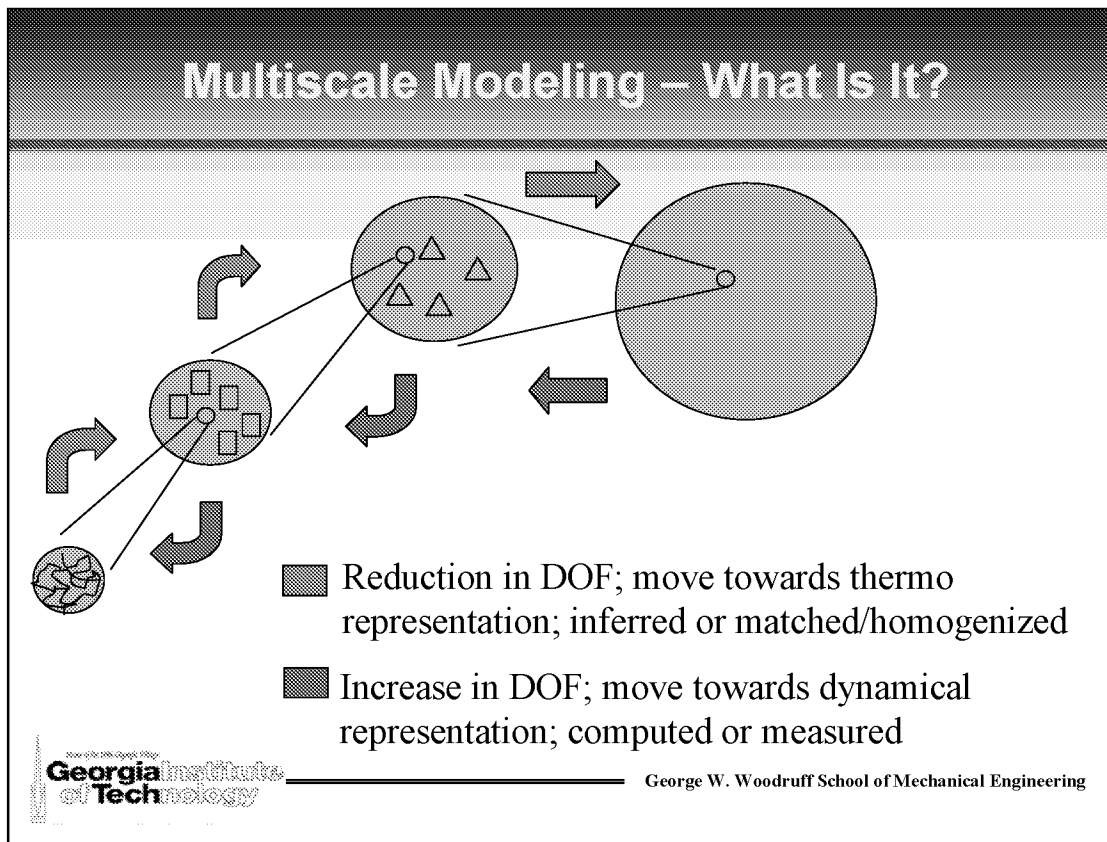


Figure 2

MULTISCALE MODELING- WHY DO IT?

The most compelling argument to develop effective multiscale models is that relevant phenomena occur at disparate length and time scales, and are not easily connected within the umbrella of a single, unified theory. This is a real challenge in materials science and mechanics. Moreover we must account for microstructure variation if the ultimate objective is not just to derive first order average properties but rather properties that depend on extremal characteristics of microstructure. The modeling goes up and down through the length scales as we seek to explore effects of variation at different scales. If the goal is to design a fracture resistant microstructure, for example, we must be able to construct as well as deconstruct the hierarchical structure in order to isolate effects of a given scale. It is complicated by significant coupling of phenomena across length scales due to long range order in solids. We advocate a multiscale approach that respects conservation of mass, momentum and energy, and reflects similar characteristics of dissipation as we move back and forth between different types of models. The identification of schemes to capture evolutionary behavior over a representative volume in this regard is of immense practical importance and represents a fertile are for further development. The objective of a single, unified model for such a hierarchical, multiscale (in both length and time) is not terribly realistic. Rather, development of principles for linking models exercised at their most relevant and appropriate scale within some overarching set of heuristics or framework is the most desirable approach.

Multiscale Modeling – Why Do It?

- Phenomena occur at different length and temporal scales
- Fine scale behavior is often relevant to phenomena that depend on extremal characteristics – fracture, fatigue, turbulence; one-way homogenization unsuited for this task
- Practical limitations on computing time; DOF
- Limitations on confidence in local properties

Georgia Tech  George W. Woodruff School of Mechanical Engineering

Figure 3

MULTISCALE MODELING EXAMPLE – CAST ALLOY FATIGUE

The first example illustrates the building of an hierarchical model for fatigue phenomena occurring over a wide range of length scales for cast A356-T6 alloys, ranging from several microns (individual Si particles) to 15-30 microns (fine scale gas pores) to 30-90 microns (dendrite cells or secondary dendrite arm spacing) to shrinkage pores (up to 1 mm) and entrapped oxides tens of microns to mm range.

Microplasticity of Cast A356-T6 / USCAR

Collaborators:

- M.F. Horstemeyer, Sandia-Livermore
- J. Fan, Alfred University
- K. Gall, Univ. Colorado

Sponsors:

- Sub-contract with Sandia National Laboratories through CRADA with DOE/Big 3

 George W. Woodruff School of Mechanical Engineering

Figure 4

REGIMES OF FATIGUE FOR CAST A356-T6

It was found from elastic-plastic finite element analysis of individual cracked and debonded particles as well as ensembles of particles that the HCF-LCF transition corresponds to the percolation limit for cyclic microplasticity in the eutectic (interdendritic) channels. The transition is highly nonlinear.

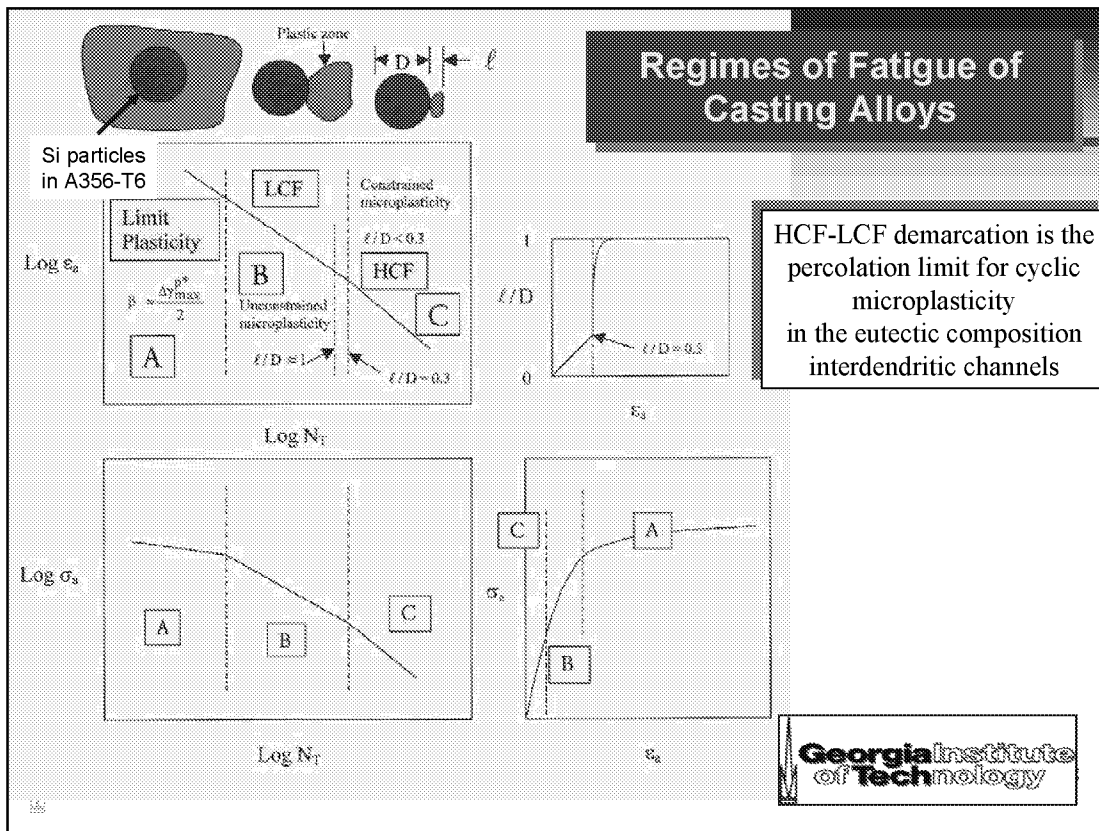


Figure 5

FINITE ELEMENT SIMULATIONS

Simulations were performed of debonded particles, including effects of particle-matrix contact during the compressive part of the cycle. This information was used to develop the structure of an R-ratio dependent correlation of cyclic microplastic shear strain over some characteristic length scale at the notch root (pore or particle).

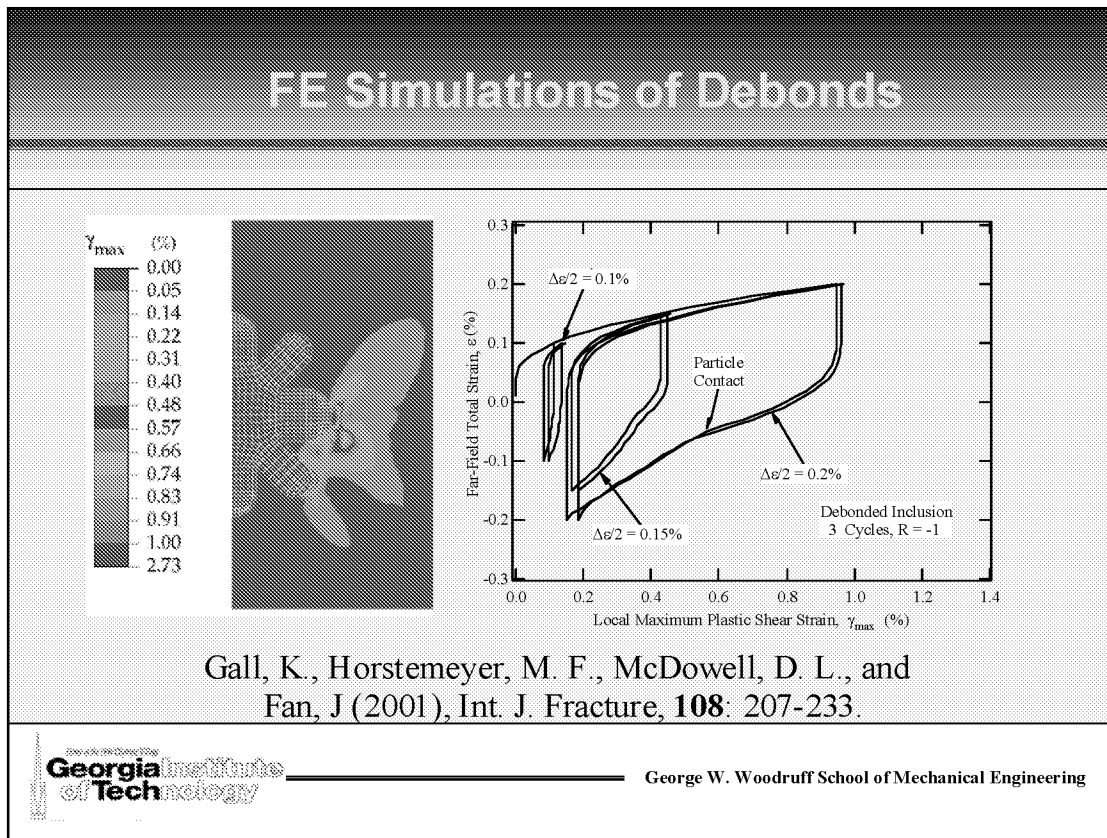


Figure 6

PREDICTIONS OF THE OVERALL MULTISCALE FATIGUE MODEL

Note two major aspects of the predictions for number of cycles to form a 1 mm fatigue crack. First, for various types of defects, the HCF life scatters over the observed experimental range for these types of defects. These calculations are deterministic for each type of defect – the scatter arises from variation of defect severity. Secondly, note the crossover in the LCF regime due to crack-particle and crack-pore coalescence. Higher levels of initial porosity are highly detrimental in the HCF regime, but are beneficial in the LCF regime.

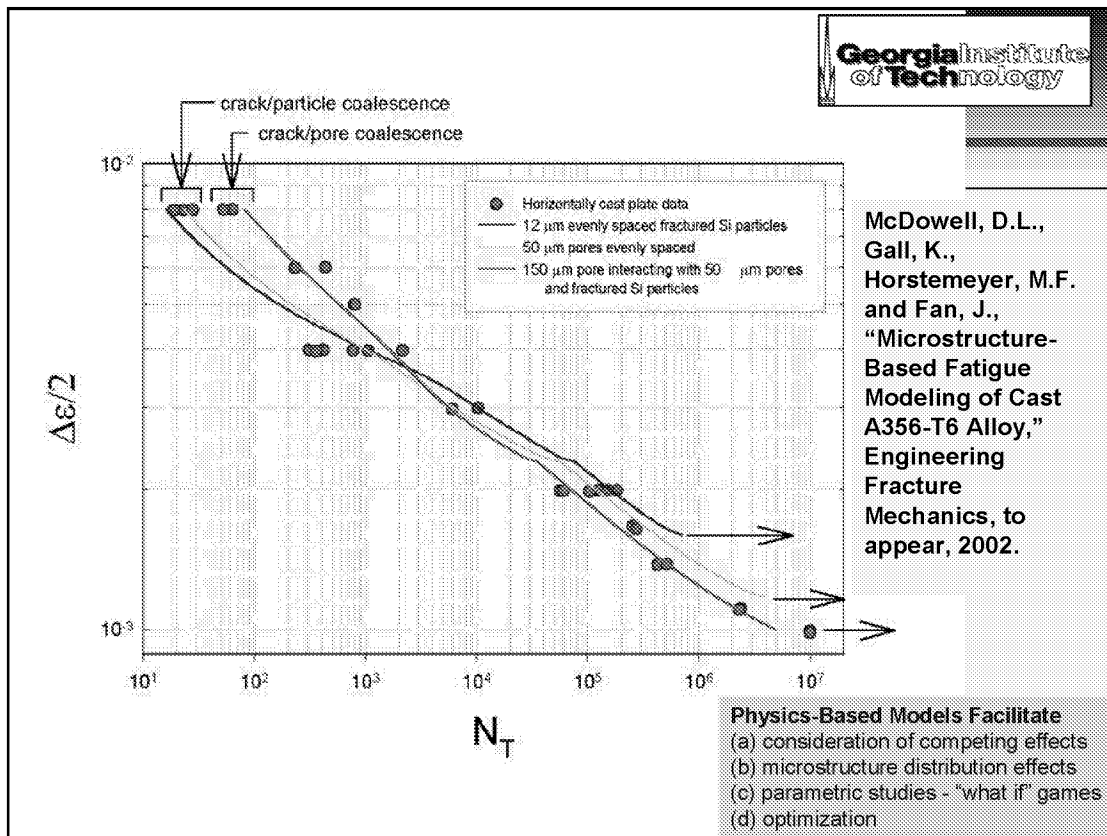


Figure 7

MULTISCALE MODELING EXAMPLE – CAST ALLOY FATIGUE

With such models it is possible to identify clear physical mechanisms for various types of fatigue thresholds, shown below on the Kitagawa diagram. The three thresholds that arise in this model are (a) absence of cyclic microplasticity in the microstructure (yellow region), (b) propagation threshold for microstructurally small cracks based on CTD in Al being less than one Burgers vector (below red line in the blue region), and (c) long crack propagation threshold (below blue line in the blue region).

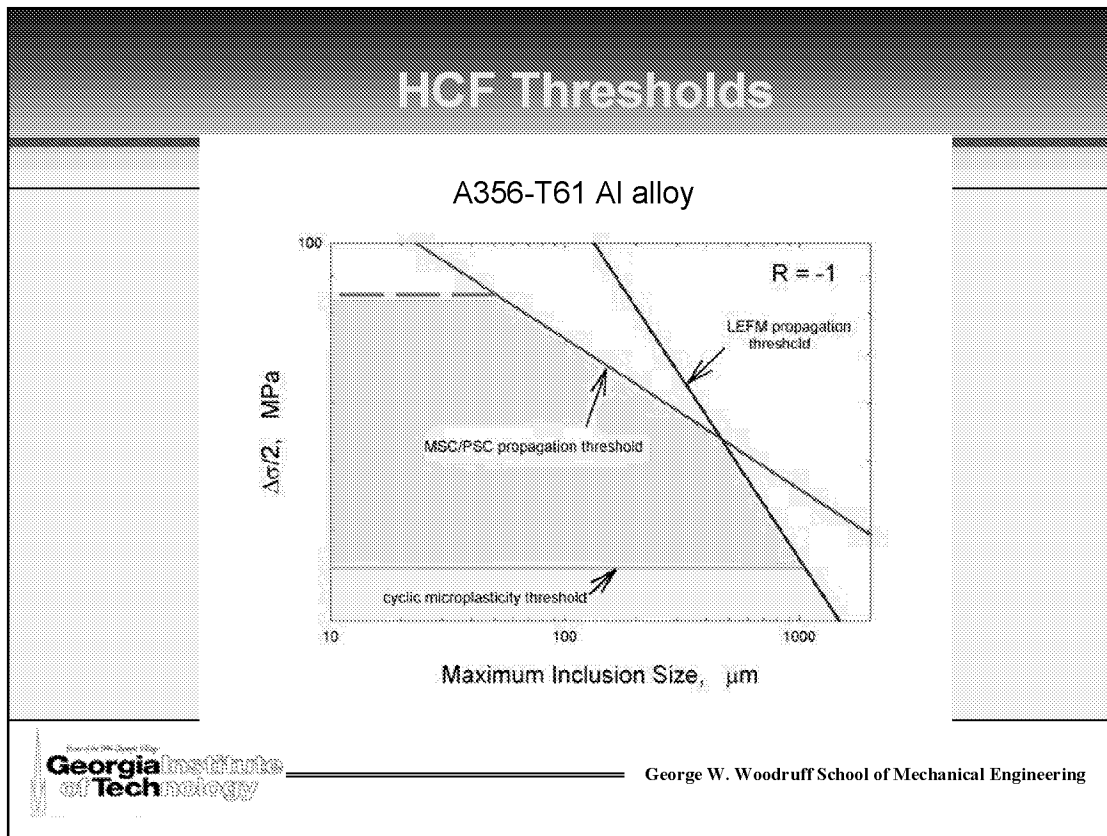


Figure 8

MULTISCALE MODELING OF FRETTING FATIGUE OF TI-6AL-4V

This work illustrates the use of microstructure-based models of a dual phase material in a multiresolution modeling scheme to better understand the phenomena of fretting fatigue.

Microplasticity of Ti-6Al-4V - USAF

Collaborators:

Chung-Hyun Goh, Georgia Tech
J. Wallace & R.W. Neu, Georgia Tech (experiments)

Sponsors:

UDRI contract (admin: J. Burns and J.P. Gallagher)
USAF Palace Knight program (R. Morrissey, co-
advised by T. Nicholas)
AFOSR (Monitor C. Hartley)

Georgia Institute of Technology

George W. Woodruff School of Mechanical Engineering

Figure 9

MICROSTRUCTURE FEATURES

The specific Ti-6Al-4V microstructure to be modeled is a one with primary alpha (HCP) and lamellar grains with BCC beta phase and secondary alpha, shown below.

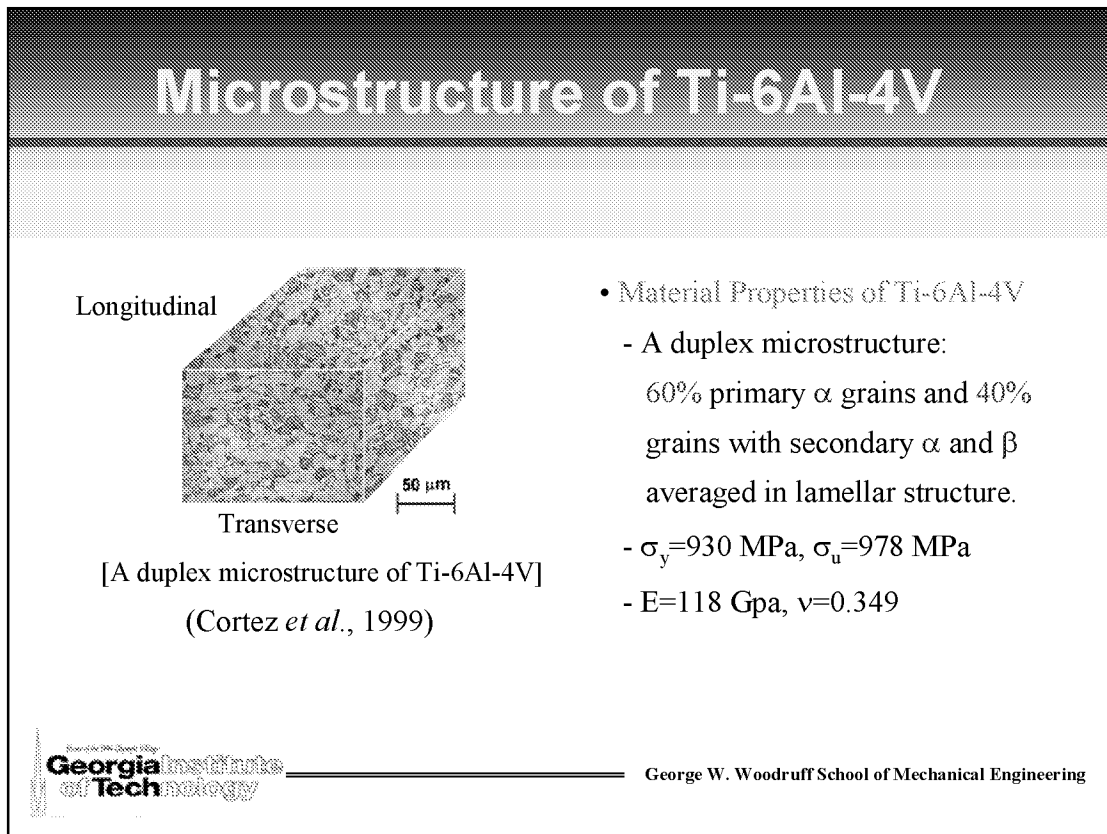


Figure 10

PLANAR TRIPLE SLIP APPROXIMATION FOR HCP ALPHA PHASE

At room temperature, prismatic slip is the principal slip mode in the alpha Ti, which is modeled using a 2D planar triple slip approximation. Of course, the 2D approximation overconstrains specification of crystallographic texture.

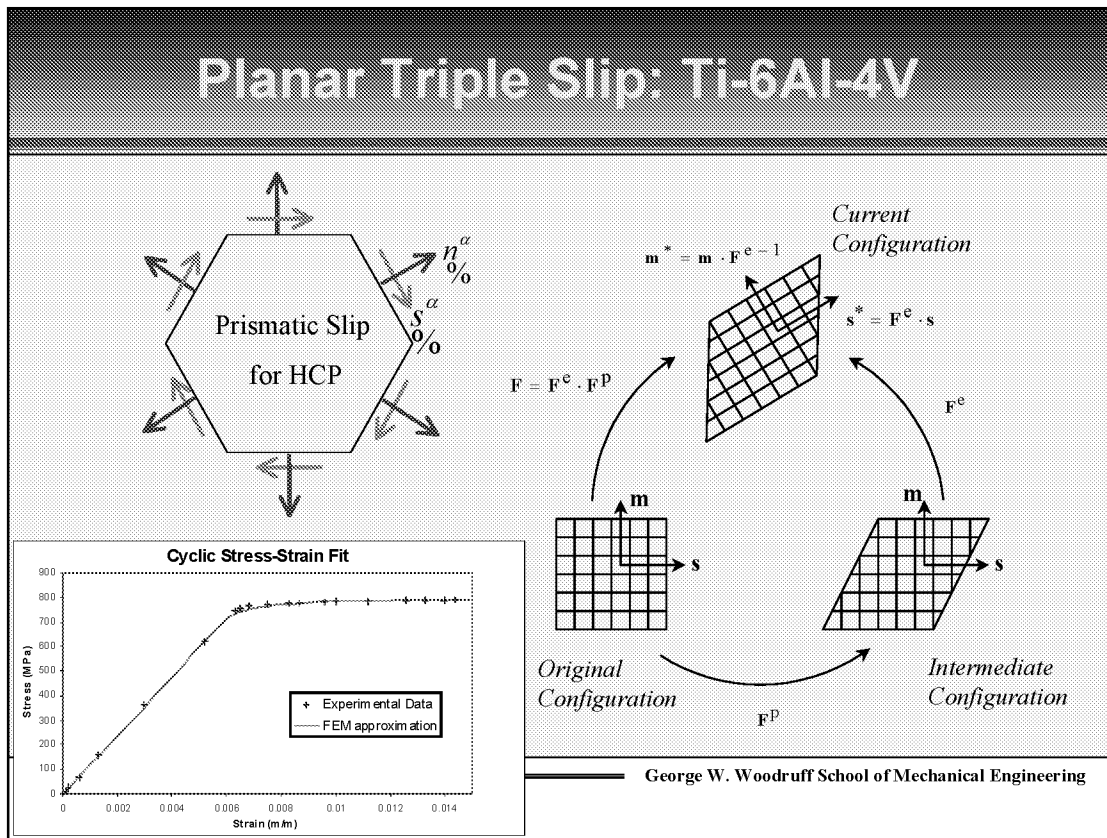


Figure 11

COMPONENT FRETTING MODEL

Using this crystal plasticity description, individual grains are modeled for the actual geometry of experimental specimen configurations, within the region of contact plasticity, while nonlinear kinematic hardening and elasticity laws are used in the intermediate and far fields from the contact, respectively.

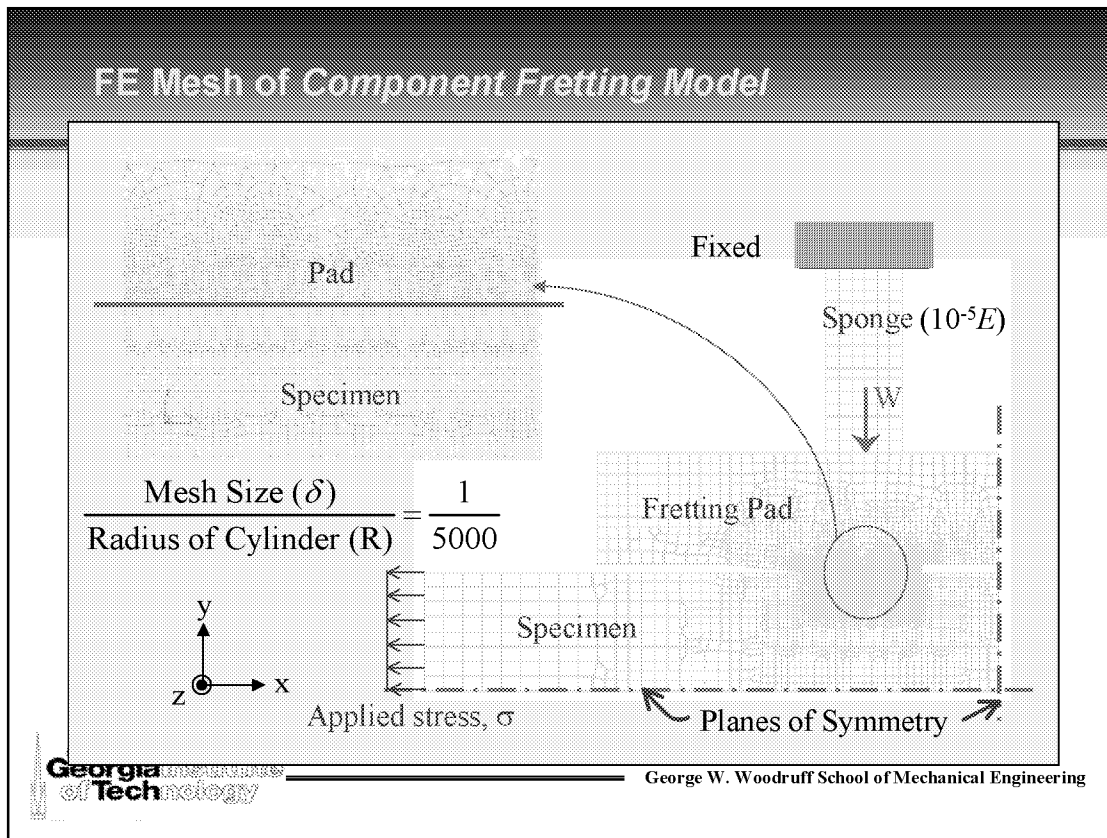


Figure 12

COMPARISON TO FRETTING FATIGUE EXPERIMENTS

The first example illustrates the building of an hierarchical model for fatigue phenomena occurring over a wide range of length scales for cast A356-T6 alloys, ranging from several microns (individual Si particles) to 15-30 microns (fine scale gas pores) to 30-90 microns (dendrite cells or secondary dendrite arm spacing) to shrinkage pores (up to 1 mm) and entrapped oxides tens of microns to mm range.

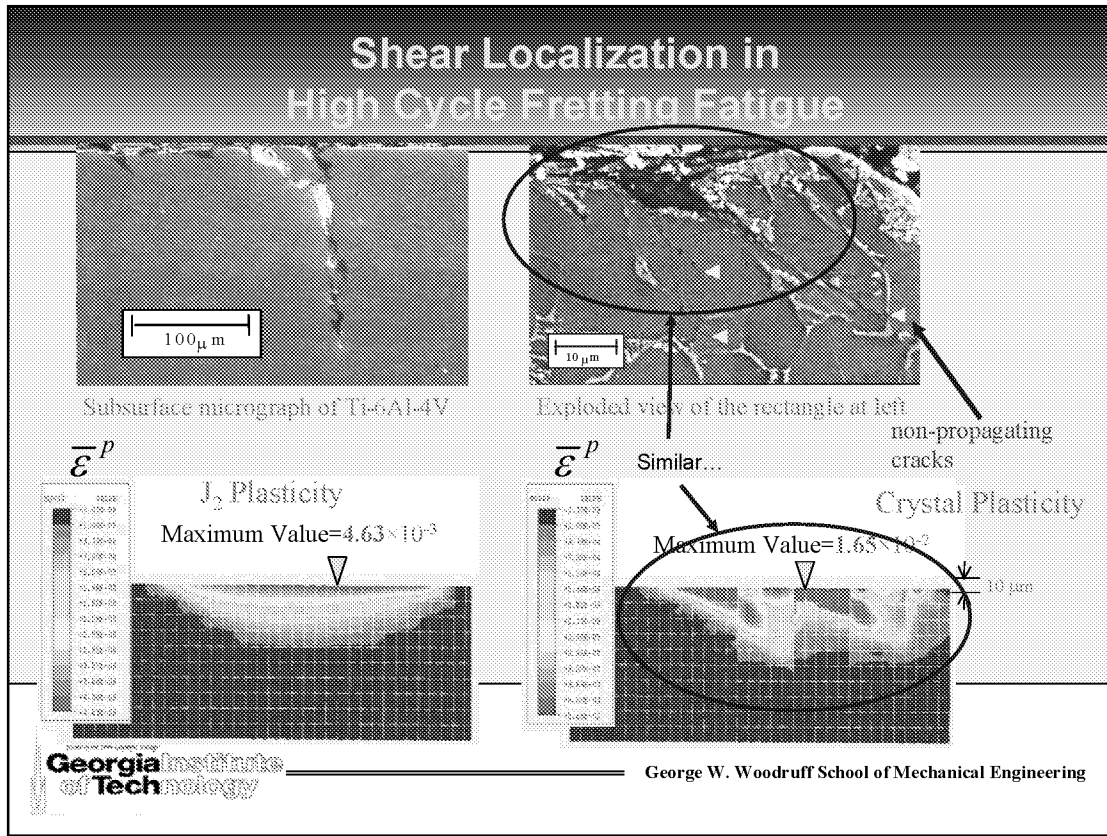


Figure 13

INTERFACE SEPARATION LAWS FROM MOLECULAR CALCULATIONS

The objective of this work is to embed results of nonequilibrium processes (i.e., dislocation generation and motion) into internal state variable continuum models for cohesive interface separation potentials to treat interfaces with one or more ductile metallic constituent. Initial applications are to twist and tilt grain boundaries in Cu. Rather than using some kind of overlapping matching scheme, we use the molecular dynamics and statics results as “numerical experiments” from which we extract information regarding the form of the potential for combined normal and shear separation. To date, such potentials are purely phenomenological and typical have nonlinear elastic character. Some recent developments have included the notion of a degradation of unloading stiffness, motivated by secant stiffness behavior of brittle microcracked solids. Such approaches are likely not descriptive for interfaces between ductile metallic constituents.

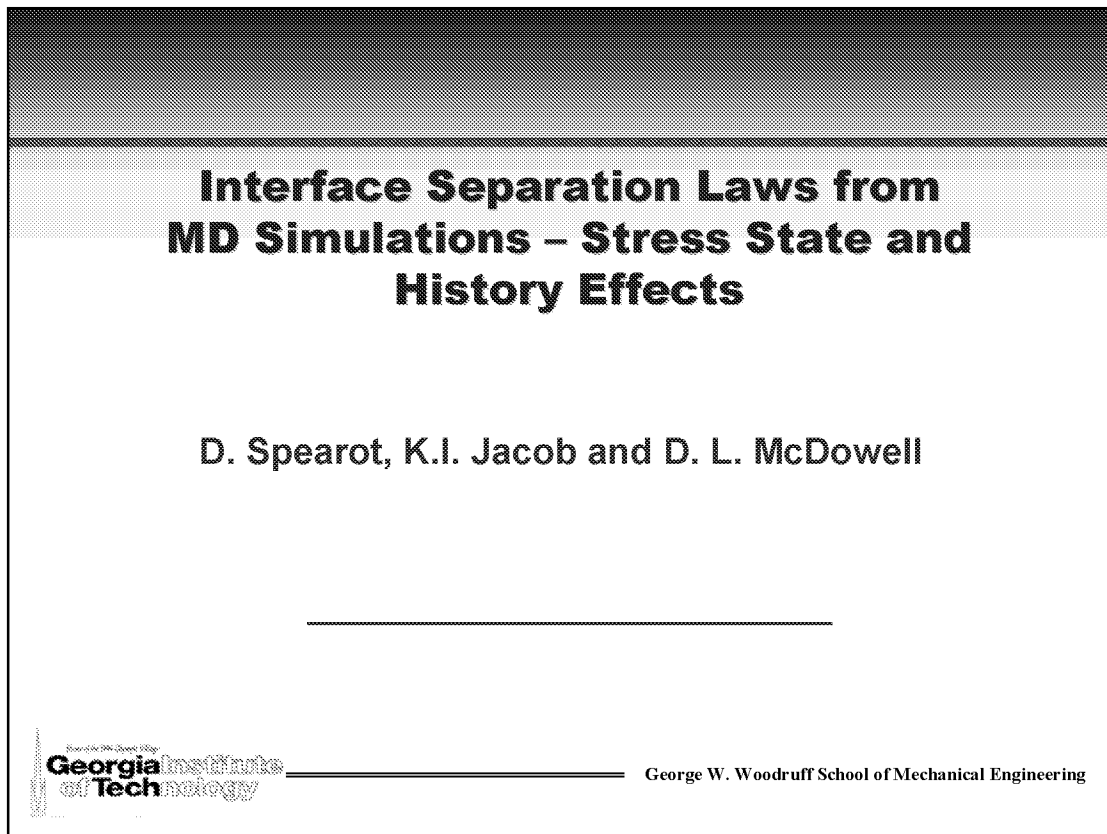


Figure 14

COHESIVE FINITE ELEMENT METHOD – A MEANS FOR ANALYZING RANDOM MICROSTRUCTURES

Distributed cohesive fracture interface elements have proven to be a useful tool for modeling the influence of microstructure morphology of multiphase brittle material systems. We cite below some aspects of the approach. Needleman (1987) was the first to use such approaches in computational schemes as an alternative to conventional fracture mechanics. The advantage of using such models is that distributions of cracks and crack growth paths are dictated naturally by microstructure without user intervention. Of course, there are issues related to convergence, mesh refinement, scaling from nanoscale separations to micron-scale separations, path history dependence, modeling cohesive versus adhesive fracture processes, modeling bulk (not just interface) fracture, and artificial compliance enhancement due to distributed separation elements through the microstructure.

INTERFACE SEPARATION MODELS

- Cohesive traction-displacement relation across interface

(Needleman, 1987)

$$\mathbf{T} = -\frac{\partial \phi}{\partial \Delta}$$

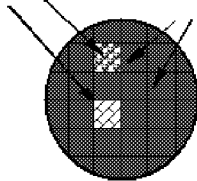
(Zhai and Zhou, 1999)

$$\phi(\Delta) = \phi_0 - \phi_0 \left(1 + \frac{\Delta_n}{\delta_n} \right) \exp\left(-\frac{\Delta_n}{\delta_n}\right) \exp\left(-\frac{\Delta_t^2}{\delta_t^2}\right)$$

- Cohesive Finite Element Method (CFEM)
 - No assignment of fracture path
 - Consideration of significant, representative volumes
 - Facilitates the introduction of lower length scales into the analysis of fracture

Individual constituent

Cohesive surfaces along element boundaries





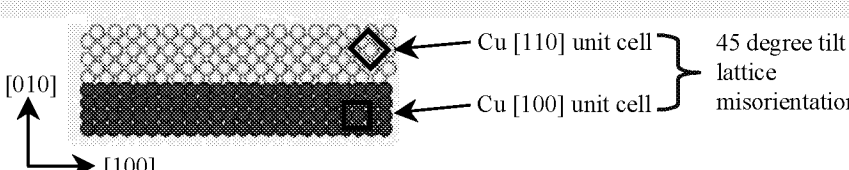
George W. Woodruff School of Mechanical Engineering

Figure 15

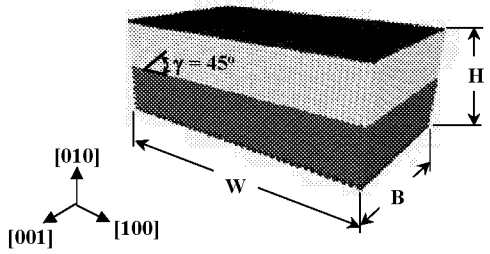
MOLECULAR DYNAMICS CALCULATIONS

The embedded atom interatomic potential is used in dynamical calculations of separation of idealized Cu-Cu grain boundaries, as shown below. We have considered effects of both periodic and non-periodic boundary conditions.

INTERFACE STRUCTURE

- Cu grain boundary interface


- Boundary conditions
 - Last plane in +/- [010] direction is frozen to remain planar
 - Tensile displacement rate of 1 Å/ps applied 'fixed' planes
 - Temperature = 300 K



George W. Woodruff School of Mechanical Engineering

Figure 16

PATH HISTORY DEPENDENCE OF NORMAL AND SHEAR SEPARATION

Significant differences are observed between normal and shear loading (deformation) paths for the interface. In particular, in tension with periodic unloading, the average stress returns to the origin. In shear, by contrast, there is a residual deformation of the representative volume of atoms, indicative of irreversible dislocation generation and motion. The degree of reversibility of the displacement in the normal separation depends on the scale of the characteristic volume of atoms considered – with relatively small volumes (thousands of atoms), the image forces on dislocations emitted from the interface are high enough to drive them back out of the surface as separation proceeds. This is not the case with shear.

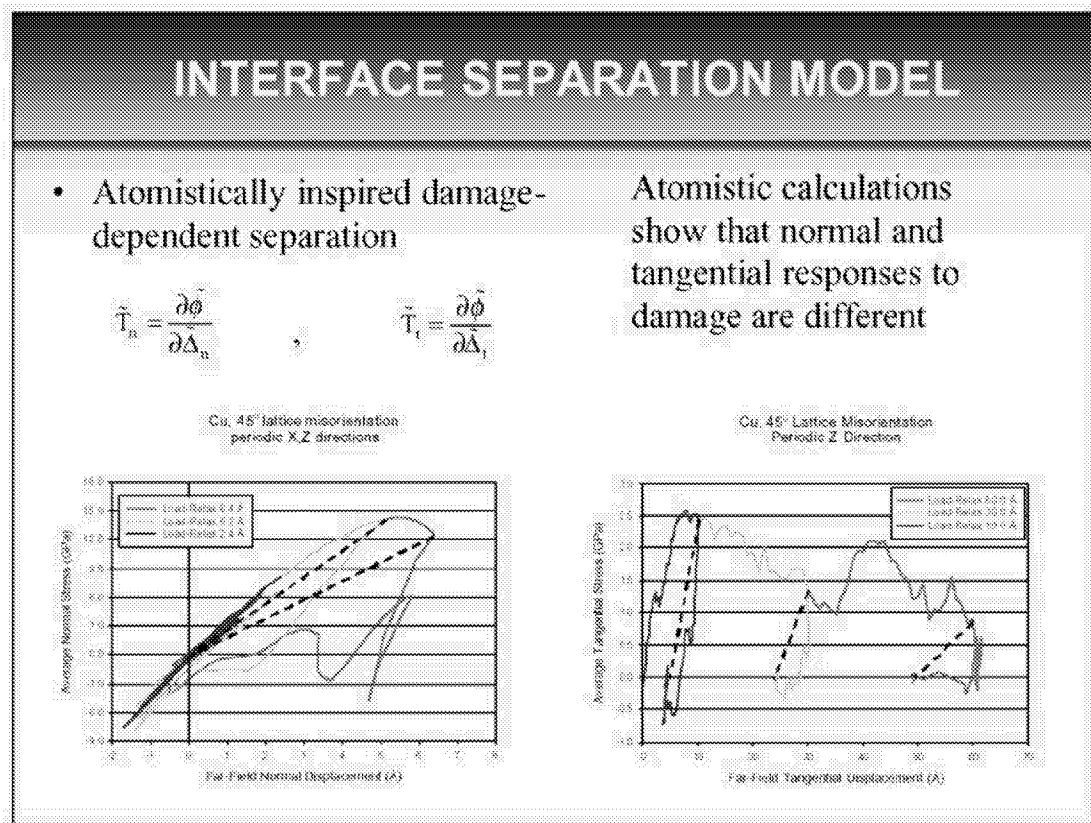


Figure 17

MD-INSPIRED CONTINUUM SEPARATION MODEL

The elements of a continuum model with structure extracted from these kinds of molecular calculations are akin to the elements of a conventional plasticity model. A hyperelastic separation potential is still assumed with regard to a relaxed configuration of separation, but internal state variables are introduced that relate to the degree of interface damage within some boundary layer (based on changes of coordination number) and a measure of dislocation density on various slip systems (ascertained from centrosymmetry parameters – still in progress). The interface separation normalizing parameters are assumed to depend on these ISVs. The ISV evolution equations are based on the MD calculations, and are size scale and interface structure dependent. A challenge is the scaling of the continuum model to address modeling of fracture processes at various length scales.

INTERFACE SEPARATION MODEL

- Embedding atomic characteristics into phenomenological model
 - Effective nonlinear elastic separation potential

$$\tilde{\phi} = \hat{\phi} \left(\frac{\tilde{\Delta}_n}{\delta_n}, \frac{\tilde{\Delta}_t}{\delta_t}; \Lambda_j \right) \iff \Lambda_j \text{ is a set of interface attributes (ISVs)}$$

$$\Lambda_j \rightarrow D_c, \rho^{\alpha}$$

- The interface topology and structure are embedded explicitly:

$$\delta_n = \hat{\delta}_n(\Lambda_j) \quad \delta_t = \hat{\delta}_t(\Lambda_j)$$
- Associated evolution equations

$$\frac{D\Lambda_i}{Dt} = \dot{\Lambda}_i = f(\Lambda_j, \Delta_n, \Delta_t; \nabla^n \Lambda_j, \nabla^n \Delta_n, \nabla^n \Delta_t)$$


George W. Woodruff School of Mechanical Engineering

Figure 18

PRINCIPLES FOR RIGOROUS EQUIVALENCE OF CONTINUUM AND PARTICLE SYSTEMS FOR MULTISCALE MODELING

One of the problems with existing propositions to link atomistic or other discrete particle system calculations with continuum fields is that many approaches seek to match only certain aspects of each solution. In this work, we propose a theoretical structure, based on the dynamic principle of virtual work, to provide transfer of all relevant information from the particle system to the continuum. In so doing, we effectively use the discrete particle system solution as the constitutive law, and construct current configuration continuum fields that are dynamically consistent. After doing this, one may then subject the resulting continuum fields to spatial and temporal averaging procedures, but these are relatively well established in the mechanics literature. It is a separate task to develop continuum constitutive equations.

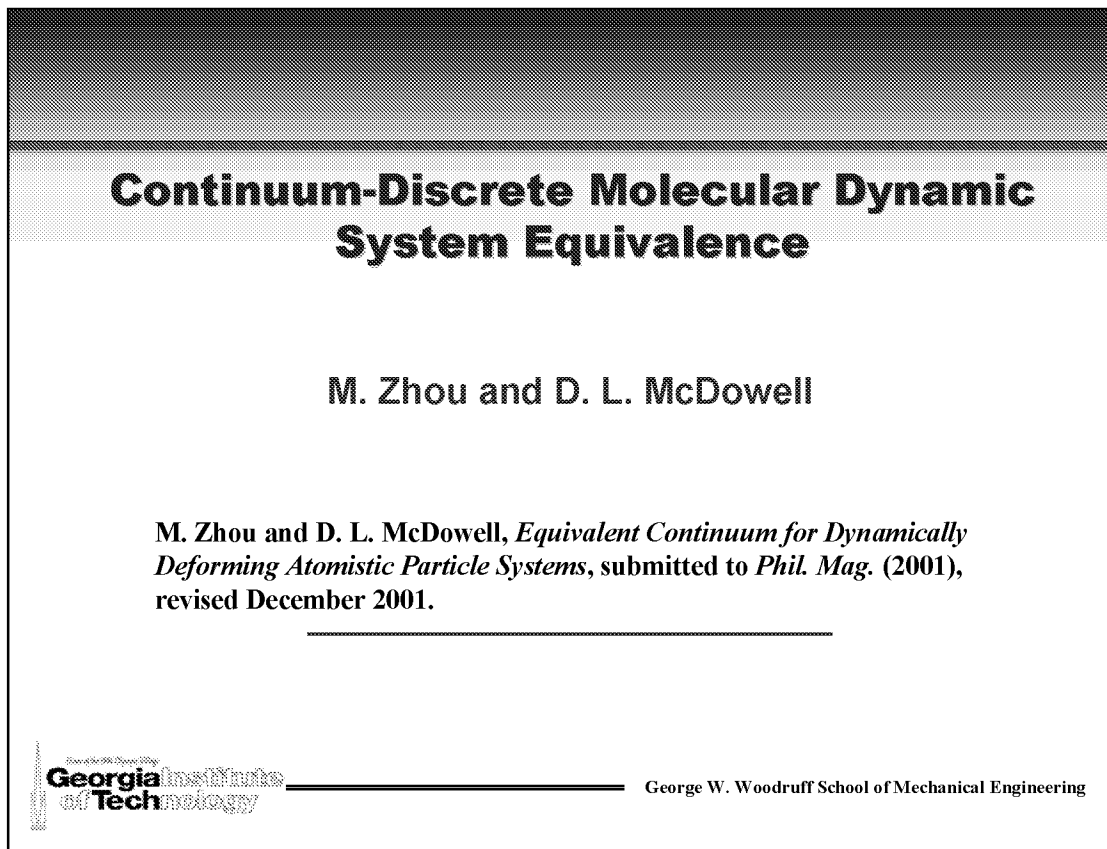


Figure 19

ELEMENTS OF DYNAMIC EQUIVALENCE OF CONTINUUM AND PARTICLE SYSTEMS

In addition to many desirable attributes of the resulting continuum, work-conjugate stress and couple stress fields emerge (the latter only in the case of non-central interatomic moments). As usual, for example, the Cauchy stress is the work conjugate to the rate of deformation tensor. We also assert that if interatomic forces are purely of central type, then any couple stresses must arise from higher scale morphological arrangements of defects. The assessment of the equivalent continuum may be performed either in parallel with the atomistics or as a post-processing step, and is computationally rather intensive. None-the-less, the proposition provides a vehicle to speak of rigorously (rather than heuristically) equivalent fields.

Elements of Fully Dynamic Equivalence

- **Equivalent continuum (EC) in fully dynamic sense:**
 - ◆ Equivalence of internal, external and inertia work rates on arbitrary scale
 - ◆ Conservation of momenta, energy and mass
 - ◆ Definition of work-conjugate deformation field
 - ◆ Account of nonlocal effects
 - ◆ Explicit account of structure
 - ◆ Account of heterogeneity

- **Work-conjugate stress and couple stress fields:**
 - ◆ Nonpolar materials: Couple stress unnecessary at nano-level; arises from scaling

- **Solution is computationally intensive**



George W. Woodruff School of Mechanical Engineering

Figure 20

NONLOCAL EFFECTS OF ATOMIC INTERACTIONS

Within some specified surface in the current configuration that passes through a series of atoms, interactions with atoms outside the surface are treated as body force and body moment fields. Hence, nonlocal action is dominant for small volumes of atoms, and is less significant as the ratio of the size of S to cut-off radius for lattice interactions increases.

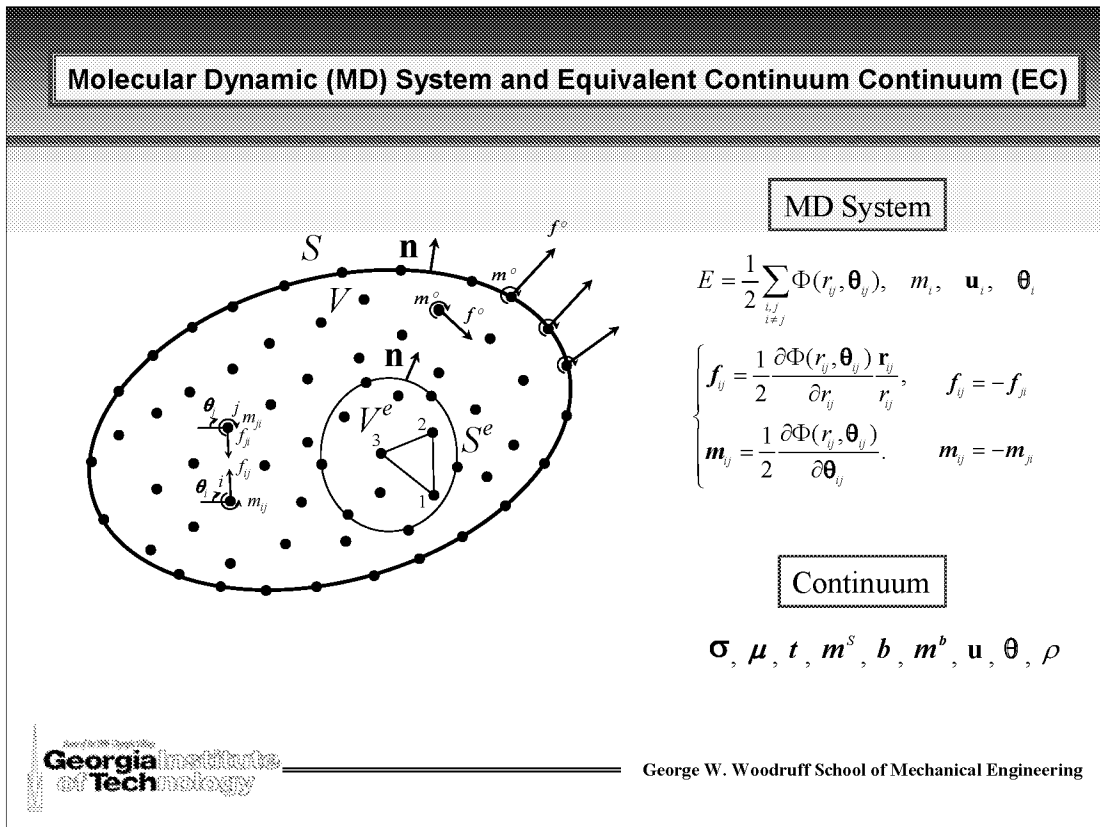


Figure 21

“CONTINUUMIZATION OF FIELDS”

The continuum is imbued with continuous mass density characteristics and continuously distributed stress and couple stress fields based on interpolation functions akin to the finite element method.

Continuum Deformation Field

$$\begin{cases} \delta \mathbf{u}^{(e)}(\mathbf{x}) = \sum_{i=1}^M N_i(\mathbf{x}) \delta \mathbf{u}_i, \\ \delta \boldsymbol{\theta}^{(e)}(\mathbf{x}) = \sum_{i=1}^M N_i(\mathbf{x}) \delta \boldsymbol{\theta}_i, \end{cases} \quad \left(\sum_{i=1}^M N_i = 1 \right)$$

$$\begin{cases} \delta \mathbf{D}^{(e)} = \frac{1}{2} \left[\frac{\partial \delta \mathbf{u}^{(e)}}{\partial \mathbf{x}} + \left(\frac{\partial \delta \mathbf{u}^{(e)}}{\partial \mathbf{x}} \right)^T \right] = \frac{1}{2} \sum_{i=1}^M (\delta \mathbf{u}_i \otimes \mathbf{B}_i + \mathbf{B}_i \otimes \delta \mathbf{u}_i), \text{ and} \\ \delta \mathbf{W}^{(e)} = \frac{1}{2} \left[\frac{\partial \delta \mathbf{u}^{(e)}}{\partial \mathbf{x}} - \left(\frac{\partial \delta \mathbf{u}^{(e)}}{\partial \mathbf{x}} \right)^T \right] = \frac{1}{2} \sum_{i=1}^M (\delta \mathbf{u}_i \otimes \mathbf{B}_i - \mathbf{B}_i \otimes \delta \mathbf{u}_i). \end{cases}$$



George W. Woodruff School of Mechanical Engineering

Figure 22

WORK EQUIVALENCE OF CONTINUUM AND DISCRETE PARTICLE SYSTEMS

Below are shown the dynamic work equivalence of internal forces (in black), external forces (in blue) and inertial forces (in red) for a current configuration volume element enclosing a finite set of particles/atoms and the equivalent continuum. It is noted that continuum stress, deformation and density fields are all expected to vary substantially over distances comparable to interatomic spacings, as they mimic the atomistic solutions. However, these continuum fields may then be subjected to classical volume and time averaging procedures, as done, for example, in turbulent flow.

**Particle System and Continuum Equivalence
(On Arbitrary Size Scale)**

Continuum $(V^* \leq V)$

$$\begin{aligned}
 & - \int_{V^*} \boldsymbol{\sigma}^{(c)} : \delta \mathbf{d}^{(c)} dV - \int_{V^*} \boldsymbol{\mu}^{(c)} : \delta \mathbf{w}^{(c)} dV + \int_{V^*} \delta^{(c)} \delta \mathbf{u}^{(c)} dV + \int_P m^{(c)} \delta \omega^{(c)} dV + \int_S f^{(c)} \cdot \delta \mathbf{u}^{(c)} dS + \int_{S^*} m^{(c)} \delta \omega^{(c)} dS = \\
 & = \int_{V^*} \rho^{(c)} \mathbf{u}^{(c)} \delta \mathbf{u}^{(c)} dV + \int_{V^*} (f^{(c)} \cdot \boldsymbol{\theta}^{(c)}) \delta \boldsymbol{\theta}^{(c)} dV
 \end{aligned}$$

Discrete atomistic

$$\sum_{i=1}^M f_i^{(a)} \cdot \delta \mathbf{r}_i + \sum_{i=1}^M m_i^{(a)} \cdot \delta \boldsymbol{\theta}_i + \sum_{i=1}^M f_i^{(e)} \cdot \delta \boldsymbol{\xi}_i + \sum_{i=1}^M m_i^{(e)} \cdot \delta \boldsymbol{\theta}_i = \sum_{i=1}^M m_i^{(a)} \delta \boldsymbol{\xi}_i + \sum_{i=1}^M (f_i \cdot \boldsymbol{\theta}_i) \cdot \delta \boldsymbol{\theta}_i$$

$(M \leq N)$



George W. Woodruff School of Mechanical Engineering

Figure 23

REFERENCES

1. Gall, K., Horstemeyer, M., McDowell, D.L., and Fan, J. "Finite Element Analysis of the Stress Distributions Near Damaged Si Particle Clusters in Cast Al-Si Alloys," *Mechanics of Materials*, Vol. 32, No. 5, 2000, pp. 277-301.
2. Gall, K., Horstemeyer, M.F., Degner, B.W., McDowell, D.L., and Fan, J. "On the Driving Force for Fatigue Crack Formation From Inclusions and Voids in a Cast A356 Aluminum Alloy," *International Journal of Fracture*, Vol. 108, 2001, pp. 207-233.
3. Fan, J., McDowell, D.L., Horstemeyer, M.F. and Gall, K., "Computational Micromechanics Analysis of Cyclic Crack-tip Behavior for Microstructurally Small Cracks in Dual-Phase Al-Si Alloys", *Engineering Fracture Mechanics*, Vol. 68, 2001, pp. 1687-1706.
4. McDowell, D.L., Gall, K., Horstemeyer, M.F. and Fan, J., "Microstructure-Based Fatigue Modeling of Cast A356-T6 Alloy," to appear in *Engineering Fracture Mechanics*, 2002.
5. Morrissey, R.J., McDowell, D.L. and Nicholas, T., "Frequency and Stress Ratio Effects in High Cycle Fatigue of Ti-6Al-4V," *International Journal of Fatigue*, Vol. 21, 1999, pp. 679-685.
6. Morrissey, R.J., McDowell, D.L. and Nicholas, T., "Strain Accumulation in Ti-6Al-4V During Fatigue at High Mean Stress," *Mechanics of Time-Dependent Materials*, Vol. 2, 1999, pp. 195-210.
7. Morrissey, R.J., McDowell, D.L. and Nicholas, T., "Microplasticity in HCF of Ti-6Al-4V," *International Journal of Fatigue*, Vol. 23, 2001, pp. 55-64.
8. Goh, C.-H., Wallace, J.M., Neu, R.W. and McDowell, D.L., "Polycrystal Plasticity Simulations of Fretting Fatigue," *International Journal of Fatigue*, Vol. 23, 2001, pp. S423-S435.
9. Morrissey, R., Goh, C.-H., and McDowell, D.L., "Microstructure-Scale Modeling of HCF Deformation," to appear in special issue of *Mechanics of Materials on Experiments and Modeling of Failure of Modern Materials*, honoring Professor Sia Nemat-Nasser, 2002.
10. Goh, C.-H., Neu, R.W. and McDowell, D.L., "Influence of Nonhomogeneous Material in Fretting Fatigue," to appear in *ASTM STP on Fretting Fatigue, Symp. On Fretting*, Tokyo, Japan, 2002.

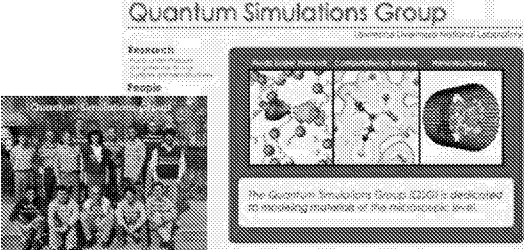
11. Goh, C.-H., Neu, R.W. and McDowell, D.L., “Crystallographic Plasticity in Fretting of Ti-6Al-4V,” submitted to the International Journal of Plasticity, February 2002.
12. McDowell, D.L., “Materials Design: A Useful Research Focus for Inelastic Behavior of Structural Metals,” Special Issue of the Journal of Theoretical and Applied Fracture, Prospects of Mesomechanics in the 21st Century: Current Thinking on Multiscale Mechanics Problems, eds. G.C. Sih and V.E. Panin, Vol. 37, 2001, pp. 245-259 (invited).
13. Zhou, M. and McDowell, D.L., “Equivalent Continuum for Dynamically Deforming Atomistic Particle Systems,” submitted to Philosophical Magazine, May 2001; revised January 2002.
14. Spearot, D.E., Jacob, K.I., Zhou, M. and McDowell, D.L., “Nonlocal Separation Constitutive Laws for Interfaces and their Relation to Nanoscale Simulations,” 1st Georgia Tech Conference on Nanoscience and Nanotechnology, October 16-18, 2000, Atlanta, GA.

Quantum Simulations of Solids, Liquids and Nanostructures

Giulia Galli
Lawrence Livermore National Laboratory
Livermore, CA

Quantum simulations of solids, liquids and nanostructures

Giulia Galli
Lawrence Livermore National Laboratory



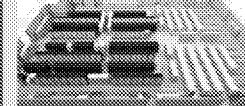
Quantum Simulations Group
Lawrence Livermore National Laboratory

Work carried by DOE for the University of California under contract no. Eng-048

Figure 1

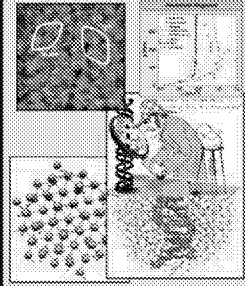
Quantum Simulations of Matter: solids, liquids and nanostructures

High Performance Computing

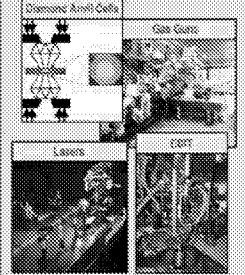


ASCI WHITE
Density Functional code: JEEP
Quantum Monte Carlo codes

Quantum Simulations



State of the Art Experiments



Dimension Annel Cells
Gas Cells
Layers
DOT



- PREDICT physical properties of materials with great accuracy
- INVESTIGATE properties not directly accessible to experiments
- INTERPRET and COMPLEMENT experiments

P81238-gagg-u-001

Figure 2

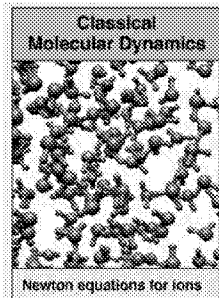
Computation as a tool for scientific investigation



- Why ab-initio simulations?
- Some interdisciplinary problems where ab-initio simulations can have an impact
- How the methods developed in the solid state physics community have evolved and where they have `spread`
- How these methods `join` quantum chemistry methods and how they are reaching out to the biology arena
- Major limitations and challenges

Figure 3

Microscopic modeling based on classical molecular dynamics may have limited predictive power



- The materials properties are computed assuming a given **interatomic potential fitted to experiment**.
- Fits are done using data taken over a limited range of thermodynamic conditions
- No explicit description of bond formation and breaking → *no chemistry*
- No explicit description of electronic properties

Complex states of matter involving forming and breaking of bonds and involving different phases cannot be described with classical molecular dynamics

Figure 4

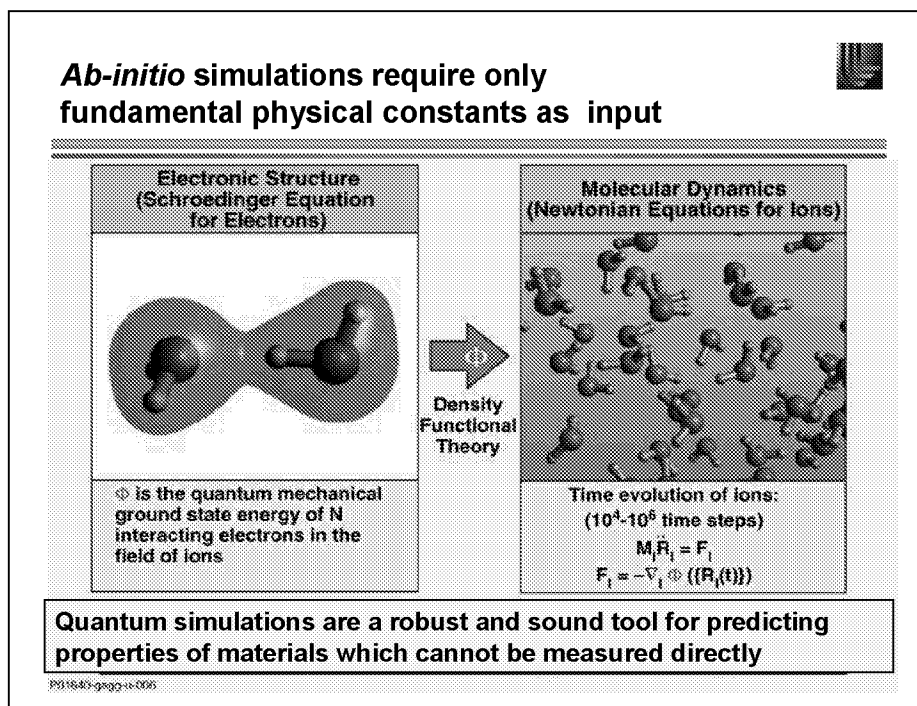


Figure 5

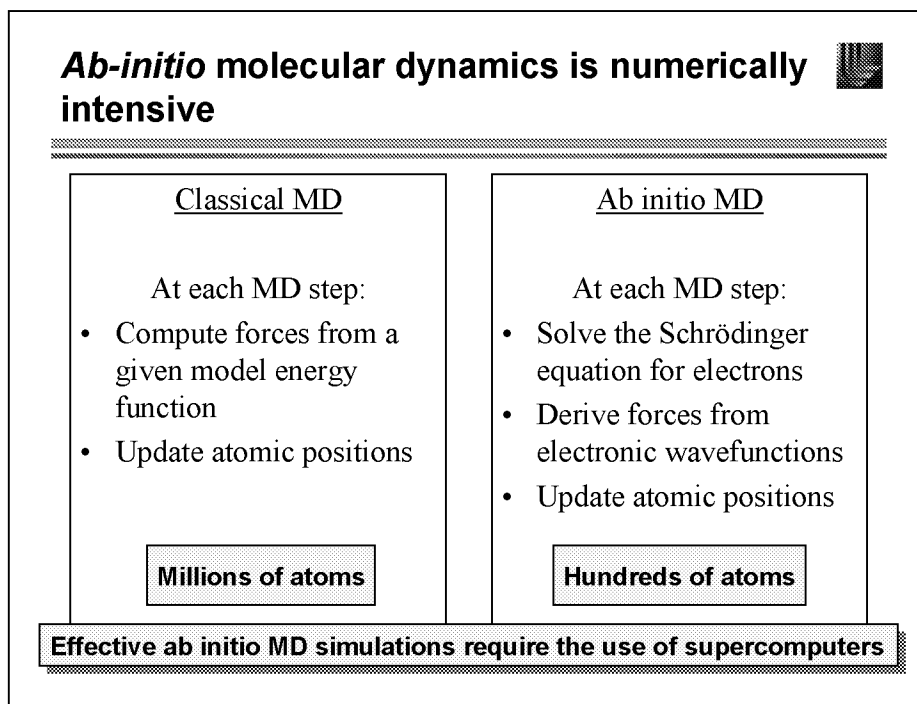


Figure 6

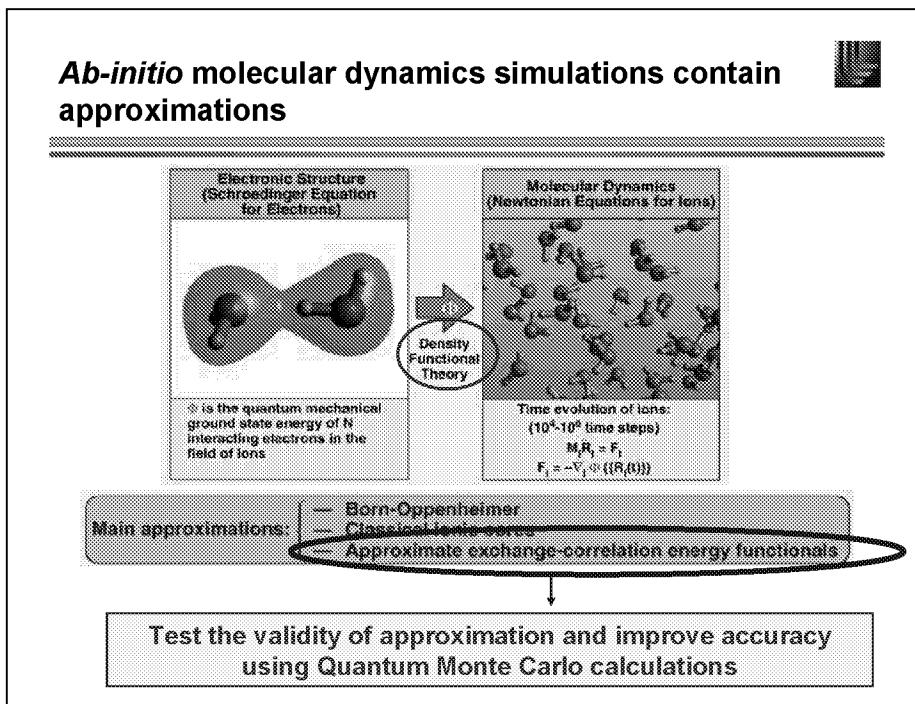


Figure 7

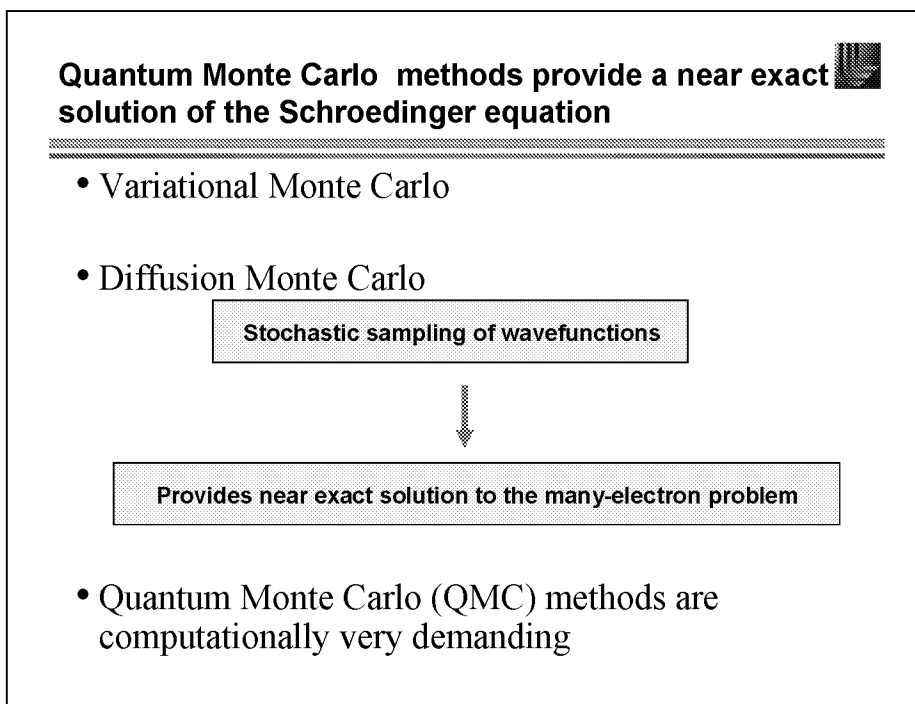


Figure 8

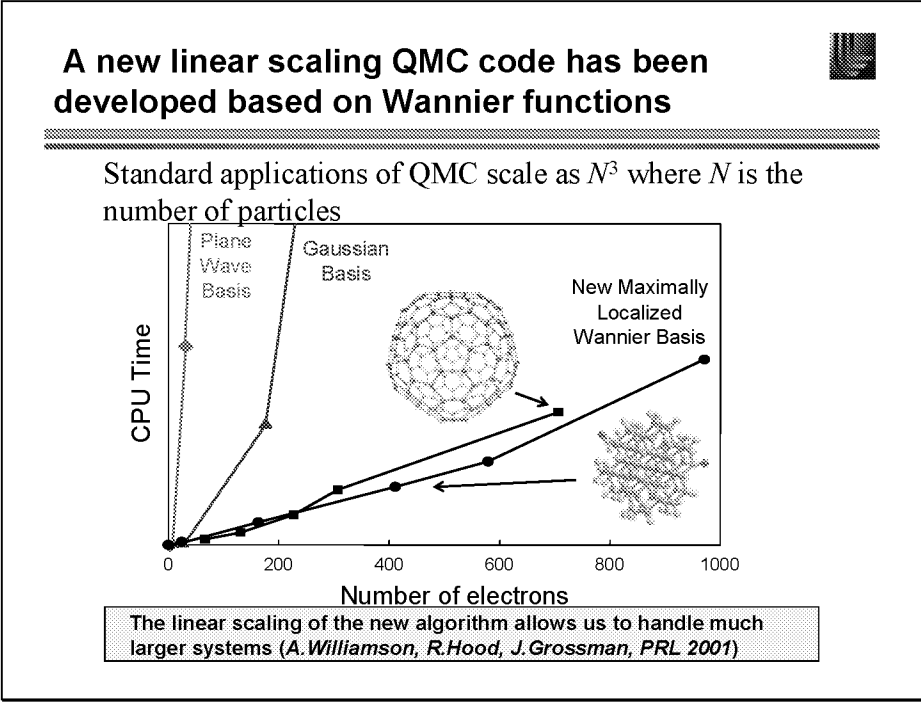


Figure 9

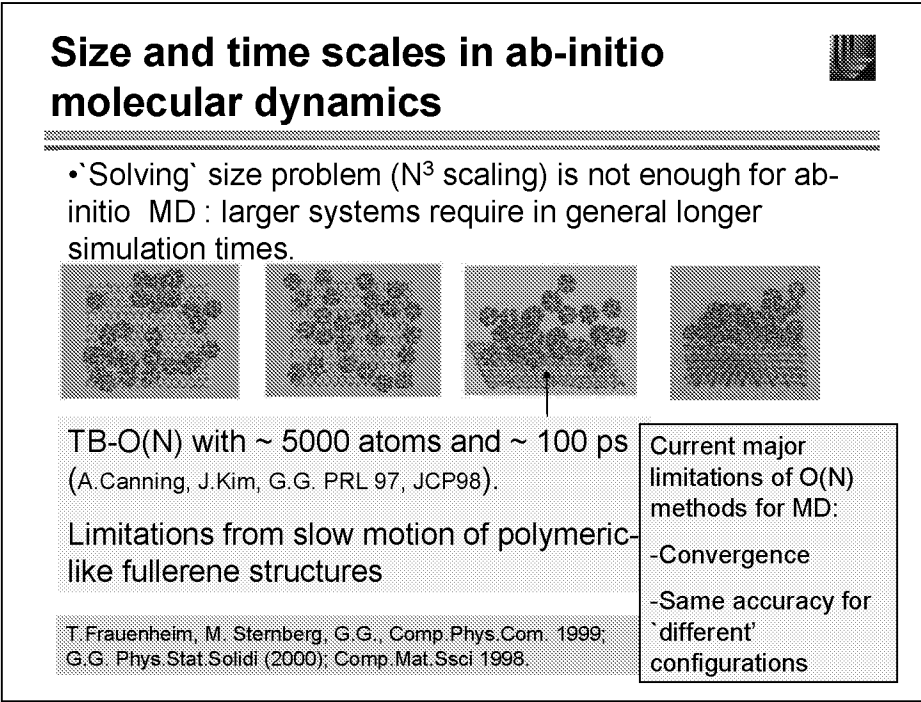


Figure 10

From solid state physics to chemistry and 'biology'



- 'Standard model of solid' (Kohn-Sham, 1965 → M.Cohen et al. 1979)
- Combine statistical mechanical methods (Molecular Dynamics) and the 'Standard Model for Solids' (Density Functional Theory): R.Car and M.Parrinello, 1985 →
- Improve Density Functionals (Gradient Corrections): ca. 1990 → from condensed matter physics to chemistry
- Quantum Monte Carlo calculations for real materials (D.Ceperley et al.) : ca. 1990 →
- Coupling classical/quantum methods → towards biology.

Figure 11

Progress in condensed matter physics, materials science and chemistry using computations



- Progress in 'traditional materials modeling' at different length scales: predict new materials, predict new properties, "maneuver atom by atom"
- Progress at the interface between "hard" and "soft" matter: microscopic materials modeling into the biology world
- Progress at a "new" length scale, in the nanoscience world

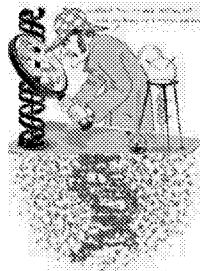


Figure 12

Complex systems can be modeled using ab-initio molecular dynamics

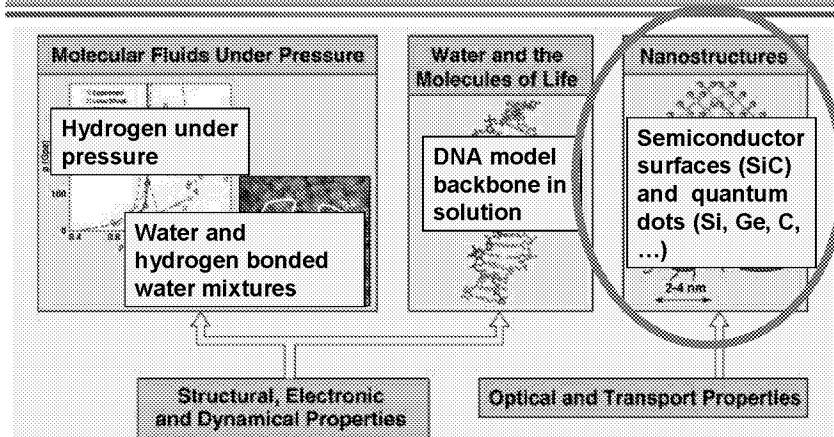


Figure 13

What can we learn about surfaces using first-principles calculations?

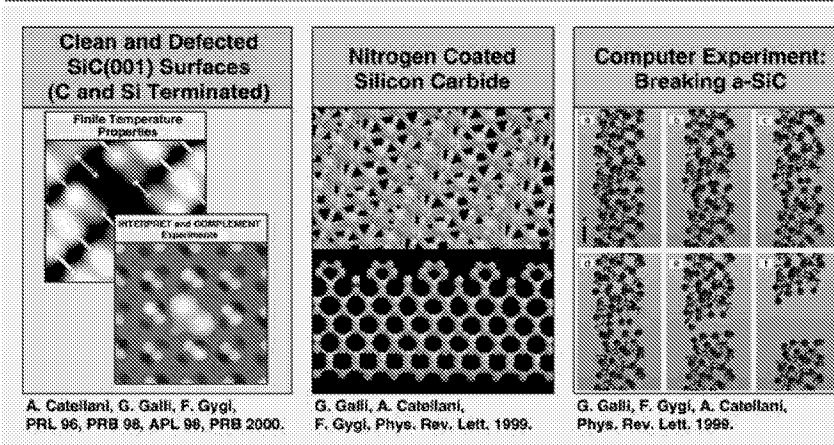


Figure 14

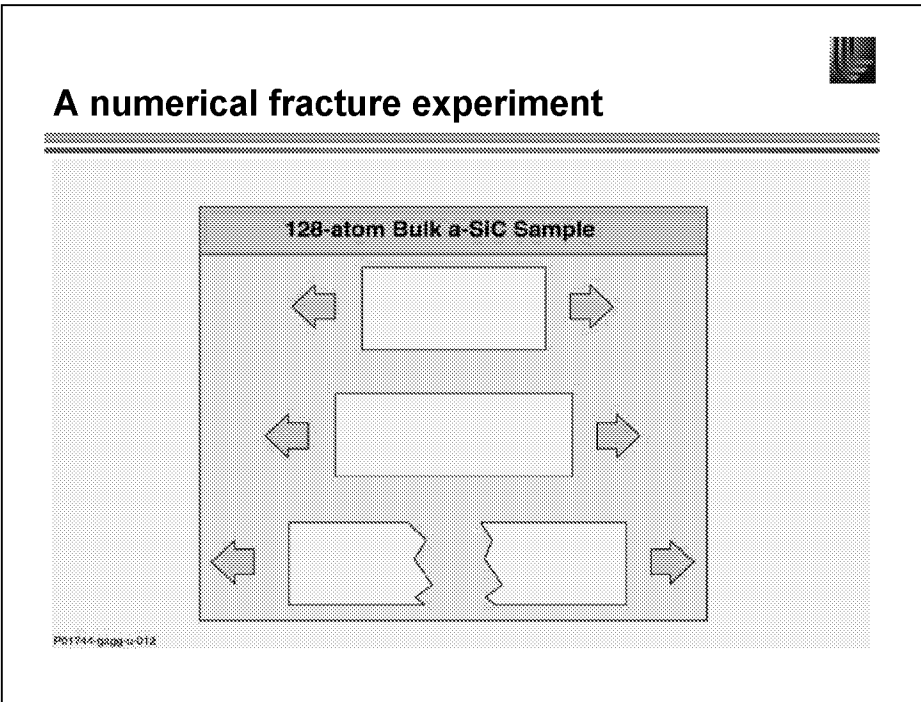


Figure 15

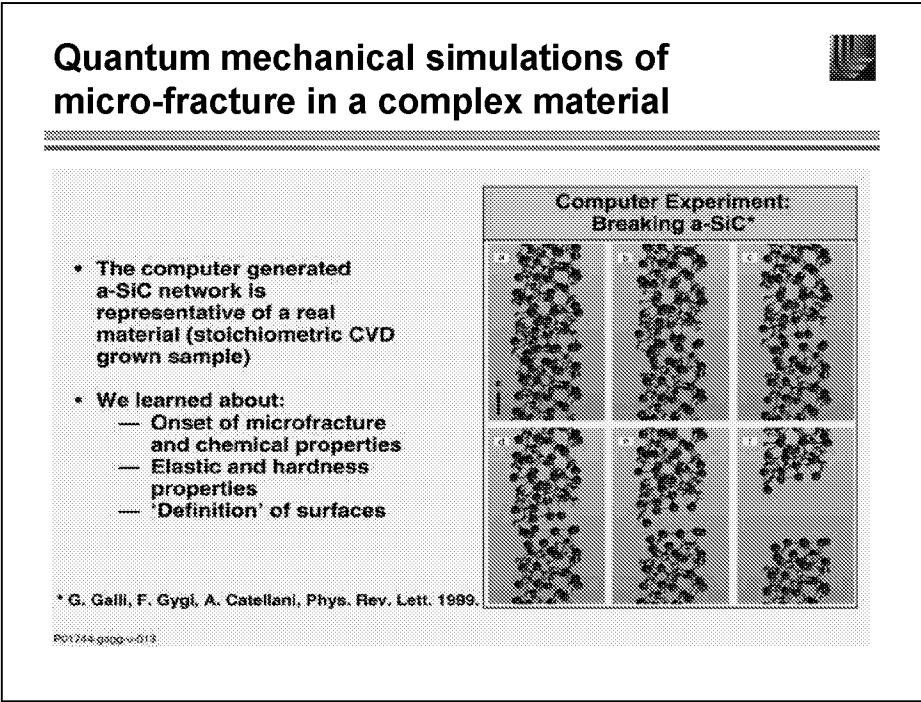


Figure 16

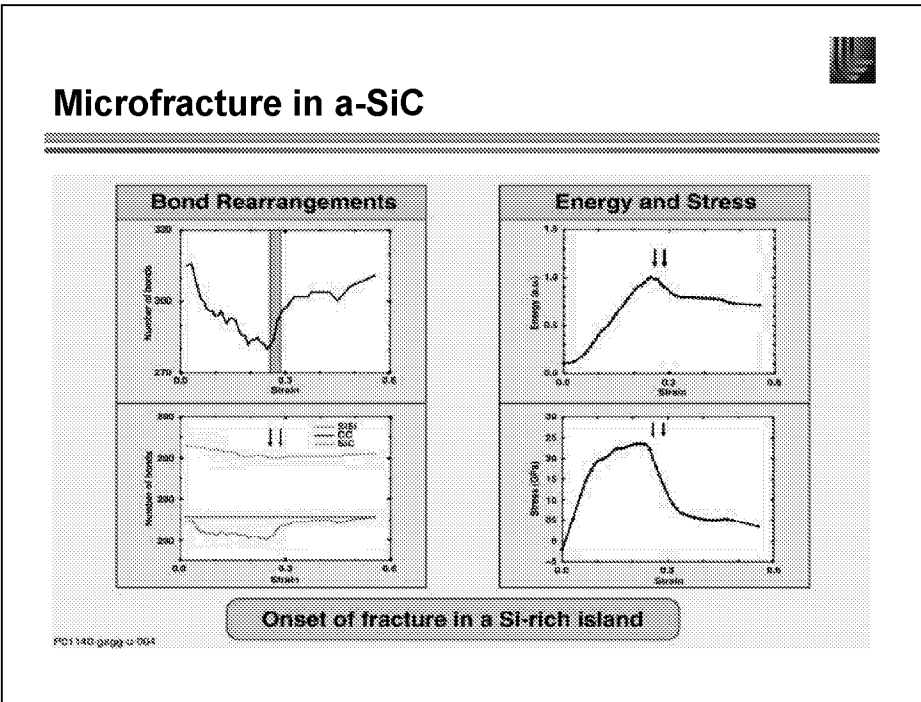


Figure 17

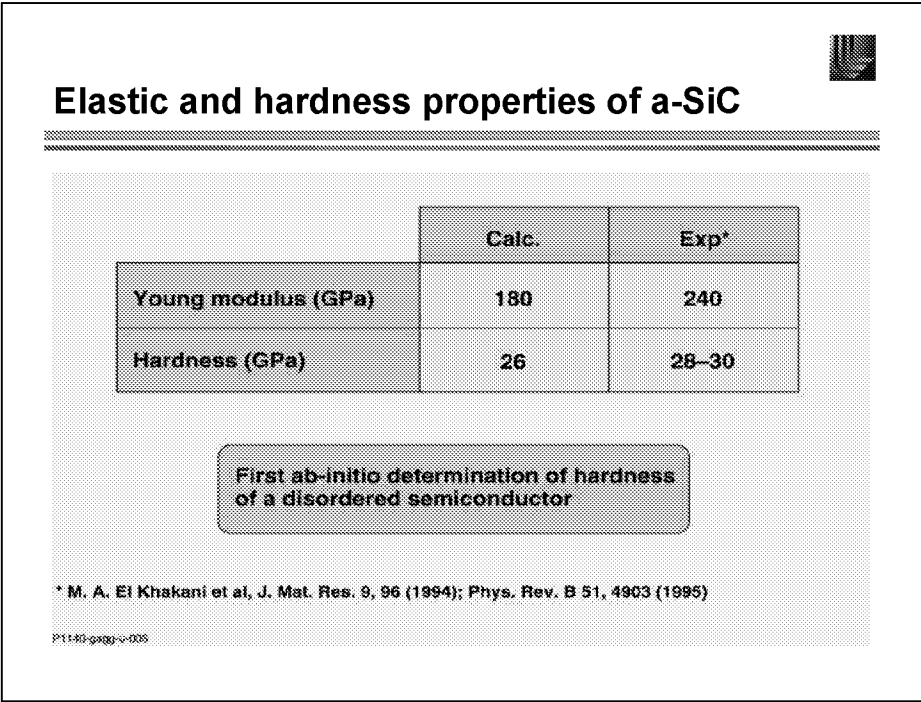


Figure 18

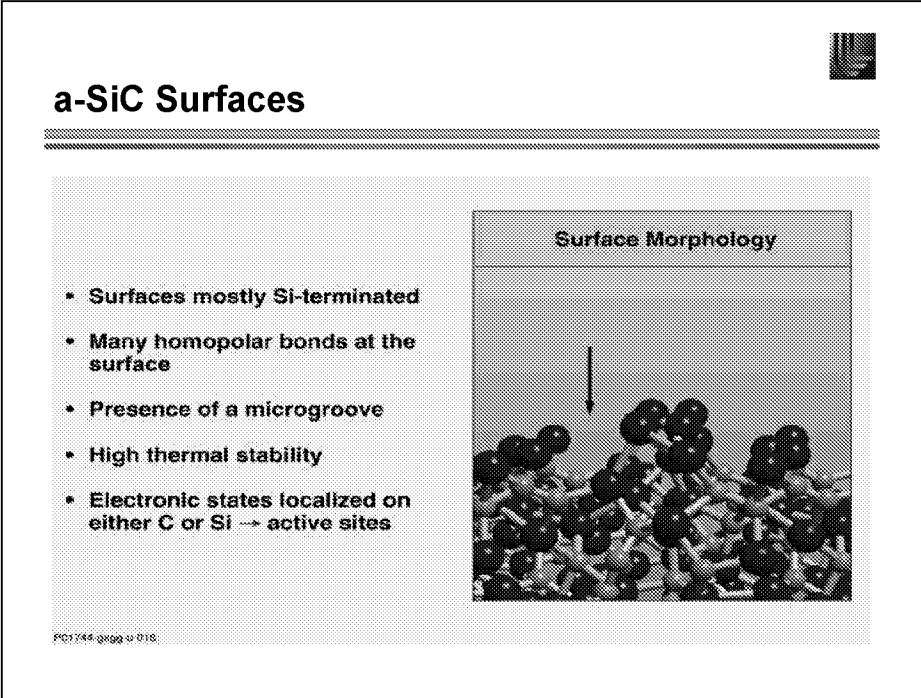


Figure 19

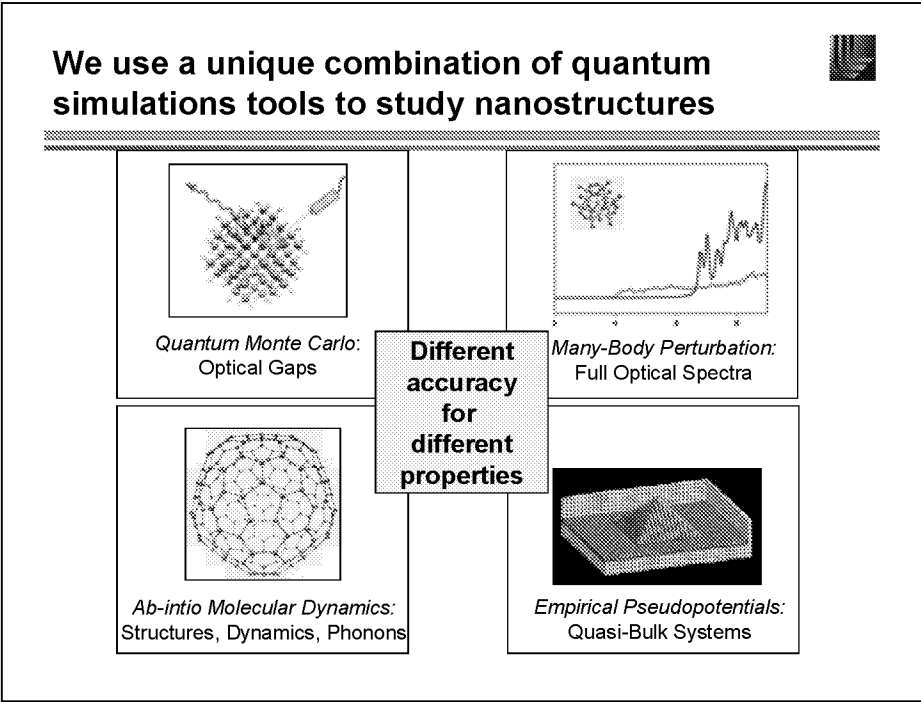


Figure 20

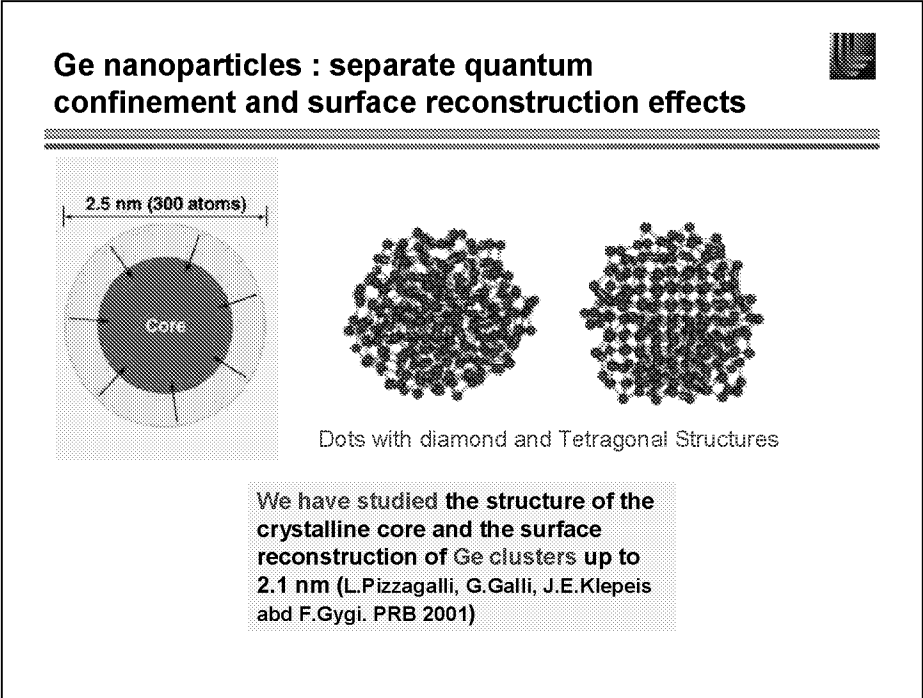


Figure 21

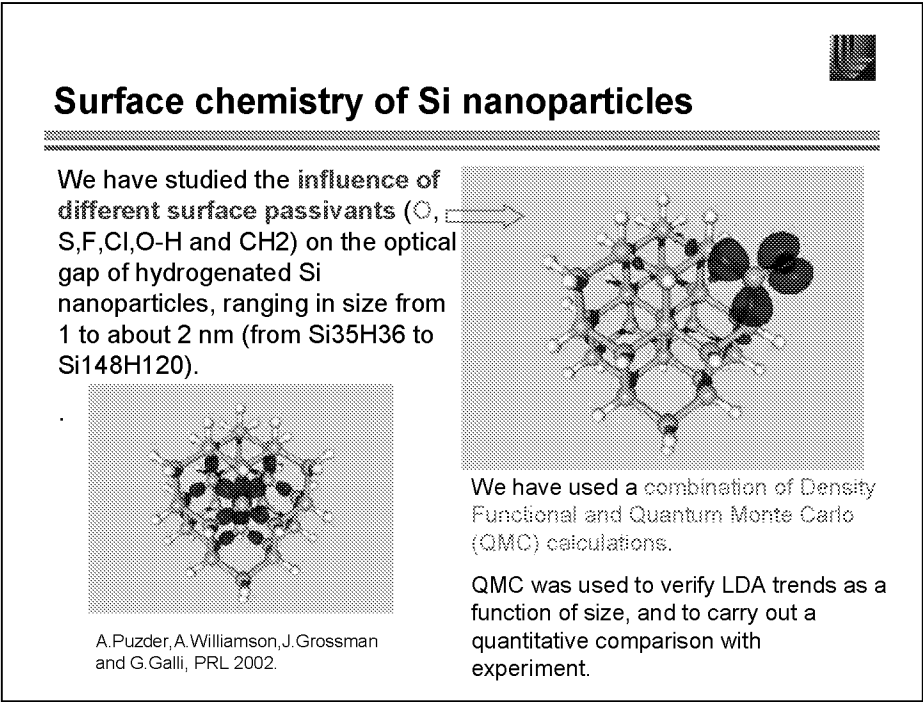


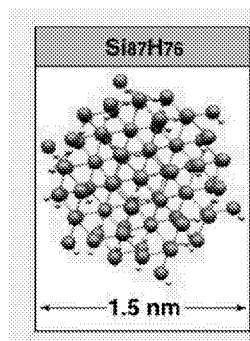
Figure 22

Surface chemistry of Si nanoparticles

We found that a double bonded oxygen atom on the surface greatly reduces the single particle and optical gap for hydrogenated Si dots with diameters less than 2 nm.

For sizes larger than 2 nm, oxygen states disappear from the gap and the HOMO-LUMO states are Si core states.

These results provide a consistent interpretation of several experiments appeared in the recent literature (Van Buuren 1998, Schlupper 1994 and Wolkin 1999).



A. Puzder, A. Williamson, J. Grossman and G. Galli

Figure 23

Surface chemistry of Si nanoparticles: work in progress

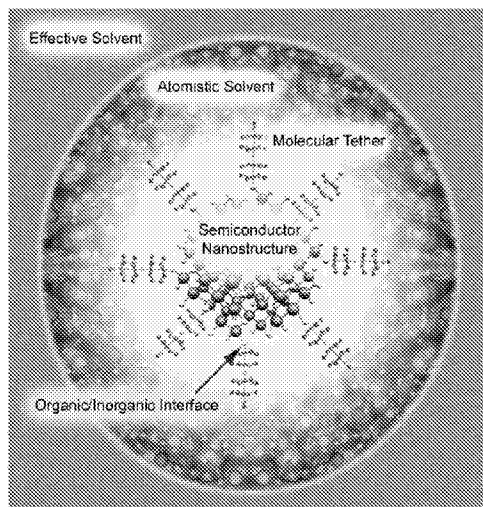


Figure 24

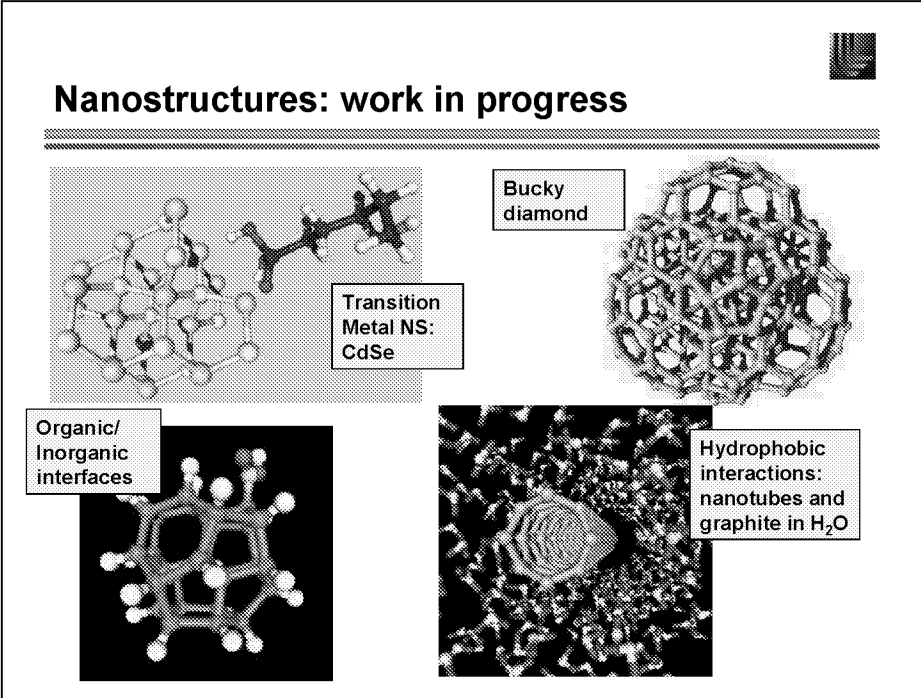


Figure 25

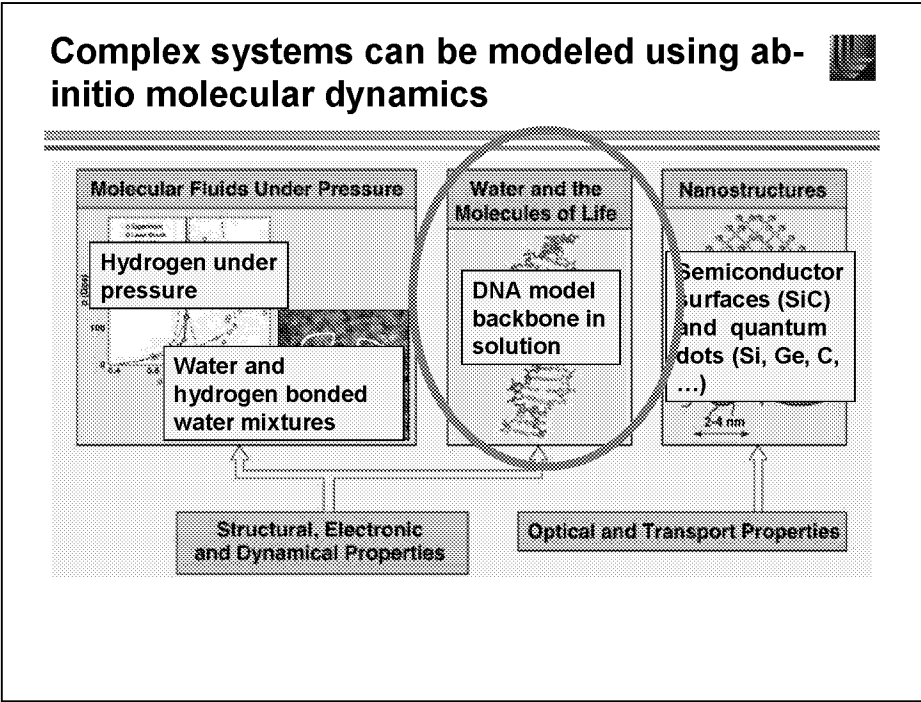
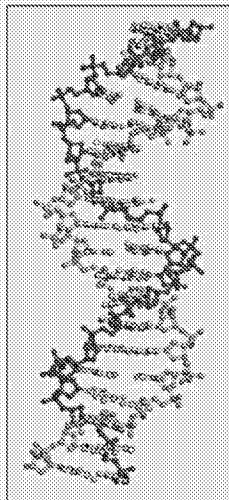


Figure 26

How does DNA interact with its environment?

- Water solvation
- Effect of counter ions
- Role of hydrogen bonding
- Factors that affect structural stability
- "Active" sites



PS1238-ggg-v-013

Figure 27

How does DNA interact with its environment?

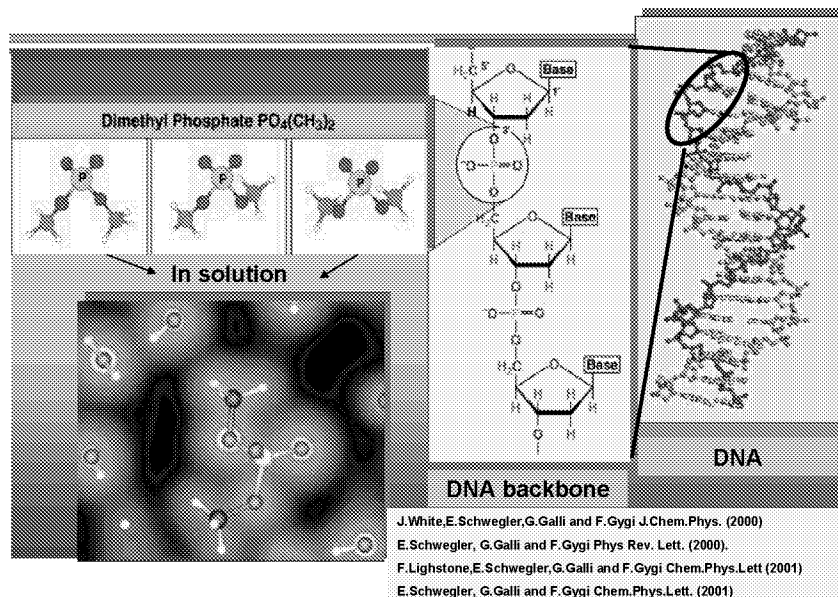


Figure 28

Model of the DNA backbone

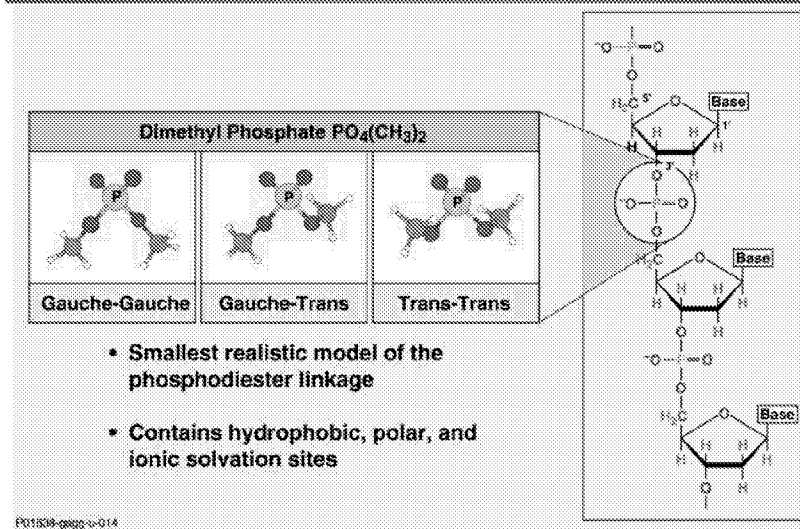


Figure 29

The importance of counter ions on DNA backbone structure

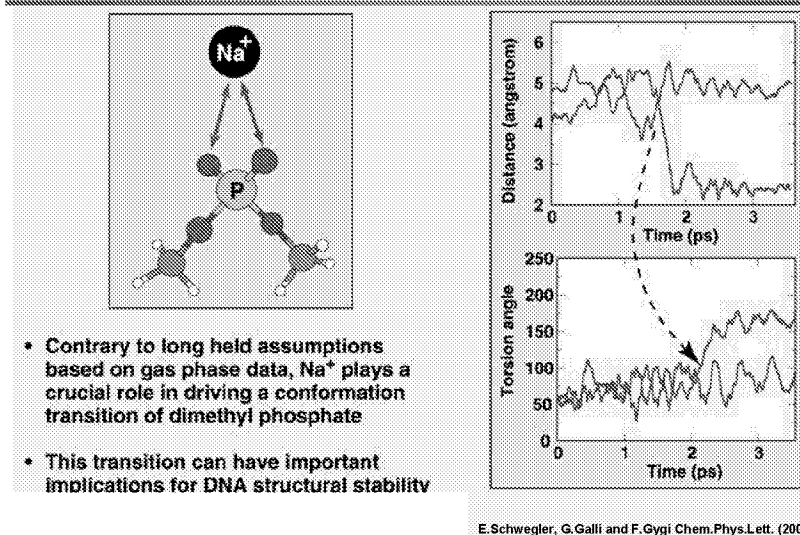
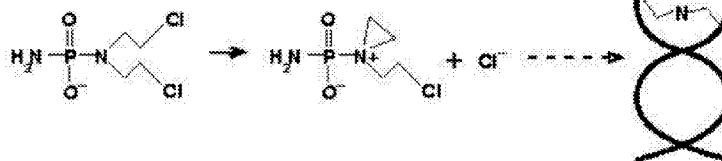


Figure 30

Work in progress: understanding the reactivity of anti-cancer drugs



Nitrogen mustard based DNA alkylating agents



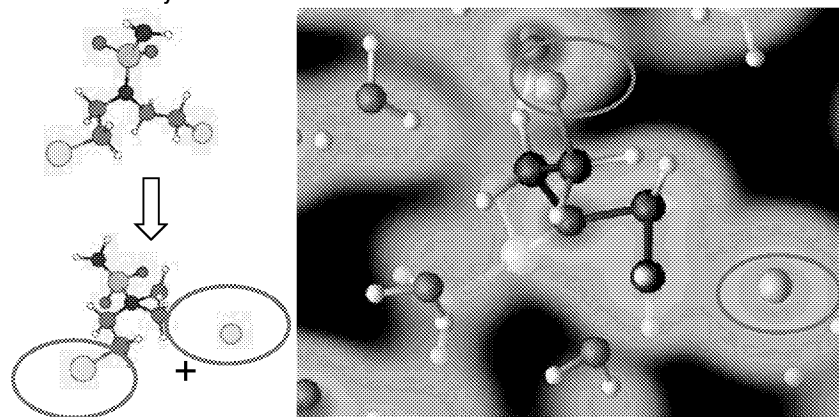
Activation steps involve intramolecular cyclization reactions that are poorly understood

Figure 31

Work in progress: understanding the reactivity of anti-cancer drugs



Cyclization reaction in solution using constrained ab-initio molecular dynamic simulations



E.Schwegler et al.

Figure 32

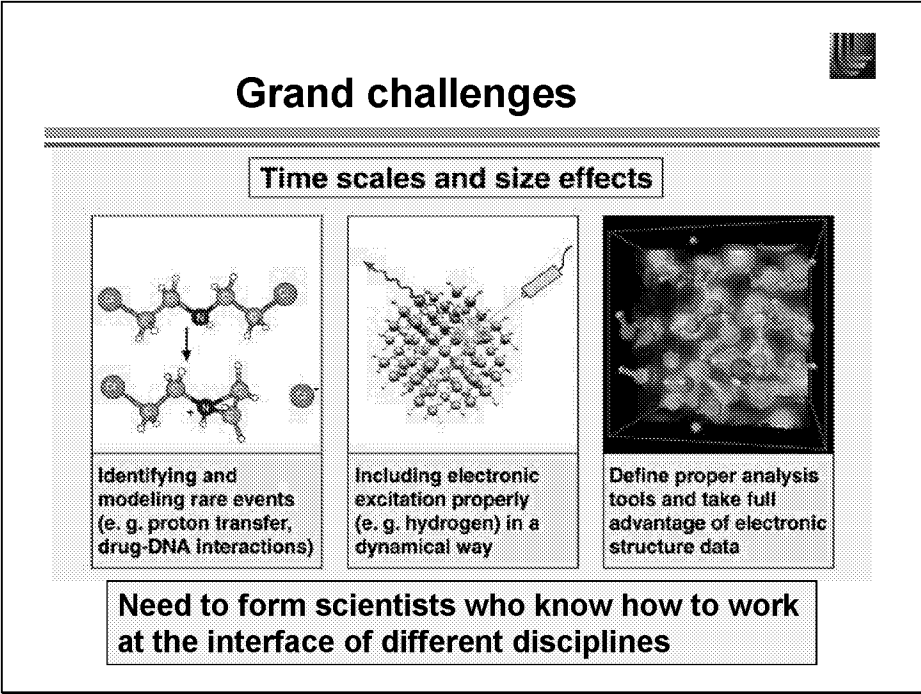


Figure 33

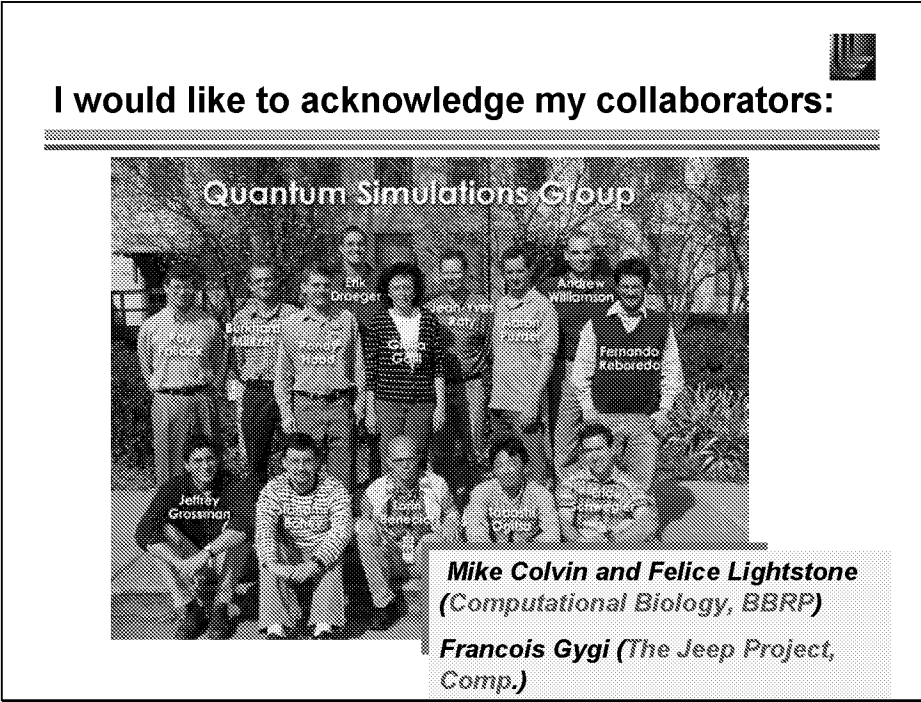


Figure 34

**Exploration in Accurate Atomistic, Coarse Grain and Mesoscopic
Simulations of Structured Solutions**

John C. Shelley
Schrodinger, Inc.
Portland, OR

OVERVIEW AND LIST OF COLLABORATORS AT VARIOUS STAGES OF THIS WORK

Cleaning solutions, LCDs, and biophysical systems all rely on structured solutions for key aspects of their behavior. Simulations have a useful role to play in examining, learning about, making predictions concerning, and utilizing these systems. Atomistic simulations can be fairly routine but even if enormous resources are used in such studies many important phenomena lie outside their range of applicability. As a result simplified models with dramatically higher computational efficiencies have been used for many such studies. Generally, such approaches have used generalized models that do not correspond well to specific systems. Here we describe largely successful attempts at creating models with mimic specific systems fairly well.

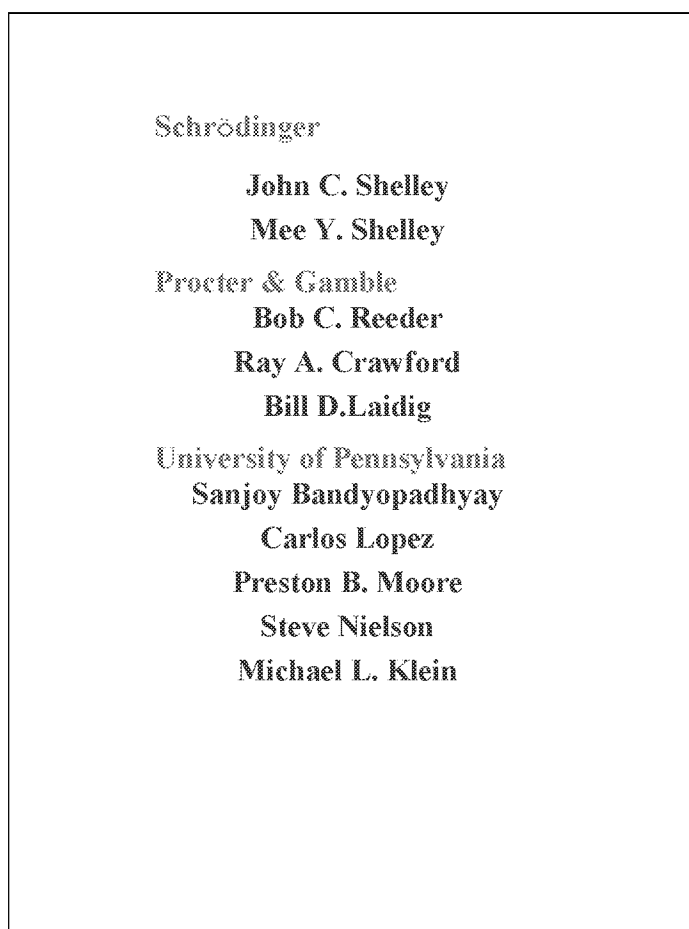


Figure 1

OUTLINE

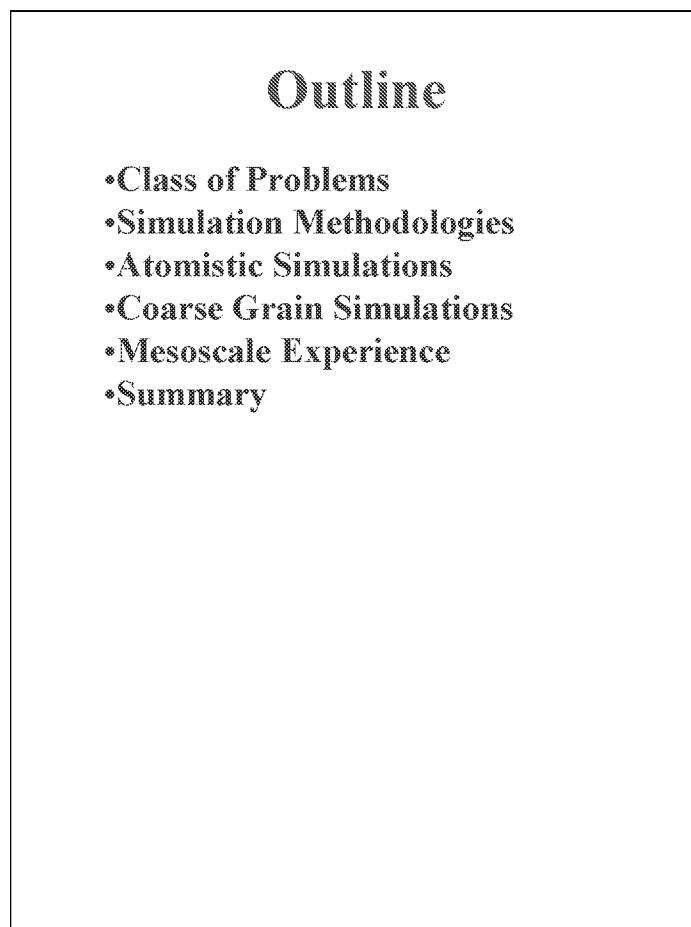


Figure 2

THE FOCUS OF OUR STUDIES

Our focus is currently on structured aqueous solutions such as those formed by surfactants or phospholipids.

The types of phenomena of most interest to us generally involve collective behaviors that are beyond what can be studied using atomistic simulations.

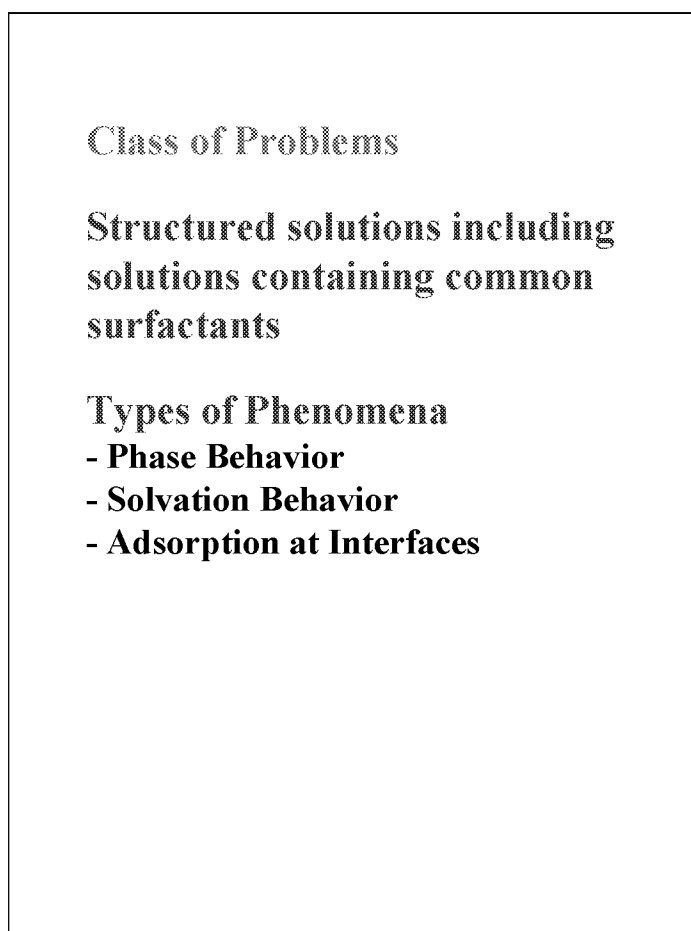


Figure 3

EXAMPLES OF STRUCTURED SOLUTIONS

These are images from atomistic simulations of a commonly studied surfactant SDS (sodium dodecyl sulfate). The molecules in our studies consist of a hydrophilic group attached to one or two hydrophobic groups. The competing drives to maintain contact between the water and the hydrophilic groups while minimizing water-hydrophobic contacts leads to aggregation into structures with spacial extents limited by the size of the molecules involved. The top image is of a roughly spherical micelle while the bottom is from a lamellar liquid crystalline phase consisting of bilayers of surfactants. Colors: small yellow, sodium ions; large yellow, sulfur; red, oxygen; gray, hydrogens and carbons. Water is present but not shown in the micellar system.

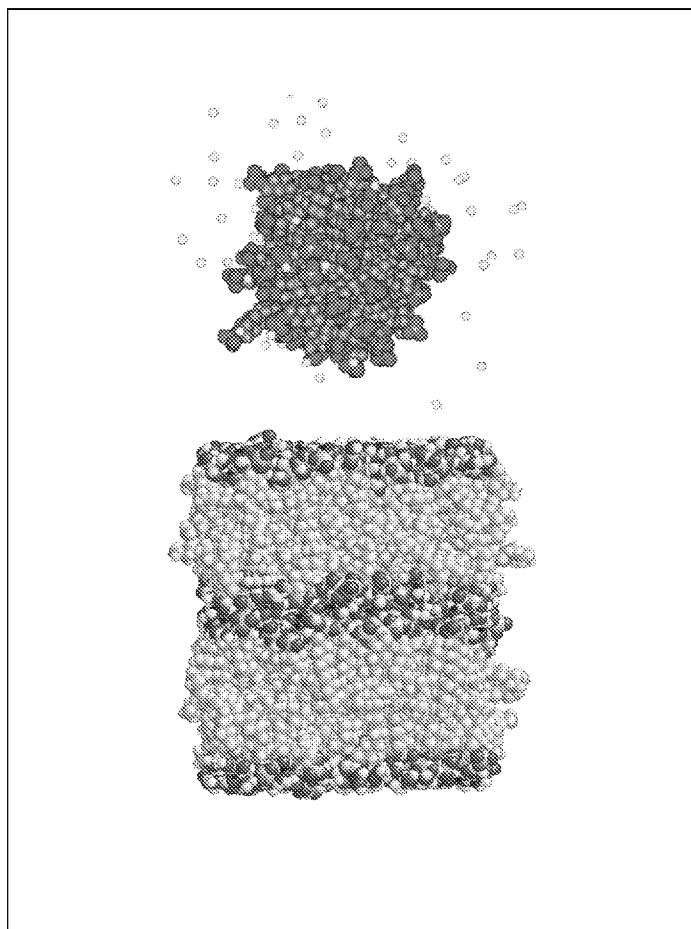


Figure 4

SIMULATION METHODOLOGIES

Different levels of simulation methodology that may be applied to surfactant systems. Quantum mechanical studies, involve solving Schrödinger's equation for the electrons in the system. Atomistic models generally treat atoms as spheres which may be linked together to form molecules. Electrostatic interactions are included by placing fractional point charges on the nuclei of the atoms. Coarse grain models (not shown) involve representing local groups of atoms that are fairly rigid by single sites. Such sites can also be linked together to represent molecules. Mesoscopic models are similar except that they generally represent many atoms with considerable internal flexibility. A number of continuum approaches exist, including computational fluid mechanics. The amount of computer resources needed to study a given volume of solution dramatically decreases as one goes from quantum, through atomistic, coarse grain, mesoscopic to continuum methods.

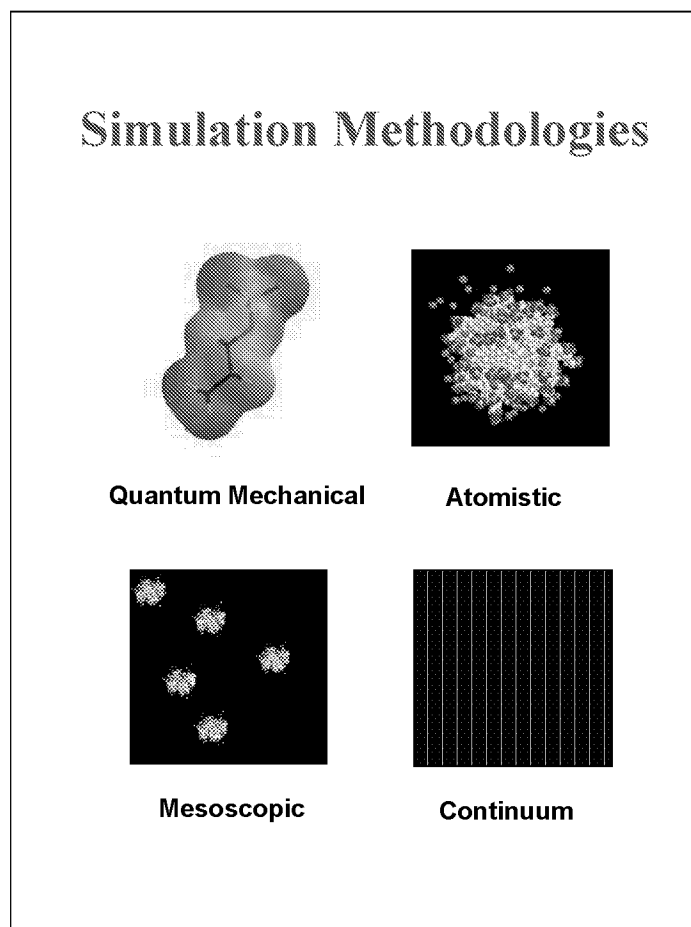


Figure 5

SIMULATION CAPABILITIES VS. LENGTH AND TIME-SCALES FOR SDS

This is a rough plot of the regions of applicability in study duration and system size for various computational methods. As well, key time and length scales for SDS are indicated. Many important phenomena in these solutions are related to aggregate formation and evolution and currently require coarse grain or mesoscopic methods.

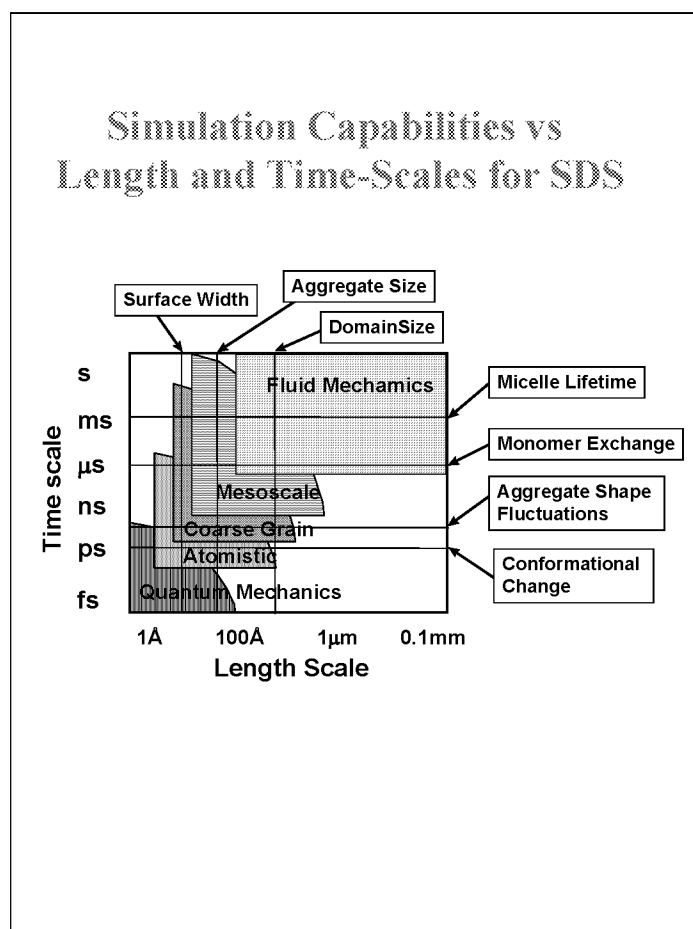


Figure 6

ATOMISTIC SIMULATIONS

Applications of atomistic simulations to structured solutions is illustrated in the earlier images for SDS and here for a commonly studied phospholipid, dimyristoylphosphatidylcholine (DMPC). These studies almost always require that the system be constructed with roughly the right structures prior to conducting the simulation itself. The models employed for this type of system are fairly mature these days and many properties can be reliably estimated from such simulations.

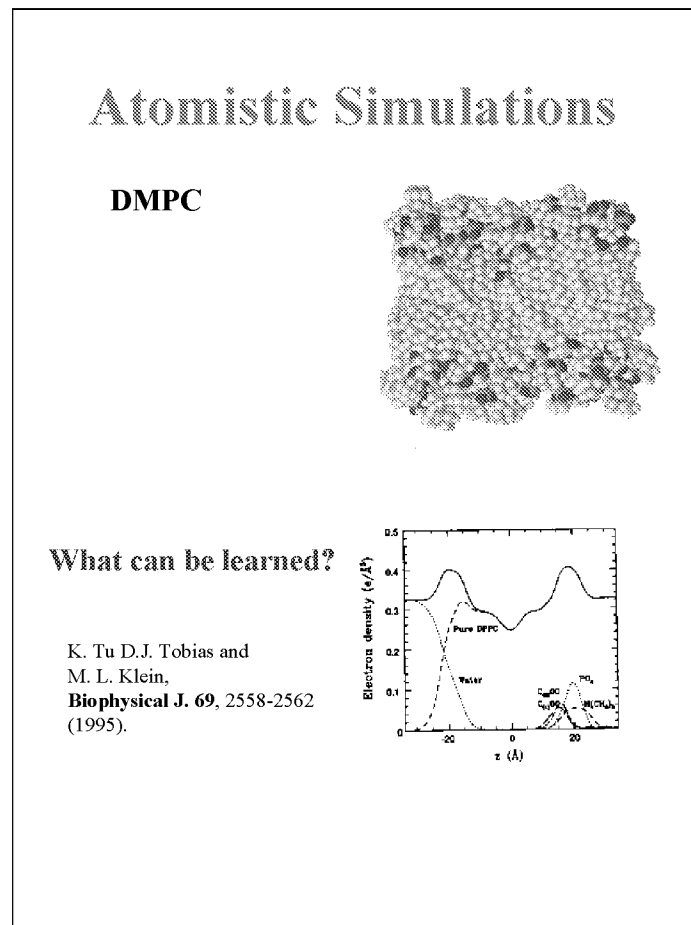


Figure 7

WHAT CAN BE LEARNED FROM ATOMISTIC STUDIES?

While atomistic simulations can be used to study local structure and dynamics, length and time-scale limitations force us to consider other methods.

What can be learned from atomistic studies?

Local structure and dynamics can be well characterized:

- **chain conformation,**
- **association of small species**
- **diffusion of small species**
- **surface tension/surface area per lipid**

Limitations

- **System size (<100 Å) is smaller than many phenomena of interest.**
- **Time simulated (<10 ns) is generally too short to study many collective behaviors.**

Cannot study large-scale motion and reorganization.

Figure 8

COARSE GRAIN

Coarse grain models are the next level of simplification above atomistic models. The use of coarse grain models in studying structured solutions is not new. While such studies generally involve simple models that do not mimic specific systems, they have shown that these models can capture many of the phenomena present in the real systems. Our work is an experiment to see if coarse grain models can be parameterized to accurately mimic specific systems (chosen in advance). To do this we force the models to reproduce key structural features from experiment and atomistic simulations. We will describe how such a model was constructed for DMPC.

Coarse Grain

To Get Beyond The Limits of Atomistic Models Simplify The Representation.

Coarse grain models are the Next Level up in simplification.

- **General phenomena reproduced fairly well (Gary Larson) by simple models**
- **No serious attempt to make such models accurate.**

Our Goal

- **To see if simplified models can be made accurate.**

Method

- **Force model to reproduce key structural features from experiment and atomistic simulation (similar to A. Lyubartsev's work).**

Figure 9

SOME ASPECTS OF THE MODEL ARE DERIVED FROM SEPARATE SIMULATIONS

As much as possible a divide and conquer approach is used in parameterization of coarse grain models. Models for bulk water and hydrocarbons can be constructed separately. Each coarse grain water site represents 3 water molecules. Similarly hydrocarbon site represents 3 carbon atoms and their associated hydrogen atoms. Hydrocarbon sites can be linked together to represent hydrocarbon chains. The parameters used in the models were adjusted to reproduce the bulk densities and vapor pressures of pure water and hydrocarbons as determined by experiment. As well as the average length and stiffness of hydrocarbon chains as estimated by atomistic simulations is reproduced.

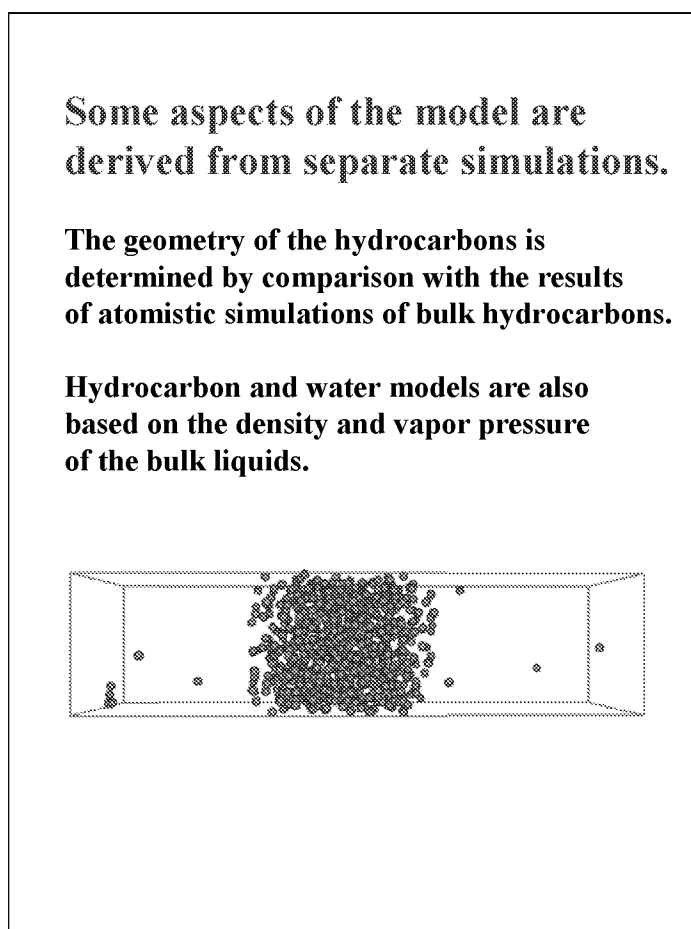


Figure 10

WATER/HYDROCARBON INTERACTIONS

The parameters governing the interaction between water and hydrocarbon sites were adjusted until the width of the water-hydrocarbon interfaces was about 5 Å (roughly the value found in atomistic simulations).

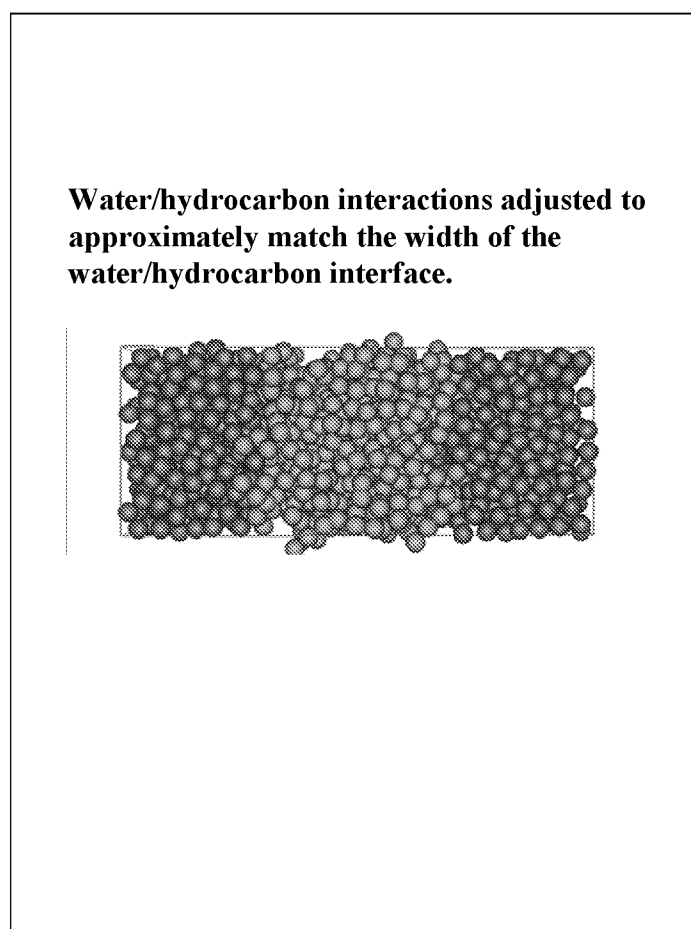


Figure 11

SITE MAPPING FOR THIS COARSE GRAIN MODEL

The mapping atoms to sites for the coarse grain model is not unique. Generally, it involves identifying groups of atoms that are essentially rigid and representing them by single sites in the coarse grain model.

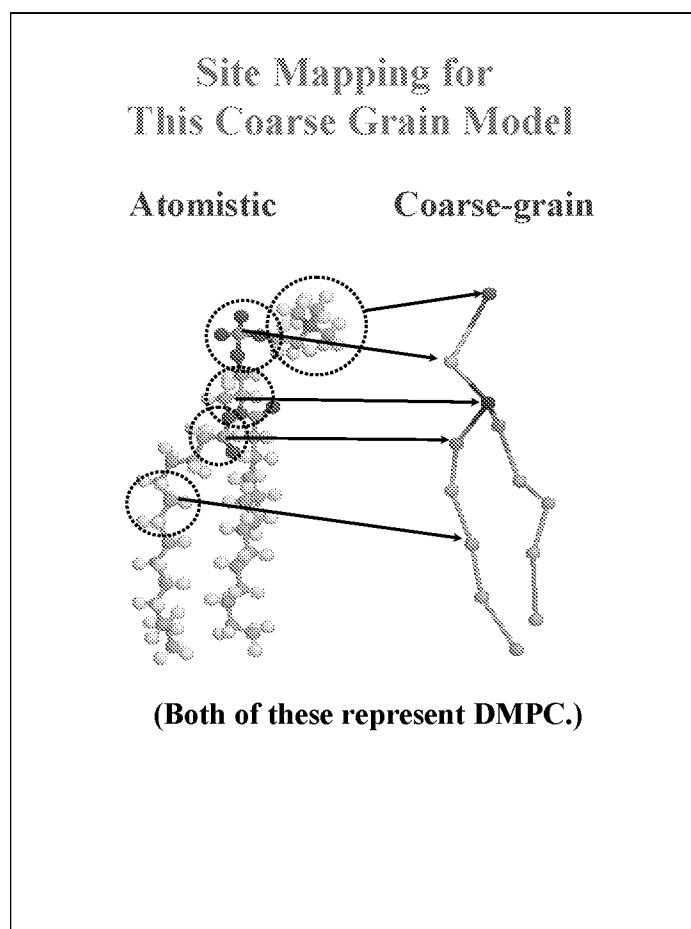


Figure 12

HOW TO MAKE THIS WORK?

There are many parameters in our coarse grain model for DMPC, nearly all of which are determined by comparison with atomistic simulations. The procedure involves choosing an initial set of parameters, performing a simulation using the coarse grain model, comparing the results with a related atomistic simulation and adjusting the parameters in the coarse grain model to improve agreement. This procedure is repeated many times until acceptable agreement is obtained. The parameters controlling the internal geometry of these molecules converge quickly. Non-bonded interactions between sites are parameterized based upon the radial distributions functions, $g(r)$ (essentially, the density of a type of site as a function of distance from the site of interest, normalized by dividing by the average density).

How to make this work?

Strategy:
Try to match atomic level structure as closely as possible using the coarse grain model.

Choose bond lengths (14) and angles (16) and their force constants appropriately.

Non-bonded interactions:
Electrostatics (2) and van der Waals potentials (28) chosen to match atomistic $g(r)$'s.

Figure 13

INTERACTION POTENTIAL

Most $g(r)$'s are relatively unstructured and so the corresponding potential can have a simple form (e.g. a Lennard-Jones 9-6). However, $g(r)$'s amongst the hydrophilic groups are highly structured in a complex manner. For these interactions, we use tabulated potential (following Lyubartsev's approach). These potentials are adjusted until the corresponding $g(r)$'s match closely. In the top figure the atomistic (solid lines) and coarse grain (dashed) $g(r)$'s for the choline group are given. The bottom figure gives the corresponding tabulated potentials obtained from the iterative fitting procedure.

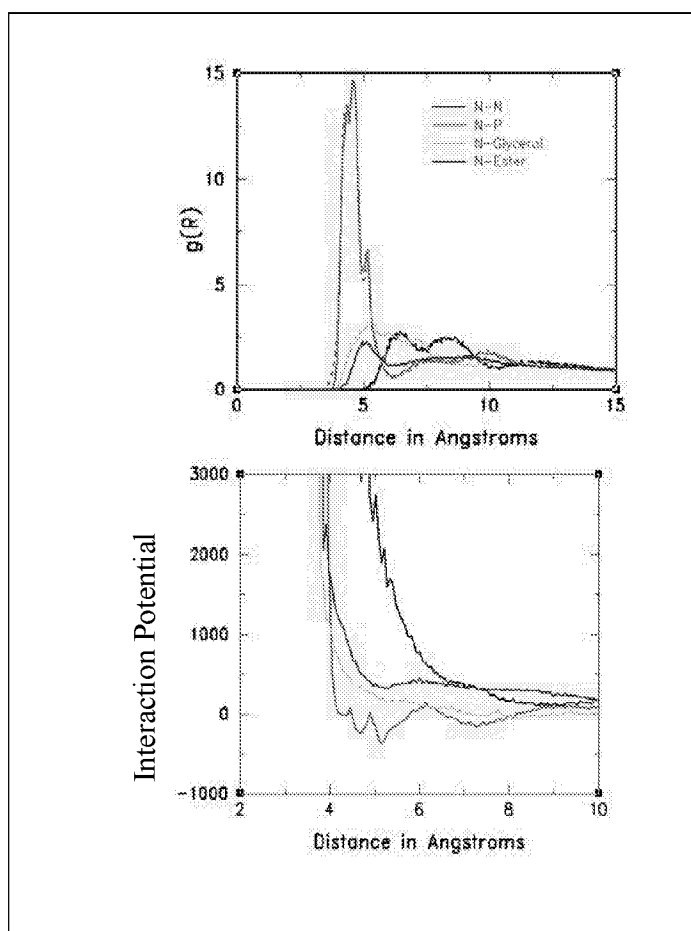


Figure 14

APPLICATION TO PREASSEMBLED DMPC BILAYERS

A Monte Carlo simulation using our DMPC coarse grain model is about 100 times more efficient than the corresponding atomistic simulation. The density profiles of the various groups are in very good agreement with those obtained from the corresponding simulation.

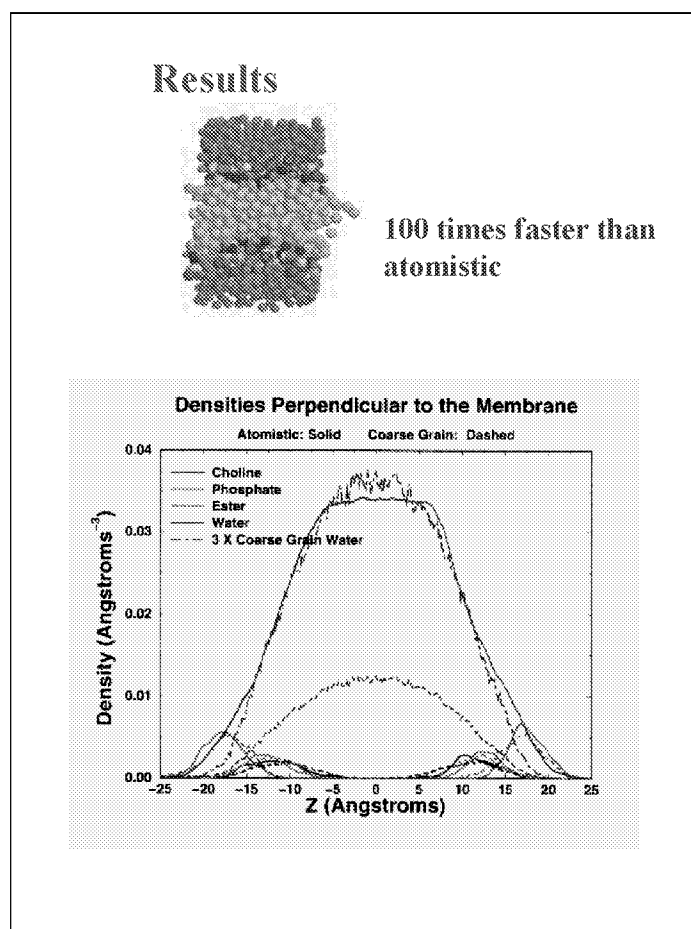


Figure 15

SELF-ASSEMBLY OF A DMPC BILAYER

Using the coarse grain model it takes only a few days to simulate the self-assembly of a DMPC bilayer from a random initial state on a typical workstation. The assembly process is far more efficient if we switch from a Monte Carlo simulation method to a molecular dynamics simulation method.

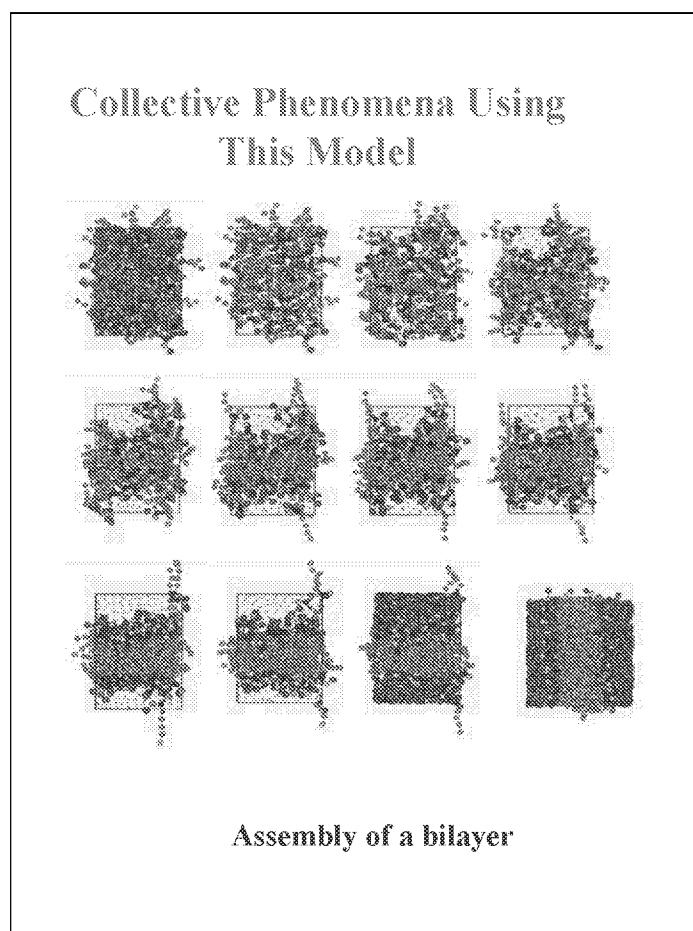


Figure 16

SIMULATING LARGE SYSTEMS

Using these models it is fairly easy to simulate large systems such as the DMPC system depicted below which contains 1024 phospholipids. Note that the color scheme is somewhat different than previously described: light blue, water; dark blue, hydrocarbons; yellow, hydrophilic groups.

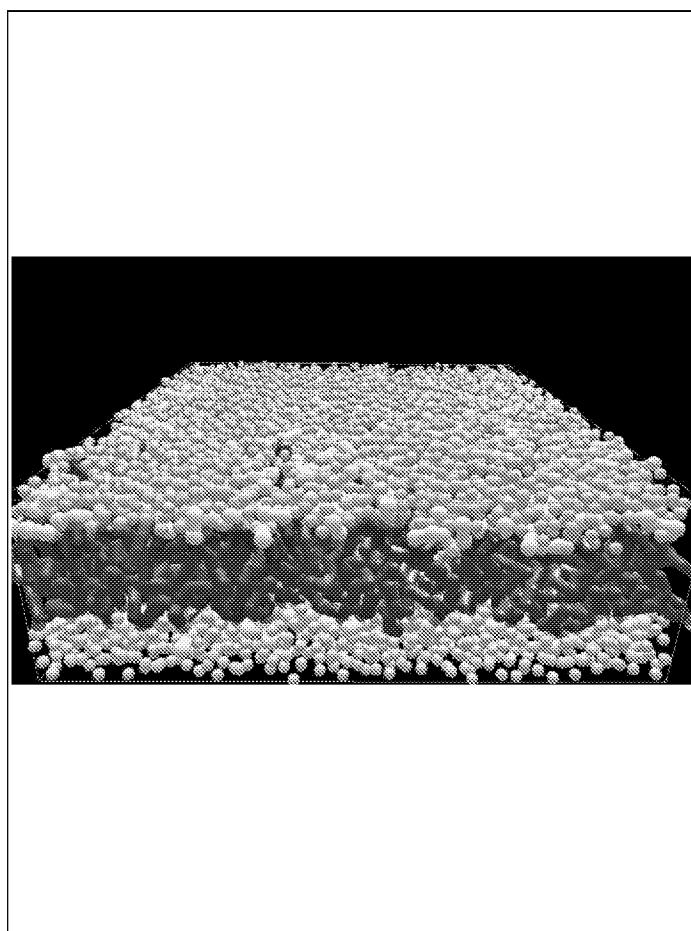


Figure 17

DMPC DIFFUSION

These figures contain the root mean-square displacements of DMPC molecules during simulations employing atomistic (top) and coarse grain (bottom) models. Estimates for the diffusion constant, can be obtained from the limiting slopes of these curves. Atomistic simulation gives a value of $6.5 \times 10^{-8} \text{ cm}^2/\text{sec}$ which is in the range of experimental values available for this system. The coarse grain model gives a value of $6.3 \times 10^{-6} \text{ cm}^2/\text{sec}$ or roughly 100 times larger than the atomistic simulation. This discrepancy is both worrying and encouraging. Worrying because it's different than experiment but encouraging because it may mean that these models may evolve much faster than expected. We are investigating this further.

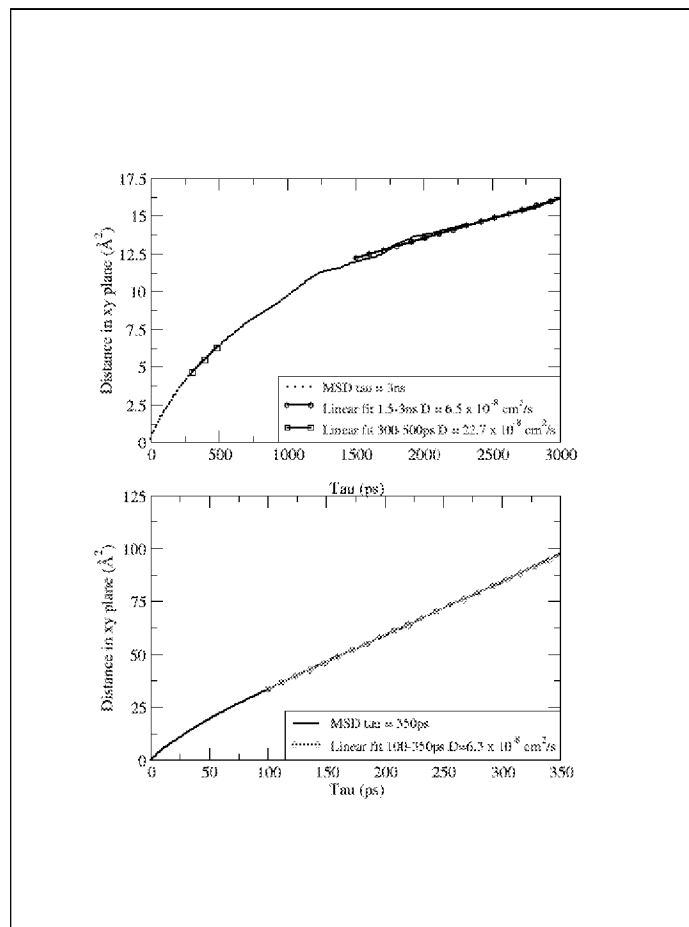


Figure 18

SELF ASSEMBLY INTO A REVERSE HEXAGONAL PHASE

As an added test we studied the self-assembly of a reverse hexagonal phase. We were only able to study systems large enough to contain one or two repeat units of this phase. However, all three studies of this phase resulted in the self assembly of the correct number of structures for the size of the systems studied. Below is an example from a system which was large enough to contain one repeat unit.

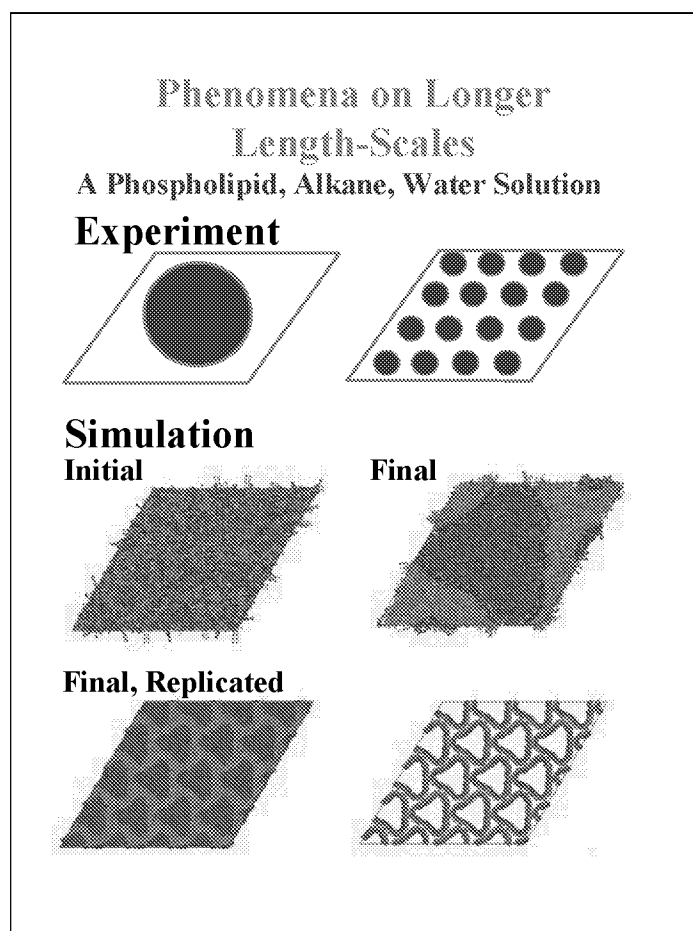


Figure 19

INITIAL STAGES OF A SIMULATION CONTAINING TWO REPEAT UNITS

Monte Carlo simulation was used to randomly construct the initial structure and to relax it somewhat. However, as noted earlier for lamellar systems, Monte Carlo simulations were not very efficient at forming aggregates.

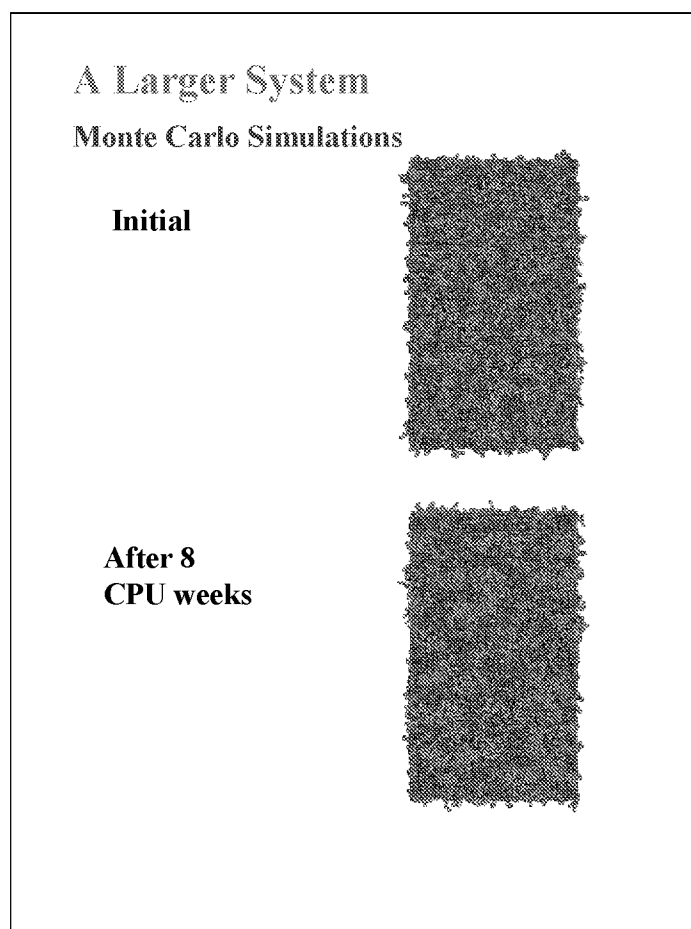


Figure 20

SELF ASSEMBLY OF A SYSTEM CONTAINING TWO REPEAT UNITS

Switching to molecular dynamics from Monte Carlo for this simulation lead to rapid evolution of the system into a structure containing the two repeat units.

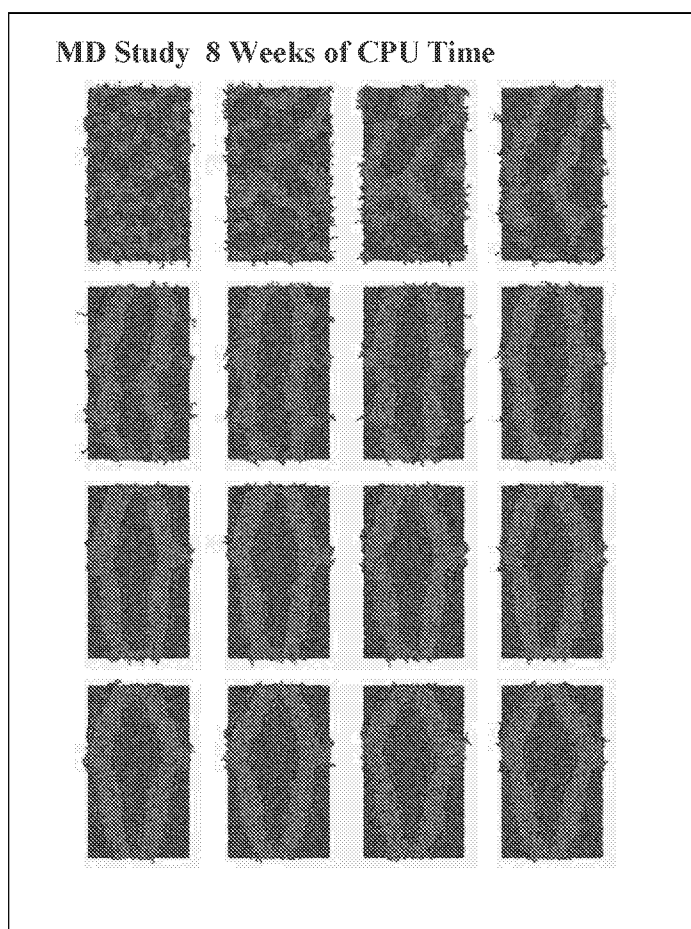


Figure 21

A COARSE GRAIN SUCCESS STORY

Our studies show that it is indeed possible to construct models which mimic specific systems fairly accurately. The range of systems covered by a consistent set of such models needs to be broadened.

Coarse Grain Simulation Summary

- About 10,000 times faster for phospholipids**
- Have adapted to a number of surfactant systems both ionic and non-ionic with both implicit and explicit solvation models.**
- These seem to form the basis of a self-consistent set of coarse grain models.**
- Huge amount of work involved in creating these models.**
- Still need to develop models for longer length and time-scales.**

Figure 22

MESOSCALE MODELS

The coarse grain models that we have constructed are still too slow to study all of the phenomena of interest. So we must consider further simplification of the models to the mesoscale level. The sites are becoming quite large and there are only a few of them per molecule in the systems that we are studying. As a result the molecular shape, something which is fundamental in determining the behavior of the system that we are interested in, becomes distorted and constructing accurate models becomes problematic.

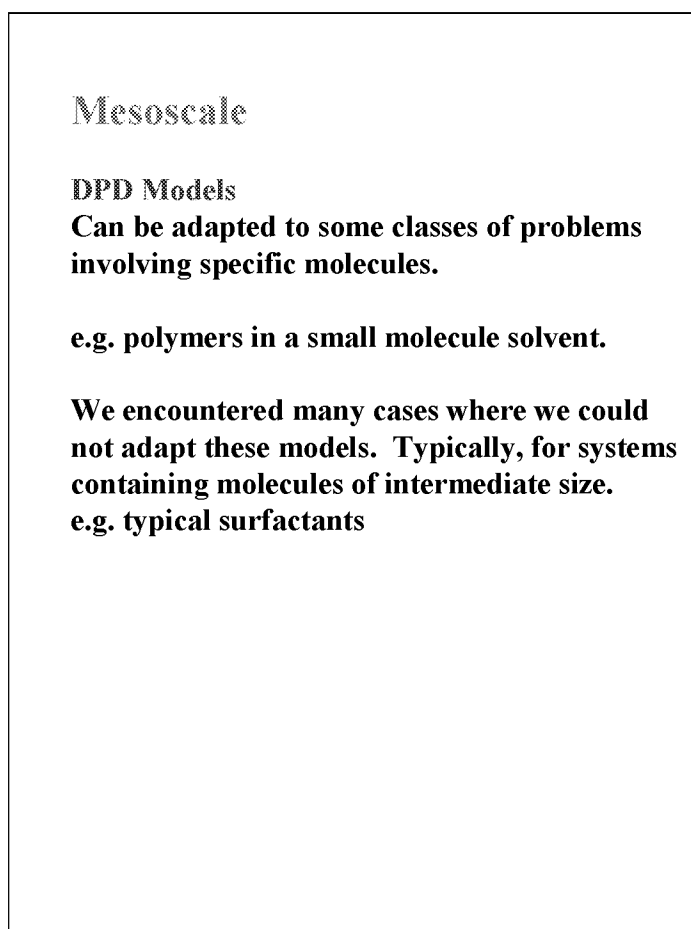


Figure 23

A POTENTIAL SCHEME FOR CONSTRUCTING A MESOSCALE MODEL

Instead of using sites to represent atoms with a single molecule one could use sites to represent atoms across adjacent molecules as illustrated below. However, this approach is not entirely satisfactory in part because it restricts the association of molecules.

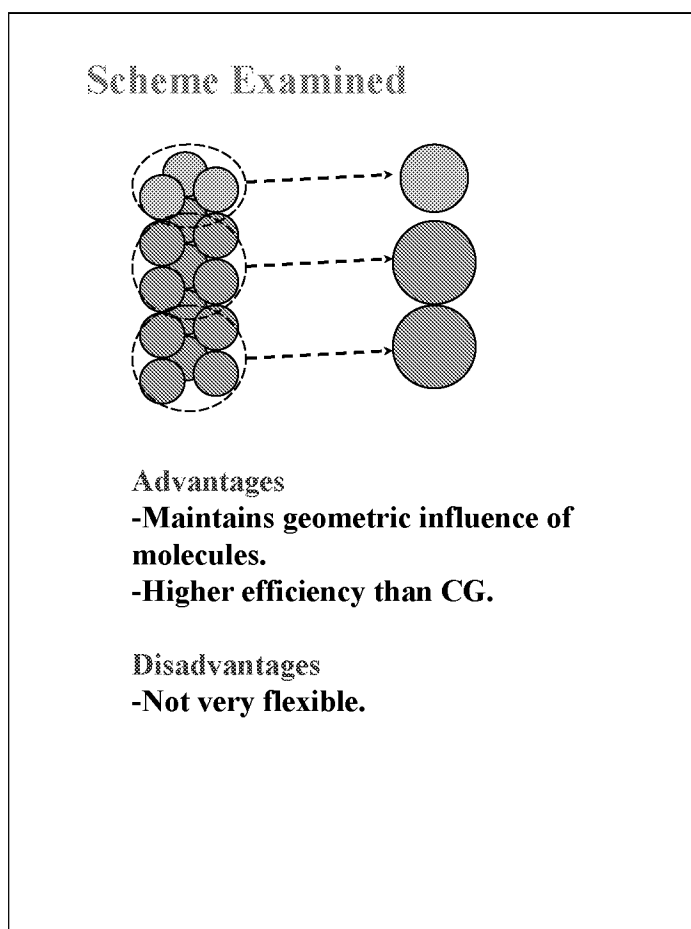


Figure 24

SUMMARY

Atomistic and coarse grain models can be constructed to fairly accurately mimic surfactant and phospholipid systems and together they provide complementary information. The application of mesoscale models to these systems is problematic and basic model construction strategies need to be explored further.

Summary

- **Atomistic Models are fairly mature in many cases... still need to exercise care.**
- **Have demonstrated that coarse grain models can, after considerable effort, be made to accurately describe specific systems.**
- **Typical Mesoscopic models can be made to work in some cases. Likely need more complicated and accurately derived models to make them work in general.**

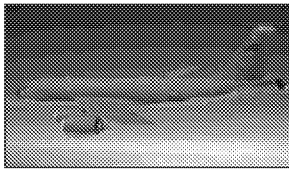
Figure 25

**A Multiscale Modeling Approach to Crack
Initiation in Aluminum Polycrystals**

A.R. Ingraffea
Cornell University
Ithaca, NY USA

INTRODUCTION

A Multiscale Modeling Approach to Crack Initiation in Aluminum Polycrystals



10m

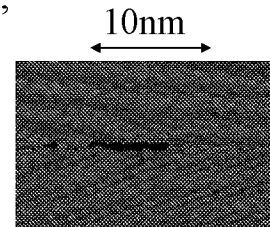
A. R. Ingraffea

Computational Materials Institute
Cornell University
www.tc.cornell.edu/Research/CMI

In collaboration with

E. Iesulauro, T. Creteigny, C.-S. Chen,
K. Dodhia, C. Myers, J. Sethna

With Support from: NSF-KDI, AFOSR



10nm

Figure 1

PRESENTATION OUTLINE

A current issue facing our aging fleet of commercial and military aircraft is what is the residual strength of components, such as fuselage and wing skins, after undergoing damage such as corrosion and fatigue crack initiation. Corrosion and fatigue crack initiation are inherently multiscale problems. The following discusses why we are looking at fatigue crack initiation and tools developed to study how fatigue cracks initiate and begin to propagate. These tools have been developed to study 2D representations of metallic polycrystals at the mesoscale that can then be used as part of a multiscale simulation involving continuum as well as atomics models. Recent work has involved transitioning these tools to 3D.

Presentation Outline

- Overview:
 - What is the problem, and why are we working on it?
- Mesoscale (Polycrystal) Modeling
 - Modeling Issues
 - 2D Simulation Results
 - Recent 3D Progress
- Atomistic (Grain and Particle Boundary, Crack Tip) Modeling
 - Modeling Issues
 - Preliminary Simulation Results
- Observations To Date

Figure 2

MOTIVATION: FATIGUE CRACKS INITIATE IN ALUMINUM ALLOYS IN AGING AIRCRAFT—HOW?

As current aircrafts are flown well beyond their original design lifetime concerns and research begin to focus on maintenance and repair as well as understanding how damage occurs. A major damage mechanism of aircraft fuselages is fatigue cracking. An aircraft is exposed to a corrosive environment that damages the outer surface of the aluminum alloy components. Fatigue cracks can then nucleate and propagate from features such as corrosion pits. To better see the complex physics that is going on we reduce our length scale to the meso-scopic level at which polycrystals become visible. Below this scale are networks of dislocations opening up locations for corrosive elements to penetrate deeper into the allow.

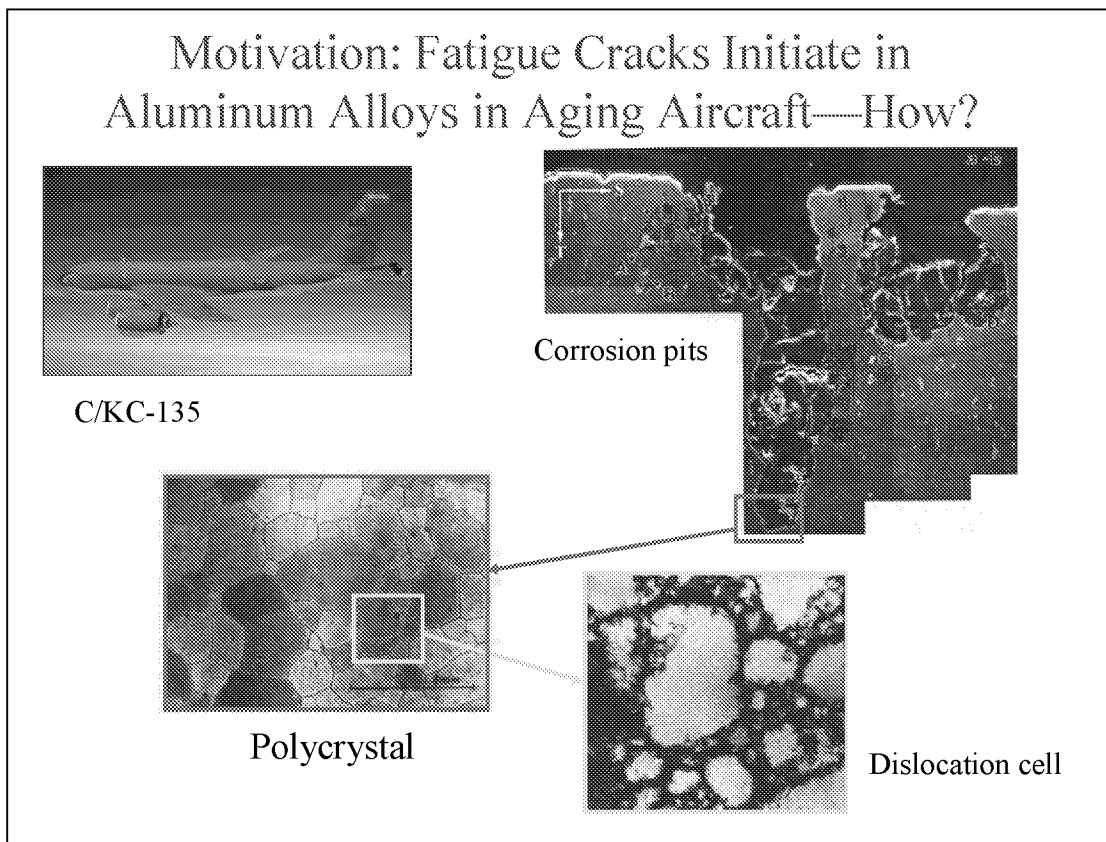


Figure 3

MULTISCALE MODELING: THE CONCEPT

Most analyses model components as continua. However, this approach smears out smaller scale features that may be the direct cause of failure at the macro-scale. Here a pipe is modeled with a strain field due to thermal boundary conditions on its internal surface. An area of high temperature can be zoomed in on and discretized to the mesoscopic scale, explicitly representing polycrystals. This simulation can be used to determine if the temperature field is resulting in decohering grain boundaries and crack initiation. The grain boundaries or crack tips can also be further discretized to the atomic scale to determine grain boundaries strength and behavior.

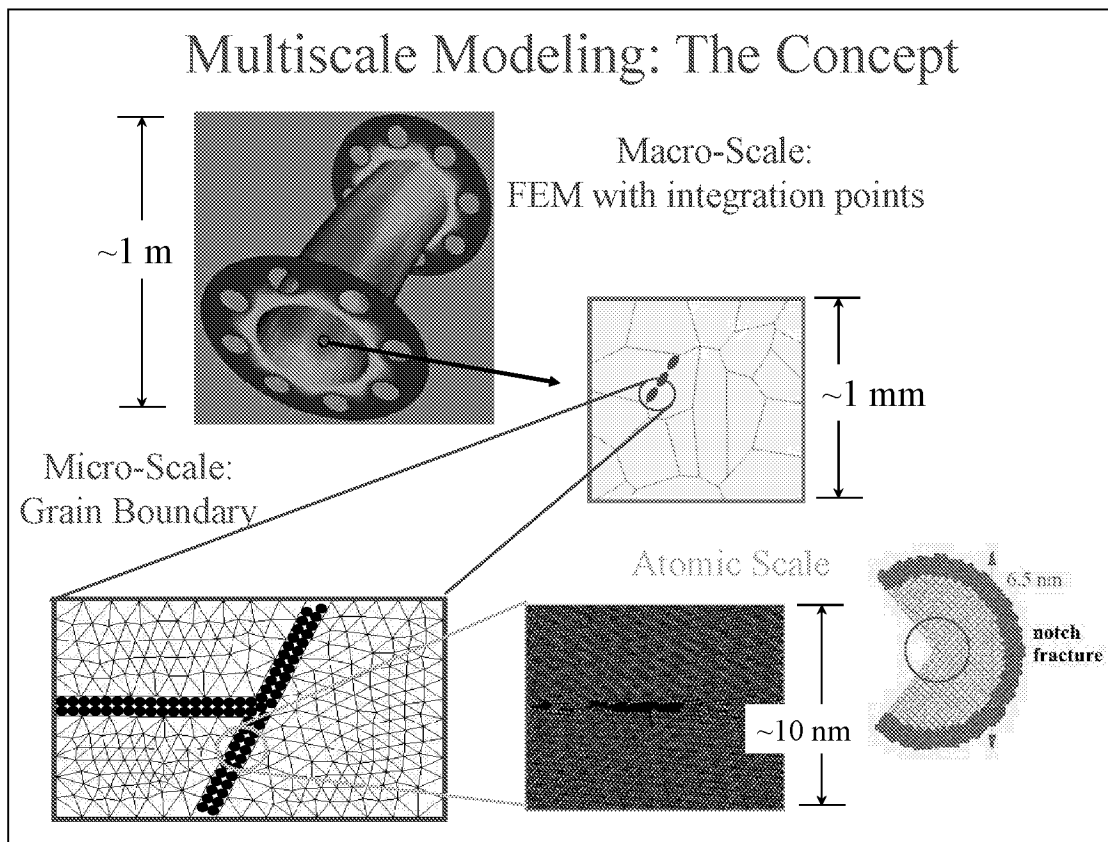


Figure 4

POLYCRYSTAL MODELING

Computational modeling of the mesoscopic scale at which many grains or crystals are explicitly represented can be broken in several steps. The steps presented here include determining the grain geometry and meshing for finite elements analysis, determining the constitutive model to be for the grains, determining the constitutive model to be used to describe the behavior of the grain boundaries and the grain-particle interfaces, and finally statistical modeling for determining grain geometry and constitutive properties.

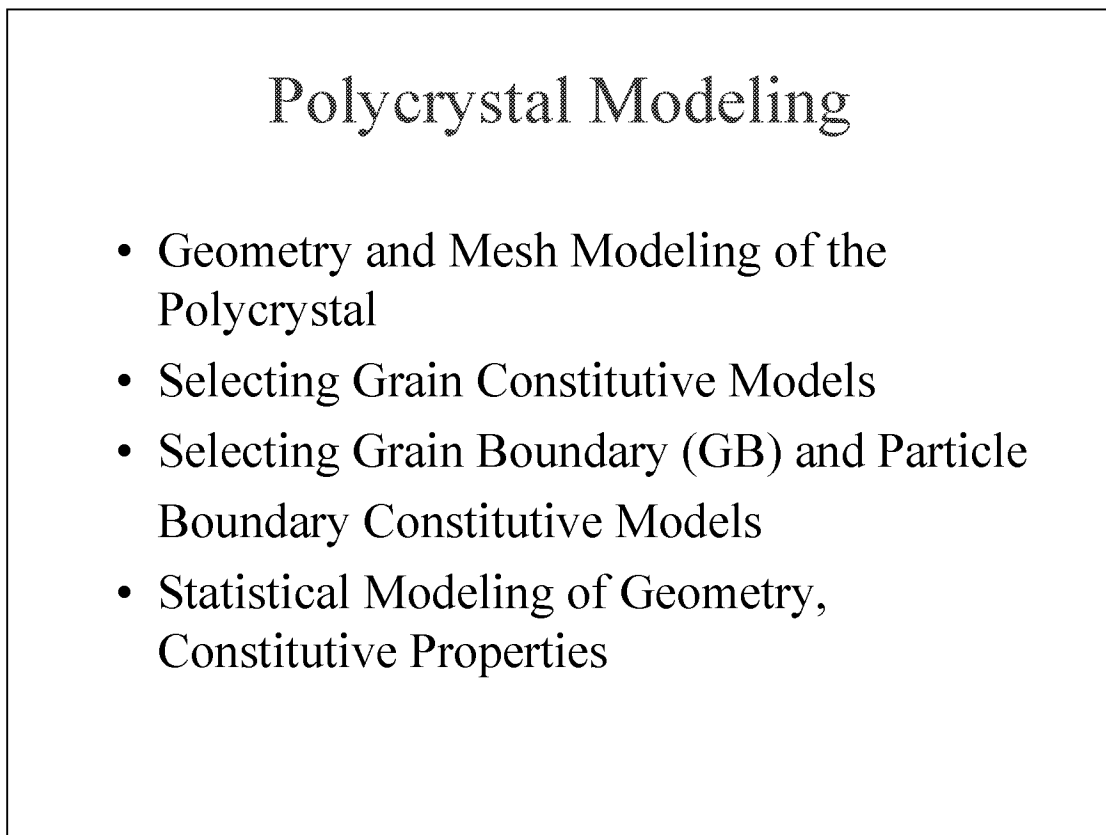


Figure 5

MODELING: GRAIN GEOMETRY AND MATERIAL PROPERTIES

Currently the 2D grain structure is generated using Voronoi tessellation. Each polygon then is taken to represent a grain. For annealed or newly crystallized metals this can be a good representation assuming randomly distributed initiation sites and isotropic grain growth at an uniform rate. This model however does not represent metals after processing such as rolling that results in elongated grains. The Voronoi tessellation was used for a first approximation. Initial simulations also did not consider sub-grain features such as particles, dispersoids, and precipitates. Fracture was also limited to intergranular debonding. Once the grain geometry is determined each grain is assigned an individual set of constitutive parameters from one of the models listed. Although a single constitutive model is chosen for the over all sample, each grain is assigned different parameters allowing for heterogeneity to be represented. The distribution of nano-sized precipitates and other hardening features are not consist from grain to grain resulting in heterogeneous material properties at this scale. Each parameter of the chosen constitutive model is randomly selected from a uniform distribution of possible values. In the case of orthotropic models the crystallographic orientation is sampled from the Orientation Distribution Function (ODF) which can be determined experimentally for the given alloy.

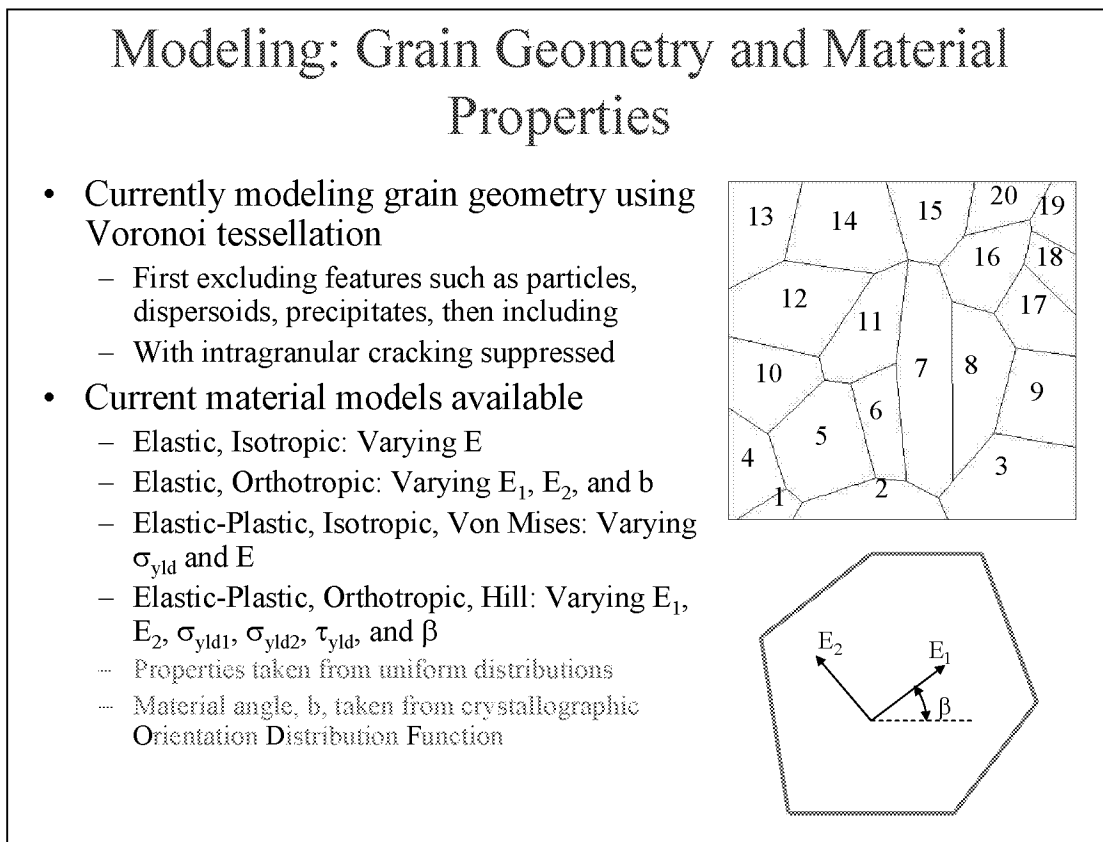


Figure 6

MODELING: GRAIN BOUNDARY CONSTITUTIVE RELATIONSHIP, CCZM

The constitutive model used to describe the grain boundary response is a traction-displacement relationship. A coupled cohesive zone model from Tvergaard and Hutchinson was chosen from implementation through interface elements. Due to the random orientation of the grain boundaries mixed mode fracture is expected along the grain boundaries. For this reason a couple model was chosen. The interface elements are zero volume elements placed between elements in different grains. These elements were placed along all grain boundaries in the sample. Since the goal of the final simulations is to observe crack initiation the use of the cohesive zone model and interface elements allows for natural decohesion between grains due to the local stress and strain fields rather than explicit placement of a crack by the user.

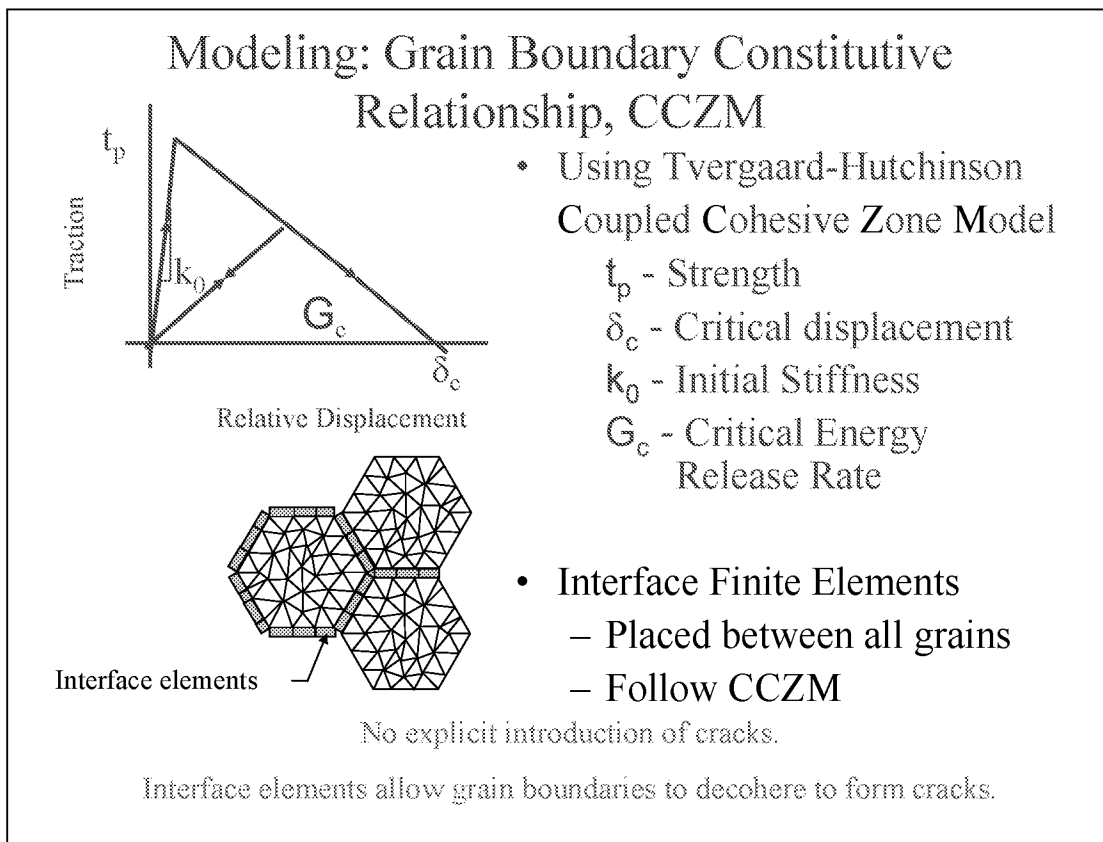


Figure 7

OBSERVATIONS UNDER MONOTONIC LOADING

To observe the influences of geometry, constitutive modeling, and grain boundary properties on crack initiation a parametric study was conducted. The affect of geometry, grain constitutive model and parameters, and grain boundary parameters were studied. Alteration of the geometry had little affect. For all geometries generated initiation was primarily in Mode I. For elastic constitutive modeling, initiation paths were most sensitive to the presence of orthotropy. The addition of plasticity was shown to shift some damage to plastic deformation of the grains. For samples with large variation in the grain boundary strength the strain level for initiation was lowered. This was lowered even further when orthotropy of the grains was introduced. The key observation was the role of the relationship between the grain boundary strength and the grain yield stress. This relationship determined how much plasticity was seen in the grains and whether or not decohesion occurred in the grain boundaries.

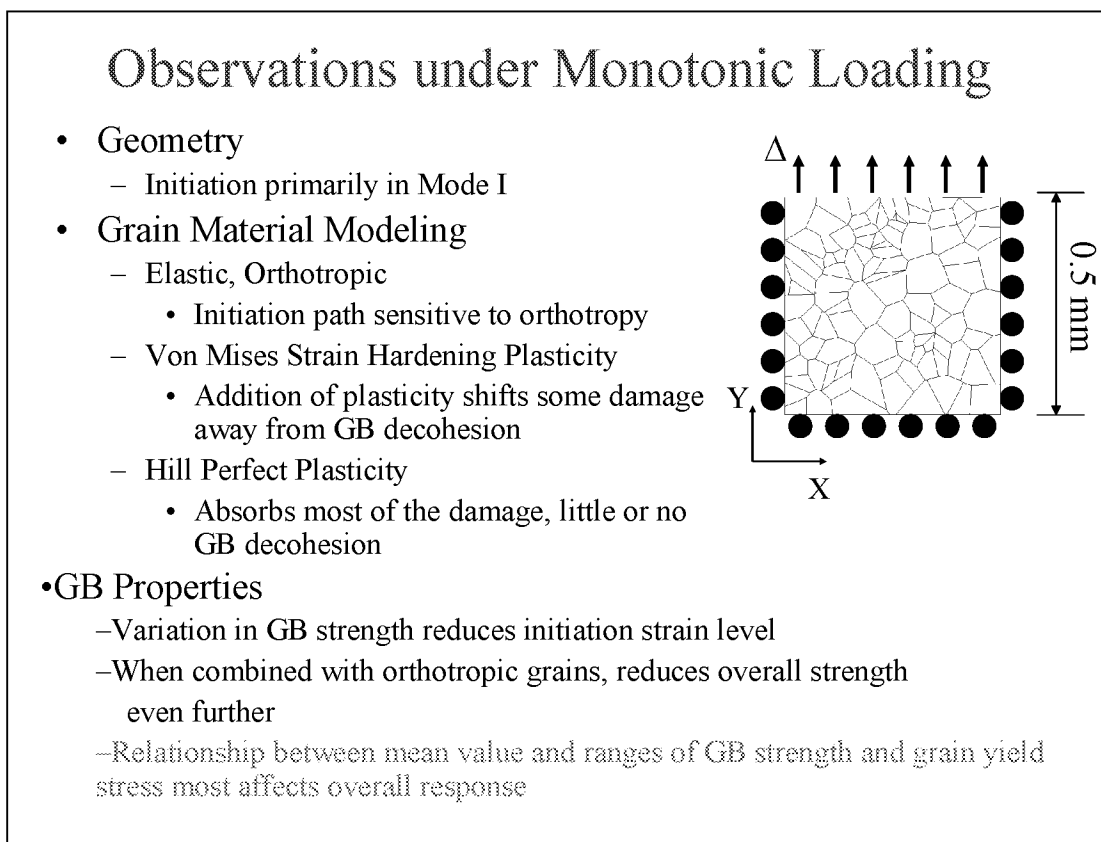


Figure 8

FATIGUE SIMULATION RESULT

After completing the parametric study a fatigue test was conducted. The grain geometry shown was used with 100 grains modeled using Hill plasticity with mean primary yield stress of $500 \text{ MPa} \pm 5\%$. The mean grain boundary strength was also $500 \text{ MPa} \pm 5\%$. The sample was then loaded under displacement control to a strain of 0.69%, 98% of the approximate global yield strain, and unloaded twice. The third loading was taken to a strain of 0.70%, 99% of the approximate global yield strain. Initial decohesion can be seen at point 1, the first peak loading. At unloading the stress throughout the polycrystal did not return to 0, resulting in the presence of residual stresses at the beginning of the second loading. Additional opening can be seen at the second peak. Again residual stresses were present at the beginning of the third loading. This demonstrates the accumulation of damage possible throughout the sample and initiation points due to fatigue loading. Stress concentrations can also be seen at grain boundary triple points at the ends of the decohering grain boundaries. At these locations the adjacent grain boundaries are at high angles which would require more Mode II decohesion. It is possible that at these points the initiating crack might propagate into the grains. However, the current implementation does not allow for cracks to transition from intergranular to intragranular.

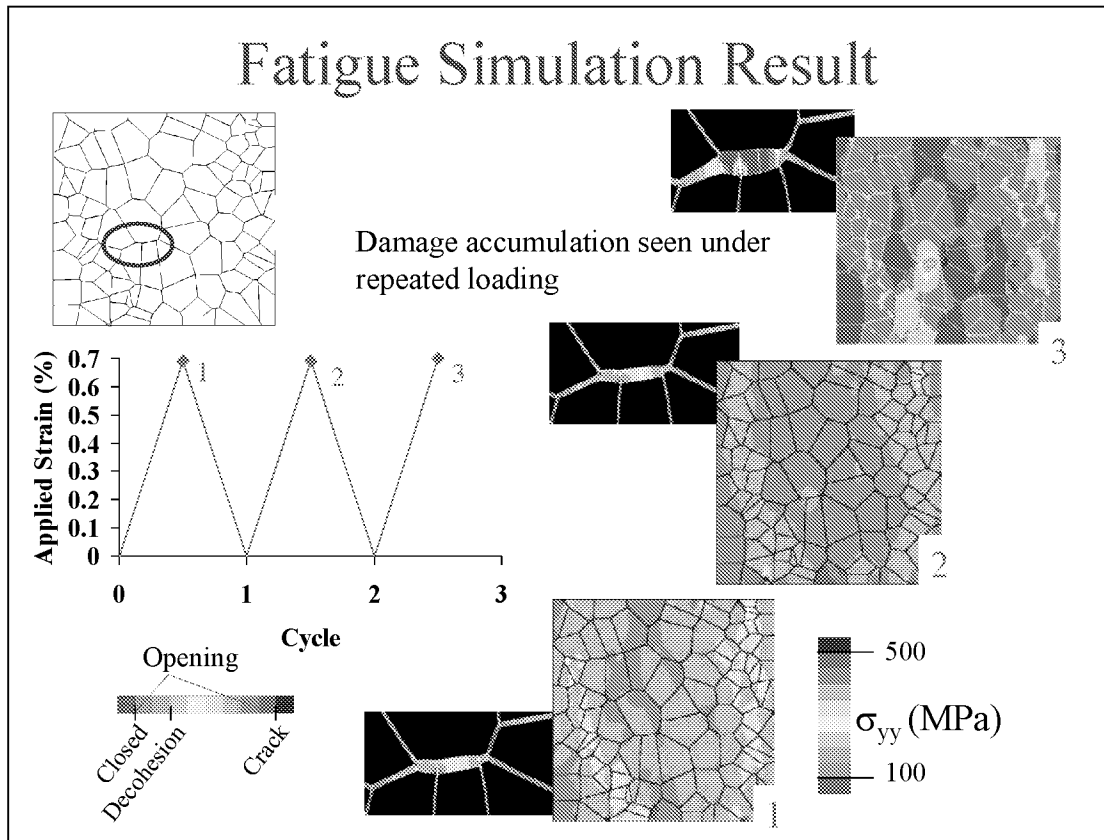


Figure 9

POLYCRYSTALS WITH INCLUSION PARTICLES

After testing of the 2D polycrystal samples additional refinement was added through the addition of sub-grain sized particles. Again the nano-sized particles are considered to be smeared out and accounted for through the variation in the constitutive parameters of the grains. Where the nano-sized precipitates help to increase strength larger particles, or inclusions, can actually be detrimental to the strength of an alloy. Experimental observations have also shown hard particles to be initiation sites for fatigue cracks.

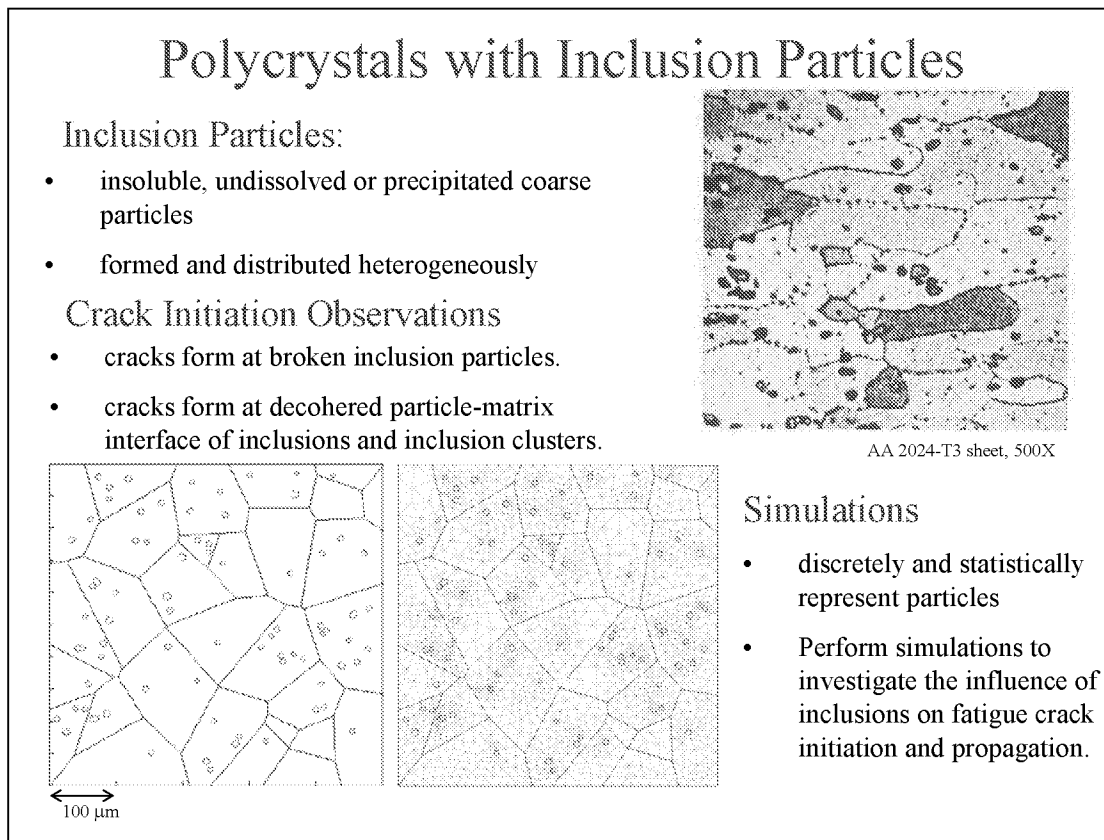


Figure 10

MODELING: PARTICLE-MATRIX BOUNDARY CONSTITUTIVE RELATIONSHIP, CCZM

Larger particles have been observed to be much harder than the surrounding matrix and well as brittle. These particles have also been shown to be poorly bonded to the matrix and thus sites for decohesion, void formation, and crack initiation. Cracking of the brittle particles is ignored for these simulations but decohesion is included. Again the particle-matrix boundary is modeled using the Tvergaard and Hutchison couple cohesive zone model. Interface elements are placed between the particles and the grains. Again this allows for natural decohesion of the particles from the matrix forming voids and initiating cracks.

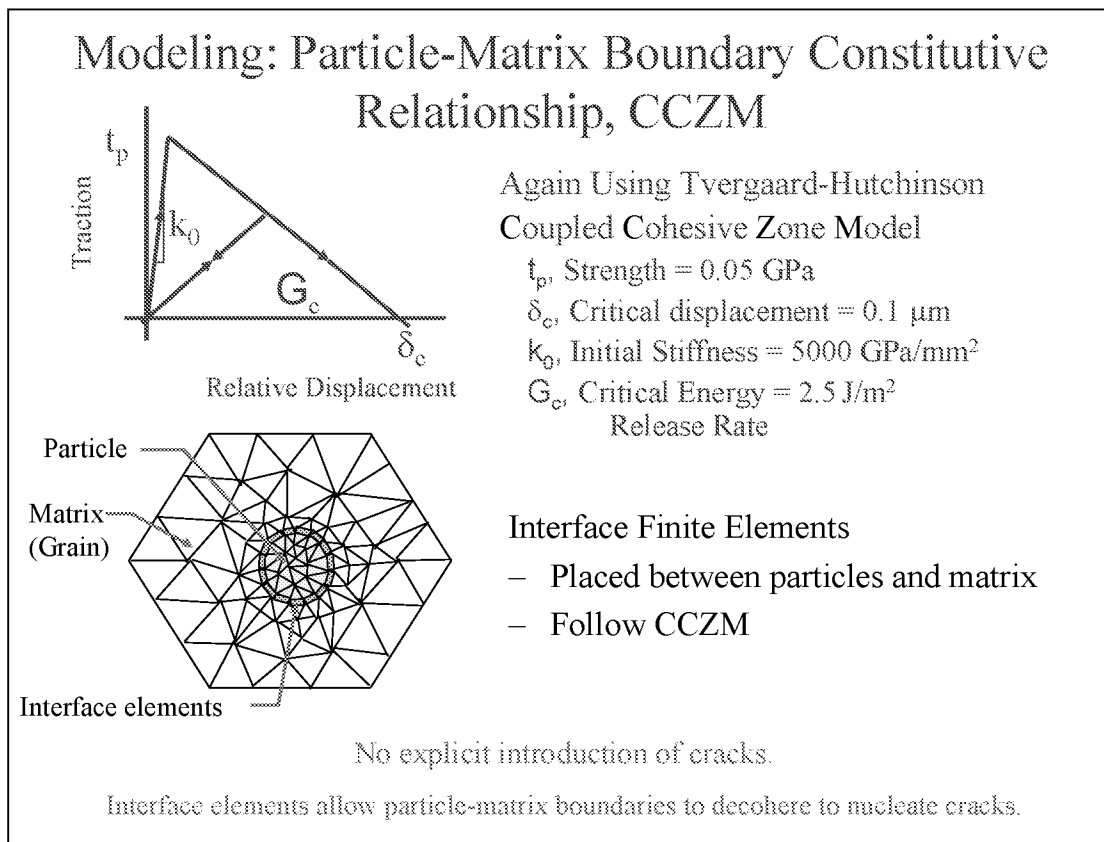


Figure 11

0.4% APPLIED STRAIN

A polycrystal sample was generated with elastic, isotropic particles with an average grain size of 0.017 mm^2 and particle volume fraction of 2%. The grains were modeled using Von Mises plasticity with a yield stress of 0.5 GPa. The particle-grain interfaces were given a strength of 0.05 GPa. The sample was then loaded under an applied strain of 0.4%. The sample showed stress concentrations are the particles as expected. Debonding of the particles was also seen.

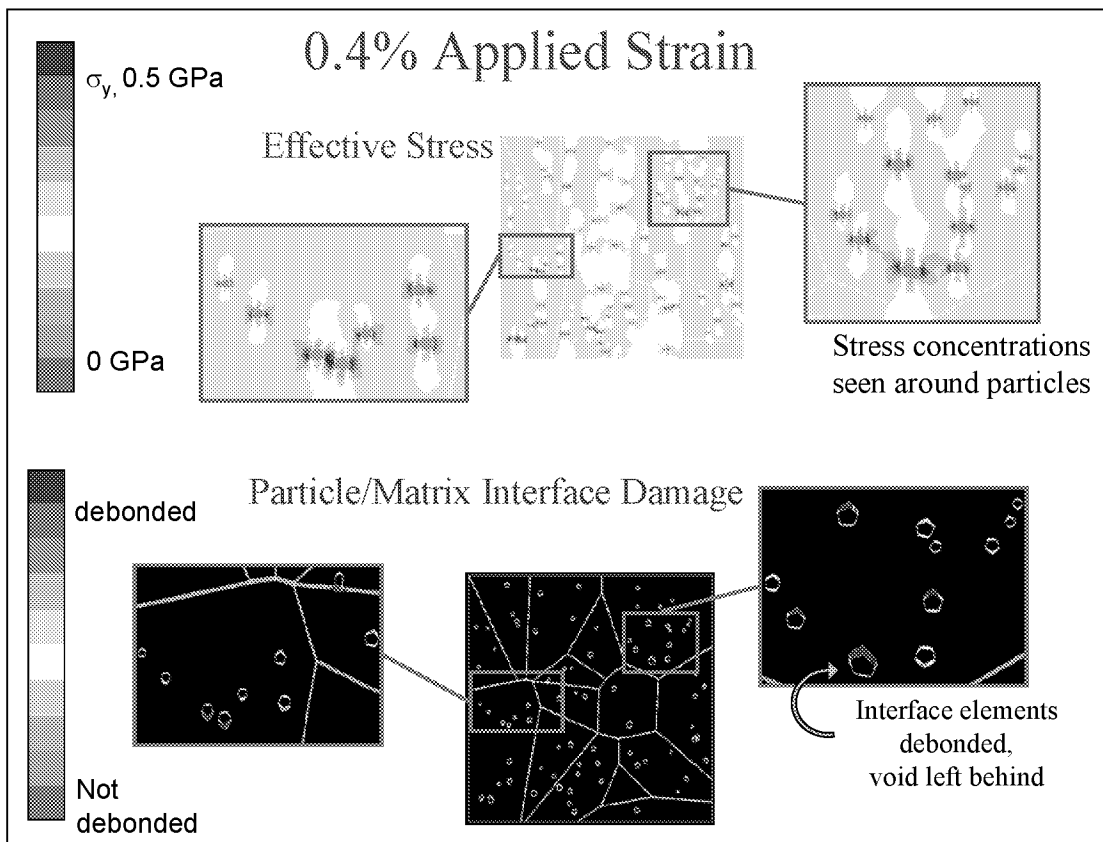


Figure 12

DEBONDED PARTICLES PROVIDE NUCLEATION SITES FOR MICROCRACKS

The debonded particles provide sites for nucleation and propagation of cracks as seen in this example.

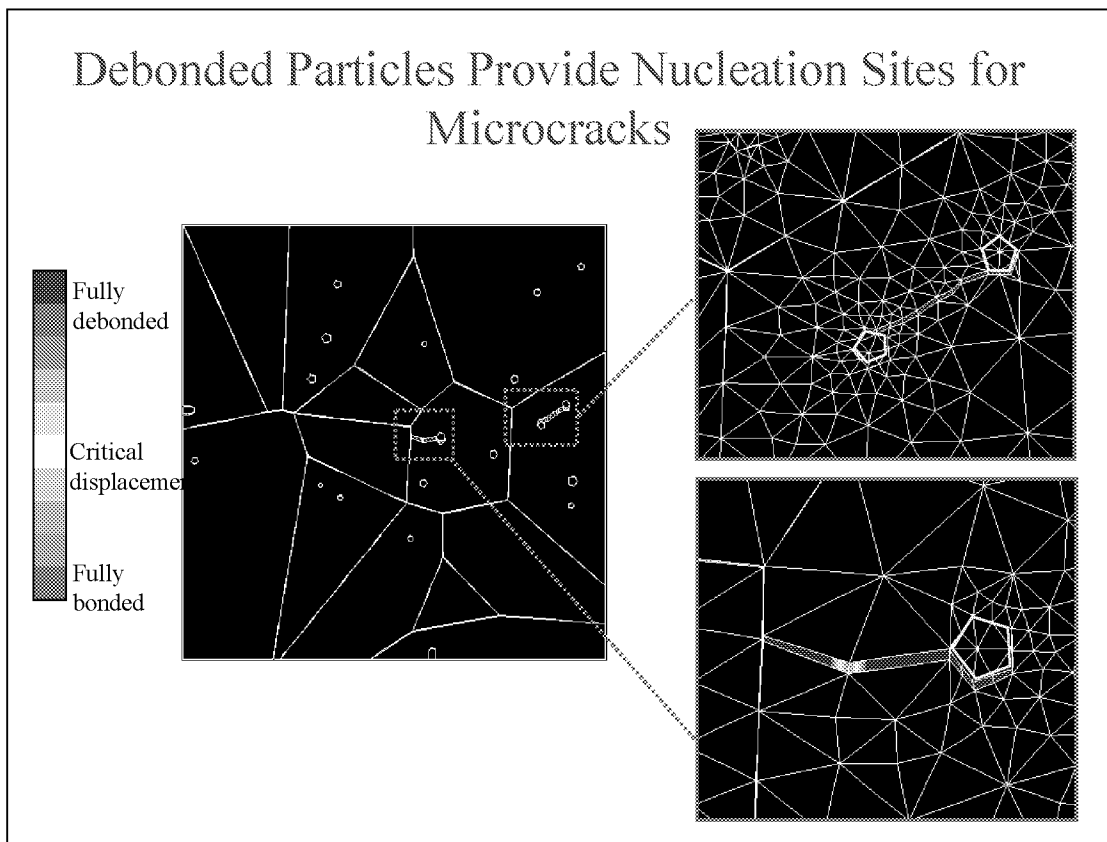


Figure 13

STEPS FOR TRANSITIONING TO 3D

While 2D plane strain or plane stress approximations give initial insights, the problem of crack propagation in metallic polycrystals is a 3D problem. The tools discussed so far have been for 2D representations and analyses. Transitioning these tools to 3D will require several steps. First a 3D representation needs to be generated. The subsequent meshing of such a geometry is more difficult than for 2D samples. Again material properties are assigned to each grain and boundary conditions are applied. The large increase in the number of finite elements demands extra consideration before choosing a solution technique. The needed storage for such a representation and memory and computational time for solving will put a strain on computational resources that needs to be considered.

Steps for Transitioning to 3D

- Creating grain geometry
- Meshing for FEM simulations
- Assigning individual material properties for each grain
- Determining appropriate boundary conditions
- Selecting solution techniques
- Determining necessary computational power

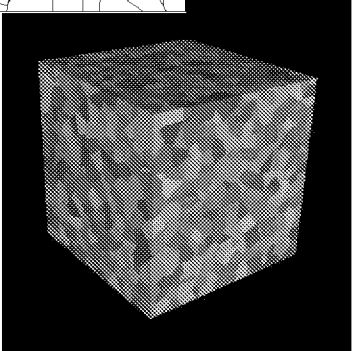
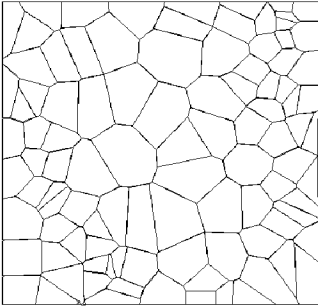


Figure 14

GENERATING 3D POLYCRYSTAL MESH

For a small example a 50 grain sample was generated using a 3D Voronoi tessellation. The sample was meshed using QMG 2.0 an octree mesh generator created by Professor Steven Vavasis at Cornell University. The resulting mesh had over 800,000 10-noded tetrahedral elements and over 3.3 million degrees of freedom. This is a huge increase from the 12,000 degrees of freedom for a 100 grain 2D sample. The overall project of which this research is only a small part will involve several different software applications each operating on the same data. To facilitate the use of a single set of data by many application the mesh data was stored in a database using SQLServer 2000. Simple SQL queries can be written to extract the necessary information into a suitable format for the desired application. This also allows for our collaborators at other universities including Mississippi State University and the College of William and Mary to share a single set of data.

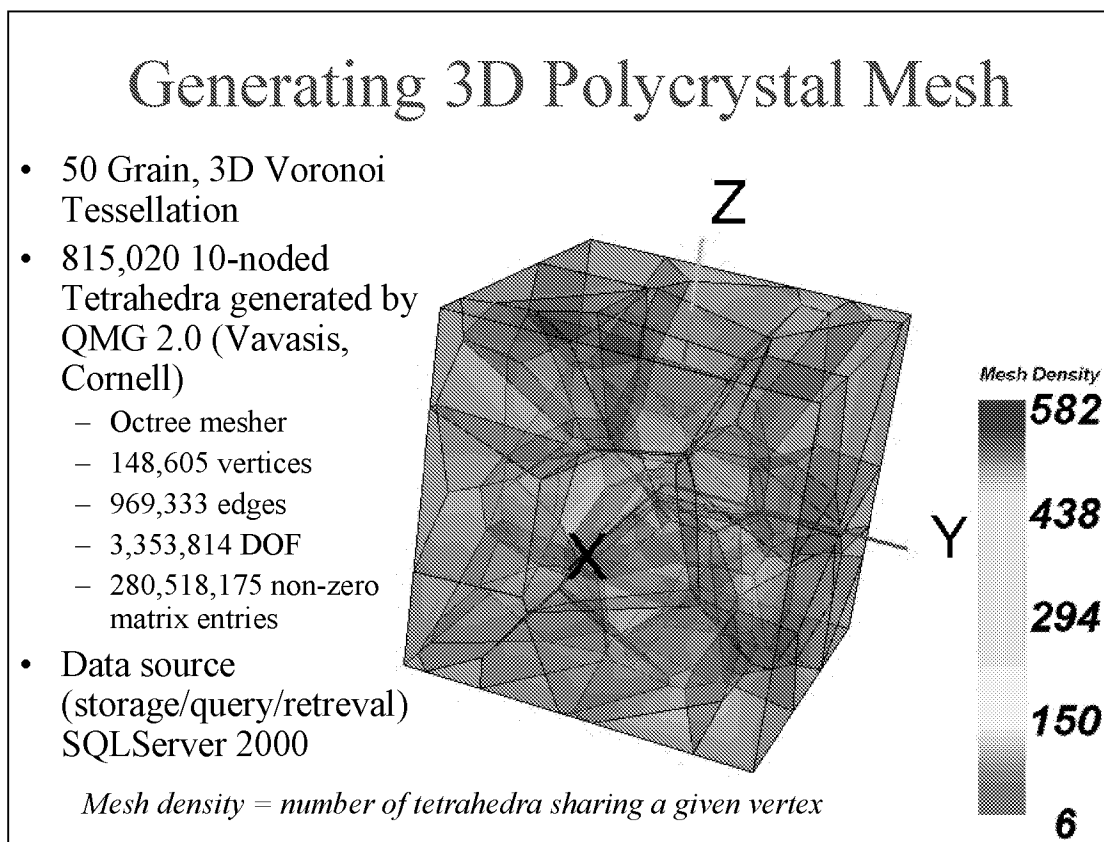


Figure 15

TENSION TEST UNDER APPLIED DISPLACEMENT

Each grain in the sample was randomly assigned material properties for an elastic, isotropic constitutive model. Three sides of the cube were then fixed as shown. The negative XZ face was fixed in the Y direction. The negative YZ face was fixed in the X direction. The XY face was fixed in the Z direction. Finally a strain of 1% was applied in the Z direction to the positive XY face.

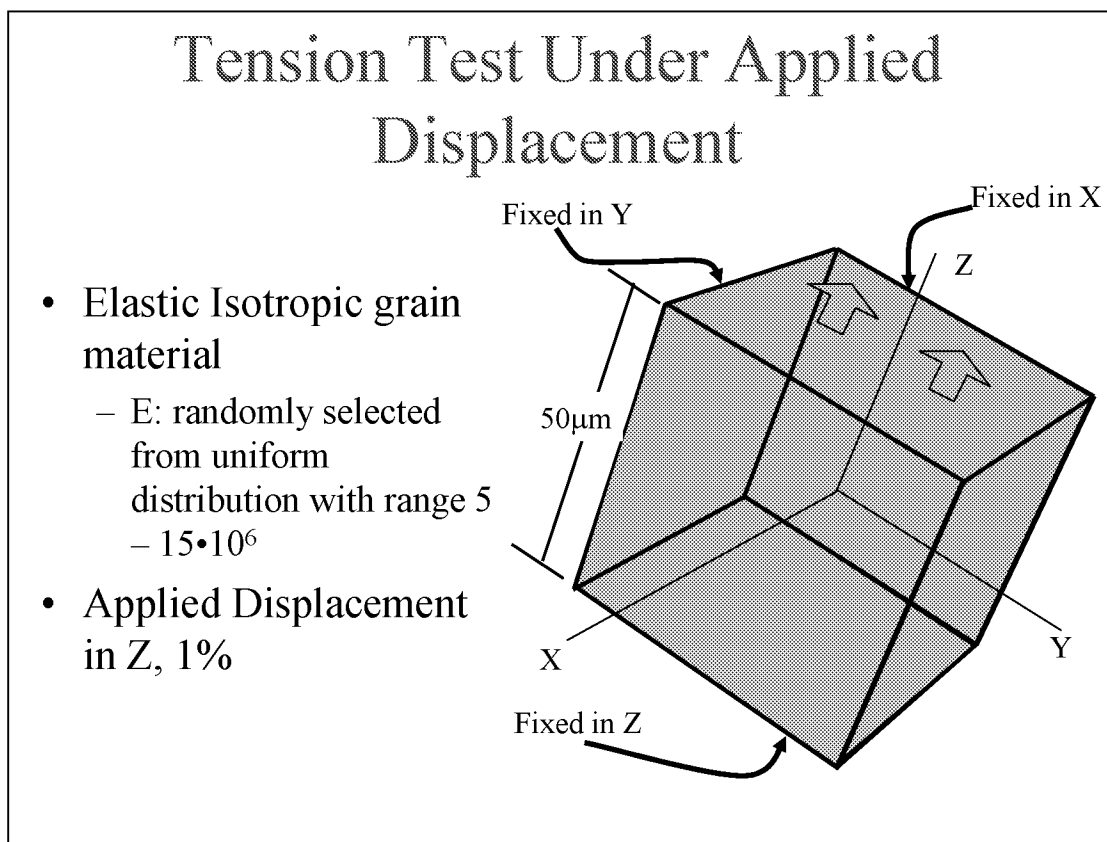


Figure 16

TENSION TEST UNDER APPLIED DISPLACEMENT

The problem was solved using 64 servers. Each server has 2 processors of which only 1 was used. Using the 64 processors the solution took less than 28 minutes. Due to the variation in the Young's Modulus of each grain the resulting displacement field is not uniform. The wireframe polycrystal shown is the displaced shape. The Poisson effect can be seen as the YZ and XY faces have contracted. The color contour is shown over the original configuration. Visualization was created using VTK.

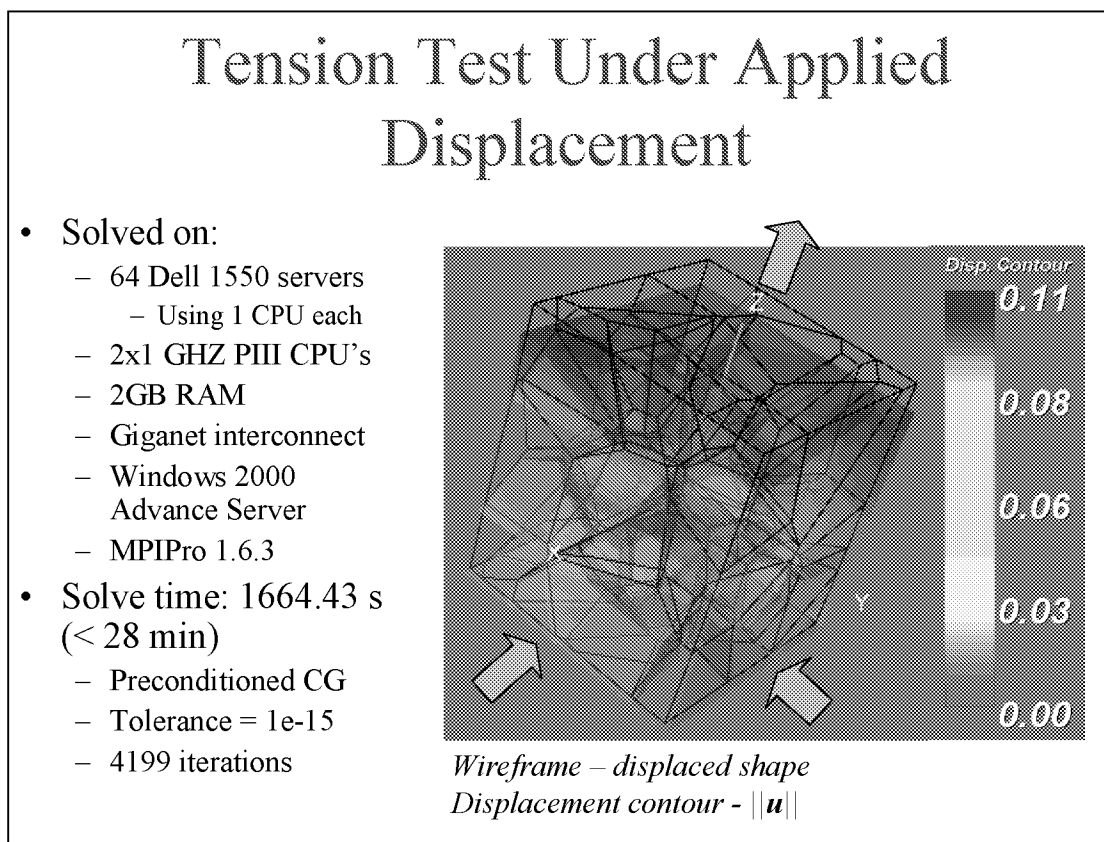


Figure 17

COUPLING MD TO FINITE ELEMENTS

Techniques are being investigated to transition between molecular dynamics representations at the atomic scale and finite element representations of the meso-scale. One technique currently being looked at is overlapping a region of atoms over the finite element representation. The atomic scale captures the nonlinear behavior in small areas of interest such as at a crack tip which is then added to the linear response determined by the finite elements.

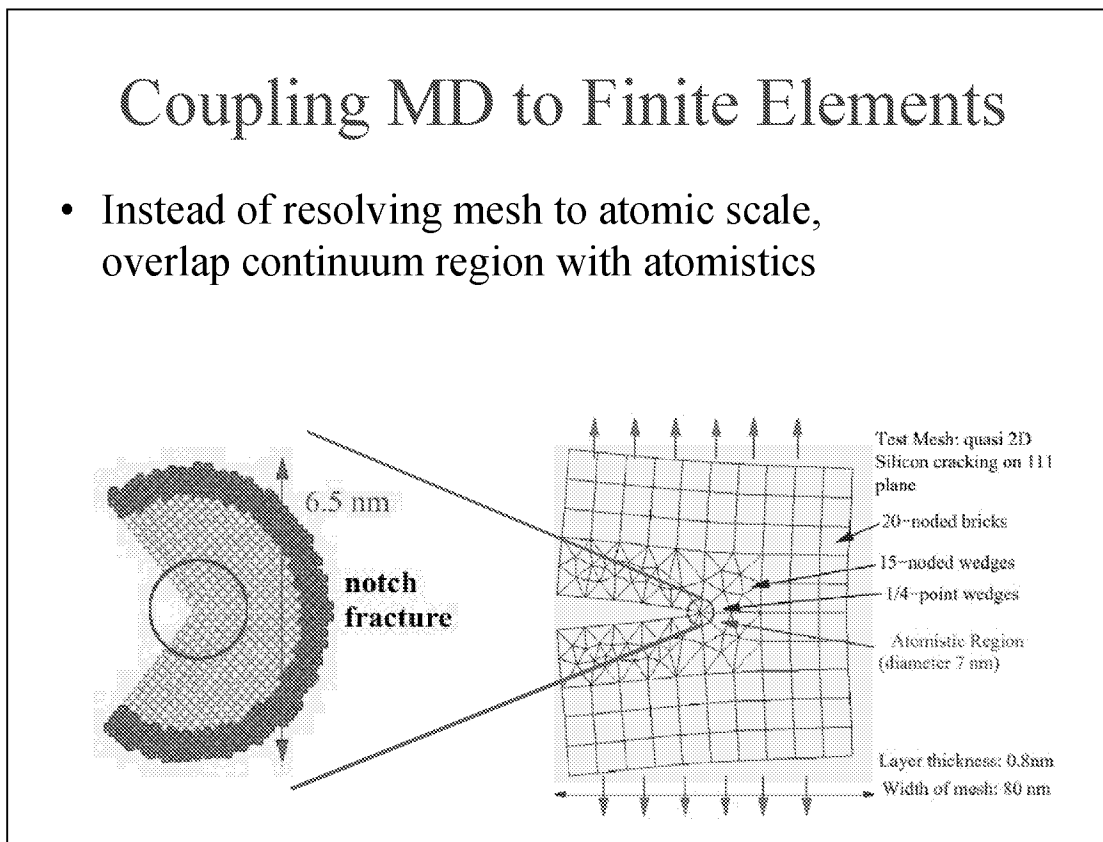


Figure 18

WORK IN PROGRESS

There is still much work to be done in the areas discussed in this presentation. Although simple 3D polycrystal examples have been created and solved, several of the tools available in 2D need to be implemented in 3D. These include generating and meshing samples with hard particle inclusions as well as 3D cohesive elements for grain boundary and particle-grain interface decohesion. In order to facilitate meshing and solving of the samples, parallel implementations are needed. We are also still investigating techniques for bridging the length scales between meso- and atomic scale representations. These include techniques such as quasi-continuum approach and overlaying an atomic region as shown previously. The goal of this work is to incorporate the pieces shown here along with other simulators to create an adaptive software environment in which to study multiscale phenomenon.

Work in Progress

- Model polycrystal samples with particles and cohesive separation in 3D.
- Bridge the length scale between meso- and atomic scales: quasi-continuum approach, overlaying atomic region.
- Understand relation between atomistic modeling and CZM in simpler systems, e.g., single crystals.
- Implement parallel versions of meshers and simulators: essential for 3D
- Create adaptive software environments to facilitate multiscale simulations.

Figure 19

Scale-Bridging in Dislocation-Based Multi-Scale Modeling

Kyung-Suk Sim
Brown University
Providence, RI

INTRODUCTION

Three examples of scale bridging problems in nano- and micro-mechanics of solids will be discussed in this presentation.

Scale-bridging in dislocation-based multi-scale modeling

**Kyung-Suk Kim
Brown University
Providence, RI 02912**

Introduction

- 1. Generalized stacking fault energy, dislocation-nucleation instability, and its effects on flow stress of the slip process.**
- 2. Multiple-dislocation cooperative slip bridging dislocation nucleation processes and pile-up termination processes.**
- 3. Continuum plastic-flow-field transition from small scale to a large scale, caused by elastic and plastic anisotropy incompatibilities.**

Supported by NSF/MRSEC, Ford and ONR
Presented at NASA Langley, March 6, 2002

Figure 1

CHARACTERISTICS OF DISLOCATIONS AT DIFFERENT LENGTH SCALES

Plastic flow of crystalline solids is primarily governed by the motion of dislocations. The motion is controlled by various dislocation characteristics at different length scales. Therefore, the plastic flow and the failure processes led by plastic flow must be analyzed by multi-scale modeling, if responsible micro-mechanisms for an upper-scale phenomena are to be understood and interlinked between different length scales. This slide shows typical characteristics of dislocations at different length scales, that have to be modeled with scale bridging.

Plasticity theory of crystalline solids

Dislocation theory (1-10 nm, 10-100nm, 0.1-5 μ m, 0.2-10 μ m, 2-100 μ m)

Core-level dislocation model; configurational degree of freedom in the core

Line-level dislocation model; configurational degree of freedom in the curve

Dislocations/atmosphere interaction model; degree of freedom in the atmosphere

Dislocation – dislocation interaction model; degree of freedom in the forest

Dislocation – wall interaction model; degree of freedom near a wall

Continuum theory (0.2-10 μ m, above 10 μ m)

Strain gradient theory

Single crystal plasticity

Twinning and phase transformations

Grain boundary sliding and grain growth

Diffusion-coupled plasticity

Void nucleation and growth

Polycrystal plasticity and texture formation

Figure 2

MAP OF DEFORMATION-MEASUREMENT TECHNIQUES

Experimental techniques should be also scale-bridged because the resolution of an experimental technique has a limited domain of validity on the scale map of the field of view and the strain resolution. In multi-scale modeling the model at a specific length scale has to be checked with experimental verification at the corresponding physical length scale, and proper experimental techniques have to be used for the validation and the scale bridging.

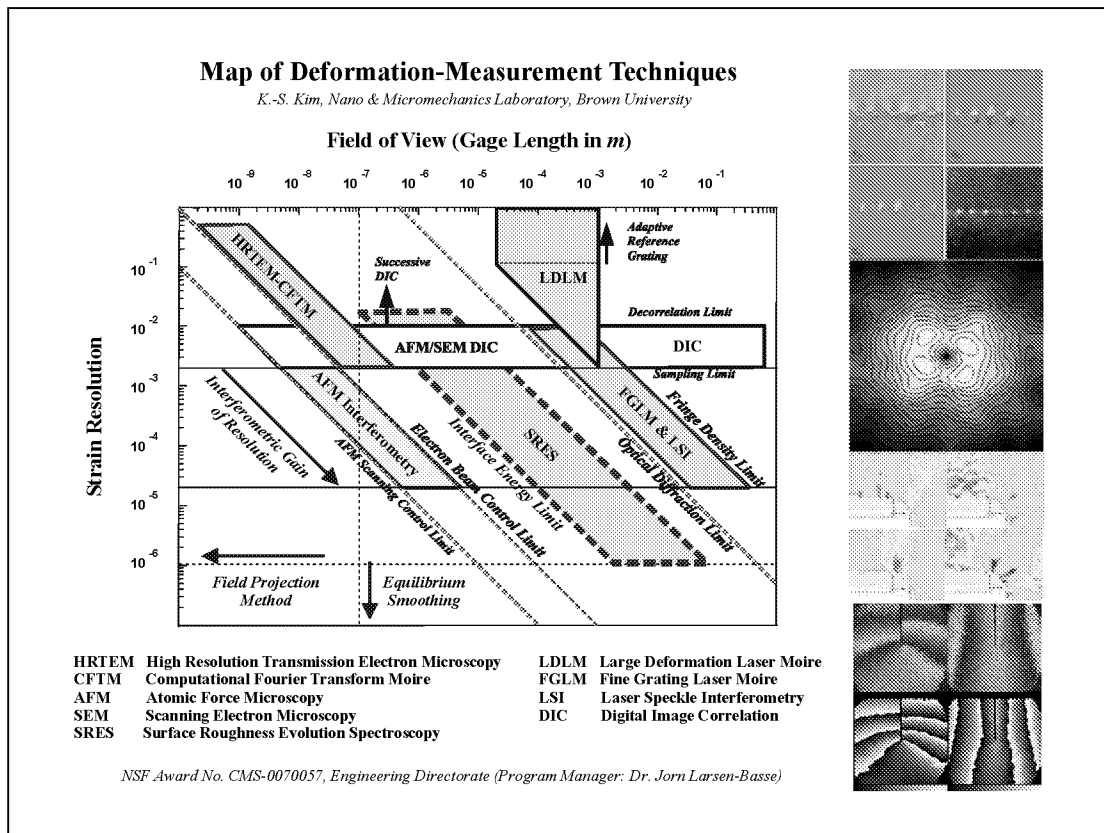


Figure 3

GENERALIZED STACKING FAULT ENERGY

Some irreversible slip processes at a nano- and micro- meter scales are predominantly determined by an instability of the motion of a dislocation.

The characteristics of some slip process can be described by the generalized. Stacking fault energy. The generalized stacking fault energy can be obtained by ab-initio calculations, and it can be connected to a continuum mechanics modeling of the slip instability as initiation of dislocation motion.

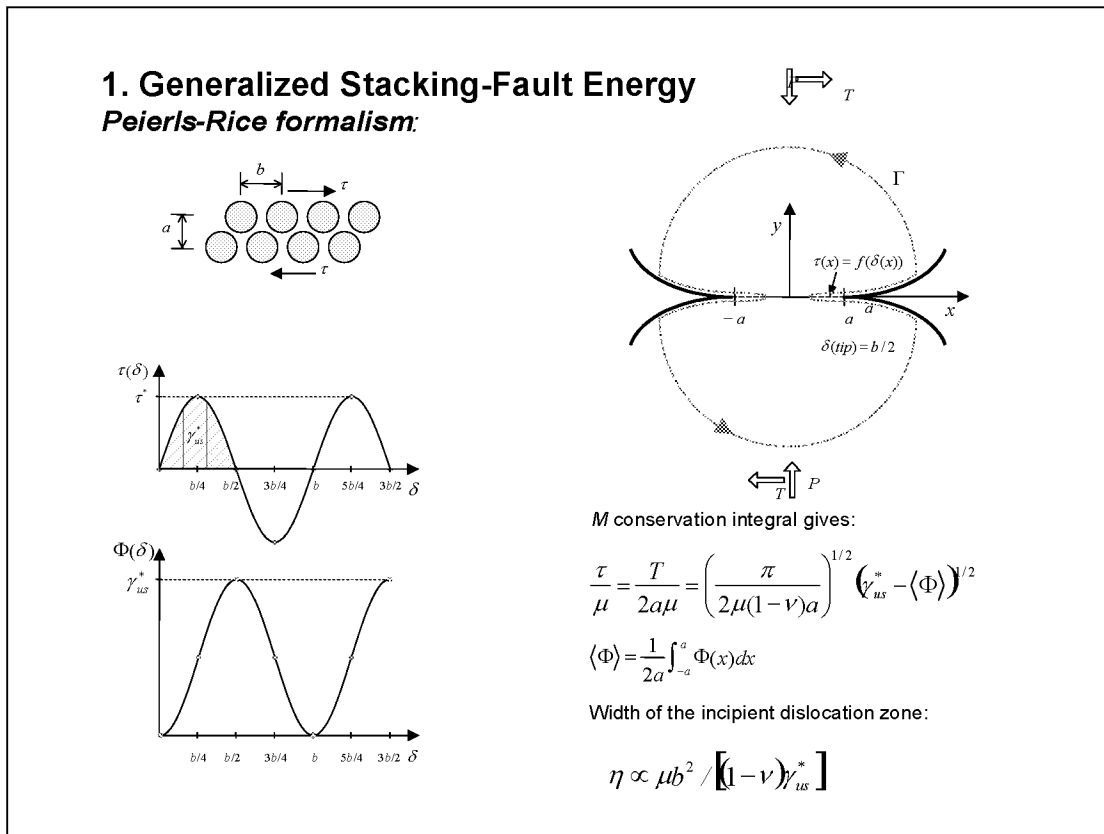


Figure 4

SINGLE-ASPERITY CONTACT FRICTION

The friction force required to slide a single asperity contact used to be considered to be proportional to the contact area, since Bowden and Tabor made the conjecture based on macroscopic experimental observation. The friction force divided by the contact area is called the contact stress, and indeed the friction stress has been measured to be constant within a contact radius range of 3 – 14 nm in UHV AFM friction experiments. The friction stress has been also observed to be constant in Surface-Force-Apparatus (SFA) experiments within a contact radius range of 40 – 250 microns. However, the friction stress of the AFM experiment is about 1/30 of the shear modulus of the contact joint, and that of the SFA is about 1/1300 of the shear modulus. These results contradict the Bowden and Tabor conjecture, and the friction stress between the two different length scales could not be measured so far.

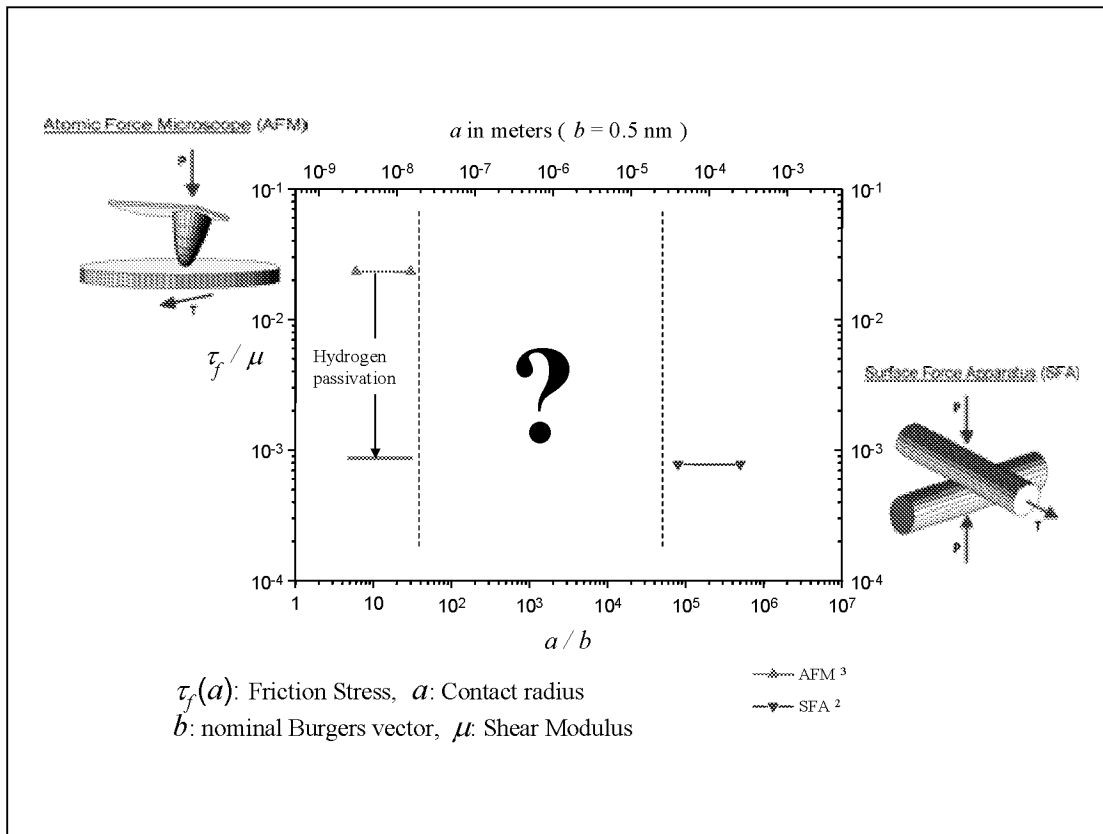


Figure 5

MAP OF SINGLE-ASPERITY-FRICTION MECHANISMS

Recent analysis based on the Peierls-Rice formalism with the generalized stacking fault energy shows that the single asperity friction has different mechanisms of slip at different length scales of the contact radius. At a nano-meter scale the contact area is so small that it can not contain a well-defined dislocation loop and corresponding dislocation core structures for the slip process; therefore, the slip process is considered to be a concurrent slip and the friction stress is close to the theoretical strength of the joint. As the contact area becomes larger than a certain critical size, a mobile dislocation is nucleated at the edge of the contact and it self-annihilates due to its line-tension energy before the next dislocation is nucleated, assisting the slip process; this slip mechanism is called “Single Dislocation Assisted (SDA)” slip. As the contact size gets to be larger, the leading dislocation is stabilized with in the contact area before the trailing dislocations are nucleated; this mechanism is called “Multiple-Dislocation-Cooperated” slip and the friction stress is contact-size independent.

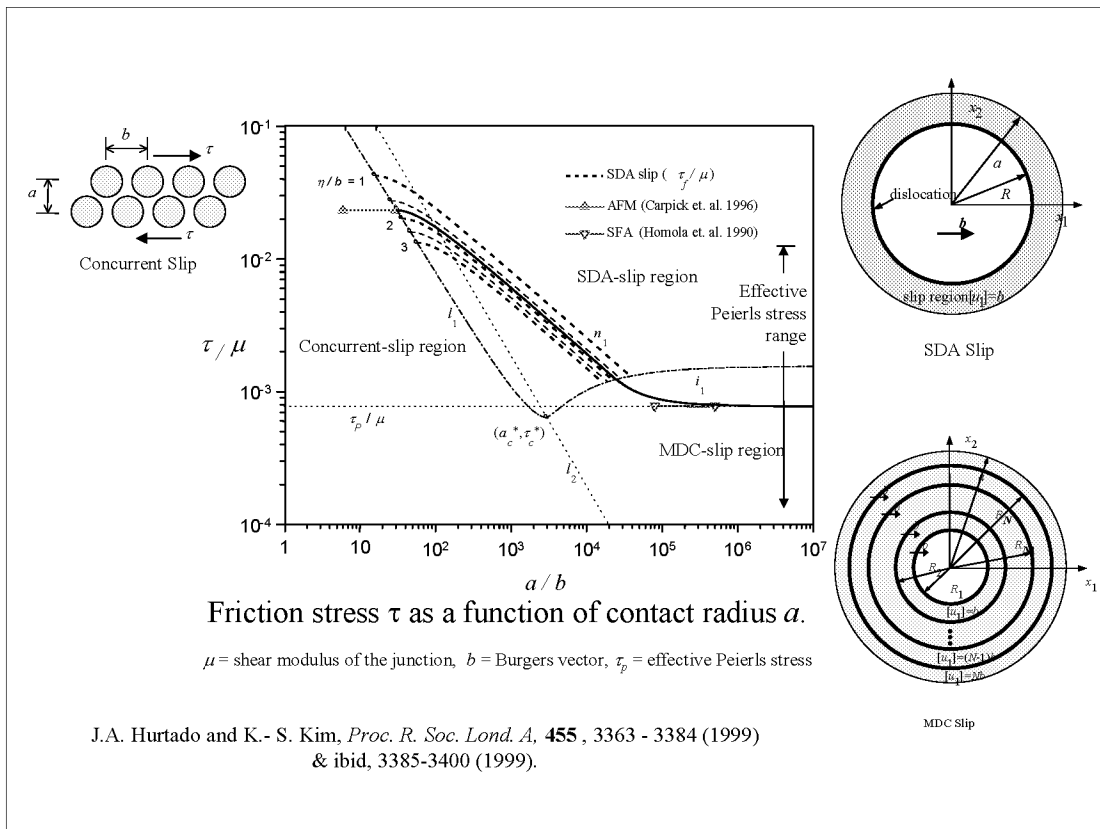


Figure 6

CONCLUSION ON GENERALIZED STACKING FAULT ENERGY

The evaluation of the generalized stacking fault energy is sensitive to the modeling scheme such as the density functional theory or an embedded-atom- potential method. It is a good testing entity for checking the validity of the modeling scheme. Other utilities of the generalized stacking fault energy as a scale-bridging scheme are listed on the slide.

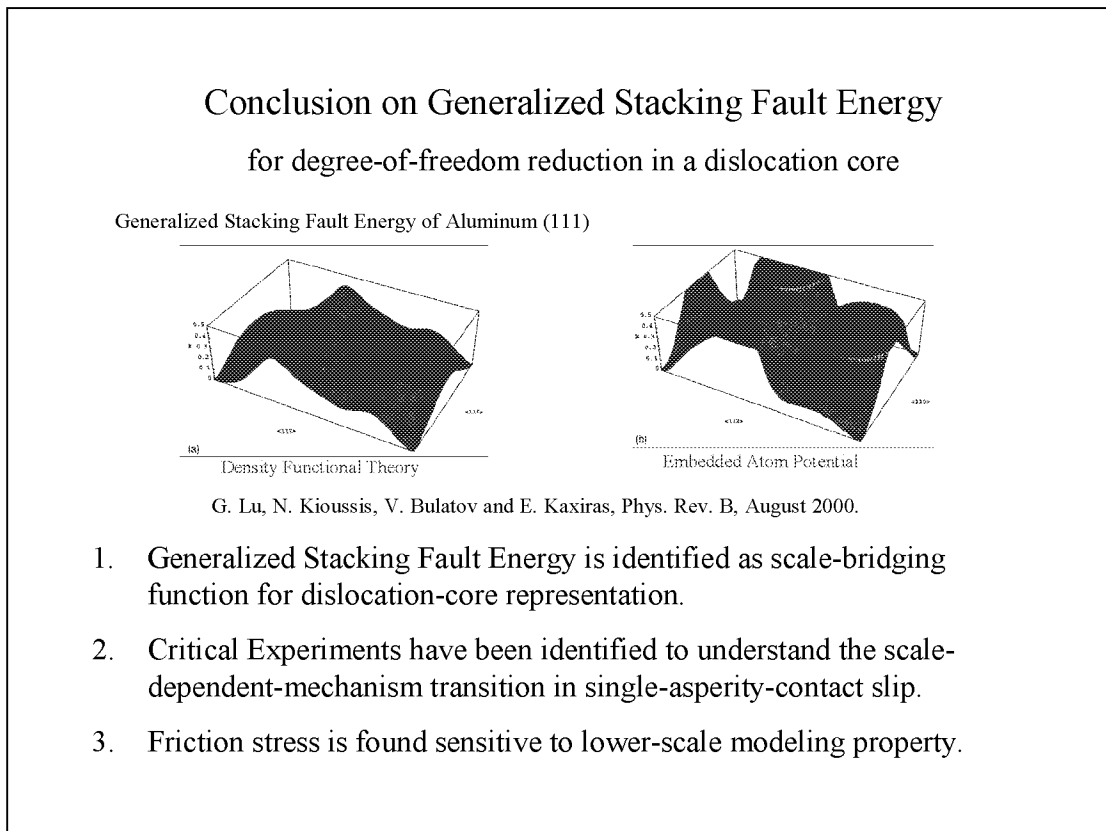


Figure 7

2. MULTIPLE-DISLOCATION-COOPERATIVE SLIP MODELING (A356-T6)

Another scale-bridging example for multi-scale modeling is discrete dislocation modeling for multi-dislocation cooperated slip processes. The example is the inverse size effect of the plastic flow stress observed in a cast aluminum A356-T6. The flow stress for a fine structure of secondary dendrite arm spacing is lower than that of a coarse structure. The cast aluminum is a multi-phase alloy containing pro-eutectic phase surrounded by silicon- aluminum eutectic phase. The pro-eutectic phase is softer than the eutectic phase as shown on the hardness distribution near the interface between the two phases.

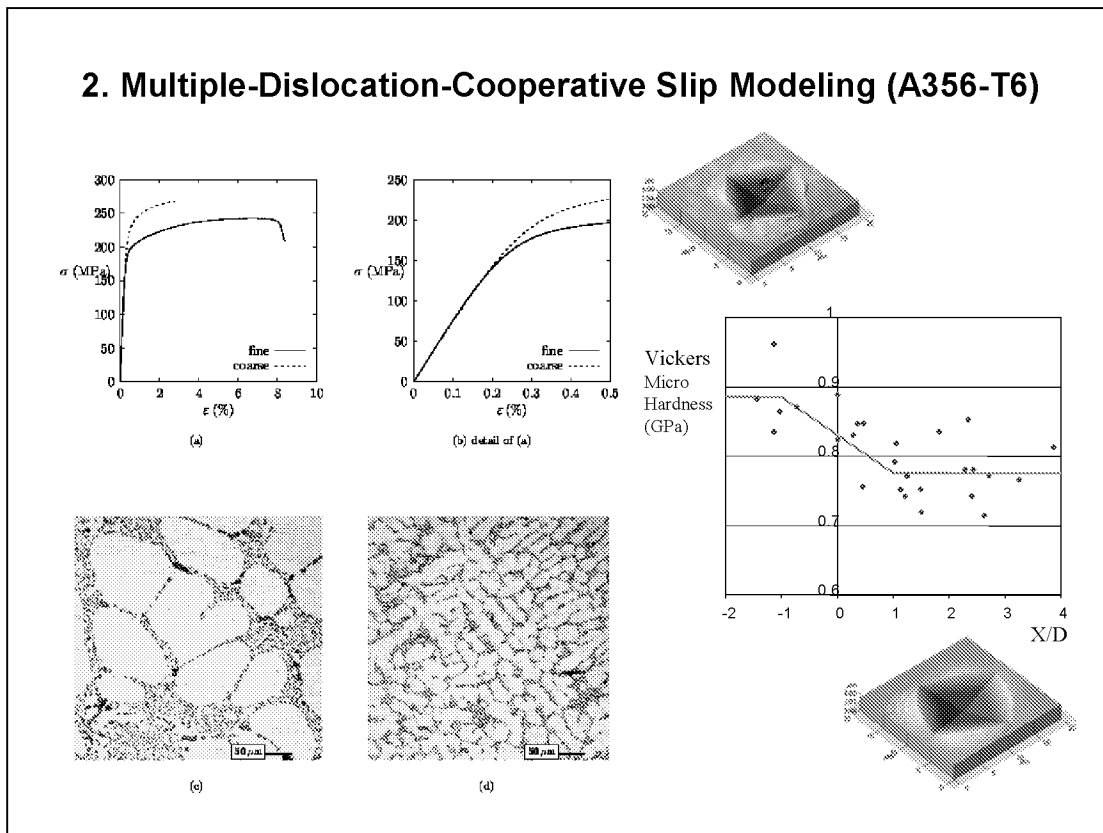


Figure 8

DISLOCATION BLOCKING MECHANISMS OF A A356-T6

This slide shows dislocation slip bands in the pro-eutectic phase, blocked by the eutectic phase. This type of plastic flow requires multi-scale modeling of the collective dislocation motion. The first inset shows an optical view graph of the slip bands and the other insets show AFM view graph of the slip bands. The height of the slip steps in the AFM view graphs show that dislocations are nucleated in the pro-eutectic phase and blocked by the eutectic phase.

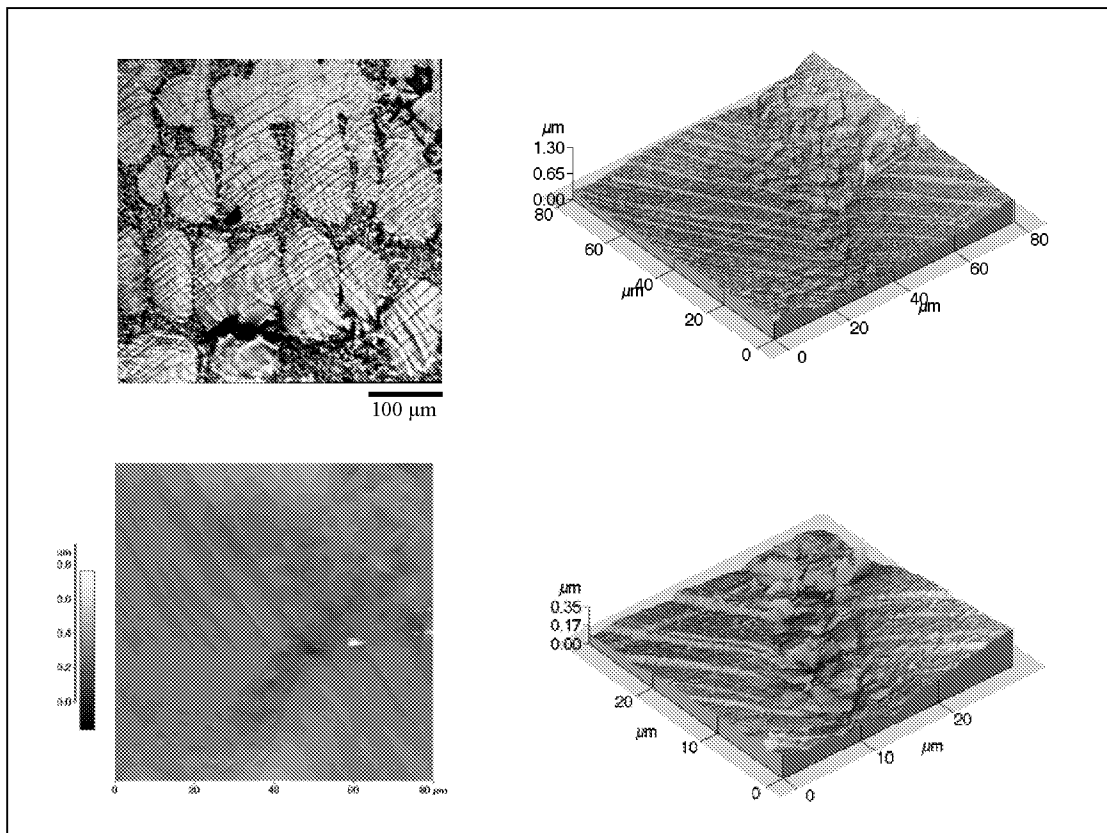


Figure 9

DISCRETE DISLOCATION MODELING

For the multi-scale modeling of the collective dislocation motion Needleman and his associates have developed a discrete-dislocation FEM methods. The method employs mechanism-based constitutive rules of the dislocation motion, which requires the long-range interaction stress field. The stress field is computed by an FEM analysis. The constitutive rules coupled with the FEM analysis make the multi-scale modeling algorithm.

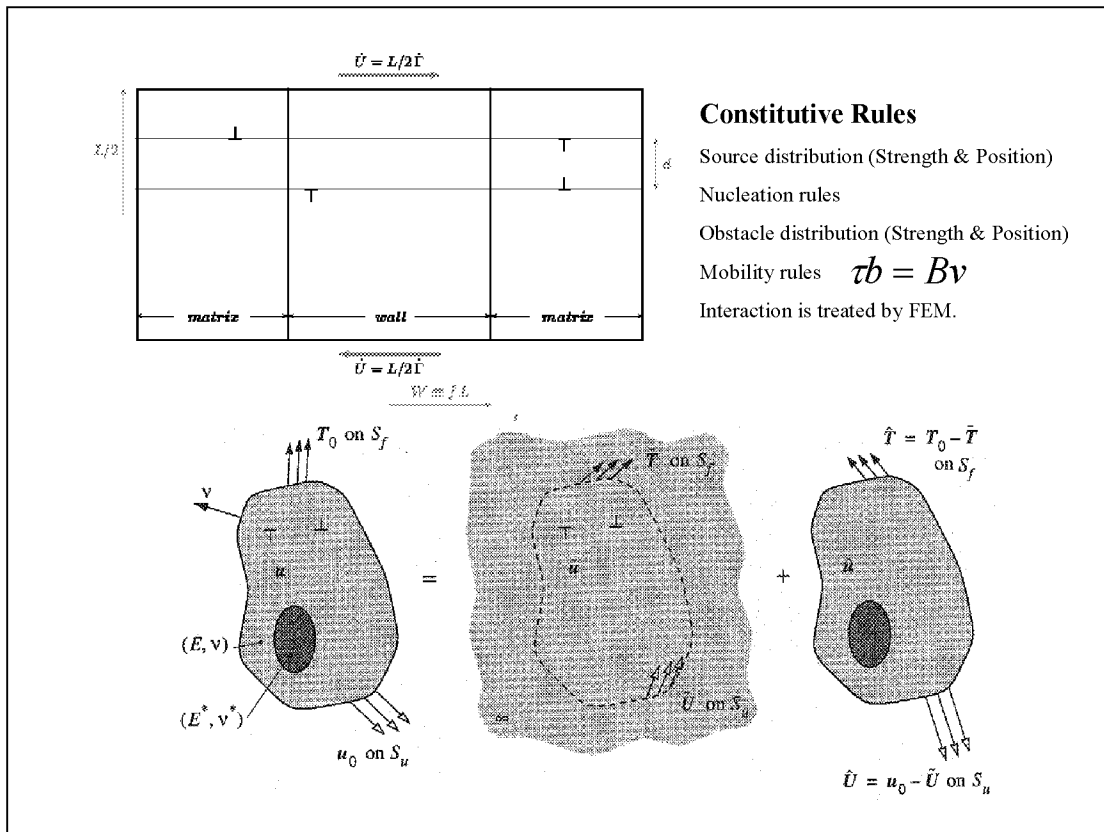


Figure 10

CONCLUSION ON MULTIPLE-DISLOCATION COOPERATIVE SLIP

The conclusion page is self explanatory. The left inset shows the inverse-size effect observed on the stress strain relation predicted by the discrete dislocation modeling. Right side insets show dislocation-slip-band configurations for different-size microstructures, generated by the computational modeling. In smaller microstructures the slip band can penetrate and glide through the eutectic phase, while the slip bands can only penetrate a skin depth in the eutectic phase. The skin depth forms a boundary layer of the dislocation penetration.

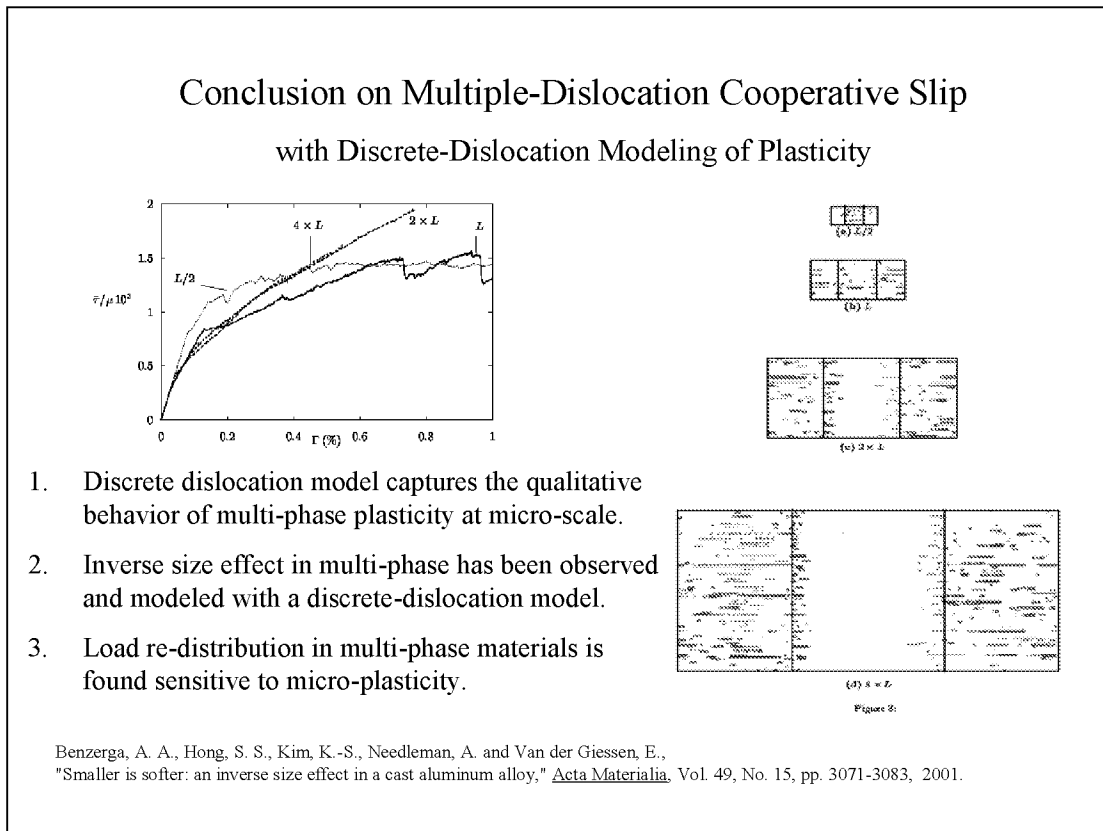


Figure 11

SYMMETRY TRANSITION FROM ASYMPTOTIC CRACK-TIP PLASTIC TO ELASTIC FIELDS

The asymptotic mode-I crack-tip plastic-strain fields on (101) have been considered identical for [10-1] and [010] cracks in both BCC and FCC crystals, because the continuum yield surfaces are identical for the two crack orientations [Rice, 1987]. We will see the experimental results on the next slide.

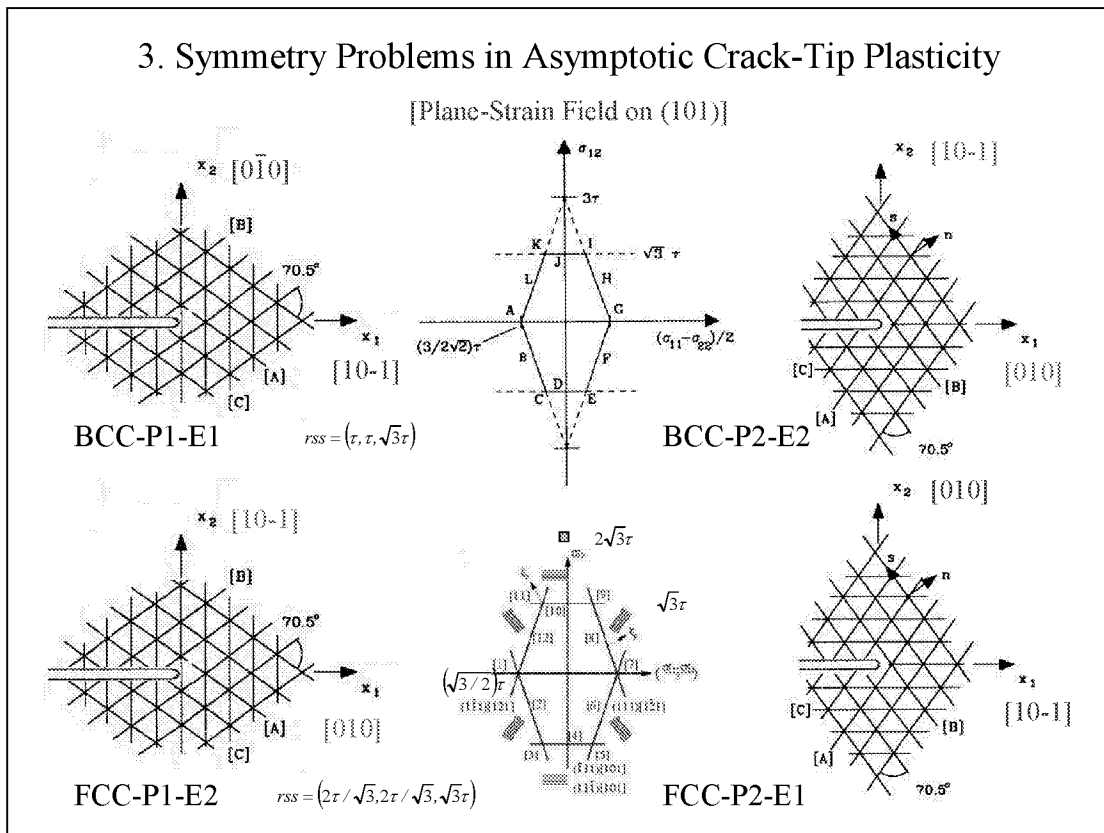


Figure 12

EXPERIMENTAL OBSERVATIONS OF THE CRACK-TIP SLIP SECTORS

In contrast to the predictions the experimental observations on the slide show completely different slip sectors for the two orientations. The upper diagrams depict activated slip systems predicted by Rice [1987], while the lower pictures show the slip traces and slip sectors in Iron-Silicon3% for the two orientations.

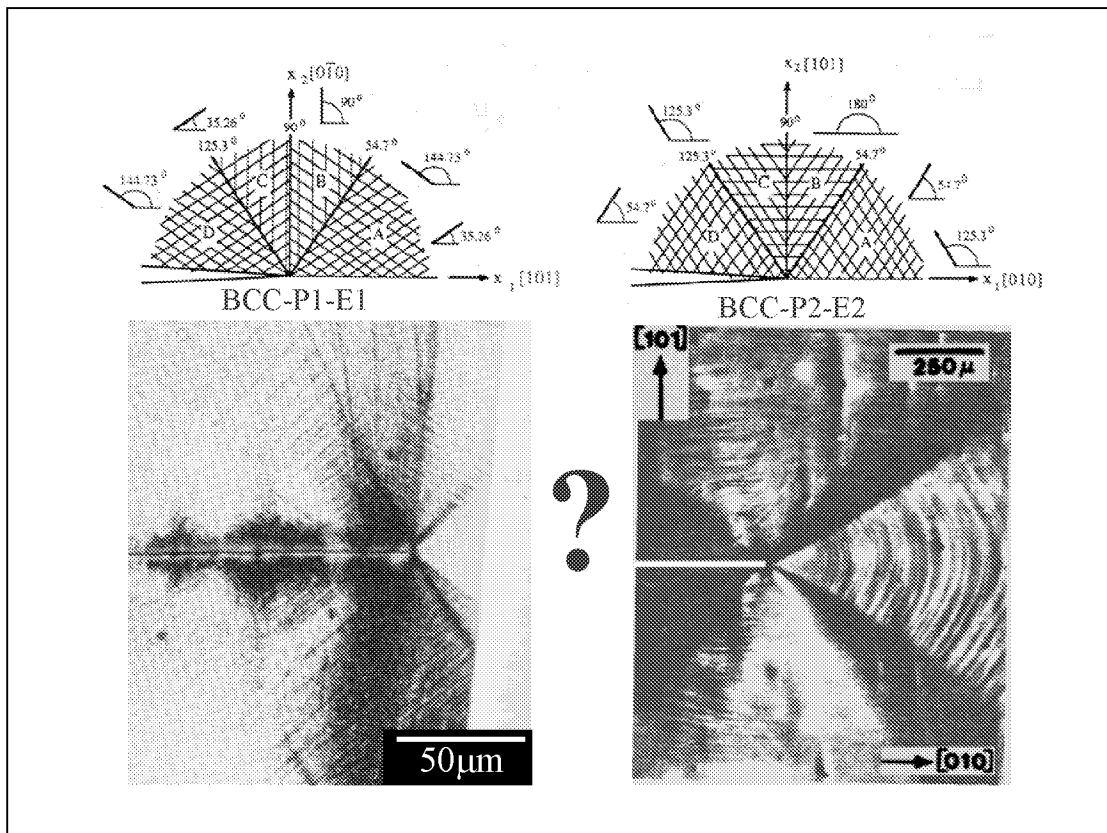


Figure 13

COMPARISON BETWEEN EXPERIMENTS AND COMPUTATIONAL MODELING

The data (a) and (b) shown in the red inset are the angular distribution of Mohr strain $\{(\epsilon_{xx} - \epsilon_{yy})/2, \epsilon_{xy}\}$ in the asymptotic plastic-strain fields around the crack tips of the two orientations. The distributions are distinctly different. However, the analytical and small-strain FEM simulation in (c), a large-deformation FEM simulation in (d) and discrete dislocation models in the other two insets could not capture the characteristics of the strain distribution in (b). All the computational simulations assumed isotropic elasticity.

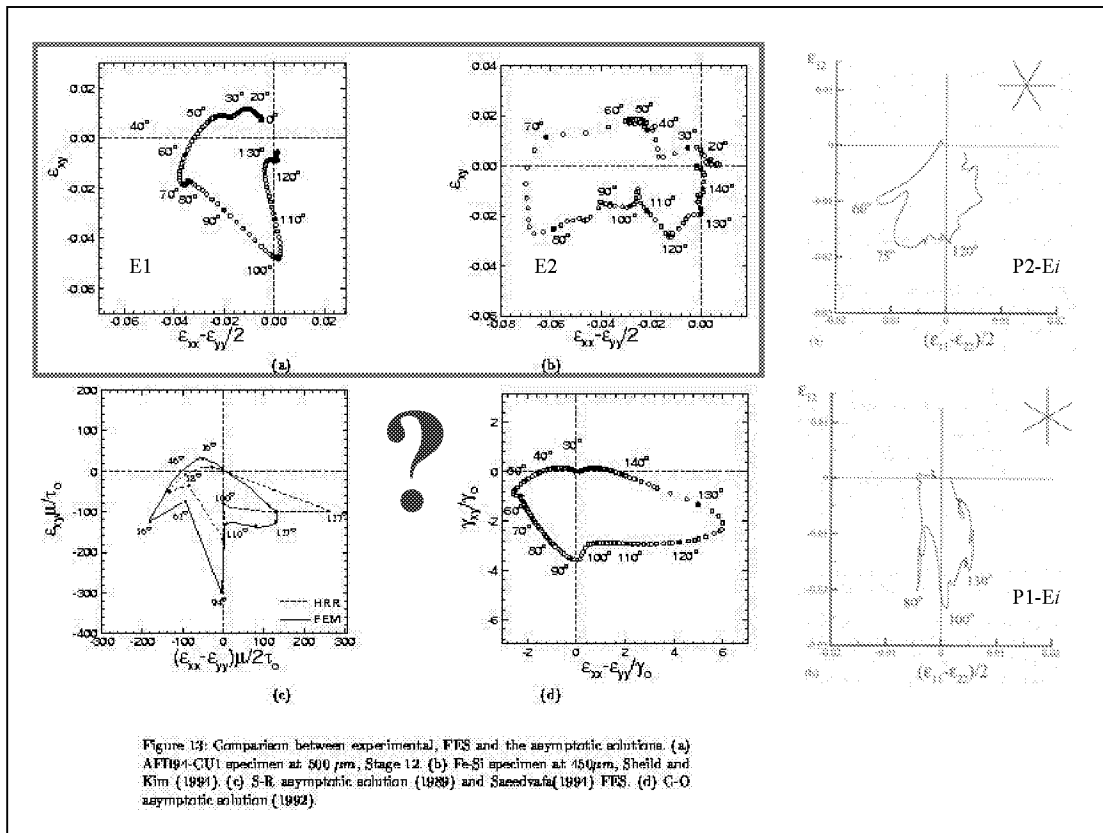


Figure 14

CONCLUSION ON SYMMETRIES IN CRACK TIP PLASTICITY

Experimental measurements show that the asymptotic plastic-deformation field of (b) exhibits counter-intuitive unloading sectors ahead of the crack tip as shown in the first figure of the slide. The second figure shows the asymptotic elastic-field Mohr-strain distribution around the crack tips of the two orientations. The distribution shifted to the right is not coherent with the asymptotic plastic-deformation field, generating the unloading sectors. The crack-front unloading sectors make the crack growth torturous as shown in the third picture. The fourth figure shows the Mohr-stress distribution around the crack tip. As seen in this example, the scale bridging between the asymptotic plastic field and the outer elastic field is essential to capture proper physical processes.

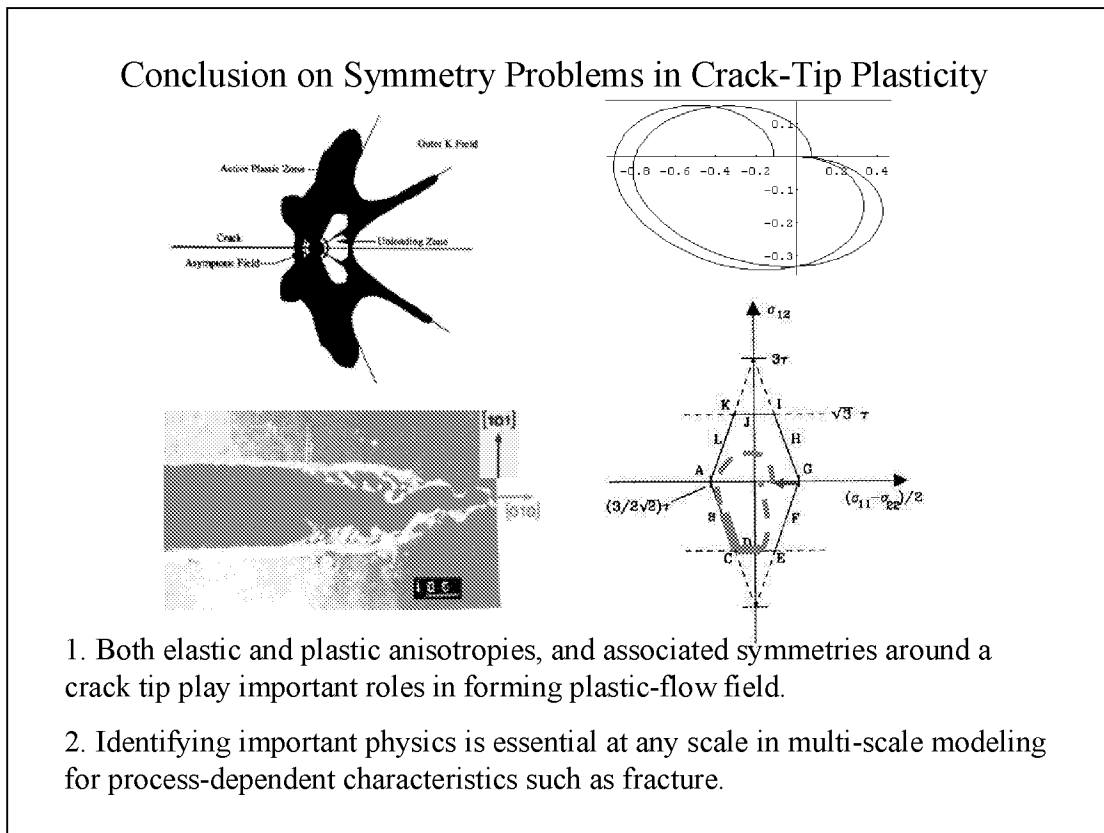


Figure 15

CONCLUSION

It is self-explanatory.

Conclusion

1. Scale-bridging concepts such as dislocation model and cohesive-zone model - generalized stacking fault energy are essential for multi-scale modeling of plastic flow and friction.
2. Right model has to be selected to capture right physics of the phenomena; discrete dislocation model captured the inverse size effects in multi-phase plastic flow.
3. Identifying important physics is essential at any scale in multi-scale modeling for process-dependent characteristics such as fracture; symmetry problems are shown for single crystal crack-tip plasticity.
4. Critical experiments are always needed at any scale for reliable multi-scale modeling.

Figure 16

**Yield Criteria for BCC Metals that Include Effects of Non-Glide
Stresses Based on Understanding the Atomic Level Features of
Dislocation Motion**

Vaclav Vitek
University of Pennsylvania
Philadelphia, PA

INTRODUCTION

Yield Criteria for BCC Metals That Include Effects of Non-glide Stresses Based on Understanding the Atomic Level Features of Dislocation Motion

V. Vitek

Department of Materials Science and Engineering,
University of Pennsylvania, Philadelphia

J. L. Bassani

Department of Mechanical Engineering and Applied Mechanics,
University of Pennsylvania, Philadelphia

SUPPORT

NSF, Engineering Division, CMS99-00131
ASCI through Lawrence Livermore National Laboratory

Figure 1

GENERAL FRAMEWORK OF CRYSTAL PLASTICITY

The criterion for the activation of a slip system α is that a yield function reaches a critical value. This function depends, in general, on the whole tensor of the applied stress and crystallography of the material studied.

CRYSTAL PLASTICITY

GENERAL FRAMEWORK

Define a yield function Φ^α for a slip system α which is a function of the applied stress tensor σ^a

A slip system α is activated when the yield function reaches a critical value $\Phi_{\text{critical}}^\alpha$

$$\Phi^\alpha [\sigma^a; \text{crystallography}] = \Phi_{\text{critical}}^\alpha$$

Figure 2

SCHMID'S LAW

This criterion for the activation of a slip system states that the plastic flow commences when the shear stress in a given slip plane in the slip direction reaches a critical value. It is implicitly assumed that the components of the applied stress tensor other than the shear stress in the slip direction have no influence on plastic flow and that the sense of shearing plays no role. This criterion was deduced experimentally in studies of slip in hcp (zinc) and fcc (copper, gold) materials.

SCHMID'S LAW

PLASTIC FLOW WILL COMMENCE WHEN THE RESOLVED SHEAR STRESS ON THE OPERATIVE SLIP SYSTEM REACHES A CRITICAL VALUE

INCLUDES TWO DISTINCT ASSERTIONS

- **The components of the applied stress tensor other than the shear stress in the slip direction have no influence on plastic flow**
- **The critical resolved shear stress does not depend on the sense of shearing**

Figure 3

SCHMID'S LAW AND YIELD FUNCTION

The yield function attains a very simple form when the Schmid's law applies. For a slip system α , corresponding to a slip plane and a slip direction, it is just equal to the shear stress in the slip plane in the slip direction, i.e. to the Schmid stress. The yield criterion is then that the Schmid stress reaches a critical value.

SCHMID BEHAVIOR

The yield function for the slip system α is equal to the Schmid stress for this system, τ^α

When the critical resolved shear stress for the slip system α is $\tau_{\text{critical}}^\alpha$ the yield criterion is

$$\Phi^\alpha = \tau^\alpha = \tau_{\text{critical}}^\alpha$$

Figure 4

SLIP CHARACTERISTICS OF FCC MATERIALS

The most important characteristics of the slip in pure fcc metals, and also pure hcp metals when the slip is along basal planes, are very weak temperature dependence of the flow and yield stress indicating no significant lattice friction Peierls stress. Close packed planes, i.e. $\{111\}$ in fcc and basal in hcp, are the only slip planes and no asymmetries between tension and compression are observed. The Schmid's law applies for this type of gliding and the only important stress component governing the plastic flow in fcc materials is the shear stress in $\{111\}$ planes in $\langle 110 \rangle$ directions. However, deviations from the Schmid's law occur in the case of cross slip.

SCHMID'S LAW APPLIES IN CLOSE PACKED STRUCTURES SUCH AS FCC AND HCP

CHARACTERISTICS OF SLIP IN FCC MATERIALS

- Well defined slip planes $\{111\}$
- Weak dependence of the yield and flow stress on temperature
- No significant lattice friction, i. e. Peierls stress
- The same behavior in tension and compression

Figure 5

SLIP CHARACTERISTICS OF BCC MATERIALS

The most important characteristics of the slip in pure bcc metals are the very strong temperature dependence of the flow and yield stress indicating large lattice friction Peierls stress, complex slip geometry, pronounced asymmetry between tension and compression. The Schmid's law does not apply. For reviews see [1-3].

1. Christian, J. W., *Metall. Trans. A* Vol. 14, 1983, p.1237.
2. Vitek, V., *Dislocations and Properties of Real Materials*, edited by Lorretto, M., (London: The Institute of Metals) 1985, p. 30.
3. Duesbery, M. S., *Dislocations in Solids*, edited by Nabarro, F. R. N., (Amsterdam: North Holland) Vol. 8, 1989, p. 67

CHARACTERISTICS OF SLIP IN BODY-CENTERED CUBIC METALS

- **Strong temperature and strain rate dependence of the flow stress and slip geometry**
As $T \rightarrow 0K$ the flow stress $\sim 10^{-2}G$
- **Strong and unusual orientation dependencies and asymmetries of the flow stress and slip geometry**
- **Slip planes are not always well defined**
- **SCHMID'S LAW IS NOT VALID**

Figure 6

OTHER MATERIALS WITH ANALOGOUS SLIP PROPERTIES

Materials with bcc structure are no exception. The Schmid law is not valid and strong temperature and orientation dependencies of the yield stress are observed in many intermetallic compounds and non-cubic structures. Rather, fcc materials and hcp gliding on basal planes are a special case when Schmid's law applies. An example is the molybdenum di-silicide (MoSi_2). In this material dislocation glide occurs on several slip systems. The most important is $\{013\}\langle 331\rangle$ which displays large asymmetry, in particular for the orientation of the compression axis close to $[001]$.

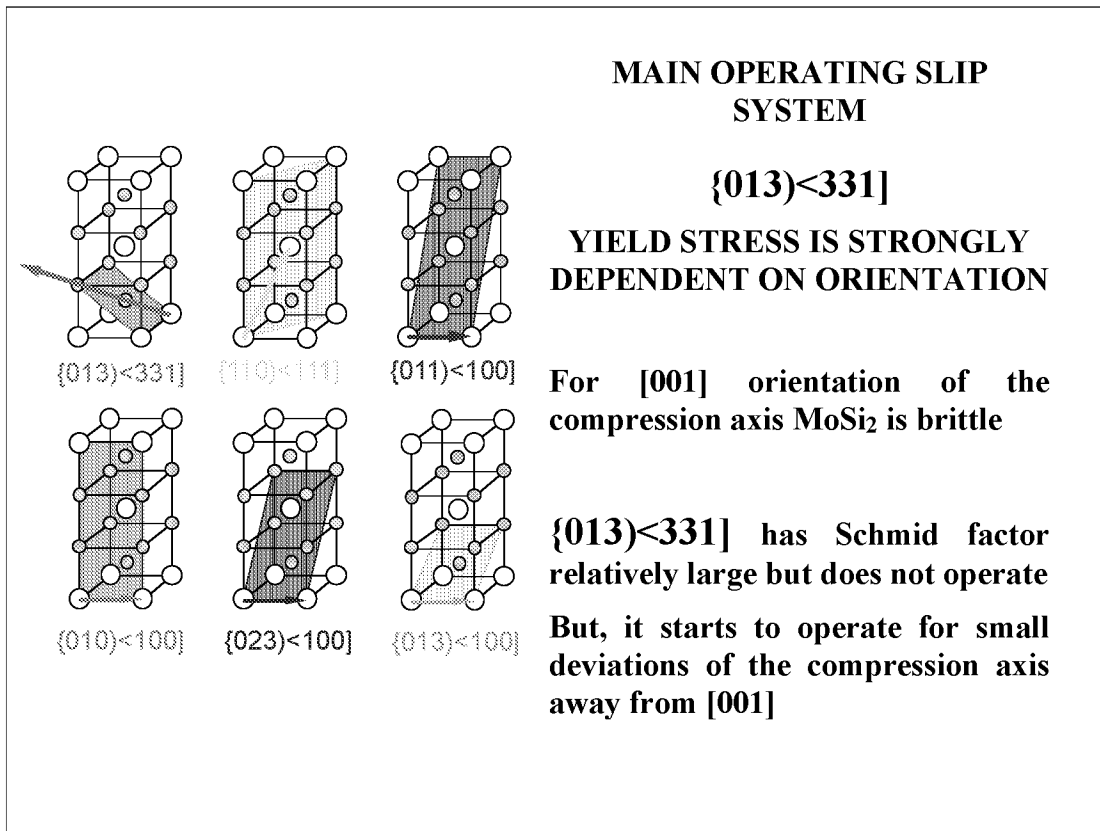


Figure 7

SIGNIFICANT CONSEQUENCES OF THE BREAK DOWN OF THE SCHMID'S LAW FOR THE PLASTIC BEHAVIOR

When the Schmid law does not apply the plastic deformation displays asymmetries that are most frequently characterized by different behavior in tension and compression. Such unique stress-state dependence of flow properties arising when Schmid's law does not apply can significantly affect critical phenomena such as strain localization, evolution of the texture of grains, and failure mechanisms at mesoscopic and macroscopic length scales.

CONSEQUENCE OF NON-SCHMID BEHAVIOR

- **Tension-compression asymmetry in single and polycrystals**
- **Elevation of stresses due to restriction of slip in polycrystals**
- **Strain localization - formation of shear bands**
- **Affects evolution of textures and failure mechanisms**

Figure 8

NON-PLANAR DISLOCATION CORES

The most common reason for the very high Peierls stress and associated asymmetries of dislocation motion that lead to the break down of the Schmid law are dislocation cores spread into several non-parallel planes. Schematic picture of such dislocation cores is shown below. In bcc metals the screw dislocations possess such cores.

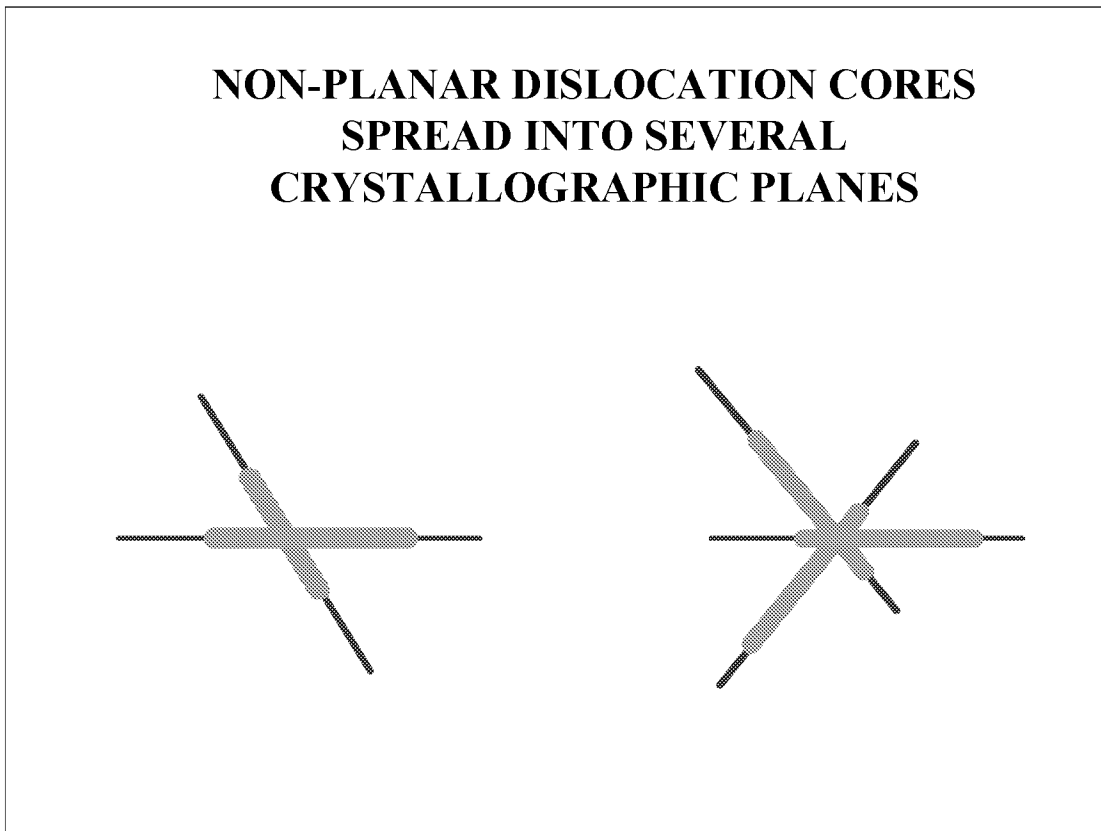


Figure 9

SCREW DISLOCATIONS IN BCC METALS

It is now generally accepted that in bcc metals screw dislocations control their characteristic plastic properties, in particular temperature and orientation dependencies of the yield stress as well as their slip geometry [1-3].

1. Christian, J. W., *Metall. Trans. A* Vol. 14, 1983, p.1237.
2. Vitek, V., *Dislocations and Properties of Real Materials*, edited by Lorretto, M., (London: The Institute of Metals) 1985, p. 30.
3. Duesbery, M. S., *Dislocations in Solids*, edited by Nabarro, F. R. N., (Amsterdam: North Holland) Vol. 8, 1989, p. 67

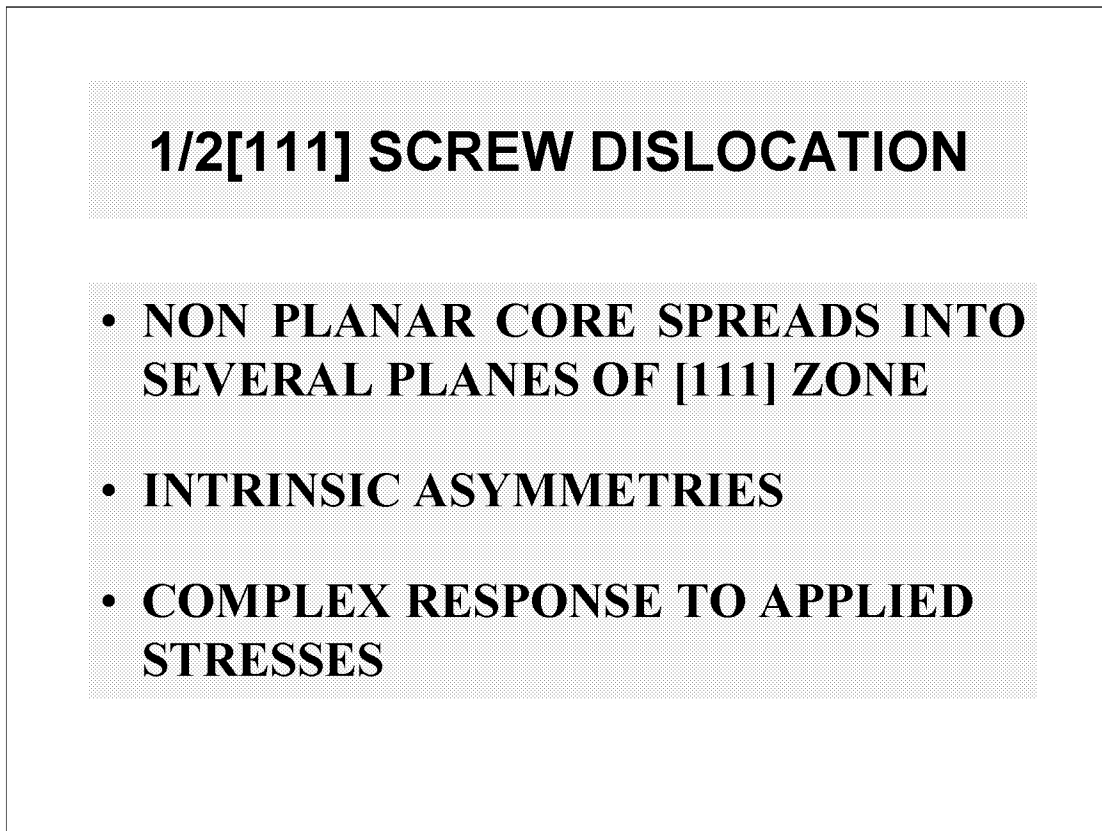


Figure 10

ATOMISTIC COMPUTER MODELING OF SCREW DISLOCATION IN TRANSITION BCC METALS

Computer simulation of the dislocation core was done using a molecular statics method and central-force many-body potentials for Mo and Ta. The core structure is represented using the method of differential displacements. The atomic arrangement is shown in the projection perpendicular to the direction of the dislocation line ($[111]$) and circles represent atoms within one period without distinguishing their positions in three successive (111) planes. The relative displacement of the neighboring atoms produced by the dislocation in the $[111]$ direction is depicted as an arrow between them. In the case of Mo the core spreads in a three-fold manner into the three $\{110\}$ planes while in the case of Ta it spreads in a six-fold manner into the same planes [1,2].

1. Duesbery, M. S. and Vitek, V., *Acta Mater.* Vol. 46, 1998, p. 1481.
2. Ito, K. and Vitek, V., *Philos. Mag.* Vol. 81, 2001, p. 1387.

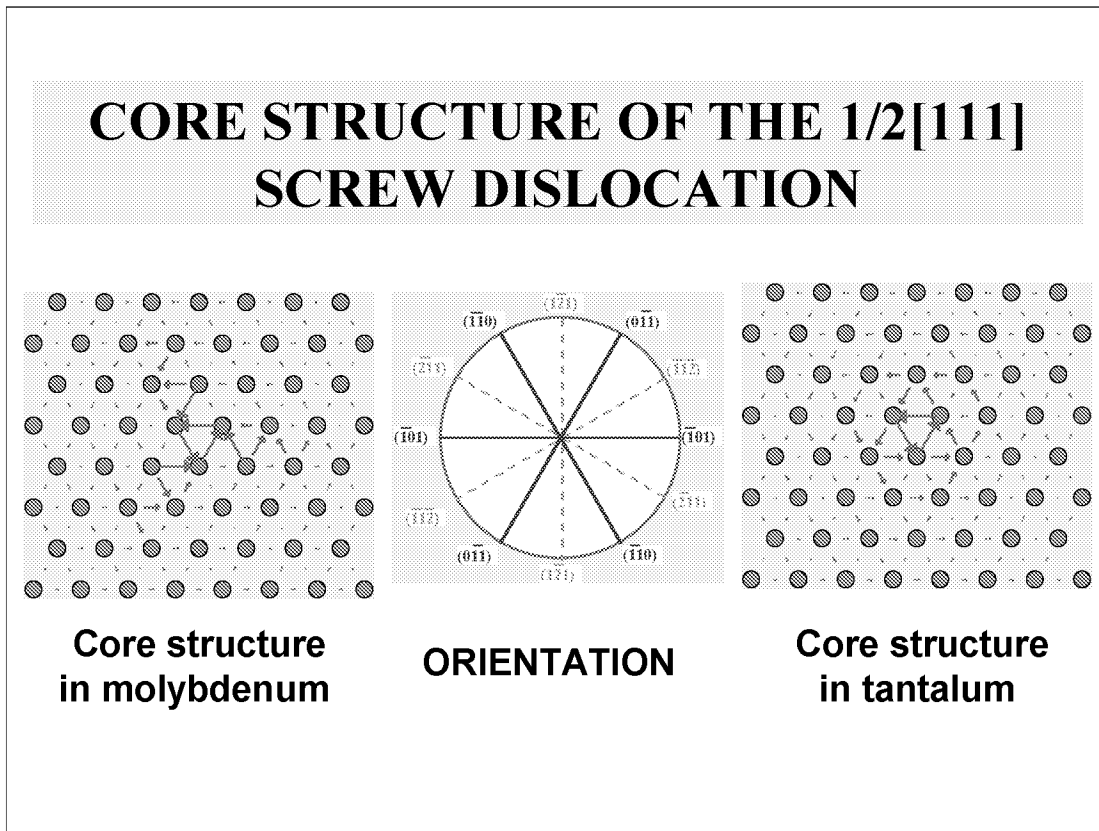


Figure 11

TRANSFORMATION OF THE CORE PRIOR TO THE DISLOCATION MOTION

The most important aspect of non-planar dislocation cores is that their structure transforms under the influence of applied stresses prior to the dislocation motion. An example presented here shows changes in the core of the $1/2[111]$ screw dislocation under the effect of pure shear in the $[111]$ direction in the plane.

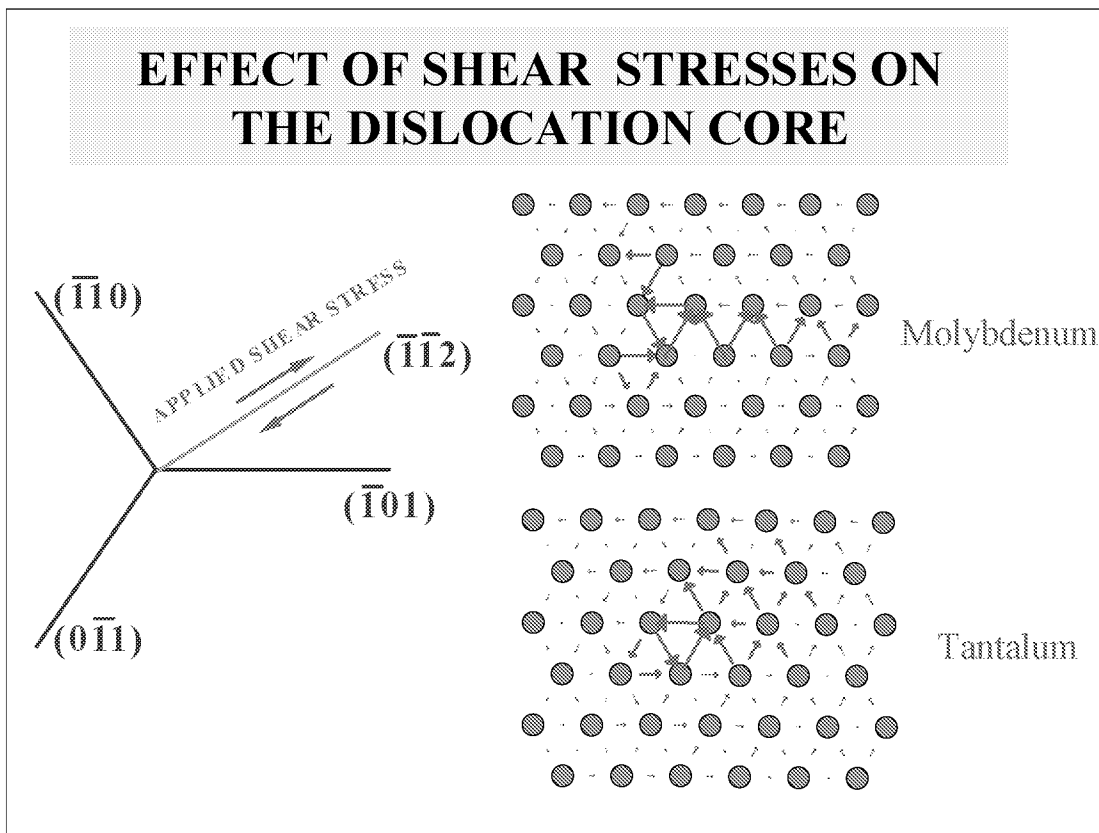


Figure 12

DEPENDENCE OF THE CRITICAL RESOLVED SHEAR STRESS (CRSS) ON THE ORIENTATION OF THE PLANE OF THE MAXIMUM RESOLVED SHEAR STRESS (MRSSP)

The calculated dependence of the CRSS on the orientation of the MRSSP in molybdenum shows the break down of the Schmid's law and asymmetric behavior of this dependence.

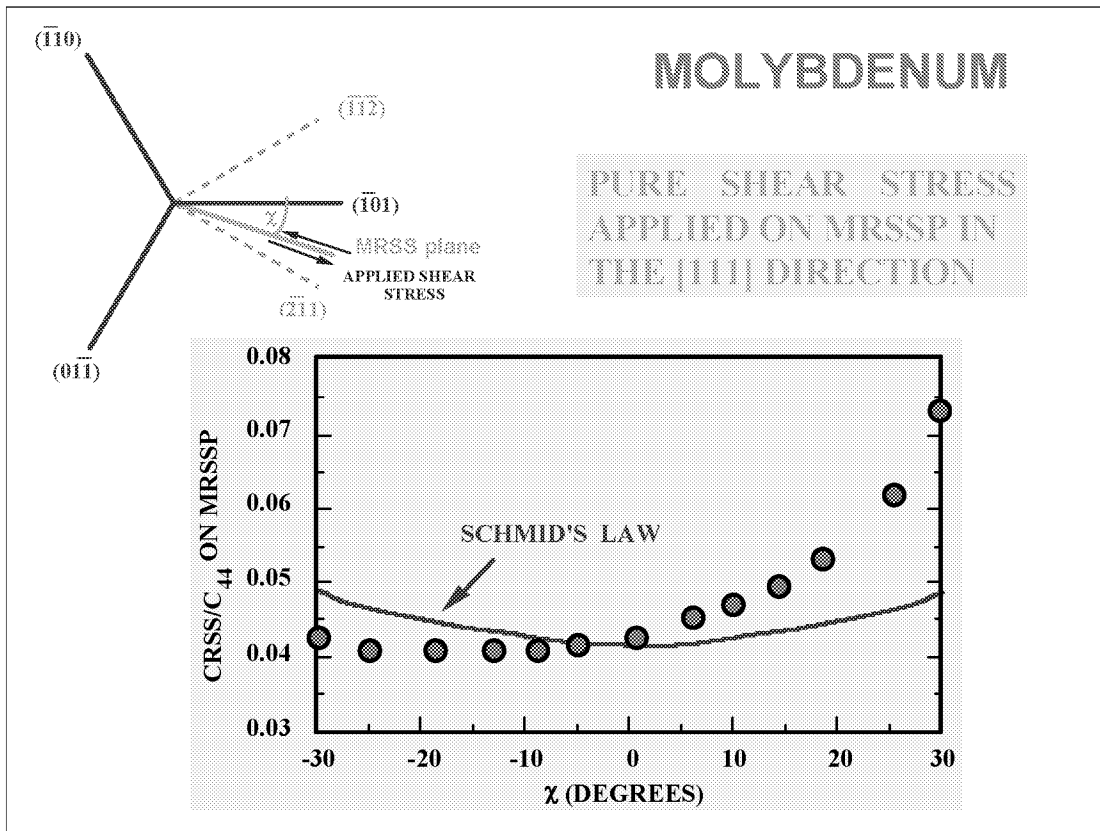


Figure 13

TENSILE AND COMPRESSIVE LOADING

Atomistic modeling of the dislocation motion was performed for a number of different tensile and compressive axes marked in the standard triangle. The three groups of the tensile and compressive axes correspond to three different maximum resolved shear stress planes.

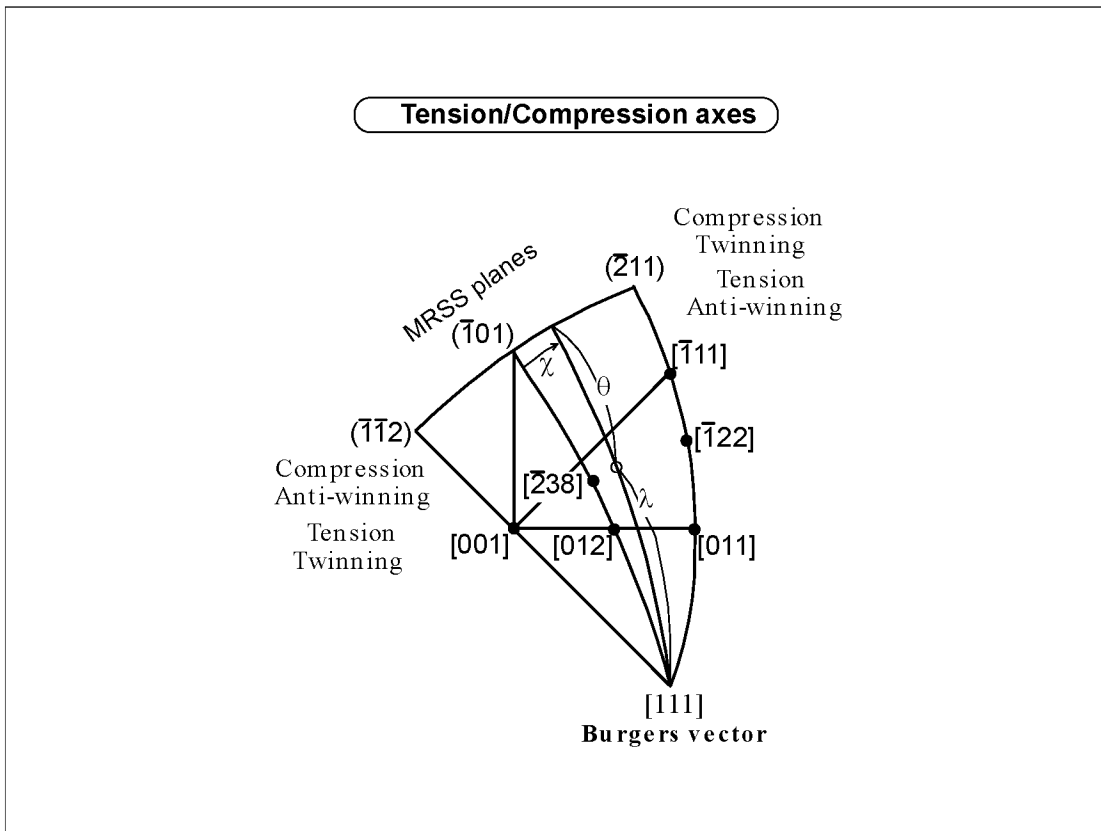


Figure 14

MOLYBDENUM TENSION AND COMPRESSION

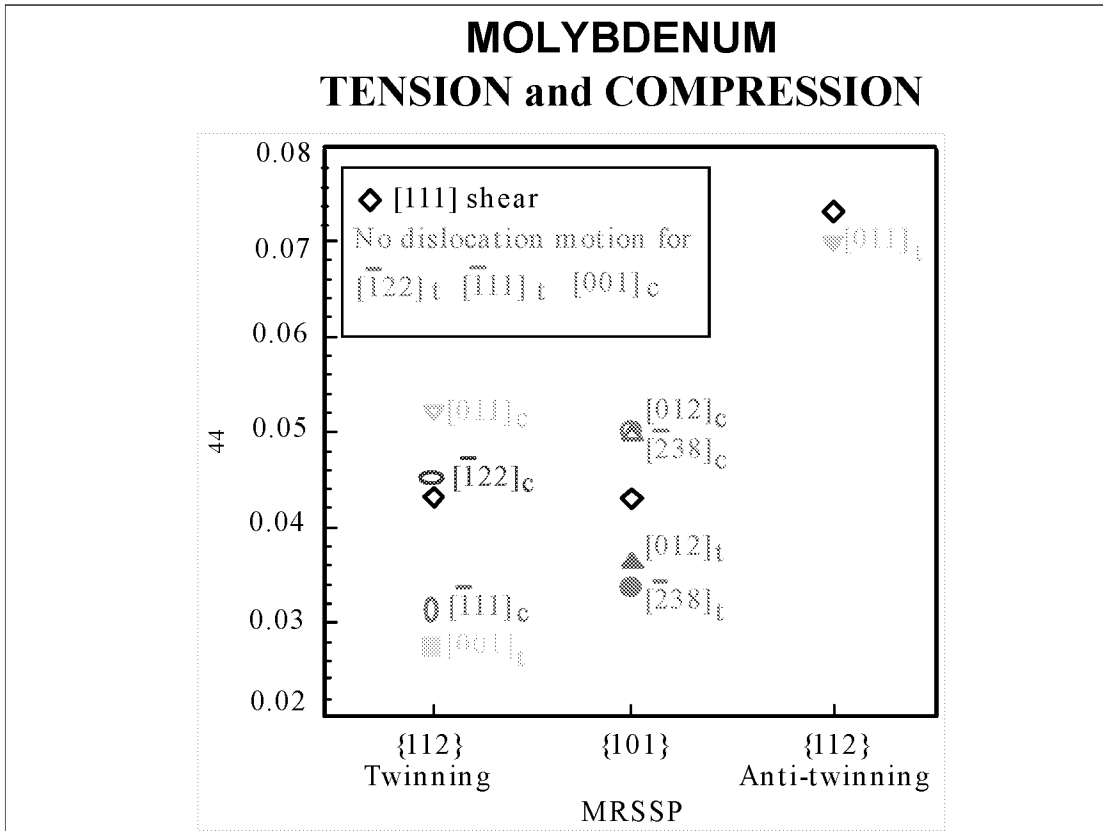


Figure 15

EFFECT OF THE SHEAR STRESS PERPENDICULAR TO THE BURGERS VECTOR ON CRSS

The stress component affecting the glide in the case of tensile/compressive loading was identified as the shear stress perpendicular to the Burgers vector, i.e. the stress that does not exert the Peach-Koehler force on the dislocation. Computer modeling combining this shear stress with the glide shear stress parallel to the Burgers vector demonstrates the dependence of the CRSS on this non- glide shear stress and shows that tensile/compressive data fit into this dependence.

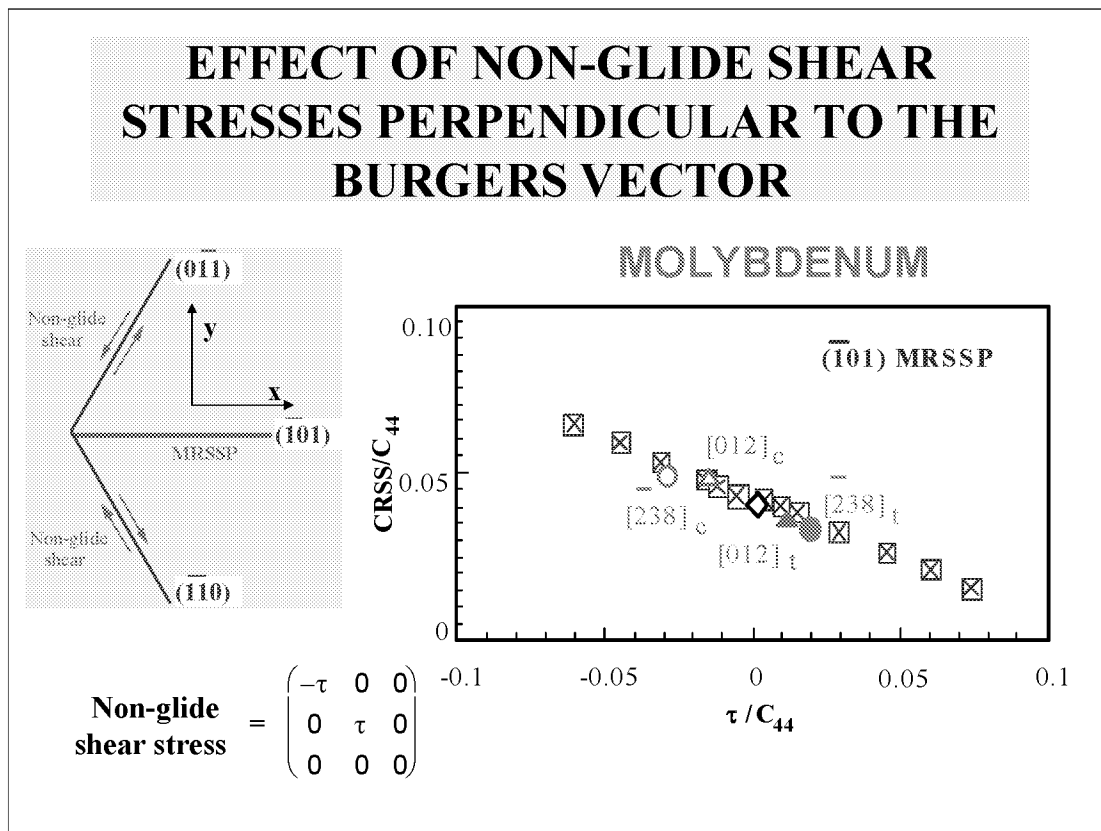


Figure 16

EFFECT OF THE SHEAR STRESS PERPENDICULAR TO THE BURGERS VECTOR ON THE DISLOCATION CORE

The reason why the non-glide shear stress perpendicular to the Burgers vector affects significantly the CRSS is that it induces changes in the dislocation core that may either help or hinder the eventual glide, depending on the orientation of the non-glide stress.

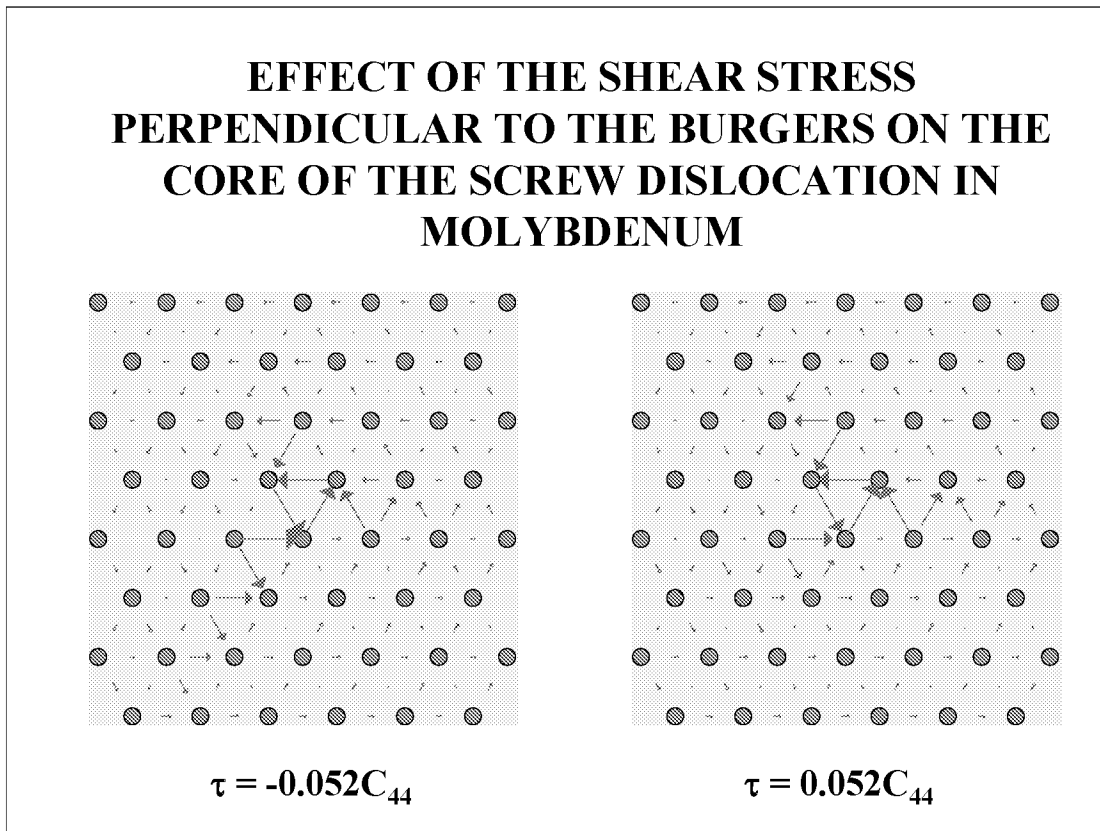


Figure 17

MOST IMPORTANT PHYSICAL FINDING BASED ON THE ATOMISTIC MODELING OF THE CORE OF THE SCREW DISLOCATION

The glide of the dislocation is affected and governed by shear stresses both parallel and perpendicular to the Burgers vector that act in the $\{110\}$ planes of the $[111]$ zone.

PHYSICAL CONCLUSION

THE YIELD FUNCTION DEPENDS ON

- **SHEAR STRESSES PARALLEL TO THE BURGERS VECTOR ACTING IN THREE $\{110\}$ PLANES OF THE $[111]$ ZONE**
- **SHEAR STRESSES PERPENDICULAR TO THE BURGERS VECTOR ACTING IN THREE $\{110\}$ PLANES OF THE $[111]$ ZONE**
- **BOTH THESE DEPENDENCIES HAVE BEEN DETERMINED BY ATOMISTIC MODELING OF THE DISLOCATION MOTION**

Figure 18

COMBINING THE RESULTS OF ATOMISTIC STUDIES WITH CONTINUUM CRYSTAL PLASTICITY

Based on the findings of atomistic modeling of the glide of $1/2\langle 111 \rangle$ dislocations in Mo and Ta the yield function depends on shear stresses in the $\{110\}$ planes both parallel and perpendicular to the Burgers vector. A feasible approximation is that the yield function is a linear combination of the Schmid stress and non-glide stresses. The corresponding coefficients need to be determined so as to reproduce the results of atomistic modeling [1-3].

1. Qin, Q. and Bassani, J. L., *J. Mech. Phys. Sol.* Vol. 40, 1992, p. 813, 835.
2. Bassani, J. L., *Adv. Appl. Mech.* Vol. 30, 1994, p. 191.
3. Bassani, J. L, Ito, K. and Vitek, V., *Mat. Sci. Eng. A* Vol. 319, 2001, p. 97.

YIELD FUNCTIONS WITH NON-GLIDE STRESSES

Schmid stress on slip system α : $\tau^\alpha = \mathbf{n}^\alpha \bullet \boldsymbol{\sigma} \bullet \mathbf{m}^\alpha$

slip plane normal
stress tensor
slip direction

Non-glide stress components: $\tau_\eta^\alpha = \mathbf{n}_\eta^\alpha \bullet \boldsymbol{\sigma} \bullet \mathbf{m}_\eta^\alpha$

\mathbf{n}_η^α and \mathbf{m}_η^α are crystallographic vectors that resolve each of the ($\eta = 1, n_{ng}$) non-glide stress components

YIELD FUNCTION for slip system α $\Phi^\alpha = \tau^\alpha + \sum_{\eta=1}^{n_{ng}} a_\eta^\alpha \tau_\eta^\alpha$

non-glide stress yield parameters

Figure 19

YIELD FUNCTION FOR APPLICATION OF PURE SHEAR STRESSES PARALLEL TO THE BURGERS VECTOR

When a shear stress parallel to the Burgers vector is applied in a MRSSP making angle χ with the slip plane we can choose the shear stress in any other plane of the [111] zone as the non-glide stress entering the yield function.

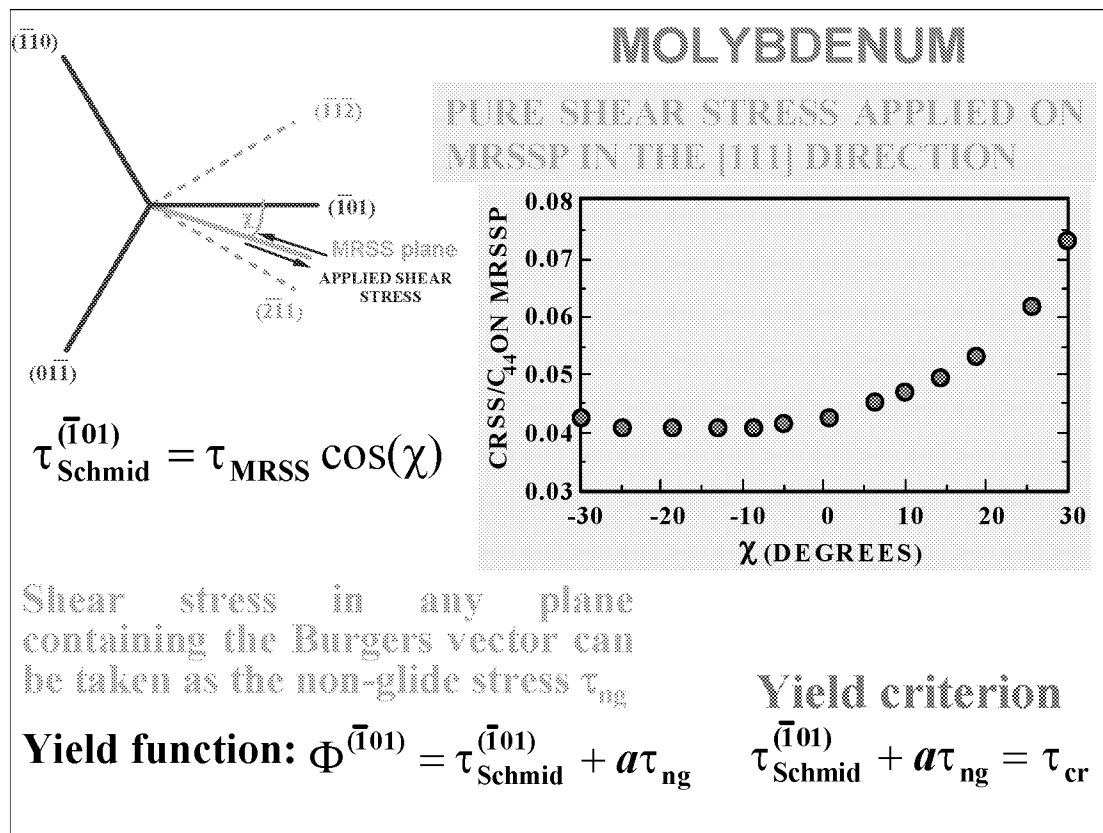


Figure 20

**YIELD FUNCTION FOR APPLICATION OF THE PURE SHEAR STRESS
PARALLEL TO THE BURGERS VECTOR**

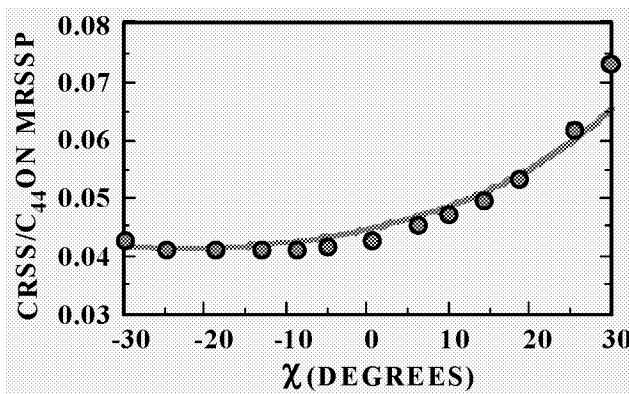
The atomistic studies suggest to choose the non-glide shear stress entering the yield function the shear stress in one of the two $\{110\}$ planes that are not the slip planes. Here we choose the shear stress in the plane.

Choosing the non-glide stress as the shear stress in the $(\bar{1}10)$ plane

$$\tau_{\text{ng}}^{(\bar{1}10)} = \tau_{\text{MRSS}} \cos(\chi + 60) \quad \text{and the yield criterion reads}$$

$$\tau_{\text{Schmid}}^{(\bar{1}01)} + a\tau_{\text{ng}}^{(\bar{1}10)} = \tau_{\text{MRSS}} [\cos(\chi) + a\cos(\chi + 60)] = \tau_{\text{cr}}$$

$$\text{CRSS} = \tau_{\text{cr}} [\cos(\chi) + a\cos(\chi + 60)]^{-1}$$



τ_{cr} and a fitted to results of atomistic calculations

$$\tau_{\text{cr}} = 0.0586C_{44}$$

$$a = 0.641$$

Figure 21

GLIDE ON ALL POSSIBLE SLIP SYSTEM IN A BCC CRYSTAL

There are twenty four $\langle 111 \rangle \{110\}$ slip systems (considering positive and negative slip directions as different). Each of these slip systems follows the same yield criterion but they all may operate at the same time.

<111> {110} Slip Systems for BCC Crystals

Slip System α	Slip Direction \mathbf{m}^α	Slip Plane \mathbf{n}^α	Non-Glide Stress Plane \mathbf{n}_1^α	Slip System α	Slip Direction \mathbf{m}^α	Slip Plane \mathbf{n}^α	Non-Glide Stress Plane \mathbf{n}_1^α
1	111	0 $\bar{1}$ 1	$\bar{1}$ 01	13	$\bar{1}\bar{1}\bar{1}$	0 $\bar{1}$ 1	$\bar{1}$ 10
2	111	$\bar{1}$ 01	0 $\bar{1}$ 1	14	$\bar{1}\bar{1}\bar{1}$	$\bar{1}$ 01	$\bar{1}$ 10
3	111	$\bar{1}$ 10	0 $\bar{1}$ 1	15	$\bar{1}\bar{1}\bar{1}$	$\bar{1}$ 10	10 $\bar{1}$
4	$\bar{1}$ 11	0 $\bar{1}$ 1	101	16	1 $\bar{1}\bar{1}$	0 $\bar{1}$ 1	$\bar{1}\bar{1}$ 0
5	$\bar{1}$ 11	101	0 $\bar{1}$ 1	17	1 $\bar{1}\bar{1}$	101	$\bar{1}\bar{1}$ 0
6	$\bar{1}$ 11	110	0 $\bar{1}$ 1	18	1 $\bar{1}\bar{1}$	110	101
7	$\bar{1}\bar{1}$ 1	101	011	19	11 $\bar{1}$	101	1 $\bar{1}$ 0
8	$\bar{1}\bar{1}$ 1	011	101	20	11 $\bar{1}$	011	1 $\bar{1}$ 0
9	$\bar{1}\bar{1}$ 1	$\bar{1}$ 10	101	21	11 $\bar{1}$	$\bar{1}$ 10	011
10	1 $\bar{1}\bar{1}$	$\bar{1}$ 01	011	22	$\bar{1}\bar{1}\bar{1}$	$\bar{1}$ 01	110
11	1 $\bar{1}\bar{1}$	011	$\bar{1}$ 01	23	$\bar{1}\bar{1}\bar{1}$	011	110
12	1 $\bar{1}\bar{1}$	110	$\bar{1}$ 01	24	$\bar{1}\bar{1}\bar{1}$	110	0 $\bar{1}\bar{1}$

Schmid stress: $\tau^\alpha = \mathbf{m}^\alpha \cdot \boldsymbol{\sigma} \cdot \mathbf{n}^\alpha$ Non-glide stress: $\tau_1^\alpha = \mathbf{m}^\alpha \cdot \boldsymbol{\sigma} \cdot \mathbf{n}_1^\alpha$

Effective flow stress: $\tau^{*\alpha} = \tau^\alpha + a \tau_1^\alpha$

Figure 22

TAYLOR MODEL WITH NON-GLIDE STRESSES

For the polycrystal made of randomly oriented grains of bcc Mo we assume that the strain in each crystal is the same as the macroscopic strain (Taylor hypothesis). At the same time each grain satisfies the yield criterion involving the non-glide stresses. The Taylor factor demonstrates the tension-compression asymmetry in this polycrystal induced by the effect of non-glide stresses.

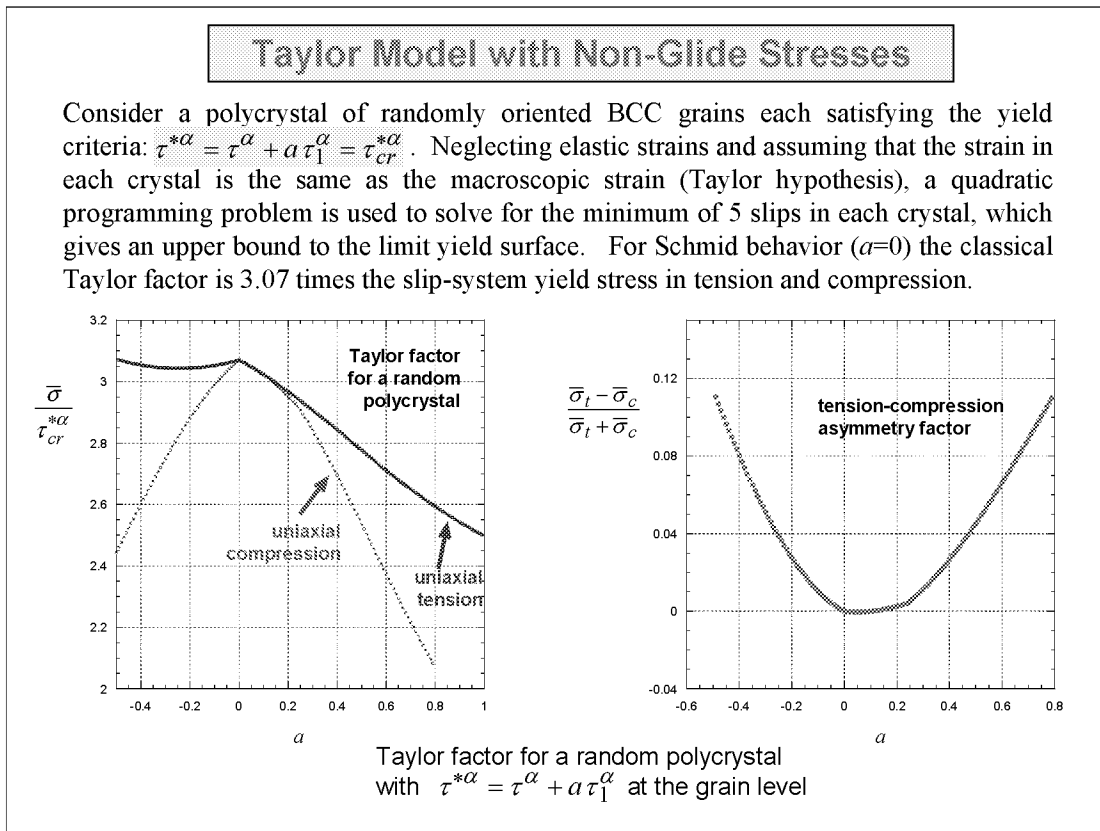


Figure 23

EFFECT OF NON-GLIDE STRESSES ON THE YIELD SURFACE AND HARDENING

The calculated yield surface and stress-strain curves demonstrate asymmetries induced by the effect of non-glide stresses and thus the effect of non-Schmid behavior that occurs on the macroscopic scale owing due to the atomic level properties of dislocations in bcc metals.

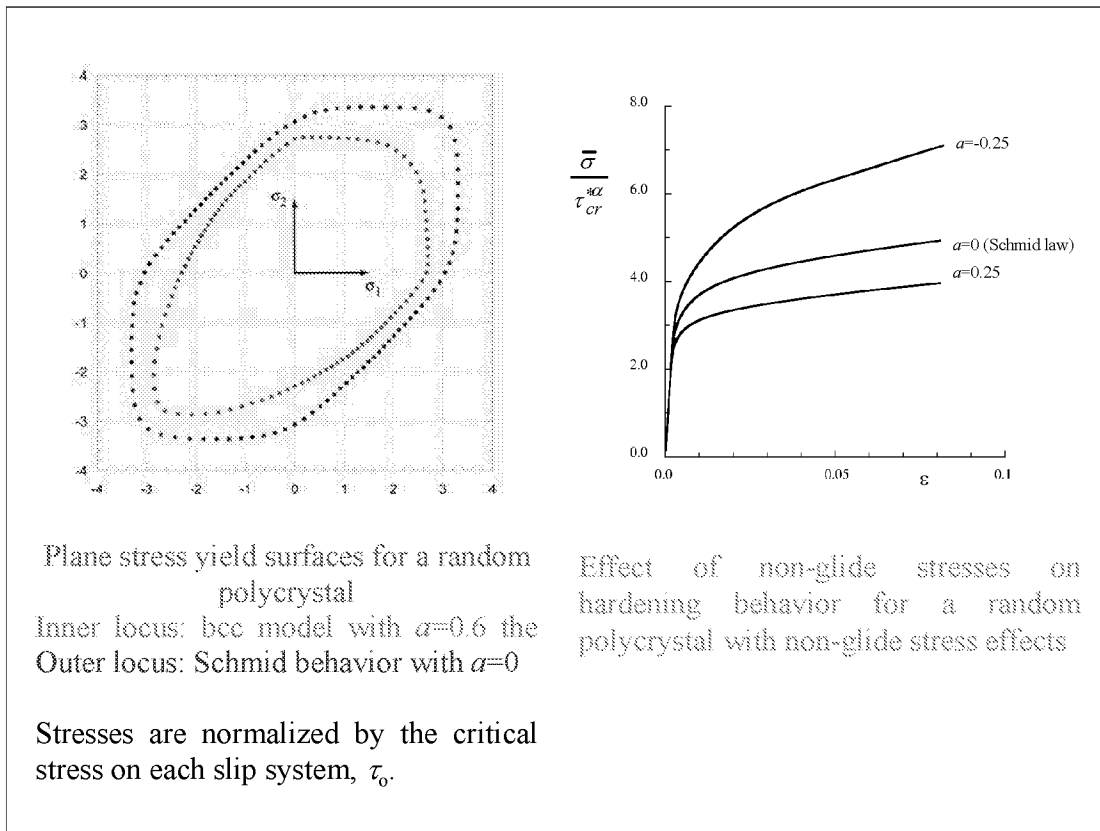


Figure 24

CONCLUSIONS

Atomistic modeling of dislocation cores and their response to applied stresses determine for a given slip system:

- (i) Those components of the stress tensor that drive and affect the dislocation motion.
- (ii) Relative importance of different stress components in determination of the yield stress.

The yield function for crystal plasticity is defined based on these results of atomistic calculations.

This yield function is then employed in studies of plastic yielding in both single and polycrystals.

Atomic level behavior of dislocations percolates into the mesoscopic and macroscopic plastic behavior.

CONCLUSIONS

Atomistic modeling of dislocation cores and their response to applied stresses determine for a given slip system:

- (i) Those components of the stress tensor that drive and affect the dislocation motion**
- (ii) Relative importance of different stress components in determination of the yield stress**

The yield function for crystal plasticity is defined based on these results of atomistic calculations

This yield function is then employed in studies of plastic yielding in both single and polycrystals

ATOMIC LEVEL BEHAVIOR OF DISLOCATIONS PERCOLATES INTO THE MESOSCOPIC AND MACROSCOPIC PLASTIC BEHAVIOR

Figure 25

FUTURE DEVELOPMENT

Quantum mechanics based description of atomic interactions in transition metals and alloys reflecting mixed metallic and covalent bonding.

Present development: Bond-order potentials.

Temperature and strain rate dependence of the yield stress based on mesoscopic models that incorporate the results of atomistic studies via the dependence of the activation enthalpy on the relevant components of the stress tensor.

Incorporation of temperature and strain rate effects together with hardening into yield criteria that will be used continuum studies, for example finite elements calculations, of deformation under complex applied stresses.

FUTURE DEVELOPMENT

Quantum mechanics based description of atomic interactions in transition metals and alloys reflecting mixed metallic and covalent bonding

Present development: Bond-order potentials

Temperature and strain rate dependence of the yield stress based on mesoscopic models that incorporate the results of atomistic studies via the dependence of the activation enthalpy on the relevant components of the stress tensor

Incorporation of temperature and strain rate effects together with hardening into yield criteria that will be used continuum studies, for example finite elements calculations, of deformation under complex applied stresses

Figure 26

**Multiscale Modeling of Crystalline Metals
with Experimental Verification**

Sia Nemat-Nasser
University of California at San Diego
San Diego, CA


UC San Diego
University of California, San Diego
*Center of Excellence for
Advanced Materials*

**Multiscale Modeling of Crystalline Metals
with Experimental Verification**

Sia Nemat-Nasser

Multiscale Modeling, Simulation & Visualization
NASA Langley Research Center
Hampton, Virginia
March 5-6, 2002

CEAM/UCSD

Figure 1

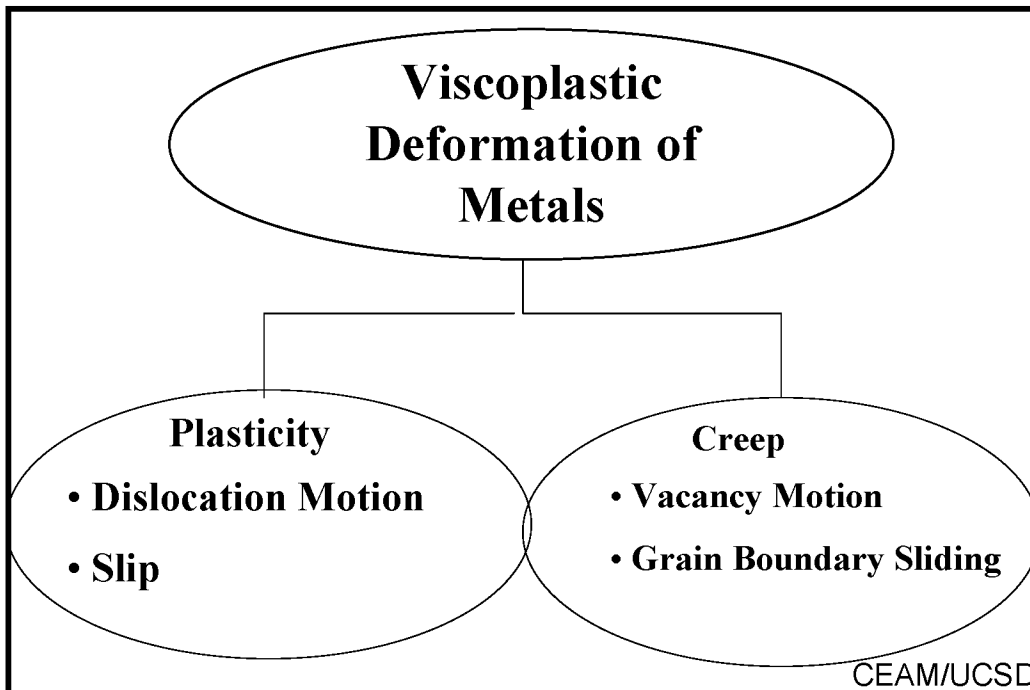


Figure 2

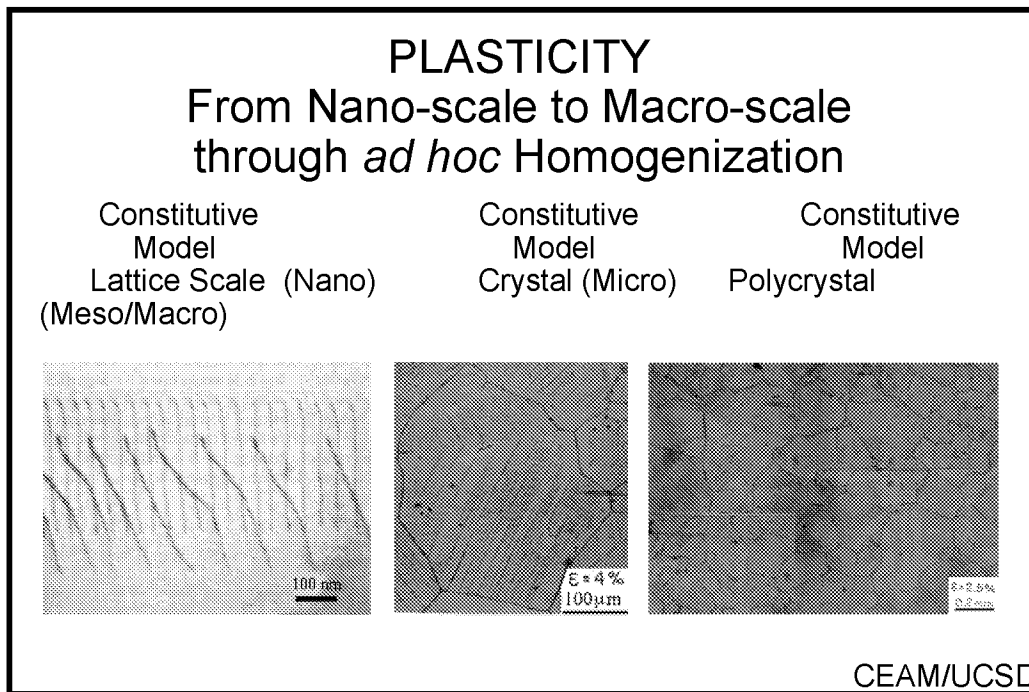


Figure 3

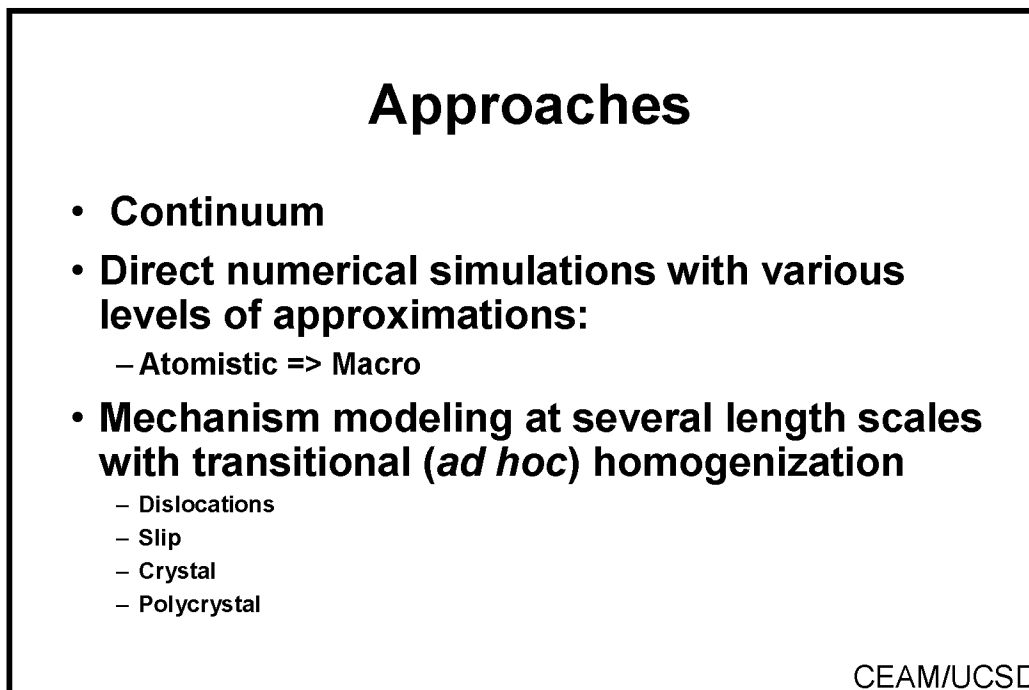


Figure 4

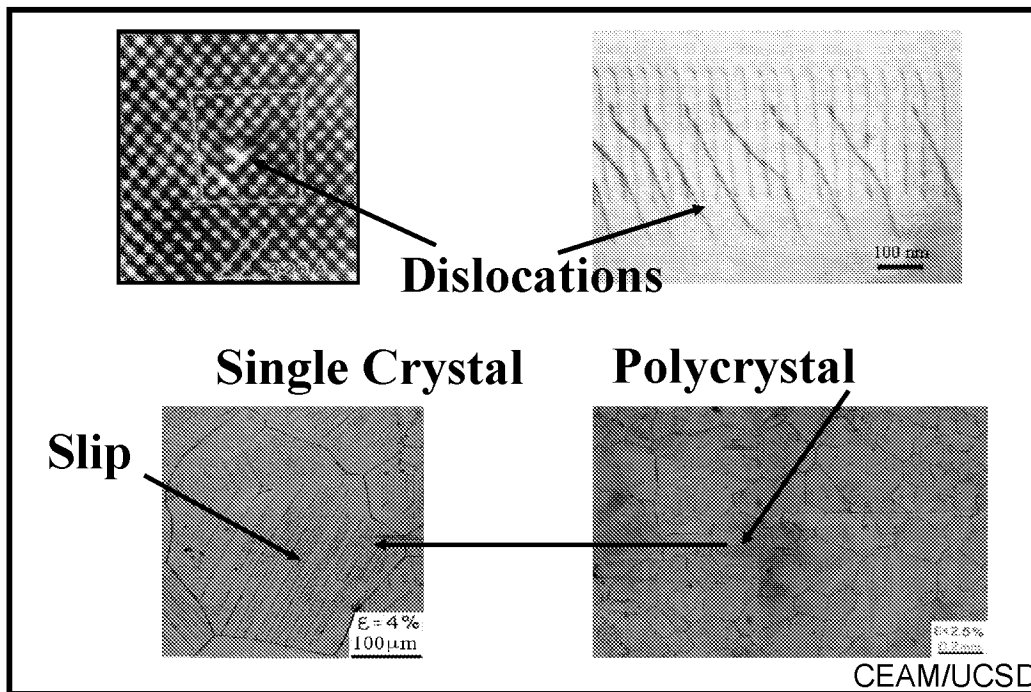


Figure 5

Length-scale as Internal-state Variable

- **Strain gradient exists at all scales:**
 - around dislocation lines
 - near slip planes
 - within each crystal
 - over many crystals
 - at continuum scale around geometric & material discontinuities
- **Strain fields are obtained by solving initial-boundary-value problems at relevant length scale**
- **Constitutive relations must reflect essential structural characteristics at relevant length scales**
- **Dislocation density *provides* a natural length scale in continuum plasticity**
 - $(\text{average dislocation density})^{-1/2} = \text{length scale}$

CEAM/UCSD

Figure 6

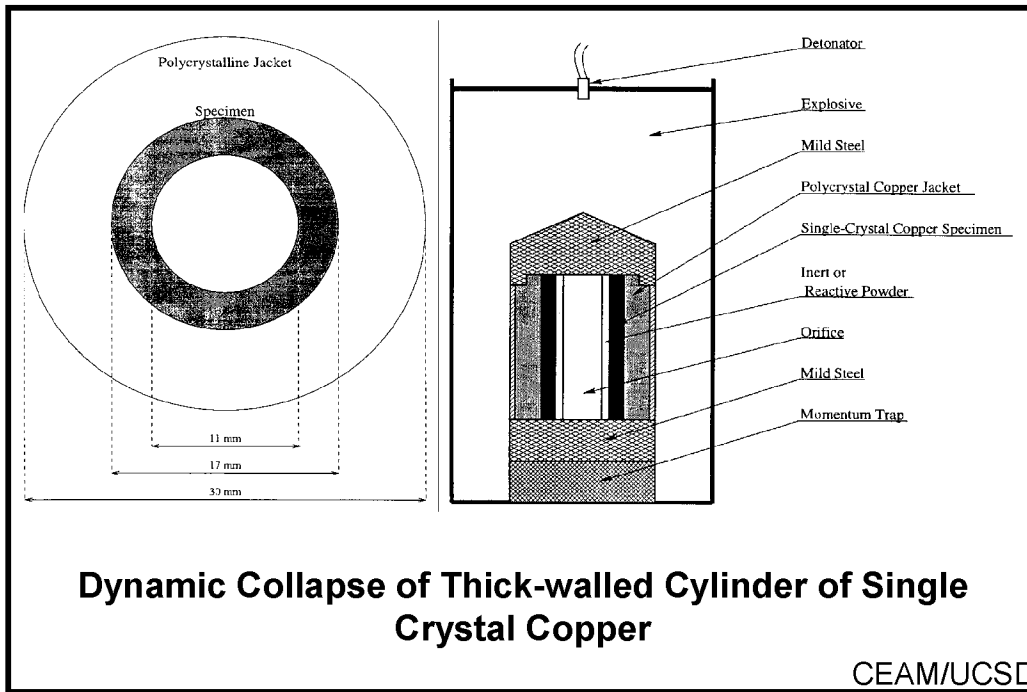


Figure 7

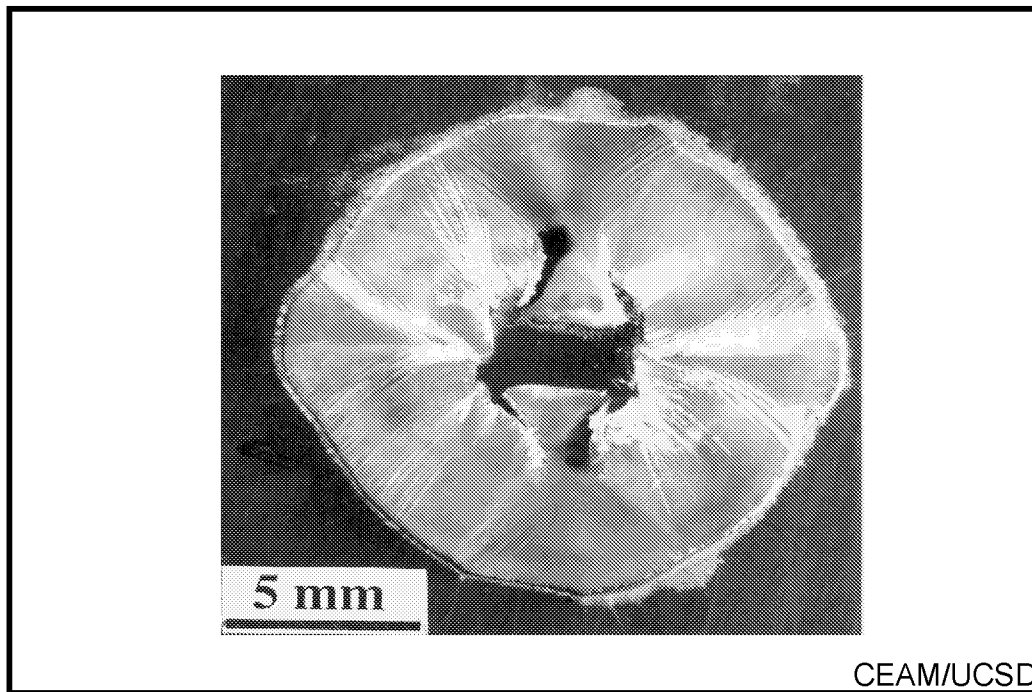


Figure 8

Figure 10

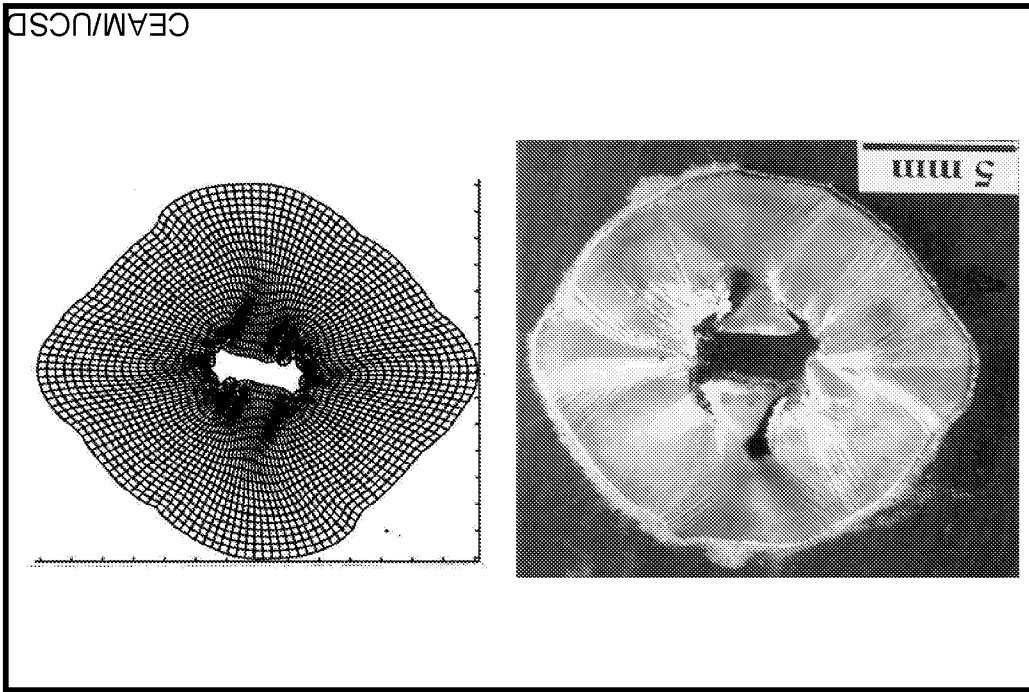
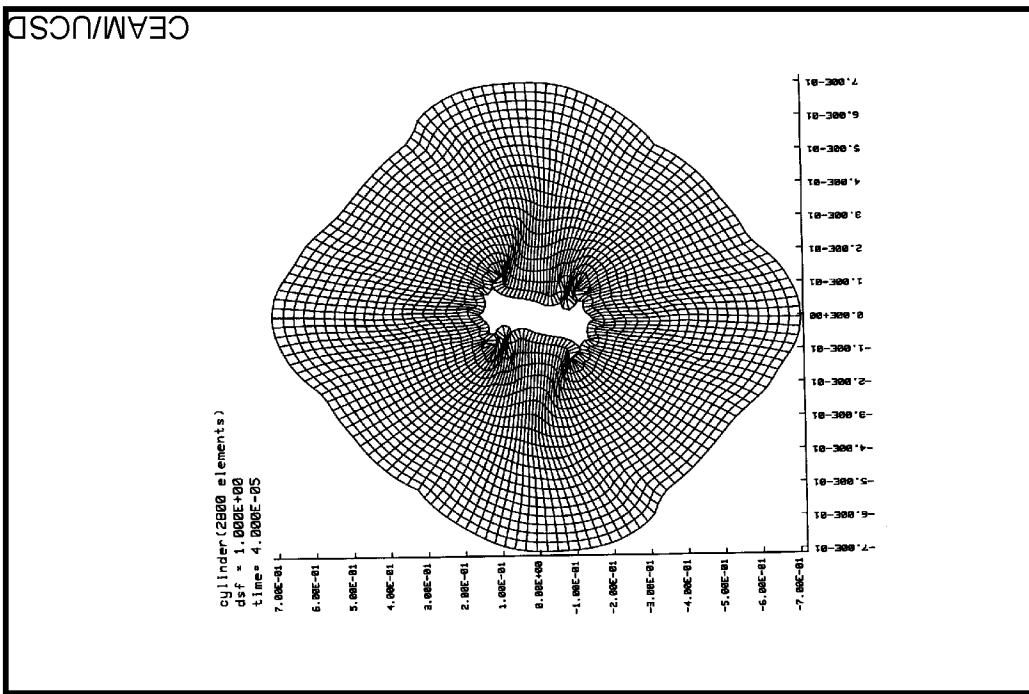


Figure 9



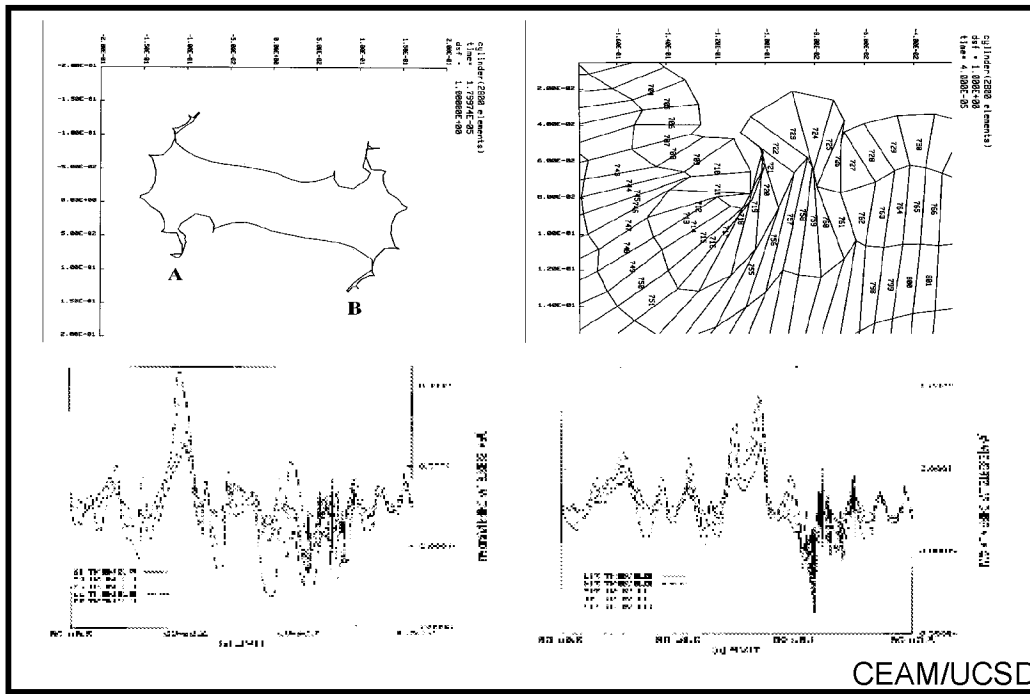


Figure 11

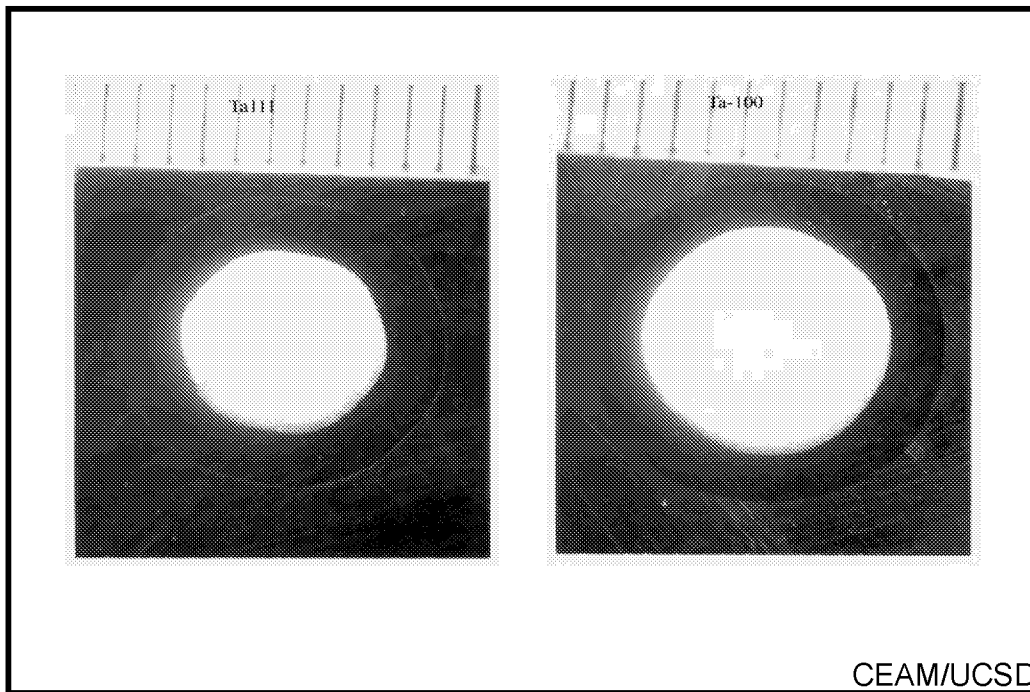


Figure 12

WHAT IS NEEDED IN THE SCIENCE OF DEFORMATION MODELING

- **Experimental Techniques & Tools**
- **Nano/Microstructure-Properties Relations: Mechanisms Identification**
- **Physics-based Nano- Micro- & Macro-mechanical Modeling**

CEAM/UCSD

Figure 13

Experimental Tools

- **Recovery Hopkinson Technique**
 - * **Compression Tests**
 - * **Tension Tests**
 - * **Compression-Tension Tests**
 - * **Tension-Compression Tests**
- **Isothermal and Adiabatic Tests**
 - * **Strain Rate to 50,000/s**
 - * **Temperature Range -200 to 1500 C**
- **Tri-axial Hopkinson Techniques**

CEAM/UCSD

Figure 14

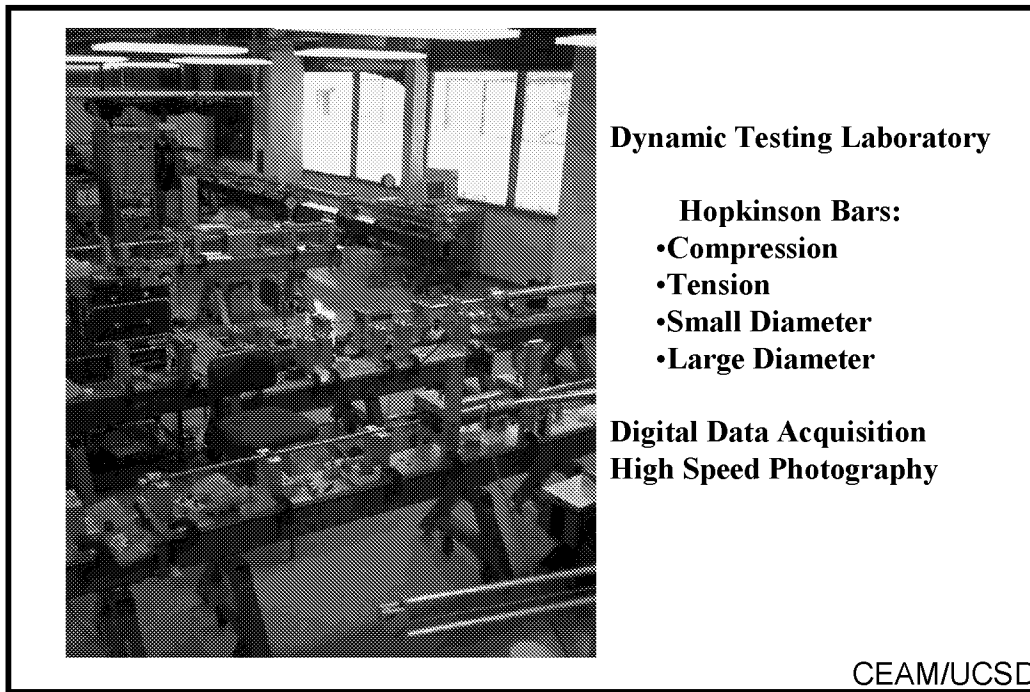


Figure 15

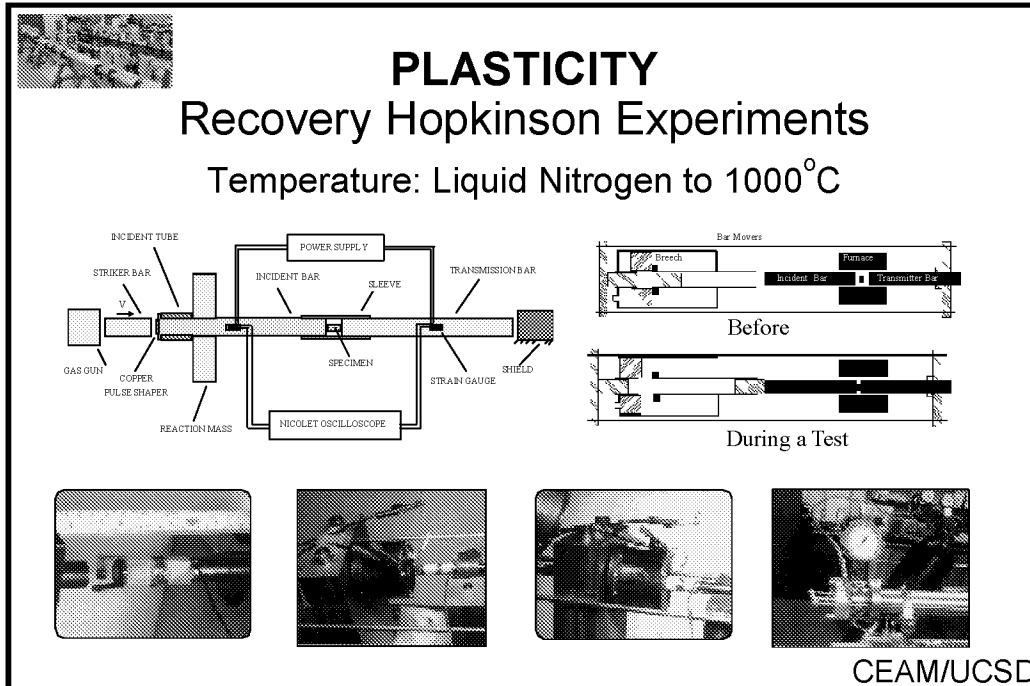


Figure 16

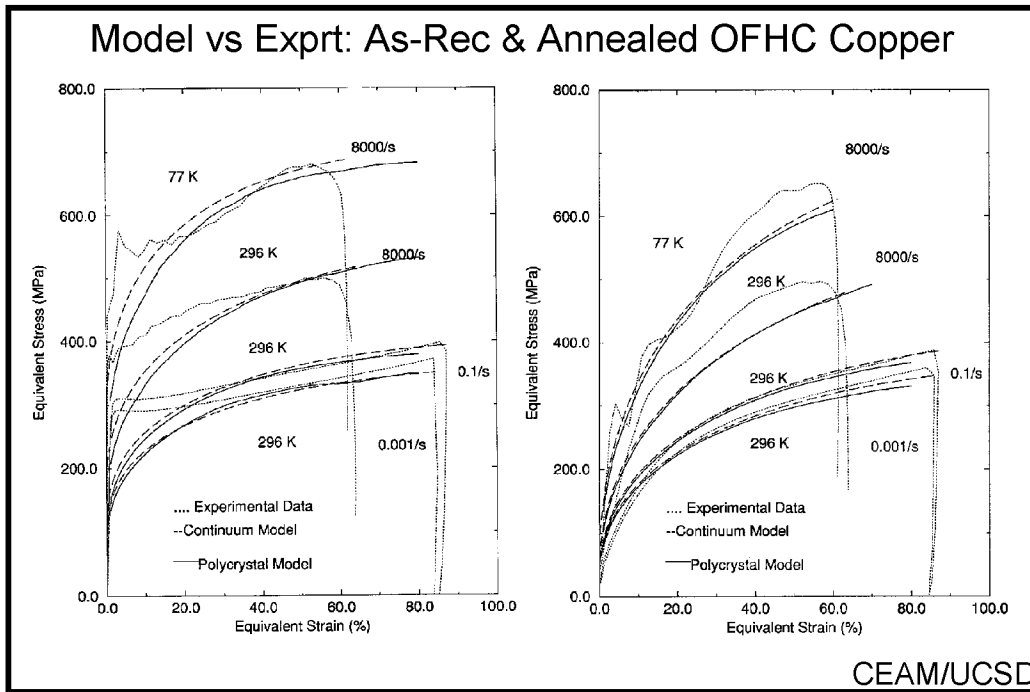


Figure 17

Flow Stress

Dislocation Motion Leads to Plastic Flow

- Resistance to Dislocation Motion Leads to Flow Stress and Workhardening

Barriers to Dislocation Motion

- Short-range Barriers
- Long-range Barriers
- Viscous Drag

CEAM/UCSD

Figure 18

Barriers to Dislocation Motion

Short-range Barriers

- Lattice Resistance = Peierls Barrier
- Dislocations Intersecting Slip Planes
- Solute Atoms
- Vacancies and Interstitials
- Precipitates, etc.

Long-range Barriers

- Grain Boundaries
- Farfield Forests of Dislocations
- Other Farfield Inhomogeneities

CEAM/UCSD

Figure 19

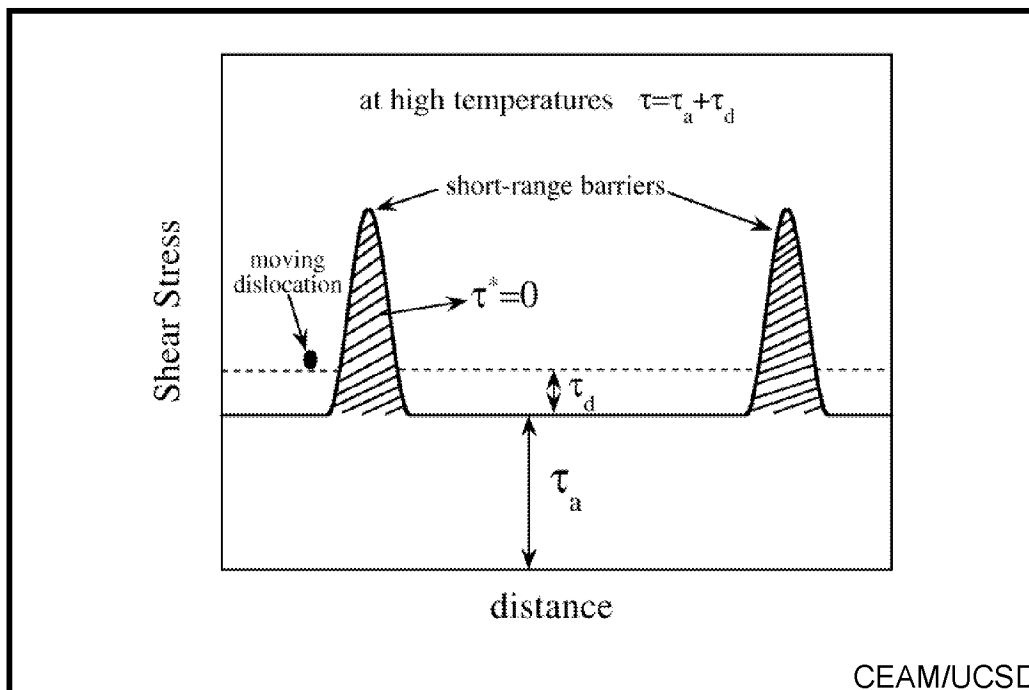


Figure 20

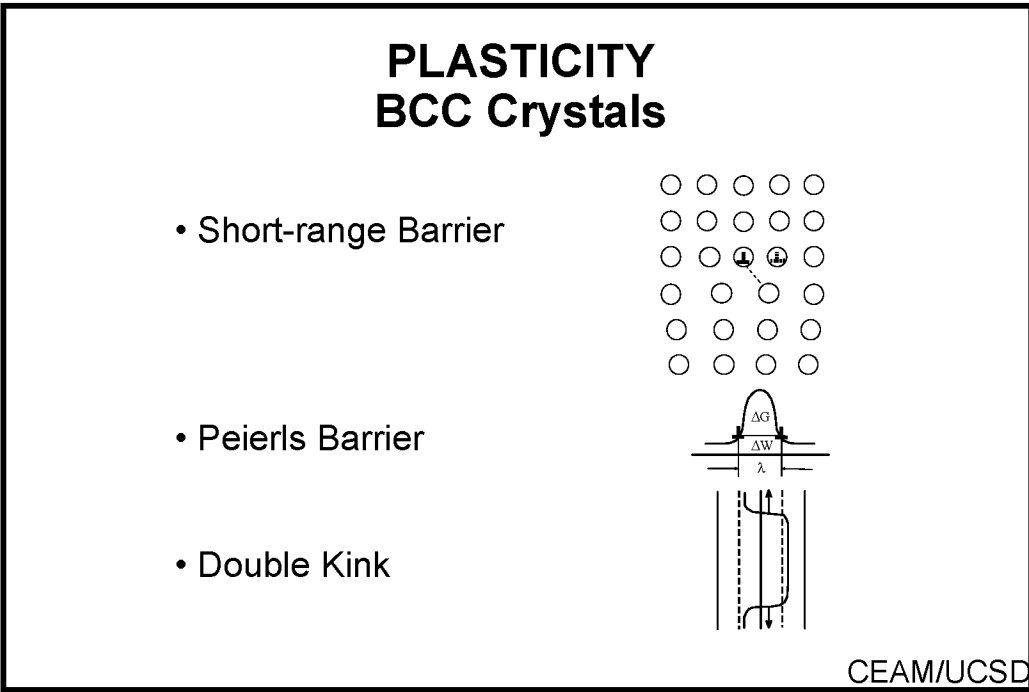


Figure 21

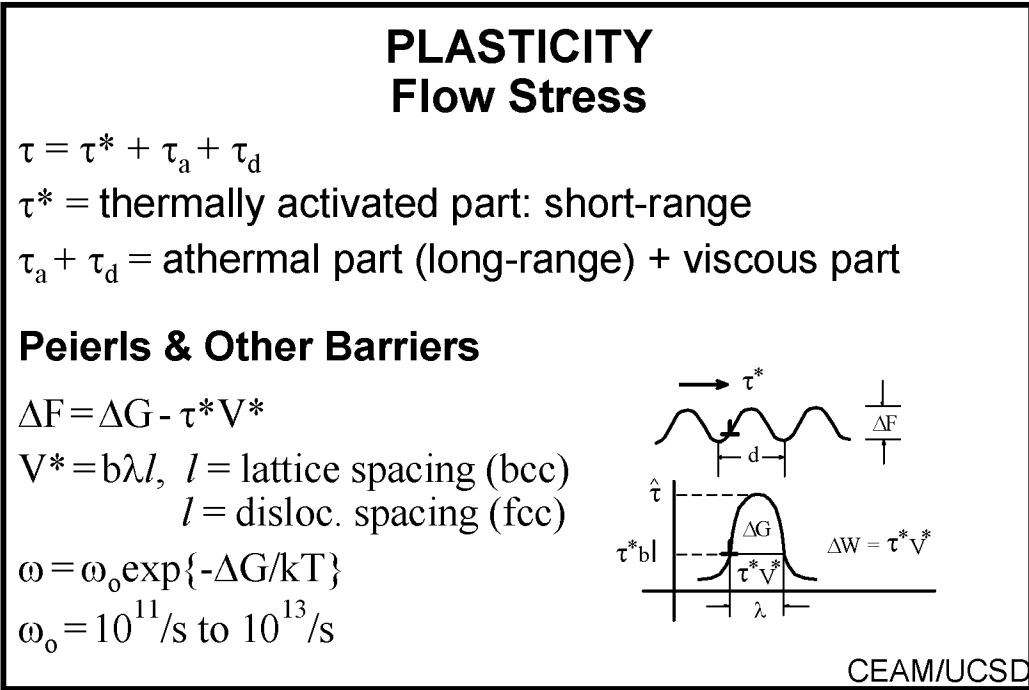


Figure 22

Direct Experimental Strategy

- At fixed strain rate, obtain high-temperature strain-stress relation => athermal part
- At fixed strain, obtain high-temperature stress/strain-rate relation => drag part
- Subtract athermal & drag parts from total flow stress => thermally activated part

CEAM/UCSD

Figure 23

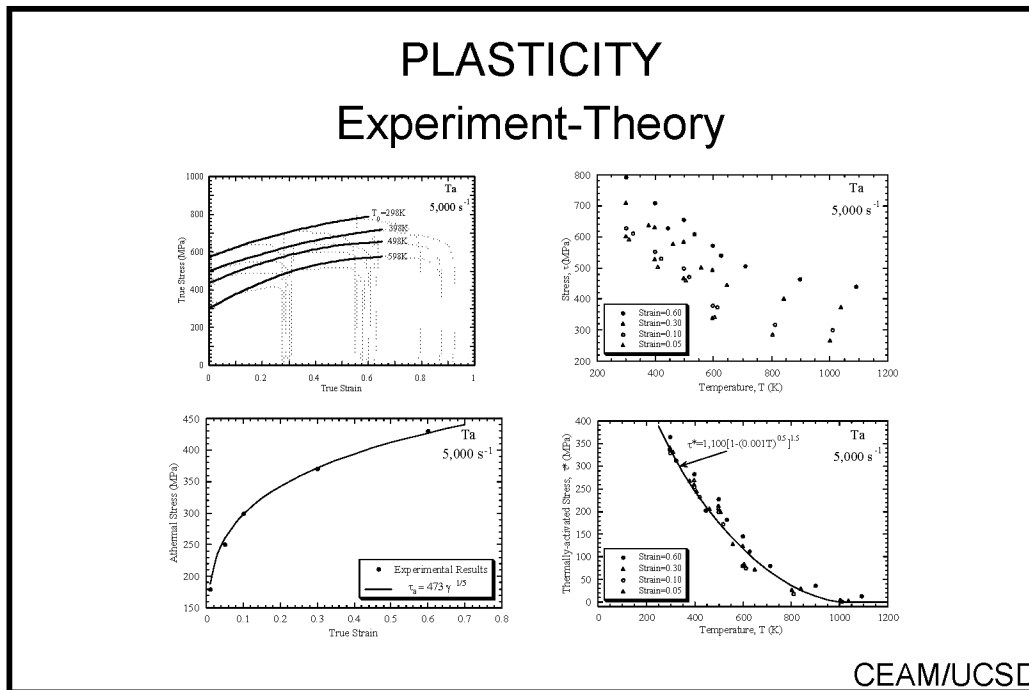


Figure 24

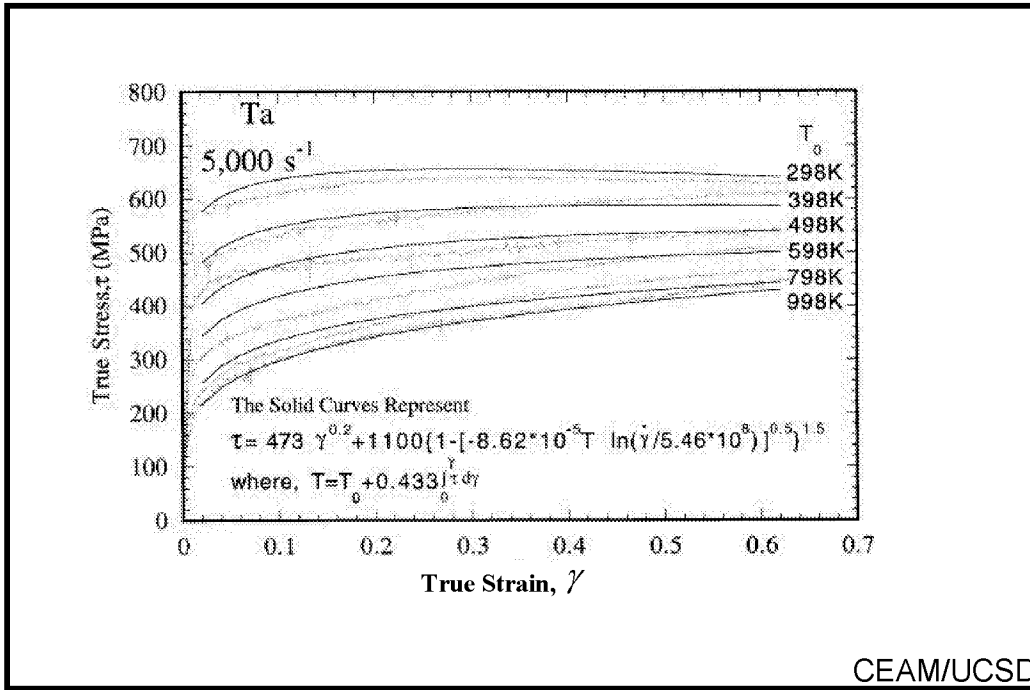


Figure 25

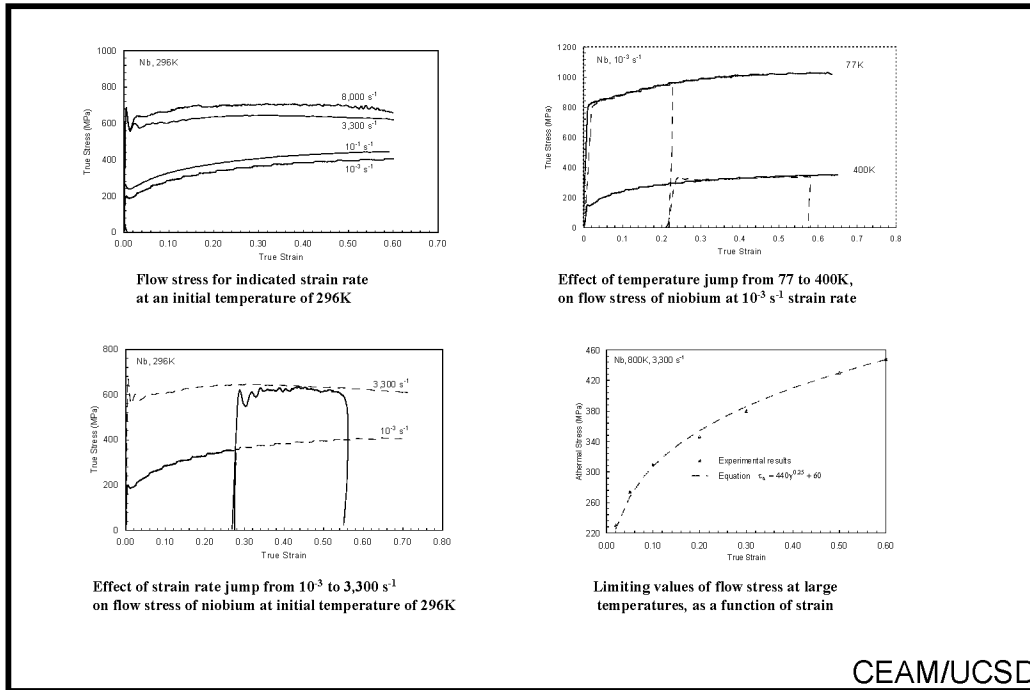


Figure 26

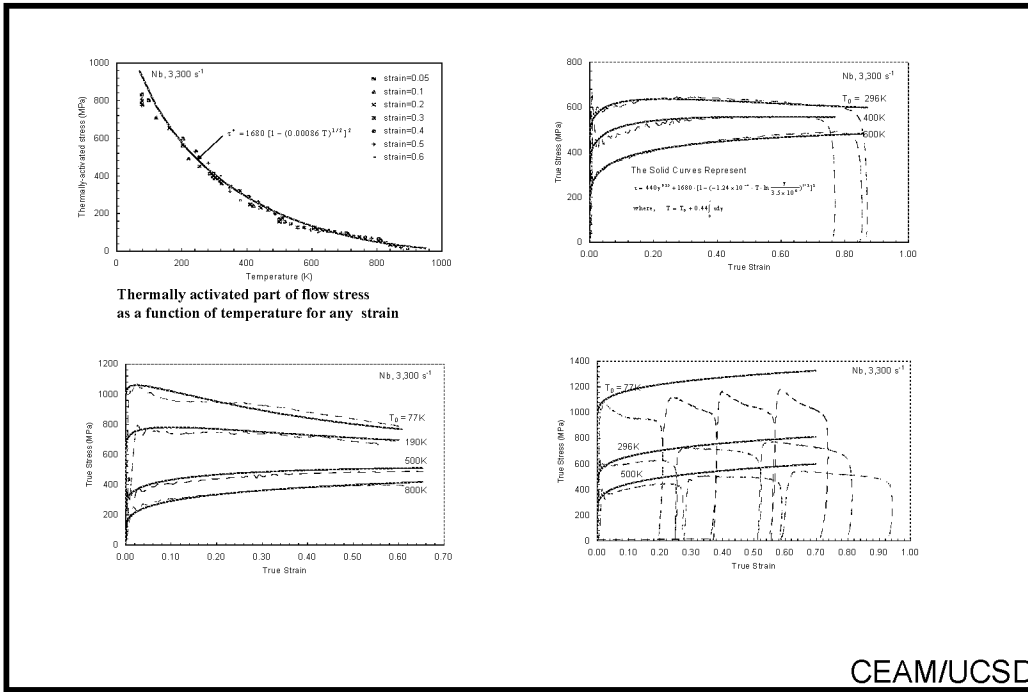


Figure 27

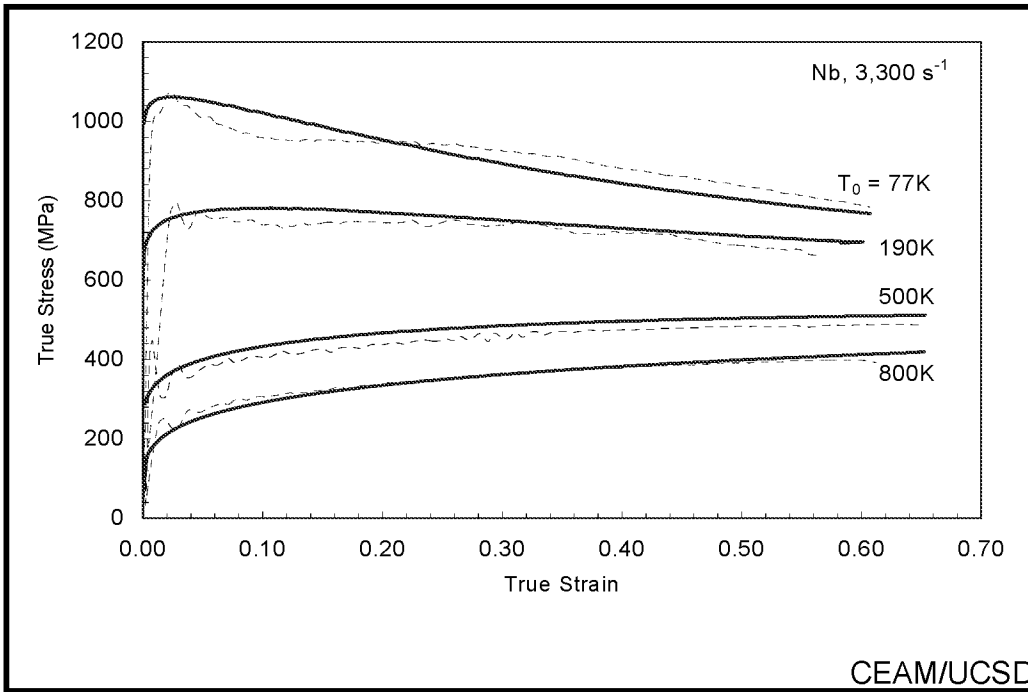


Figure 28

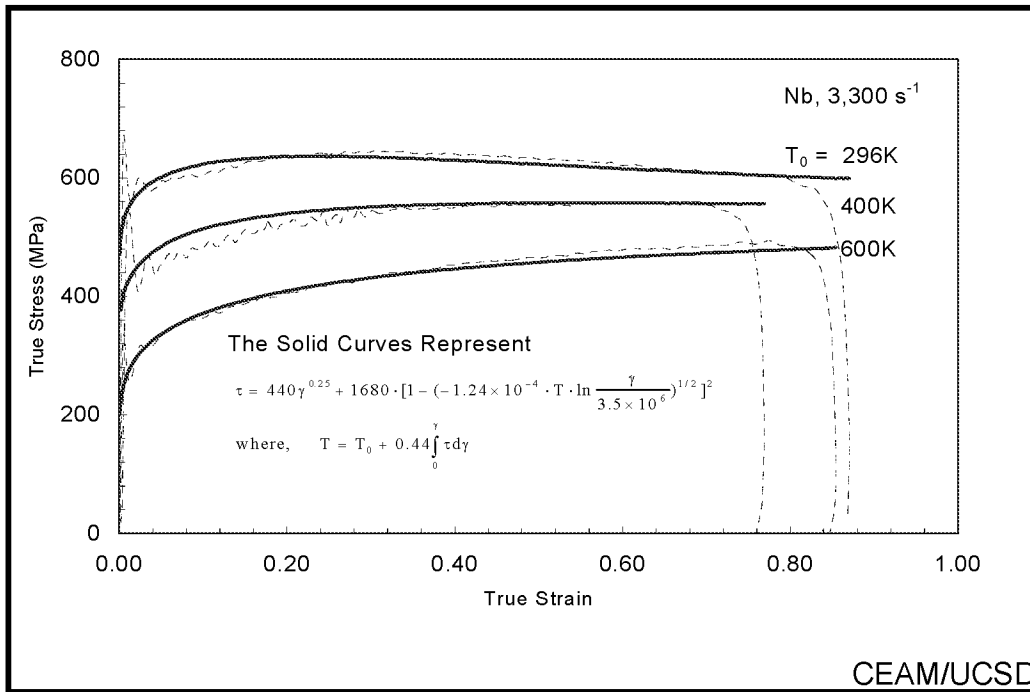
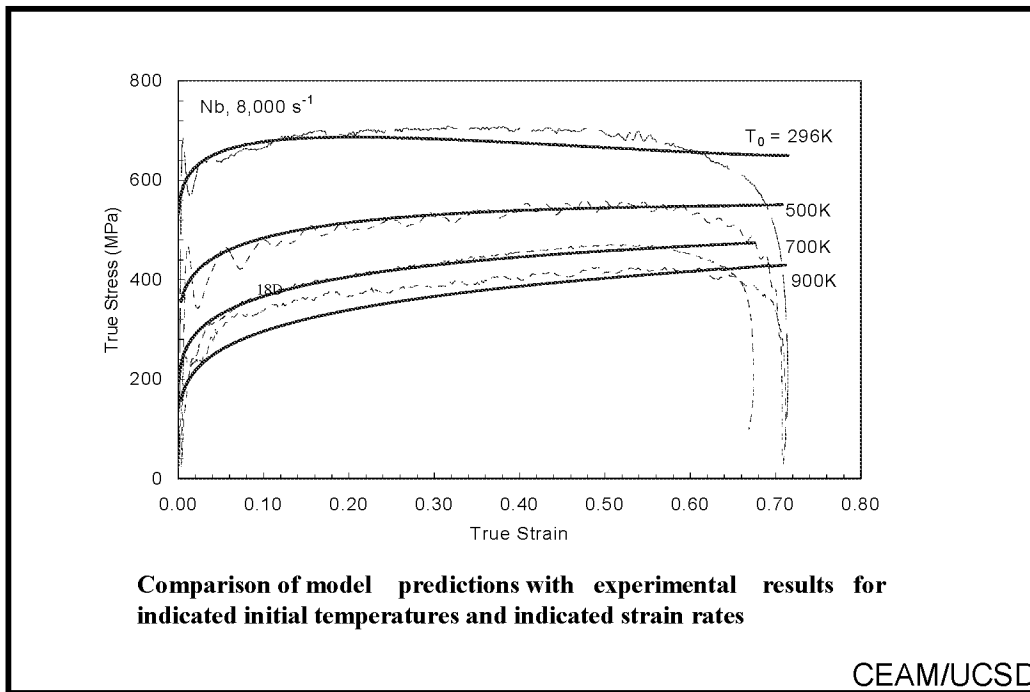


Figure 29



Comparison of model predictions with experimental results for indicated initial temperatures and indicated strain rates

Figure 30

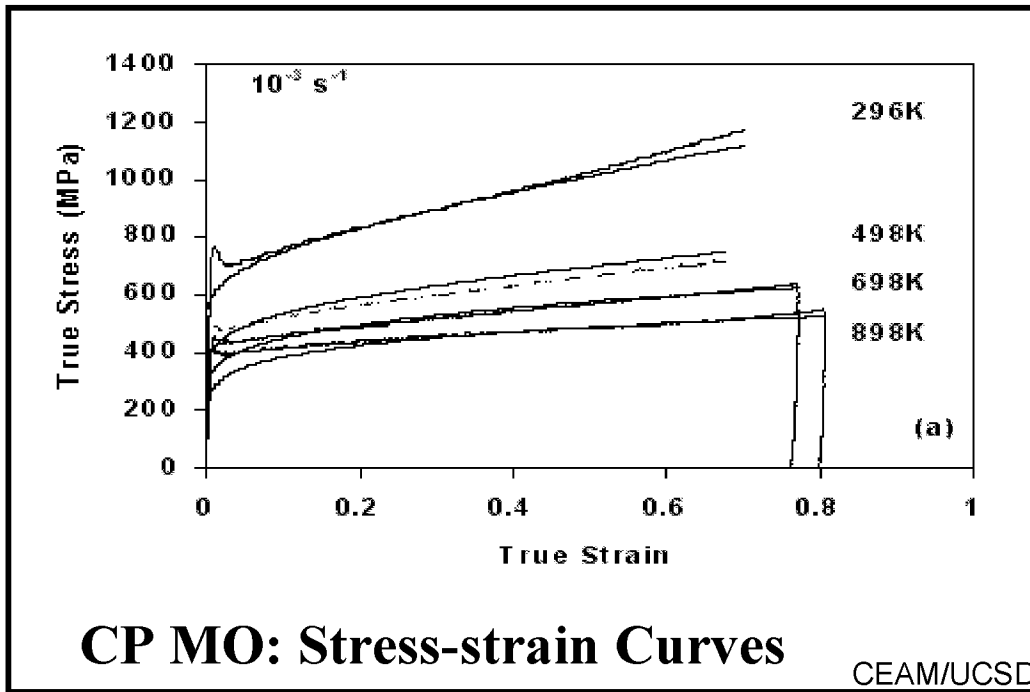


Figure 31

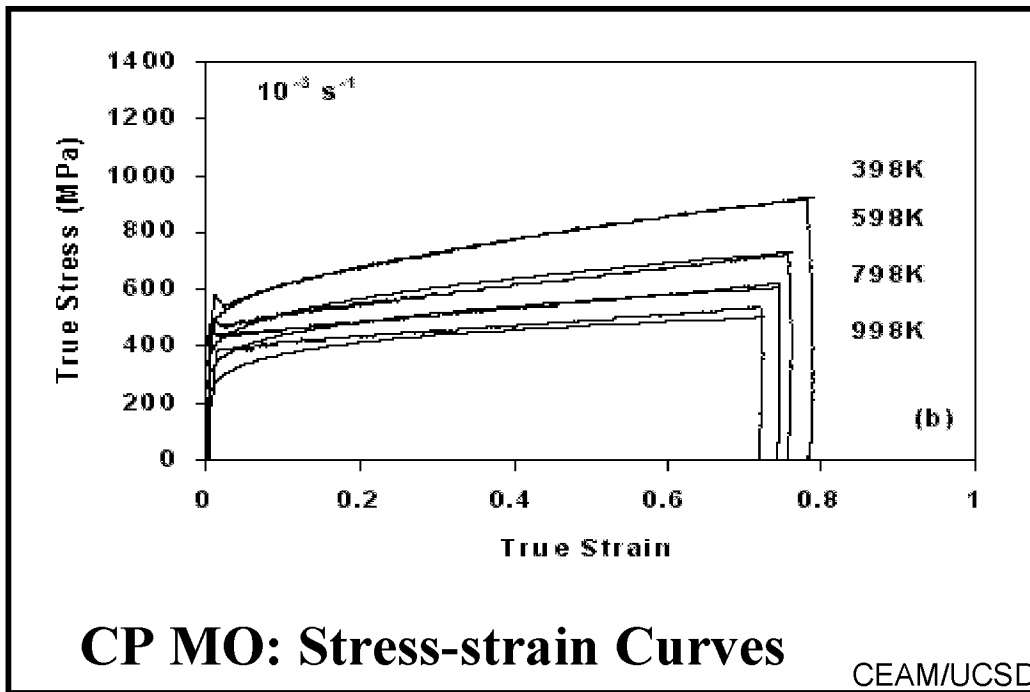


Figure 32

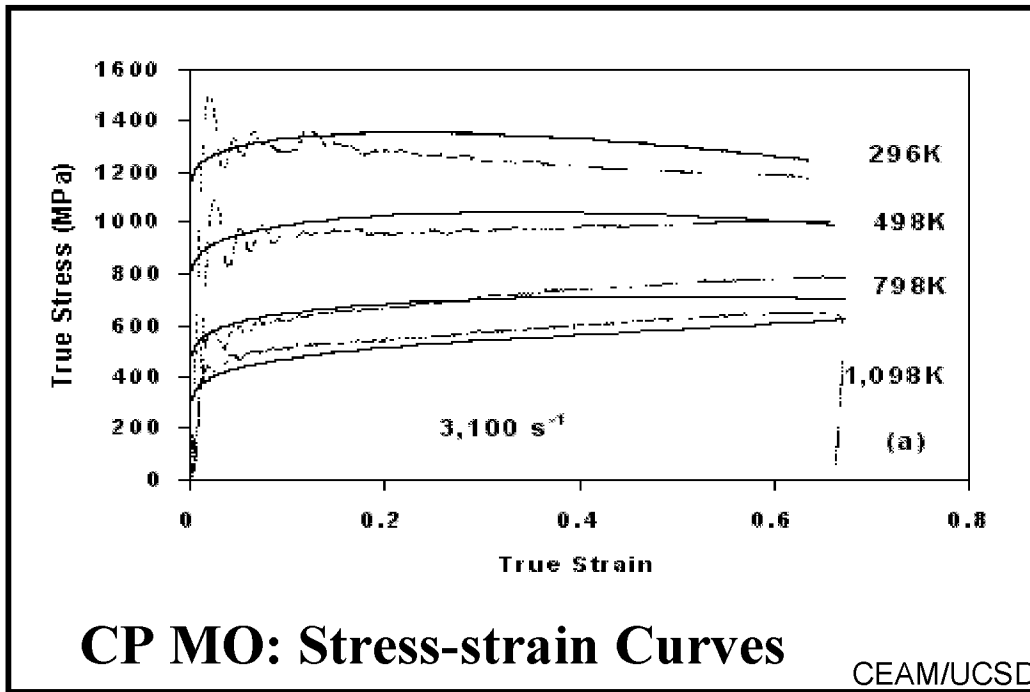


Figure 33

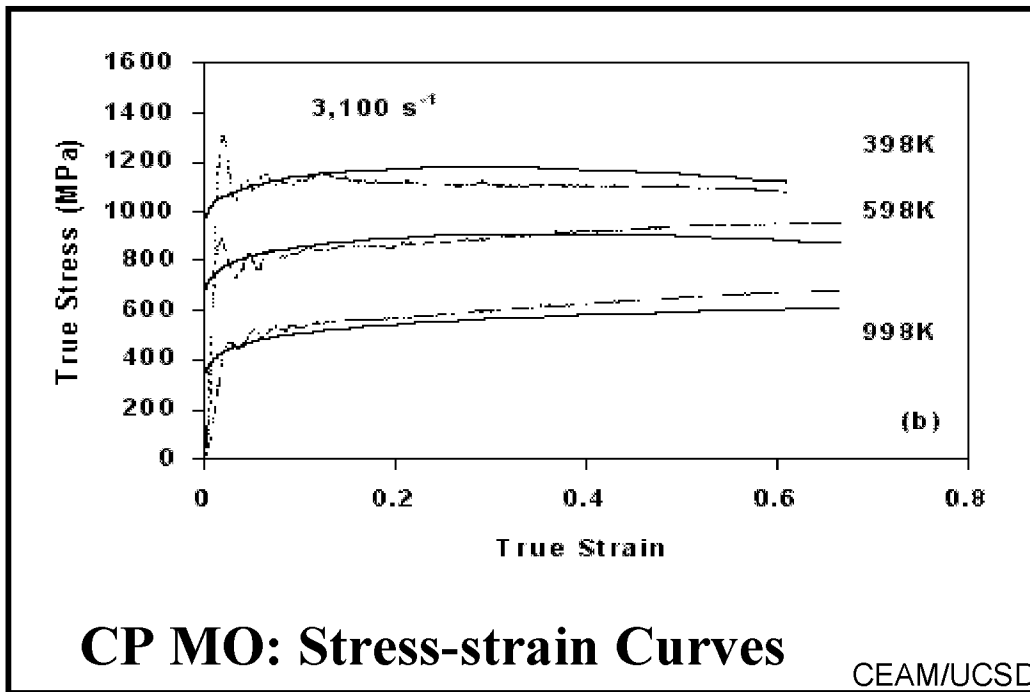


Figure 34

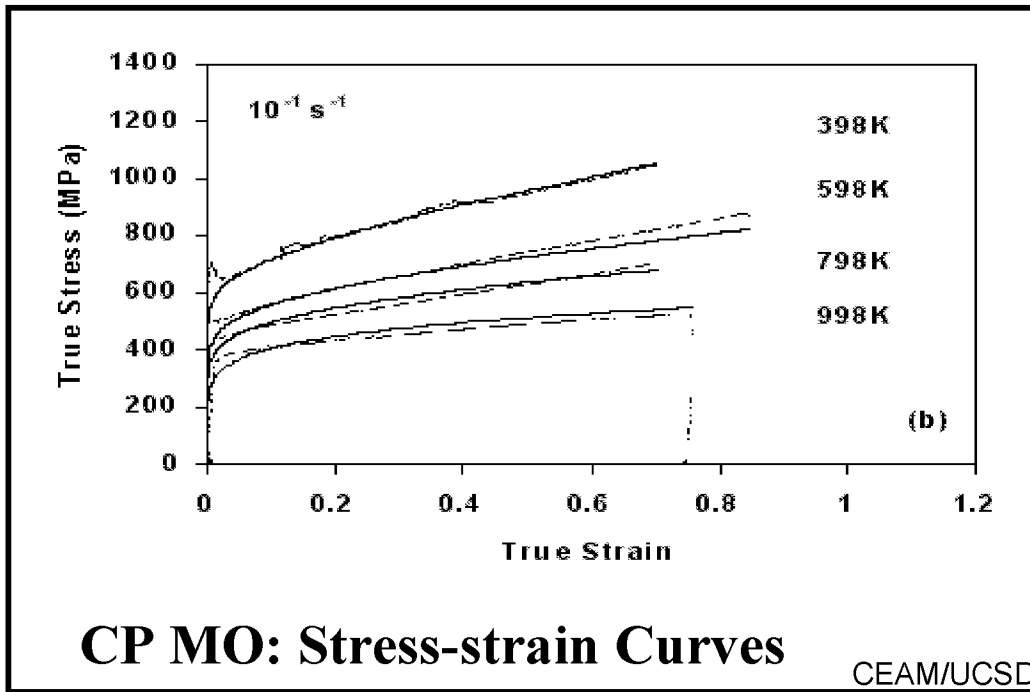


Figure 35

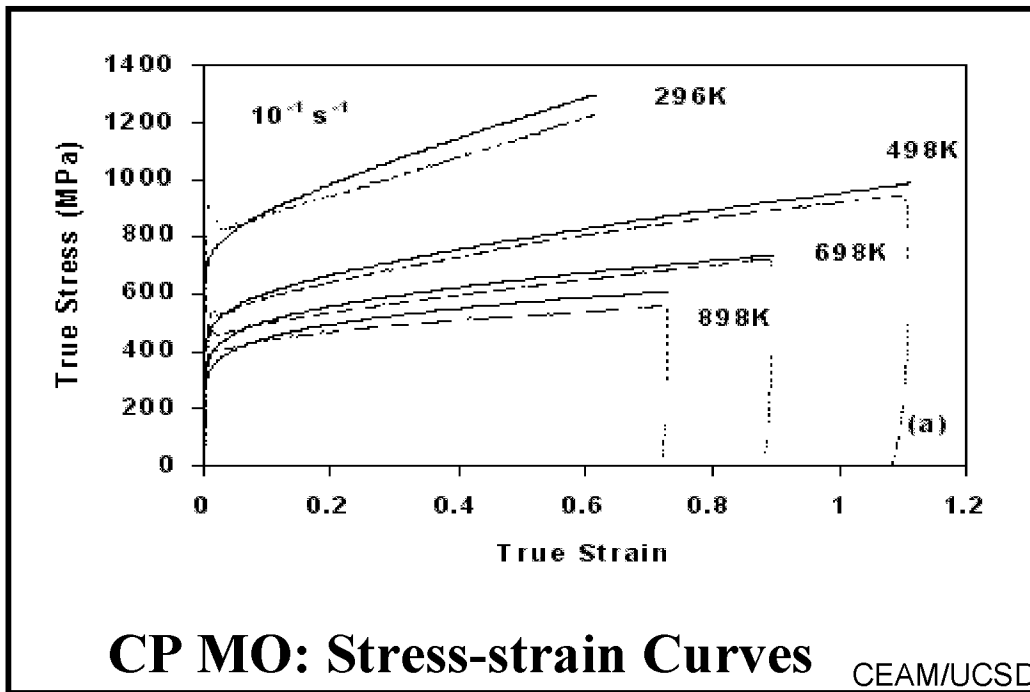


Figure 36

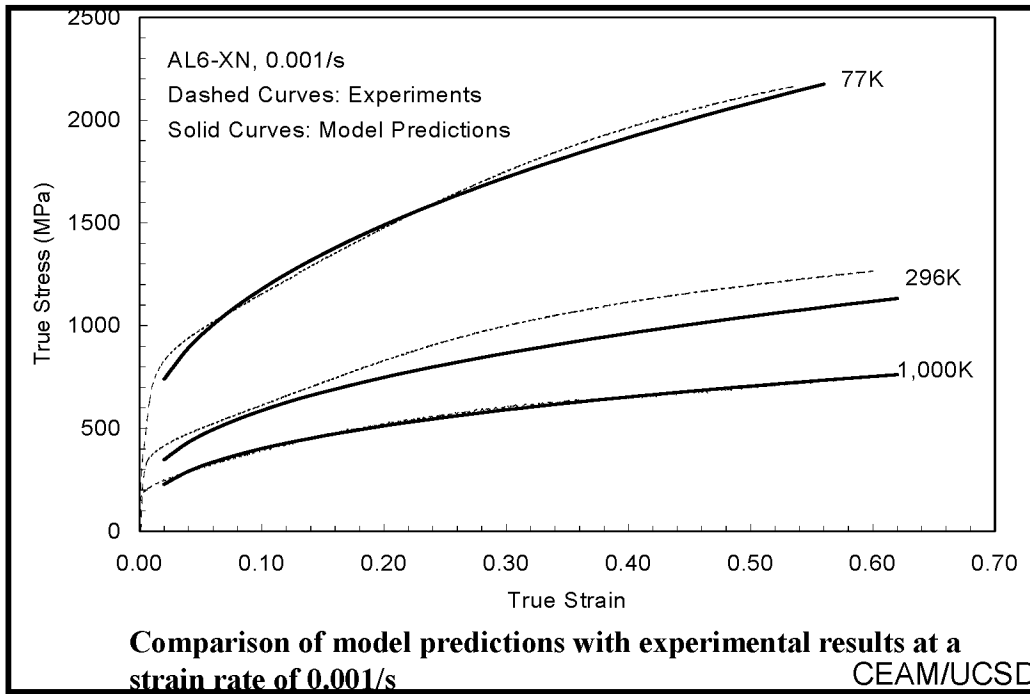


Figure 37

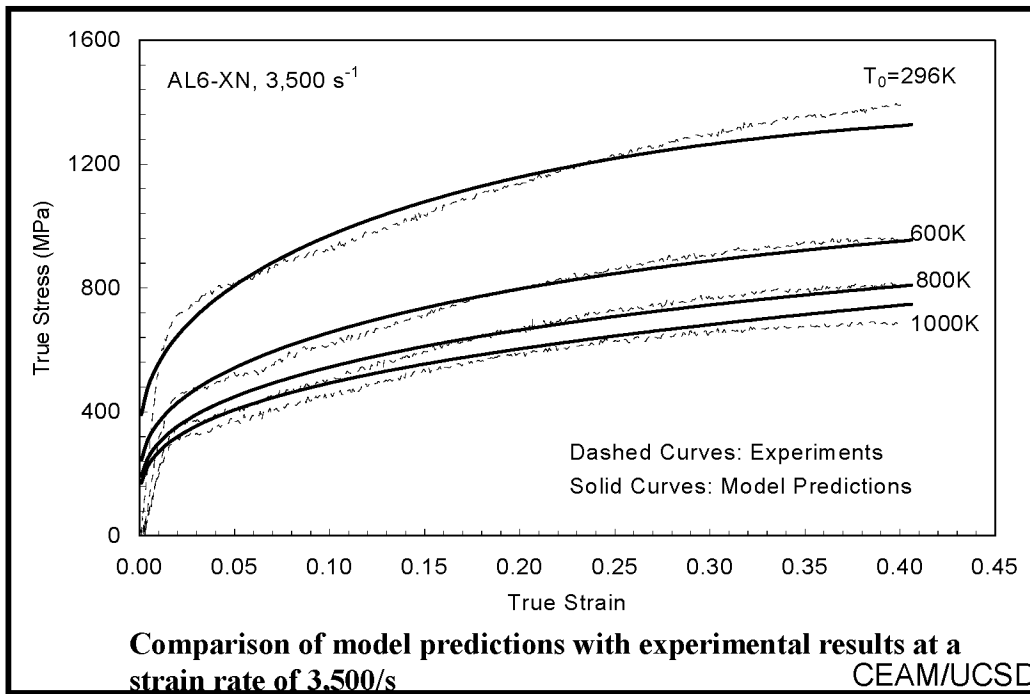


Figure 38

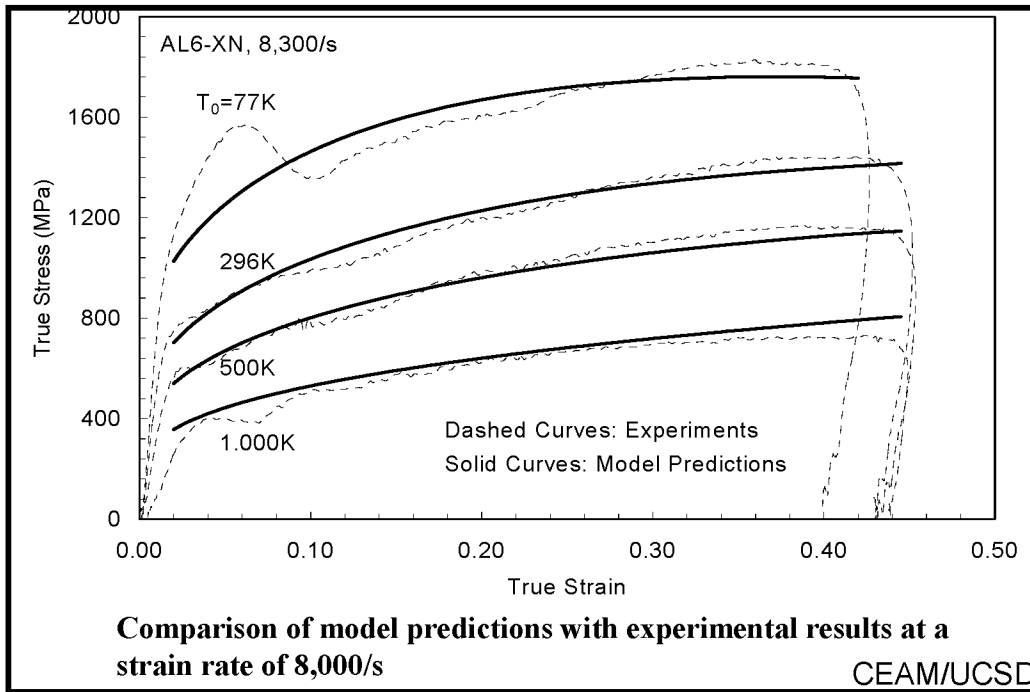


Figure 39

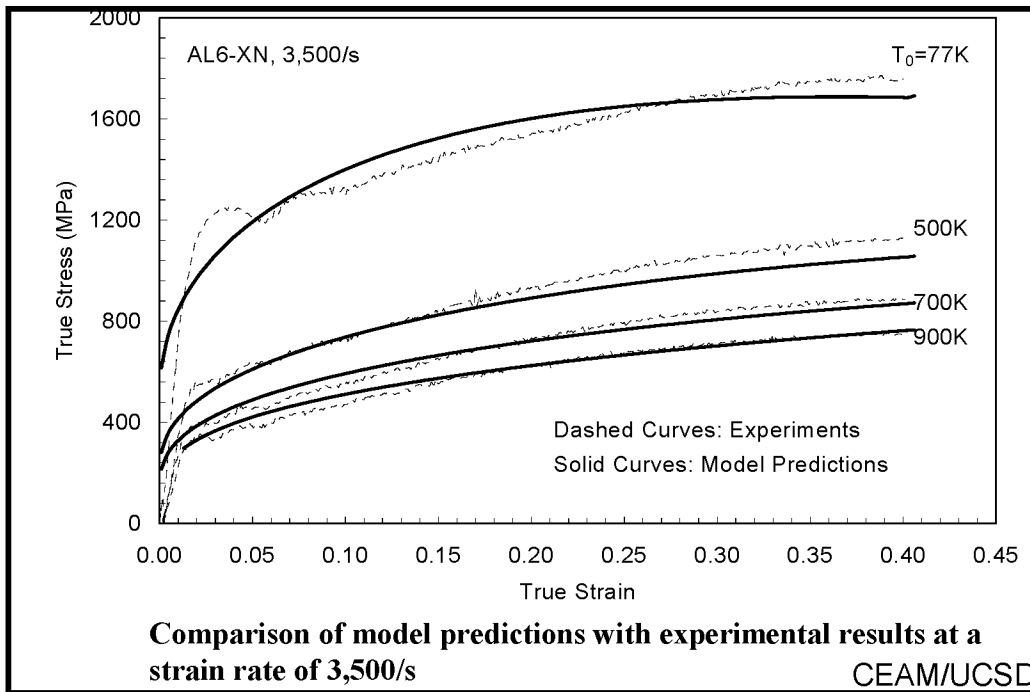


Figure 40

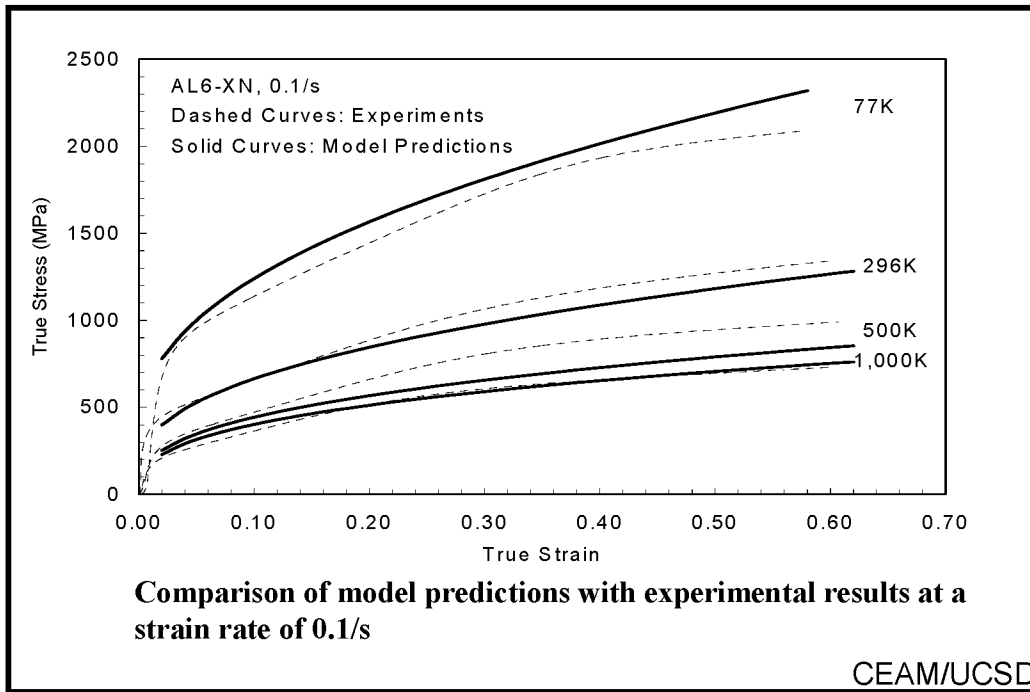


Figure 41

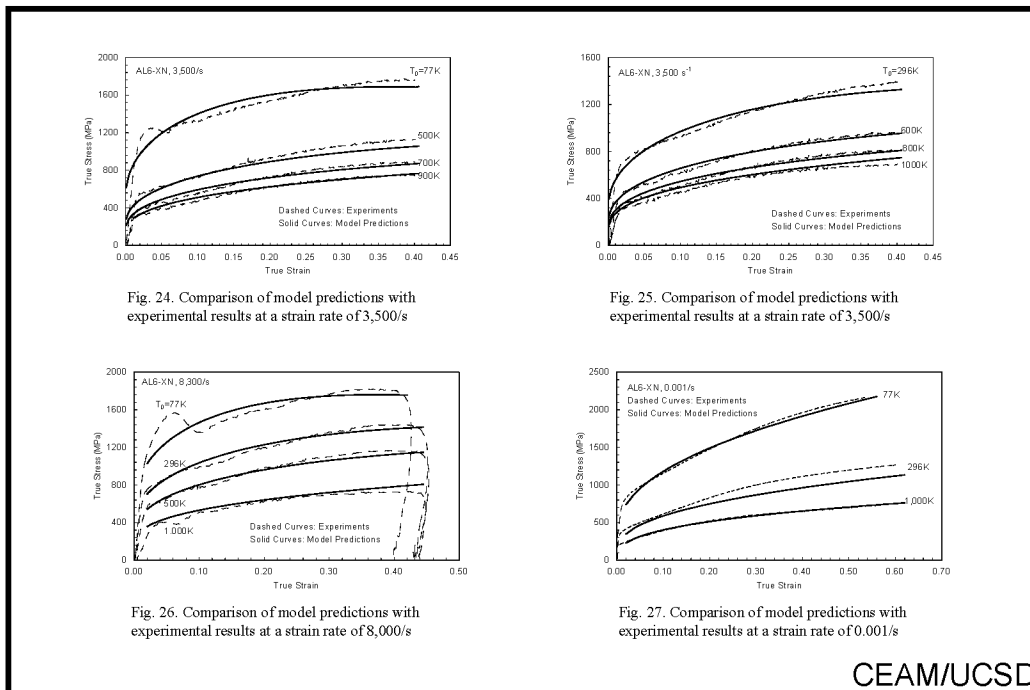


Figure 42

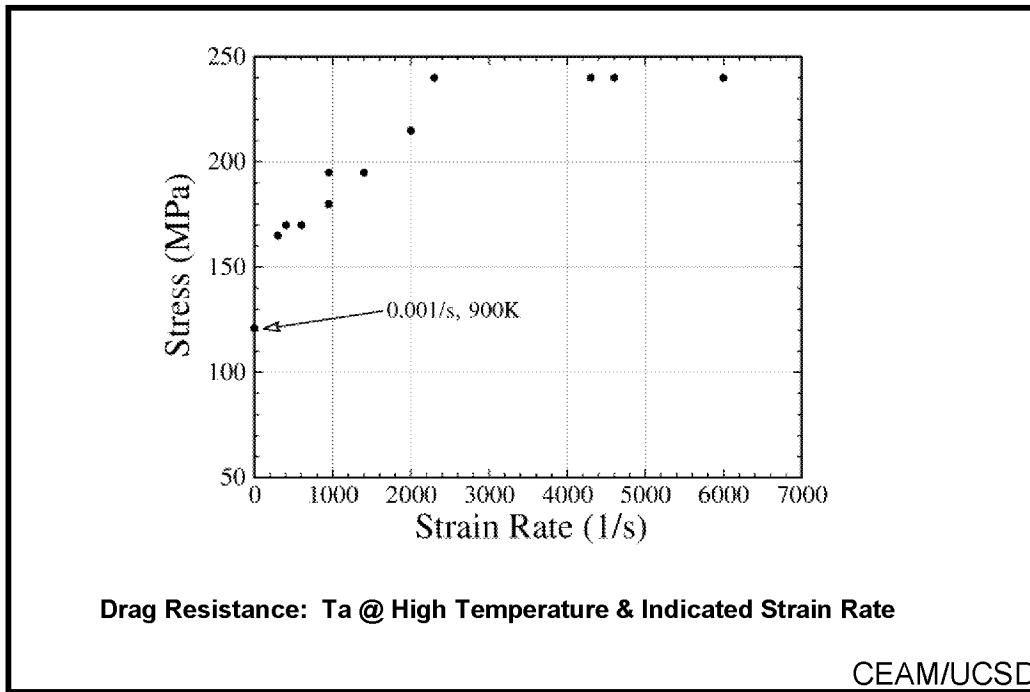


Figure 43

$$\Delta G = G_0 \left[1 - \left(\frac{\tau^*}{\hat{\tau}} \right)^p \right]^q$$

$$G_0 = \hat{\tau} b \lambda l, \quad l = \rho^{-1/2}$$

$$\hat{\tau} = \frac{G_0}{b \lambda l} = \frac{G_0}{b \lambda l_0} \frac{l_0}{l}$$

CEAM/UCSD

Figure 44

$$\dot{\gamma} = \dot{\gamma}_r \exp(-\Delta G / kT)$$

$$\dot{\gamma}_r = b \rho_m \omega_0 \ell$$

$$\Delta G = G_0 \left[1 - \left(\frac{\tau^*}{\hat{\tau}} \right)^p \right]^q$$

$$\tau = \tau^* + \tau_a + \tau_d$$

$$\tau_a = A_0 f(\rho(\gamma), d_G, \dots) \approx a_0 \gamma^n$$

$$\tau_d = \tau_d^0 (1 - \exp(-\alpha \dot{\gamma})) \quad \alpha = \frac{M^2 B}{\rho_m b^2 \tau_y}$$

CEAM/UCSD

Figure 45

$$\tau^* = \tau^0 \left\{ 1 - \left[-\frac{kT}{G_0} \ln \frac{\dot{\gamma} \cdot f(\gamma, T)}{\dot{\gamma}_0} \right]^{1/q} \right\}^{1/p} f(\gamma, T) \quad \text{for } T \leq T_c,$$

$$\tau^0 = \frac{G_0}{b \lambda \ell_0}, \quad \dot{\gamma}_0 = b \rho_m \omega_0 \ell_0, \quad f(\gamma, T) = 1 + a \left[1 - \left(\frac{T}{T_m} \right)^2 \right] \gamma^m$$

$$T_c = -\frac{G_0}{k} \left(\ln \frac{\dot{\gamma} \cdot f(\gamma, T_c)}{\dot{\gamma}_0} \right)^{-1}$$

CEAM/UCSD

Figure 46

Table 1. Constitutive Parameters for Indicated Commercially Pure Metal

Metal, bcc, $f = 1$	a_1 (MPa)	n	p	q	τ^0 (MPa)	$\frac{k}{G_0}$ (K^{-1})	$\dot{\gamma}_0$ (s^{-1})
Tantalum	473	0.20	2/3	2	1,100	8.62×10^{-5}	$5. \times 10^8$
Molybdenum	720	0.25	2/3	2	2,450	8.62×10^{-5}	1.45×10^7
Niobium	440	0.25	2/3	2	1,680	1.24×10^{-4}	3.5×10^6
Vanadium	342	0.15	1/2	2	1,260	1.24×10^{-4}	3.5×10^6

Table 2. Constitutive Parameters for Indicated Metal

Metal, $p = 2/3,$ $q = 2$	a_1 (MPa)	n	τ^0 (MPa)	$\frac{k}{G_0}$ (K^{-1})	$\dot{\gamma}_0$ (s^{-1})	m_0 (MPa)	α (s)	a	m
OFHC Cu, annealed	220	0.3	46	4.9×10^{-5}	2×10^{10}	NA*	NA*	20	0
OFHC Cu, as- received	220	0.3	400	4.9×10^{-5}	2×10^{10}	NA*	NA*	1.8	0
AL6-2N	900	0.35	630	6.6×10^{-5}	2×10^{10}	140	3	5	1/2
Ti-6Al-4V	685	0.05	1,560	6.2×10^{-5}	1.32×10^{10}	NA*	NA*	2.4	1

*NA = Not available

CEAM/UCSD

Figure 47

Constitutive Parameters for Various Titanium 6Al-4V

Values of various constitutive parameters for the three Ti64 materials

Parameter	p	q	k/G_0 ($\times 10^{-5} K^{-1}$)	$\dot{\gamma}_0$ ($\times 10^{10} s^{-1}$)	a_0	$\tau_{\alpha}^{0,0}$	n
Commercial Ti64	1	2	6.2	1.32	2.4	1560	0.05
RS-Mil-Hip Ti64	1	2	6.2	1.32	2.4	1900	0.03
RS-Hip Ti64	1	2	6.2	1.32	2.4	1620	0.04

CEAM/UCSD

Figure 48

Single Crystal Deformation

Crystallographic slip leaves the lattice

unaffected

Plastic flow consists of *simple shearing* due to dislocation motion associated with a finite number of active slip systems, resulting in both *plastic deformation and rigid-body rotation of the material relative to the lattice*

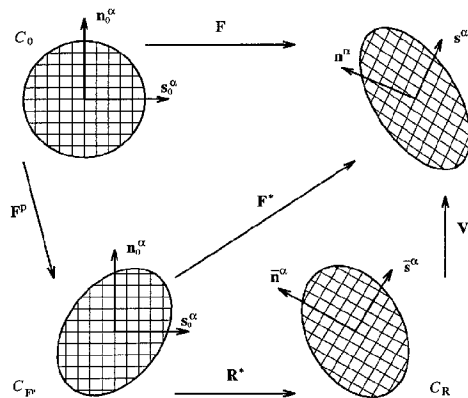
Elastic deformation is by lattice distortion

CEAM/UCSD

Figure 49

Single Crystal: Decomposition of Deformation

$$\mathbf{F} = \mathbf{F}^* \mathbf{F}^P = \mathbf{V}^e \mathbf{R}^* \mathbf{F}^P, \quad \mathbf{F}^* = \mathbf{V}^e \mathbf{R}^*$$



Decomposition of deformation gradient \mathbf{F} into plastic deformation \mathbf{F}^P , lattice rotation \mathbf{R}^* , and lattice distortion (elastic deformation) \mathbf{V}^e , $\mathbf{F}^* = \mathbf{V}^e \mathbf{R}^*$ and $\mathbf{F} = \mathbf{F}^* \mathbf{F}^P$

CEAM/UCSD

Figure 50

A Simple Continuum Model

$$\dot{\boldsymbol{\tau}} = \mathbf{L} : \left(\mathbf{D} - \dot{\gamma} \frac{\boldsymbol{\mu}}{\sqrt{2}} \right)$$

$\mathbf{L} = \text{Elasticity Tensor}$

$\mathbf{D} = \text{Deformation Rate Tensor}$

CEAM/UCSD

Figure 51

General Continuum Model

$$\dot{\boldsymbol{\tau}} = \mathbf{L} : \left(\mathbf{D} - \dot{\gamma} \frac{\partial \Phi}{\partial \boldsymbol{\tau}} \right)$$

$\Phi = \text{Flow Potential}$

CEAM/UCSD

Figure 52

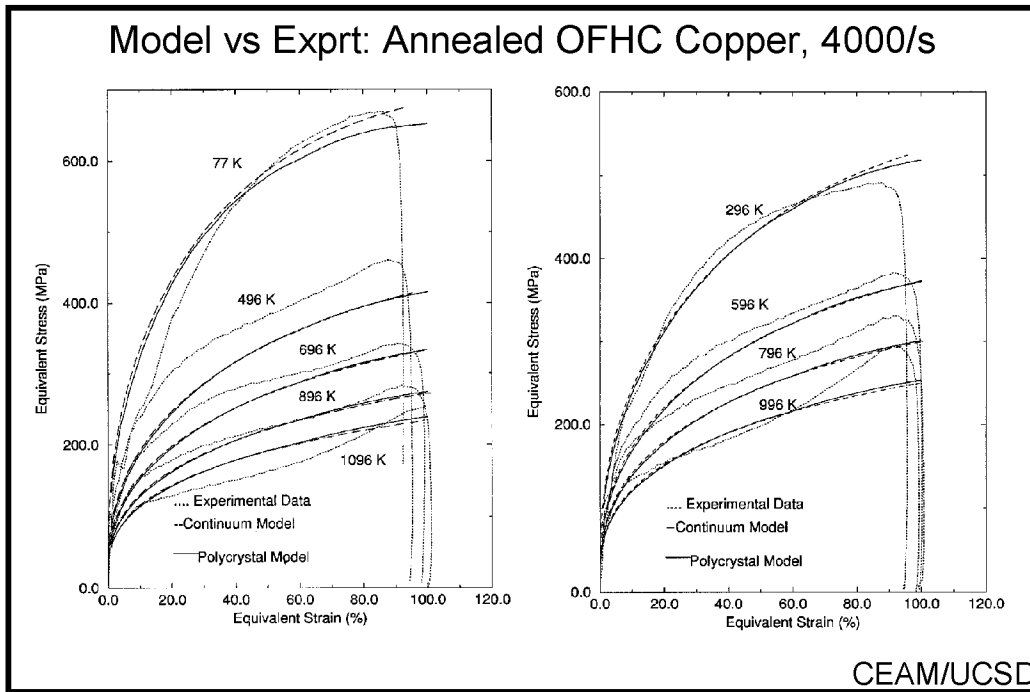


Figure 53

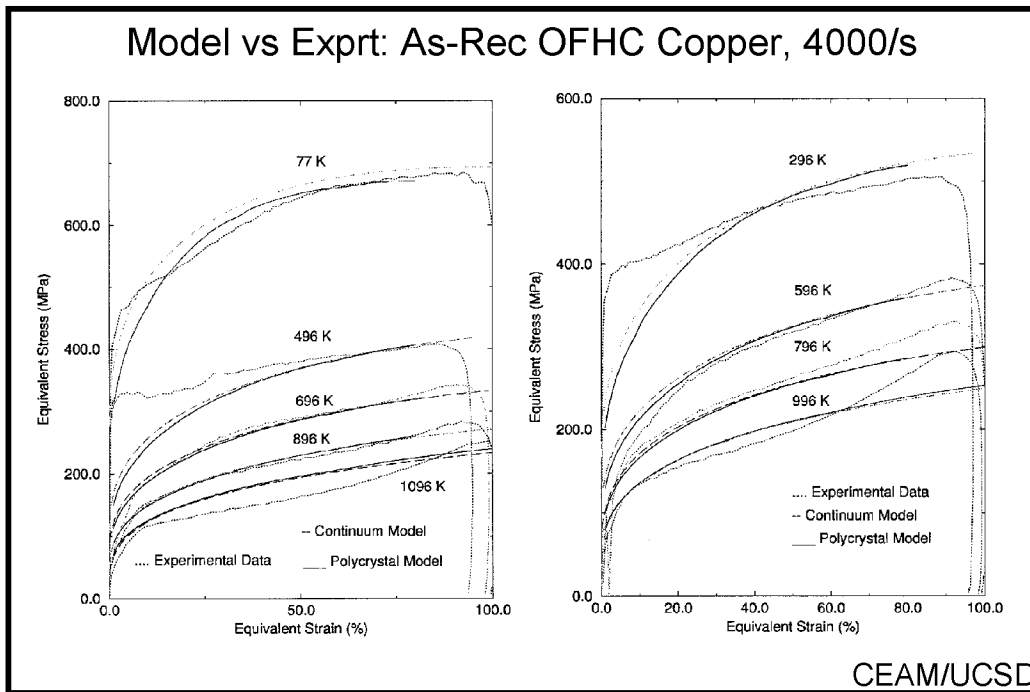


Figure 54

**Multiscale Simulation of Grain Growth IN
Nanocrystalline Thin Films**

Dorel Moldovan
Argonne National Laboratory
Argonne, IL

INTRODUCTION

*Multiscale Simulation of Grain Growth in
Nanocrystalline Thin Films**

Dorel Moldovan, Dieter Wolf, Simon R. Phillpot
and Andrew J. Haslam

Materials Science Division, Argonne National Laboratory
Argonne, IL 60439

*work supported by the U.S. Department. of Energy

*Interfacial Materials Group, Materials Science Division
Argonne National Laboratory*



Figure 1

ABSTRACT

We have combined molecular-dynamics simulations with mesoscopic simulations to study the mechanism and kinetics of grain growth in a thin film of nanocrystalline palladium with a columnar grain structure. The conventional picture is that grain growth results solely from the migration of grain boundaries in response to the driving force associated with the reduction in the grain-boundary area. However, our molecular-dynamics simulations suggest that, at least in a nanocrystalline microstructure, grain rotations play an equally important role. Based on this insight we have developed a kinetic model for grain-boundary-diffusion accommodated grain rotation, extending the formalism of Raj and Ashby (1971) for grain-boundary sliding. We have incorporated this model into a mesoscopic-simulation code based on the Needleman-Rice (1980) variational formalism for the dissipated power. The presence of both grain-boundary migration and grain rotation introduces a *physical* length scale, R_c , into the system. The growth process is characterized by two regimes: if the average grain size is smaller than R_c , grain growth is grain-rotation dominated; by contrast, if the average grain size is greater than R_c , grain growth is dominated by grain-boundary migration. Our study reveals that the growth exponents characterizing the power-law time dependence of the average grain size are different for the two growth regimes. We discuss how this methodology can be extended to allow the study of deformation process. This combination of atomic-level with mesoscopic simulations then enables the investigation, in a physically realistic manner, of grain growth in systems containing a large number of grains and over long times.

*Work supported by the U.S. Department of Energy, Office of Science under Contract W-31-109-Eng-38.

OUTLINE

- Atomistic simulations
 - Evidence of grain-rotation during grain growth
- Mesoscopic simulations
 - The model
 - Variational formulation for dissipated power
 - Atomistic and mesoscale modeling of a 25 grain system
 - Validation of the mesoscale model
 - Isotropic and anisotropic grain growth
 - Grain growth by grain rotation only
 - Grain growth in the presence of both GB migration and grain rotation
- Conclusions

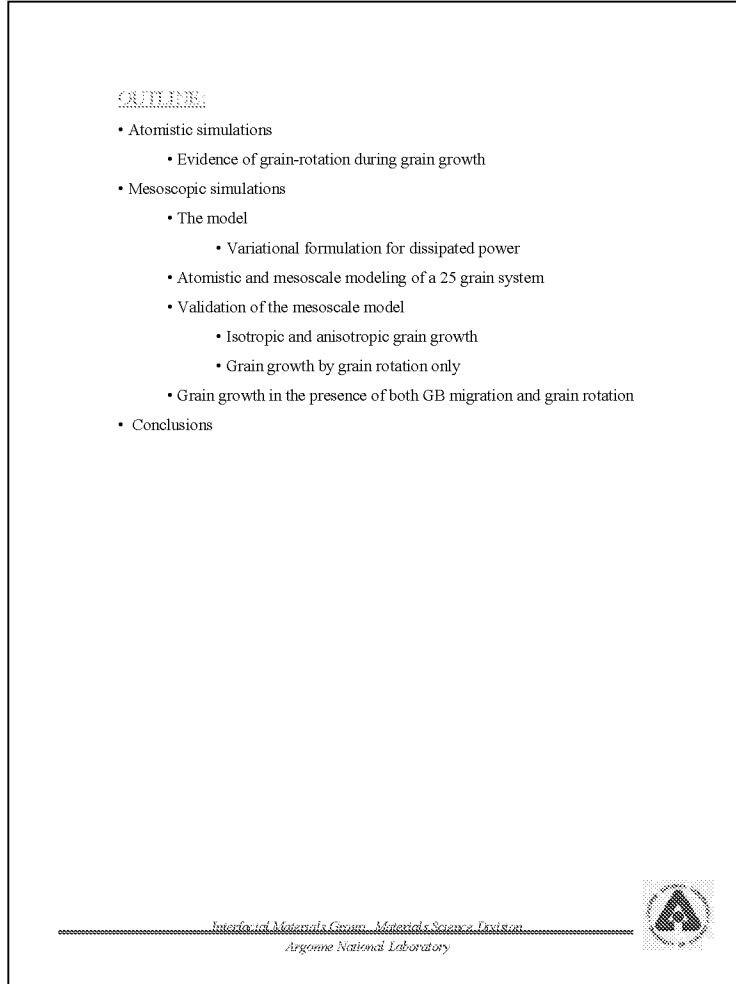


Figure 2

DETAILS ON THE MOLECULAR DYNAMICS SIMULATIONS

An embedded atom method potential parameterized for Pd is used in these molecular dynamics (MD) studies. A textured columnar microstructure was selected with the $\langle 001 \rangle$ direction as the common texture axis; therefore all GBs are $\langle 001 \rangle$ tilt boundaries. The initial microstructure contains 25 grains (388,656 atoms) with an average grain size of about 14nm. The constant pressure MD simulations with 3D-periodic border conditions were carried out on this microstructure using 5th order Gear predictor-corrector algorithm to solve the equations of motion. The simulation temperature was about 0.9 of the melting temperature for the simulated potential and the simulation was carried on for about 7.2ns (1.4 million MD steps).

(A.J. Haslam, *et al.*, Materials Science and Engineering A318,293-312, 2001)

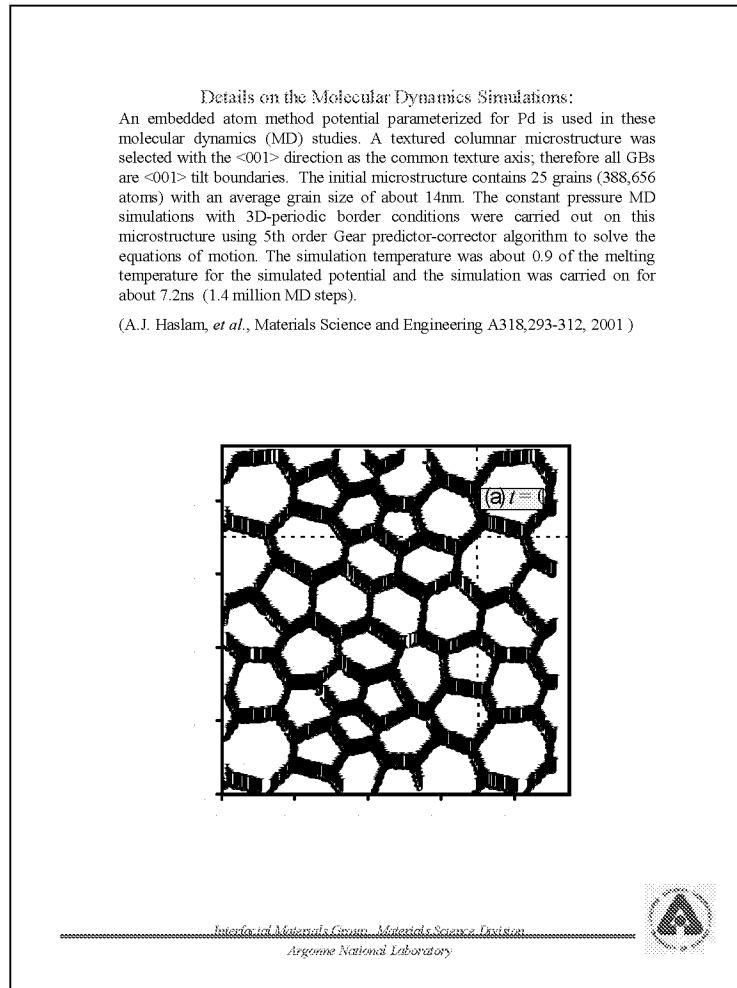


Figure 3

GRAIN GROWTH ON MD TIME SCALE

The positions of the miscoordinated atoms in one of the (001) planes of the simulation cell at the beginning and end of the simulation are shown. It is obvious the substantial amount of grain growth that has taken place.

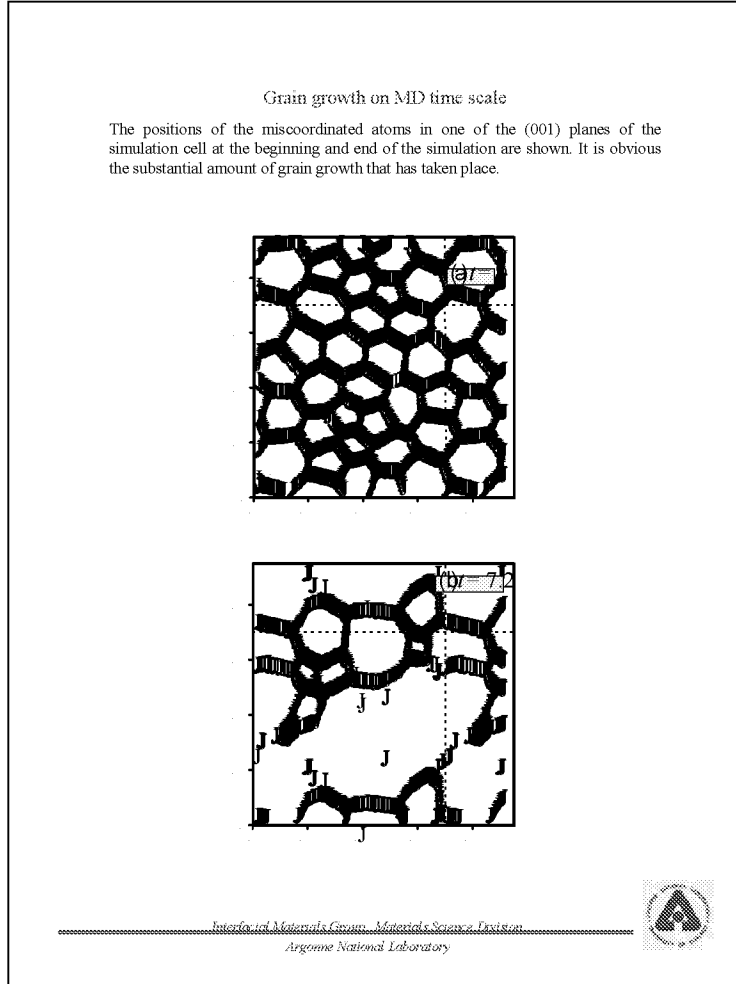


Figure 4

MD SIMULATIONS

Our MD simulations shows that there are two growth mechanisms which lead to the final microstructure. These are grain boundary migration and grain rotation - grain coalescence. The two figures bellow focusing on three representative grains in the microstructure by plotting all the perfect fcc coordinated atoms shows a grain rotation grain coalescence event.

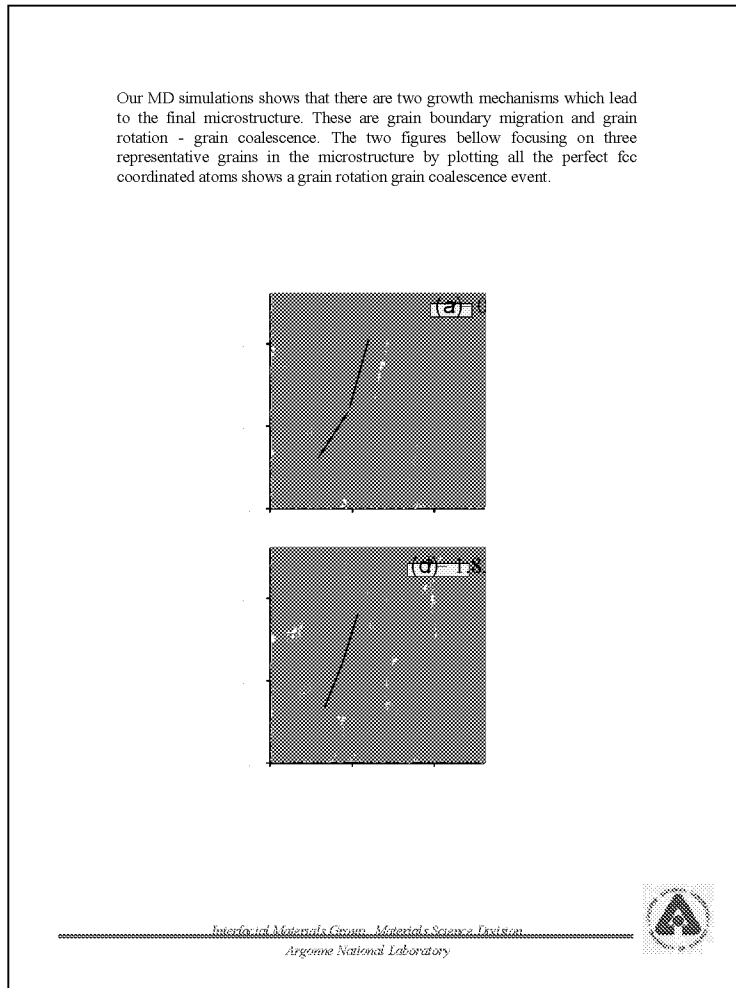


Figure 5

SUMMARY OF MD SIMUALTIONS

- We have observed **two** mechanisms for grain growth:**grain rotation / grain coalescence** grain-boundary (GB) migration
- At the nanoscale, **grain rotation and GB migration are intricately coupled** and play equally important roles in the grain-growth process.
- MD provides **input** for **mesoscale simulations**

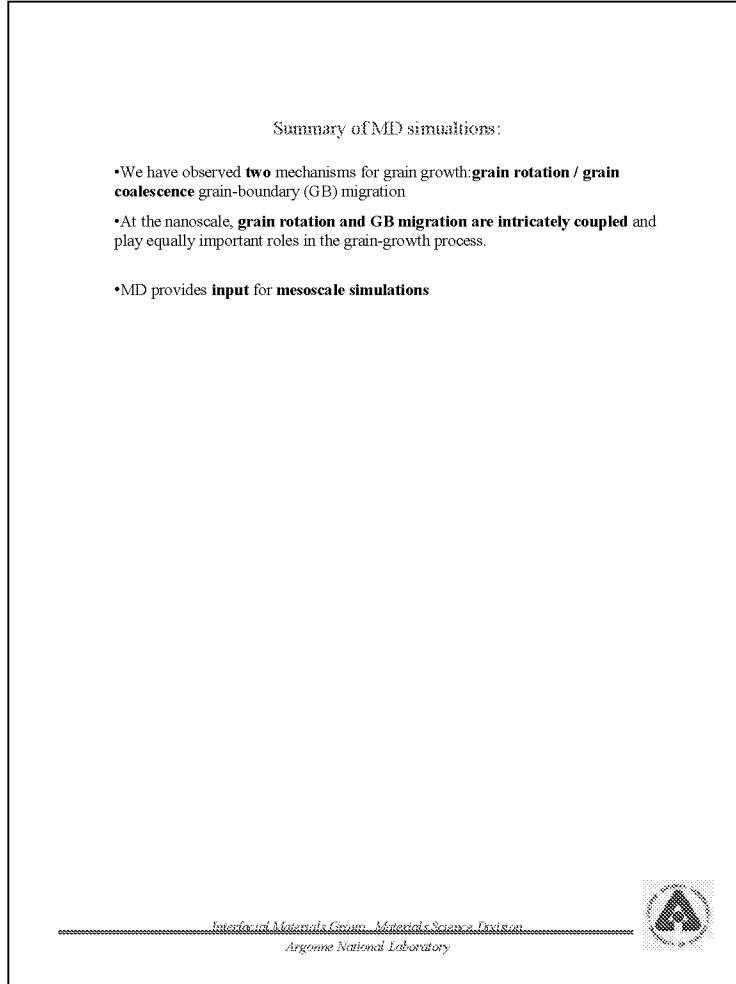


Figure 6

MESOSCOPIC MODEL OF A 2D POLYCRYSTALLINE MICROSTRUCTURE

- At the mesoscale level the microstructure consists of interconnected polygons initially generated by a Voronoi construction with periodic border conditions. In our representation each grain boundary connecting two triple-points is represented by a set of straight segments.
- GB energy and mobility

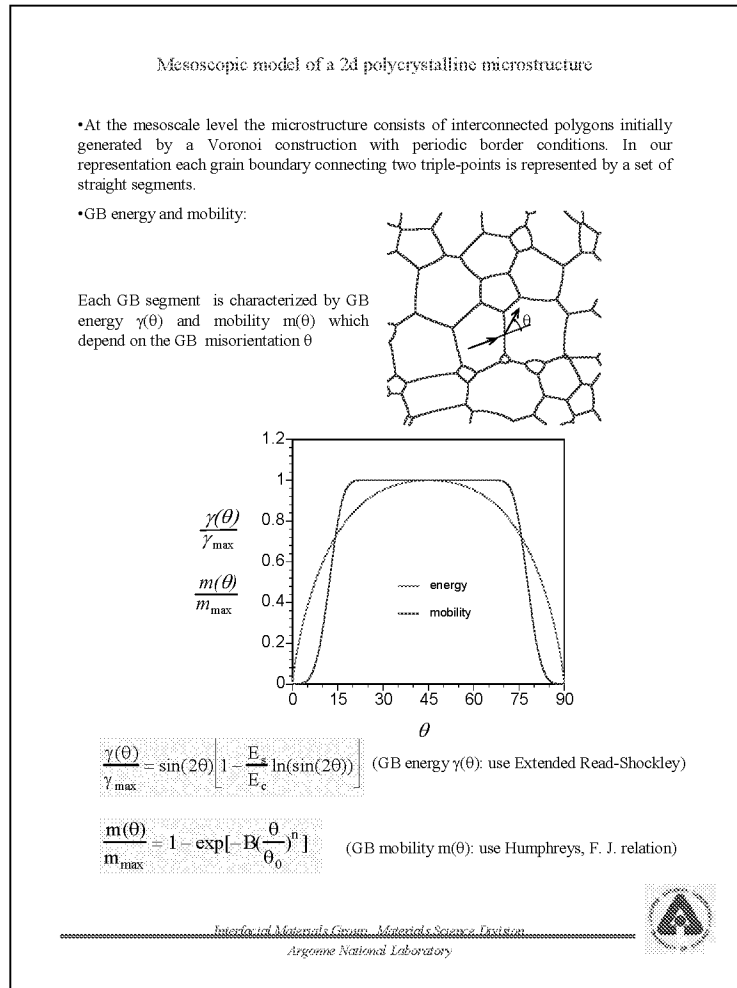


Figure 7

GRAIN-BOUNDARY ENERGY

Grain-boundary energy parameters used in the mesoscale simulations are fitted from MD simulations (Pd, <001> tilt boundaries).

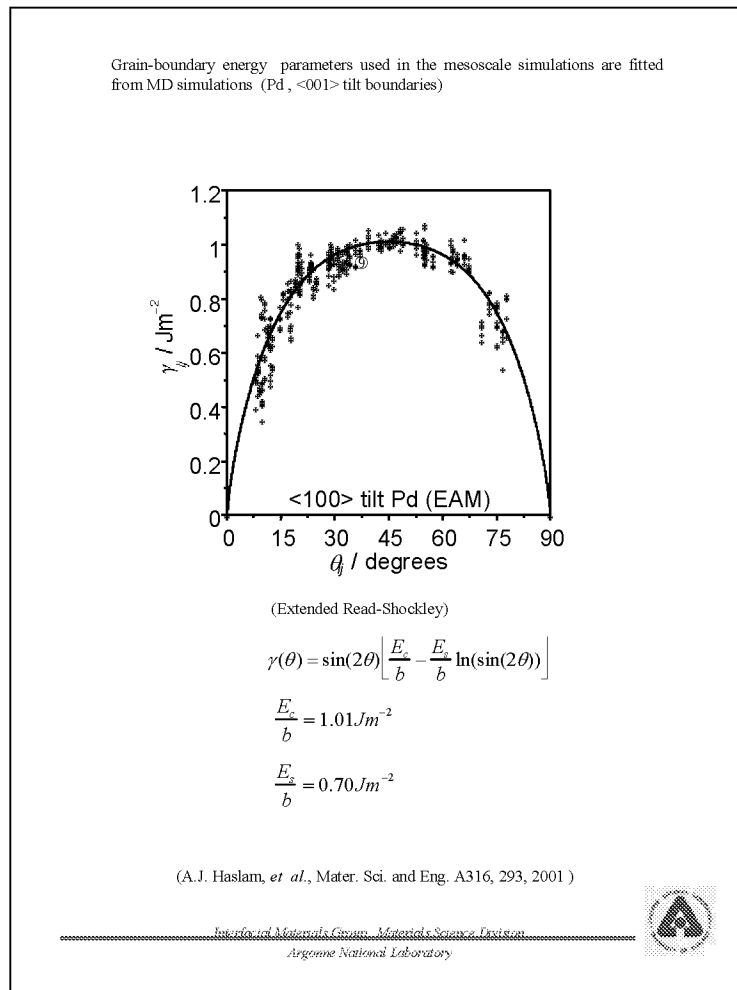


Figure 8

THEORY OF DIFFUSION ACCOMMODATED GRAIN-ROTATION

(D. Moldovan, *et al.*, Acta Mater. 49, 3521, 2001; based on Raj&Ashby 1971)

Based on the theory of diffusion-accommodated grain-boundary sliding by Raj and Ashby we have developed a kinetic theory of grain rotation in columnar polycrystalline microstructures. The driving force for rotation of any given grain is the aggregate torque on the grain due to the misorientation dependence of the grain boundaries delimiting the grain.

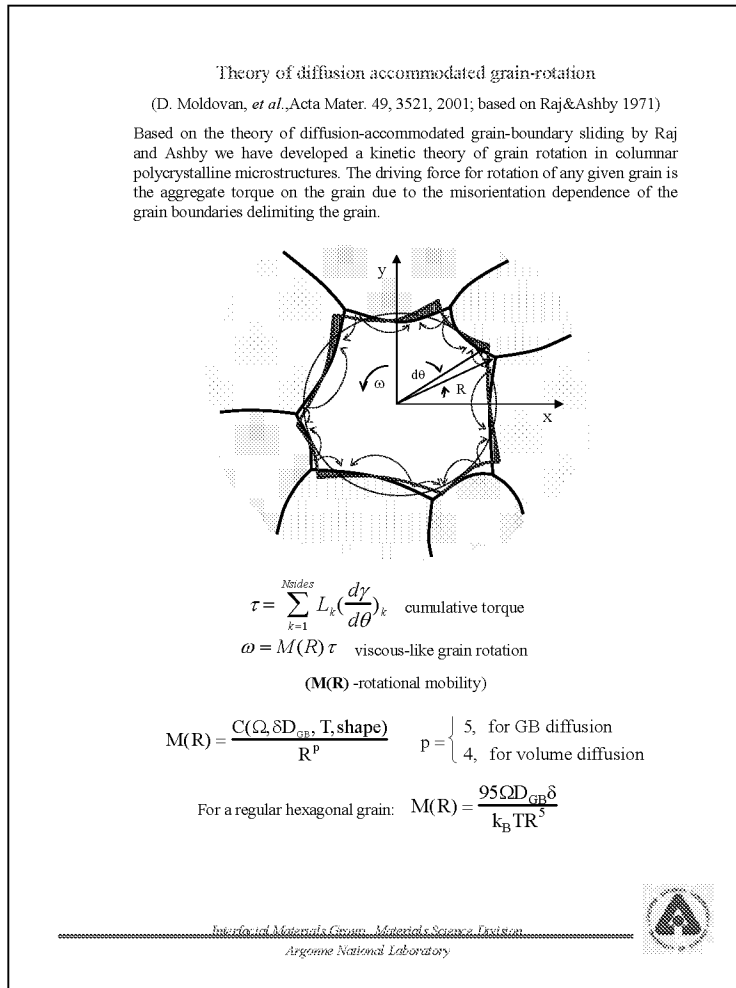


Figure 9

VARIATIONAL FORMULATION

As the formal basis for our mesoscale simulations we adopt the theoretical approach of Needleman and Rice based on variational principle for dissipative systems, originally formulated for GB and surface diffusion in the context of GB void growth studies. Later this was adapted for the simulation of curvature-driven grain growth by Cocks and Gill; their modification describes the rate of power dissipation due to the competition between the reduction of GB energy and the viscous drag during GB migration.

(Needleman & Rice, *Acta Metall.*,28, 1315, 1980); Cocks& Gill, *Acta Mater.*,44, 4765, 1996)

Our extension includes an additional dissipative process due to grain rotation. (Moldovan, D., Wolf D., Phillpot S.R. and Haslam A.J., *Acta Mater.* (in press) 2002)

Variational Formulation

As the formal basis for our mesoscale simulations we adopt the theoretical approach of Needleman and Rice based on variational principle for dissipative systems, originally formulated for GB and surface diffusion in the context of GB void growth studies. Later this was adapted for the simulation of curvature-driven grain growth by Cocks and Gill; their modification describes the rate of power dissipation due to the competition between the reduction of GB energy and the viscous drag during GB migration.

(Needleman&Rice, *Acta Metall.*,28, 1315, 1980); Cocks& Gill, *Acta Mater.*,44, 4765, 1996)

Our extension includes an additional dissipative process due to grain rotation.

(Moldovan, D., Wolf D., Phillpot S.R. and Haslam A.J., *Acta Mater.* (in press) 2002)

Two dissipative processes are considered:

- grain-boundary migration ($\{\mathbf{v}\}, \{\mathbf{r}\}$)
- grain rotation($\{\omega\}, \{\phi\}$)

$\Pi(\{\mathbf{v}\}, \{\omega\}; \{\mathbf{r}\}, \{\phi\})$

The problem is reduced to finding the variational parameters $\{\mathbf{v}\}$ and $\{\omega\}$ such that:

$\delta\Pi = 0$

Interfacial Materials Group, Materials Science Division
Argonne National Laboratory



Figure 10

VARIATIONAL FUNCTIONAL TERM FOR A GB SEGMENT

Here is the explicit relation of the variational functional term corresponding to a GB segment of length L_i moving with the velocities v_{i1} and v_{i2} .

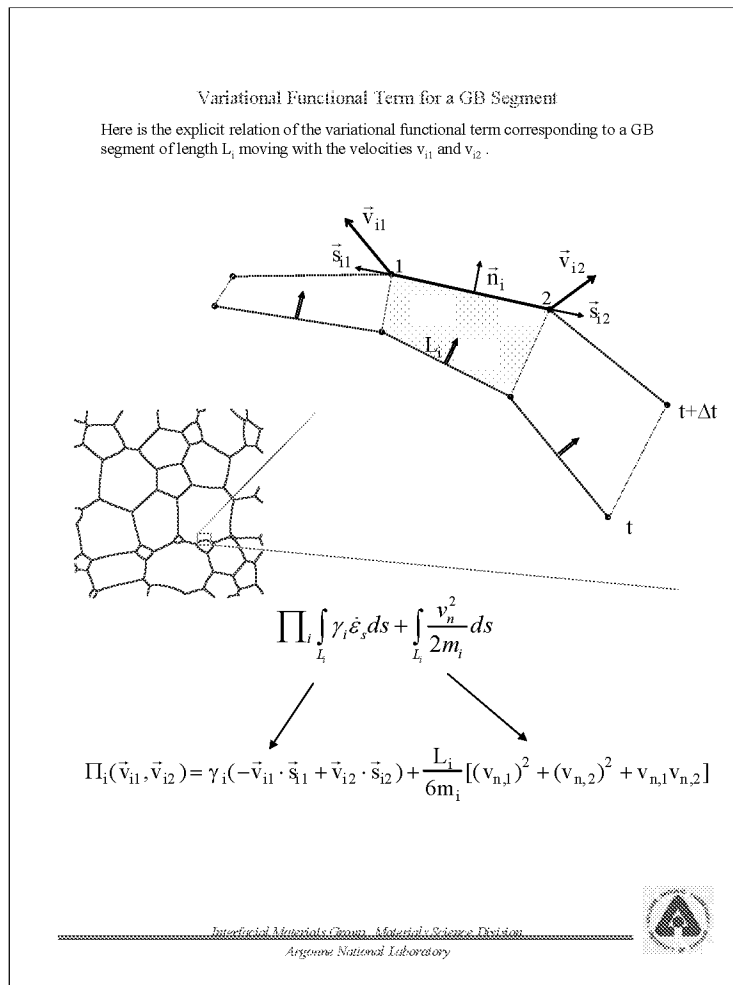


Figure 11

VARIATIONAL FUNCTIONAL TERM FOR A ROTATING GRAIN

The variational functional term corresponding to a rotating grain with the angular velocity ω . The rotational mobility of the grain is M .

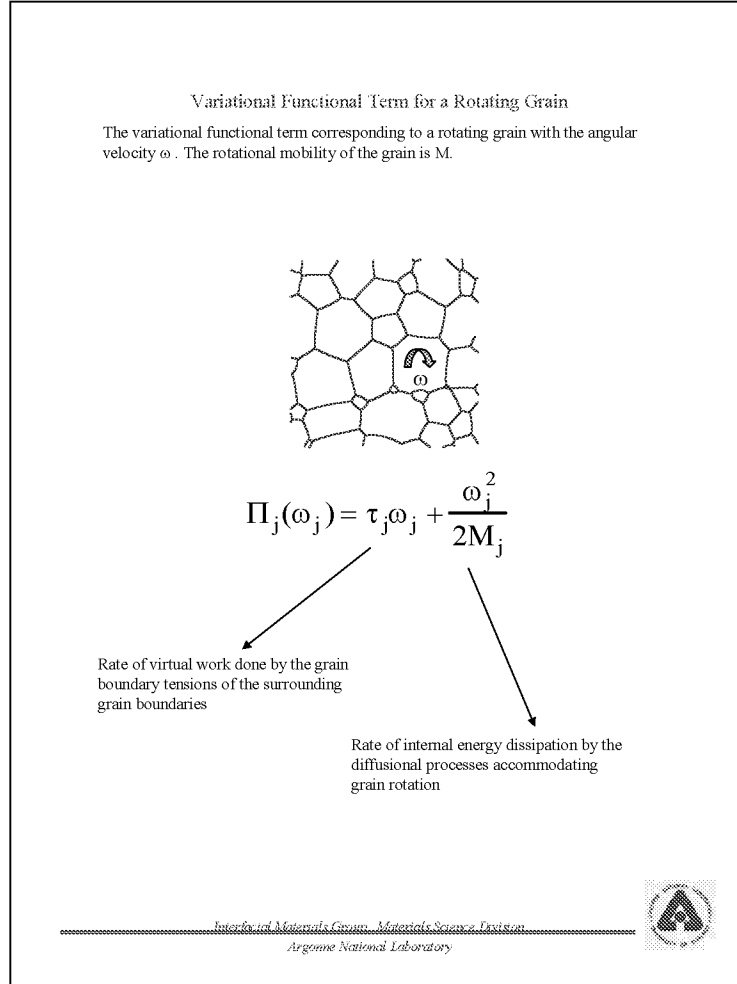


Figure 12

ALL TOGETHER: THE GENERAL FORM OF THE VARIATIONAL FUNCTIONAL

The general form of the variational functional for a microstructure comprised of N_{GBsegm} GB segments and N_{grains} grains.

All Together: The General Form of the Variational Functional

The general form of the variational functional for a microstructure comprised of N_{GBsegm} GB segments and N_{grains} grains.

$$\Pi(\{\mathbf{r}\}, \{\phi\}; \{\mathbf{v}\}, \{\omega\}) = \sum_i^{\text{GBsegm}} \left[\gamma_i (\mathbf{v}_{i1} \cdot \mathbf{s}_{i1} + \mathbf{v}_{i2} \cdot \mathbf{s}_{i2}) + \frac{L_i}{6m_i} [(v_{i1}^x)^2 + (v_{i2}^x)^2 + (v_{i1}^y)^2 + (v_{i2}^y)^2] \right] + \sum_{j=1}^{N_{\text{grains}}} \left[\tau_j \omega_j + \frac{\omega_j^2}{2M_j} \right]$$

Find the variational parameters $\{\mathbf{v}\}$ and $\{\omega\}$ such that: $\delta\Pi = 0$

- 1) Global (Finite element method)
- 2) Local (Monte Carlo)

We use the velocity Monte Carlo approach to find the set of variational parameters.
(F. Cleri, *Physica A* 282, 339, 2000)

After each VMC step using $\{\mathbf{v}\}$ and $\{\omega\}$ update $\{\mathbf{r}\}$ and $\{\phi\}$ using a simple forward integration

Interfacial Materials Group, Materials Science Division
Argonne National Laboratory



Figure 13

DIMENSIONAL ANALYSIS; CHARACTERISTIC LENGTH AND TIME SCALES IN THE PRESENCE OF BOTH GB MIGRATION AND GRAIN ROTATION

Grain growth due to either GB migration or grain rotation alone exhibits no physical length scale. However the presence of both GB migration and grain rotation introduces a physical length scale R_c . This is determined solely by the material parameters and temperature

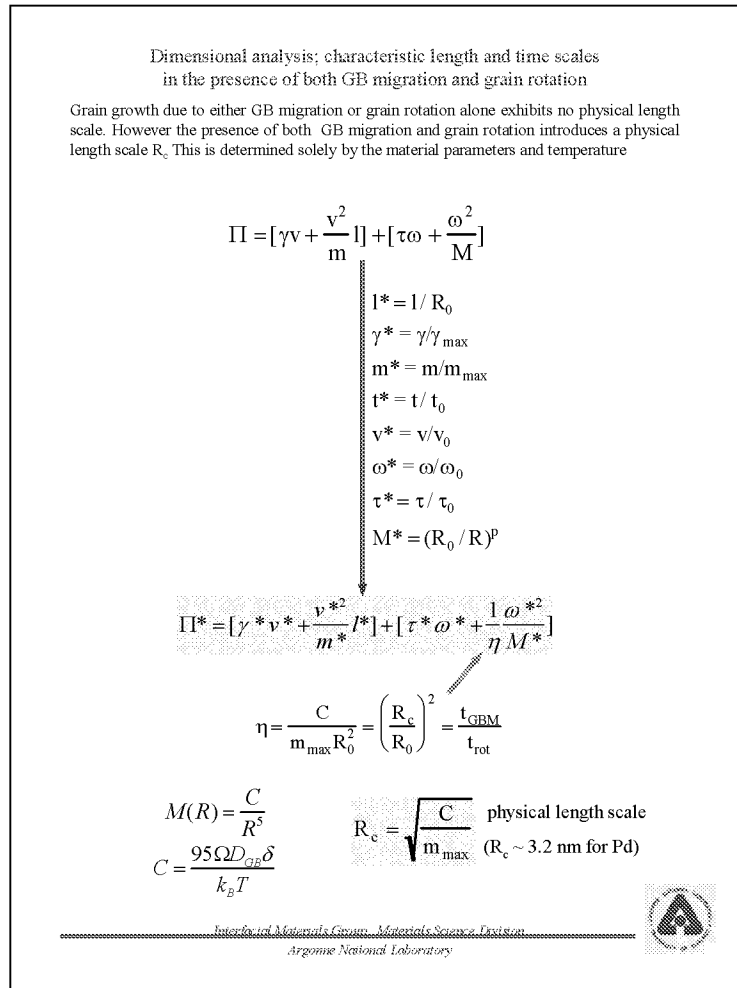


Figure 14

TOPOLOGICAL CHANGES

To account for the discontinuities occurring during the evolution of the microstructure certain topological changes has to be implemented. In addition to the well known neighbor switching (T1) and grain disappearance (T2) events we have introduced an additional topological change: the grain disappearance by grain coalescence.

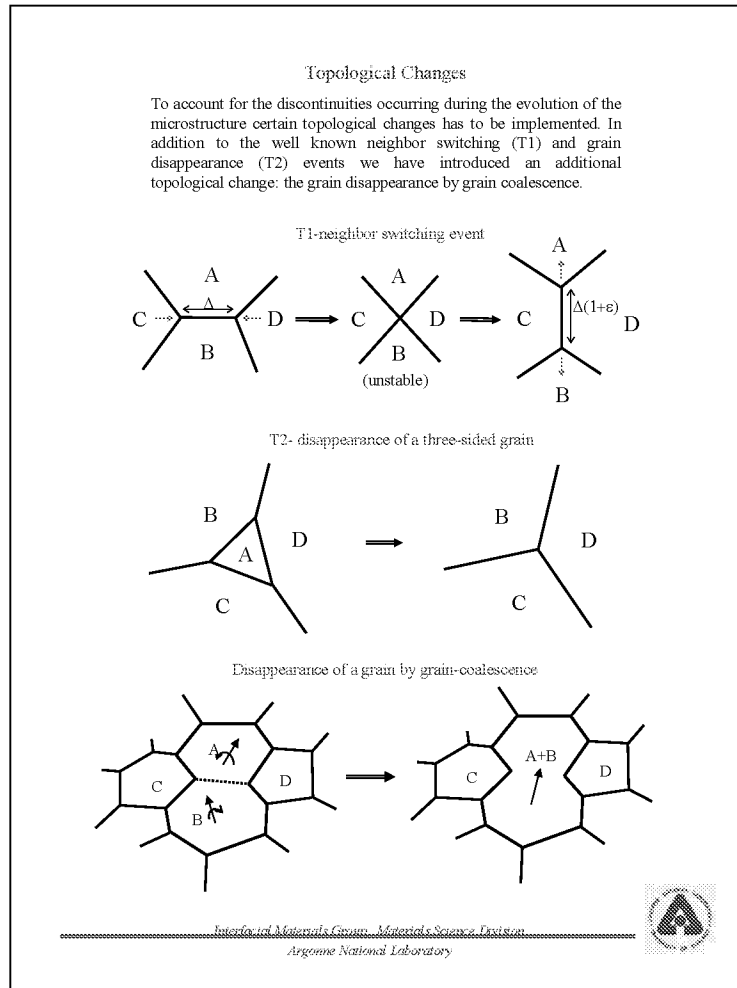


Figure 15

GRAIN GROWTH IN THE PRESENCE OF BOTH GB MIGRATION AND GRAIN ROTATION. COMPARISON BETWEEN ATOMISTIC AND MESOSCALE SIMULATION OF A 25 GRAIN SYSTEM

Here are shown side by side a few snapshots of the evolving microstructure. These are obtained from MD and mesoscale simulations. The parameters listed below and characterizing the mesoscale model were extracted from MD simulations:

$$\gamma_{\max} = 1.01 \text{ J m}^{-1}; m_{\max} = 9.27 \times 10^{-8} \text{ m}^4/(\text{Js}); R_0 = 14 \text{ nm}; R_c = 3.2 \text{ nm}; \eta = (R_c/R_0)^2 = 0.05$$

initial microstructure, $t=0.0 \text{ ns}$

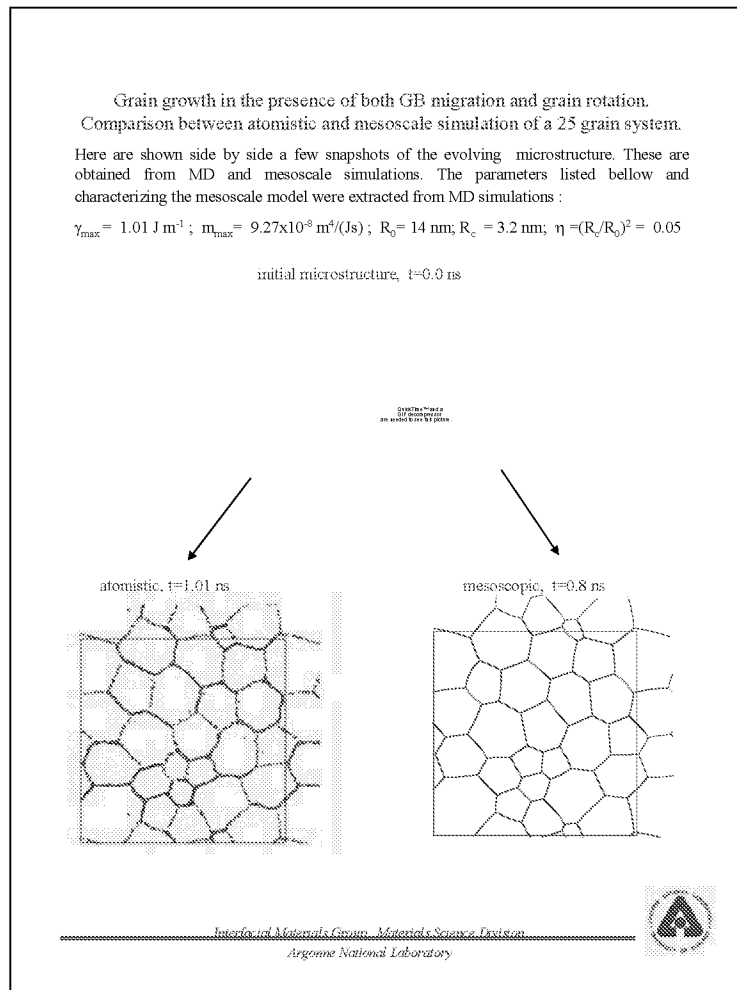


Figure 16

ATOMISTIC AND MESOSCOPIC

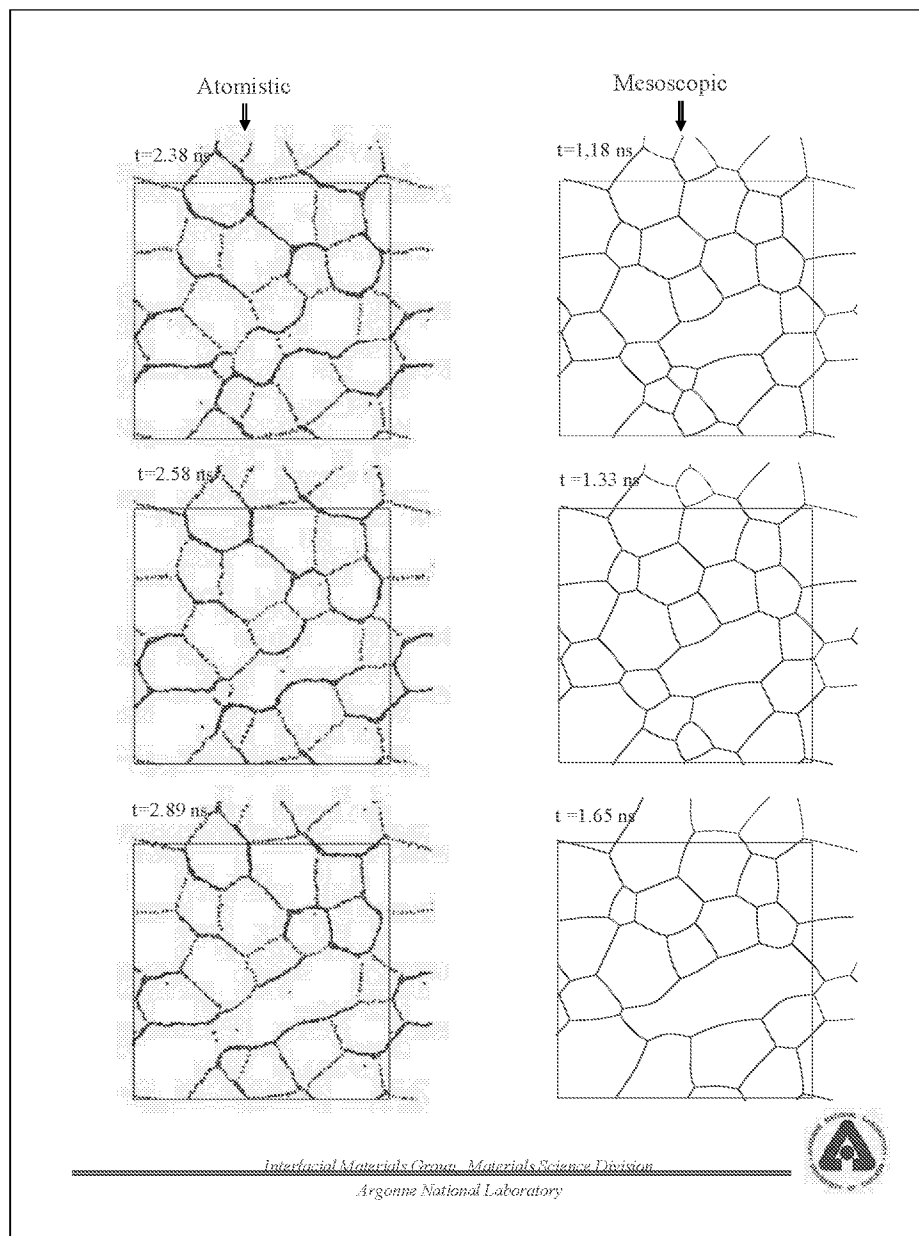


Figure 17

VALIDATION OF GRAIN GROWTH SIMULATIONS BASED ON VARIATIONAL FUNCTIONAL FOR THE DISSIPATED POWER.

Grain growth study in the presence of GB migration only:

1. Isotropic GBs
2. Anisotropic GBs

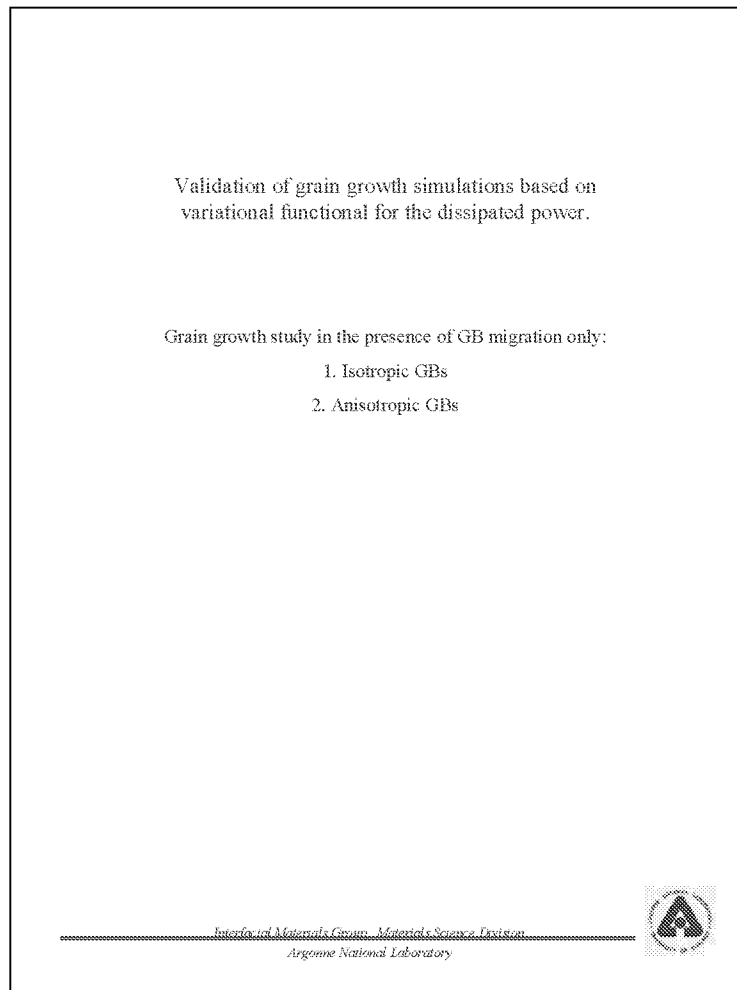


Figure 18

GROWTH LAW IN THE PRESENCE OF GB MIGRATION ONLY

(D. Moldovan *et al.*, Phil. Mag. A, 2002 (in press))

The kinetics of the growth process is characterized by the growth law. The average grain area is plotted as a function of time for both the isotropic and anisotropic systems. After some initial time the two systems reach the scaling regime, showing linearity in the long-time behaviour which is characterized by a grain-growth exponent n , that is, $A(t) \sim t^n$. Specifically for the isotropic system the mean grain area increases linearly with time (i.e. $n=1.0$) while for the anisotropic system we obtain $n=0.71$.

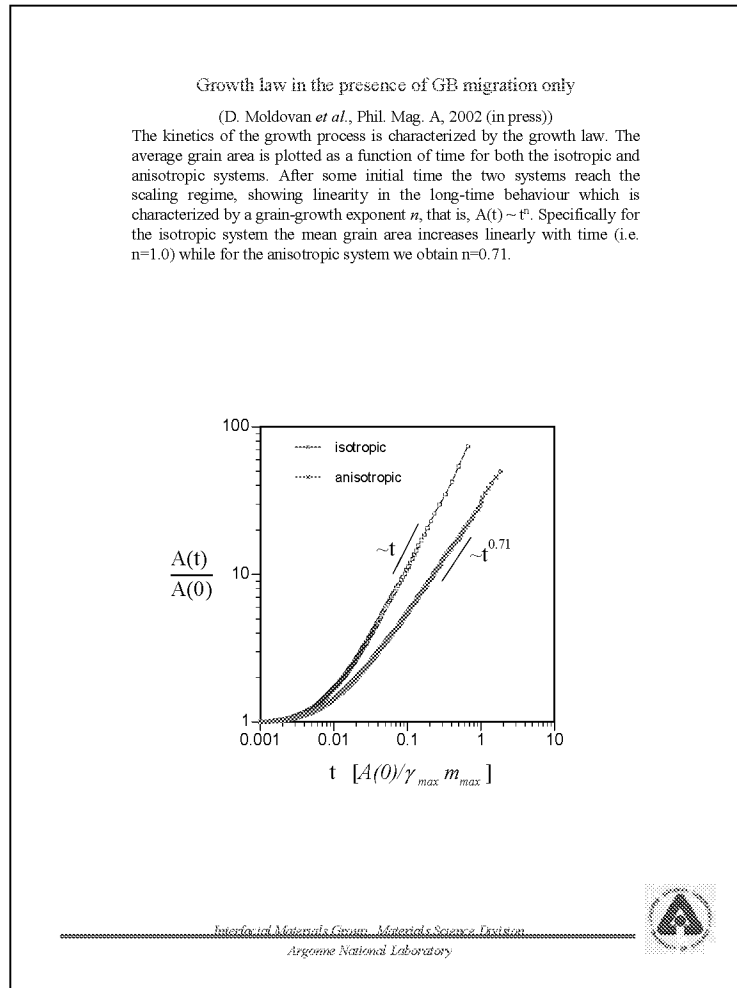


Figure 19

GRAIN GROWTH CHANGES THE FRACTION OF LOW-ANGLE AND HIGH-ANGLE GBS

The fraction of low-angle and high-angle GBs is being modified during growth. This is best characterized by the misorientation-angle distribution function, which basically gives the fraction of the total number of GBs with a given misorientation. The increase of the fraction of small-angle (low-energy, low-mobility) boundaries in the system explains the lower growth-law exponent for the anisotropic system compared with the isotropic case. This is mainly because the average driving force, proportional to $\langle\gamma(t)\rangle/\langle R(t)\rangle$, decreases gradually with time.

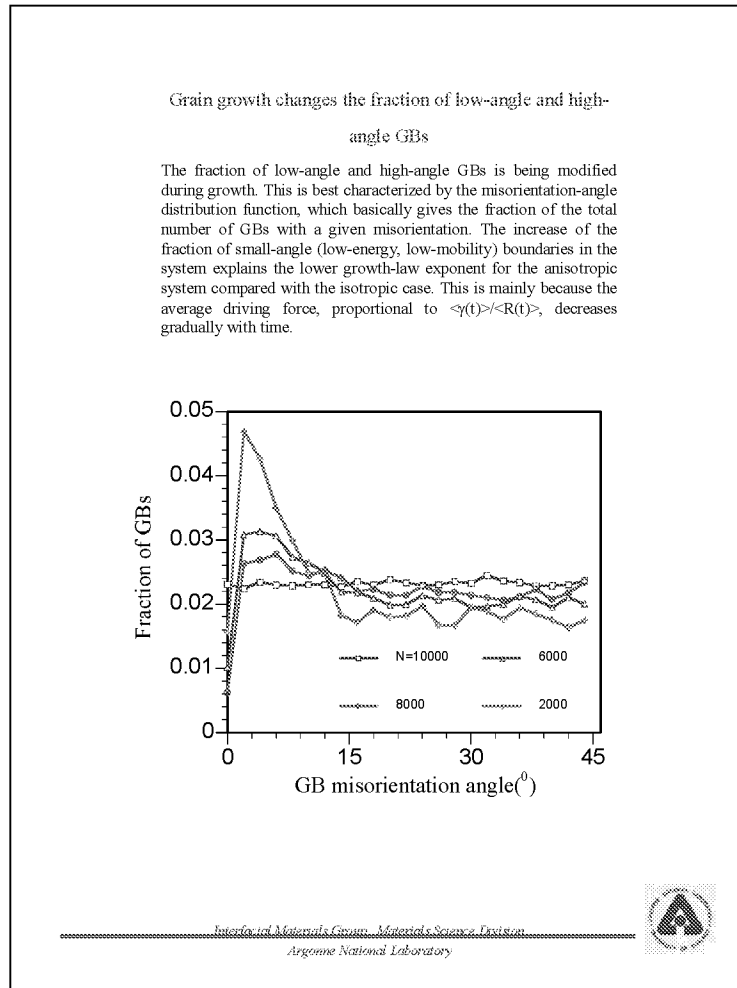


Figure 20

GRAIN-SIZE DISTRIBUTION FUNCTIONS

The grain-size distribution functions for the isotropic and anisotropic systems averaged over a few configurations in the scaling regime are compared with the fitted log-normal distribution and the theoretical distribution functions of Hillert and Louat. It can be seen that both distributions obtained from simulations the cut-off value of the reduced grain size is about $x_c = 2.2$. Moreover the shapes and the positions of the peaks are nearly the same for both the isotropic and the anisotropic systems. At small grain sizes they follow closely the Hillert's distribution whereas at large grain sizes they decrease less steeply and come close to Louat's distribution.

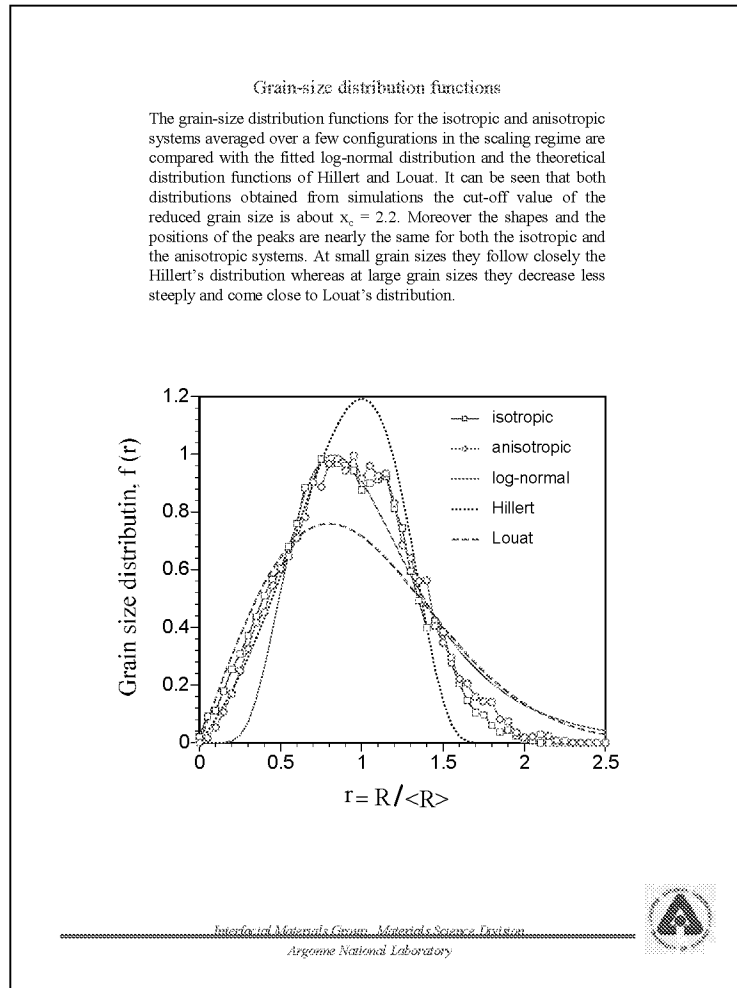


Figure 21

THE EFFECT OF GB DISCRETISATION ON THE TRIPLE-POINT ANGLE DISTRIBUTION FUNCTION

For an isotropic system it is well known that the triple-point angles are all equal to 120° , and this value is predicted by the Herring relation (given at the bottom of this page). However in our simulations with discretized GBs the adherence to Herring relation depends on the degree of discretization of each GB. The ability of each GB to assume a curved configuration depends on the number of boundary nodes along each boundary. The effect of the number of boundary nodes on the triple-point equilibrium angles can be understood best by plotting the triple-point distribution for systems with various numbers of boundary nodes. For the isotropic case the deviation from 120° is a measure of the effect of the degree of boundary discretization on the triple point-equilibrium condition. According to the Herring relation in the anisotropic system the triple-point angles may be substantially different from 120° . However, the extent to which the Herring relation is obeyed can be established by plotting the triple-point angle-deviation distribution function.

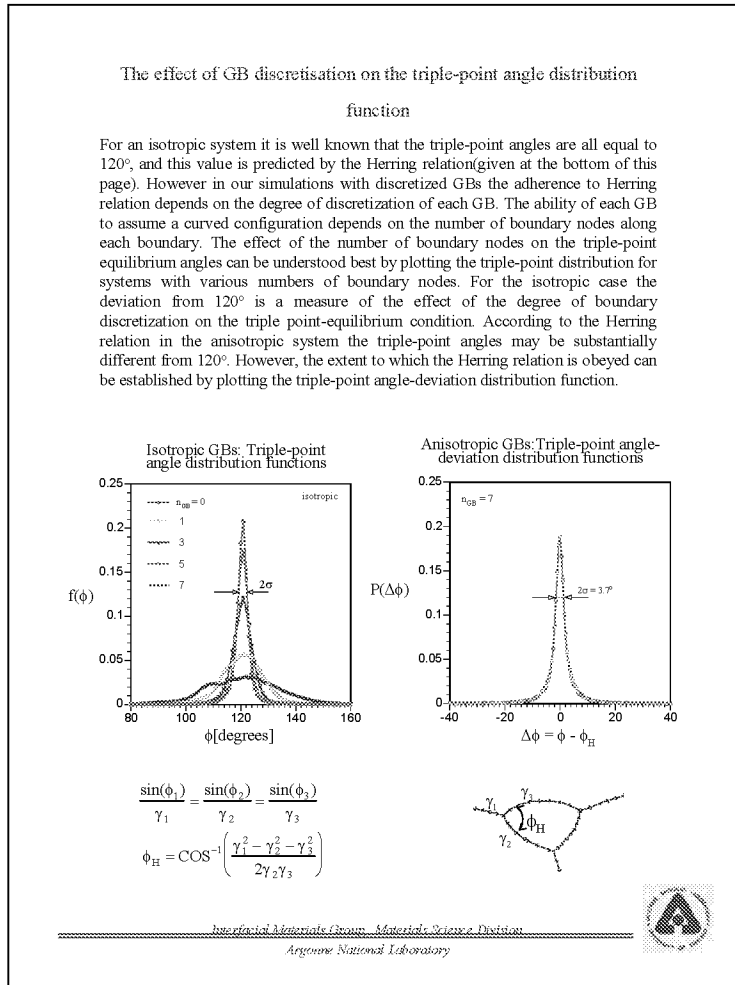


Figure 22

GROWTH LAW IN THE PRESENCE OF GRAIN ROTATION ONLY

The effect of the grain rotation on the kinetics of grain growth are best revealed by investigating the time evolution of the average grain area. To emphasize the differences in growth the results obtained for $\eta = \infty$ (grain rotation only) are analyzed. Our simulations show that the growth exponent n in the presence of grain rotation only is smaller than in the presence of GB migration only. Moreover the growth exponent depends on the actual grain size dependence of the grain rotational mobility considered in the simulations

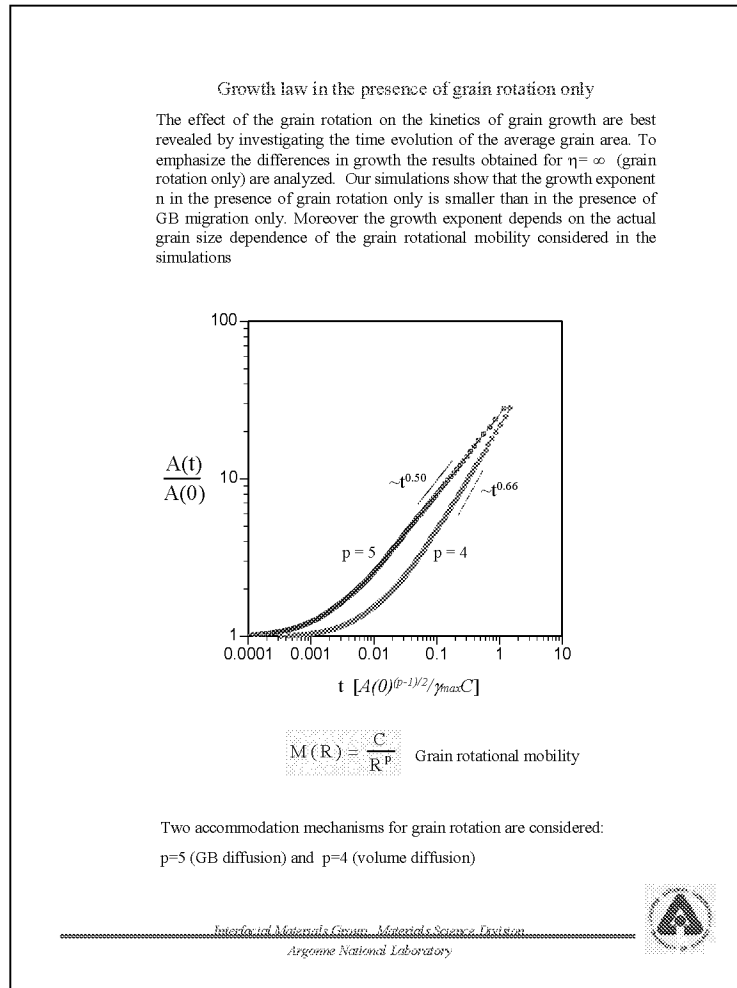


Figure 23

GRAIN-COALESCENCE CHANGES THE FRACTION OF LOW-ANGLE AND HIGH-ANGLE GBS

The fraction of low-angle and high-angle GBs is being modified during growth by grain rotation grain coalescence only. In particular one can see that there is significant decrease of the low-angle GBs fraction.

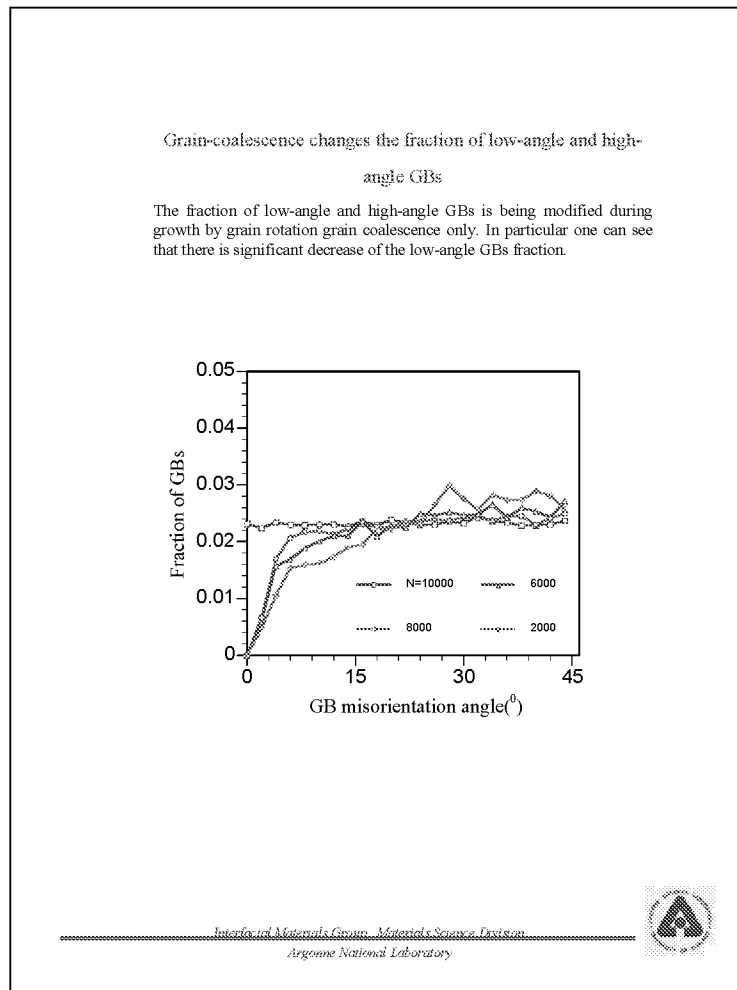


Figure 24

**GRAIN GROWTH IN THE PRESENCE OF
BOTH GB MIGRATION AND GRAIN ROTATION.**

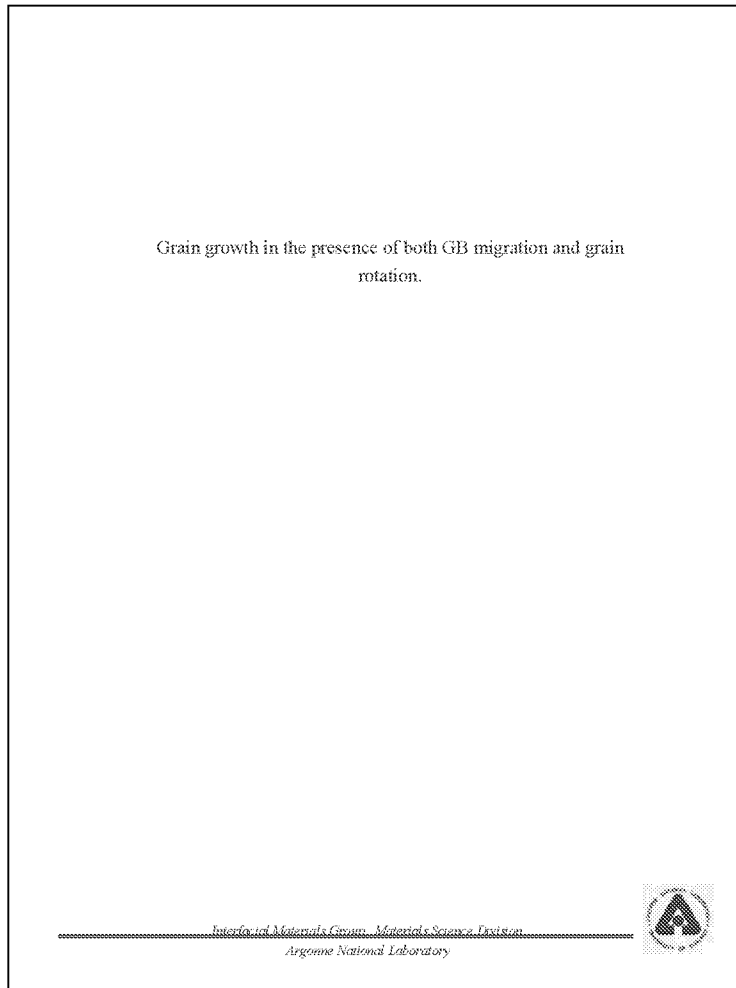


Figure 25

GROWTH LAW IN THE PRESENCE OF BOTH GB MIGRATION AND GRAIN ROTATION (P = 5 MODEL)

The effect of the grain rotation on the kinetics of grain growth are best revealed by investigating the time evolution of the average grain area. As shown in the figures below the value of the growth exponent, n , depends on the parameter h . Specifically we find that for $\eta < 10$, the growth exponent is practically equal to $n=0.71$, which is the same as the value for the system in the presence of GB-migration only. Similarly, for $\eta > 3000$ we find $n=0.5$, i.e., the same as the value obtained in the presence of growth by grain rotation-coalescence only. In the range $10 < \eta < 3000$, n decrease smoothly from $n=0.71$ to $n=0.5$. This is the crossover regime where both growth mechanisms have comparable contribution to the growth process.

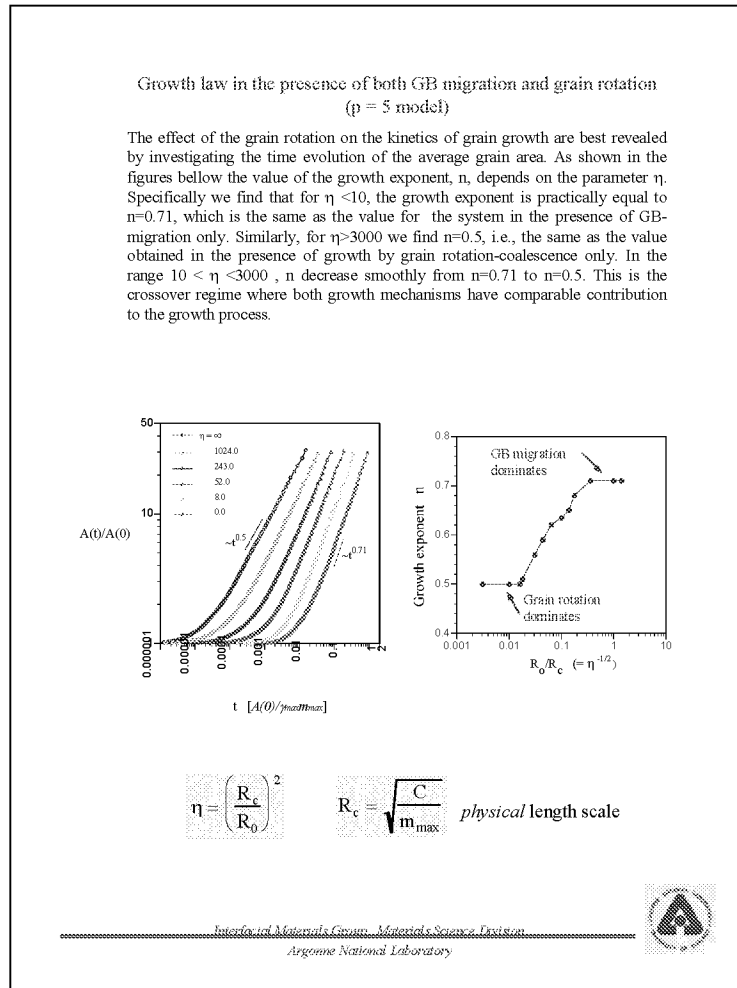


Figure 26

MISORIENTATION DISTRIBUTION FUNCTION IN THE PRESENCE OF BOTH GB MIGRATION AND GRAIN ROTATION

The fraction of low and high-angle GBs in the system evolves quite different when both GB migration and grain rotation are present. As previously shown during the growth by grain rotation-coalescence alone, the fraction of low-angle decreases significantly, while for curvature-driven GB migration alone the opposite trend is observed. In the crossover regime when migration and rotation have comparable contributions to the growth both trends are present. For example figure below shows for $\eta=250$ that initially when the grains are small, rotation-coalescence dominates and the fraction of low-angle GBs decrease. However as the average grain size increases the GB migration starts to dominate and the fraction of low-angle GBs increases.

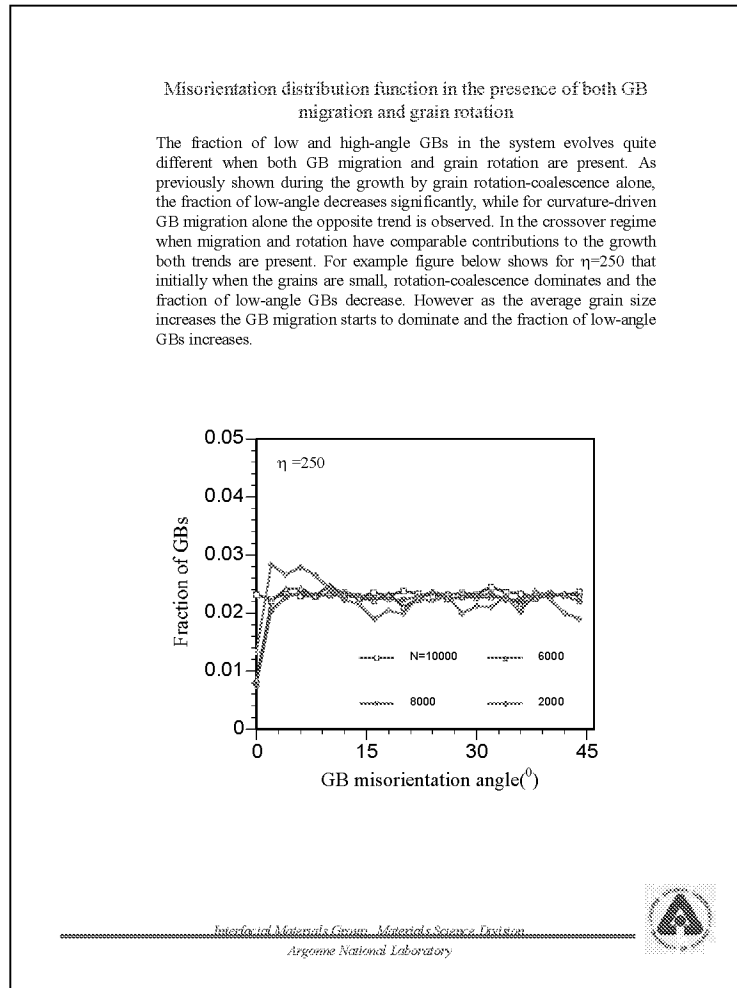


Figure 27

GRAIN SIZE DISTRIBUTION FUNCTION

The effect of the presence of both GB migration and grain rotation on the grain size distribution function is illustrated below by plotting them for systems with $h=\infty$ (grain rotation only), $\eta=250$ (migration+rotation) and $\eta=0$ (GB migration only). For comparison, we also show the log-normal distribution function fitted to the distribution in the presence of GB migration only ($\eta=0$). The shapes and peak positions are different for the three distribution functions. The distribution function for $\eta=\infty$ is narrower than for the others two systems and has a higher peak value; notice also that the distribution function drops more quickly to zero at small grain sizes, showing an apparent cut-off at $x_c=0.2$. The presence of GB migration leads to a widening of the grain-size distribution and a shift of the peak positions towards larger reduced grain sizes.

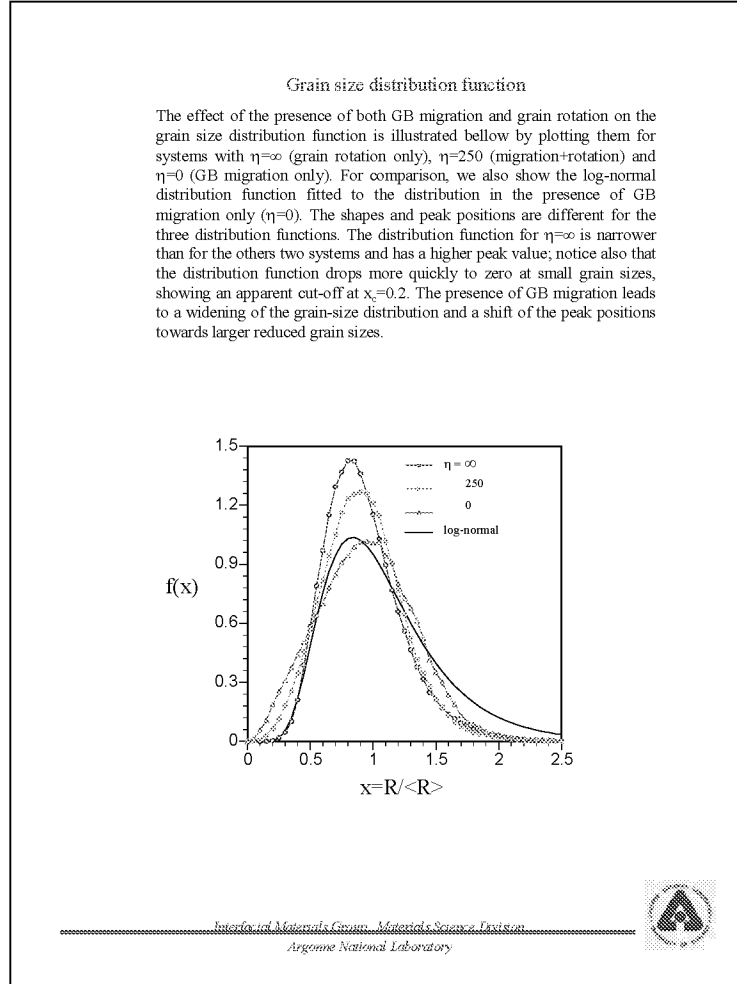


Figure 28

CONCLUSIONS

- Our MD simulations show that at least at the nanoscale grain sizes there are two equally important grain-growth processes: GB migration and grain rotation.
- We have developed a mesoscale model for grain growth which incorporates GB anisotropy and grain rotation.
- The presence of both GB migration and grain rotation introduces a physical length scale R_c into the system. If the average grain size is smaller than R_c , grain-growth is grain-rotation dominated; by contrast if the average grain size is larger than R_c , grain growth is dominated by GB migration.

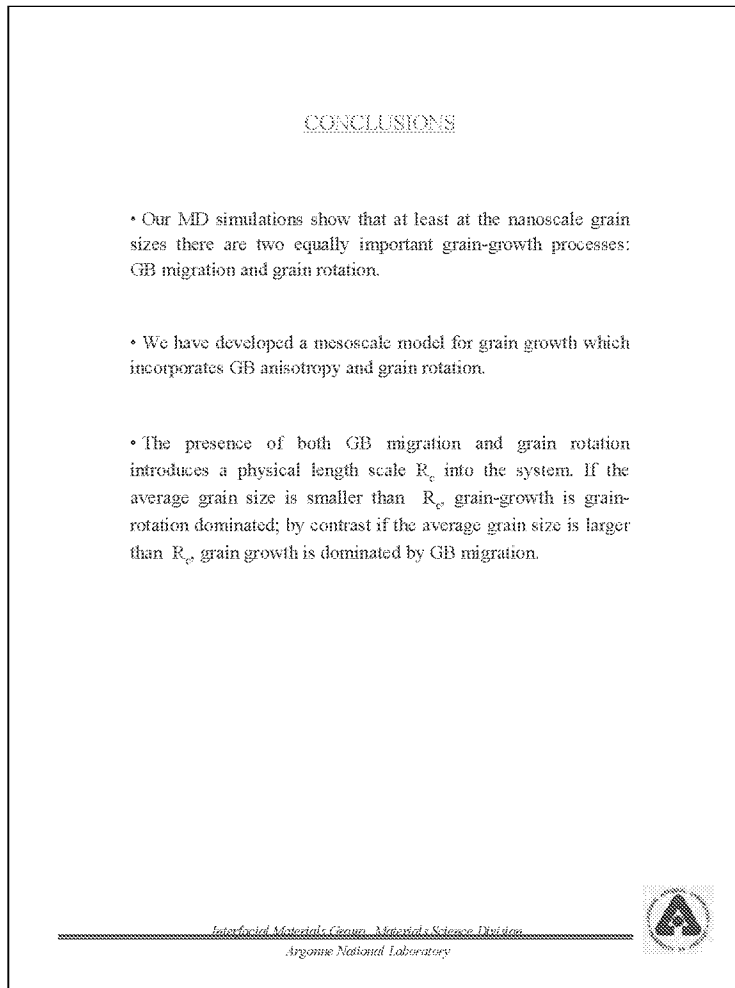


Figure 29

**Anisotropic Materials Properties:
Functional Forms for Multiscale Modeling**

Nicholas Bailey
Cornell University
Ithaca, NY

INTRODUCTION

This talk is about a particular aspect of the "parameter passing" method of multiscale modeling, namely the mathematical representation of the parameters in question. Typically the information to be passed is more than a few numbers; it's functions of several variables: orientation, stress etc. From our experience in three different contexts we have abstracted an approach to designing functional forms which is rooted in basic physics principles. The examples are (1) the stress dependence of Peierls barriers of dislocations (2) the orientation dependence of atomistically computed surface energies and (3) the orientation dependence of the etching rate of silicon by KOH.

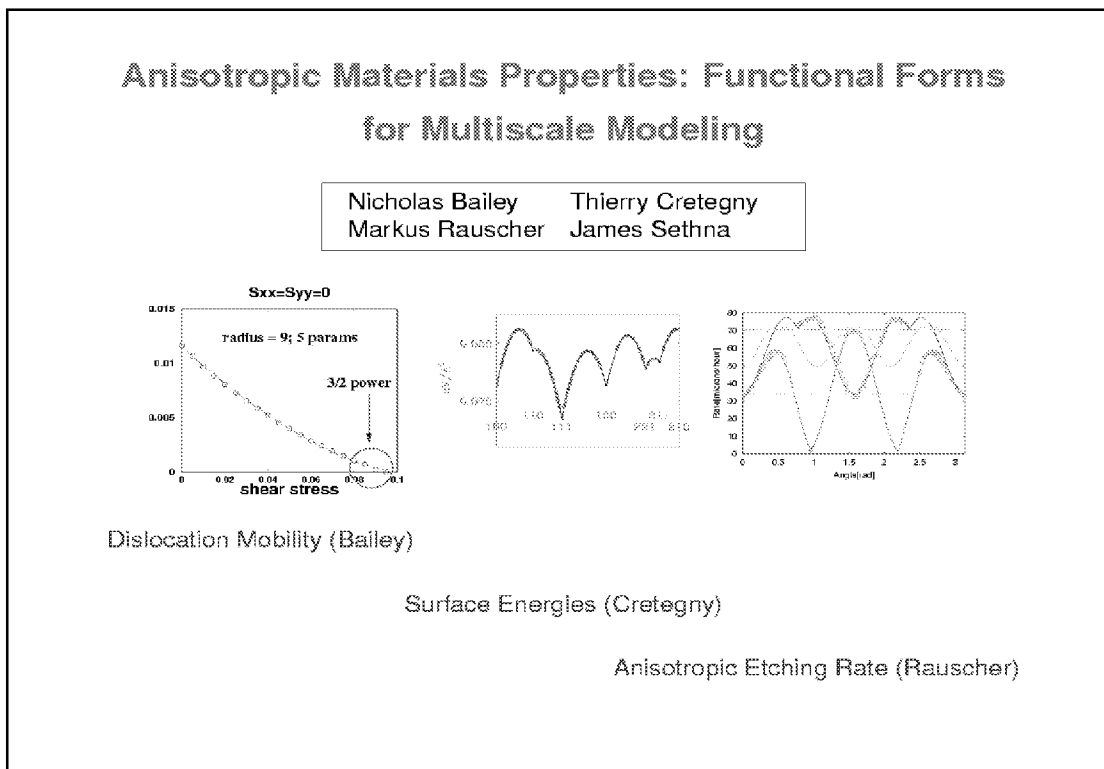


Figure 1

MULTISCALE MODELING

In multiscale modeling we have atomistic simulations dealing with the smallest scales and some combination of continuum models and defect dynamics at larger scales. Going from atomistic-based modeling to defect based modeling means changing the mathematical description of the material; defects are primary entities rather than emergent entities. We reduce the number of degrees of freedom, but also in a sense increase the precision of the description, (e.g. by requiring a defect to have an exact location). This is an artifact of the change of description but it means that care must be taken in the formulation of defect rules. The rules are those of defect dynamics: e.g. mobilities as a function of all continuum parameters. The parameters come first from geometry: There are fewer entities, but it takes more numbers to specify their geometry (five numbers for a grain boundary). Then there is the interaction of a defect with its environment: effect fields at the position of the defect (stress, electric field, concentration of hydrogen etc) but also the contribution to these fields elsewhere in the material from the defect.

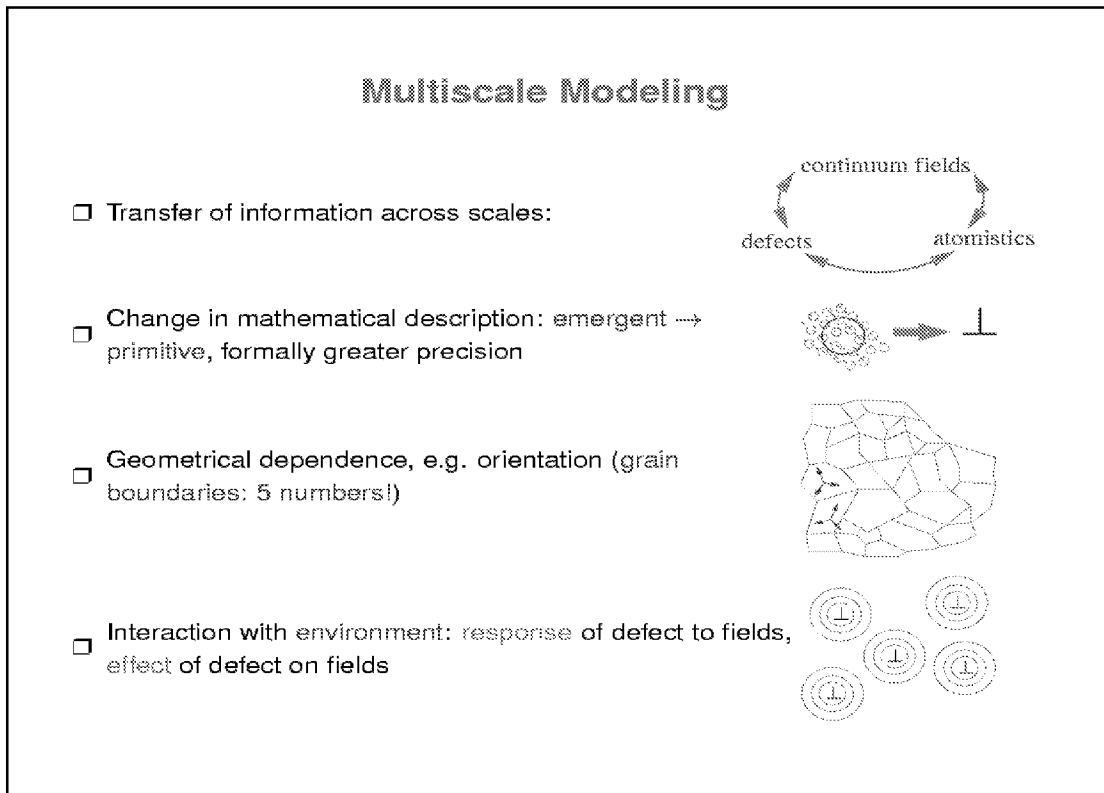


Figure 2

FUNCTIONAL FORMS PHILOSOPHY

We have a philosophy for producing functional forms. The purpose is to create functional forms requiring the fewest fitting parameters, which can be fit with the fewest data points, given that there are typically many independent variables. There are five ingredients of the philosophy. Symmetry that is known to be present in the data, such as crystal symmetry (e.g. cubic), must be built into the functional forms. The same goes with singularities which are known to be in the data, such as cusps---a naïve approach to fitting data would be to use an analytic expansion, but that would take many terms to reproduce a singularity. It makes much more sense to include this right in the functional form (compare quarter point elements in fracture modeling). To actually suggest a functional form one looks for a very simple physical model of the defect. A model too simple to be of quantitative use can often suggest appropriate functional forms. The final ingredients are subtleties in definitions (features of the continuum description that are missing from the atomistic description) and extra physics associated with singularities.

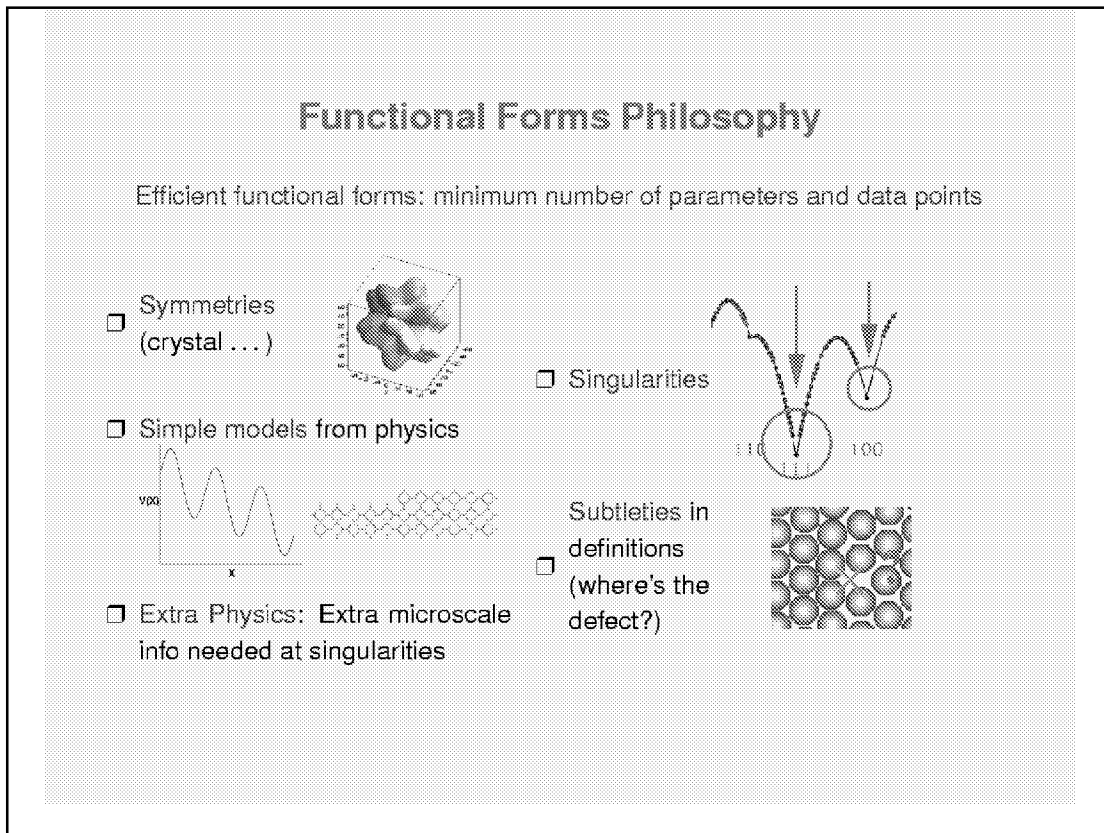


Figure 3

DISLOCATION GLIDE

My first example is the calculation of the Peierls barrier as a function of stress for 2D edge dislocations. This is connected to dislocation glide (in a 2D crystal, glide at low temperatures is given simply by thermal activation over the Peierls barrier). We use flexible boundary conditions (boundary atom positions are given by linear elasticity including multipole terms) and the Nudged Elastic Band method to compute the barrier for a range of applied stresses. The symmetry is the periodicity of the lattice, which implies a relation between the forward and backward barriers (positive and negative shear stress). The singularity is the vanishing of the barrier at the Peierls stress as a 3/2 power law (saddle-node bifurcation). See next slide for the functional form. The subtlety is the definition of the center of the dislocation, which is connected with the multipole coefficients (a change of the center can be absorbed into a change in multipole coefficients, so there is a choice, like choosing a gauge in electromagnetism). The extra physics is that as the barrier vanishes at large stress, double and multiple jumps become important (before continuous sliding happens).

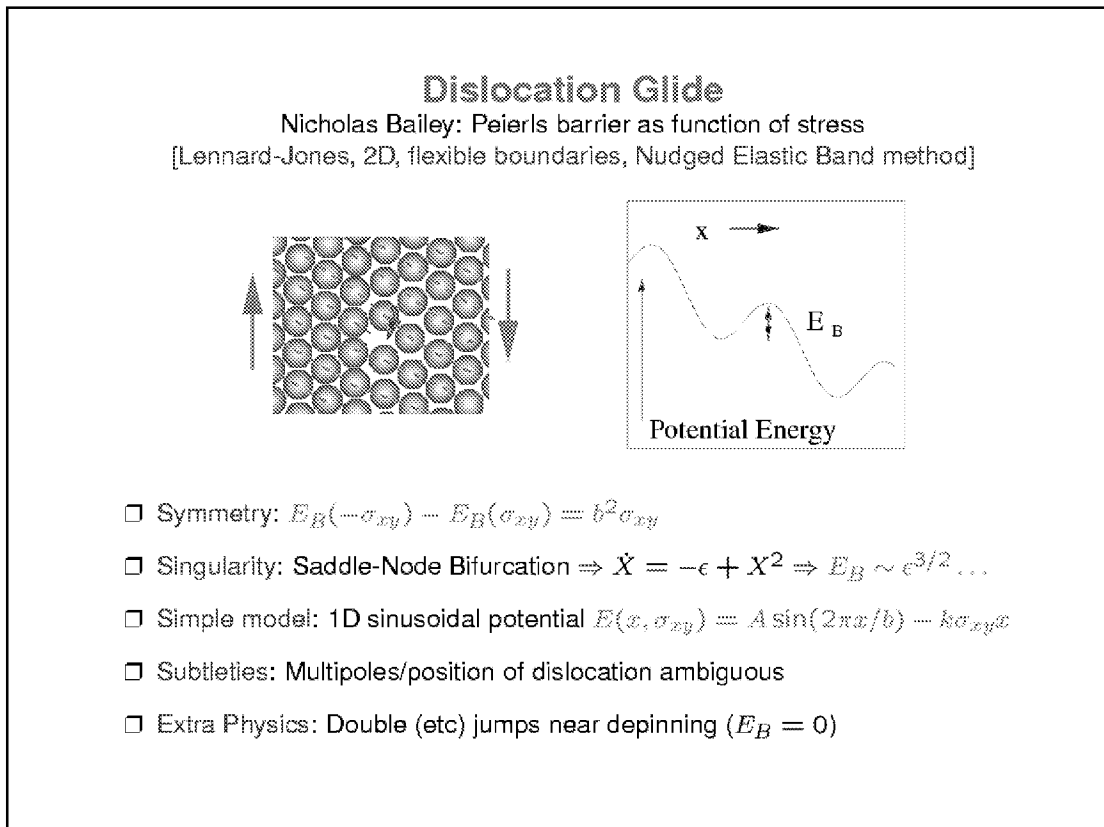


Figure 4

FUNCTIONAL FORM FOR BARRIER DATA

Here is the functional form we are using. We consider a one-dimensional potential, with sinusoidal and linear terms, for which we can calculate the barrier exactly without the analytic factor h it is exact for the sinusoidal potential. Putting in the h allows fitting to real data. Choosing h in this way maintains the symmetry and the correct form of the power law singularity. Here is one possible choice of h ; others can be imagined. Ideally only one or two terms in the h series are needed. The figure on the left shows a two parameter fit to the dependence on shear stress; on the right is a contour plot of σ_{xx} and σ_{yy} . The dependence on the other components of stress is nearly linear so we include it by making the parameters of the functional form shown here depend on those components and expand to quadratic order (so the total number of parameters is three times the number in the single-variable function).

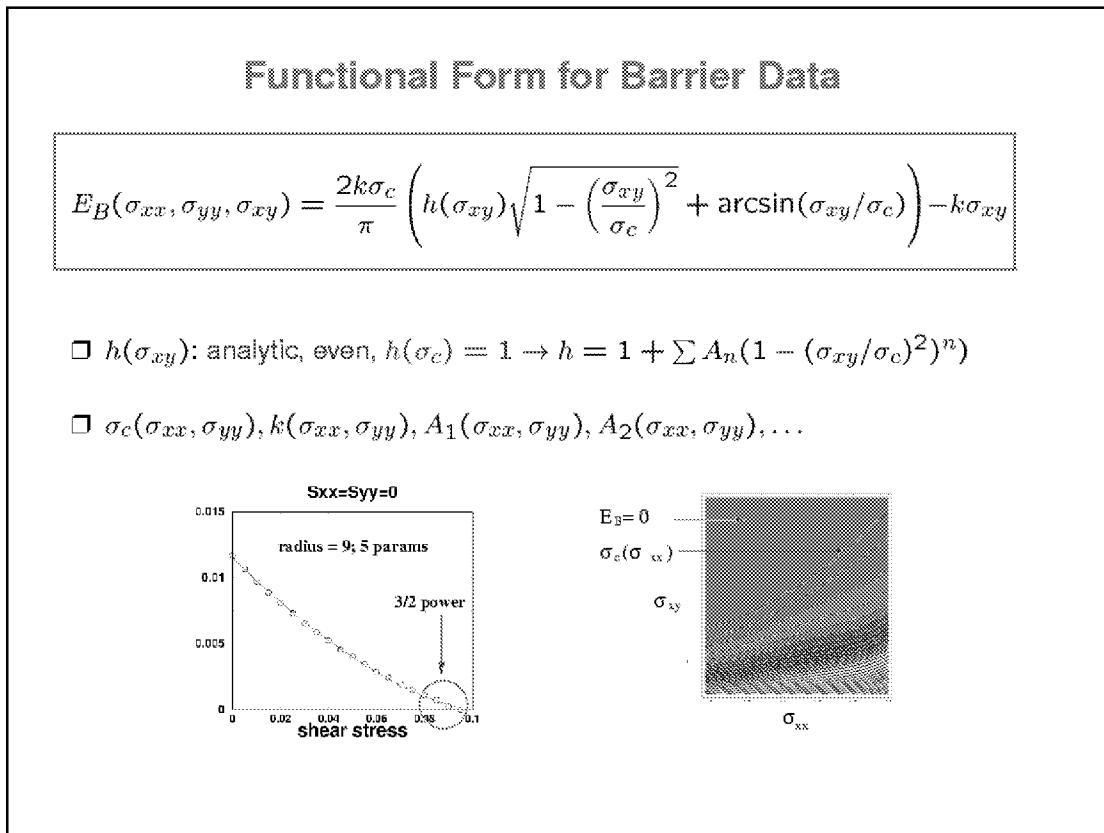


Figure 5

SURFACE PROPERTIES: NEAR EQUILIBRIUM

My second example, due to Thierry Cretegy, is about the orientation dependence of surface energies (computed from an empirical potential though they could be from an ab initio calculation). This function will be a single function of two angular variables. The symmetry in this case is cubic, so rather than the whole unit sphere we consider a triangular patch (figure on the left). Plotting energies along the indicated path gives the figure on the right. The dots are individually calculated energies; the line is a two-parameter fit to all the data in the triangular plot. Near high symmetry directions there are cusps in the surface energy (nearby surfaces are like steps on the high symmetry surface, the energy is proportional to the step density and hence the absolute value of the angle). To get a functional form we use a “broken bond model” which estimates the energy of a surface simply counting dangling bonds (ignoring relaxation of the atoms, which takes place in the actual computation). For an FCC lattice one needs only consider the cusp functions from the first and second neighbor bonds (110 and 100 directions).

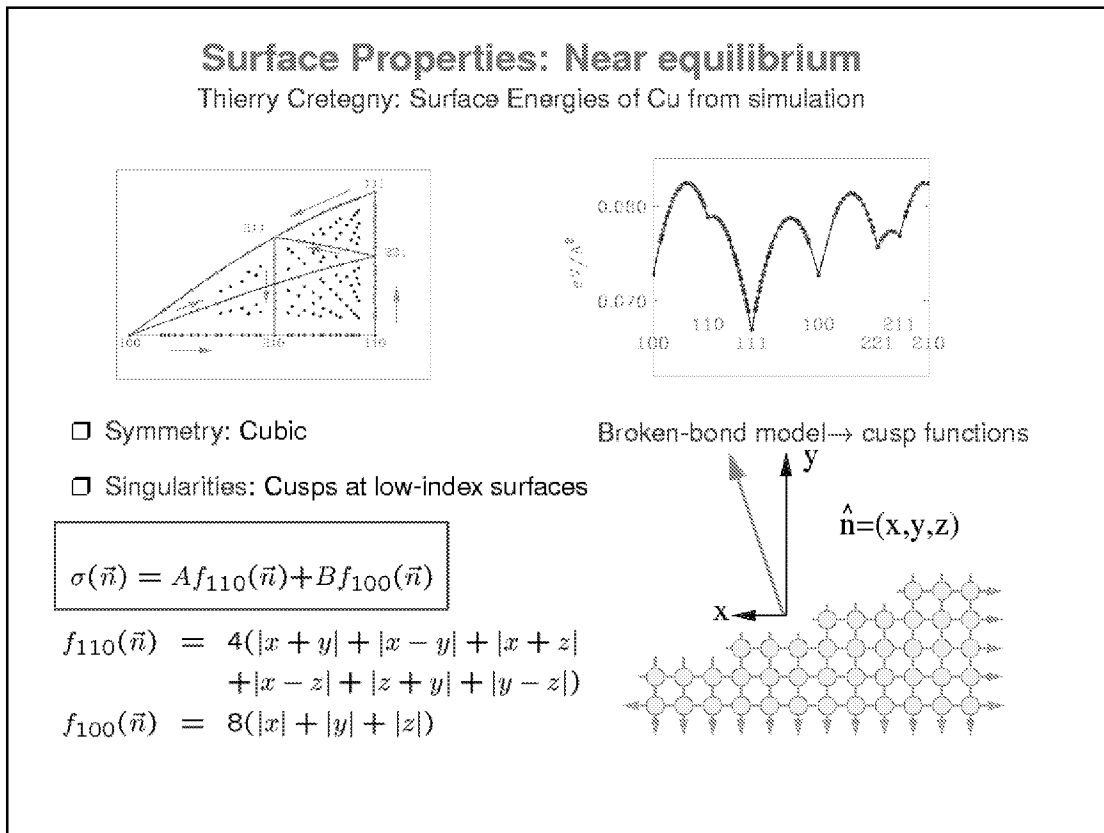


Figure 6

SURFACE ENERGIES: SUBTLETIES

The subtlety in the case of the surface energies is that not all orientations yield a stable surface. Instead the surface tends to facet into two different surfaces. However for use in multiscale modeling, or say for making a Wulff plot to find the equilibrium crystal shape, it is desirable to have a surface energy for all orientations. To do this Thierry did a constrained minimization by choosing boundary conditions such that only one step fits. Extra physics is needed for example if studying growth of crystal surfaces in a continuum model. At the singularities in this data, the mobility of the surface vanishes, which corresponds to the fact that growth of the surface requires nonlinear effects coming from island nucleation etc.

Surface Energies: Subtleties

- Subtlety: some surfaces are unstable!
 - for continuum model need all orientations
 - reconstructions, step bunching, faceting
 - prevent by only allowing one step within periodic boundary conditions

- Extra Physics:
 - Nonlinear mobility at cusps (facets have zero mobility in linear response)
 - Need nucleation of islands and pits, etc.

Figure 7

SURFACE PROPERTIES: FAR FROM EQUILIBRIUM

My last example is from Markus Rauscher and concerns modeling of experiments by Wind and Hines. They measure the etching rate of silicon by KOH within a particular crystallographic zone by fabricating a "pie" which is then cut into 1 degree wedges as shown. This creates a direct map of the etching rate within this zone (110 or 100). The modeling is to understand the faceting that occurs for certain orientations. His input was the measured rate, apart from the orientations where faceting occurs. The symmetry and singularities here are as for surface energies: silicon is cubic, and in a simple model the etching rate is proportional to the number of dangling bonds, i.e. a broken bond model again (now for the diamond lattice). As well as one cusp function (111) from the broken bond model he also added cubic harmonics (analogous to spherical harmonics but with the cubic symmetry built in). The middle figure shows the data from two different zones, along with the five parameter fit in those zones and the 111 zone. The figure on the right is a 3D plot of the fit.

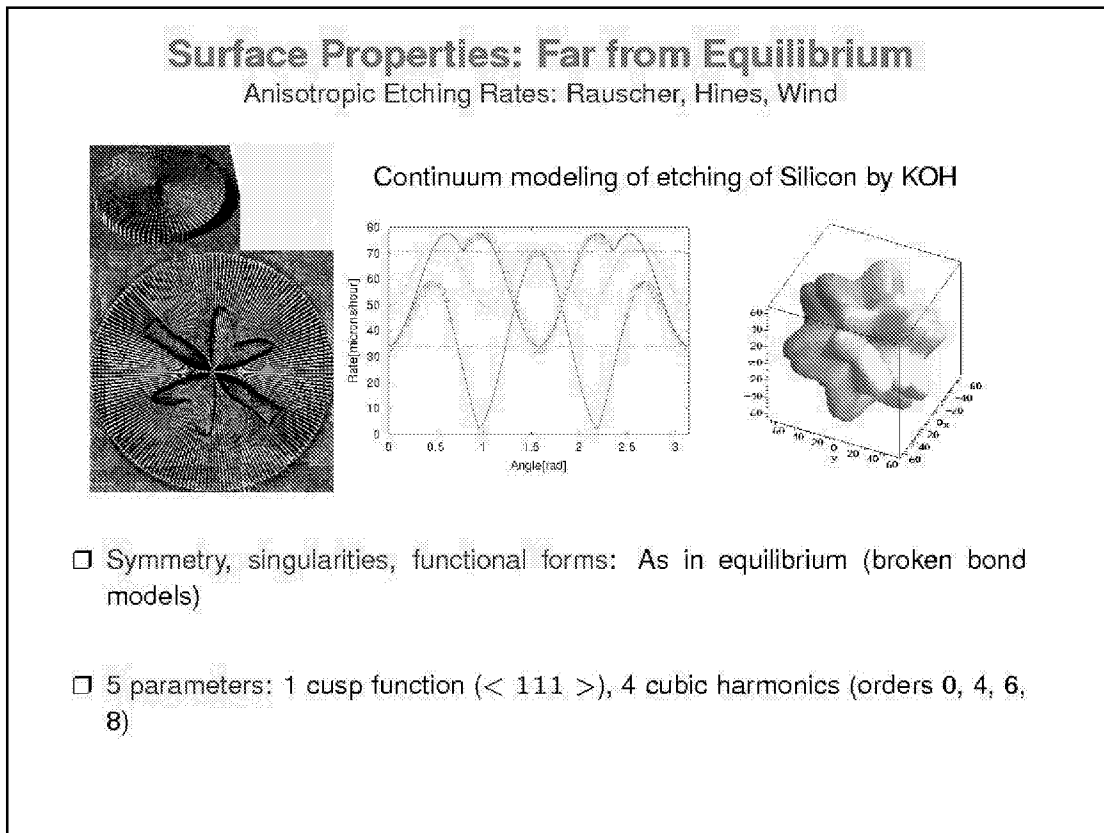


Figure 8

ETCHING SUBTLETIES

The subtlety here is very important; otherwise it might not make sense to use experimental data as input to a model whose outcome is to be compared to experiment. Because faceting appears in certain orientations, namely those near cusps as shown in the figure, the nominal measured rate there is an average over the facets and cannot be used. The data used is that corresponding to smooth surfaces and the cusps themselves. The model's purpose is to understand the faceted regions and the transition from smooth to faceted, so there is indeed a separation between the input and the output of the model. The new physics needed here arises from the fact the PDE in the continuum model is not very well behaved and tends to form its own singularities; these are related to the faceting transition; when solved numerically without special treatment the solution blows up. This can be avoided by adding some diffusion (viscosity solution), but this leads to eventually flattening rather than facets. The problem was solved by including surface tension which comes into play near regions of high curvature.

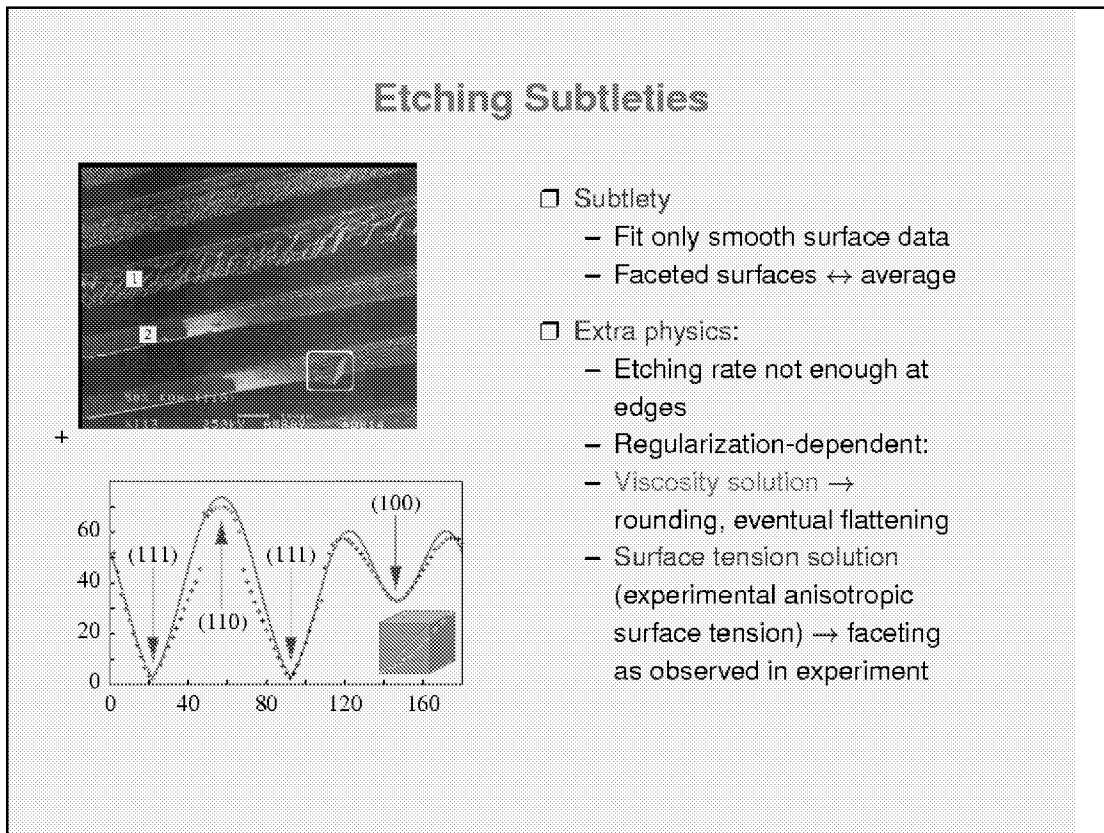


Figure 9

SUMMARY: GUIDING PRINCIPLES FOR USEFUL FUNCTIONAL FORMS

To sum up, I want to reiterate that what we are presenting is more than a recipe, it is a philosophy, a way of thinking: symmetry, singularities, simple models, subtleties and extra physics.

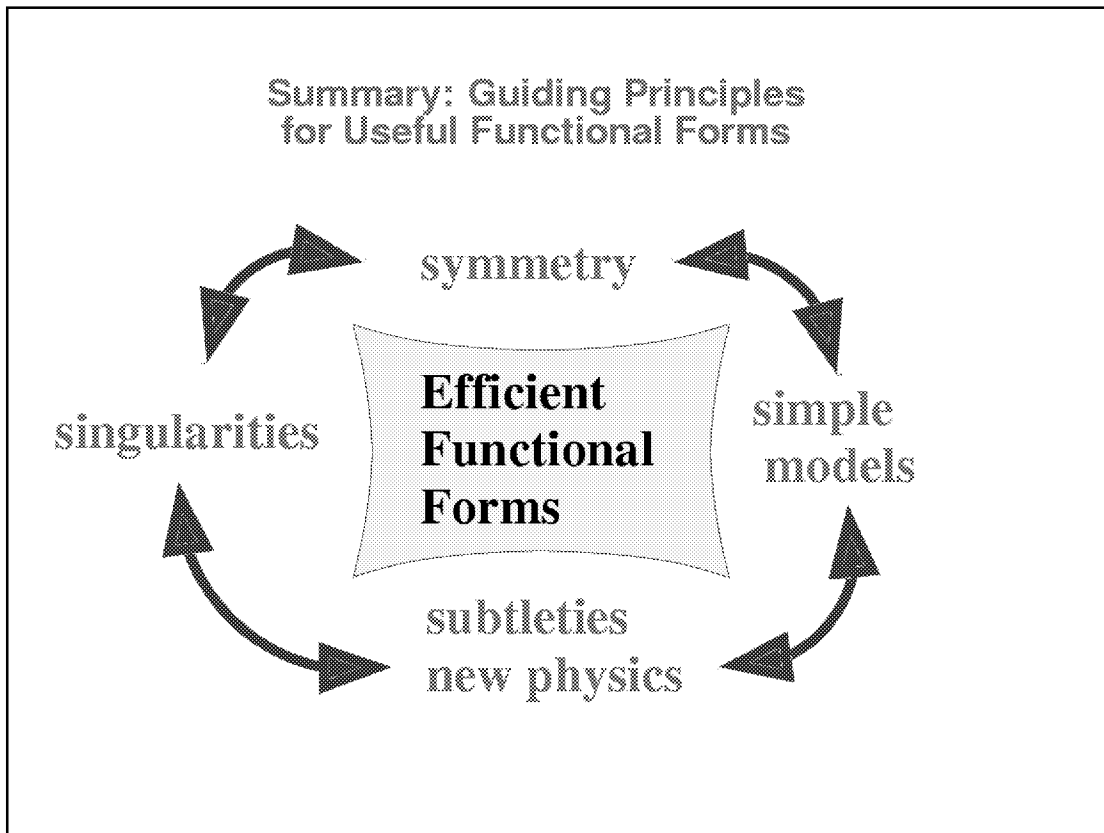


Figure 10

**Multiscale Modeling for Linking Growth, Microstructure, and
Properties of Inorganic Microporous Films**

Dion G. Vlachos
University of Delaware
Newark, DE

INTRODUCTION

The focus of this presentation is on multiscale modeling in order to link processing, microstructure, and properties of materials

Multiscale Modeling for Linking Growth, Microstructure, and Properties of Inorganic Microporous Films

Dion G. Vlachos

Department of Chemical Engineering and
Center for Catalytic Science and Technology

University of Delaware

Newark, DE 19716

vlachos@che.udel.edu
www.che.udel.edu/vlachos

Figure 1

NUCLEATION AND GROWTH OF MATERIALS

Overview of problems we study (clockwise): Growth mechanisms in chemical and physical vapor epitaxy, thin films of zeolites for separation and sensing, thin Pd films for hydrogen separation, and pattern formation by self-regulation routes

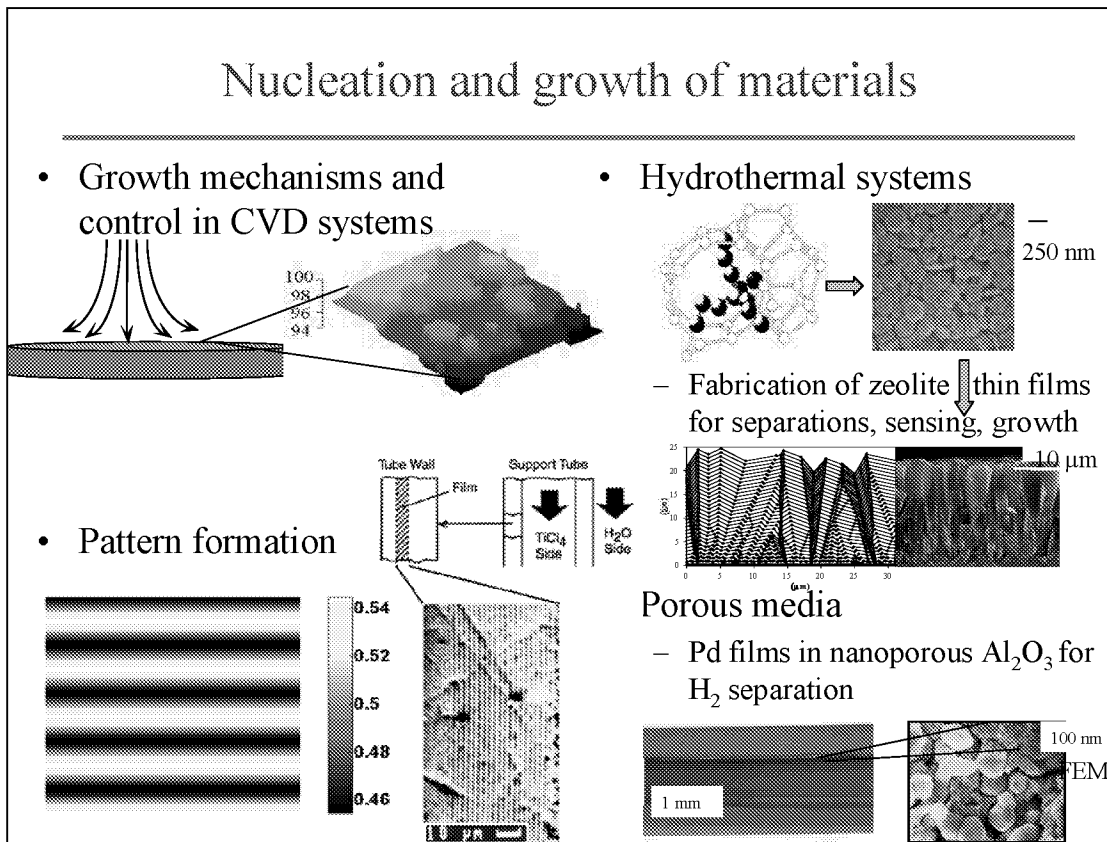


Figure 2

CHEMICAL REACTORS EXHIBIT MULTIPLE SCALES

Schematic of multiple length scales in a deposition process. Three broad scales can be distinguished: The reactor scale, where the continuum approximation is valid, the mesoscale where the microscopic mechanisms control growth mode and crystal morphology, and the quantum scale. Quantum scale controls intermolecular forces which in turn affect nucleation and the kinetics of diffusion and surface reactions. Phenomena at each scale are coupled in a two-way manner. From a controls point of view, solving at least the reactor and mesoscale models simultaneously is necessary.

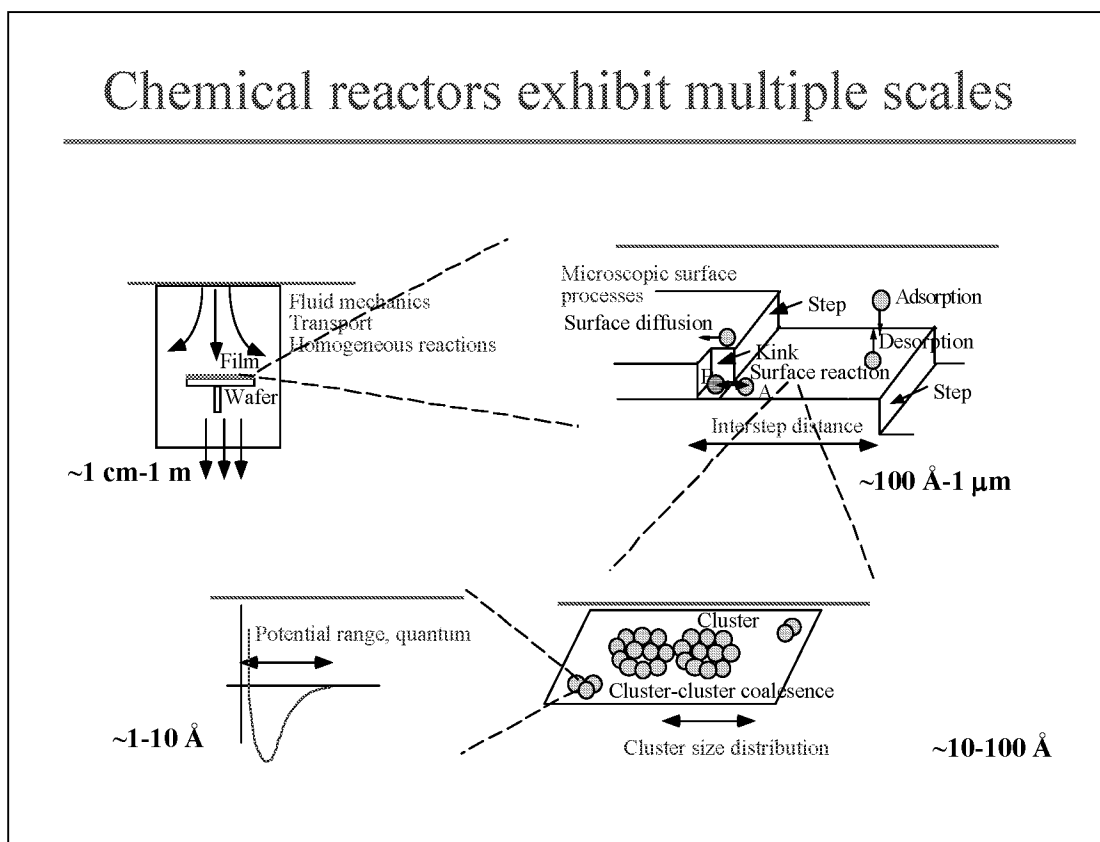


Figure 3

OVERALL MULTISCALE MODELING APPROACH

Overall approach we undertake. First, three levels of models are bridged together: chemistry from semi-empirical methods (especially for large reaction mechanisms) or DFT, kinetic MC for the surface, and continuum models for the reactor. Through semi-empirical parametrization or lookup tables, we decouple the quantum and mesoscale simulations. Meso- and macro-scale models are fully coupled. Methods for achieving this are described in Raimondeau and Vlachos, Chem. Eng. J. (accepted).

In a number of problems, kinetic MC is inadequate to capture realistic length scales. Mathematically rigorous coarse-grained models are then derived from the master equation in order to replace MC in multiscale frameworks. We present an example of this approach in this talk.

Finally, control of microstructure of materials demands reduction of these complex models to a small number of ODEs. An example is discussed in this talk.

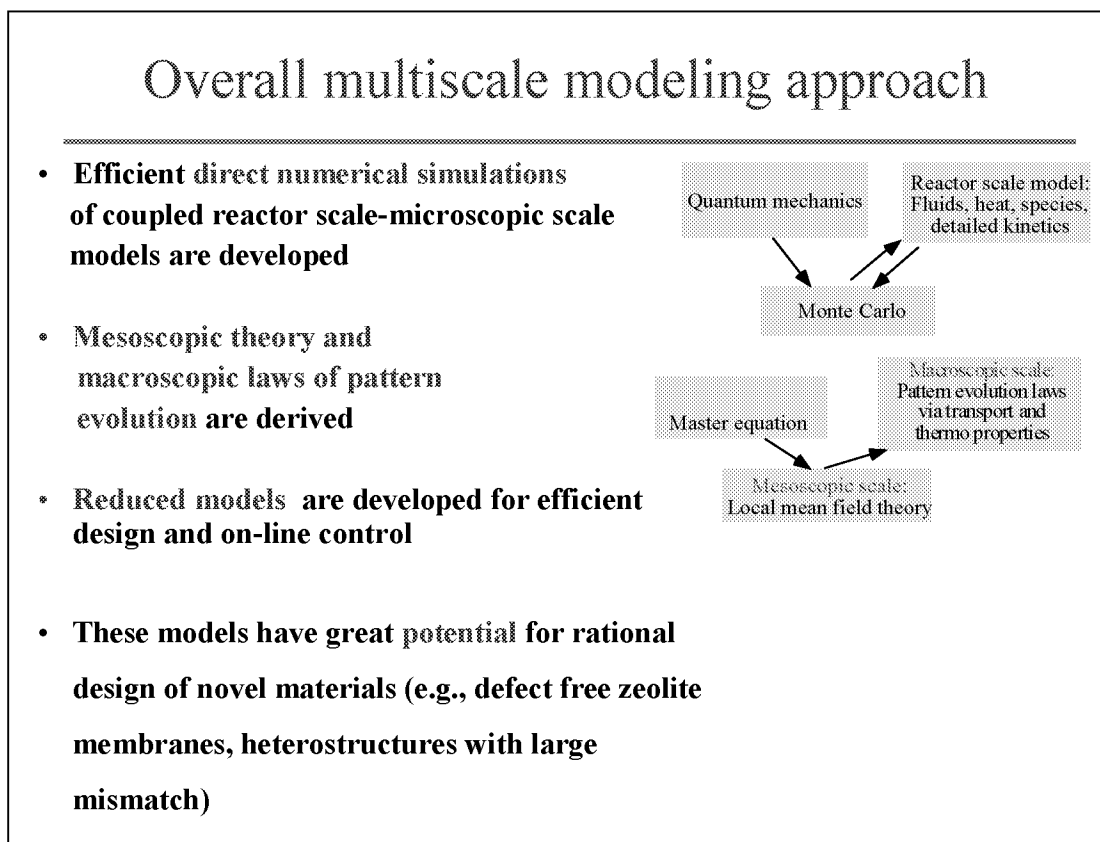


Figure 4

FULL COUPLING BETWEEN FLUID (MACRO) AND SURFACE (MESO) SCALES

The first example discussed is a simple model system that illustrates the coupling of meso and macro scales in a vertical reactor. Spatially average rates are computed at each time step of MC and fed into the boundary conditions of the continuum model, which in turn provides the concentrations at the gas-solid interface needed in the MC.

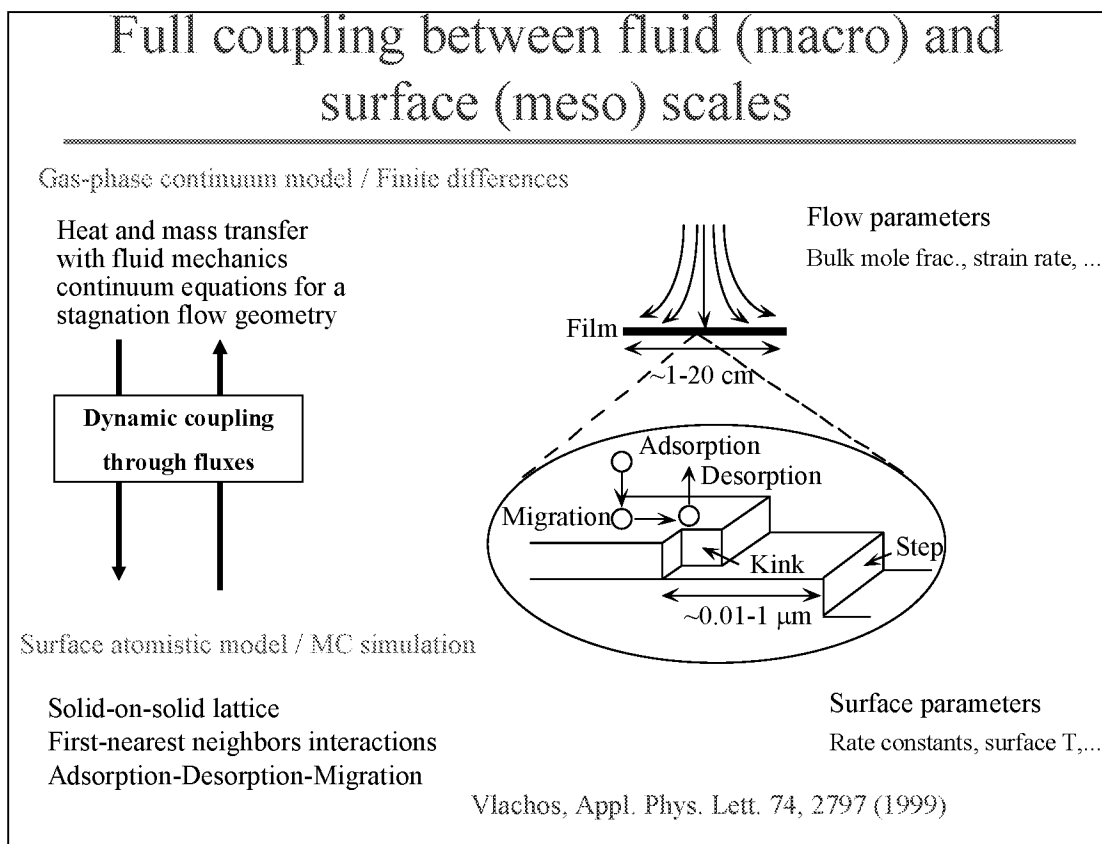


Figure 5

MACROSCOPIC PARAMETERS CONTROL MICROSTRUCTURE

Example of coupled, multiscale growth simulations. These graphs show the effect of substrate temperature on growth rate and microroughness at three strain rates (proportional to flow rates). At high temperatures step flow is observed, whereas at lower temperatures, 2D nucleation dominates giving rise to increased roughness. These simulations provide for the first time insight into the role of macroscopic, experimentally accessible quantities, such as temperature and flow rate, into the transition from one growth mode to the other (demarcated by open circles).

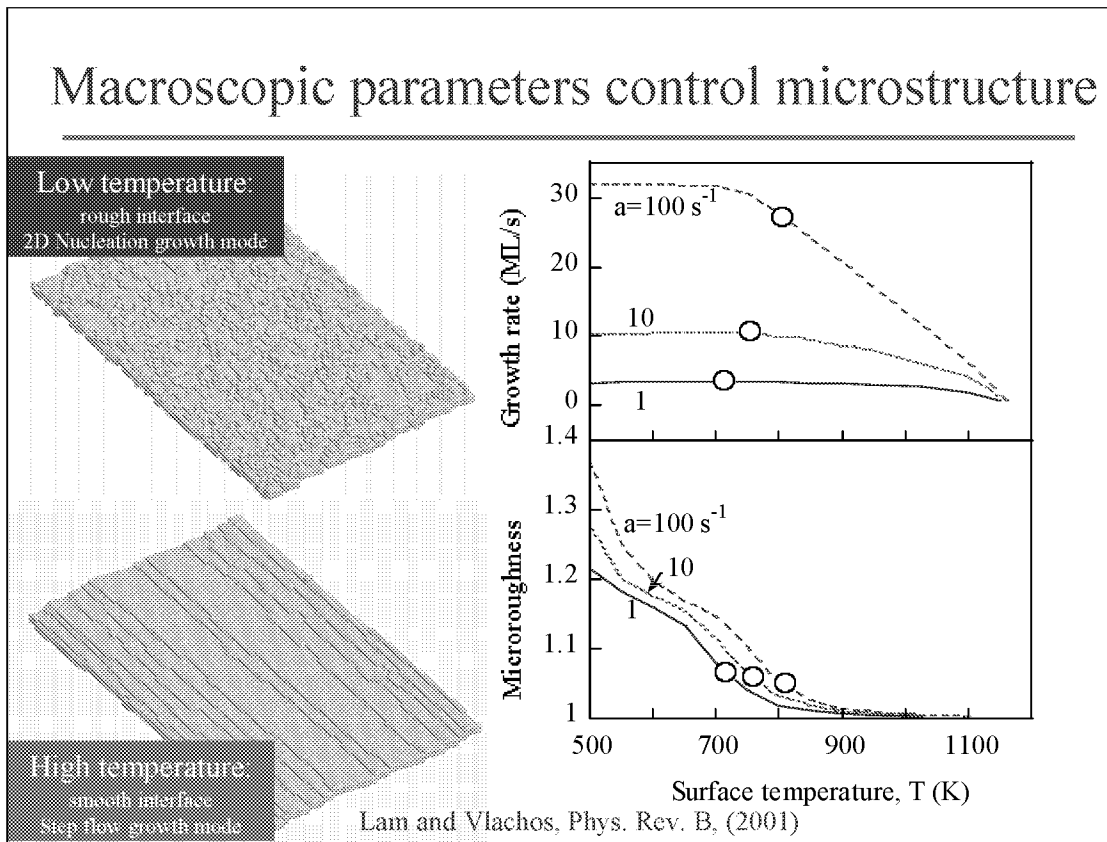


Figure 6

PROPER ORTHOGONAL DECOMPOSITION (POD)

Model reduction is essential from an engineering perspective in order to develop efficient models that can be used for on-line control. The POD method is used for fluid phase and surface data reduction obtained from hybrid, multiscale simulations.

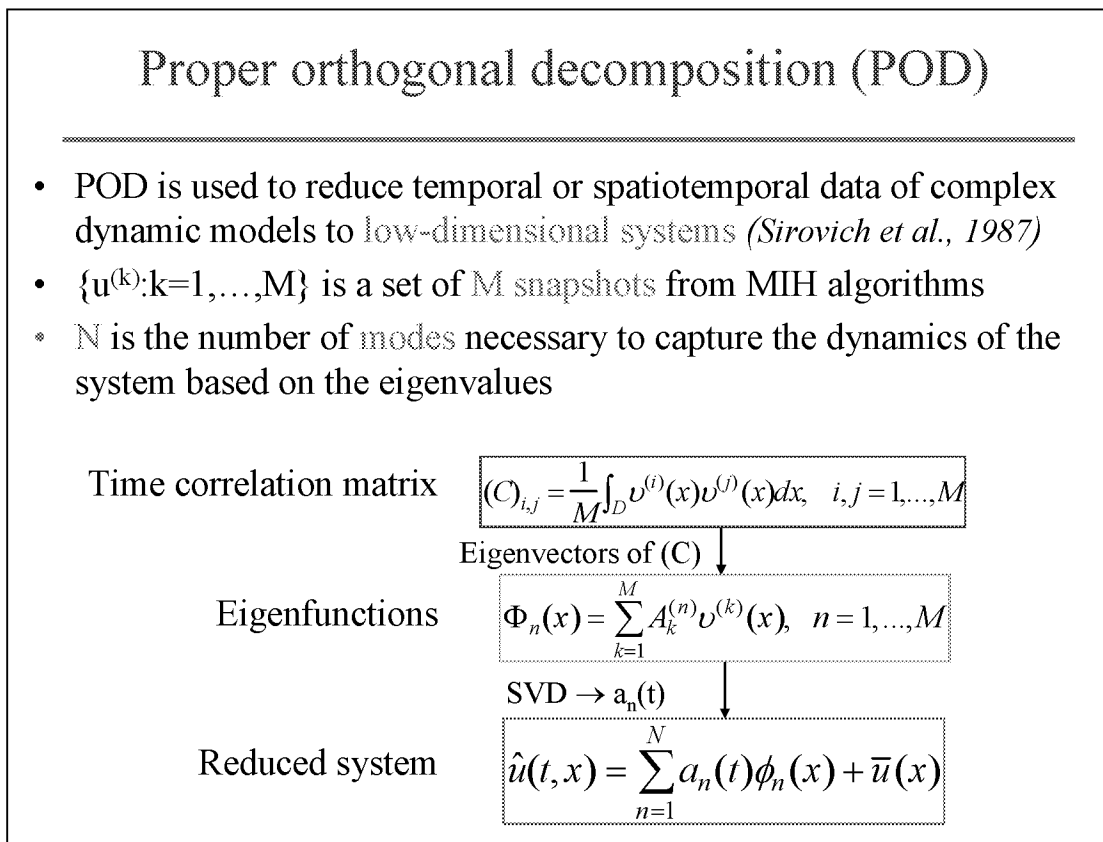


Figure 7

RESULTS OF MODEL REDUCTION

Example of model reduction. A step change in the precursor concentration is introduced, and the dynamics of the system is monitored. The reduced model (~6 ODEs) does an excellent job for the fluid phase. Surface morphology is also well captured, but some smearing does occur. DNS stands for direct numerical simulations and POD represents the reduced model.

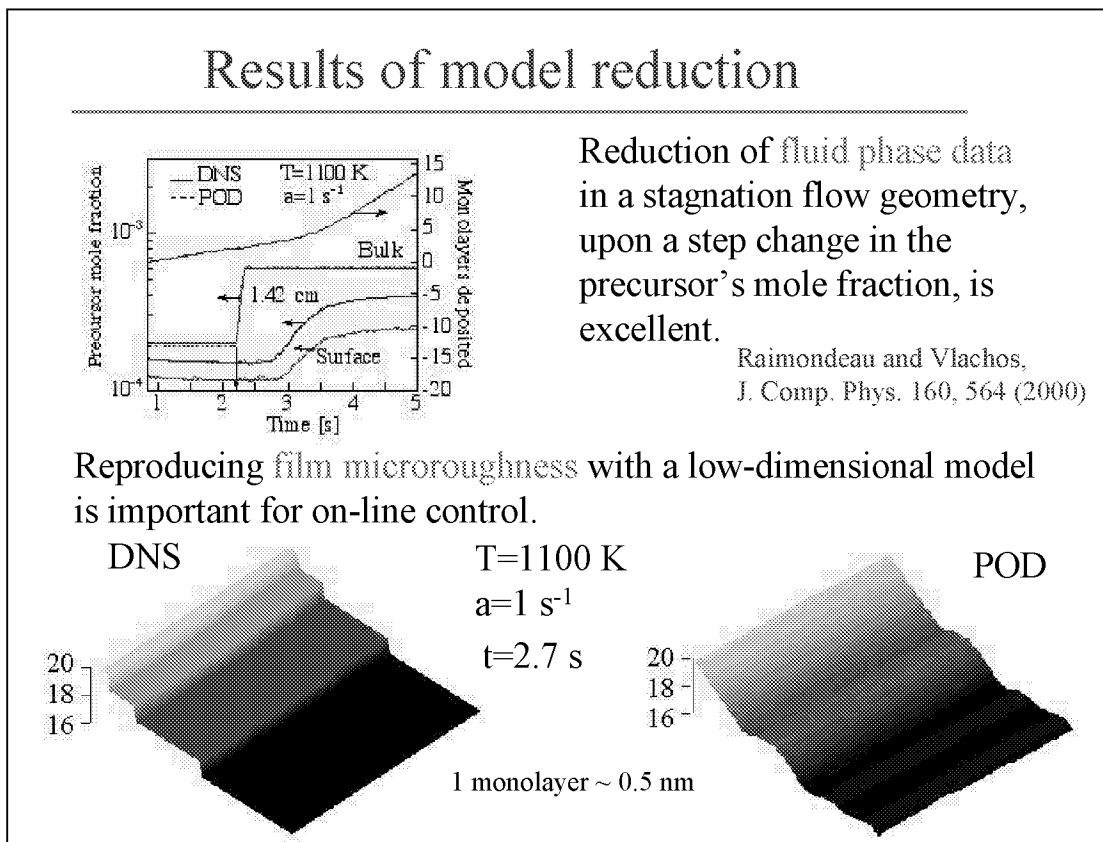


Figure 8

RESULTS OF MODEL REDUCTION (CONTINUED)

Example of model reduction at low temperatures. Now, 2D nucleation prevails. The reduction is again reasonable. The bottom right graph shows the average microroughness as a function of time. Upon introduction of a step change in the precursor, a new quasi-steady state is attained. The reduced model captures this information reasonably well, despite the fact that it was not directly trained for this task. Such data can be collected experimentally by STM or AFM. The performance of the reduced model indicates that it would be possible to use a STM or AFM tip as a sensor and reduced models derived from first principles, multiscale simulations, for on-line control of microstructure.

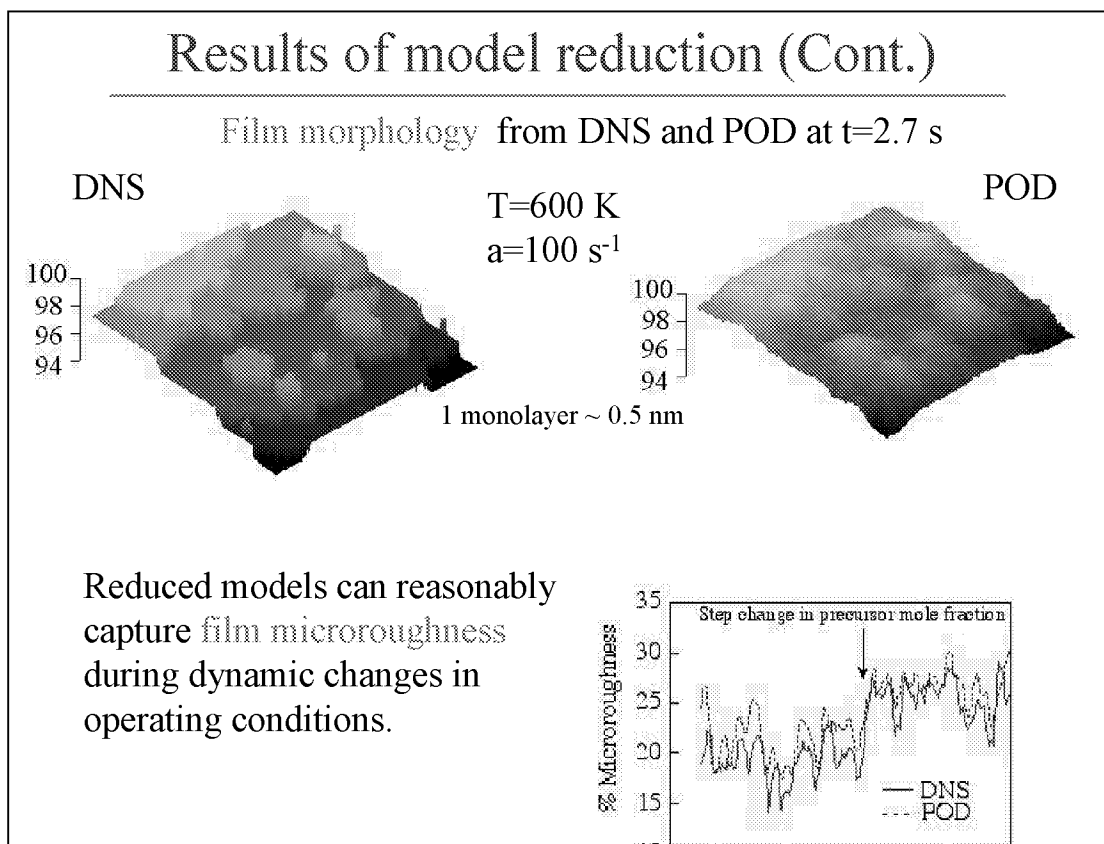


Figure 9

MULTISCALE MODELING OF ZEOLITE MEMBRANES

Introduction to zeolites and their applications as another example of multiscale simulations. Summary of three-step synthesis of zeolite films developed by M. Tsapatsis and co-workers. Controlling properties of membranes demands an understanding of the fundamentals of growth, which are discussed next.

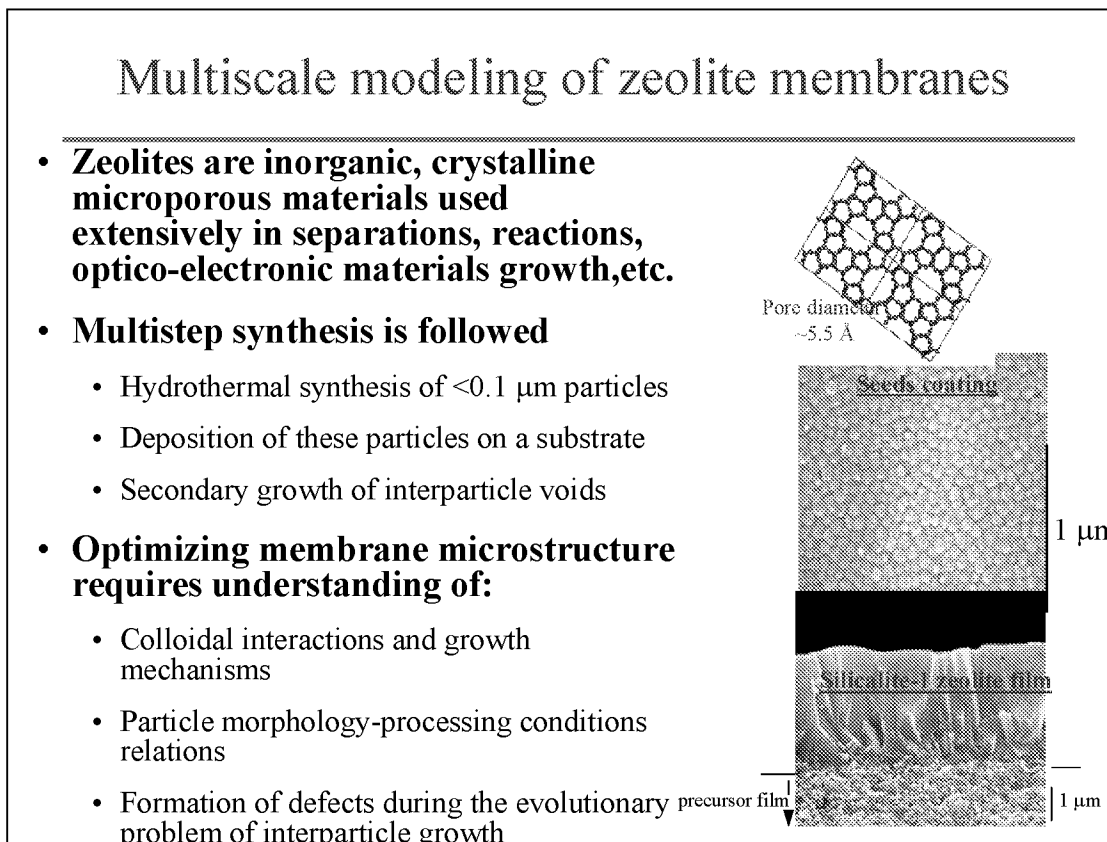


Figure 10

SILICALITE-1 SYNTHESIS FROM CLEAR TPAOH-TEOS-H₂O SOLUTIONS

Synthesis of zeolite nanoparticles takes place in aqueous solution, by adding a SiO₂ source and a template (a structure directing agent). Hydrolysis and condensation reactions lead to a plethora of siliceous species and nanoparticles seen by a variety of experimental techniques indicated. The growth unit that contributes to growth has been, however, speculative till recently.

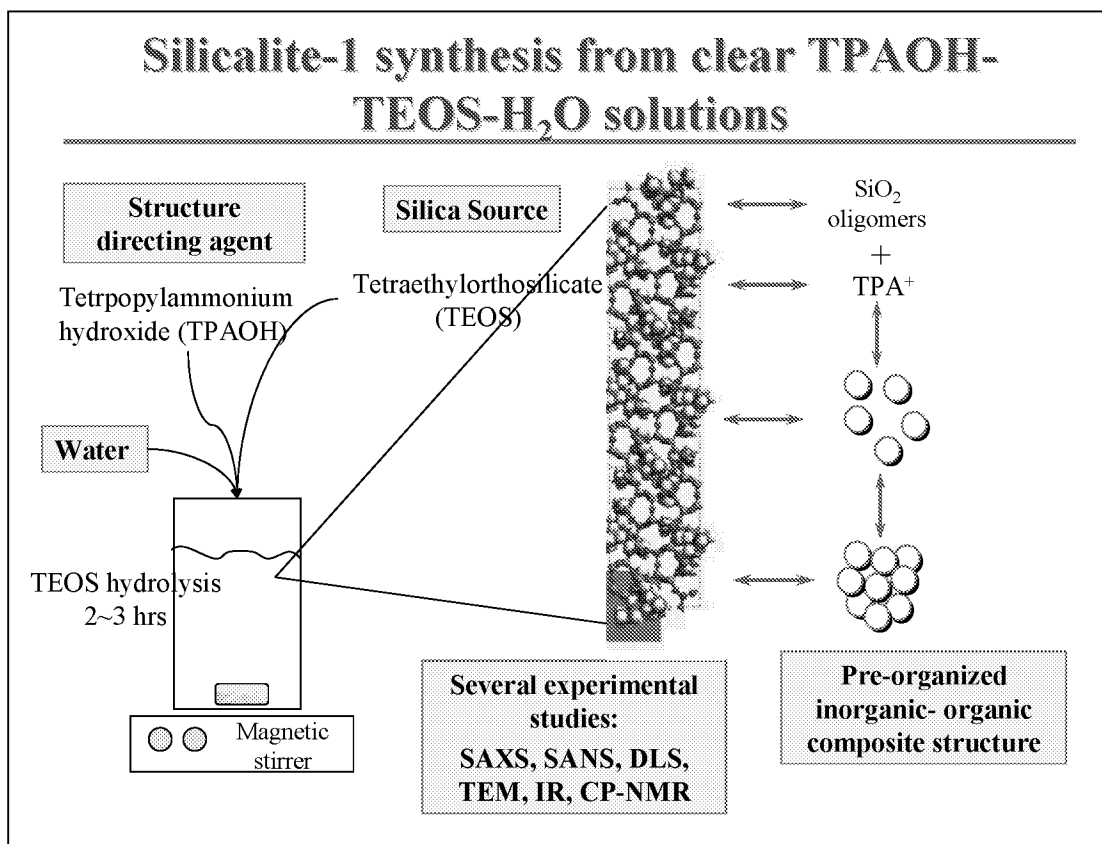


Figure 11

MODELING OF GROWTH

To understand the growth and isolate it from nucleation, DLS experiments have been carried out for seeded growth and modeled with a transport model based on the chemical potential formulation. The chemical potential considers the Brownian motion of growth units and interactions between particles with the DLVO potential. Good agreement is found. Model parameters have been obtained from independent experiments in this case. A primary outcome of this work is that the growth unit appears to be nanoparticles of ~ 3 nm in diameter.

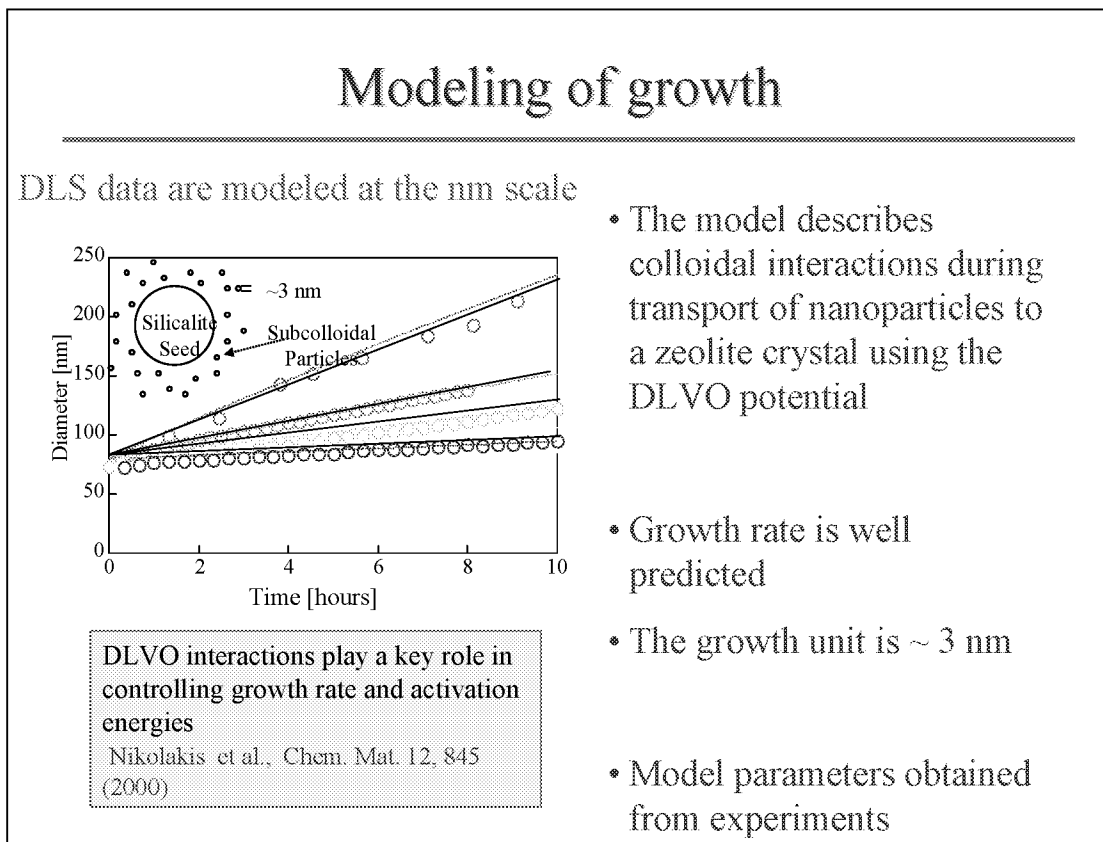


Figure 12

AFM MEASUREMENTS OF FORCES VALIDATE DLVO POTENTIAL

AFM experiments between a glass sphere and a zeolite film have been used to validate the DLVO potential used in the growth model. The force can be described reasonably by the DLVO potential.

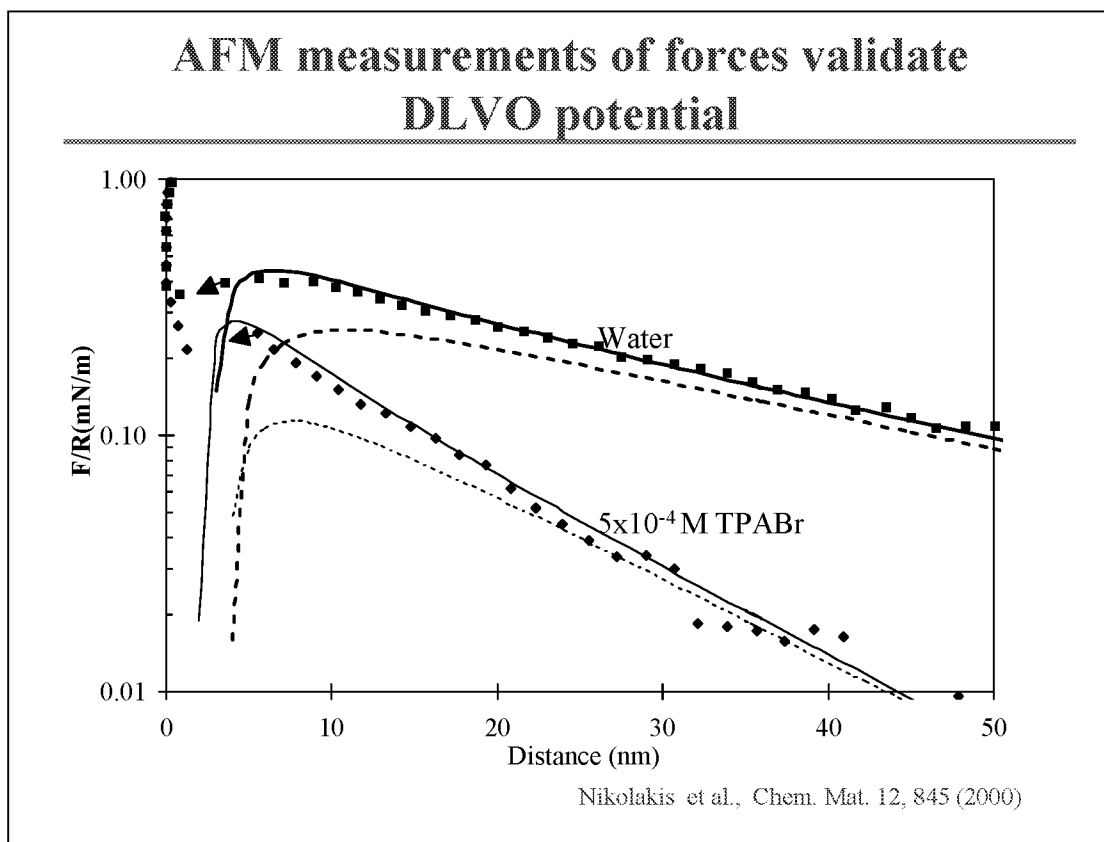


Figure 13

TEM INDICATES THE EXISTENCE OF SUBCOLLOIDAL PARTICLES

High resolution TEM indicates the existence of nanoparticles predicted by the model. Models and experiments have been used in a symbiotic manner for model validation.

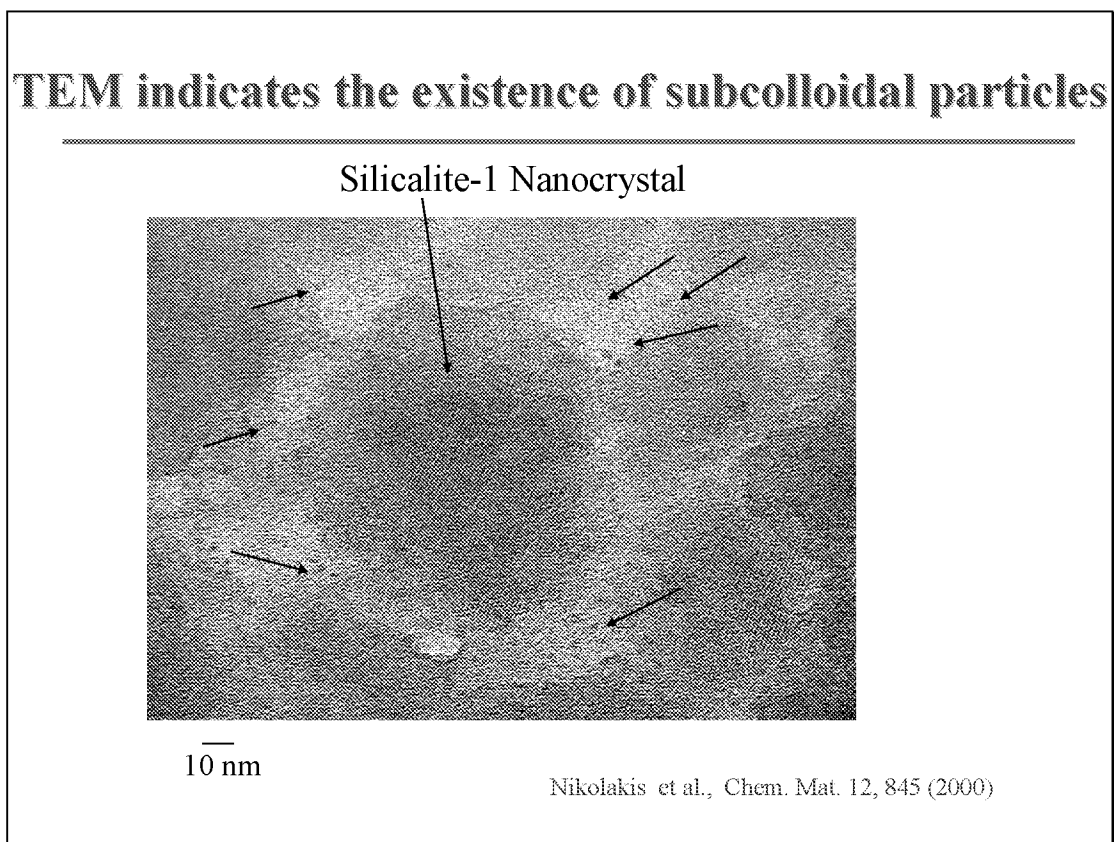


Figure 14

MODELING AT VARIOUS SCALES

Armed with a growth model that describes growth at the nanometer scale, we are currently exploring ways to predict particle anisotropy and particle morphology evolution as a function of processing conditions. It turns that particle morphology strongly affects membrane microstructure.

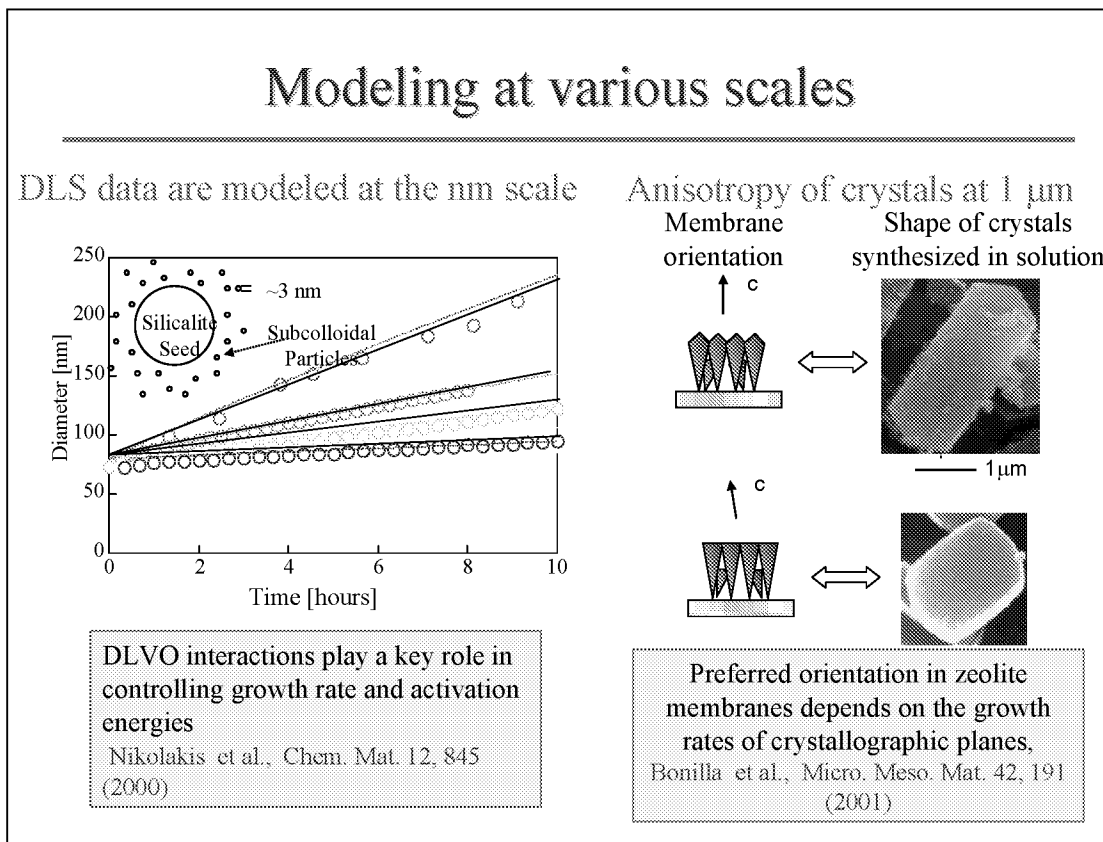


Figure 15

ZEOLITE MEMBRANE GROWTH IS MODELED

Fundamental growth models can be used to study the evolution of thin films from an initial coating of particles. The left graph shows 2D simulations of 10,000 particles as a function of time or height. The right graph shows a cross section SEM of a silicalite-1 zeolite film. The model predicts the columnar structure of films.

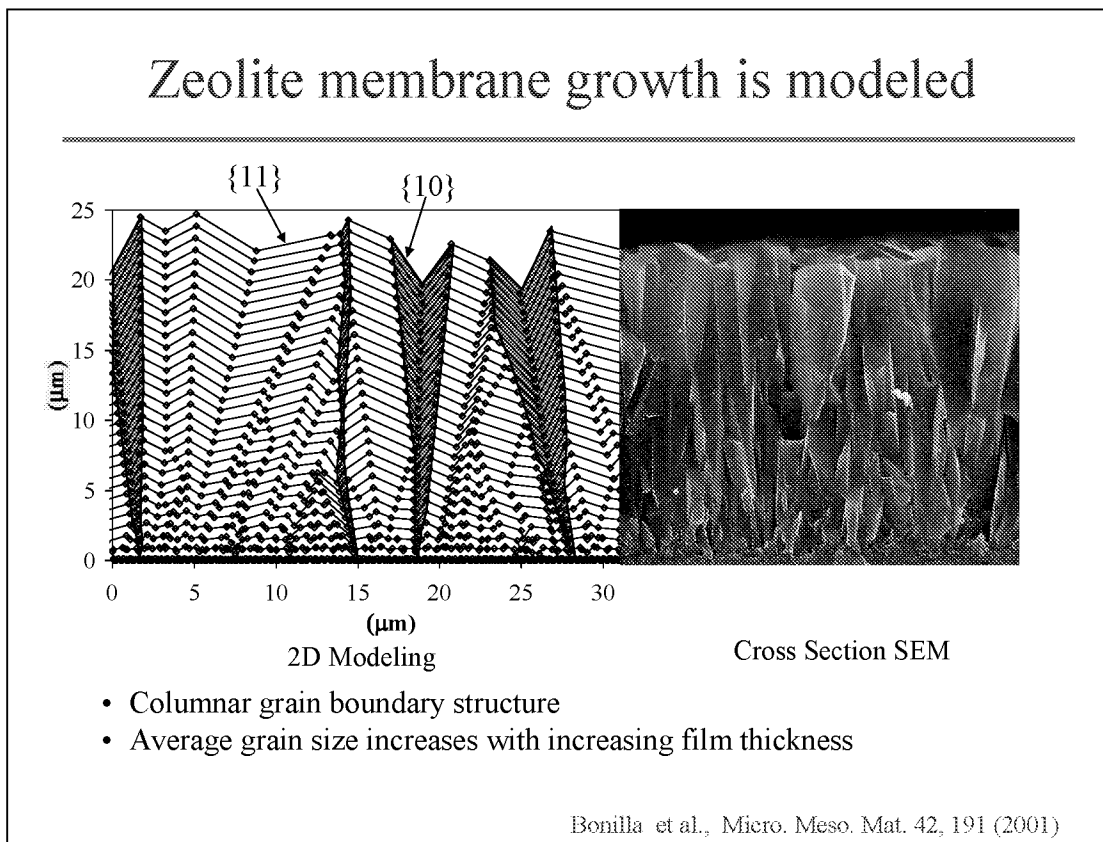


Figure 16

DEFECTS CAN BE PREDICTED AND CONTROLLED

Defects can also be predicted that happen near the zeolite/substrate interface. Simulations show that the most critical factor controlling defects is the growth factor, α , which is the ratio of velocities of different particle facets. Under more isotropic growth conditions, defects are minimized. Thus, it is important to link processing conditions with particle morphology.

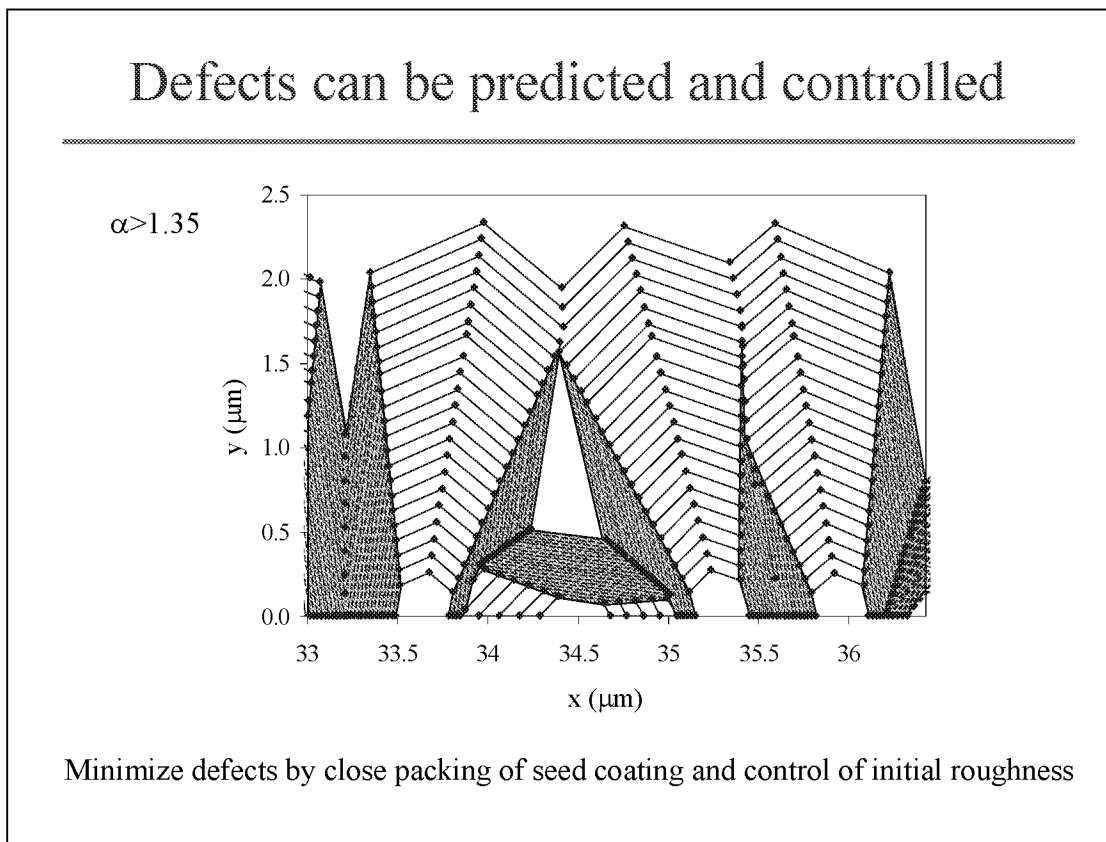


Figure 17

XRD POLE FIGURE RESULTS

Experiments for the primary orientation of these films indicate that either 2 or 1 peaks, depending on growth conditions.

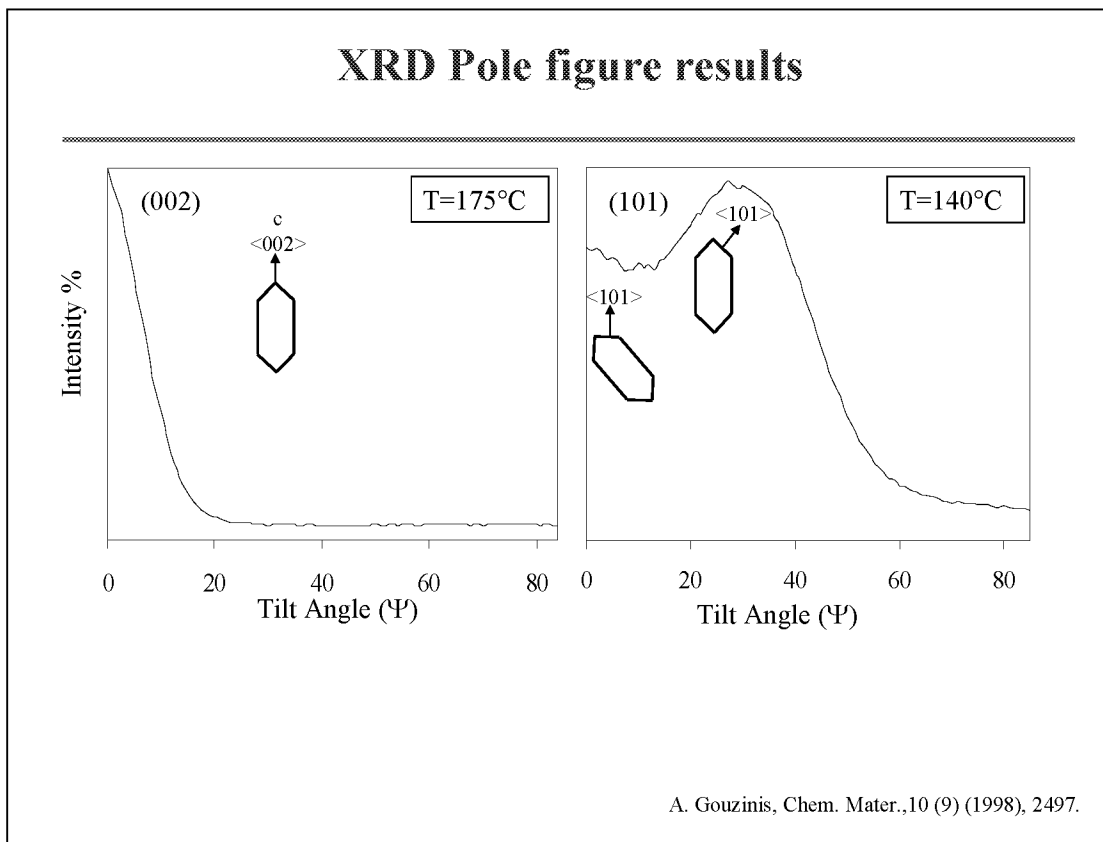


Figure 18

MEMBRANE ORIENTATION IS AFFECTED BY PARTICLE MORPHOLOGY AND GROWTH CONDITIONS

The model can explain the formation of single or double peaks. The key again is the growth factor. These simulations provide insight into how to control the orientation of polycrystalline films that can have a significant impact on performance.

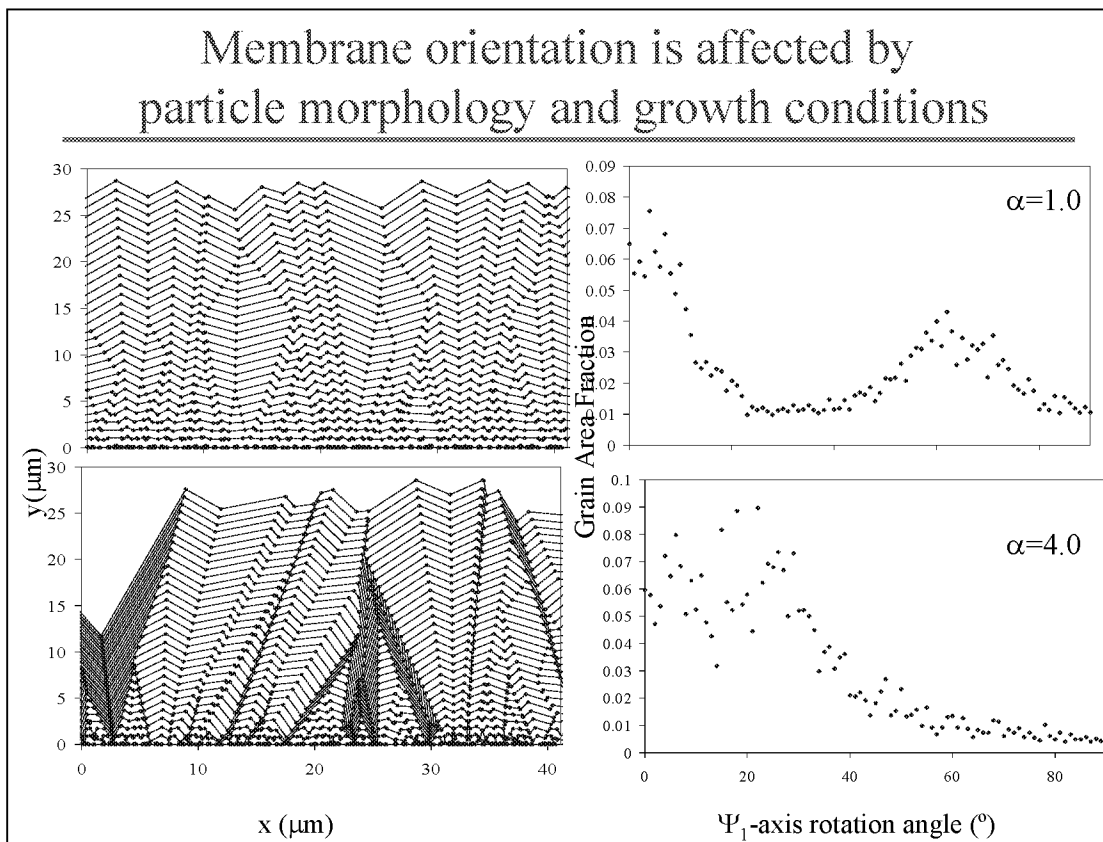


Figure 19

DIFFUSION/REACTION THROUGH MEMBRANES

Confocal micrograph of zeolite films indicates the presence of grain boundaries. Prediction of transport of molecules through these films is a challenging, multiscale problem that direct molecular simulations cannot handle. Mesoscopic theory emerges as an invaluable tool in bridging the length and time scales problem in predicting properties of polycrystalline films.

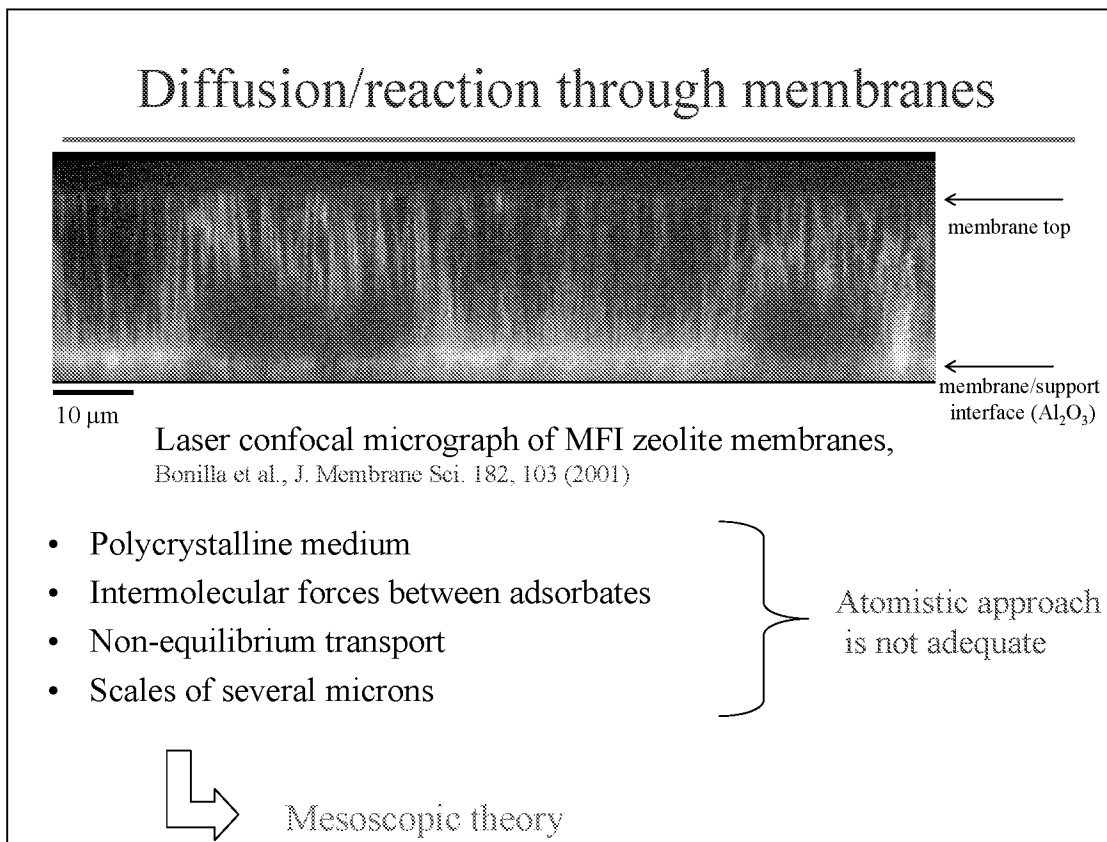


Figure 20

MESOSCOPIC THEORY OF PATTERN EVOLUTION

Mesoscopic theory is developed from the microscopic master equation by non equilibrium statistical mechanics. This mesoscopic theory captures the details of microscopic mechanisms and is exact when the interaction potential is infinite ranged. Thermodynamic and transport macroscopic equations (e.g., velocity of moving interfaces, mobility, critical nucleus size, surface tension) can also be derived by further coarse-graining using homogenization theory and asymptotic expansion of traveling waves.

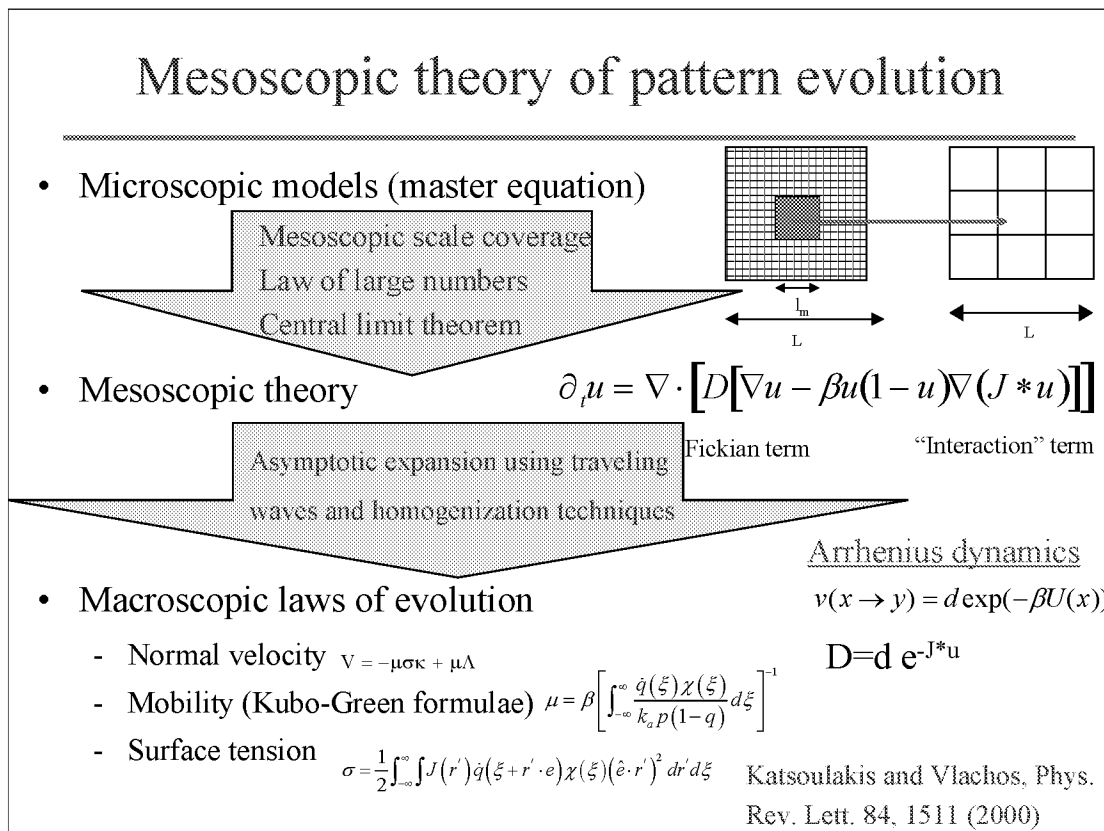


Figure 21

VALIDATION OF MESOSCOPIC THEORY

Numerical simulations in thin, single crystal films show excellent agreement between gradient (no equilibrium) MC simulations and mesoscopic simulations for various strengths of the interaction potential for relatively short ranged potentials. This result is a consequence of a Large Deviation Principle that these equations satisfy.

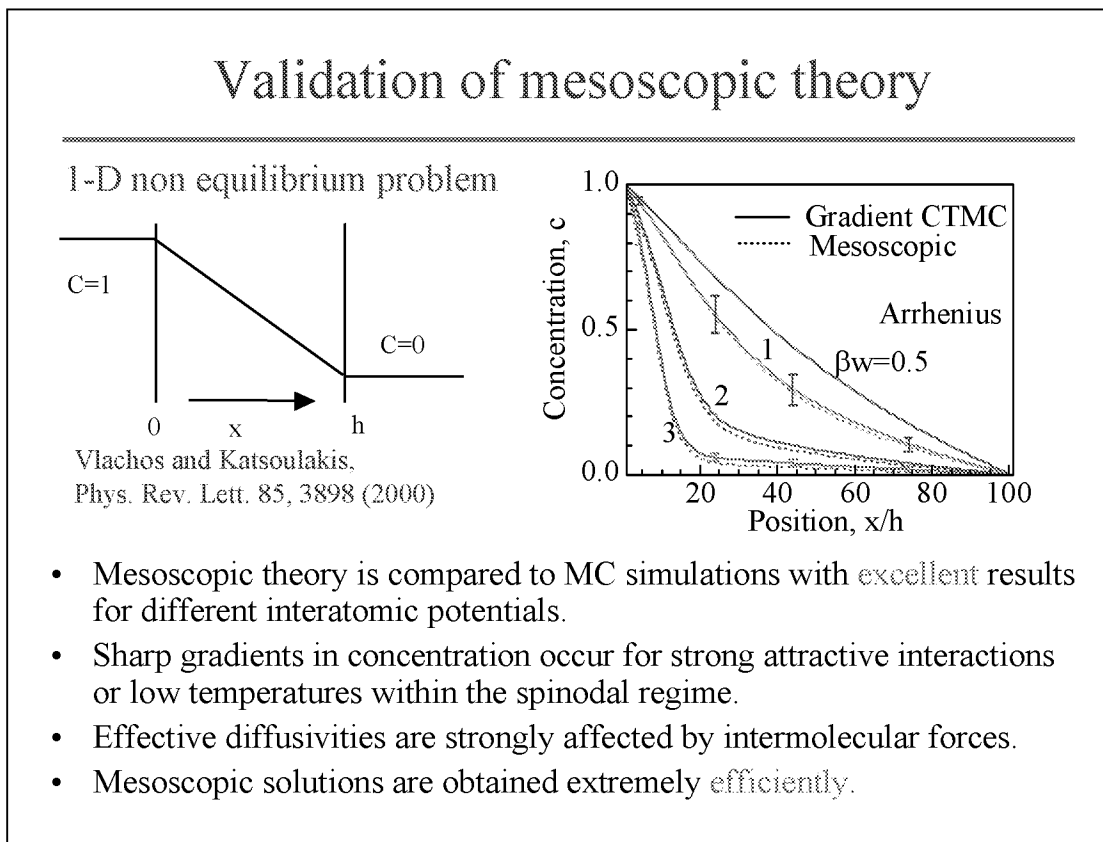


Figure 22

BREAK OF MEMBRANE SYMMETRY

Extension of mesoscopic theory from single crystal to polycrystalline materials can be achieved using homogenization theory. Simulations depicted here indicate that both the concentration and location of defects are important factors in controlling permeation properties. For example, the performance of a membrane depends on which side is exposed to the high pressure (feed side) when intermolecular forces dominate transport of species through a membrane.

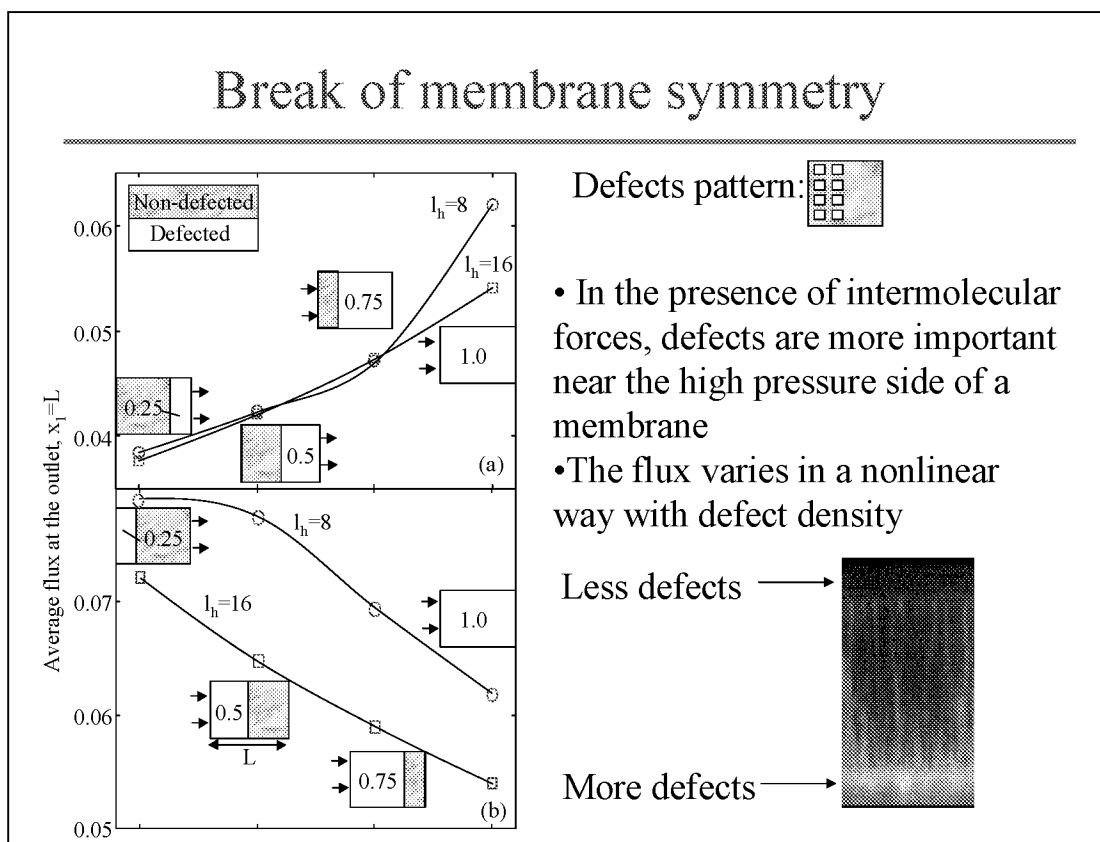


Figure 23

Mesoscopic theory: How good is it?

- Mesoscopic equations have been validated by comparison of MC to mesoscopic theory (FD and Spectral solutions) for a variety of potentials, microscopic dynamics, steady state and transients
- The excellent performance of mesoscopic theory is a result of a Large Deviation Principle
- Mesoscopic equations can be used to describe the behavior of heterogeneous systems (polycrystalline membranes, catalysts, composite materials) in the presence of intermolecular forces by extending homogenization techniques
- Mesoscopic theory is an attractive alternative to atomistic simulations for larger scales and heterogeneous media

Figure 24

Summary

- We show the feasibility of applying multiscale hybrid (quantum/atomistic/continuum) models to homogeneous-heterogeneous reactors
 - Surface chemistry developed assures thermodynamic consistency and coverage dependence of kinetic parameters.
 - Surface reaction mechanisms with predictive capabilities are developed.
- Reduction of multiscale models is feasible and enables design and control of materials' microstructure at the atomic level
- Mesoscopic theory is a viable substitute to traditional molecular simulations for larger time and length scales
 - The theory compares well to Monte Carlo simulations in 1D and 2D even for short range interactions.
 - Solution of mesoscopic theories are obtained in seconds.

Figure 25

Acknowledgements

- Funding
 - NSF-Career, NASA, NSF-NIRT, NSF-Nanotechnology
- Students and postdocs
 - R. Lam, S. Raimondeau, J. Reese, M. Snyder, V. Nikolakis, G. Bonilla
- Colleagues
 - M. Tsapatsis, M. Katsoulakis

Figure 26

References on multiscale simulations

1. Y. K. Park, P. Aghalayam, and D. G. Vlachos, "A generalized approach for predicting coverage-dependent reaction parameters of complex surface reactions: Application to H₂ oxidation over platinum," *J. Phys. Chem. A* **103**(40), 8101-8107 (1999).
2. V. Nikolakis, E. Kokkoli, M. Tirrell, M. Tsapatsis, and D. G. Vlachos, "Zeolite growth by addition of subcolloidal particles: Modeling and experimental validation," *Chem. Mater.* **12**, 845-853 (2000).
3. M. Katsoulakis and D. G. Vlachos, "From microscopic interactions to macroscopic laws of cluster evolution," *Phys. Rev. Letters* **84**(7), 1511-1514 (2000).
4. S. Raimondeau and D. G. Vlachos, "Low-dimensional approximations of multiscale epitaxial growth models for microstructure control of materials," *J. Comp. Phys.* **160**, 564-576 (2000).
5. P. Aghalayam, Y. K. Park, and D. G. Vlachos, "Construction and optimization of complex surface reaction mechanisms," *AIChE J.* **46**(10), 2017-2029 (2000). *This paper was selected in the highlights of Chem. Eng. Progress (paper of the month), p., Oct. issue, 2000.*
6. G. Bonilla, M. Tsapatsis, D. G. Vlachos, and G. Xomeritakis, "Fluorescence confocal optical microscopy of the grain boundary structure of zeolite MFI membranes made by secondary (seeded) growth," *J. Membrane Sci.* **182**(1-2), 103-109 (2001).
7. D. G. Vlachos and M. Katsoulakis, "Derivation and validation of mesoscopic theories for diffusion of interacting molecules," *Phys. Rev. Letters* **85**(18), 3898-3901 (2000).
8. G. Bonilla, D. G. Vlachos, and M. Tsapatsis, "Simulations and experiments on the growth and microstructure of zeolite MFI films and membranes by secondary growth", *Micropor. Mesopor. Mat.* **42**(2-3), 191-203 (2001).
9. R. Lam and D. G. Vlachos, "A multiscale model for epitaxial growth of films: Growth mode transition," *Phys. Rev. B* in press (2001). -6403(3)-July 15, 2001 (electronic number 035401)
10. J. Reese, S. Raimondeau, and D. G. Vlachos, "Monte Carlo algorithms for complex surface reaction mechanisms: Efficiency and accuracy," *J. Comp. Phys.* **173**(1), 302-321 (2001).
11. D. J. Horntrap, M. A. Katsoulakis, and D. G. Vlachos, "Spectral methods for mesoscopic models of pattern formation," *J. Comp. Phys.* **173**(1), 364-390 (2001).

Figure 27

References (Cont.)

12. R. Lam, T. Basak, D. G. Vlachos, and M. A. Katsoulakis, "Validation of mesoscopic theories and their application to computing effective diffusivities," *J. Chem. Phys.* **115(24)**, 11278-11288 (2001).
13. R. Lam, D.G. Vlachos, and M.A. Katsoulakis, "Homogenization of mesoscopic theories: Effective properties of model membranes," *AIChE J.*, accepted (2001).
14. S. Raimondeau and D. G. Vlachos, "Recent developments on multiscale, hierarchical modeling of chemical reactors," *Chem Eng. J.*, accepted (2001).
15. S. Raimondeau and D. G. Vlachos, "The role of adsorbate-layer nonuniformities in catalytic reactor design: Multiscale simulations for CO oxidation on Pt," *Comput. Chem. Eng.*, accepted (2001).

Figure 28

Multiscale Modeling of Polycrystalline Materials

Olga Shenderova
North Carolina State University
Raleigh, NC

TALK OUTLINE AND COAUTHORS

In the first part of this presentation, a combination of atomic-scale structural modeling, density functional calculations and mesoscale theory will be presented that yields predictions of the mechanical properties of polycrystalline materials. This is an example of *hierarchical* multiscale modeling in which results at one scale are used as input for methods appropriate at the next larger scale. This project is collaboration between Donald Brenner of North Carolina State University, Airat Nazarov and Alexei Romanov, of Russian Academy of Science, and Lin Yang of Lawrence Livermore National Laboratory. The Office of Naval Research provided support for this work.

At the end of the presentation, a multiscale model of polymer nanocomposites which is another example of serial approach will be briefly outlined. The hierarchy of computational methods will include atomistic, mesoscopic and analytic levels. This work is a collaboration effort between Leonid Zhigilei, Dana Elzey and Ioannis Chasiotis of University of Virginia, Deepak Srivastava of NASA Ames Research Center and computational group of International Technology Center.

Talk Outline & Coauthors

- **Multiscale Modeling of Polycrystalline Materials**
Donald Brenner (*NCSU*)
Airat Nazarov and Alexei Romanov (*RAS, Russia*)
Lin Yang (*LLNL*)
- **Multiscale Modeling of Carbon Nanotubes/
Polymer Composites** (*Introductory remarks*)
Leonid Zhigilei, Dana Elzey, Ioannis Chasiotis (*UVA*)
Deepak Srivastava (*NASA Ames Research Center*)
International Technology Center, NC

Figure 1

MULTISCALE MODELING OF POLYCRYSTALLINE DIAMOND: ULTIMATE GOAL

Accurate first-principles predictions of macroscopic-scale materials properties strictly from theory remain a long-standing goal of the materials modeling community. Regarding polycrystalline materials, it would be beneficial to accurately predict properties of their grain boundaries (GBs), since it is well recognized that many of the properties of polycrystals depend to a large extent on the properties of their internal interfaces and their junctions. GBs contribute to strength, ductility, toughness, corrosion resistance as well as thermal and electronic properties. In our research we concentrated mostly on prediction of mechanical properties of polycrystalline diamond according to an interest of ONR, however the developed approach is quite general.

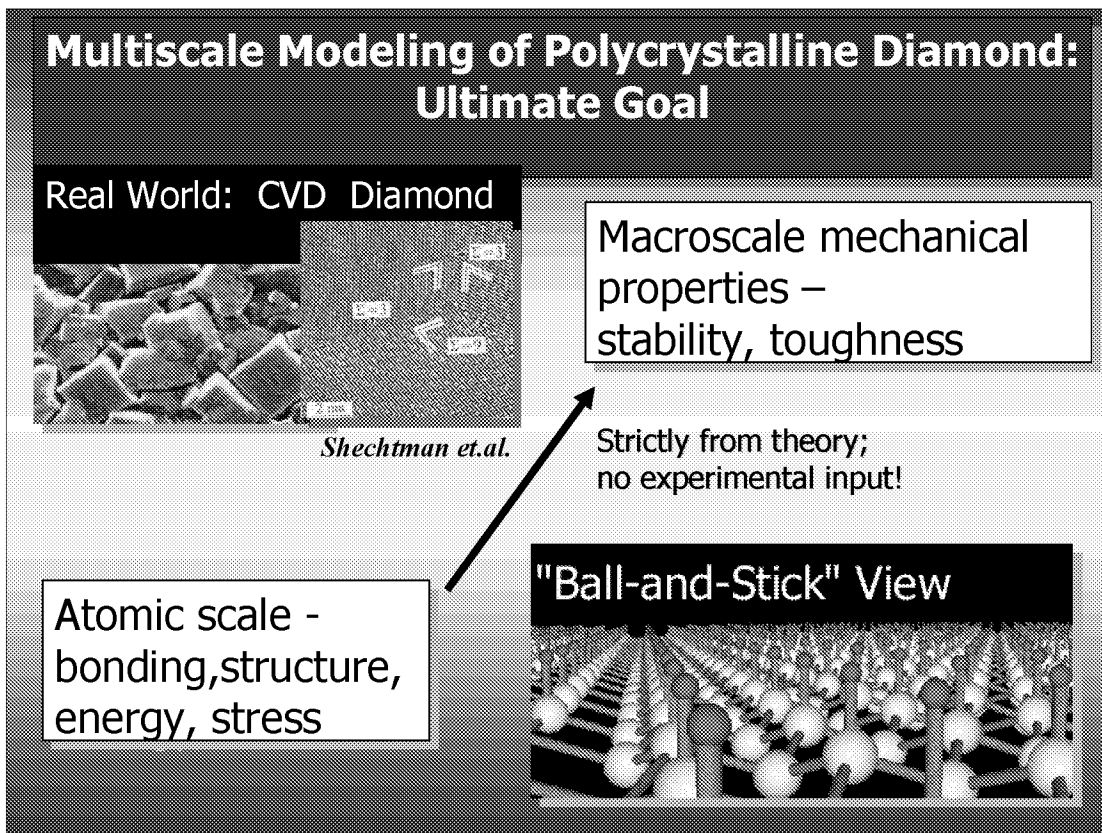


Figure 2

MULTISCALE MODELING OF POLYCRYSTALLINE DIAMOND

While density functional methods are capable of accurately predicting properties of ideal structures and selected localized defects for many systems, they remain too computationally intensive to model extended defects typical of macroscopic-scale engineering materials. In contrast, continuum-based methods are ideal for accurately describing long-range stresses but are inappropriate for modeling atomic-scale chemical dynamics from which processes such as crack propagation originate. Intermediate between these two length scales is atomistic modeling using analytic interatomic potentials. While powerful, especially given current computing capabilities that allow very large systems to be modeled, this approach can yield results for which the range of validity is difficult to access due to possible inaccuracies in the interatomic potential.

Multiscale Modeling of Polycrystalline Diamond

How do we attack this problem?

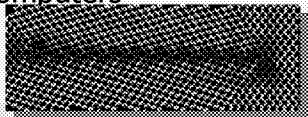
Direct First Principles Methods (e.g. density functional theory):

- Accurate total energies
- But ... limited to ~ 1000 's of atoms on supercomputers



Analytic Potentials (e.g. EAM or bond order):

- 50,000 atoms on workstations/ 10^6 - 10^8 + on parallel computers
- qualitative stress/energies and dynamics
- but ... not always quantitatively accurate



Continuum Models/Finite Element Methods

- Well developed for microstructure evolution
- but ... missing atomic-level 'chemistry' of fracture

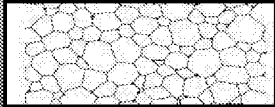


Figure 3

MULTISCALE MODELING OF POLYCRYSTALLINE DIAMOND

That is why we used the following combined approach. In this scheme, the mesoscopic model gives a way to predict the energies and stresses for GBs in the entire misorientation range for a given tilt axes based only on a few reference structures of low-sigma GBs. These structures are small systems accessible to the first principles (FPs) density functional calculations. This leads to a completely first-principles estimate of the energy of tilt grain boundaries at any arbitrary tilt angle. Analytic potential calculations are used in the present scheme to prove the validity of disclination approach to the covalent materials; generate starting configurations for the FPs calculations and to evaluate the extension of stress fields and consequently the sizes of computational cell for FPs calculations. In addition, large-scale molecular dynamics simulations with analytical potentials provide qualitative insight on dynamics of fracture initiation and propagation in polycrystalline materials.

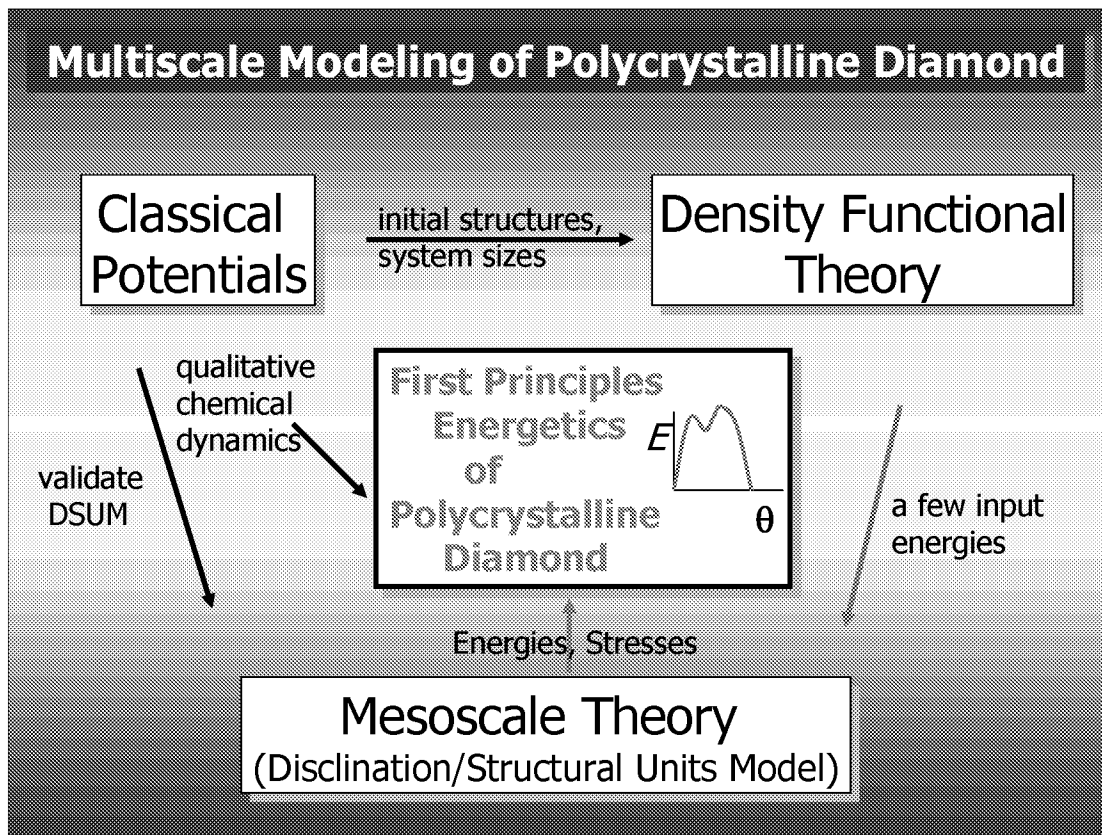


Figure 4

ATOMISTIC SIMULATION METHODS

The analytic potential energy function used in the present simulations is a many-body bond order potential developed by Donald Brenner that mimics bonding in carbon systems for a wide range of atomic hybridizations. The function reproduces a relatively large database of molecular properties of hydrocarbons as well as solid-state properties of carbon, including the in-plane lattice constant, cohesive energy and elastic properties of graphene sheets as well as cohesive energy and elastic properties of diamond. Density functional with local density approximation calculations had been carried out by Lin Yang of LLNL.

Atomistic Simulation Methods

Analytic Bond Order Potential for Hydro-carbons

- Second moment approximation to local DOS
- Near neighbor pair sum modulated by analytic bond order
- Empirical corrections for radicals, conjugation, dihedral rotation
- Fit to extensive solid state and molecular data base

First Principles Calculations

- Density functional local density approximation
- Plane wave basis/60 Ry cut-off
- Norm-conserving pseudopotentials
- Effective k-point sampling
- Relaxation of nuclear degrees freedom

Figure 5

DISCLINATION-STRUCTURAL UNITS MODEL

Disclination-structural units model (DSUM) [1] combines the disclination description of GBs and structural units (SUs) concept. A GB, being a rotational defect, is described more simply by disclinations, the linear rotational defects. A wedge disclination forms when one extracts or inserts a sector of the material from cylinder or disk. According to the disclination model, a general GB can be considered to consist of alternating areas of two special GBs. The junctions of these areas are partial disclinations, and the boundary is represented as a disclination dipole wall (DDW). However, it was unknown how the period of DDWs scales with the geometrical period given by a coincidence site lattice. Later atomic calculations by Sutton and Vitek, which lead to the structural units model, demonstrated that the decomposition of general GB into sections of two low energy boundaries occurs within the geometrical period. All intermediate boundaries in a range delimited by two neighbor special boundaries are composed of the mixture of their SUs in a certain proportion and arrangement. The disclination formalism was subsequently combined with the structural units model to calculate grain boundary energies for metals [1].

[1] V. Gertsman, A.A. Nazarov, A.E. Romanov, *et.al. Philos. Mag. A* **59**, 1113 (1989)

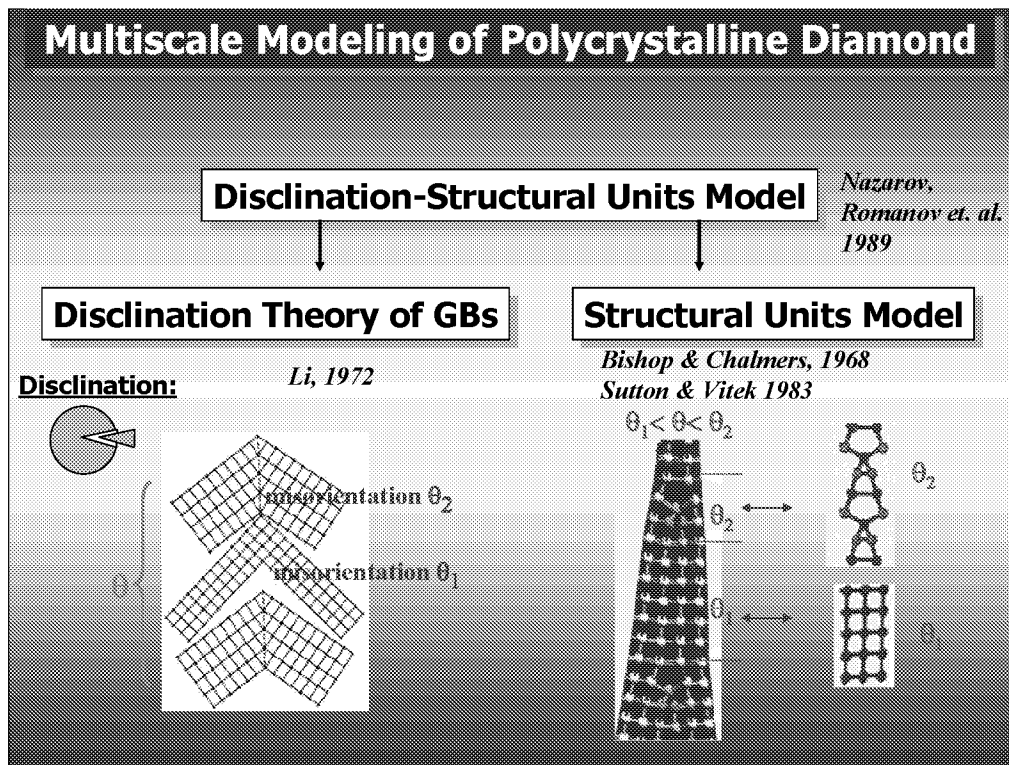


Figure 6

GB ENERGY CALCULATIONS USING DSUM

According to DSUM, at the lines along a GB where SUs of different types meet, the local misorientation angle alternates between θ_1 and θ_2 and therefore, these lines are partial wedge disclinations and the minority SUs can be considered as disclination dipoles. Because the DDW period is known from the coincidence site lattice parameters for the given boundary, its elastic energy is explicitly known. The energy of a GB is then given as a weighted sum of the energies of the individual SUs plus the elastic energy of the DDW and the energy of the disclination cores. This leads to a set of equations involving only the energies of the key single-SUs grain boundaries, bulk elastic properties, and a single unknown disclination core parameter. This parameter can be uniquely determined from the energy of a single GB containing a combination of structural units. The whole set of input parameters can be obtained from the first principles simulations leading to the accurate prediction of GBs energetics for the entire misorientation range for a given tilt axis. It should be noticed, that dislocation-structural units multiscale model for prediction of GB energetics had been developed by Wang and Vitek (1986), but it requires larger number of input parameters than DSUM.

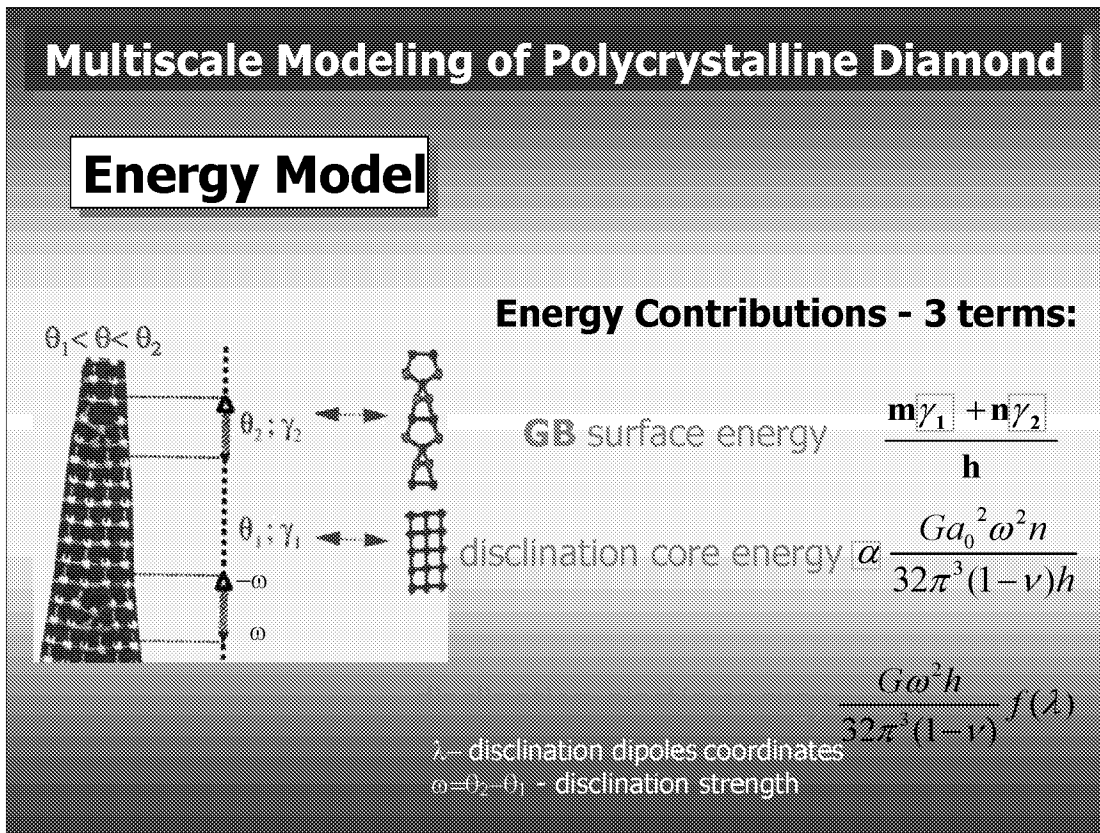


Figure 7

VALIDATION OF THE MODEL: GB ENERGY CALCULATION WITH ANALYTICAL POTENTIAL

To demonstrate accuracy of the DSUM approach for covalent materials, energies obtained directly from the bond-order potential for <001> symmetrical tilt GBs in diamond at different misorientation angles (indicated by the circles in the figure) were compared to values predicted by the DSUM (solid curve) [1]. As input parameters for the DSUM the energies of two S=1 GBs, two S=5 GBs and S=29 GB from analytic potential calculations had been used (solid circles). Very good agreement can be seen between the energies predicted with DSUM and those calculated with the analytic potential. This demonstrates the validity of the disclination approach to covalent crystals.

[1]O.A.Shenderova, D.W.Brenner , A.I.Nazarov, A.E.Romanov, L.Yang. 'Multiscale modeling approach for calculating grain boundaries energies from first principles', *Phys.Rev.B*, **57**, R3181 (1998).

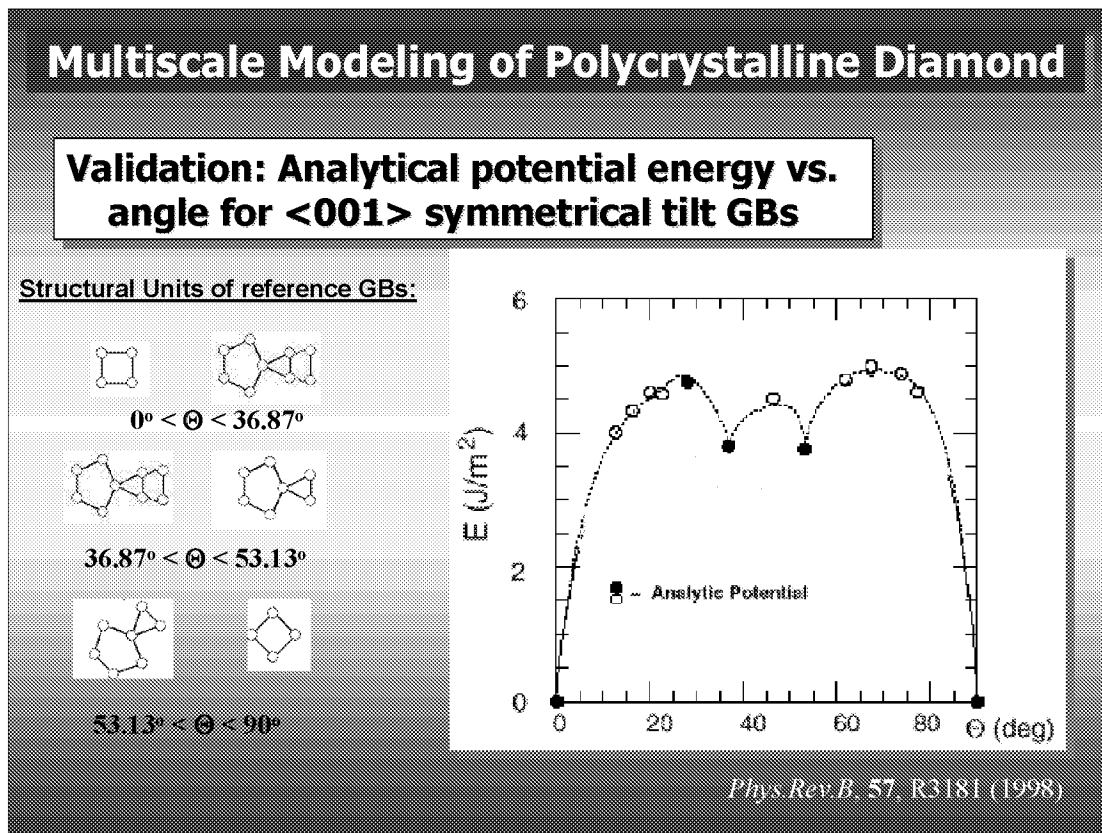


Figure 8

ACCURATE PREDICTION OF GBS ENERGIES USING FIRST PRINCIPLES SIMULATIONS

Below is GB energy versus misorientation curve obtained with input energies of special GBs and one intermediate GB calculated from the density functional approach. Energies of special GBs calculated from first principles are about 1.3-1.5 times less those calculated with bond order potential due to electronic system relaxation. Necessary elastic parameters for diamond also had been calculated using density functional approach. So taking first principle calculations only for a few special GBs we obtain realistic GBs energies in the entire range of misorientation for a given tilt axis.

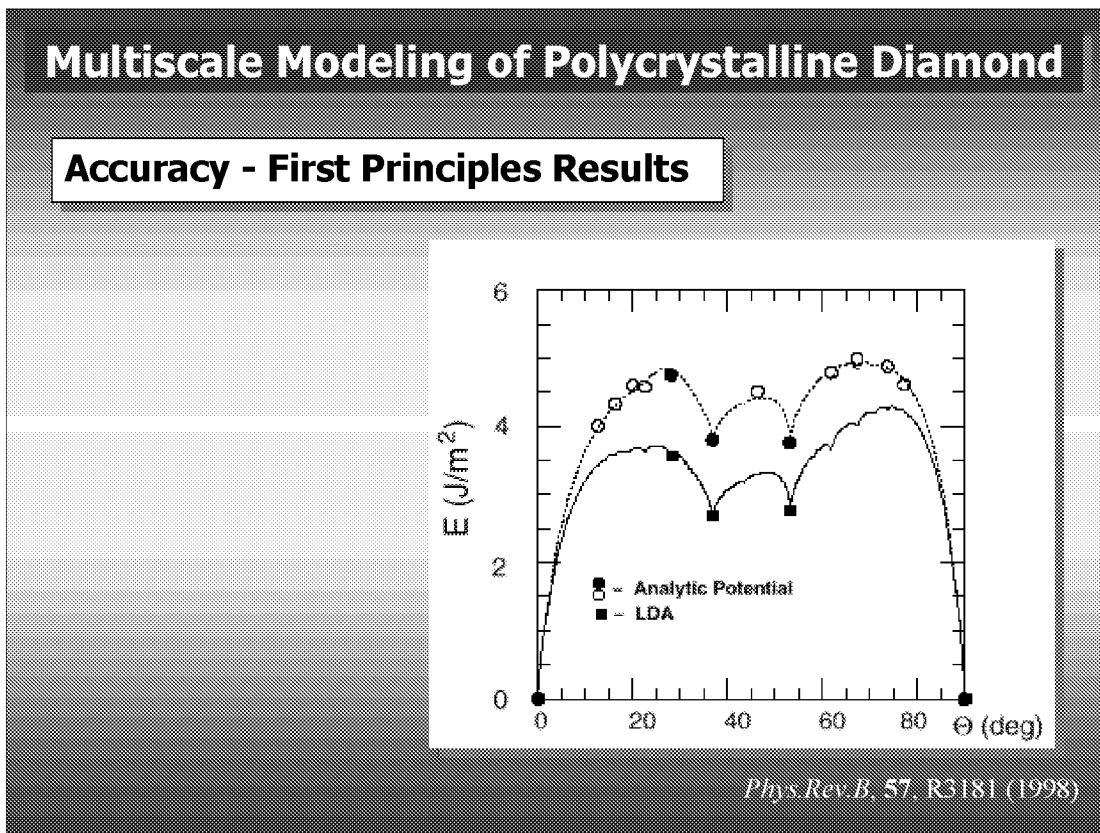


Figure 9

USING DSUM FOR STRESS CALCULATIONS: COMPARISON WITH THE STRESS DISTRIBUTION CALCULATED USING THE ANALYTIC POTENTIAL

In addition to GB energy, the disclination approach is able to provide stress distribution near GBs. Stresses near defected structures may also be calculated at the atomic level from interatomic forces and the result compared to the disclination model. The stress contribution attributed to individual atoms consist of “moments of the forces” between a central atom and its neighbors divided by the local atomic volume. Below such analysis is carried out for the $\Sigma=149(7\ 10\ 0)$ GB, which has a relatively complicated stress field and therefore is a good test model [1]. As it seen from the figure, small areas of compressive stress are inserted to more extended regions of tensile stress and vice versa.

[1] O.A.Shenderova, D.W.Brenner, 'Atomistic Simulation of Grain Boundaries, Triple Junctions and Related Disclinations', *Solid State Phenom.*, Trans Tech Publ., v.87, p.318 (2002)

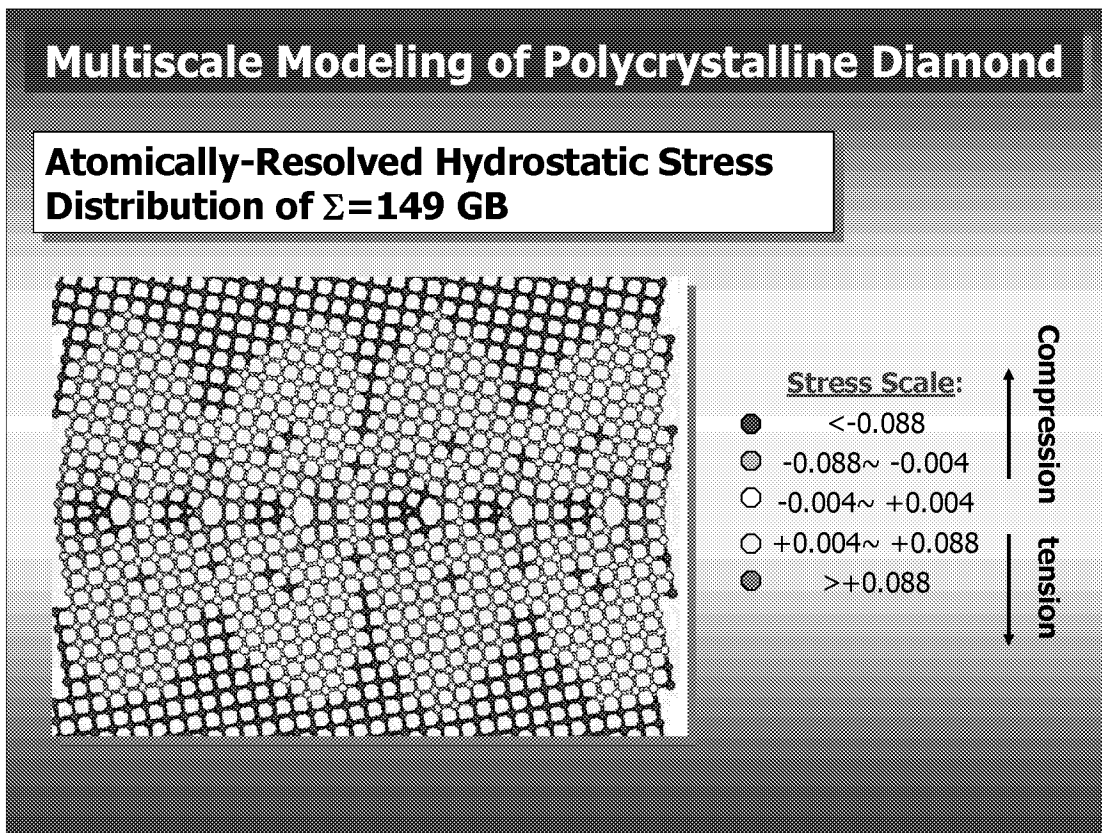


Figure 10

CALCULATION OF STRESSES USING DSUM

Figures below illustrate stresses in the vicinity of S=149 GB calculated using DSUM [1] and those calculated with the analytic bond-order potential. As it can be seen, very good agreement exist between the atomistic and mesoscopic approaches in the description of both shape of the stress distribution as well as stress magnitudes at distances from the interface more then about two interatomic distances.

[1] R.Valiev, V.Vladimirov, et.al. “Stress fields of equilibrium and nonequilibrium grain boundaries”, Fiziko-technical inst. By Ioffe, Leningrad, 1989 (in Russian).

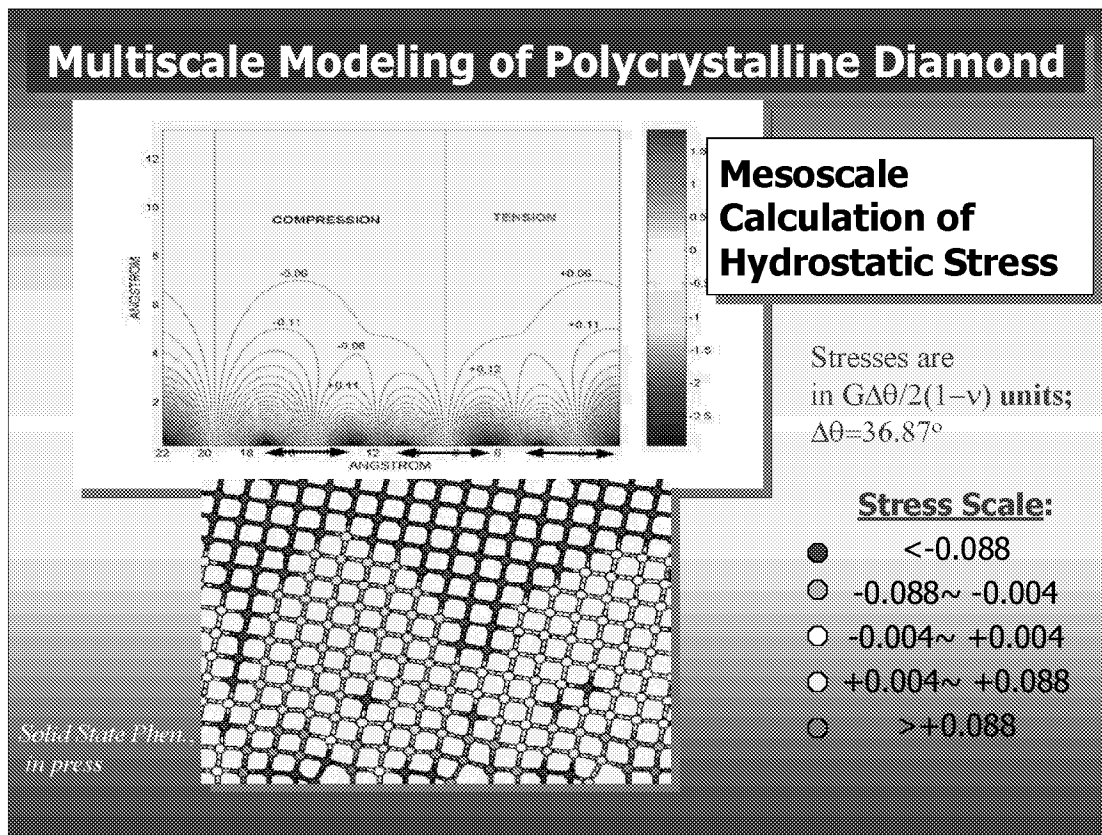


Figure 11

FIRST PRINCIPLE CLEAVAGE ENERGIES AND TOUGHNESS OF GBS IN DIAMOND

GB energy plays a central role in various GBs properties, such as GB mobility and fracture, impurity segregation, GB diffusion, to name but a few. The simulation data for first principle GBs energies combined with the energies of free surfaces (also calculated from first principles) allow to evaluate cleavage fracture energy of the internal interface [1]. The resulted curve is shown in the Figure. For comparison, the bulk ideal crystal cleavage energies are presented too. It is apparent from the Figure that special GBs possess higher cleavage energies relative to GBs in the nearby misorientation range. Cleavage energies of most <001> tilt GBs are about 60-75% of those for the ideal bulk crystals with the same orientation. Based on the cleavage energies, in turn, toughness of different GBs can be also evaluated. Results of calculations demonstrate good agreement with experimental data for CVD diamond films.

[1] O.A. Shenderova, D.W.Brenner, A.Omeltchenko, X.Su, L.H.Yang. 'Atomistic Modeling of Grain Boundaries Fracture in Diamond', *Phys.Rev.B* **61**, 3877(2000).

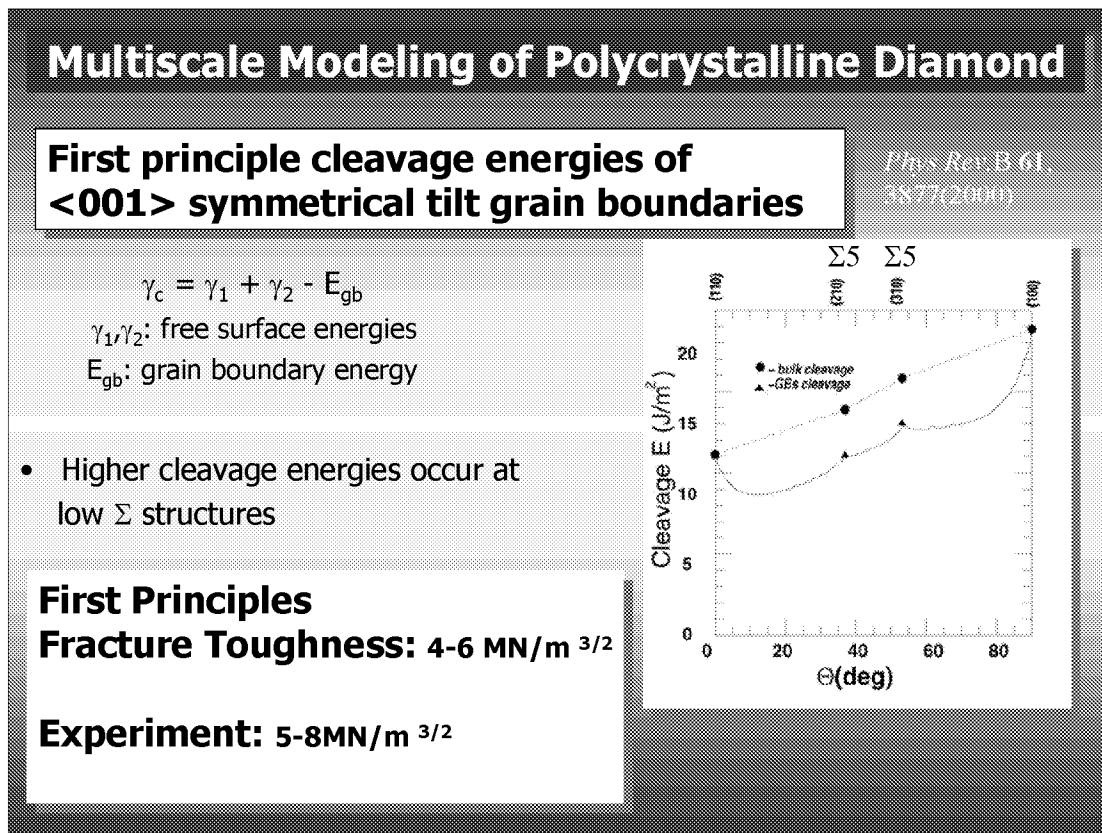


Figure 12

EXTENSION OF DSUM TO MORE COMPLICATED GB STRUCTURES.

GBs with a multiplicity of structures have been observed in Si and Ge. Some of them have been found to consist of zig-zag arrangements of structural units and others to contain dislocations having a screw component along the tilt axis. The $\langle 001 \rangle$ symmetrical tilt GBs commonly observed in materials with a diamond cubic lattice can be constructed in the entire range of misorientation from three characteristic structural units: type A, the core of a pure edge dislocation, type B, the core of a mixed 45° dislocation, and units of perfect crystal. There exist two distinct groups of $\langle 001 \rangle$ tilt GBs that are delimited by the $\Sigma=5/\theta=53.1^\circ$ boundary. Grain boundaries with minimum energies in the misorientation range $0^\circ \leq \theta < 53.1^\circ$ consist of mixture of the structural units F and A_s while GBs in the $53.1^\circ \leq \theta < 90^\circ$ misorientation range can consist of the F' , A_z and B_s units. An intermediate GB can be composed of non-dissociated dislocations consisting of pairs of A_z or B_s units, or of separated A_z and B_s units (see Figure below). All types of structures are stable, although the energies are different. DSUM had been extended to treat these more complicated GBs structures.

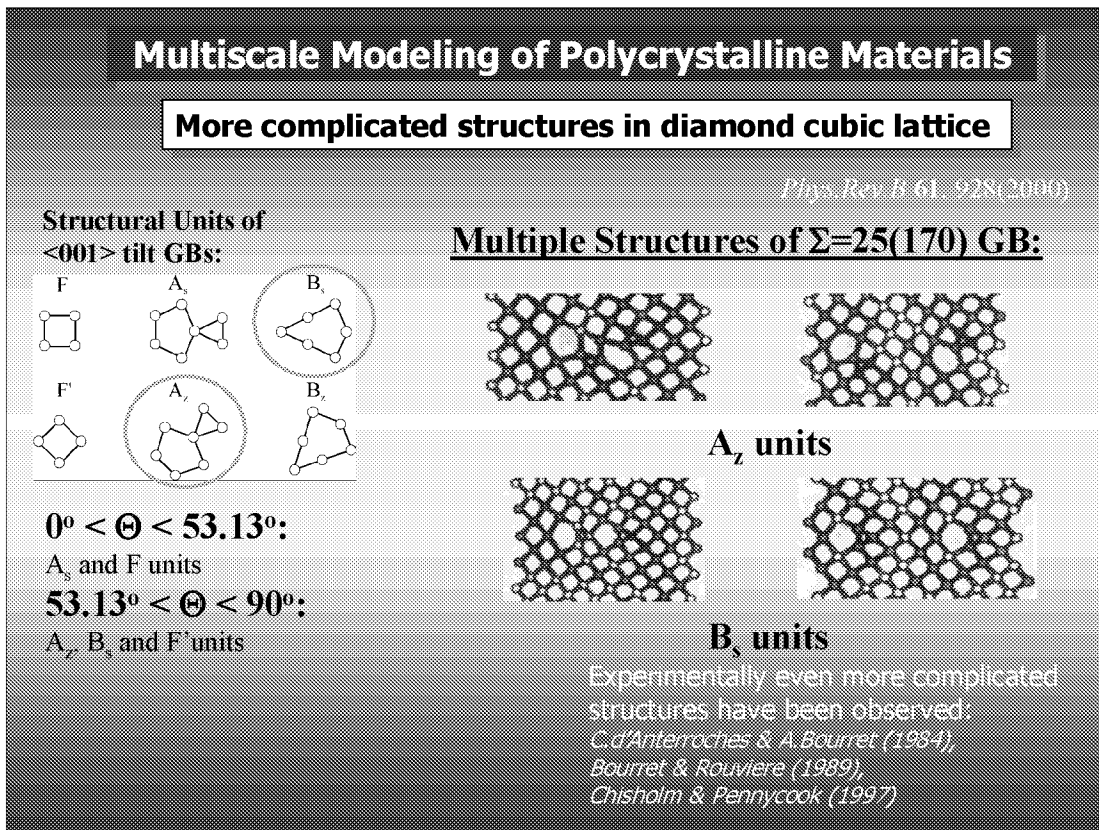


Figure 13

EXTENSION OF DSUM TO MORE COMPLICATED GB STRUCTURES.

In order to calculate GBs energies for groups of $\langle 001 \rangle$ GB models in the $53.1^\circ \leq \theta \leq 90^\circ$ misorientation range these structures were described in terms of flat and faceted disclination dipole walls and screw dislocation dipole walls (figures below), with the energies of these defects calculated from anisotropic elasticity theory. Details of the analysis are provided in [1].

[1] A Nazarov, O.A. Shenderova, D.W.Brenner, 'Elastic Models of $\langle 001 \rangle$ and $\langle 011 \rangle$ Tilt Grain Boundaries in Polycrystalline Diamond', *Phys.Rev.B* **61**, 928(2000).

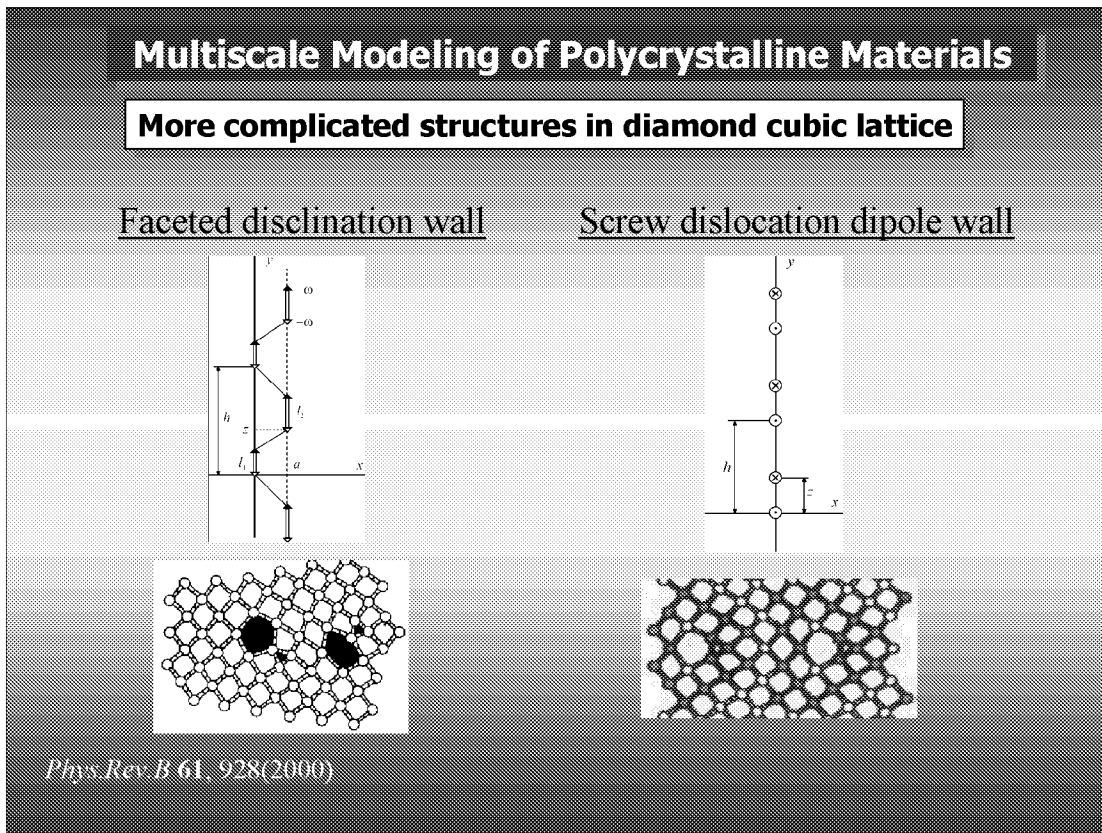


Figure 14

EXTENSION OF DSUM TO MORE COMPLICATED GB STRUCTURES.

Resulted GBs for groups of metastable GBs predicted with DSUM are illustrated in the Figure below. Grain boundary energies for the $\langle 001 \rangle$ and $\langle 011 \rangle$ tilt axes for diamond given by atomistic modeling quantitatively agree with those from the DSUM for the most stable structures. For metastable structures, the DSUM predicts the correct energy ranking for different models at a given tilt angle, although the agreement between the results of the DSUM and atomistic model is not quantitative. The calculations demonstrate that an appropriate treatment of the elastic energy of complicated structures (e.g. faceted grain boundaries and grain boundaries with dislocations containing screw components) is needed to correctly predict energy rankings [1].

[1] A Nazarov, O.A. Shenderova, D.W.Brenner, 'Elastic Models of $\langle 001 \rangle$ and $\langle 011 \rangle$ Tilt Grain Boundaries in Polycrystalline Diamond', *Phys.Rev.B* **61**, 928(2000).

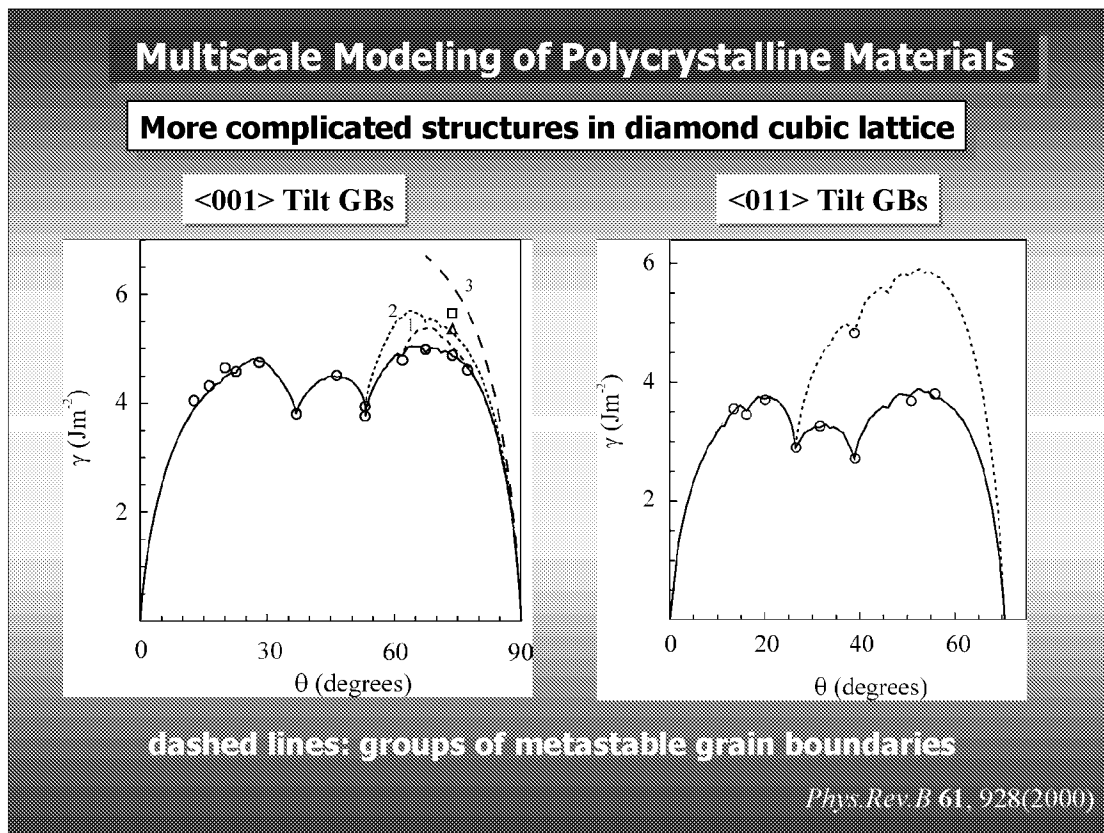


Figure 15

DSUM CALCULATIONS OF GBS ENERGIES FOR OTHER MATERIALS

Examples below illustrate results of application of DSUM to $\langle 001 \rangle$ and $\langle 111 \rangle$ GBs in copper [1]. Analytic potential calculations of energies of delimiting GBs had been used as input parameters. Good agreement can be seen for results of simulations for a variety of GBs calculated with an analytic potential and those predicted by DSUM. Even if to use only $\Sigma=1$ delimiting boundaries (no atomistic simulations are required, interface energy is zero), still obtained curves possess very high predictive capability.

[1] A Nazarov, O.A. Shenderova, D.W.Brenner, 'On the disclination-structural unit model of grain boundaries', *Mat.Sci.Eng.A*, **281**,148(2000).

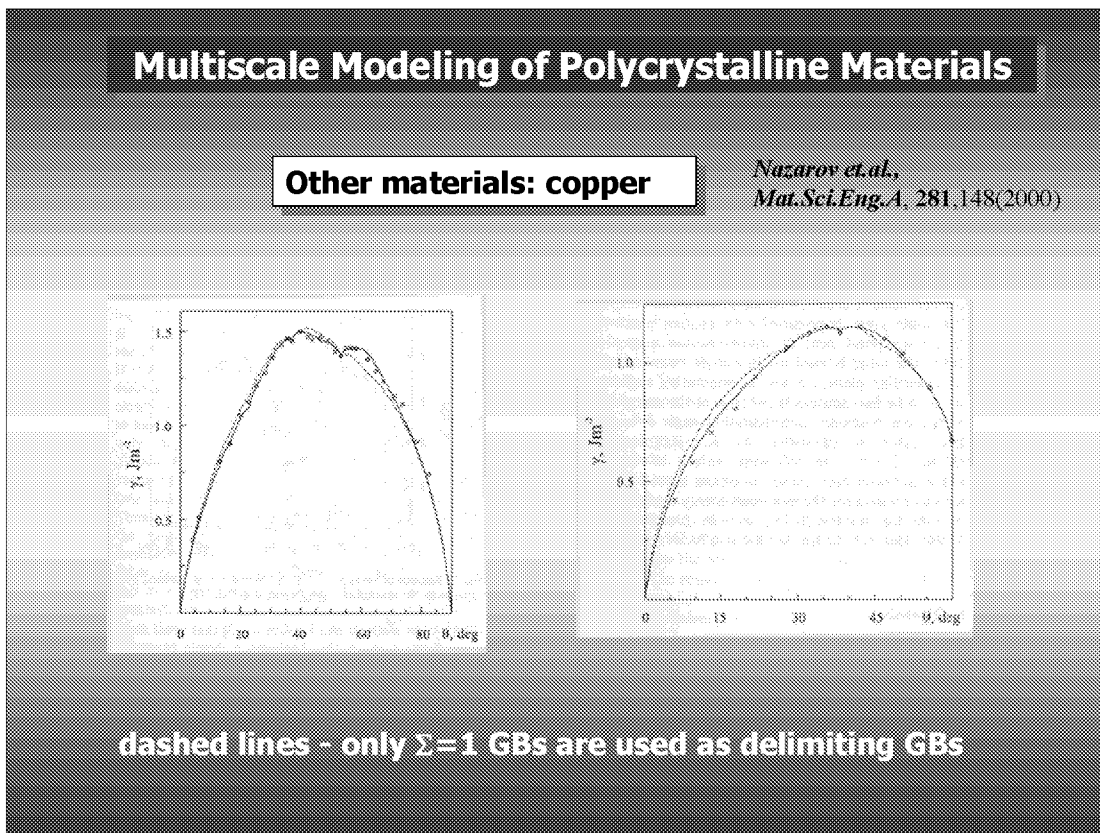
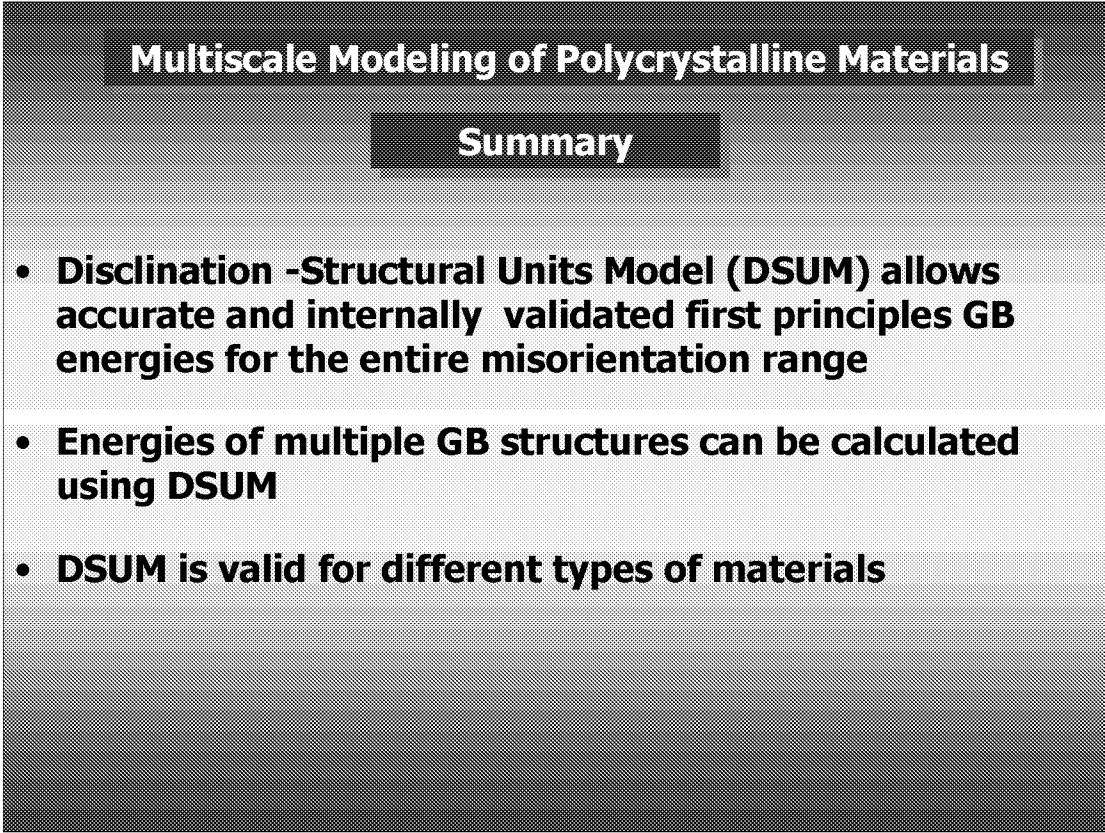


Figure 16

SUMMARY ON THE DISCLINATION-STRUCTURAL UNITS MODEL.



Multiscale Modeling of Polycrystalline Materials

Summary

- **Disclination -Structural Units Model (DSUM) allows accurate and internally validated first principles GB energies for the entire misorientation range**
- **Energies of multiple GB structures can be calculated using DSUM**
- **DSUM is valid for different types of materials**

Figure 17

GRAIN BOUNDARY TRIPLE JUNCTIONS MODELING

Grain boundary triple junctions (TJs), the intersecting points of GBs, are important microstructural elements, especially in nanocrystalline materials. TJs may contain disclination and act as stress concentrators and therefore as nuclei for both plastic deformation and microcrack generation or formation of local amorphous regions. The picture on the left illustrates the structure of TJ formed by $S=9/3/3$ GBs in diamond, which was observed experimentally. Simulations indicated that several models of the TJ with perfect matching of the SUs can exist [1]. The reconstruction along the TJ core to maintain four-fold coordination of atoms in diamond required double periodicity along the tilt axis and resulted in extended stresses in the vicinity of the TJ (fig. on the left).

[1] O.A.Shenderova, D.W.Brenner. 'Atomistic Simulations of Structures and Mechanical Properties of $\langle 011 \rangle$ Tilt Grain Boundaries and Their Triple Junctions in Diamond', *Phys.Rev.B* **60**, 7053(1999).

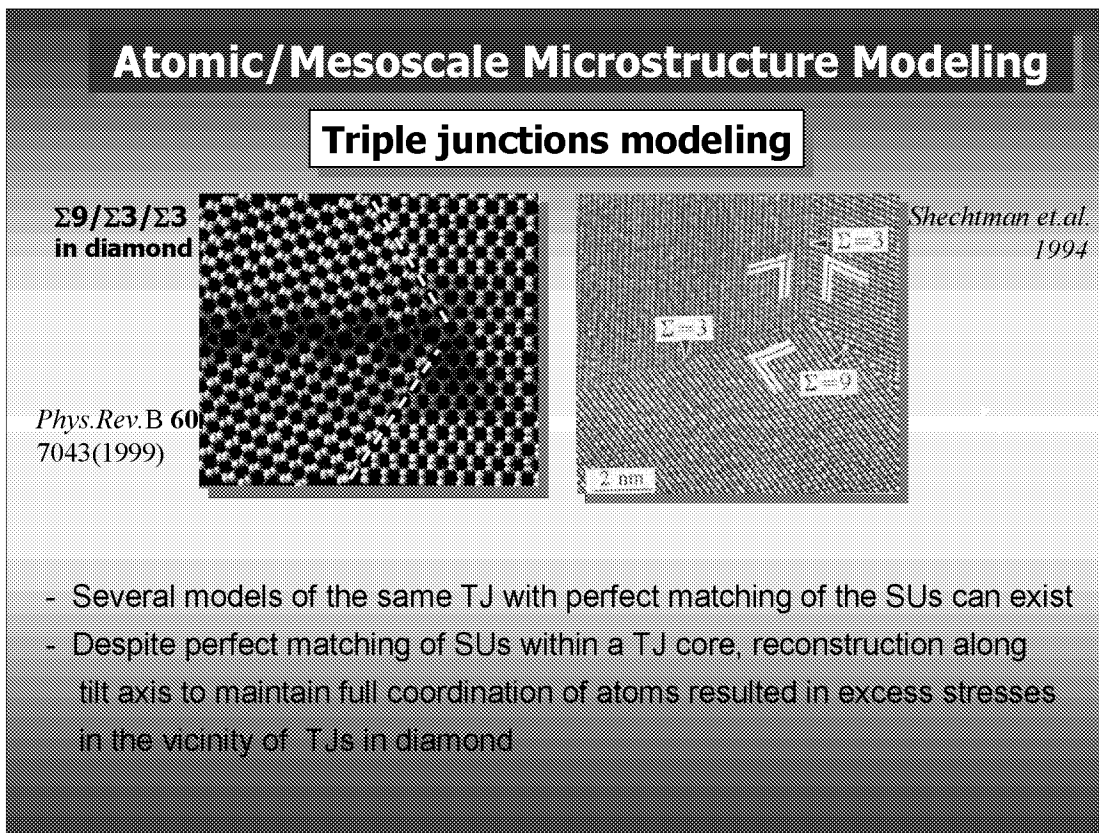


Figure 18

MULTISCALE MODELING OF MORE COMPLICATED MICROSTRUCTURAL ELEMENTS

At the present we try to extend the multiscale DSUM model to TJs in FCC metals. The general strategy is the same as that used for GBs. As a first step, a wide variety of structural models of TJs containing special GBs should be simulated as it had been done by Sutton and Vitek for the structural units model for GBs. After calculations of TJ energies, rules for combination of SUs within a TJ core leading to a minimum energy core structure can be elaborated. Representing again minority SUs as disclination dipoles, energies and stresses of three intersecting disclination dipole walls can be calculated using disclination theory. TJ core energy will be obtained from atomistic simulation. A snapshot at the bottom illustrate a geometrical construction of a periodic unit cell for an idealistic nanocrystal containing only special GBs and TJs [1]. Such system can help to understand the influence of a grain size on stability of nanocrystals. Again, multiscale DSUM can be applied to dramatically decrease computational burden of the analysis.

[1] A.Nazarov, private communication

Multiscale Modeling of Polycrystalline Materials: perspectives

Disclination - Structural Units model of grain boundary triple junctions (TJs):

- geometrical construction of special TJs
(periodic systems can be constructed-> FPs calculations!)
- minimum energy core structure
- absolute energies, stresses
- role of finite length of GBs (nanocrystals)

Periodic Network of Special GBs

- contains only $\Sigma 5$, $\Sigma 25$, $\Sigma 125$ GBs
- triple junctions are special
- system size can be controlled
- network energy vs. grain size

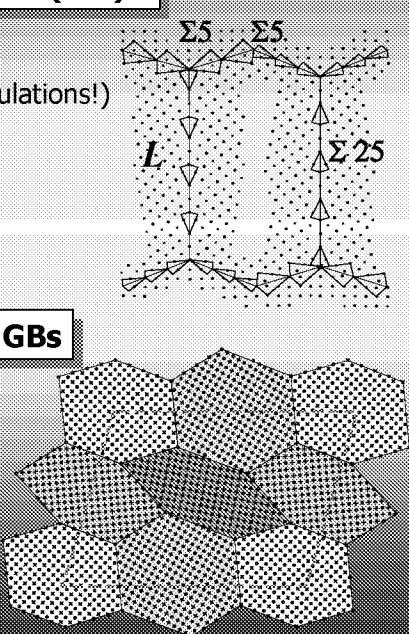


Figure 19

COMPUTATIONAL GRAIN BOUNDARY ENGINEERING

The developed multiscale approach can be useful in grain boundary engineering, the concept that had been already applied to optimize microstructures of real materials. It is well known that different types of GBs could behave differently under mechanical load and have different resistance to crack propagation. Grain boundary engineering is aimed on development of a set of thermal-mechanical treatments for a polycrystalline material resulting in a microstructure where 'good' GBs (mostly low-sigma GBs) will have certain arrangement and proportion in a sample. Different continuum level approaches (such as finite elements approach) or Monte Carlo technique are used to simulate the sintering of polycrystalline materials and can be developed to simulate microstructure evolution under thermal-mechanical treatments. To make these simulations more realistic, DSUM could be incorporated for quick estimation of the energies of the evolving GBs and TJs in the simulated systems.

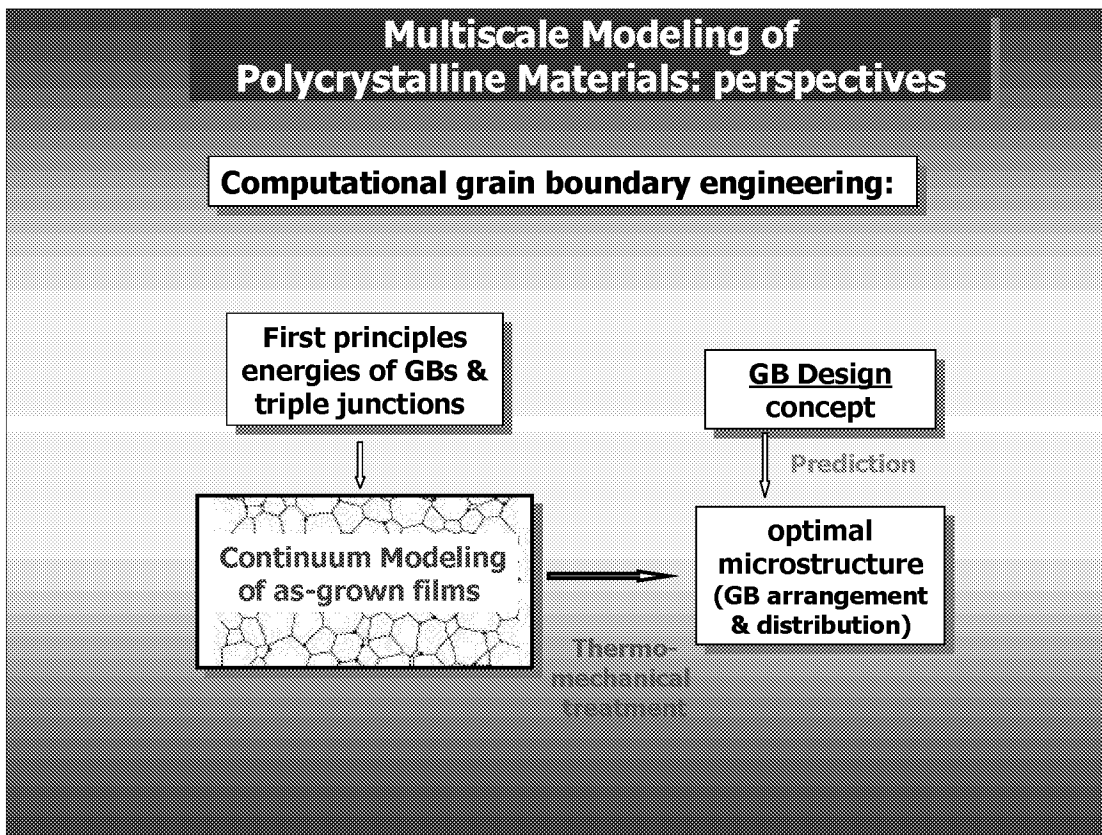


Figure 20

MULTISCALE MODELING OF CARBON POLYMER NANOCOMPOSITES

A radical alternative to conventional polymer composites which has emerged during the last decade is a class of polymer nanocomposites (PNCs) containing a uniform dispersion of nanoelements with characteristic sizes less than a hundred nanometers. A majority of polymer molecules reside near nanoelements so that the entire matrix may be considered to be nanoscopically confined. These restrictions on chain conformations alter molecular mobility and thermal transitions. Thus the crucial issues in PNC research is an understanding of characteristics of the interface region, its dependence on nanoelement geometry and surface chemistry, the relative arrangement of constituents and, ultimately, its relationship to macroscopic PNC properties. While first two issues can be addressed by large scale atomistic simulations, the issue of collective dynamics of nanoelements in a matrix can be studied only using mesoscopic simulation. The last issue can be addressed by a traditional continuum description using characteristics provided at previous structural level. All level of simulations would benefit from supporting related experiments.

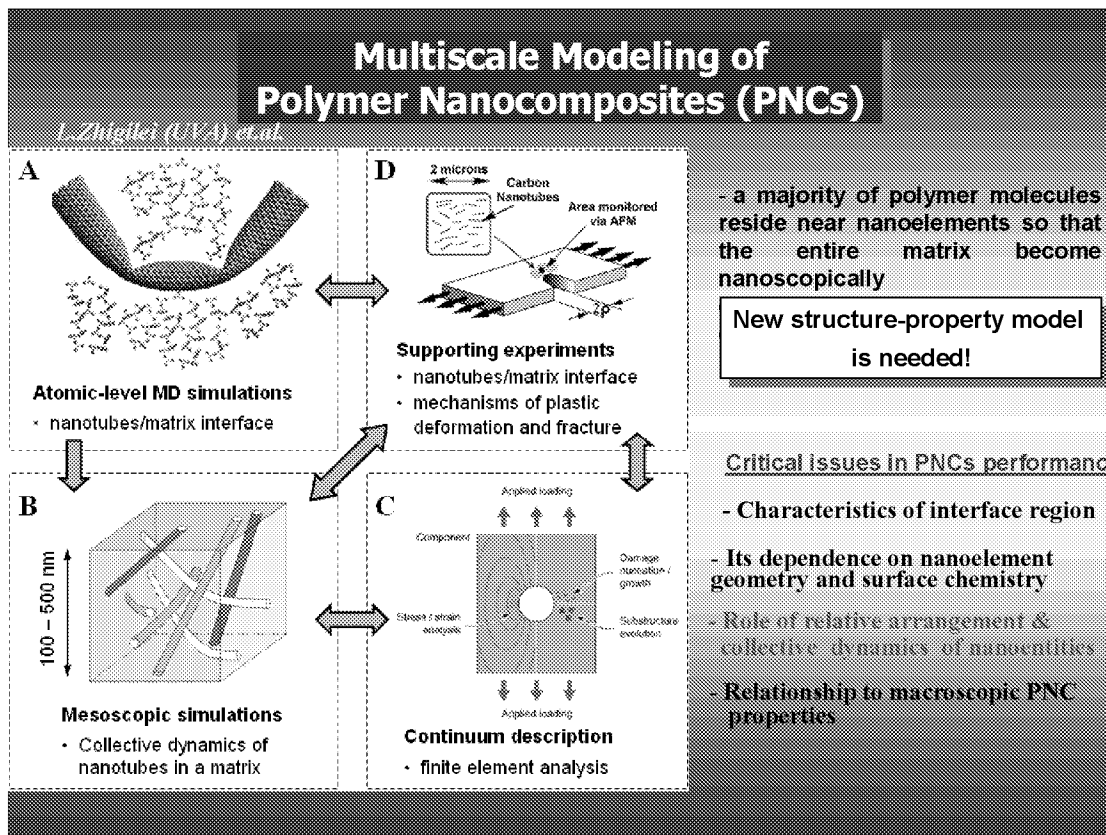


Figure 21

MESOSCOPIC DYNAMIC MODEL FOR NANOCOMPOSITE

While large-scale atomistic studies of the interface properties had been performed earlier and a continuum-beam model of a nanotube was developed by a group of researchers at NASA Langley Research Center (by Harik *et.al.*), the model of *dynamic* behavior of an ensemble of carbon nanotubes (CNTs) in an organic matrix had not been considered before and is the key of our multiscale approach. In the proposed model [1], each nanocomposite constituent (nano-fibers and matrix) is represented through coarser-grained models. In particular, each CNT is modeled as a “breathing flexible cylinder” represented by a variable number of segments (Figure below). Segment length varies along the nanotube depending on the local transverse curvature. The internal interactions within the nanotube are described through a mesoscopic many-body force field consisting of terms for stretching, bending, etc. An organic matrix will be represented by a coarse-grained “bead-and-spring” model. The functional forms of the matrix-nanotube potentials are chosen based on the results of atomic-level simulations. The equations of motion for five independent variables are integrated and classical trajectories are obtained in a manner similar to the traditional MD technique. The trajectories provide complete information on the dynamics of the nanotubes and the matrix molecules at the mesoscopic length-scale.

[1] L. Zhigilei, not published

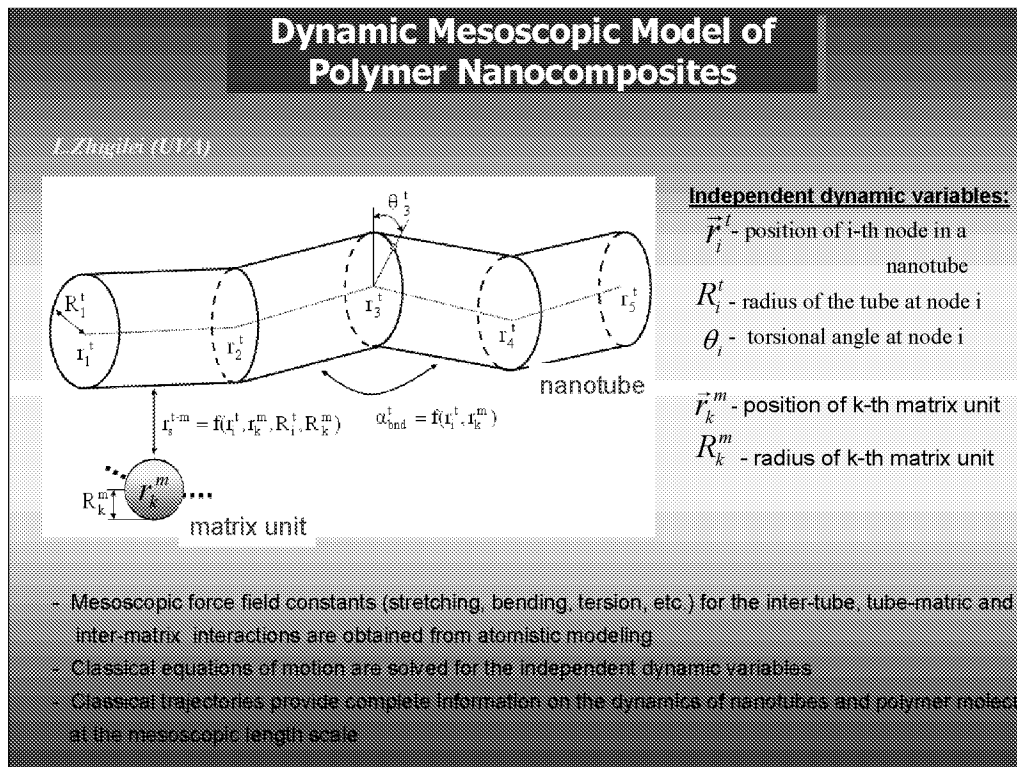


Figure 22

PERSPECTIVES

Once developed and tested, the model will be used to predict the behavior and properties of CNT-polymer nanocomposites under conditions representative of a range of practical applications. In particular, mechanisms of failure during dynamic and static loading, material response to the shock loading, as well as acoustic and thermal properties of the nanocomposites will be investigated. A range of processes involved in fabrication and processing of nanocomposites will also be studied with the goal of providing recommendations for the development and optimization of fabrication and processing technology.

It should be also emphasized that the general formalism for the description of nanocomposites implemented in the proposed model can be, in principal, extended to other polymer nanocomposite materials.

**Multiscale Model of
Polymer Nanocomposites: Perspectives**

- **Predict behavior and properties of CNT-polymer nanocomposites related to practical applications:**
 - mechanisms of failure during dynamic and static loading,
 - material response to the shock loading
 - acoustic and thermal properties of the nanocomposites
- **Provide recommendations for optimization of processing technology through simulations of processing conditions**
- **The resulting general formalism for the description of CNT-polymer nanocomposites can be extended to other polymer nanocomposite materials**

Figure 23

**On The Role of Plasticity Length Scale Parameters
in Multi-Scale Modeling**

W. O. Soboyejo
Princeton University
Princeton, NJ

INTRODUCTION

On The Role of Plasticity Length Scale Parameters in Multi-Scale Modeling

J. Lou, P. Shrotriya and W.O. Soboyejo

The Princeton Materials Institute and The Department of
Mechanical and Aerospace Engineering
Princeton University, Princeton, NJ 08544

Research Supported By NSF With Dr. K.L. Murty as
Program Monitor



Figure 1

OUTLINE OF PRESENTATION

The outline of the presentation is presented here. This includes the titles of the different sections of the presentation.

Outline of Presentation

- Introduction and Background
- Micro-Tensile Experiments
- Micro-Bending Experiments
- Nano-indentation Experiments
- Framework for multi-scale modeling
- Conclusions and Future Plans

Princeton **University** 

Figure 2

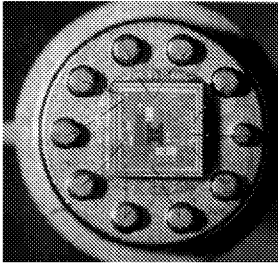
MEMS – A MOTIVATION FOR A MULTI-SCALE FRAMEWORK

This viewgraph identifies the emerging applications of MEMS structures. These include micro-motors, micro-satellites, micro-switches, accelerometers, actuators and sensors. The existing \$ 2 billion market for MEMS structures is expected to grow to ~\$ 5 billion within a year. Photographs of emerging MEMS products are presented. These include an accelerometers and a turbine rotor controlled by a fiber optic cable.

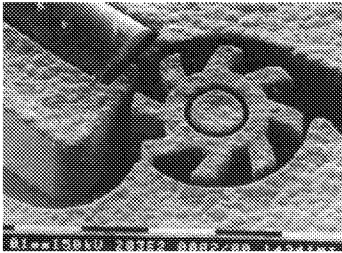
MEMS – A Motivation for a Multi-Scale Framework

- Micro-electro-mechanical systems (MEMS) have emerged in recent years
- These are machines on the micron-scale (finer than human hair of ~ 100 μm in diameter)
- Emerging systems include micro-satellites, micro-motors, micro-switches, accelerometers, actuators and sensors

Accelerometers



Turbine Rotor



Princeton University 

Figure 3

MATERIALS THAT ARE USED IN MEMS STRUCTURES

This viewgraph summarizes the materials that are used currently in MEMS structures. Most structures are fabricated from Si (single crystal or polycrystalline). SiC is also used in harsh environments or high temperature environments. Most recently, metallic MEMS structures have emerged for larger and thicker devices e.g. Ni, Ni-Fe, Ni-Co and Al structures.

Materials That Are Used in MEMS Structures

- Most of the existing MEMS structures are fabricated from single crystal or polycrystalline Si
- SiC is also used for MEMS in high temperature/harsh environments
- Metallic MEMS structures are being used increasingly in larger and thicker devices (plasticity becomes important)
 - Ni, Ni-Fe, Ni-Co
 - Al

Princeton **University**



Figure 4

INTRODUCTION TO LIGA PROCESS

This viewgraph describes the German acronym for the LIGA process that is used for the fabrication of the nickel MEMS structures that were employed in this study. The method was first developed in Germany about 20 years ago, and is now widely used for the fabrication of metallic MEMS structures.

Introduction to LIGA Process

- LIGA, an acronym of the German words for Lithographic, Galvanoformung, Abformung (lithography, electroplating, and molding), is a technique used to produce micro-electron-mechanical systems (MEMS) made from metals, ceramics, polymers and plastics
- First developed at the Forschungszentrum Karlsruhe (FZK), Germany in the mid-1980s
- Typically has 1-10 μm minimum lateral feature size, and are from hundreds of microns to a few millimeters thick. Especially advantageous for micromechanical systems such as micro-motors and micro-pumps because the high aspect ratios allow high torque to be produced

Princeton University



Figure 5

INTRODUCTION TO LIGA PROCESS (CONT.)

Further details on the LIGA processing of metallic MEMS structures are provided. The steps include the deep etching of x-ray resist materials to produce micro-moulds with high aspect ratios. Metals can then be electrodeposited into the micro-moulds to produce movable micro-devices with typical dimensions between $\sim 20 - 200 \mu\text{m}$.

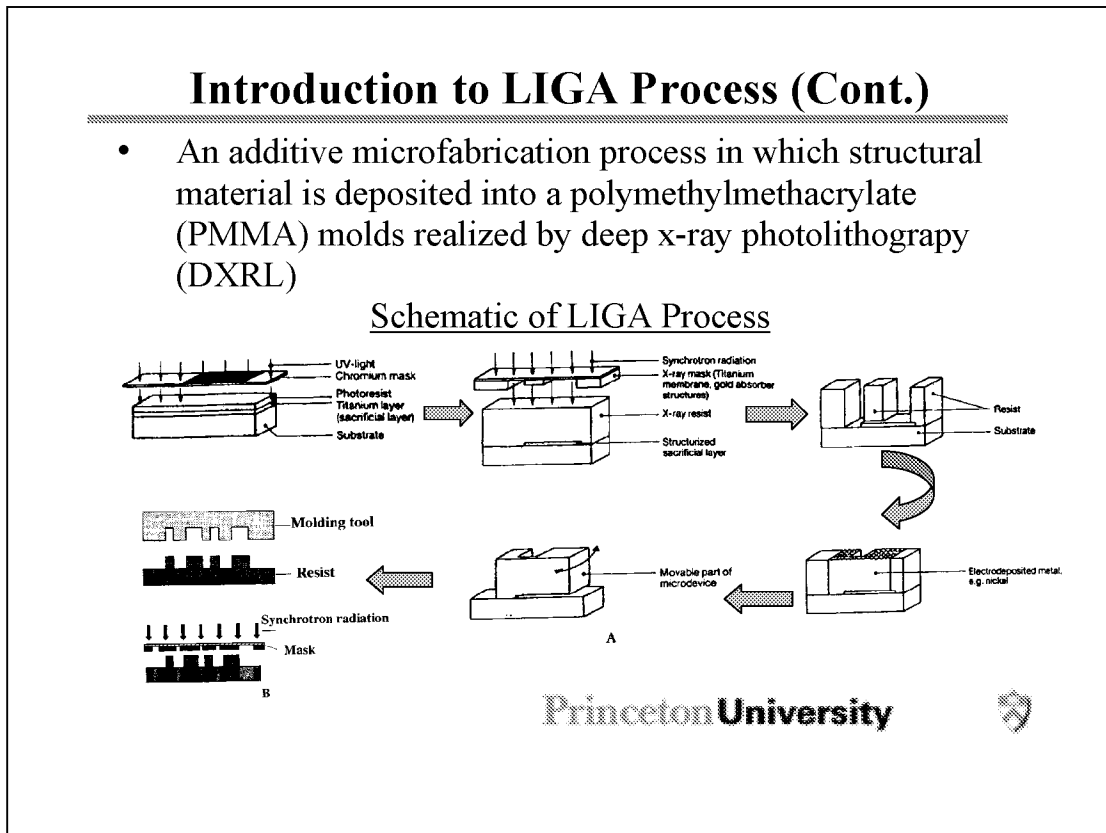


Figure 6

PLASTICITY AT THE MICRON AND SUB-MICRON SCALES

The micro-scale nature of metals MEMS structures requires a different framework for the modeling of plasticity due to contacts, fatigue and a wide range of loading conditions. Conventional J_2 plasticity theory breaks down due to the size effects that become important at the micron scale. Extended J_2 plasticity is needed along with discrete dislocations and atomistic approaches.

Plasticity at The Micron and Sub-Micron Scales

- There are several scenarios that require the constitutive modeling of plasticity at the micron- and sub-micron scales
- Conventional J_2 deformation theory breaks down in this domain since it does not contain a size-scale
- Discrete dislocation and atomistic approaches may be needed at the smallest size scales

Princeton University



Figure 7

PLASTICITY AT MICRON SCALE

Metals and their alloys exhibit significant size effects at the micron scales. This is particularly important in the case of LIGA Ni MEMS structures which have sizes between ~ 20 and $200 \mu\text{m}$. Prior evidence of size effects are also presented. These include: evidence of micro-indentation size effects on hardness data obtained for W crystals, and strong evidence of size effects obtained from torsional test on copper wire.

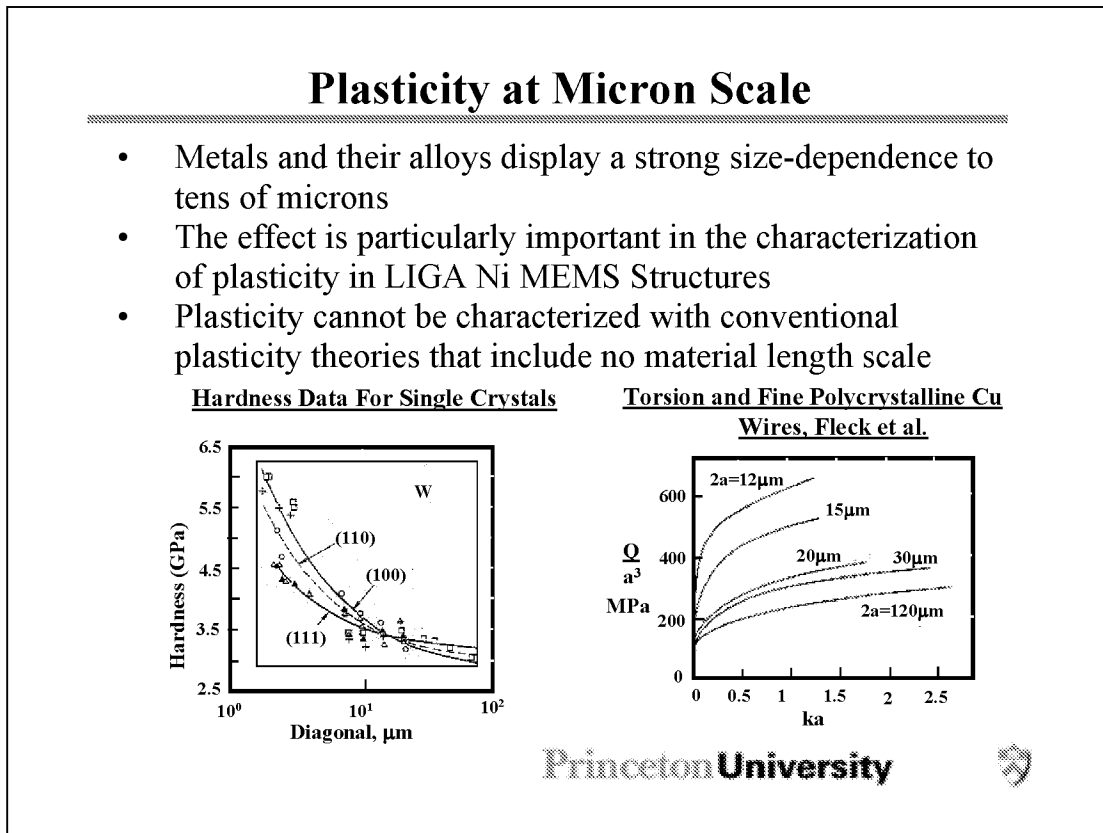


Figure 8

EXPERIMENTS OF PLASTICITY AT MICRON SCALE

In general, the microhardness should be independent of the size-scale of the indentation. However, in the range between $\sim 1 - 10 \mu\text{m}$, the hardness may become strongly dependent of the indentation size. Evidence of such size dependence has been obtained by a number of researchers. This is attributed largely to strain gradient plasticity phenomena that give rise to size dependent phenomena.

Experiments of Plasticity at Micron Scale

- Microhardness should be size-independent in the absence of a plasticity length scale
- The strong size dependence of hardness at the micron-scale is one of the most compelling pieces of evidence for the existence of a plasticity length-scale
- Strong evidence of hardness dependence observed in other metals
 - Atkinson (1995)
 - Ma and Clark (1995)
 - De Guzman et al. (1993)
 - Poole et al. (1996)
 - McElhaney et al. (1998)

Princeton University



Figure 9

MODELING OF PLASTICITY AT MICRON SCALE

A number of researchers have made significant efforts to develop strain gradient plasticity theories. Two groups have emerged. The first uses phenomenological theories to model the effects of plastic strain gradients, while the second group uses so-called mechanism-based strain gradient theories based on the strain contributions from geometrically necessary and statistically stored dislocations.

Modeling of Plasticity at Micron Scale

- Significant effort to develop new plasticity theory containing constitutive length scale that can characterize size-dependent plastic deformations
- Phenomenological plasticity theories proposed for the modeling of plastic strain gradients
 - Fleck and Hutchinson (1994, 1997)
 - Aifantis (1984, 1992)
 - Acharya and Bassani (1996)
 - De Borst and Muhlhaus (1992)
- Mechanism-based strain gradient plasticity (MSG) theory developed based on geometrically necessary dislocation
 - Gao, Huang and Nix (1999)
 - Huang, Gao and Nix (2000)
 - Nix and Gao (1998)

Princeton University



Figure 10

A FRAME WORK FOR MULTI-SCALE MODELING

In general, a multi-scale framework is needed for the modeling of plasticity. This is illustrated here for a simple nano-indentation modeling framework. At the smallest scales, electron transitions, atomistic simulations and dislocation dynamics are needed to model possible pile-up and stiction phenomena. Between the micron and sub-micron scales, strain gradient plasticity theories are needed. Finally, continuum theories are useful in the regime beyond the micron scale.

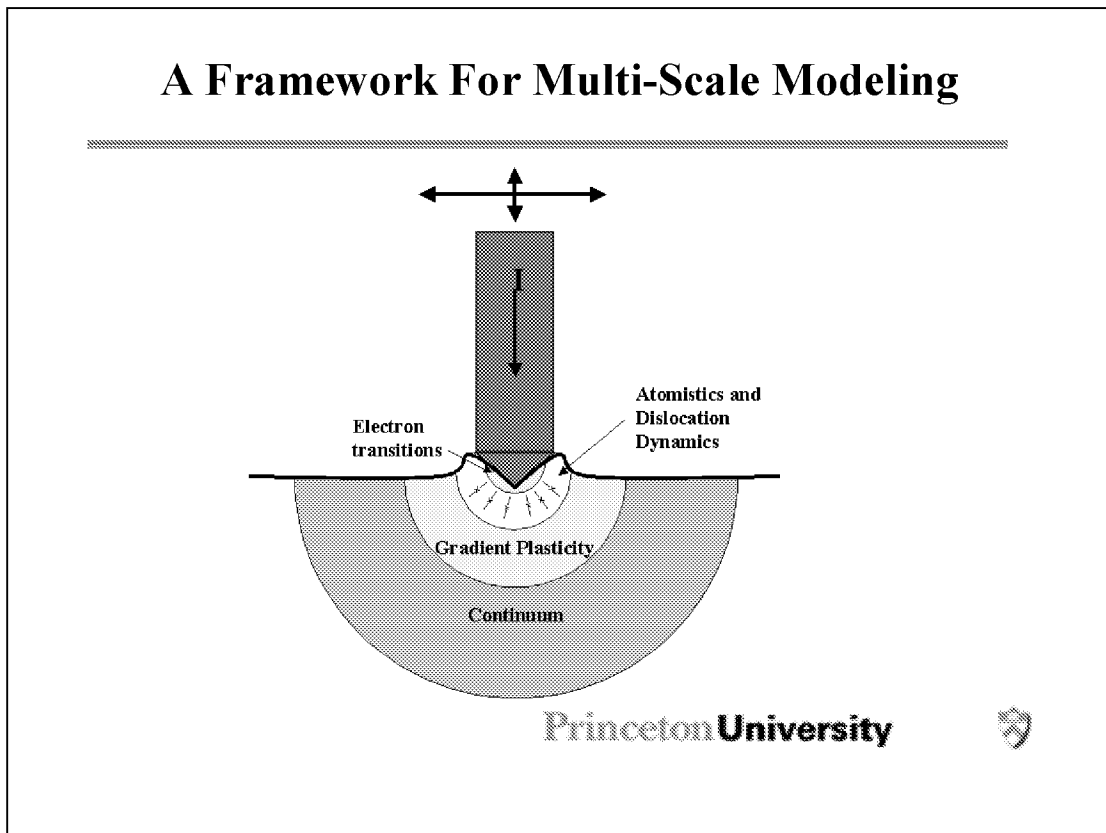


Figure 11

MATERIALS AND PROCESSING

The compositions of the sulfamate baths that were used in the LIGA processing of the electrodeposited Ni structures are presented along with the key plating conditions. Plating was done from a sulfamate bath to electrodeposit Ni into moulds at a current density of 50 mA/cm².

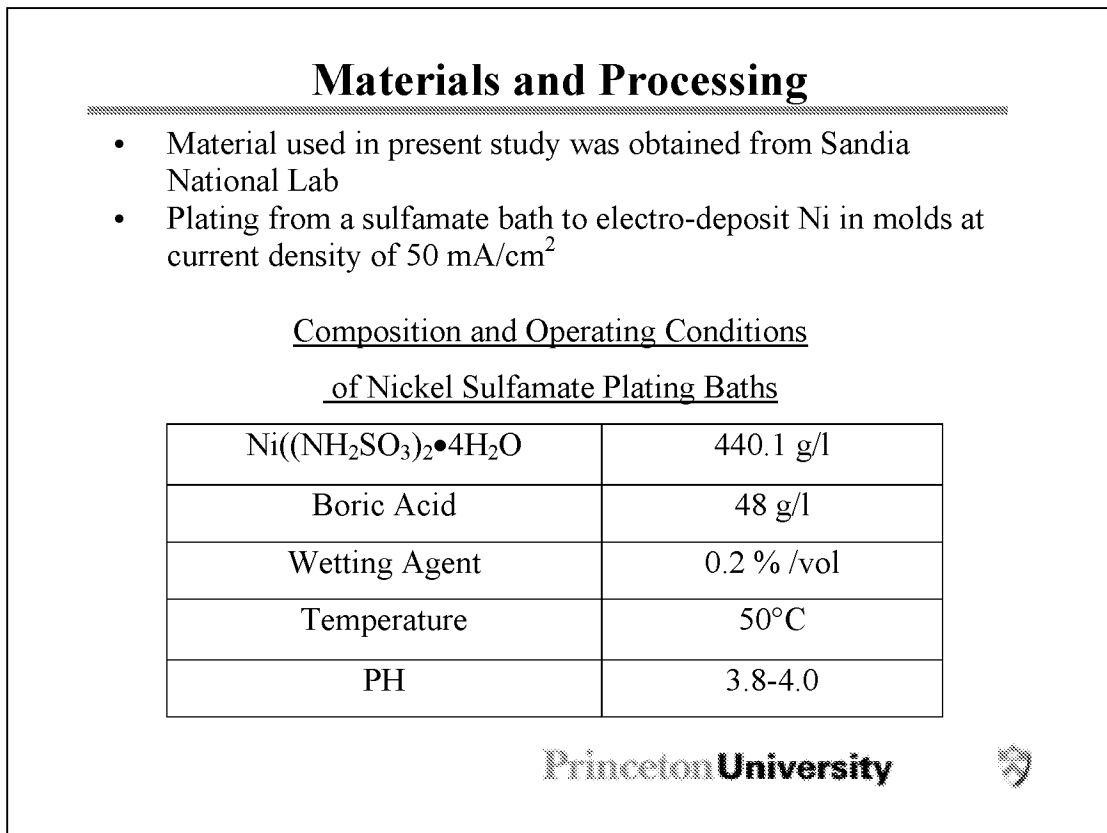


Figure 12

MICROSTRUCTURES OF LIGA NI THIN FILM

Cross-sectional micrographs of the complex material microstructure are presented. These show a refined top layer on a columnar structure with micro-scale structure. Within the columnar structure, the cross-sectional view from the focused ion beam image reveals a refined nano-scale/sub-micron structure.

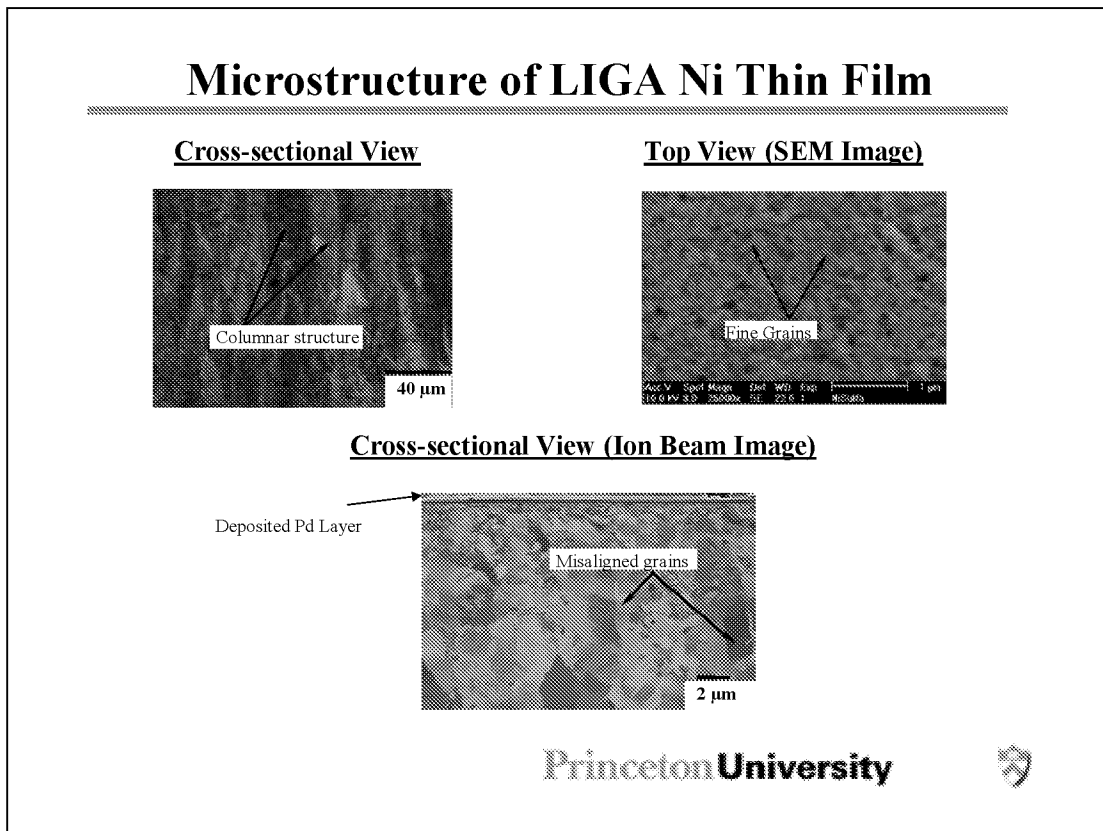


Figure 13

MICRO-TEXTURE OF LIGA NI THIN FILM

The micro-texture of the as-plated LIGA nickel material is presented. The orientation imaging microscopy (OIM) image shows strong [001] texture. However, some “black” areas are also present, for which the micro-texture has not been determined.

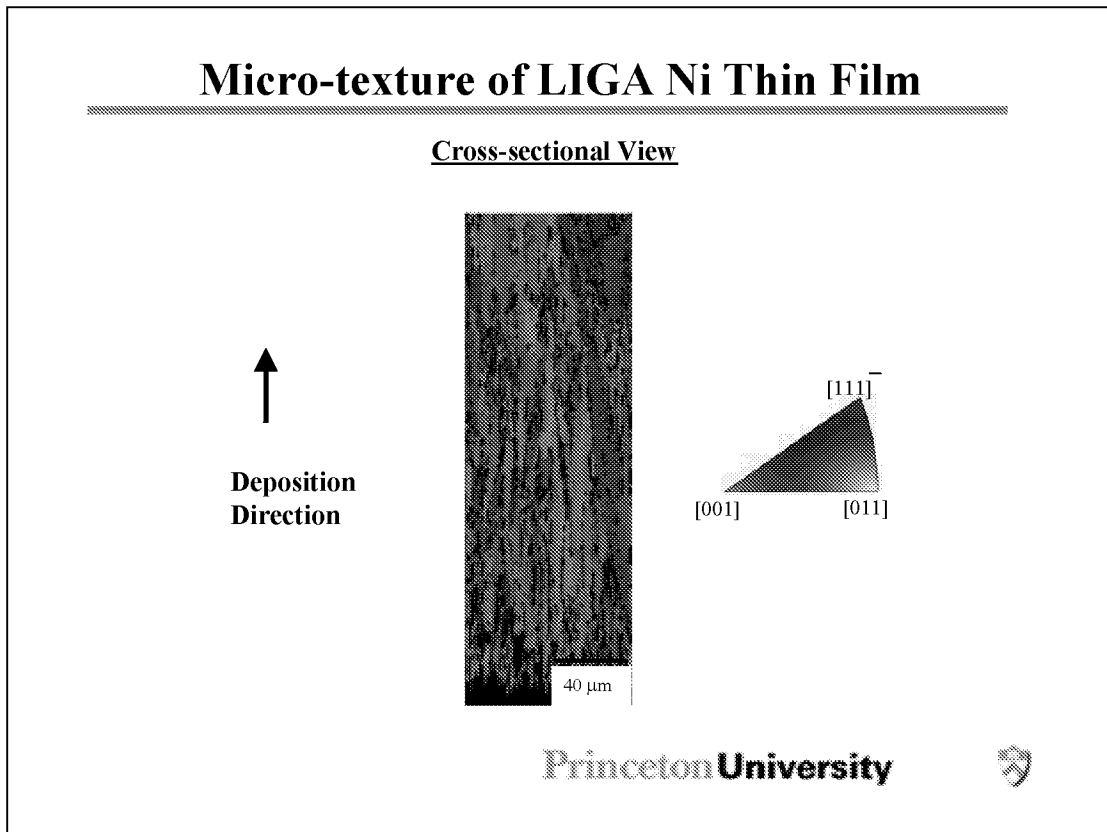


Figure 14

SCHEMATICS OF LIGA NI SPECIMENS

Schematics of the specimens that were used in the experiments are presented. These include dog-bone micro-tensile specimens and rectangular specimens that were used for micro-bending and nano-indentation testing.

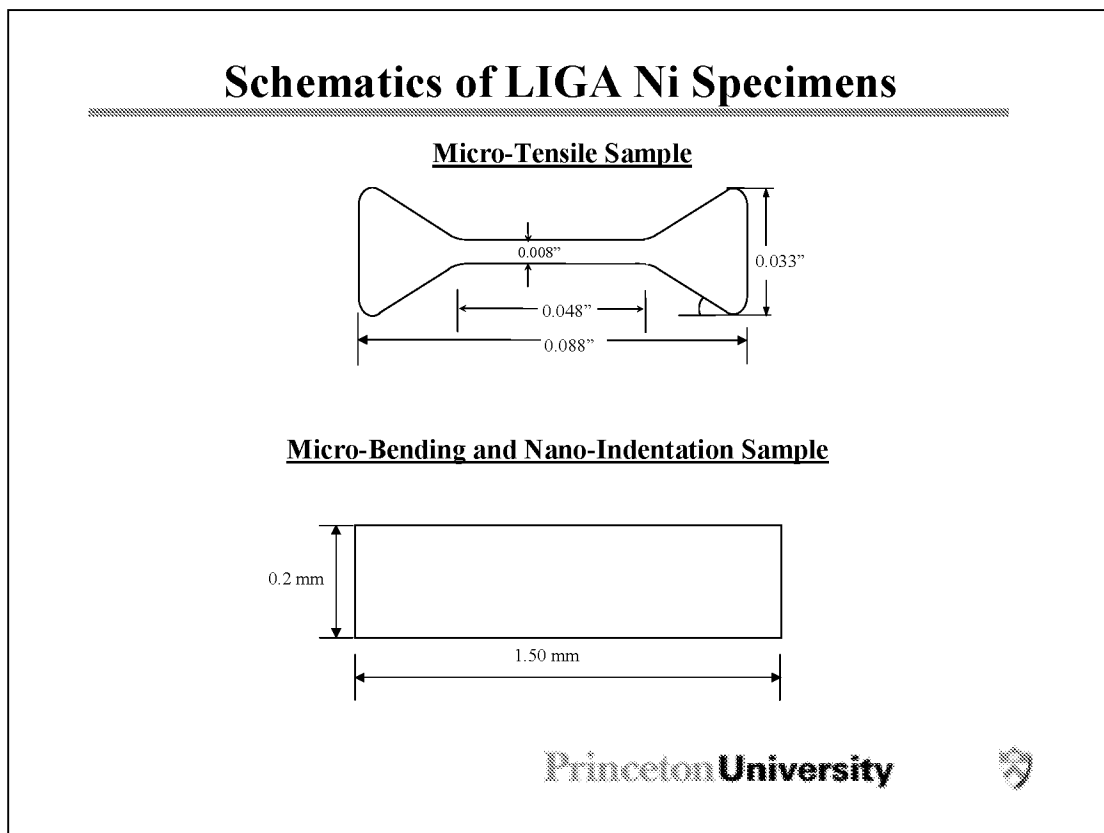


Figure 15

MICRO-TENSILE TESTING SYSTEM

A schematic of the micro-tensile testing system is presented. This shows the loading configuration, laser interferometry system for gauge strain measurement, load cell and uni-slide drive for load application. These all rest on an anti-vibration table.

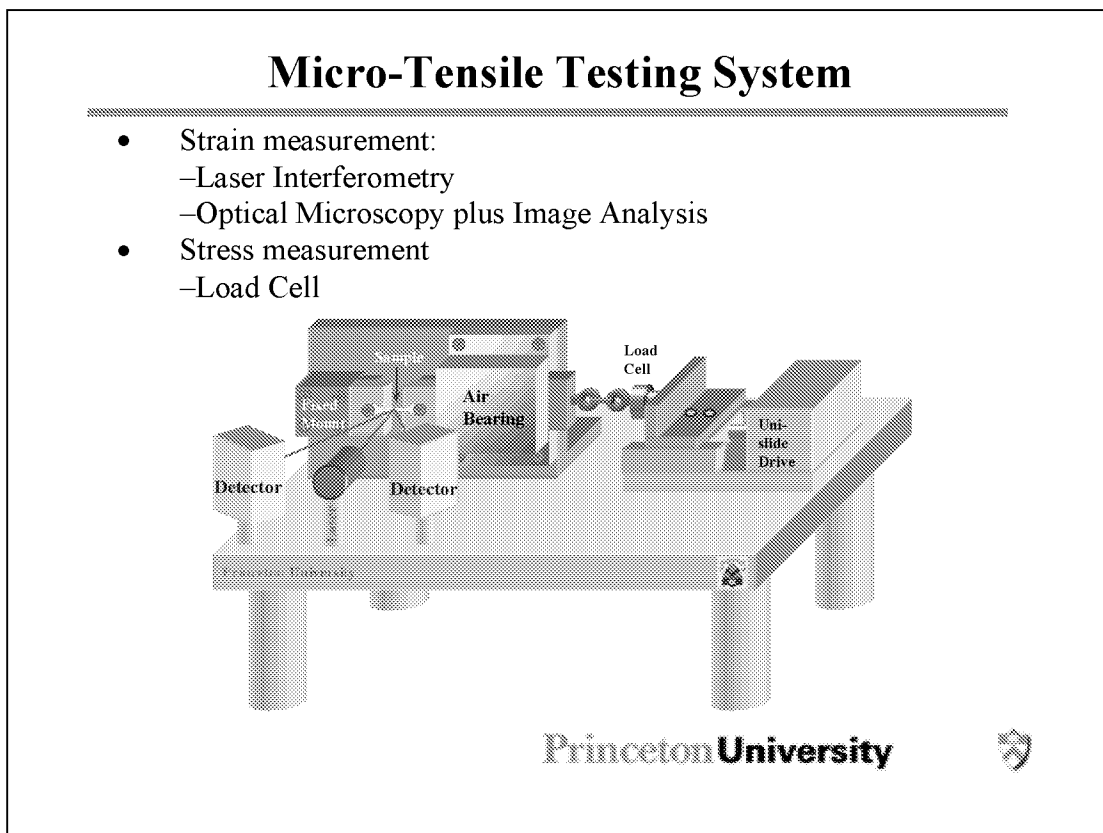


Figure 16

STRESS-STRAIN CURVES OF LIGA NI THIN FILM

The stress-strain curves obtained for LIGA Ni specimens with thickness of 50, 100 and 200 μm are presented. These show an initial elastic regime that is followed by a plastic regime with limited hardening. All the three materials exhibit similar stress-strain behavior, i.e. no significant thickness effect in tension.

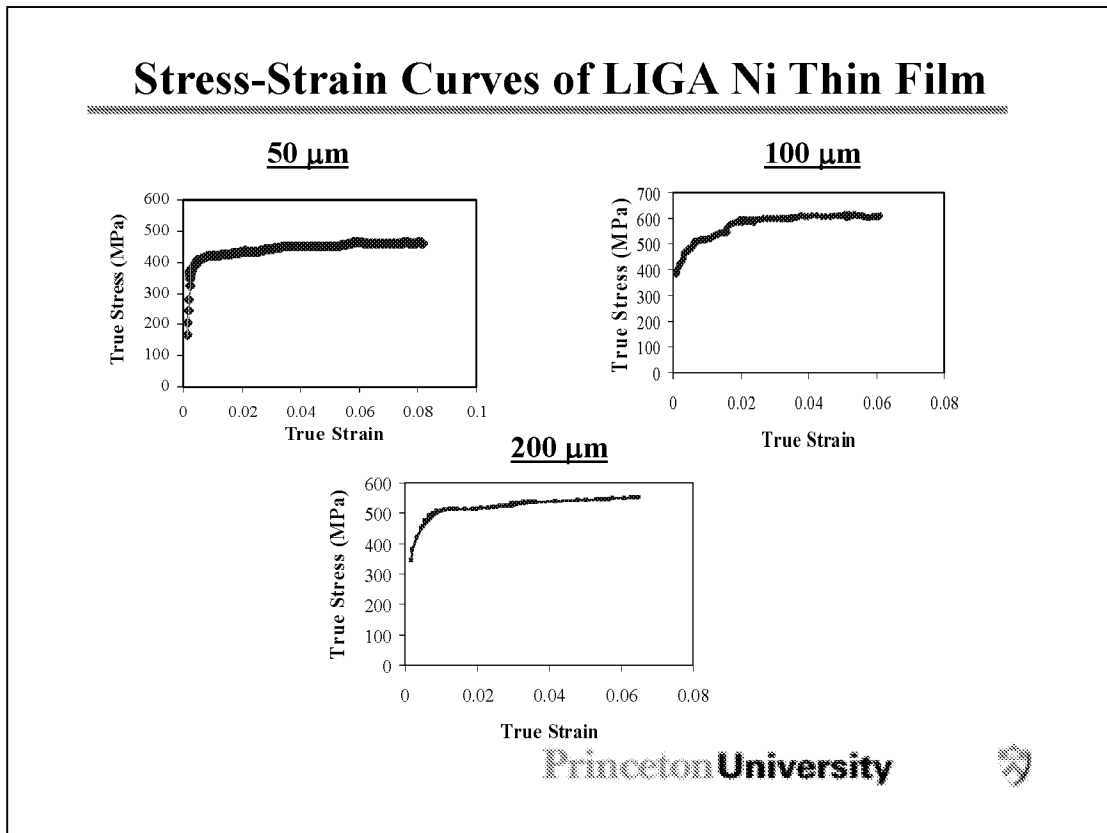


Figure 17

SUMMARY OF MICRO-TENSILE PROPERTIES

The micro-tensile properties obtained from the micro-tensile tests are presented. The measured differences obtained from the LIGA Ni MEMS structures with different thicknesses are within the limits of experimental error. Hence, there does not appear to be a significant effect of thickness on tensile properties.

Thickness of Structure (μm)	0.2% Offset Yield Stress (MPa)	Ultimate Tensile Stress (MPa)	Plastic Elongation to Failure
50 μm	405	497	6.6%
100 μm	475	587	6.2%
200 μm	450	547	8.5%

Princeton University 

Figure 18

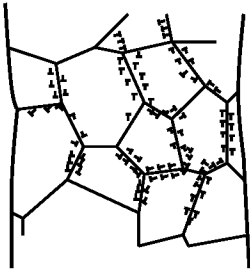
ANALYSIS OF MICRO-TENSILE TESTS

The absence of a size effect in micro-tension is associated with a statistical distribution of local short range strain gradient effects surrounding individual grains. These do not have a significant long range effect due to the different orientation of the grain boundaries. In contrast, long range applied strain gradients in bending have a significant size effect.

Analysis of Micro-Tensile Tests

- No apparent effect of thickness on the tensile properties for LIGA Ni MEMS structure has been found. This is due to the lack of contribution from the strain gradient plasticity phenomena

Schematic of local
Strain gradient



Schematic of global
Strain gradient



Princeton University 

Figure 19

SCHEMATIC ILLUSTRATION OF GEOMETRICALLY NECESSARY DISLOCATIONS CONCEPT

Schematic illustration of specimen and dislocation configurations are presented for conditions before and after bending. The schematics show that additional columns of atoms are needed for geometric compatibility when strain gradients are applied under bending loads.

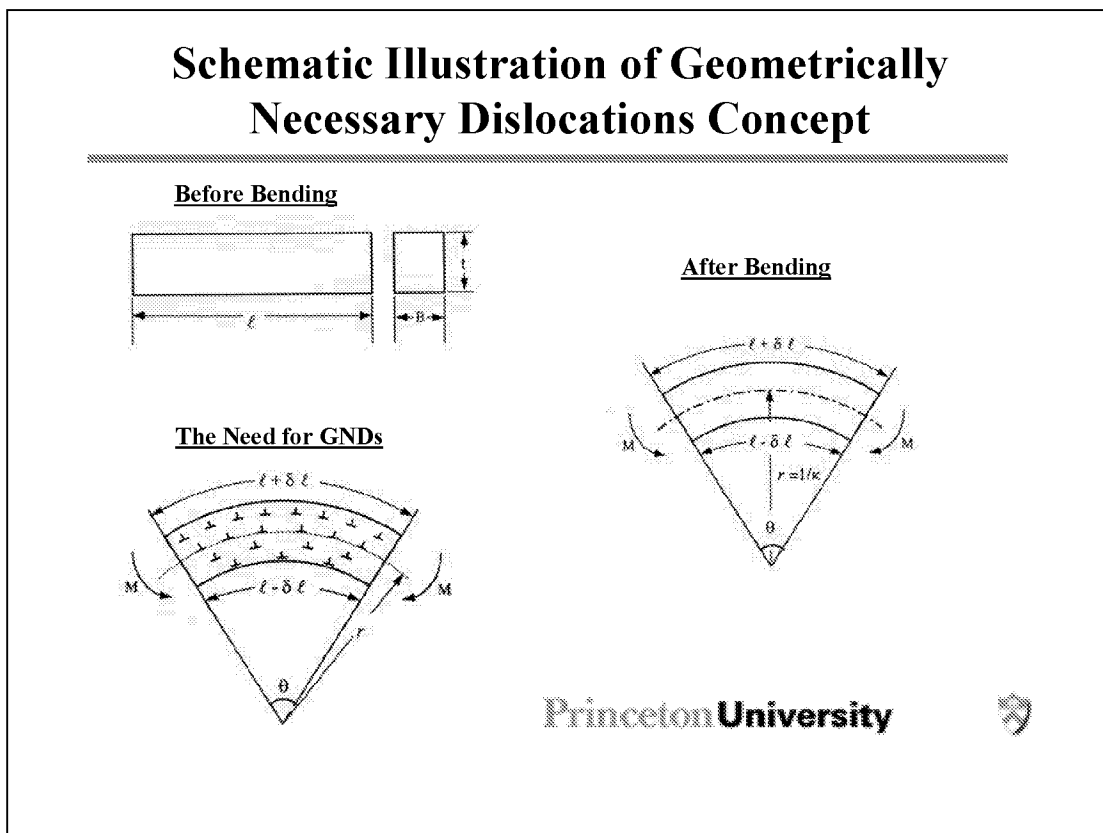


Figure 20

COMPARISON OF CURRENT AND PREVIOUS TENSILE PROPERTIES

A comparison of the current tensile properties with prior tensile results is presented. The results suggest that the current yield stresses are comparable to prior results. The Young's moduli are also comparable to prior results.

Source	Young's Modulus (GPa)	0.2% Offset Yield Stress (MPa)	Ultimate Tensile Strength (MPa)
Mazza et al.	202	405	782
Sharpe et al.	176	323	555
Hemker et al.	175	400	540
Current Study	189	437	544
Bulk Ni	207	59	317

Princeton University 

Figure 21

SCHEMATIC OF MICRO-BEND EXPERIMENT

A schematic illustration of the micro-bend test is presented along with the corresponding normal moments versus strain relationships. The stages of the micro-bend tests are illustrated with numbers 1-3, while the corresponding moment/strain relationships are labeled on the schematic.

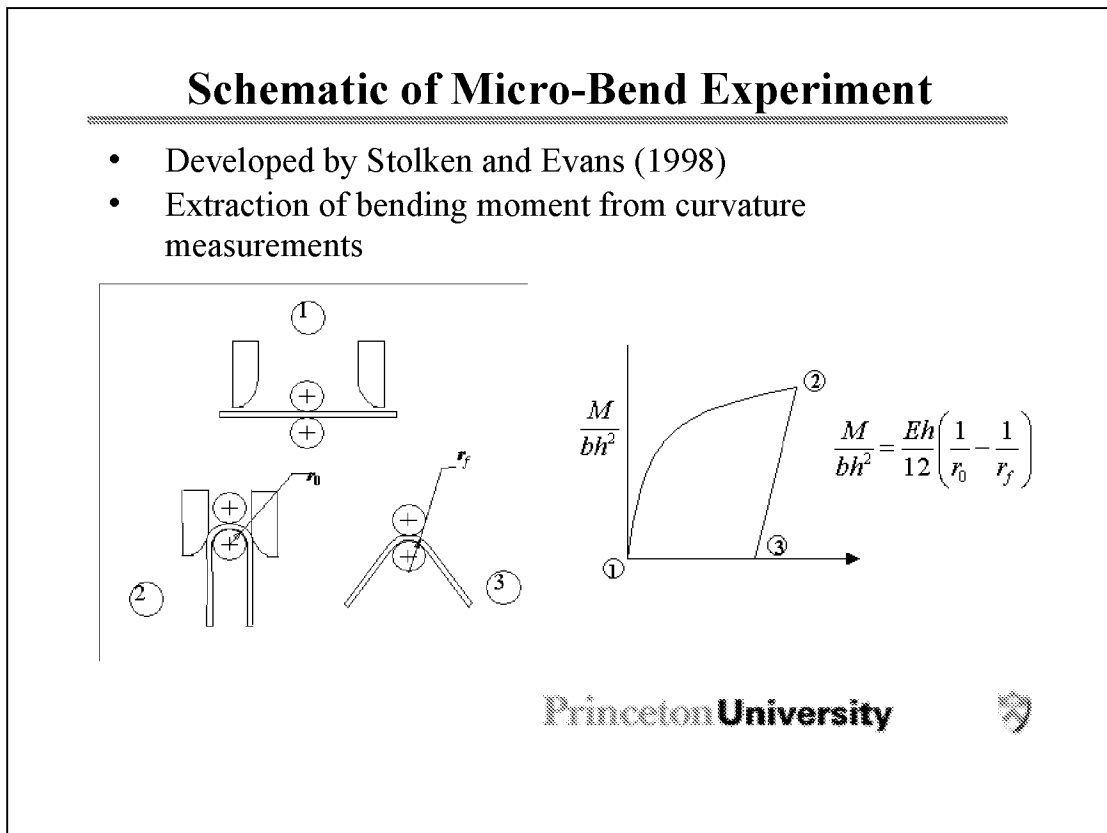


Figure 22

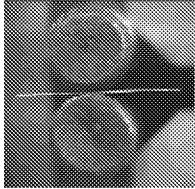
PROCEDURE OF MICRO-BEND EXPERIMENT

Actual photographs of the micro-bending test are presented (before and after spring back). The test procedure is also described in same detail. This includes descriptions of Ni foil thinning with TEM preparation techniques, micro-bend testing around W fibers, and curvature/strain measurements with micro vision system.

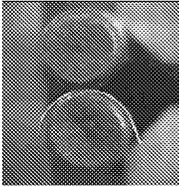
Procedure of Micro-Bend Experiment

- Ni MEMS specimens ground with TEM preparation techniques
- Experiments performed on specimens with thicknesses of 25, 50, 100 and 200mm
- Micro-bending experiments performed around W fibers with Teflon spacers
- Elastic spring-back measured by analysis of micro-vision images

Initial Configuration



After Spring-Back



Princeton University 

Figure 23

RESULTS FROM MICRO-BEND EXPERIMENTS

The results from the micro-bending tests are presented. These show a significant size effect on plots of normalized bending moment versus surface strain. The smallest thicknesses (25 μm) have normalized bending moments that are 3 times those of the thickest (200 μm) specimens.

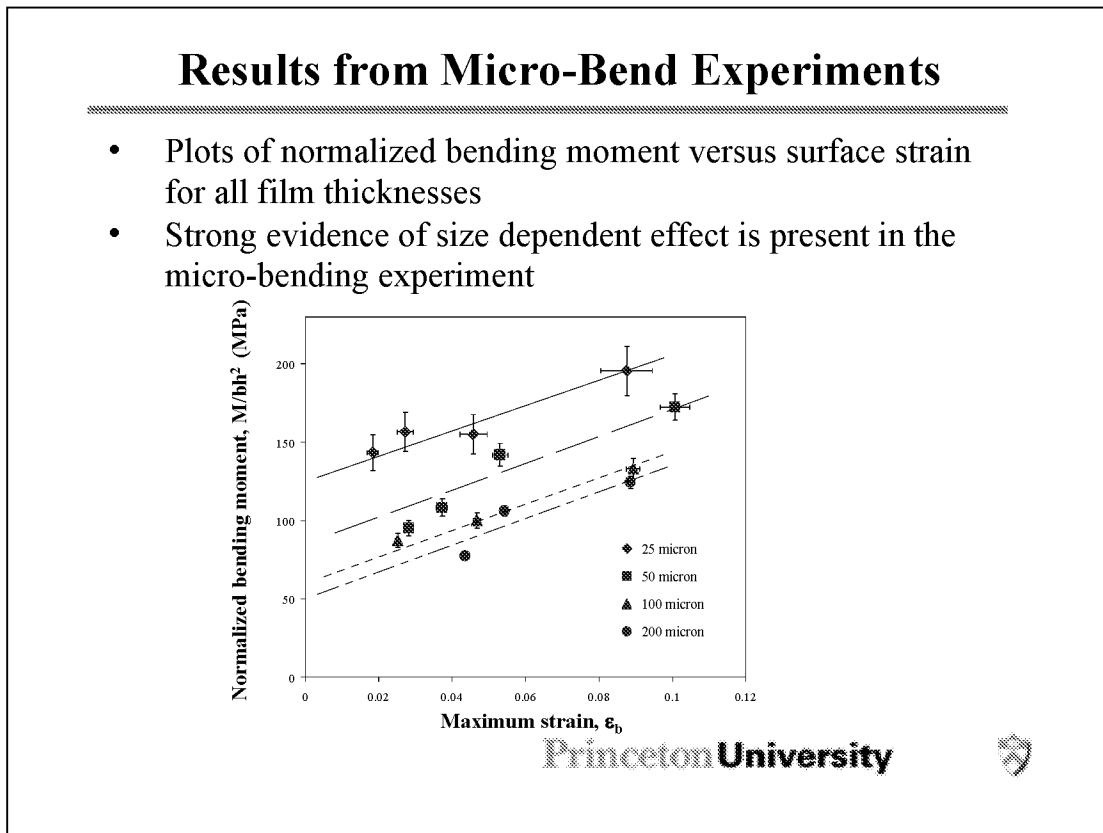


Figure 24

SGP THEORY OF THE STRETCH AND ROTATION LENGTH SCALES

An introduction to the strain gradient plasticity theory is presented. This includes a description of the strain tensor and second gradient of displacement, along with an expression for the effective strain in the extended J_2 deformation theory.

SGP Theory of The Stretch and Rotation Length Scales

- The formulation is for a small strain and non-linear elastic solid, where both strain and strain gradients contribute to the strain energy density
- The strain tensor and the second gradient of the displacement (strain gradient) is defined as following:

$$\varepsilon_{ij} = \frac{1}{2}(u_{i,j} + u_{j,i}) \quad \text{and} \quad \eta_{ijk} = u_{k,ij} = \varepsilon_{jk,i} + \varepsilon_{ik,j} - \varepsilon_{ij,k}$$

- Define the effective strain as a function of the deviatoric parts of the strain and strain gradient tensors as extension of traditional J_2 theory
- The deviatoric strain gradient tensor could be decomposed into 3 unique, mutually orthogonal third order deviatoric tensor
- The effective strain of the deformation theory can be taken as:

$$\varepsilon = \left[\left(\frac{2}{3} \varepsilon'_{ij} \varepsilon'_{ij} + l_1^2 \eta_{ijk}^{(1)} \eta_{ijk}^{(1)} + l_2^2 \eta_{ijk}^{(2)} \eta_{ijk}^{(2)} + l_3^2 \eta_{ijk}^{(3)} \eta_{ijk}^{(3)} \right) \right]^{1/2}$$

Princeton University



Figure 25

SGP THEORY OF THE STRETCH AND ROTATION LENGTH SCALES (CONT.)

The complete version of the extended J_2 theory is presented initially. However since the $\chi_{ij}\chi_{ji}$ is unessential in most problems, it is eliminated from consideration in the simple version that includes the stretch and rotational gradients. This is shown at the bottom the page.

SGP Theory of The Stretch and Rotation Length Scales (Cont.)

- The complete version of the J_2 SGP expression for the effective strain:

$$\varepsilon = \left[\left(\frac{2}{3} \varepsilon'_{ij} \varepsilon'_{ij} \right) + \left(l_1^2 \eta'_{ijk} \eta'_{ijk} \right) + \left(\frac{2}{3} (2l_2^2 + 12/5 l_3^2) \chi_{ji} \chi_{ij} \right) + \left(\frac{2}{3} (2l_2^2 - 12/5 l_3^2) \chi_{ij} \chi_{ji} \right) \right]^{1/2}$$

Where $\eta_{ijk} = \mu_{k,ij}$ is the strain gradient generated and η'_{ijk} is its deviator

- $\chi_{ij} \chi_{ji}$ is unessential in most problems (eliminated from consideration)

-The effective strain is thus given by

$$\varepsilon = \left(\left(\frac{2}{3} \varepsilon'_{ij} \varepsilon'_{ij} \right) + \left(l_{SG}^2 \eta'_{ijk} \eta'_{ijk} \right) + \left(\frac{2}{3} l_{RG}^2 \chi_{ij} \chi_{ij} \right) \right)^{1/2}$$

Where $-l_{SG}$ is the stretch length scale

$-l_{RG}$ is the rotation length scale

Princeton University



Figure 26

PLASTICITY LENGTH SCALE ANALYSIS FROM MICRO-BEND EXPERIMENT

The bilinear hardening law that was used to approximate the deformation behavior of the films is presented. A typical plot of true stress versus true strain is also presented for one of the LIGA foils. Typical values of the fitting parameters in the hardening expression are also presented.

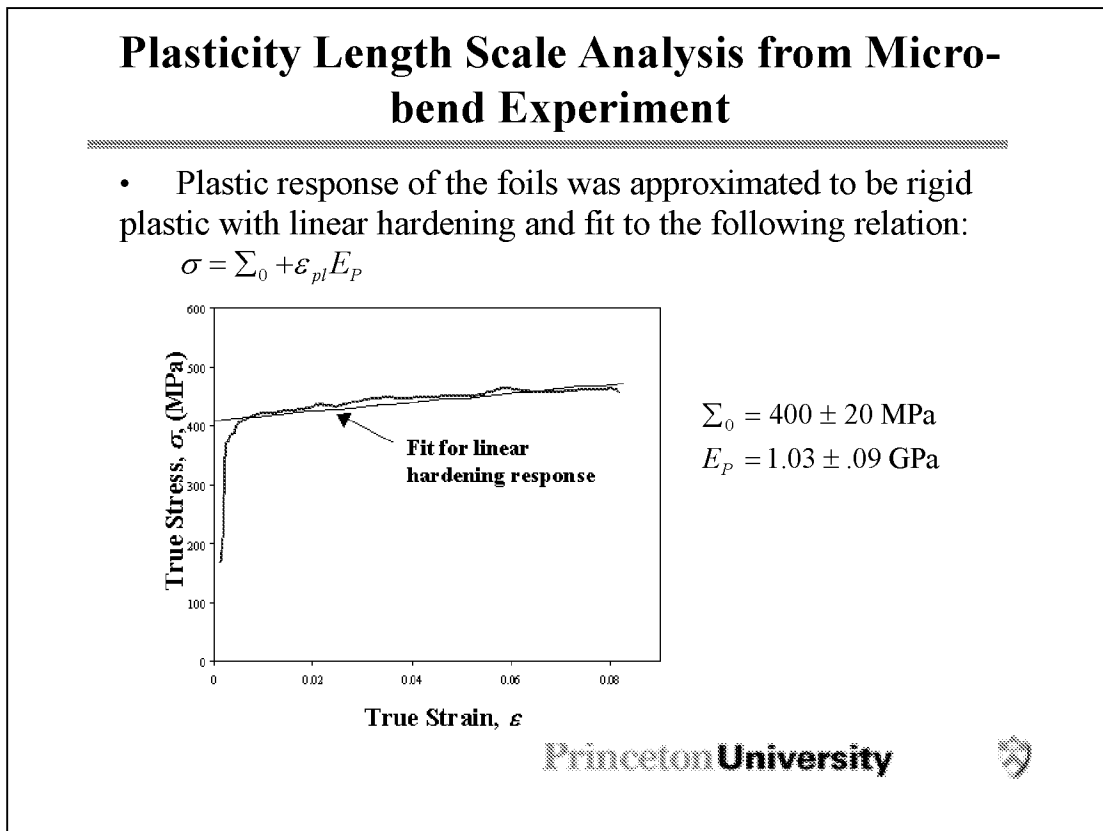


Figure 27

**PLASTICITY LENGTH SCALE ANALYSIS FROM
MICRO-BEND EXPERIMENT (CONT.)**

An outline of the plasticity length scale analysis is presented. This includes expressions for the strain energy density in the presence of strain gradient, and an expression for the bending moment as a function of surface strain.

Plasticity Length Scale Analysis from Micro-bend Experiment (Cont.)

- For a rigid-plastic material with linear hardening, the strain energy density in the presence of strain gradients can be expressed as:
- $$w = \frac{\varepsilon}{2} (E_p \varepsilon + 2 \Sigma_0)$$
- The energy density is integrated through the thickness to obtain the total energy of the beam and differentiated with respect to the neutral axis curvature in order to express the bending moment, M , as a function of the surface strain, ε_b ,

$$\frac{4M}{\Sigma_0 t h^2} = \left(\frac{2}{\sqrt{3}} \right) \left(\sqrt{2\beta^2 + 1} + 2\beta^2 \ln \left(\frac{\sqrt{2\beta^2 + 1} + 1}{\sqrt{2\beta^2 + 1} - 1} \right) \right) + \left(\frac{\varepsilon_t E_p}{\Sigma_0} \right) \left(\frac{8}{9} + \frac{16}{3} \beta^2 \right)$$

where $\beta = l_c/h$

Princeton University



Figure 28

PLASTICITY LENGTH SCALE ANALYSIS FROM MICRO-BEND EXPERIMENT (CONT.)

The extraction of the composite length scale parameter, l_c , is discussed. The value of l_c obtained for LIGA Ni foils is $5.6 \mu\text{m}$. This compares very well with values of l_c of $5.3 \pm 0.2 \mu\text{m}$ obtained by Stolken and Evans.

Plasticity Length Scale Analysis from Micro-bend Experiment (Cont.)

- The micro-bend experiments provide a measure of l_c which is given by:

$$l_c = \sqrt{l_{RG}^2 + \left(\frac{8}{5}\right) l_{SG}^2}$$

- The non-linear data fitting is performed using the built-in functions of the symbolic computation software *MATHEMATICA*
- In current study, $l_c \sim 5.6 \mu\text{m}$ in LIGA Ni MEMS structures
- This compares very well with the results of Stolken and Evans obtained from Ni foils for which $l_c = 5.3 \pm 0.2 \mu\text{m}$ and $l_{RG} \sim 5 \mu\text{m}$

Princeton University



Figure 29

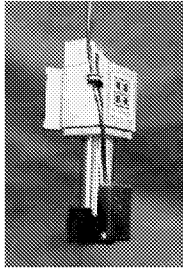
SET-UP OF NANO-INDENTATION EXPERIMENT

The set-up for nano-indentation testing is presented. This includes a TriboScope nano-indentation system produced by Hysitron, Inc, Minneapolis, MN. The system is incorporated into a DI Dimension 3100 atomic force microscope (AFM) frame. Contact mode AFM is used to image the surfaces before and after indentation.

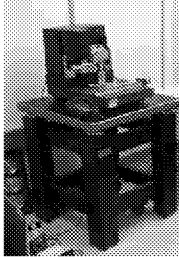
Set-up of Nano-Indentation Experiment

- The hardness measurements were performed using a TriboScope[®] (TriboScope is a registered trademark of Hysitron, Inc., Minneapolis, MN) Nanomechanical Testing System incorporated with DI Dimension 3100 AFM frame
- Contact mode Atomic Force Microscopy scans can be obtained before and after the indentation tests
- A load-displacement curve was recorded during each test

The indenter head



AFM Frame



Princeton University 

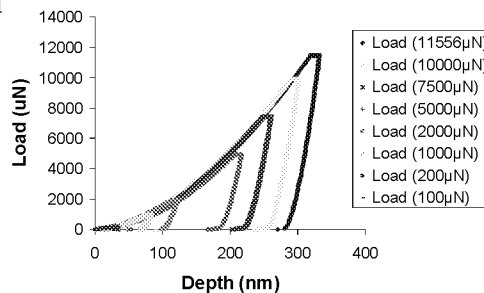
Figure 30

PROCEDURE OF NANO-INDENTATION EXPERIMENTS

The procedure for the nano-indentation experiments is described. This utilized North Star (three-sided cube corner) and Berkovich (three-sided pyramid type) indenter tips. Deformation was applied at a constant loading rate of 100 $\mu\text{N}/\text{sec}$, and a holding period of 15 seconds was applied. Consistent load-displacement plots were obtained.

Procedure of Nano-indentation Experiments

- Two types of indenter tips were used in the study
 - North Star indenter (a three-sided cube-corner type tip/sharp gradient)
 - Berkovich indenter (a three-sided pyramid type tip/weak gradient)
- Peak load ranges between 200 μN to 11000 μN were explored in the study- these show very good repeatability
- The loading rate was kept at 1000 $\mu\text{N}/\text{sec}$, and holding period of 15 sec was applied



Princeton University



Figure 31

NANO-INDENTATION SIZE DEPENDENCE

The results from the nano-indentation tests are presented. The blunt Berkovich tip (small gradients) do not show a significant size effect. However, the sharp cube corner tip (large gradients) exhibits a strong size effect, which is associated with an increase in hardness by a factor of 3.

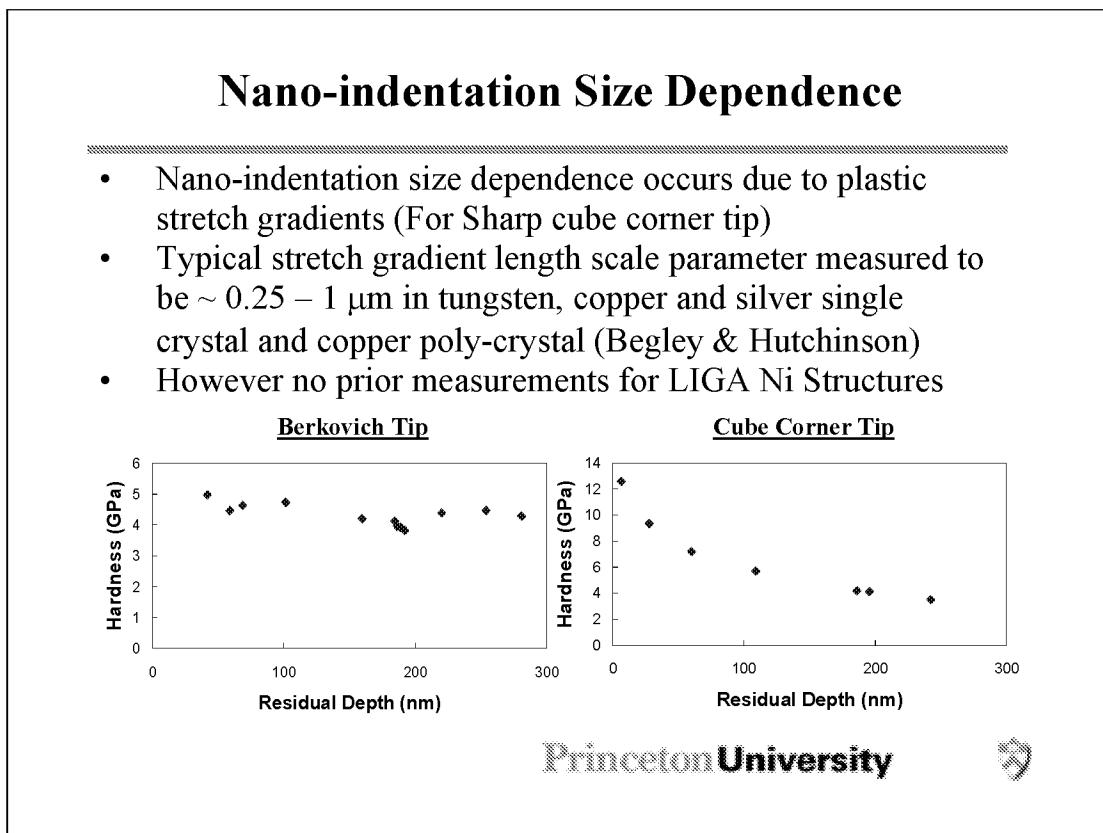


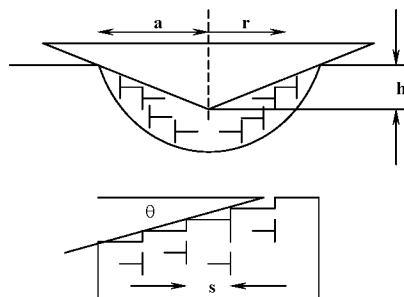
Figure 32

MSG THEORY OF PLASTICITY LENGTH SCALE

The mechanism-based strain gradient (MSG) theory is described qualitatively. The circular dislocation loops formed under the indenter are described. These are assumed to be circular loops of geometrically necessary dislocation.

MSG Theory of Plasticity Length Scale

- A modeling approach based on the geometrically necessary dislocations
- Assumption has been made that the indentation made by rigid cone is accommodated by circular loops of geometrically necessary dislocations



Princeton University



Figure 33

MSG THEORY OF PLASTICITY LENGTH SCALE (CONT.)

The Taylor's relation for the shear stress is written in terms of the separate contributions from geometrically necessary and statistically stored dislocations. Tabor's relation and the Von Mises yield condition are also used to obtain an expression for the hardness.

MSG Theory of Plasticity Length Scale (Cont.)

- Taylor's relation can be rewrite as following:

$$\tau = \alpha\mu b\sqrt{\rho_G + \rho_s} = \alpha\mu b\sqrt{\rho_s}\sqrt{1 + \frac{\rho_G}{\rho_s}}$$

where α is a constant to be taken as $\sim 1/3$ for FCC metal, μ is the shear modulus and ρ_s is the density of the statistically stored dislocations and ρ_G is the density of the geometrically necessary dislocations

- From Taylor's Relation, apply Von Mises yielding condition of $\sigma = \sqrt{3}\tau$ and take Tabor's factor to be 3, we can have:

$$H = 3\sigma = 3\sqrt{3}\alpha\mu b\sqrt{\rho_s}\sqrt{1 + \frac{\rho_G}{\rho_s}} = H_0\sqrt{1 + \frac{\rho_G}{\rho_s}}$$

Where $H_0 = 3\sqrt{3}\alpha\mu b\sqrt{\rho_s}$

Princeton University



Figure 34

MSG THEORY OF PLASTICITY LENGTH SCALE (CONT.)

The density of geometrically necessary dislocations is estimated by considering the overall length of GND loops that are induced in a hemispherical volume defined by the contact radius. An estimate of the density of statistically stored dislocations is also obtained from the plateau hardness, H_0 .

MSG Theory of Plasticity Length Scale (Cont.)

- The overall length of the geometric necessary dislocation loops induced by the indenter as modeled can be estimated by:

$$\lambda = \int_0^a 2\pi r \cdot \frac{dr}{s} = \frac{\pi h a}{b}$$

where $s = ba/h$ is the spacing between the loops of the GND

- Assume all of the injected GND loops remain within the hemispherical volume V defined by the contact radius, a :

$$V = \frac{2}{3} \pi a^3$$

- So, the density of geometrically necessary dislocations becomes:

$$\rho_G = \frac{\lambda}{V} = \frac{3h}{2ba^2} = \frac{3}{2bh} \tan^2 \theta$$

- Meanwhile, from the definition of H_0 , we can have:

$$\rho_s = \frac{H_0^2}{27\alpha^2 \mu^2 b^2}$$

Princeton University



Figure 35

MSG THEORY OF PLASTICITY LENGTH SCALE

The ratio of the hardness is shown to be related to the ratio, h/h^* , where h is the indentation depth and h^* is a characteristic length scale. The ratio of hardnesses is equivalent to the ratio of the yield strengths.

MSG Theory of Plasticity Length Scale (Cond.)

- Thus, a simple characteristic form for the depth dependence of the hardness can be obtained as:

$$\frac{H}{H_0} = \sqrt{1 + \frac{h^*}{h}}$$

where H is the hardness for a given depth of indentation, h ; H_0 is the hardness in the limit of infinite depth and h^* is a characteristic length scale which has the form as following:

$$h^* = \frac{81}{2} b \alpha^2 \tan^2 \theta \left(\frac{\mu}{H_0} \right)^2$$

- Alternatively, this form can be rewritten as:

$$\frac{\sigma}{\sigma_0} = \sqrt{1 + \frac{h^*}{h}}$$

Princeton University



Figure 36

PLASTICITY LENGTH SCALE ANALYZED USING CUBE CORNER INDENTER TIP DATA

A normalized plot of $(H/H_0)^2$ versus $1/h$ is presented for the cube-corner hardness values. This exhibits a linear relationship expected from the theory. Also, the values of h^* and H_0 extracted from the plots of experimental data compare very well with theoretical predictions.

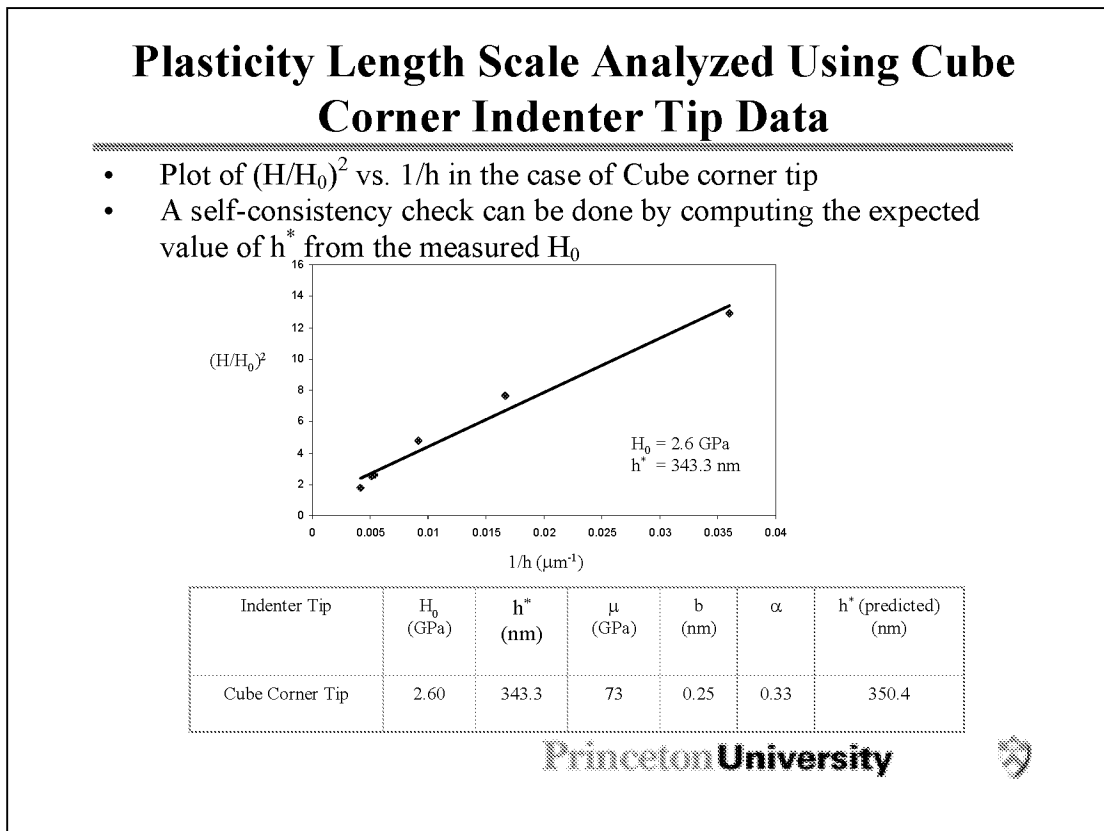


Figure 37

DETAIL OF THE PARAMETER USED IN MSG THEORY OF PLASTICITY LENGTH SCALE

A framework for the estimation of strain gradients is presented. The stress ratio expression presented earlier is also reformulated in terms of strain gradient.

Detail of the Parameter Used in MSG Theory of Plasticity Length Scale

- From geometrical consideration in the modeling, defining the strain gradient as:

$$\chi = \frac{\tan \theta}{a}$$

- Then we can rewrite the formulation in terms of strain gradient defined above:

$$\left(\frac{\sigma}{\sigma_0}\right)^2 = 1 + \frac{1}{2}b\left(\frac{\mu}{\sigma_0}\right)^2 \chi$$

where σ is the effective flow stress in the presence of strain gradient and σ_0 is the flow stress in the absence of strain gradient

Princeton University



Figure 38

DETERMINATION OF STRETCH GRADIENT LENGTH SCALE PARAMETER

An expression for the microstructural length scale parameter is presented. This has a value of $\hat{l} = 0.89 \mu\text{m}$ for LIGA Ni films. From this, the Fleck-Hutchinson stretch gradient parameter, l_{SG} is estimated to be $0.36 \mu\text{m}$.

Determination of Stretch Gradient Length Scale Parameter

- Can identify the microstructural length scale parameter as:

$$\hat{l} = \frac{1}{2}b \left(\frac{\mu}{\sigma_0} \right)^2$$

- For LIGA Ni MEMS films, the resulting value is $\hat{l} = 0.89 \mu\text{m}$
- The extracted microstructural length scale parameter is actually related to the material length scale parameter as:

$$l \approx \hat{l} \left(\frac{\sigma_0}{\sigma_{ref}} \right)^2$$

which can be approximately considered as the stretch gradient parameter since the stretch gradient plays a dominant role in the indentation experiment

$$l_{SG} = 0.36 \mu\text{m}$$

Princeton University



Figure 39

DISLOCATION PILE-UP AT SMALL SCALES

Dislocation pile-up phenomena are shown to occur around the indents obtained at small scales. These suggest a need for discrete dislocation models. The challenge is really how to interface the discrete dislocation models with anisotropic length-scale plasticity theories.

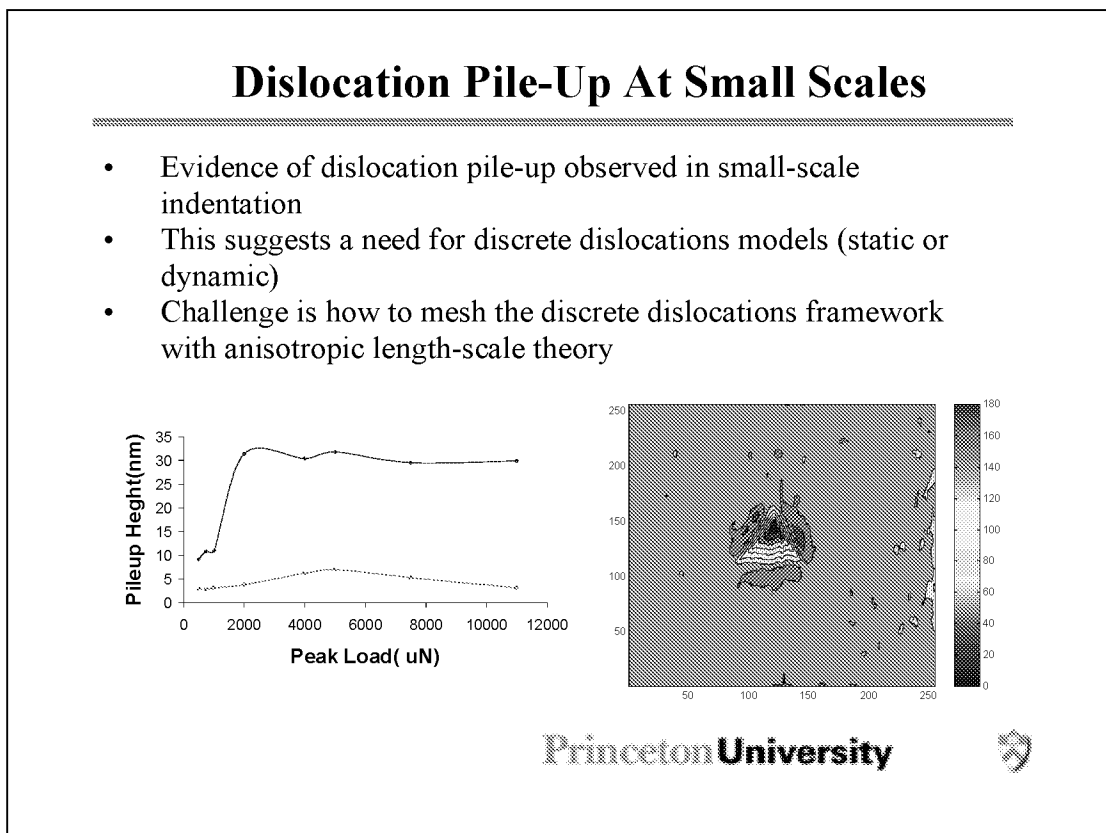


Figure 40

DETERMINATION OF ROTATIONAL GRADIENT LENGTH SCALE PARAMETER

The separate length-scale parameters are identified for LIGA Ni MEMS structures examined in this study. These give $l_c = 5.6 \mu\text{m}$, $l_{SG} = 0.36 \mu\text{m}$ and $l_{RG} = 5.58 \mu\text{m}$. These are incorporated into an extended J_2 expression for constitutive modeling of plasticity.

Determination of Rotational Gradient Length Scale Parameter

- The micro-bend experiments provide a measure of the composite strain gradient length scale parameter l_c which is given by:

$$l_c = \sqrt{l_{RG}^2 + \left(\frac{8}{5}\right)l_{SG}^2}$$

- In current study, $l_c \sim 5.6 \mu\text{m}$ in LIGA Ni MEMS structures and l_{SG} is estimated from nano-indentation study to be $\sim 0.36 \mu\text{m}$
- The rotational gradient parameter can be estimated to be $\sim 5.58 \mu\text{m}$
- These values can be incorporated into the extended J_2 theory and used for the constitutive modeling of plasticity in Ni MEMS structures plated under the similar conditions:

$$\varepsilon = \left(\left(\frac{2}{3} \varepsilon'_{ij} \varepsilon'_{ij} \right) + \left(0.36^2 \times \eta'_{ijk} \eta'_{ijk} \right) + \left(\frac{2}{3} \times 5.58^2 \chi_{ij} \chi_{ij} \right) \right)^{1/2}$$

Princeton University



Figure 41

SUMMARY AND CONCLUDING REMARKS

A summary of the microstructure, mechanical properties and observed size effects is presented. No significant size effect was observed in tension. However, significant size effects were observed in the nano-indentation and micro-bend experiments.

Summary and Concluding Remarks

- Microstructure and mechanical properties investigated in LIGA Nickel MEMS structures
- As-received structures have nano-scale grain sizes ($d \sim 50 - 80$ nm) and primarily [001] micro-texture
- No significant size effect observed under micro-tension
- Significant size effects observed under micro-bending and nano-indentation experiments (In the case of sharp cube corner tip)
- Conventional continuum plasticity theory without a length scale parameter can not explain the size dependence effect observed in the experiment

Princeton University



Figure 42

SUMMARY AND CONCLUDING REMARKS (CONT.)

A summary of the results from the mechanism-based SGP and phenomenological SGP theories is presented along with the measured length scale parameters. The constitutive expression obtained for LIGA Ni is also presented.

Summary and Concluding Remarks (Cont.)

- Both phenomenological and mechanism-based strain gradient plasticity theory were explored in the current study
- Composite length-scale parameter, l_c , of $\sim 5.6 \mu\text{m}$ established for as-plated LIGA Ni from experiments
- The stretch gradient parameter, l_{SG} is estimated to be $\sim 0.36 \mu\text{m}$ while the rotational gradient parameter, l_{RG} , for the LIGA Ni films in current study is determined to be $\sim 5.58 \mu\text{m}$
- and constitutive expressions obtained for LIGA Ni:

$$\varepsilon = \left(\left(\frac{2}{3} \varepsilon'_{ij} \varepsilon'_{ij} \right) + \left(0.36^2 \times \eta'_{ijk} \eta'_{ijk} \right) + \left(\frac{2}{3} \times 5.58^2 \chi_{ij} \chi_{ij} \right) \right)^{1/2}$$

Princeton University



Figure 43

SUMMARY AND CONCLUDING REMARKS (CONT.)

The current results are discussed within the context of a multi-scale modeling framework for the modeling of plastic deformation at the micron- and sub-micron scales. The need for anisotropic extensions to the isotropic length scale theories is also highlighted.

Summary and Concluding Remarks (Cont.)

- A framework is presented for the multi-scale modeling of plastic deformation at the micron and sub-micron scales
- Plasticity length-scale parameters are proposed for the modeling of size effects at the micron-scale
- Anisotropic extensions of the existing isotropic theory are needed
- The plasticity length scale approach may be used to model size effects down into the sub-micron regime

Princeton **University**



Figure 44

REPORT DOCUMENTATION PAGE			Form Approved OMB No. 0704-0188	
Public reporting burden for this collection of information is estimated to average 1 hour per response, including the time for reviewing instructions, searching existing data sources, gathering and maintaining the data needed, and completing and reviewing the collection of information. Send comments regarding this burden estimate or any other aspect of this collection of information, including suggestions for reducing this burden, to Washington Headquarters Services, Directorate for Information Operations and Reports, 1215 Jefferson Davis Highway, Suite 1204, Arlington, VA 22202-4302, and to the Office of Management and Budget, Paperwork Reduction Project (0704-0188), Washington, DC 20503.				
1. AGENCY USE ONLY (Leave blank)		2. REPORT DATE July 2002	3. REPORT TYPE AND DATES COVERED Conference Publication	
4. TITLE AND SUBTITLE Multiscale Modeling, Simulation and Visualization and Their Potential for Future Aerospace Systems			5. FUNDING NUMBERS 706-63-51-30	
6. AUTHOR(S) Ahmed K. Noor, Compiler				
7. PERFORMING ORGANIZATION NAME(S) AND ADDRESS(ES) NASA Langley Research Center Hampton, VA 23681-2199			8. PERFORMING ORGANIZATION REPORT NUMBER L-18216	
9. SPONSORING/MONITORING AGENCY NAME(S) AND ADDRESS(ES) National Aeronautics and Space Administration Washington, DC 20546-0001			10. SPONSORING/MONITORING AGENCY REPORT NUMBER NASA/CP-2002-211741	
11. SUPPLEMENTARY NOTES Noor: Old Dominion University, Center for Advanced Engineering Environments				
12a. DISTRIBUTION/AVAILABILITY STATEMENT Unclassified-Unlimited Subject Category 38 Distribution: Standard Availability: NASA CASI (301) 621-0390			12b. DISTRIBUTION CODE	
13. ABSTRACT (Maximum 200 words) This document contains the proceedings of the Training Workshop on Multiscale Modeling, Simulation and Visualization and Their Potential for Future Aerospace Systems held at NASA Langley Research Center, Hampton, Virginia, March 5 - 6, 2002. The workshop was jointly sponsored by Old Dominion University's Center for Advanced Engineering Environments and NASA. Workshop attendees were from NASA, other government agencies, industry, and universities. The objectives of the workshop were to give overviews of the diverse activities in hierarchical approach to material modeling from continuum to atomistics; applications of multiscale modeling to advanced and improved material synthesis; defects, dislocations, and material deformation; fracture and friction; thin-film growth; characterization at nano and micro scales; and, verification and validation of numerical simulations, and to identify their potential for future aerospace systems.				
14. SUBJECT TERMS hierarchical approaches; material modeling; atomistics; multiscale modeling; material synthesis; nano and micro scales			15. NUMBER OF PAGES 453	
			16. PRICE CODE	
17. SECURITY CLASSIFICATION OF REPORT Unclassified	18. SECURITY CLASSIFICATION OF THIS PAGE Unclassified	19. SECURITY CLASSIFICATION OF ABSTRACT Unclassified	20. LIMITATION OF ABSTRACT UL	